Regulation and function of innate-like T cells



Joachim Paul Hagel

Keble College, University of Oxford

Thesis submitted for the degree of

Doctor of Philosophy in Clinical Medicine

University of Oxford, Michaelmas Term 2021

Supervisors:

Prof. Paul Klenerman, MRCP, FRCP, DPhil

Prof. Francesca Buffa, DPhil

Dr. Christian Willberg, DPhil

Regulation and function of innate-like T cells

Joachim Hagel, Keble College

Submitted for DPhil in Clinical Medicine, Michaelmas Term 2021

Abstract

KLRB1, encoding for CD161, is one of the most favourable prognostic pan-cancer genes. It is expressed by NK- and T-cell subsets, particularly by innate-like T cells such as MAIT and γδT cells. CD161-expressing T-cell subsets share a transcriptional and functional phenotype, including the ability to be activated by cytokines in a T-cell receptor-independent manner, similar to NK cells. The regulation and function of CD161-expressing cells as well as their role in cancer is not fully understood, however. In this study, an imaging-based high-content cytometry method, called ChipCytometry, was developed as a truly viable technique to identify and deeply phenotype CD161-positive cell types in blood and tissue. Novel mechanisms for the activation of CD161-expressing T cells were discovered by stimulation with the relatively underexplored cytokine IL-32. The ability of CD161-expressing T cells to also express IL-32 upon activation was demonstrated *in vitro*. To elucidate the role of IL-32 in disease, a pan-cancer *IL32* gene signature was generated from The Cancer Genome Atlas (TCGA) RNA-seq data. The *IL32* signature genes were associated with immune response- and T-cell activation-related pathways. Single-cell RNA-seq data from breast cancer-derived immune cells showed that *IL32* gene expression and the expression of the most significant *IL32* signature genes were strongly associated with innate-like T cells, including MAIT and γδT cells, in addition to memory T cells and Tregs. Finally, estimated immune cell fractions within TCGA data revealed that the favourable prognostic association of CD161 across cancers was attributable to multiple CD161-expressing cell types. These include NK cells, γδT cells, tissue-resident memory T cells, cytotoxic T cells and the still poorly studied T follicular helper cells in cancer. In summary, the findings of this study expand the knowledge of the regulation and function of CD161-expressing immune subsets and their role in cancer, setting the stage for their use as a clinical biomarker or in cancer immunotherapy.

Acknowledgements

First and foremost, I would like to express my sincere thanks to my DPhil supervisors Prof. Paul Klenerman, Prof. Francesca Buffa and Dr. Christian Willberg for their support and guidance throughout my DPhil studies, and for always being so generous and open minded. I am grateful that I was given the opportunity to work together with you. I cannot imagine better supervisors.

Many thanks to the Nuffield Department of Medicine, the Wellcome Trust and the COVID 19 Scholarship Extensions Fund for their generous funding, which enabled me to complete this research.

I would also like to thank all lab members of the Klenerman and Buffa labs to make my DPhil studies such a great experience. In particular, I would like to thank Kate for her contribution to the tonsil project, Alessandro for providing RENOIR and his advice along the IL 32 cancer project, Manu and Ayako for their advice in various bioinformatics matters, Kyle and Jai for their contributions to the tonsil and IL 32 in vitro studies, respectively, and Hema for providing fixed E. coli. Thank you, Matt E., Prabh, Ava, Ali and Clara for proofreading a chapter of my thesis each. Thank you, Andrew, Madeleine, Lucy, Tianqi, Lian, Philipp, Chan, Hossain, Narayan, Cathy, Claire, Nick, Ray, Jonathan, Tamsin, Ryan, Bill, Ana, Avigail, Badran, Ben, Charalampos, Dawn, Fiona, Giovanna, Helen, Jagat, Jayathilake, Karen, Matteo, May, Pedro, Philip, Ryan and Wei Chen for your help in various ways.

Lastly, I would like to thank my family and friends for their continued support throughout my DPhil studies.

TABLE OF CONTENTS

THESIS CONTRIBUTIONS **7**

ABBREVATIONS **8**

1. GENERAL INTRODUCTION **11**
1.1. Innate and adaptive immunity **11**
1.2. T cells **12**
1.2.1. T-cell development 12
1.2.2. Conventional T-cell subsets 13
1.3. NK cells and other ILCs **15**
1.4. Innate-like T cells share features of NK and conventional T cells **16**
1.4.1. Characteristics of innate-like T cells 16
1.4.2. MAIT cells 17
1.4.3. γδT cells 18
1.4.4. iNKT cells 18
1.4.5. Cytokines in innate-like T-cell regulation and function 19
1.5. Anti-cancer immune response **19**
1.6. Methods for explorative immunophenotyping **21**
1.7. Aims and objectives of thesis **23**

2. GENERAL MATERIALS AND METHODS **24**
2.1. Media and buffers **24**
2.2. Cells **24**
2.2.1. Blood samples 24
2.2.2. Isolation of PCMBs 24
2.2.3. $CD3^+$ or $CD8^+$ T cell isolation 24
2.2.4. Depletion of $CD14^+$ and $CD19^+$ cells 25
2.3. Cell culture **25**
2.3.1. Cytokine stimulation 25
2.3.2. Anti-CD3/anti-CD28 stimulation 25
2.3.3. *S*timulation of MAIT cells using *E. coli* 26
2.4. Flow cytometry **27**
2.4.1. Surface staining 27
2.4.2. Intracellular staining 28
2.4.3. Data acquisition and analysis 29
2.5. ChipCytometry of cell suspensions **31**
2.6. Bioinformatic methods **32**
2.6.1. ssGSEA analysis 32
2.6.2. Survival analysis 33
2.7. Software and statistical data analysis **33**
2.7.1. Statistical analysis 33
2.7.2. Software and R packages 33

3. DEVELOPMENT OF CHIPCYTOMETRY AS A VIABLE TECHNIQUE FOR HIGH-CONTENT IMMUNOPHENOTYPING **36**
3.1. Introduction **36**
3.2. Aims **39**
3.3. Chapter-specific materials and methods **39**
3.3.1. ChipCytometry 39
3.4. Results **40**
3.4.1. Gradually increasing sample autofluorescence in the BV421 channel 40

3.4.2. Appearance of a fluorescent haze during acquisition of stained samples 42
3.4.3. Recurrent blockages of the fluidic system 42
3.4.4. Repeated photobleaching rendered samples unstainable 44
3.4.5. Inconsistent staining intensity across stained chips (x-direction) 48
3.4.6. Inconsistent staining intensity across stained chips (y-direction) 50
3.4.7. Fluorescence anomalies affecting ChipCytometry data 51
3.4.8. Antibody filtration with cellulose acetate filters causing granular background signals 54
3.4.9. Sample multiplexing using fluorescent barcodes to increase sample throughput 54
3.4.10. Excess of staining antibody causing poor distinction between positive and negative cells 56
3.4.11. Comparison of ChipCytometry with flow cytometry 57
3.5. Discussion 58
3.6. Summary 64

4. DEFINING T-CELL SUBSETS IN HUMAN TONSILS USING CHIPCYTOMETRY (PROOF-OF-PRINCIPLE) 66
4.1. Introduction 66
4.2. Aims 69
4.3. Chapter-specific materials and methods 69
4.3.1. Tissues and cells 69
4.3.2. ChipCytometry of cell suspensions 69
4.3.3. ChipCytometry of tissue sections 70
4.3.4. Data processing and statistical methods 72
4.3.5. Image processing 73
4.4. Results 73
4.4.1. Defining tonsillar architecture in humans using tissue ChipCytometry 73
4.4.2. Identification of CD4 T-cell subsets in human tonsils 74
4.4.3. Identification and phenotyping of tonsillar CD3 T-cell subsets by cell suspension ChipCytometry 75
4.4.4. Identifying rarer T-cell subsets in tonsils by tissue ChipCytometry including MAIT cells and γδT cells 78
4.4.5. Identification and phenotyping of human tonsillar MAIT cells by cell suspension ChipCytometry 80
4.5. Discussion 82
4.6. Summary 86

5. IDENTIFICATION AND PHENOTYPING OF CD161-EXPRESSING CELL TYPES IN BLOOD 88
5.1. Introduction 88
5.2. Aims 90
5.3. Chapter-specific materials and methods 90
5.3.1. Blood samples 90
5.3.2. IL-12+IL-18 stimulation 91
5.3.3. ChipCytometry 91
5.3.4. Data transformation 93
5.3.5. Identification and removal of fluorescence anomalies and rescaling of data .93
5.3.6. Pre-processing of data 94
5.3.7. Batch correction 95
5.3.8. Unsupervised clustering and dimensionality reduction 95
5.3.9. Marker Enrichment Modeling (MEM), cluster labelling and cluster matching .96
5.3.10. Differential marker expression analysis 96
5.3.11. Principal component analysis (PCA) 96
5.3.12. PubMed Central trend 97

5.4. Results 97
5.4.1. Experimental design 97
5.4.2. ChipCytometry data transformation 97
5.4.3. Identification of fluorescence anomalies with the help of computationally generated warnings 99
5.4.4. Identification and removal of any remaining extreme values by visual inspection and rescaling of data 104
5.4.5. Pre-processing of data 108
5.4.6. Batch correction of ChipCytometry data 109
5.4.7. Unsupervised clustering of ChipCytometry data 118
5.4.8. Cluster matching and cluster characterisation 120
5.4.9. Clustering of the IL-12+IL-18-stimulated condition and comparison to clusters from the unstimulated condition 127
5.4.10. Statistical analysis of differences between unstimulated and IL-12+IL-18-stimulated cells within clusters identified by FlowSOM 130
5.4.11. ChipCytometry data analysis using traditional manual gating 136
5.4.12. Phenotype of cell populations that were identified by manual gating 139
5.4.13. Comparison of unstimulated and IL-12+IL-18-stimulated immune subsets that were identified by manual gating 142
5.5. Discussion 149
5.5.1. Development of an analysis protocol for cell suspension ChipCytometry data 149
5.5.2. Identification of cell types within CD14-/CD19-depleted PBMCs and their response to IIL-12+IL-18 stimulation 159
5.6. Summary 164

6. ROLE OF IL-32 IN INNATE-LIKE T-CELL ACTIVATION 166
6.1. Introduction 166
6.1.1. IL-32 is a novel pluripotent cytokine 166
6.1.2. IL-32 is expressed by non-immune and immune cells 166
6.1.3. Effects of IL-32 on non-immune and immune cells 168
6.1.4. The role of IL-32 in cancer 169
6.2. Aims 172
6.3. Chapter-specific materials and methods 174
6.3.1. IL-32 ELISA 174
6.3.2. TCGA samples and clinical information 174
6.3.3. Generation of an *IL32* gene signature 175
6.3.4. Pathway analysis 176
6.3.5. scRNA-seq data analysis 176
6.4. Results 177
6.4.1. IL-12-, IL-18- and IL-15-induced IL-32 expression in T cells within PBMCs 177
6.4.2. IL-12-, IL-18- and IL-15-induced IL-32 expression in enriched T cells 181
6.4.3. Common γ-chain cytokine-induced IL-32 expression in T cells 185
6.4.4. Comparison of IL-32 expression in memory T and MAIT cells 186
6.4.5. E. coli- and TCR-induced IL-32 expression in T cells 187
6.4.6. Regulation and modulation of cytokine-mediated responses of CD161-expressing T cells by IL-32 190
6.4.7. Generation of a pan-cancer *IL32* gene signature 195
6.4.8. Pathway analysis of *IL32* signature genes 207
6.4.9. *IL32* expression and *IL32* signature enrichment in immune subsets from breast cancer tissue 210
6.4.10. Association of *IL32* gene expression with cancer patient survival 215
6.5. Discussion 216
6.5.1. IL-32 expression by activated T cells 216

6.5.2. IL-32 can increase cytokine-mediated responses of CD161-expressing T cells 219
6.5.3. The role of IL-32 in the anti-cancer immune response 221
6.5.4. The association of IL-32 with patient survival 223
6.5.5. Relevance of the findings of this study 224
6.6. Summary 225

7. ROLE OF CD161 IN CANCER 227
7.1. Introduction 227
7.1.1. *KLRB1* is one of the most favourable prognostic pan-cancer genes 227
7.1.2. The role of CD161-expressing immune cell types in cancer 227
7.2. Aims 235
7.3. Chapter-specific materials and methods 235
7.3.1. Data used in this study 235
7.4. Results 236
7.4.1. Identification of *KLRB1*-expressing cell types 236
7.4.2. The association of *KLRB1* expression and immune cell types that can express *KLRB1* with cancer patient survival 239
7.4.3. The association of TRM cells with cancer patient survival 243
7.4.4. Association between *KLRB1*, ImmuCellAI immune subsets and FitzPatrick TRM1 signature 245
7.5. Discussion 246
7.6. Summary 252

8. DISCUSSION 254
8.1. ChipCytometry 254
8.1.1. Key findings 254
8.1.2. Strengths and challenges of ChipCytometry 255
8.1.3. Future work 258
8.2. Expression and function of IL-32 258
8.2.1. Key findings and their relevance 258
8.2.2. Future work 262
8.3. The role of CD161 in cancer 262
8.3.1. Key findings and their relevance 262
8.3.2. Future work 265
8.4. Major limitations 266
8.5. Summary and conclusion 267

APPENDICES 271

REFERENCES 344

LIST OF PUBLICATIONS 372

THESIS CONTRIBUTIONS

Chapter 3

Christian Willberg

Helped to design adapters for the microfluidic system of the ChipCytometer.

3D Printing Service, Radcliffe Science Library, University of Oxford

3D-printed the tray of the final adapter for the microfluidic system of the ChipCytometer.

Kate Powell and Kyle Bennet

Optimised antibody concentrations for ChipCytometry tissue section staining.

Chapter 4

Kate Powell

Processed tonsil tissue sections, performed staining of tonsil tissue sections using ChipCytometry, processed ChipCytometry images from tonsil tissue sections.

Kyle Bennett

Performed ChipCytometry staining of tonsil-derived CD3-enriched T cells.

Chapter 6

Jai Bolton

Experiments from Figure 6-4b-e, Figure 6-5a-e, Figure 6-7c, Appendix Figure IV-2, Appendix Figure IV-4b and Appendix Figure IV-8 were performed with the help from Jai Bolton.

Hema Mehta

Prepared and kindly provided PFA-fixed *E. coli.*

Francesca Buffa and Alessandro Barberis

Developed the unpublished R package RENOIR (REsampliNg methOds for machIne learning). RENOIR R package was kindly provided for the generation of an *IL32* gene signature.

ABBREVATIONS

1SE	1 standard error
ACC	Adrenocortical carcinoma
APC	Antigen presenting cell
BG image	Background image
BLCA	Bladder Urothelial Carcinoma
BRCA	Breast invasive carcinoma
CCR	C-C chemokine receptor
CD	Cluster of differentiation
CDF	Cumulative distribution function
CESC	Cervical squamous cell carcinoma and endocervical adenocarcinoma
CFU	Colony-forming unit
CHOL	Cholangiocarcinoma
CITE-Seq	Cellular Indexing of Transcriptomes and Epitopes by Sequencing
COAD	Colon adenocarcinoma
CODEX	CO-Detection by indEXing
CXCR	C-X-C chemokine receptor
D	Diversity TCR segment
DC	Dendritic cell
DLBC	Lymphoid Neoplasm Diffuse Large B-cell Lymphoma
DN	Double negative
DNA	Deoxyribonucleic acid
DP	Double positive
ESCA	Oesophageal carcinoma
FL image	Fluorescence image
FMO control	Fluorescence minus one control
GBM	Glioblastoma multiforme
GDAC	Genome Data Analysis Center
GDC	Genomic Data Commons
gMFI	Geometric mean fluorescence intensity
GO	Gene Ontology
GzmA	Granzyme A
GzmB	Granzyme B
GzmK	Granzyme K
HNSC	Head and Neck squamous cell carcinoma
HR	Hazard ratio
IFN	Interferon
IL	Interleukin
ILC	Innate lymphoid cell

iNKT cell	Invariant natural killer T cell
IQR	Interquartile range
iTreg	Induced T regulatory cell
J	Joining TCR segment
KEGG	Kyoto Encyclopedia of Genes and Genomes
KICH	Kidney Chromophobe
KIRC	Kidney renal clear cell carcinoma
KIRP	Kidney renal papillary cell carcinoma
LAML	Acute Myeloid Leukaemia
LGG	Brain Lower Grade Glioma
LIHC	Liver hepatocellular carcinoma
logFC	Log-fold change
LTi cell	Lymphoid tissue inducer cell
LUAD	Lung adenocarcinoma
LUSC	Lung squamous cell carcinoma
MAIT cell	Mucosal associated invariant T cell
MEM	Marker enrichment modeling
MESO	Mesothelioma
MHC	Major histocompatibility complex
min	Minimised
MR1	Major histocompatibility complex class Ib-related protein
NA	Not available (missing value)
NCI	National Cancer Institute
NK cell	Natural killer cell
NKT cell	Natural killer T cell
nTreg	Natural T regulatory cell
OV	Ovarian serous cystadenocarcinoma
PAAD	Pancreatic adenocarcinoma
PBMC	Peripheral blood mononuclear cell
PBS	Phosphate-buffered saline
PC	Principal component
PCA	Principal component analysis
PCPG	Pheochromocytoma and Paraganglioma
PFA	Paraformaldehyde
pfp	Percentage of false positives
PRAD	Prostate adenocarcinoma
PRECOG	PREdiction of Clinical Outcomes from Genomic Profiles
PRR	Pattern recognition receptor
Q	Quartile
READ	Rectum adenocarcinoma
REAP-seq	RNA expression and protein sequencing
RENOIR	REsampliNg methOds for machIne learning

RMSD	Root-mean-square distance
RNA	Ribonucleic acid
RNA-seq	RNA sequencing
RT	Room temperature
SARC	Sarcoma
scRNA-seq	Single-cell RNA sequencing
SD	Standard deviation
SEM	Standard error of the mean
SKCM	Skin Cutaneous Melanoma
SOM	Self-organising map
SP	Single positive
ssGSEA	Single-sample gene set enrichment analysis
STAD	Stomach adenocarcinoma
TC cell	Cytotoxic T cell
TCGA	The Cancer Genome Atlas
TCGA-CDR	The Cancer Genome Atlas Clinical Data Resource
TCM cell	T central memory cell
TCR	T cell receptor
TEM cell	T effector memory cell
TEMRA cell	T effector memory CD45RA+ cell
Tex	Exhausted T cell
TFH cell	T follicular helper cell
TGCT	Testicular Germ Cell Tumours
TH cell	T helper cell
THCA	Thyroid carcinoma
THYM	Thymoma
TL image	Transmitted light image
Tr1 cell	T regulatory type 1 cell
Treg	T regulatory cell
Treg cell	T regulatory cell
TRM cell	Tissue-resident memory T cell
t-SNE	t-distributed stochastic neighbour embedding
UCEC	Uterine Corpus Endometrial Carcinoma
UCS	Uterine Carcinosarcoma
UMAP	Uniform Manifold Approximation and Projection
UVM	Uveal Melanoma
V	Variable TCR segment

1. GENERAL INTRODUCTION

1.1. Innate and adaptive immunity

The immune system protects the host from pathogens, eliminates allergenic and toxic substances, and removes abnormal cells to prevent the development of cancer (1, 2). In addition, the immune system plays an important role in regeneration and tissue repair (3). Discrimination between self and nonself is crucial, however, to avoid that the multitude of immune effector mechanisms unleash against the tissues of the host (1).

The immune system is composed of two major arms, the innate and the adaptive immune system. Cellular components of the innate immune system include neutrophils, basophils, eosinophils, mast cells, dendritic cells (DCs), macrophages and innate lymphoid cells (ILCs), such as natural killer (NK) cells (1, 4). Innate immune cells express germline-encoded invariant receptors for the discrimination between self and nonself. For example, pattern recognition receptors (PRRs) recognise conserved molecular structures on pathogens, termed pathogen-associated molecular patterns (5, 6). Other receptors, particularly expressed by NK cells, can recognise stress signals from infected and transformed cells (7, 8). Innate immune responses can be mobilised very rapidly and provide the first line of defence through mechanisms such as phagocytosis, expression of antimicrobial peptides and direct cytotoxicity by NK cells. In addition, innate immune cells process and present antigens on MHC (major histocompatibility complex) molecules and produce pro-inflammatory cytokines and chemokines, which can recruit and activate cells of the adaptive immune system (4, 9).

The cells of the adaptive immune system, including B and T lymphocytes, express highly diverse receptors, generated through somatic recombination of receptor gene elements, which allow the recognition of foreign substances. An individual lymphocyte expresses a single type of receptor specific for a distinct antigenic determinant. Upon recognition of its

specific antigen, a B or T cell becomes activated and undergoes clonal expansion and differentiation, resulting in a large number of identical effector cells (10–13). B and T cells provide protection by the production of antibodies (B cells), cytotoxicity (T cells) and the release of cytokines (both). Further hallmarks of the adaptive immunity include a slower onset of responses compared to innate immune responses, education in form of deletion of self-reactive clones, and the formation of memory cells, which provide long-lasting protection for re-encounters with a pathogen (13–16).

The dichotomy between the innate and adaptive immune system is bridged by the existence of innate-like T cells, which possess both features of innate and adaptive immune cells (17, 18).

1.2. T cells

1.2.1. T-cell development

T cells originate in the bone marrow and then migrate into the thymus where they further develop. An extremely diverse repertoire of T cells bearing different T-cell receptors (TCRs) is formed during T-cell development by the process of somatic recombination of variable (V), diversity (D) and joining (J) TCR gene segments. There are 4 loci encoding for different TCR chains, including α, β, γ, δ. Depending on the successful rearrangement, T cells bearing either an αβTCR or γδTCR can be generated (12, 19–22).

Upon egress from the thymus, freshly generated conventional αβT cells remain naive until they encounter their cognate antigen presented by MHC molecules on antigen presenting cells (APCs) in secondary lymphoid organs. Besides TCR recognition of the antigen in context of MHC molecules, conventional T cells require two other signals for antigen-specific activation, including costimulatory signals mediated via the engagement of CD28 with ligands expressed by activated APCs and polarising signals consisting of APC-derived cytokines.

T-cell activation induces clonal expansion, differentiation of T cells in highly specialised subsets and acquisition of effector functions (9, 23–25). Arising clones develop into short-lived effector or long-lived memory cells (26, 27). Based on the expression of CCR7 in combination with CD45RA or CD45RO, different memory T-cell subsets can be defined representing different differentiation stages. This includes $CCR7^{+}CD45RA^{-}CD45RO^{+}$ central memory T cells (TCM), $CCR7^{-}CD45RA^{-}CD45RO^{+}$ effector memory T cells (TEM) and $CCR7^{-}CD45RA^{+}CD45RO^{-}$ terminally differentiated RA-positive effector memory T cells (TEMRA). In contrast, naive T cells are $CCR7^{+}CD45RA^{+}CD45RO^{-}$. While differentiating from TCM to TEM, and finally to TEMRA, there is a decrease in lymphoid homing properties, proliferation and self-renewal potential, but an increase in peripheral homing capacity, effector function and antigen dependence (28).

In contrast to conventional αβT cells, unconventional T-cell subsets, such as γδT cells, can acquire their effector functions during thymic development (29), although it is suggested that some unconventional T-cell populations require cues from commensal microorganisms in the periphery for their development and homeostasis (30, 31).

1.2.2. Conventional T-cell subsets

Conventional αβT cells are characterised by the expression of CD4 and CD8 co-receptors, which bind the MHC molecules during TCR-MHC interaction. CD4 single positive (SP) and CD8 SP T cells, but also $CD4^{+}CD8^{+}$ double positive (DP) and $CD4^{-}CD8^{-}$ double negative (DN) T cells are observed in the periphery. However, DP and DN cells are relative rare compared to CD4 and CD8 T cells (32–35).

CD4 T cells, which recognise antigenic peptides in context of MHC class II molecules, are called T helper (TH) cells, because upon activation, they help to drive the adaptive immune responses of B cells and other T cells, such as CD8 T cells. Depending on the co-stimulatory signals that naive CD4 T cells receive during priming, they differentiate into different

specialised subsets, including TH1, TH2, TH17, T follicular helper (TFH) and T regulatory cells (Tregs). Figure 1-1 shows the polarising cytokines for the differentiation into each subset, the master transcription factors involved in determining the subset identity, and the surface markers expressed and effector cytokines secreted by each subset. TH1, TH2 and TH17 cells provide protection against different types of pathogens, including intracellular pathogens, extracellular parasites and extracellular bacteria and fungi, respectively. TFH cells provide help to B cells for the generation of antibodies and Tregs are crucial for maintaining self-tolerance and homeostasis (25, 36–40).

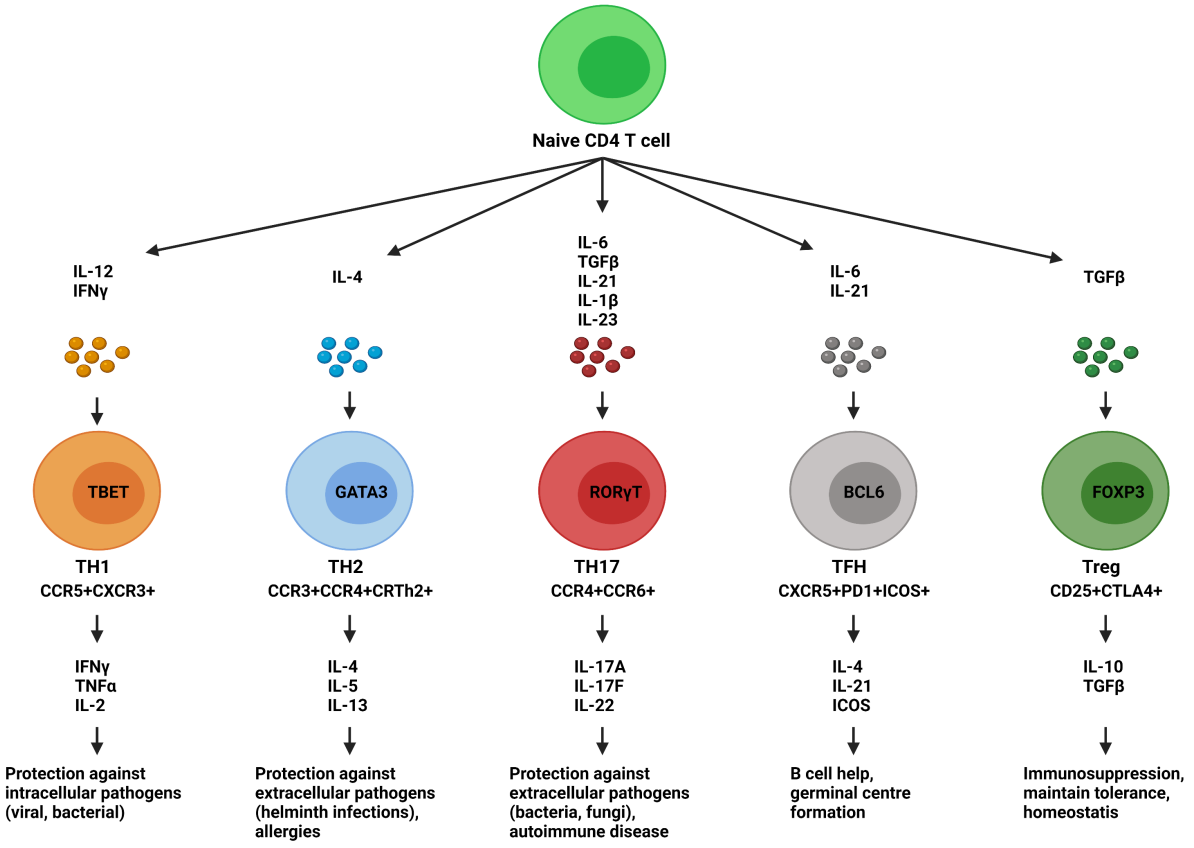


Figure 1-1. CD4 T-cell subsets. The illustration depicts polarising cytokines which instruct naive CD4 T cells during activation to differentiate into specialised CD4 T-cell subsets as indicated. The key transcription factors that determine the subset identity, subset-specific surface markers, effector cytokines and functions are shown (25, 36–40). This figure was created with BioRender.com.

CD8 T cells, which recognise antigenic peptides in context of MHC class I molecules, are called cytotoxic T cells (TC). Cytotoxic T cells kill infected or abnormal cells by the targeted

release of cytotoxic molecules, such as granzymes and perforin, which are stored in granules within the cells. They can also kill via the expression of ligands for death receptors, such as FASL and TRAIL. In addition, there are subsets of cytotoxic T cells that can express type 1, type 2 or type 17 effector cytokines and are termed TC1, TC2 and TC17 cells, respectively (41–43).

1.3. NK cells and other ILCs

NK cells are lymphocytes that express germline-encoded receptors that allow them to detect the lack of MHC class I molecule expression ("missing self") of virus-infected or cancerous cells and the expression of stress-induced self-ligands. In addition, NK cells can be alerted by PRR ligands and antibody-coated cells (44). Besides the activation via NK receptors, NK cells are responsive to cytokine stimulation, including IL-12, IL-18 and IL-15 (45–48). Some of the main effector functions of activated NK cells include target cell killing, for example, by the release of granzymes and perforin, and cytokine production, such as IFNγ (41, 48). IFNγ mediates a multitude of effects, including the upregulation of MHC expression, promotion of antigen presentation, activation of macrophages, promotion of TH1 responses, induction of antiviral mediators and inhibition of tumour cell proliferation (49). NK cells are characterised by the expression of CD56, which divides NK cells into two subsets according to its expression levels: $CD56^{dim}$ ($CD56^{+}$) and $CD56^{bright}$ ($CD56^{++}$) NK cells. The $CD56^{++}$ subset is considered an immature precursor of the finally differentiated $CD56^{+}$ subset (50–52). The majority of NK cells expresses the C-type lectin-like receptor CD161, whose ligation can inhibit NK-cell cytotoxicity (46, 53, 54). Cytokine responsiveness within NK cells correlates positively with CD56 and CD161 expression levels (46). The NK-cell phenotype includes expression of PLZF, EOMES, TBET, IL-18Rα, Granzyme A (GzmA), Granzyme B (GzmB), Granzyme K (GzmK), CD16 and CD57, although their expression levels can vary between $CD56^{+}$ and $CD56^{++}$ subsets as well as CD161-negative and CD161-positive subsets (45, 46).

The frequency of circulating NK cells is about 5-20% within human peripheral blood mononuclear cells (PBMCs) (55).

There are other ILCs besides NK cells that do not express adaptive antigen receptors generated by the recombination of receptor gene elements. ILCs are stratified into subsets according to their functions, which are considered counterparts of T-cell subsets. NK cells, for example, are considered to be the counterpart of cytotoxic T cells. ILC subsets that produce TH1-associated, TH2-associated and TH17-associate cytokines, are termed ILC1s, ILC2s, and ILC3s, respectively. In addition, there are lymphoid tissue-inducer (LTi) cells that can orchestrate the formation of secondary lymphoid tissues. LTi cells are considered to belong to the group of ILC3s (56, 57). Similar to NK cells, other ILCs can also express CD161 (58). The frequency of non-NK ILCs is very low with about 0.01-0.23% of $CD45^+$ leucocytes in human blood (59).

1.4. Innate-like T cells share features of NK and conventional T cells

1.4.1. Characteristics of innate-like T cells

Innate-like T cells, including mucosal-associated invariant T (MAIT), γδT and invariant natural killer T (iNKT) cells, are characterised by expressing TCRs with limited diversity, having public antigen specificity and being able to be activated in response to cytokine stimulation in a TCR-independent manner similar to NK cells (18, 60–67). These cell types can mount very rapid responses. The time required to induce effector functions of innate-like T cells ranges from hours to days, in contrast to days to weeks required by conventional T cells. Thus, innate-like T cells bridge innate and adaptive immune responses (18). Innate-like T-cell subsets express high levels of the NK receptor CD161, which is, however, also expressed by various conventional αβT-cell subsets (67–69). For example, TH17 cells and a subset of tissue-resident memory T (TRM) cells express intermediate levels of CD161 (70–74). Within the adult circulation, CD161 expression is associated with a memory T-cell phenotype (75).

Importantly, CD161-expressing T-cell subsets share a transcriptional and functional phenotype. This includes the ability to respond to cytokines such as IL-12+IL-18 in a TCR-independent manner, where cytokine responsiveness and response magnitude correlates with CD161 expression levels on T cells (66, 68). Thus, CD161-intermediate conventional αβT cells, but not CD161-negative subsets can respond to cytokine stimulation with IL-12+IL-18, similar as innate-like T cells. The fraction of cytokine-responsive cells within CD161-intermediate conventional T cells and their response levels are much lower compared to innate-like T cells, however (68). The function of CD161 on T cells is less clear than on NK cells due to conflicting evidence (53, 54, 75, 76). A recent study by Mathewson et al. makes a strong case for CD161 being an inhibitory receptor on T cells, however, as its genetic inactivation or blockade with monoclonal antibodies increased T cell-mediated tumour cell killing (77).

1.4.2. MAIT cells

MAIT cells express a semi-invariant TCR consisting of Vα7.2-Jα12/20/33 combined with β-chains of limited diversity (78). The MAIT cell TCR recognises microbial-derived riboflavin metabolites presented by the highly conserved and nonpolymorphic MHC class I-related molecule 1 (MR1) (79, 80). Besides TCR stimulation, MAIT cells can be activated by cytokines in a TCR-independent manner, such as IL-12, IL-18, IL-15 and TL1A (64, 65, 81–83). Main effector functions of MAIT cells include the expression of IFNγ and IL-17, and target cell killing via the release of granzymes and perforin (84–86). MAIT cells have an antigen-experienced memory phenotype and express innate-associated markers such as NK receptors. The typical MAIT cell phenotype includes CD3, Vα7.2, high levels of CD161, CD26, IL-18Rα, 2B4, CD45RO, PLZF, RORγT, TBET, EOMES, GzmA and GzmB expression, but a lack of CD45RA and CCR7 expression (68, 84, 87–91). In human blood, MAIT cells comprise up to 1-10% of T cells, of which the majority is $CD8^+$ and a small fraction is DN and a minority expresses CD4 (92).

1.4.3. γδT cells

γδT cells express TCRs comprised of a γ- and δ-chain. Two major γδT-cells subsets have been identified based on the utilization of variable δ gene segments, including $Vδ2^+$ and $Vδ2^-$ γδT cells, the latter largely consisting of $Vδ1^+$ γδT cells (93). Within γδT cells, the $Vδ2^+$ subset shows typical “innate” characteristics having relatively low TCR diversity. Up to 95% $Vδ2^+$ γδT cells show pairing with Vγ9, forming a TCR which recognise microbial-derived phosphorylated non-peptide antigens also known as phosphoantigens (66, 94, 95). The endogenous ligand isopentenyl phyrophosphate can also activate Vδ2Vγ9 cells, but only in presence of high concentrations found upon cellular transformation (96). The presentation of phosphoantigens is not fully understood but requires CD277 (95, 97). $Vδ2^-$ subsets, such as $Vδ1^+$ γδT cells, have a relatively diverse TCR repertoire and a relatively high fraction of naive cells, which are characteristics of conventional T cells (66, 98). $Vδ1^+$ subsets recognise various different ligands, including lipid antigens presented by CD1b, CD1c and CD1d (99–101). Most of the $Vδ2^+$ γδT cells express CD161 (75-80%), while only about 25% of $Vδ1^+$ T cells are CD161-positive. $Vδ2^+$ γδT cells can respond to cytokines in a TCR-independent manner. In contrast to $Vδ2^+$ cells, the cytokine responsiveness of $Vδ1^+$ cells is low. Cytokine responsiveness is higher within CD161-expressing subsets than in CD161-negative subsets within both $Vδ2^+$ and $Vδ1^+$ cells. In addition, the ability of γδT cells to respond to cytokines corresponds also with the expression of other innate-associated markers such as IL-18Rα and PLZF (66). γδT cells have a multitude of different effector functions, including the secretion of TH1, TH2 and TH17 cytokines, regulatory function, cytotoxic activity and antigen-presenting capacity (96). In human blood, γδT cells comprise about 2-10% of T cells (94).

1.4.4. iNKT cells

Another subset of innate-like T cells are iNKT cells, expressing a semi-invariant TCR consisting of Vα24-Jα18 combined with β-chains of limited diversity. The TCRs of iNKT cells recognise exogenous and endogenous glycolipid antigens presented by CD1d, an MHC class

l-like molecule (61, 62). Murine NKT cells can be activated by cytokines like IL-12+IL-18 in a TCR-independent manner (60). Human iNKT cells need some transient TCR stimulation to acquire the ability to respond to IL-12+IL-18 stimulation in a TCR-independent manner. Suboptimal TCR stimulation is sufficient to induce cytokine responsiveness, such as exposure to self-antigen from CD1d-expressing APCs (63). Analogous to CD4 T-cell subsets, there are different iNKT-cell subsets that produce TH1, TH2, TH17 cytokines, respectively, provide B cell help or have regulatory function (102, 103). Similar to γδT cells and MAIT cells, iNKT cells express CD161 (67, 69, 104). In human blood iNKT cells are rare with a frequency of 0.01-1% of total T cells (67, 69).

1.4.5. Cytokines in innate-like T-cell regulation and function

NK cells and innate-like T cells share the ability to respond to a range of cytokines, including IL-12, IL-18, IL-15, TL1A and type I IFNs (45–48, 63–66, 81–83, 105–107). The novel and understudied cytokine IL-32, which will be further introduced in the chapter-specific introduction of chapter 6, can directly act on NK cells and regulate their activity (108), but its effect on innate-like T-cell activity is currently unknown.

In addition, IL-12+IL-18 can induce the expression of IL-32 by NK and $CD4^+$ T cells (109, 110). As CD161-expressing and particularly innate-like T cells are the T-cell subsets that can respond to IL-12+IL-18-stimulation (66, 68), it warrants investigating whether IL-32 expression is a novel function of cytokine-stimulated innate-like T cells.

1.5. Anti-cancer immune response

MacFarlane Burnet and Lewis Thomas formulated the concept of immune surveillance, which proposes that the immune system surveys the host and detects and eliminates continuously arising transformed cells (111–115). The protective role of the immune system against cancer has been demonstrated by various models of immunodeficient mice leading to an increased

susceptibility to spontaneous and carcinogen-induced tumours. These murine models include RAG2-deficient and SCID mice lacking B and T lymphocytes, mice with experimentally deleted immune subsets including αβT, γδT, NKT, or NK cells, and mice with genetically inactivated immune effectors molecules, such as IL-12, IFNγ or perforin (116, 117). In line with this, immunocompromised human individuals, such as immunosuppressed transplant recipients, show an increased incidence of various cancers that are not linked to viral aetiology (118–120). In addition, a significant association between tumour infiltrating lymphocytes, such as CD8 T cells, and favourable prognosis in cancer has been observed (121–123). There are different mechanisms for the induction of anti-cancer immune responses, including immune responses generated against neoantigens that arise due to the genetic instability of cancer cells, or NK cell-mediated responses against cancer cells due to dysregulated MHC molecule expression and expression of stress-induced ligands for activating NK-cell receptors (124, 125).

Since the formulation of the concept of immune surveillance, a more complex model called cancer immunoediting has been proposed. It considers not only the protective role of the immune system against cancers but also its ability to sculpt tumour immunogenicity. This model consists of three phases, of which the first phase, the elimination phase, represents immune surveillance that can mediate protection from malignant disease as explained above. In case the immune system is not completely successful at eliminating transformed cells, the second phase follows, called equilibrium phase. In this phase, the immune system hinders the outgrowth of the tumour, but cancer cells can persist due to mutations acquired that aid their survival. In this process, the selective pressure imposed by the anti-cancer immune response continuously shapes the cancer cell properties. When the balance between the anti-tumour immune response and the ability of the tumour to mutate and resist is tilted towards favouring tumour growth, the escape phase begins. In this phase, the tumour grows progressively and avoids immune detection and elimination by various mechanisms (116, 126, 127). For example, anti-cancer T-cell responses can be negatively regulated by

inhibitory immune checkpoint receptors, which are pathways that normally control the magnitude and duration of immune responses, limit tissue damage during immune responses and contribute to maintain self-tolerance. Tumours can exploit these inhibitory immune checkpoint pathways such as PD1, CTLA4, TIM3 and LAG3 (128). As successful tumours evade and manipulate anti-cancer immune responses, evading immune destruction has been declared a hallmark of cancer (129).

KLRB1, encoding for CD161, has been described as the most favourable prognostic pan-cancer biomarker in a meta-analysis of transcriptomic data from about 18,000 tumours across 39 different cancer types (130). CD161 is expressed by subsets of NK and T cells (46, 66, 68, 75), suggesting that one or multiple CD161-expressing immune cell types can be beneficial for patient survival in cancer. Little is known, however, to which subset the favourable prognostic association of *KLRB1* across cancers can be attributed to. Further knowledge about which subset is involved could allow the development of novel immunotherapeutic strategies, in which the relevant CD161-expressing subset is exploited to achieve positive results in the treatment of cancer patients.

CD161-expressing immune subsets and their proposed roles in cancer will be further introduced in the chapter-specific introduction of chapter 7.

1.6. Methods for explorative immunophenotyping

Flow cytometry has been the gold standard for the characterisation of single cells in the field of cytometry since its development in 1965 (131–133). But there is a need for increasing panel sizes of staining antibodies to allow the analysis of the highly complex immune system. Panels need to simultaneously allow the identification of a large number of cell types, the detection of complex cell types that require a large number of phenotyping markers for their definition and the accommodation of a large number of functional markers, which pushes flow

cytometry to its limits. Therefore, several novel technologies for high-content immunophenotyping have been developed that overcome the limits of flow cytometry, such as spectral flow cytometry (134, 135), mass cytometry (136) and ChipCytometry (137). ChipCytometry is an emerging imaging-based method, where markers are acquired in iterative cycles consisting of sample staining, image acquisition and subsequent photobleaching. With this serial process, an unlimited number of markers can theoretically be accumulated on a single sample (137). Despite ChipCytometry has been described previously (137), there are multiple technical issues and limitations to overcome. In addition, studies are lacking that explore the high-content nature and possible limits of ChipCytometry. ChipCytometry is further introduced in chapter-specific introductions of chapters 3, 4 and 5.

1.7. Aims and objectives of thesis

The aim of this thesis is to investigate the regulation and function of CD161-expressing T cells and to study their role in cancer.

The objectives are:

- To develop ChipCytometry as a truly viable technique in order to identify and deeply phenotype CD161-expressing immune cells types and particularly innate-like T cells in blood and tissue (Chapters 3-5).
- To investigate whether IL-32 expression is a novel effector function of cytokine-stimulated innate-like T cells (Chapter 6).
- To investigate whether IL-32 can directly regulate innate-like T-cell activity (Chapter 6).
- To generate a pan-cancer *IL32* gene signature to investigate its role in cancer (Chapter 6).
- To explore to which CD161-expressing immune cell type the favourable prognostic association of *KLRB1* across cancers can be attributed to (Chapter 7).

2. GENERAL MATERIALS AND METHODS

2.1. Media and buffers

R10 cell culture medium

RPMI 1640 (Sigma Aldrich) + 10% heat-inactivated fetal calf serum (Gibco) + 2mM L-Glutamine (Gibco) + 1X Penicillin-Streptomicin solution (Gibco)

MACS buffer

Phosphate-buffered saline (PBS) + 2mM ethylenediaminetetraacetic acid (Sigma Aldrich) + 0.5% heat-inactivated FCS (Gibco)

2.2. Cells

2.2.1. Blood samples

Human blood samples were obtained from the National Health Service Blood and Transplant, John Radcliffe Hospital, Oxford.

2.2.2. Isolation of PCMBs

PBMCs were isolated by density gradient centrifugation. Whole blood was diluted 1:2 with PBS and layered on top of Lymphoprep™ density gradient medium (STEMCELL Technologies). Samples were centrifuged at 800 x g for 22 minutes at 22°C without brake. The PBMC layer was collected using a Pasteur pipette and washed twice with PBS (centrifugation at 350 x g for 10 minutes at room temperature (RT)).

2.2.3. $CD3^+$ or $CD8^+$ T cell isolation

$CD3^+$ were isolated from PBMCs or tonsil-derived single-cell suspensions using either CD3 Microbeads (Miltenyi Biotec) or the Pan T Cell Isolation Kit (Miltenyi Biotec) following manufacturer's instructions. $CD8^+$ cells were isolated from PBMCs using CD8 Microbeads (Miltenyi Biotec) following manufacturer's instructions.

2.2.4. Depletion of $CD14^+$ and $CD19^+$ cells

$CD14^+$ and $CD19^+$ cells were depleted from PBMCs by magnetic separation using CD14 and CD19 MicroBeads in combination with LD Columns and QuadroMACS Separator (Miltenyi Biotec), following the manufacturer's protocol.

2.3. Cell culture

2.3.1. Cytokine stimulation

Cells were stimulated with cytokines at concentrations specified in Table 2-1, with the exception of dose-response studies.

Table 2-1. List of cytokines used.

Cytokine	Concentration	Manufacturer
IL-12	10 ng/mL (suboptimal) 50 ng/mL (optimal)	Miltenyi Biotec
IL-18	10 ng/mL (suboptimal) 50 ng/mL (optimal)	MBL International
IL-15	10 ng/mL (suboptimal) 50 ng/mL (optimal)	Miltenyi Biotec
IL-2	50 ng/mL	BioLegend
IL-4	50 ng/mL	Miltenyi Biotec
IL-7	50 ng/mL	BioLegend
IL-9	50 ng/mL	Miltenyi Biotec
IL-21	50 ng/mL	Miltenyi Biotec
IL-32α	100 ng/mL	R&D Systems
IL-32β	100 ng/mL	R&D Systems
IL-32y	100 ng/mL	R&D Systems

2.3.2. Anti-CD3/anti-CD28 stimulation

Nunc™ MaxiSorp™ ELISA flat-bottom 96-well plates were coated overnight at 4°C with anti-CD3 antibodies (clone UCHT1, Mouse IgG1κ, BioLegend) at a concentration of 5 µg/mL in PBS. As a negative control, wells were treated with IgG isotype (Mouse IgG1κ Isotype, BioLegend) diluted in PBS at a concentration of 5 µg/mL. The next day, wells were washed three times with R10 medium and subsequently blocked with FCS-containing R10 medium

for 1 hour at 37°C. Cells were added to the wells and anti-CD28 antibodies (clone CD28.2, Mouse IgG1κ, Biolegend) or IgG isotype were added at a final concentration of 2 µg/mL.

2.3.3. *S*timulation of MAIT cells using *E. coli*

First, fixed *E. coli* were prepared. Colonies of *E. coli* (DH5α, Invitrogen) were picked with a sterile pipette tip from a Luria-Bertani (LB) agar plate (Lennox, Sigma Aldrich), added to LB Broth medium (Lennox, Sigma Aldrich) at 1 colony / 10mL medium and cultured in a shaking incubator at 37°C for 16 hours. A fresh tip was incubated in LB Broth medium as a sterility control. *E. coli* were pelleted, fixed in 1% paraformaldehyde (PFA) for 20 minutes and subsequently washed twice with sterile, filtered PBS. The sterility control was processed in an identical manner. For the quantification of the *E. coli*, serial dilutions were prepared from an aliquot taken prior to fixation. The dilutions were plated on LB agar plates and incubated overnight at 37°C. The colonies of plates containing between 30-300 colonies were counted to determine the number of colony-forming units (CFUs).

Then, bacterial activation of MAIT cells was performed by stimulating 10^6 PBMCs with $3x10^7$ CFU of fixed *E. coli* in presence or absence of blocking agents or isotype controls (listed in Table 2-2) for 24 hours or 48 hours, as indicated in the results section.

Table 2-2. List of blocking agents used.

Reagent	Type of reagent	Clone	Working concentration	Manufacturer
Anti-MR1	Monoclonal antibody	26.5	10 µg/mL	BioLegend
Vaccinia Virus B18R	Soluble type I IFN receptor	NA	1 µg/mL	eBioscience
Anti-IL-12/IL-23 p40	Monoclonal antibody	C8.6	10 µg/mL	BioLegend
Anti-IL-15	Monoclonal antibody	34559	10 µg/mL	R&D Systems
Anti-IL-18	Monoclonal antibody	125-2H	10 µg/mL	MBL
Anti-TNFα, Adalimumab	Monoclonal antibody	NA	10 µg/mL	Kindly provided by Dr. Nicholas Provine, Nuffield Department of Medicine, University of Oxford
Anti-IFNγ	Monoclonal antibody	B27	10 µg/mL	BioLegend
IgG1 Isotype	Monoclonal antibody	MG1-45	30 µg/mL	BioLegend

2.4. Flow cytometry

2.4.1. Surface staining

Cells were washed with PBS and resuspended in 50µL of antibody mix containing a viability dye (Live/Dead fixable near-IR dead cell stain kit, Invitrogen, final dilution: 1/500) and fluorescently-labelled staining antibodies diluted in PBS (Table 2-3). Cells were incubated for 20 minutes at 4°C. After washing with PBS, cells were fixed in 2% formaldehyde (Sigma Aldrich) for 10 minutes at 4°C. Then, cells were washed and resuspended in PBS for data acquisition.

Table 2-3. Antibodies used for flow cytometry.

Antibody	Colour	Clone	Dilution	Manufacturer
CCR7	FITC	G043H7	1/50	BioLegend
CD3	eFluor 450	OKT3	1/100	Invitrogen
	VioGreen	BW264/56	1/25	Miltenyi Biotec
	PerCP-Cy5.5	UCHT1	1/100	eBioscience
	PE-Cy7	UCHT1	1/100	eBioscience
CD4	PerCP-Cy5.5	RPA-T4	1/100	BioLegend
CD8	VioGreen	BW135/80	1/25	Miltenyi Biotec
	PerCP-Cy5.5	SK1	1/50	BioLegend
	PE-Cy7	BW135/80	1/50	Miltenyi Biotec
	APC	BW135/80	1/50	Miltenyi Biotec
	APC	RPA-T8	1/50	BioLegend
CD14	APC-Cy7	HCD14	1/100	BioLegend
CD19	APC-Cy7	HIB19	1/100	BioLegend
CD25	PerCP-Cy5.5	M-A251	1/50	BioLegend
CD45RA	PE-Cy7	HI100	1/100	BioLegend
CD56	BV421	HCD56	1/50	BioLegend
	PE-Cy7	HCD56	1/50	BioLegend
CD62L	PE	DREG-56	1/50	BioLegend
CD69	FITC	FN50	1/50	eBioscience
CD161	PE	191B8	1/50	Miltenyi Biotec
	APC	191B8	1/50	Miltenyi Biotec
	BV421	HP-3G10	1/50	BD Biosciences
Vα7.2	APC	3C10	1/50	BioLegend
	FITC	3C10	1/50	BioLegend
	PerCP-Cy5.5	3C10	1/50	BioLegend
γδTCR	PE	5A6.E9	1/50	Invitrogen
	FITC	5A6.E9	1/50	Invitrogen
	PE	11F2	1/50	Miltenyi Biotec
	APC	B1	1/50	BioLegend
Vδ2	FITC	B6	1/50	BioLegend
	PerCP-Cy5.5	B6	1/50	BioLegend
PD1	PE-Cy7	eBioJ105	1/50	eBioscience
LAG3	PE	3DS223H	1/50	eBioscience
TIM3	PerCP-Cy5.5	F38-2E2	1/50	BioLegend
IFNγ	PE-Cy7	4S.B3	1/50	BioLegend
	PerCP-Cy5.5	4S.B3	1/50	eBioscience
TNFα	PerCP-Cy5.5	MAb11	1/25	BioLegend
GzmB	APC	GB12	1/100	Invitrogen

2.4.2. Intracellular staining

For intracellular staining, Brefeldin A (eBioscience, final dilution: 1/1000) was added to the cells 4 hours before harvesting. Following surface staining and fixation, cells were

resuspended in permeabilization buffer (10X Permeabilization buffer, eBioscience) and incubated for 10 minutes at 4°C. After centrifugation, cells were resuspended in 50 µL of antibody mix containing staining antibodies diluted in permeabilization buffer (Table 2-3). After 20 minutes incubation at 4°C, cells were washed and resuspended in PBS for data acquisition.

Intracellular staining for IL-32 was performed in a two-step process. First, cells were stained with biotin-labelled IL-32αβγδ antibody (clone KU32-52, BioLegend, final dilution: 1/50), diluted in permeabilization buffer. After washing twice with permeabilization buffer, cells were stained with either anti-Biotin-PE (clone Bio-18E7, Miltenyi Biotec, final dilution: 1/100 or clone 1D4-C5, BioLegend, final dilution: 1/200) or streptavidin-BV421 (BioLegend, final dilution: 1/1000), diluted in permeabilization buffer.

2.4.3. Data acquisition and analysis

Stained samples were measured using a MACSQuant Analyzer 10 (Miltenyi Biotec). Flow cytometry data was analysed using FlowJo (Beckton Dickinson) or R as further detailed in the results. The gating strategy applied is shown in Figure 2-1, if not stated otherwise.

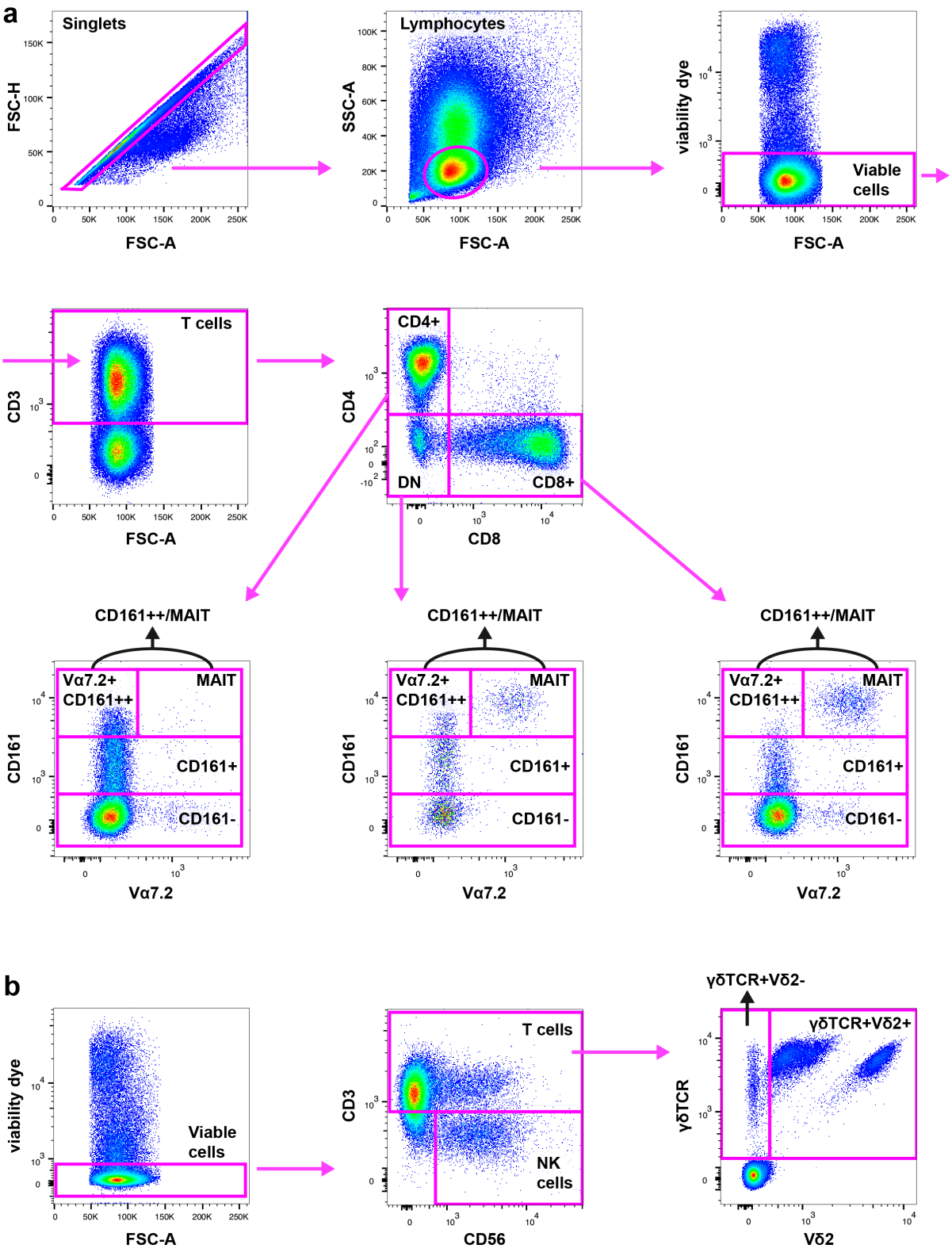


Figure 2-1. Gating strategy used to identify NK cells and T-cell subsets. (a) Identification of MAIT cells: Cells were gated as singlets, lymphocytes, viable cells and T cells. Within T cells, $CD4^+$, $CD8^+$ and DN T cells were identified. Within these subsets, $CD161^-$, $CD161^+$ and $CD161^{++}$/MAIT populations were identified. The $CD161^{++}$/MAIT-cell population can be further divided into $V\alpha7.2^+CD161^{++}$ MAIT and $V\alpha7.2^-CD161^{++}$ non-MAIT cells. (b) Identification of NK and γδT cells: After identifying singlets, lymphocytes and viable cells, NK cells were defined as $CD3^-CD56^+$ cells. Within $CD3^+$ T cells, γδT-cell subsets were identified as $\gamma\delta TCR^+V\delta2^+$ and $\gamma\delta TCR^+V\delta2^-$ cells. In order to clean up the gating process shown in (a) and (b), the channel for the viability dye

was often used as dump channel. In this case, CD14 and CD19 were placed in the same channel as the viability dye to exclude $CD14^+$ and $CD19^+$ cells from the analysis.

2.5. ChipCytometry of cell suspensions

The ChipCytometer (Zellscanner ONE, Zellkraftwerk, Leipzig, Germany) setup consisted of a modified ZEISS Axio Observer Z1 fluorescence microscope equipped with a mercury short arc lamp (HBO 100) and suitable filter sets for the used dyes (BUV395, BV421, FITC, PE, PerCP). Single-cell suspension samples were treated with Human TruStain FcX (BioLegend) to block unwanted Fc receptor-mediated staining (15 minutes, RT). Barcoding was performed to allow the analysis of multiple samples (multiple donors or conditions) on a single microfluidic chip. Sample barcodes consisted of anti-CD45 antibodies (pan-leucocyte marker) coupled to different fluorophores (BUV395, BV421, FITC, PE, or PerCP-Cy5.5). More complex barcoding strategies were realised by using barcodes that consisted of specific combinations of differently labelled anti-CD45 antibodies as further detailed in the results section. Barcode staining (5 minutes, 4°C), viability dye (LIVE/DEAD™ Fixable Green Dead Cell Stain Kit, Invitrogen) staining (5 minutes, 4°C) and staining with antibodies that do not recognise fixed epitope such as chemokine receptors (15 minutes, RT) was performed using unfixed samples prior to chip loading. Barcoded samples were mixed and cells were then loaded onto cell suspension chips (ZellSafe Cells – Chips, Zellkraftwerk, Leipzig, Germany) at a concentration of 10 million cells/mL. Cells were allowed to adhere to the chip surface for 10 minutes at RT, then non-adhered cells were washed off with PBS. Initial acquisition with the ChipCytometer was performed to acquire barcode, viability and chemokine receptor staining. Afterwards, samples were fixed (Fixation buffer, Zellkraftwerk, Leipzig, Germany) for 5 minutes at RT or 15 minutes at 4°C, as indicated in the chapter-specific materials and methods section (According to the manufacturer, prolonged incubation for sample fixation can improve sample stability for long-term storage. In this study, prolonged incubation for fixation also resulted in certain antibodies requiring higher concentrations for optimal sample staining). Subsequent markers were acquired in iterative rounds of photo-bleaching, staining

and imaging. Fluorochrome-coupled antibodies were applied in mixes (up to 5 per round), diluted in PBS. For the staining of surface markers, antibody mixes were first applied through the chip inlet and incubated for 7.5 minutes at RT and subsequently additional staining solution was applied for 7.5 minutes through the chip outlet, unless stated otherwise. For the staining of intracellular markers, cells were treated with Brefeldin A (eBioscience) for 4 hours before harvesting. Cell permeabilization was performed using True-Nuclear Transcription Factor Buffer Set (BioLegend) as follows: chips were rinsed and incubated with permeabilization buffer for 1 hour, followed by rinsing and incubation with fixation buffer for a further hour before finally washing with permeabilization buffer. Antibody mixes for intracellular staining were prepared in permeabilization buffer and staining was performed similar to surface staining but with extended incubation of 2 x 15 minutes, unless stated otherwise. All permeabilization and staining steps were performed at RT. IL-32 was stained in a two-step process. Samples were first stained with biotin-labelled IL-32 antibody (2 x 15 minutes), then thoroughly rinsed with permeabilization buffer, and finally stained with anti-biotin-PE antibody (2 x 7.5 minutes). Staining antibodies that were used and dilutions that were applied are detailed in the chapter-specific materials and methods section of chapters 3, 4 and 5. For storage, the chips were rinsed with storage buffer and tightly sealed with sealing plugs (Zellkraftwerk, Leipzig, Germany). Data processing, including cell segmentation and fluorescence intensity calculation was performed using the ZKWApp (Zellkraftwerk, Leipzig, Germany). Data analysis was performed using FlowJo (Beckton Dickinson) or R as further detailed in the results section.

2.6. Bioinformatic methods

2.6.1. ssGSEA analysis

Enrichment of signature genes within RNA sequencing (RNA-seq) or single-cell RNA sequencing (scRNA-seq) data samples was calculated via single sample gene set enrichment analysis (ssGSEA) using GSVA R package.

2.6.2. Survival analysis

The association between an explanatory variable and patient survival (overall survival) was analysed by univariate Cox proportional hazards regression analysis using survival R package. Prior to this analysis, the explanatory variable was z-score normalised. Forest plots were generated using ggforestplot R package indicating hazard ratio (HR) and 95% confidence intervals. Significant associations were defined having a likelihood ratio test p-value ≤ 0.05.

2.7. Software and statistical data analysis

2.7.1. Statistical analysis

Statistical tests were either performed in R using stats, emmeans or rstatix R packages, or in GraphPad Prism, unless stated otherwise.

2.7.2. Software and R packages

The software and R packages used are listed in Table 2-4.

Table 2-4. Software and R packages.

Software	Version
R	4.0.4
Rstudio	1.4.1106
GraphPad Prism	9.1.2
Microsoft Excel	210880801
FlowJo	10.7.1
R packages	**Version**
boot	1.3-28
caret	6.0-88
CATALYST	1.14.1
circlize	0.4.12
clusterProfiler	4.0.2
ComplexHeatmap	2.6.2
ConsensusClusterPlus	1.54.0
cowplot	1.1.1
cydar	1.10.0

CytoNorm	0.0.5
data.table	1.14.0
DataCombine	0.2.21
diffcyt	1.10.0
dplyr	1.0.4
emmeans	1.5.4
EnhancedVolcano	1.8.0
enrichplot	1.12.2
flowCore	2.2.0
FlowSOM	1.22.0
flowWorkspace	4.2.0
gdata	2.18.0
ggcyto	1.18.0
ggforestplot	0.1.0
ggfortify	0.4.11
ggplot2	3.3.3
ggpubr	0.4.0
ggsignif	0.6.2
GSVA	1.40.1
hdf5r	1.3.3
limma	3.46.0
ncdfFlow	2.36.0
org.Hs.eg.db	3.13.0
parallel	4.1.0
pheatmap	1.0.12
plyr	1.8.6
presto	1.0.0
RankProd	3.18.0
RColorBrewer	1.1-2
readxl	1.3.1
reshape2	0.8.8
rlang	0.4.10
rstatix	0.7.0.999
scales	1.1.1
Seurat	4.0.2
SeuratDisk	0.0.0.9019
stats	4.0.4
stringr	1.4.0
SummarizedExperiment	1.22.0
survival	3.2-11
TCGAbiolinks	2.20.0
tidyr	1.1.3
tidyverse	1.3.0

uwot	0.1.10
VennDiagram	1.6.20
viridis	0.5.1

3. DEVELOPMENT OF CHIPCYTOMETRY AS A VIABLE TECHNIQUE FOR HIGH-CONTENT IMMUNOPHENOTYPING

3.1. Introduction

ChipCytometry is an imaging-based high-content immunophenotyping method first described by Hennig et al. (137) (Figure 3-1a). Samples, which can be either cell suspensions or tissue sections, are loaded onto microfluidic chips and are fixed. The cell suspension chips have a proprietary surface coating in the internal channel allowing live cells to adhere and self-immobilise in a monolayer. Tissue sections, on the other hand, are mounted on coverslips and then get assembled with an adhesive to an open tissue chip that lacks a bottom cover forming a closed microfluidic chamber. On the ChipCytometer, which is a modified and automated ZEISS Axio Observer Z1 fluorescence microscope powered by a mercury short arc lamp, the analysis process begins with a photobleaching step to remove the background fluorescence of the chip-immobilised sample. Afterwards, the sample is stained with an antibody cocktail of up to five antibodies coupled to different fluorochromes (BUV395, BV421, FITC, PerCP-Cy5.5 and PE). The stained sample is then imaged on the ChipCytometer to record its fluorescence. After completion of this cycle, the remaining sample fluorescence can be removed by photobleaching. By performing iterative cycles of photobleaching, staining and imaging one can accumulate in theory a virtually unlimited number of markers on a single sample.

For cell suspension analysis, the software divides the surface area of each cell suspension chip into 44 discrete positions that are scanned sequentially (Figure 3-1b). During the photobleaching cycle, the ChipCytometer takes a transmitted light image, photobleaches for the selected period of time and records the background fluorescence (Figure 3-1c). All of these three steps are performed in a position-by-position-wise manner. Data acquisition after sample staining is performed in a similar manner to data acquisition during the

photobleaching cycle. First, a transmitted light image is acquired, followed by the acquisition of the fluorescence signals of each position. The ChipCytometer software (ZKWapp) performs cell segmentation based on the transmitted light images, which allows individual cells to be tracked across all cycles. The pattern formed by the cells on the transmitted light images also allows exact re-positioning of the microfluidic chip during all photobleaching and acquisition cycles. The ZKWapp software automatically calculates fluorescence intensity values for each individual cell and for each stained parameter. In this process, corrections are made for autofluorescence and optical artefacts by the subtraction of the background fluorescence from the recorded fluorescence signals of the stained samples. The obtained fluorescence intensity values are provided in FCS file format in addition to other parameters including spatial information. The spatial information defines a unique position for each cell on the chip, consisting of the chip position number and x- and y-coordinates on the particular chip position (137).

To accommodate the size of tissue section samples, histology chips have a larger interior chip chamber (1x2 cm^2), which is partitioned by the software into 560 adjacent positions for sequential image acquisition. After initial image acquisition of the entire chamber area, further analysis can be limited to a few selected, particularly interesting positions of a tissue section in order to speed up the acquisition process. Automated cell segmentation and fluorescence intensity value calculation for the analysis of tissue samples is being developed by the manufacturer and is currently in beta stage 2.

At any point during sample interrogation, samples can be stored in a proprietary storing solution within the chip for up to 20 months without significant biomarker degradation, which allows re-analysis with further markers later on and offers the potential for biobanking (138).

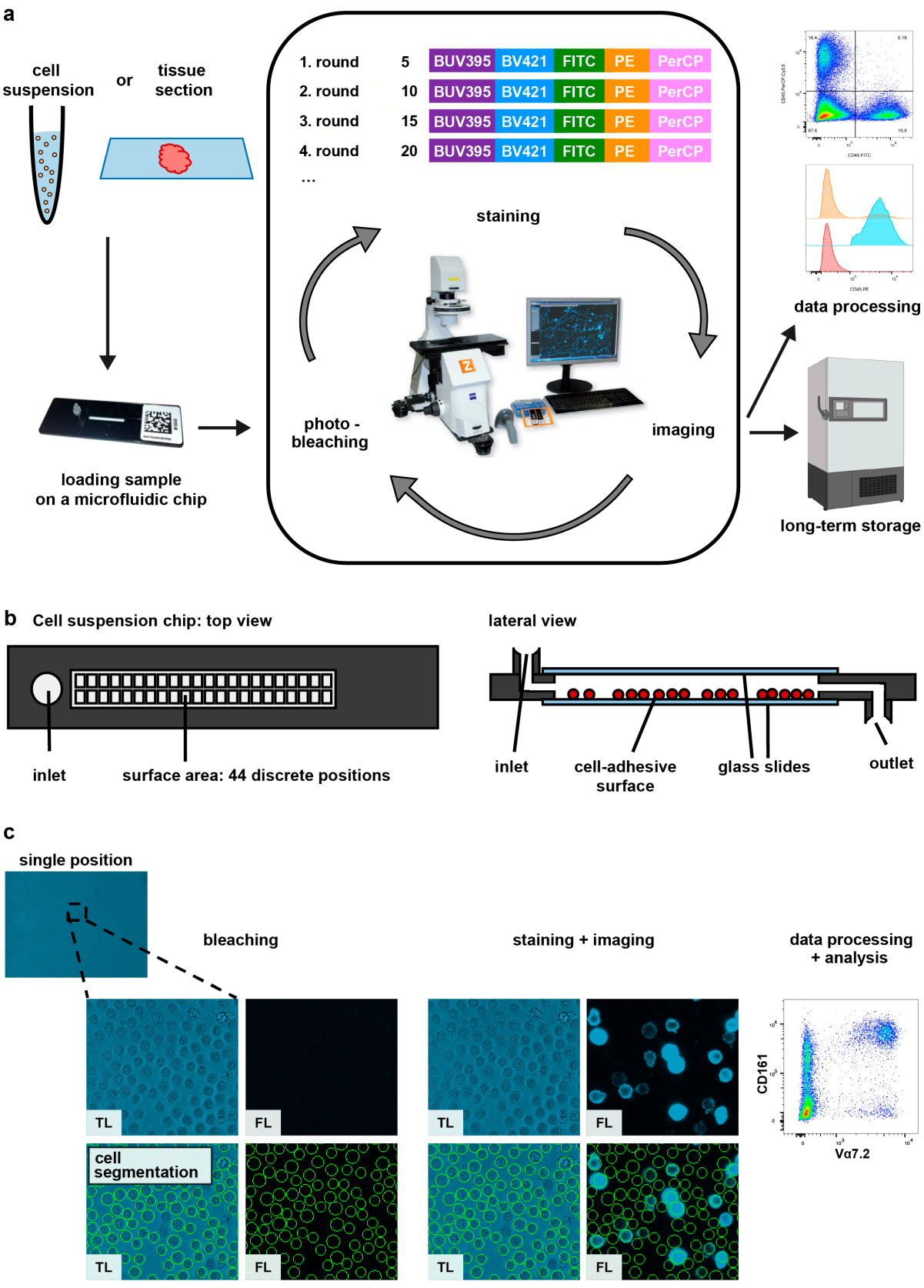


Figure 3-1. ChipCytometry allows to accumulate in theory a virtually unlimited number of markers on a single sample. Illustration of the ChipCytometry workflow. ChipCytometry requires dissociated cells or tissue sections to be loaded into a microfluidic chip. Iterative cycles of staining with fluorescently labelled antibodies, imaging and photobleaching allows in theory the acquisition of an unlimited number of markers on a single sample. In each cycle, the signals of up to five different antibody-fluorochrome conjugates can be recorded (BUV395,

BV421, FITC, PE and PerCP). Samples can be stored long-term in a proprietary storage buffer at 4°C for subsequent re-analysis or biobanking purposes. The ChipCytometry ZKWapp software allows automated data processing to obtain fluorescence intensity information for acquired cells, provided in FCS file format for further analysis. (b) Design of microfluidic chips for analysis of cell suspensions. The chips consist of a microfluidic chamber with an inlet and an outlet. The centre chamber is covered by glass slides at the top and the bottom. The bottom class slide is treated with a proprietary compound that allows cells to adhere and self-immobilise. The ZKWapp software divides the surface area of cell suspension chips into 44 positions, which are scanned sequentially. (c) Example images of the ChipCytometry workflow. Images show magnified sections of one of 44 chip positions. Left: Transmitted light (TL) images are recorded at the start of each photobleaching and imaging step. The software uses the TL images for automated cell segmentation, which allows individual cells to be tracked across all acquisition cycles. The pattern of cells in the TL images also allows precise chip (re-)positioning across all photobleaching and acquisition cycles. The photobleaching step at the start of a cycle removes sample autofluorescence or remaining fluorescence of previous stains. After subsequent imaging of the stained sample, the software automatically calculates the fluorescence intensity values of the cells. Fluorescence intensity value calculation includes the subtraction of the background fluorescence from the recorded fluorescence signals of stained samples, which allows for some corrections for non-bleachable autofluorescence and optical artefacts. The processed data is provided in FCS file format for further analysis. Part of this figure was created with BioRender.com.

Although ChipCytometry has been described previously (137), I discovered that there were multiple unresolved technical problems and limitations. I aimed to overcome those issues to establish ChipCytometry as a truly viable method.

3.2. Aims

1. To identify possible technical problems and limitations of the ChipCytometry method
2. To find solutions for technical problems and limitations, and develop ChipCytometry as a truly viable method

3.3. Chapter-specific materials and methods

3.3.1. ChipCytometry

ChipCytometry was performed as described in GENERAL MATERIALS AND METHODS-2.5, with the following changes: Samples were fixed (Fixation buffer, Zellkraftwerk, Leipzig, Germany) for 5 minutes at RT. Surface antibodies were applied through the chip inlet according to manufacturer's instructions and incubated for 10 minutes at RT, unless stated otherwise. If bi-directional staining was performed, staining antibodies were applied through the chip inlet and incubated for 5 minutes and subsequently more staining antibodies were

applied through the chip outlet and incubated for additional 5 minutes. Analogous to the surface staining protocol, antibody mixes for intracellular staining were applied through the chip inlet and incubated for 30 minutes (or 2 x 15 minutes in case of bi-directional staining) at RT. Antibodies used and optimised in this study are listed in Appendix Table I-1, Appendix Table I-2 and Appendix Table I-3.

3.4. Results

3.4.1. Gradually increasing sample autofluorescence in the BV421 channel

An increase in sample autofluorescence in the BV421 channel was observed over time. Experimentally, autofluorescence in this channel could be induced by repeated rounds of photobleaching (Figure 3-2a), while other channels were only negligibly affected (Figure 3-2b). BV421-autofluorescent cells were also observed after storing a sample on a chip at 37°C for 3 days (data not shown). Upon request, the manufacturer confirmed that samples can develop autofluorescence over time and that the appearance of this autofluorescence is promoted by heat (like the one generated during the photobleaching process), oxygen exposure and increased sample age. According to the manufacturer, the acquired sample autofluorescence is caused by pigments such as lipofuscins, which are generated over time in ongoing metabolic processes despite sample fixation. Therefore, the BV421 channel was only used as long as a clear positive population could be observed after background subtraction.

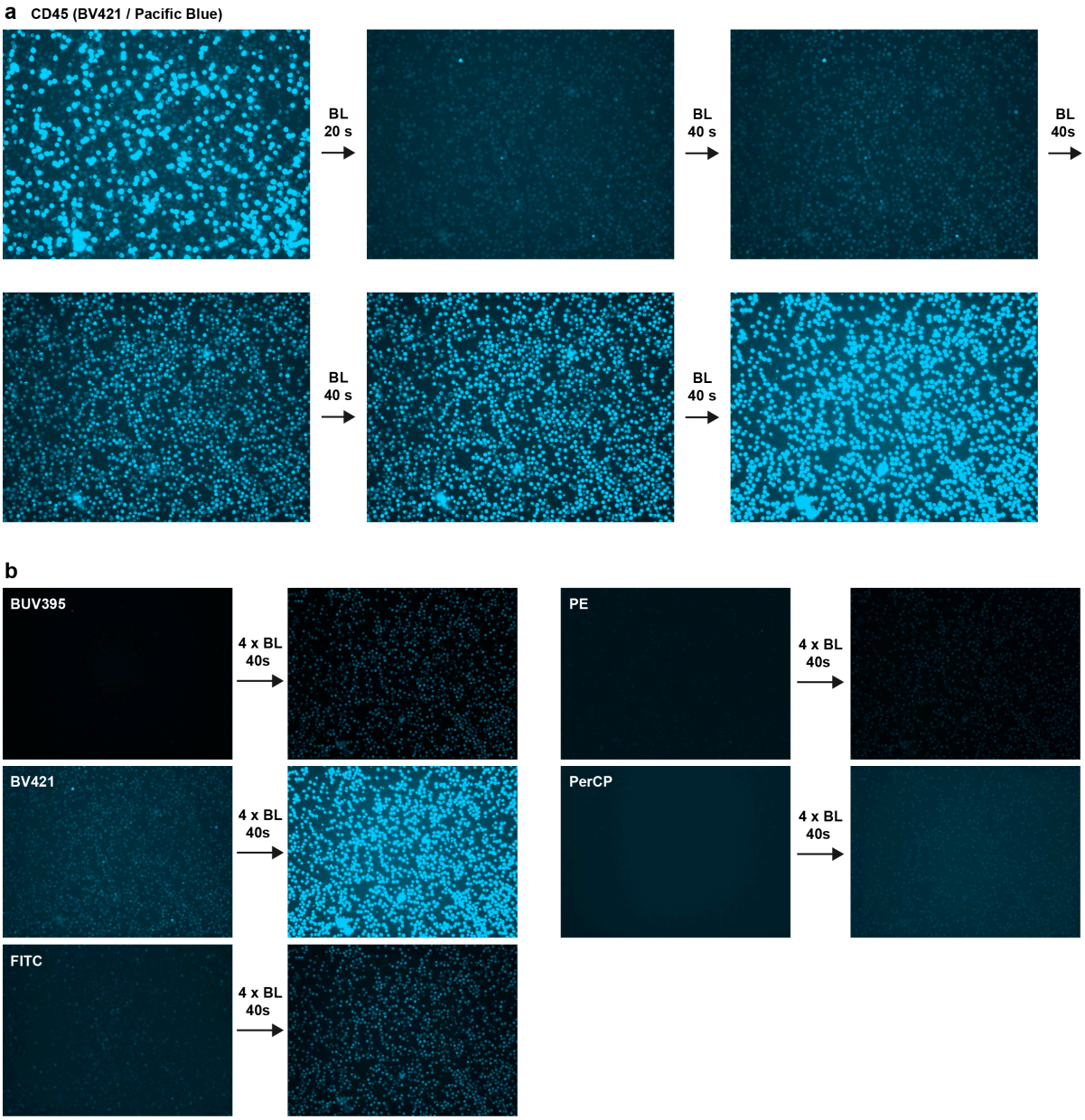


Figure 3-2. Gradual appearance of sample autofluorescence within the BV421-channel limited its usage. Human PBMCs were stained with either CD45-B395, -BV421, -FITC, -PE or -Per-CP-Cy5.5. Unstained and stained cells were mixed and analysed by ChipCytometry. (a) After acquisition of the BV421 signal, the chip was bleached (BL) five times for the indicated time. After every round of photobleaching, an increase in the autofluorescent BV421 signal of the sample was observed. (b) Comparison of background fluorescence of all five channels before and after 4 rounds of 40 s photobleaching.

3.4.2. Appearance of a fluorescent haze during acquisition of stained samples

During the imaging process of stained samples, the appearance of a fluorescent haze was observed on the recorded images (Figure 3-3a). This haze could influence the fluorescence intensity values of local cells and therefore pollute the acquired data. The fluorescent haze was not visible on the background images prior to sample staining and could be removed after its appearance on stained samples by photobleaching. The fluorescent haze was not antibody- or fluorochrome-specific. The use of extended washing protocols for stained samples prior to their acquisition could not prevent the generation of the fluorescent haze. The provision of a continuous flow of PBS across the stained samples during image acquisition successfully eliminated the fluorescent haze, however (Figure 3-3b).

3.4.3. Recurrent blockages of the fluidic system

Means to connect the pump-driven PBS supply tube with the chip inlet had to be developed. In the first approach, the tube was directly inserted into the chip inlet (Figure 3-3c). Even though degassed PBS was used, the formation of air bubbles within the fluidic system was observed over time. If air bubbles were trapped in the chip inlet or outlet, they could cause a blockage and flooding of PBS across the chip and the instrument. Therefore, adapters had to be engineered to connect the fluidic system permanently with the chip.

A cylindrical adapter with a funnel at the bottom was developed, into which the PBS was dripped. This should allow air that is trapped within the fluidic system to escape through the opening at the top (Figure 3-3d). In practise, however, air bubbles could still get trapped at the bottom of the funnel, causing blockages and overflow of the adapter. To prevent the chip and instrument from being flooded with PBS, the top of the adapter was sealed and an outflow pipe was attached so that accumulating PBS can be drained off in case of a blockage (Figure 3-3e). In practise, however, the accumulating PBS created in case of a blockage pressure within the adapter, which forced the trapped air through the microfluidic chip. This resulted in the loss of the sample. In the final approach, PBS was dripped into a funnel, which was tightly

inserted within a 3D-printed tray containing a slope (Figure 3-3f-h). In case of a blockage, PBS was redirected to drip into a collection device below the chip. The material of the 3D-printed tray was found to be reflective, which polluted the acquired images. By covering the tray with light-absorbent foil, this issue was overcome.

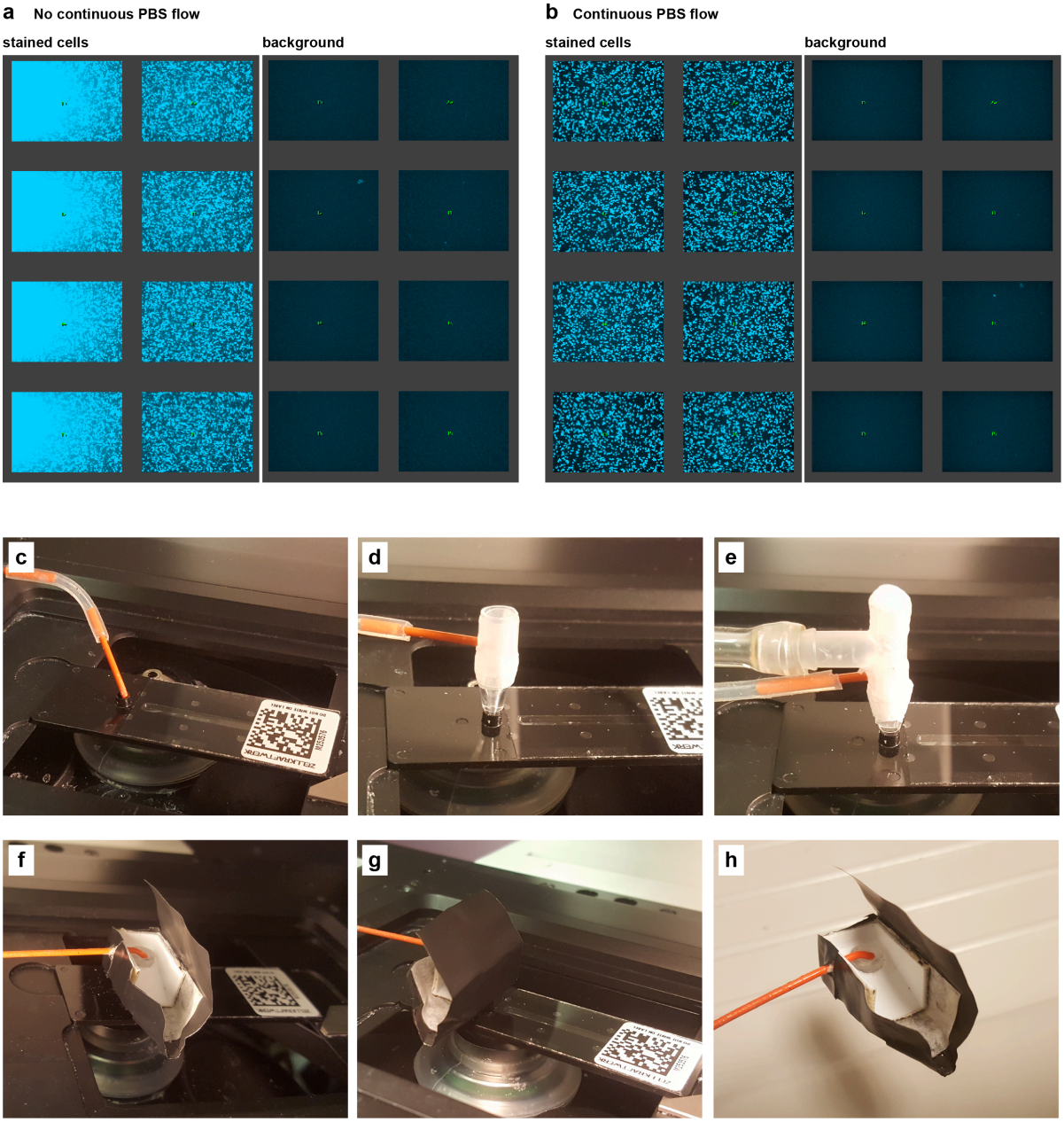


Figure 3-3. A continuous flow of PBS across the sample was required to eliminate a fluorescent haze that appeared after sample staining. Human PBMCs were stained and analysed by ChipCytometry (a) without providing a continuous PBS flow and (b) with providing a continuous PBS flow across the sample during data acquisition. After imaging of stained cells, the chip was bleached and the background fluorescence of the sample was acquired. (c)-(h) Adapters that connect the pump-driven PBS supply tube with the inlet of the microfluidic chip were developed to prevent flooding of the chip and instrument in case of a blockage. (c) The PBS supplying tube was directly inserted into the inlet of the chip. Despite the use of degassed PBS, air bubbles could form within the fluidic system over time. In case air bubbles got trapped in the chip inlet or outlet, they could cause the chip and

the instrument being flooded with PBS. (d) PBS was dripped into a cylindrical adapter with a funnel at the bottom, supplying the chip with PBS. Air bubbles within the fluidic system could escape through the opening at the top of the funnel. In practise, however, air could still get trapped at the bottom of the funnel causing blockages and overflow of the adapter. (e) To prevent the chip and instrument being flooded with PBS, the top of the adapter was sealed and an outflow pipe for accumulating PBS in case of blockages was attached. In practice, however, the accumulating PBS created in case of blockages pressure within the adapter and forced trapped air through the microfluidic chip, which resulted in the loss of the sample. (f)-(h) PBS was dripped into a funnel, which was tightly inserted within a 3D-printed tray containing a slope. In case of a blockage, PBS was redirected to drip into a collection device below the chip. The material of the 3D-printed tray was reflective and could pollute the acquired data. Therefore, the tray was covered with light-absorbent foil.

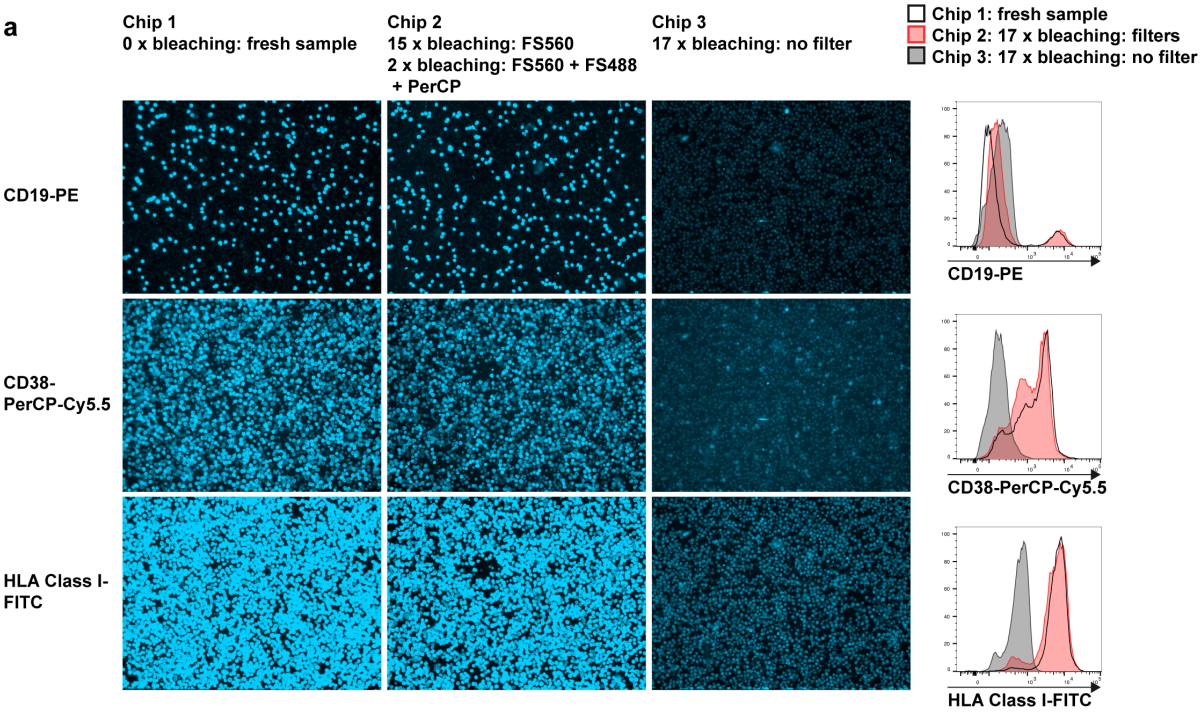
3.4.4. Repeated photobleaching rendered samples unstainable

After completion of several photobleaching cycles, it was no longer possible to stain samples with markers that were known to work. Most markers were affected after about 5-10 cycles, but some susceptible markers even after 1-2 cycles. In a test, PBMCs from one donor were loaded onto three different chips. All chips were stained with the same antibody cocktail. Chip 1 was stained directly after sample loading (= fresh sample), and chip 2 and chip 3 were stained after 17 consecutive staining and photobleaching cycles. Chip 2 was bleached 15 times using the PE filter module (bandpass 550/25, 605/70) alone, and twice using the sequential combination of PE, FITC (bandpass 470/40, 525/50) and PerCP (bandpass 435/40, 710/75) filter modules. By photobleaching through the respective filter modules, the channels get photobleached one at a time. Chip 3 was bleached 17 times without any filters using the white light filter module (no filter installed), as recommended by the manufacturer, resulting in all channels getting bleached simultaneously. Cells on chip 1 and chip 2 showed similar staining results. In contrast, chip 3 showed either no stained cells or cells that were stained but had greatly reduced fluorescence intensities compared to chip 1 and chip 2 (Figure 3-4a).

The simultaneous photobleaching of all channels with the white light filter module uses the full light spectrum of the mercury lamp. This includes light at the UV end of the spectrum (<300nm). These wavelengths can be absorbed by proteins and damage epitopes (139, 140), which is most likely the reason why repeated photobleaching through the while light filter

module rendered the sample on chip 3 unstainable. Using PE, FITC or PerCP filter modules to individually photobleach corresponding channels on chip 2 prevented the samples from being exposed to damaging low-wavelength radiation. Photobleaching each channel consecutively through its respective filter unit is very time consuming, however. Thus, the manufacturer subsequently provided an instrument upgrade consisting of a 364 nm longpass filter to block damaging UV light in front of the white light filter module. This setup allowed to bleach samples for more than 11 consecutive minutes per position in one go (equivalent of the exposure of 17 photobleaching cycles), without an observable loss in the staining ability of a selected 5-marker panel compared to a fresh sample that had only 40 seconds exposure to photobleaching (1 photobleaching cycle) per position (Figure 3-4b). This upgrade permanently impeded efficient photobleaching of the BUV395 channel through the while light filter module, however. Photobleaching of BUV395 individually through the BUV395 filter module required a considerable amount of extra time.

Although the 364 nm longpass filter improved epitope stability of some makers significantly, others were still strongly affected by cumulative photodamage after repeated photobleaching cycles. Therefore, longpass filters with higher cut-on wavelengths (420 nm and 493 nm) were tested within the white light filter module for their ability to prevent photodamage.


a
Chip 1
0 x bleaching: fresh sample
Chip 2
15 x bleaching: FS560
2 x bleaching: FS560 + FS488
+ PerCP
Chip 3
17 x bleaching: no filter
Chip 1: fresh sample
Chip 2: 17 x bleaching: filters
Chip 3: 17 x bleaching: no filter
CD19-PE
CD38-PerCP-Cy5.5
HLA Class I-FITC
CD19-PE
CD38-PerCP-Cy5.5
HLA Class I-FITC

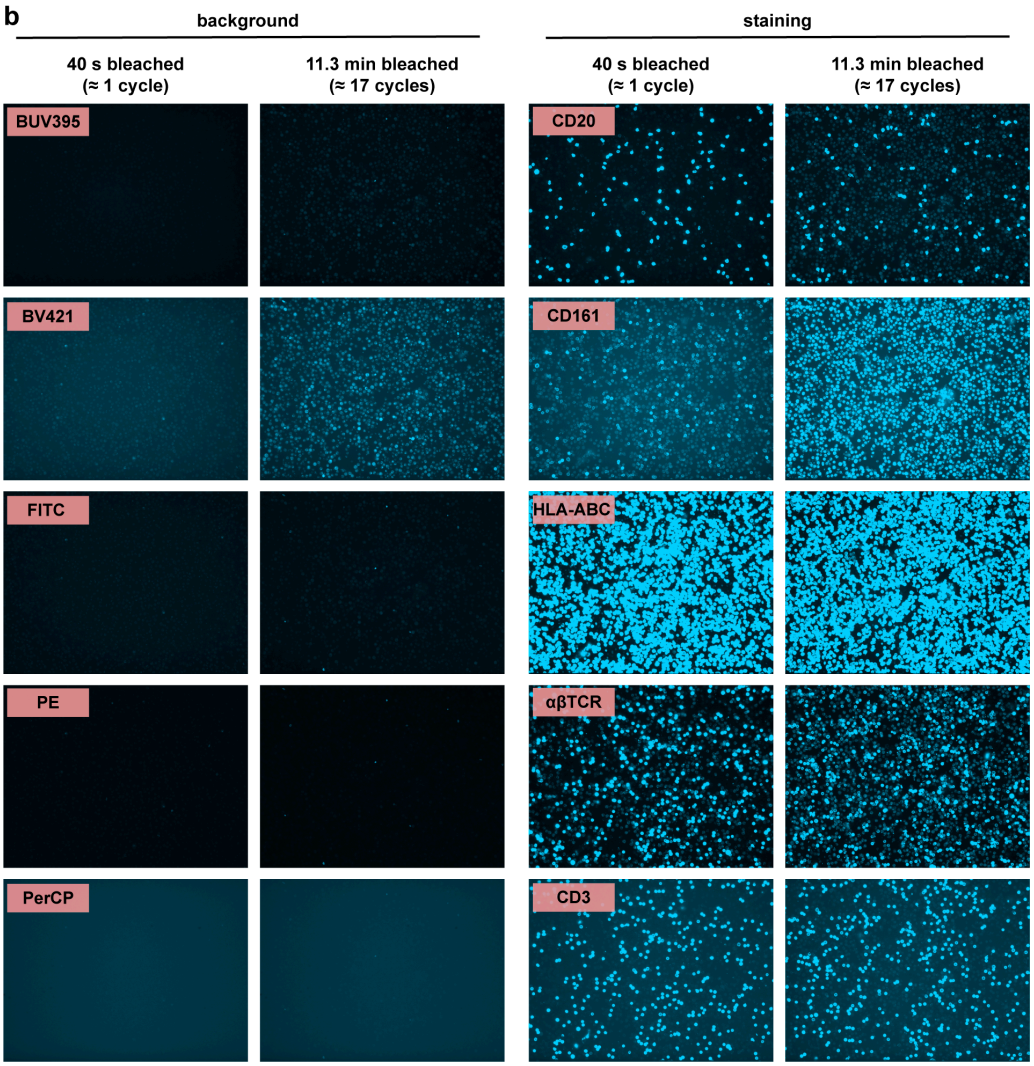

b
background
staining
40 s bleached
(≈ 1 cycle)
11.3 min bleached
(≈ 17 cycles)
40 s bleached
(≈ 1 cycle)
11.3 min bleached
(≈ 17 cycles)
BUV395
CD20
BV421
CD161
FITC
HLA-ABC
PE
αβTCR
PerCP
CD3

Figure 3-4. Repeated photobleaching cycles rendered samples unstainable. (a) Human PBMCs from one donor were loaded on three different chips. All chips were stained with CD19, CD38 and HLA Class I. Chip 1 was stained immediately after sample loading. Chip 2 was stained after 15 x photobleaching through the PE filter module (FS560) and 2 x photobleaching through the PE, FITC (FS488) and PerCP filter modules. Chip 3 was stained after 17 x photobleaching without any filters (white light filter module). Left: Examples of fluorescence images of each stain. Right: Histograms of the stained markers from the different chips. (b) Human PBMCs from one donor were loaded onto two different chips. Both chips were bleached using the white light filter module with a 364 nm longpass filter installed. One chip was bleached for 40 seconds (1 photobleaching cycle), the other chip for 11.3 minutes (equivalent of 17 photobleaching cycles). Chips were subsequently stained with a panel of 5 antibodies (CD20-BUV395, CD161-BV421, HLA-ABC-FITC, aβTCR-PE, CD3-PerCP-Cy5.5) and imaged on the ChipCytometer. Images show the recorded background after photobleaching and the acquired fluorescence signals after subsequent sample staining.

The higher the cut-on wavelength of the longpass filter, the better was the longevity of the sample epitopes (data not shown). But the installation of longpass filters also had some disadvantages.

First, similar to the 364 nm longpass filter, the 420 and 493 nm longpass filters prevented efficient photobleaching of both the BUV395 and BV421 channels when using the white light filter module for photobleaching. Using the BUV395 and BV421 filter modules instead of the white light filter module to individually bleach respective channels increased the time that was required for a photobleaching cycle two- to three-fold. In addition, photobleaching through the BUV395 filter module also caused some photodamage. Therefore, it was concluded that only three filter modules including FITC, PE and PerCP are useful for routine staining of cells via ChipCytometry.

Secondly, the higher the cut-on wavelength of the installed longpass filter, the longer was the time required to photobleach each position when the white light filter module was used. The time required to photobleach one of the 44 chip positions ranged from 20-40 seconds without any filters and increased to 40 -160 seconds with a filter installed, which can have a significant negative impact on the sample throughput.

3.4.5. Inconsistent staining intensity across stained chips (x-direction)

When the antibody staining cocktail was applied to the sample via the chip inlet according to the manufacturer's protocol, there was a trend of decreasing fluorescence intensity values across the chip, i.e., cells furthest away from the inlet had the lowest fluorescence intensities (Figure 3-5a-c). The decrease of fluorescence intensity values across the chip is most likely caused by a concentration gradient of staining antibodies between the chip inlet and the chip outlet. Increasing the volume of applied antibody staining mixes from 200 µL to 300 µL and increasing the incubation temperature during staining from 4°C to RT could not abrogate this trend (Figure 3-5c). Applying the antibody mix through the outlet resulted in the opposite trend, with a decrease of fluorescence intensity values across the chip where cells furthest away from the outlet had the lowest fluorescence intensities (Figure 3-5d). The trend of decreasing fluorescence intensity values across the chip was less pronounced, however, when staining antibodies were applied through the outlet. This is most likely due to the fact that the distance from the chip outlet to the sample is longer than the distance from the chip inlet to the sample, which could result in a less steep gradient of antibody concentration across the sample area. The problem of inconsistent staining intensity across a chip was prevented by applying the antibody staining cocktail first through chip inlet and then staining the sample again by applying more of the antibody staining cocktail in reverse through the chip outlet (Figure 3-5e). There was no trend of decreasing fluorescence intensity values across the chip when cells were stained prior to loading them onto the chip (Figure 3-5f). This confirmed that the issue of inconsistent staining intensity across stained chips in x-direction was a problem with the protocol and not with the machine.

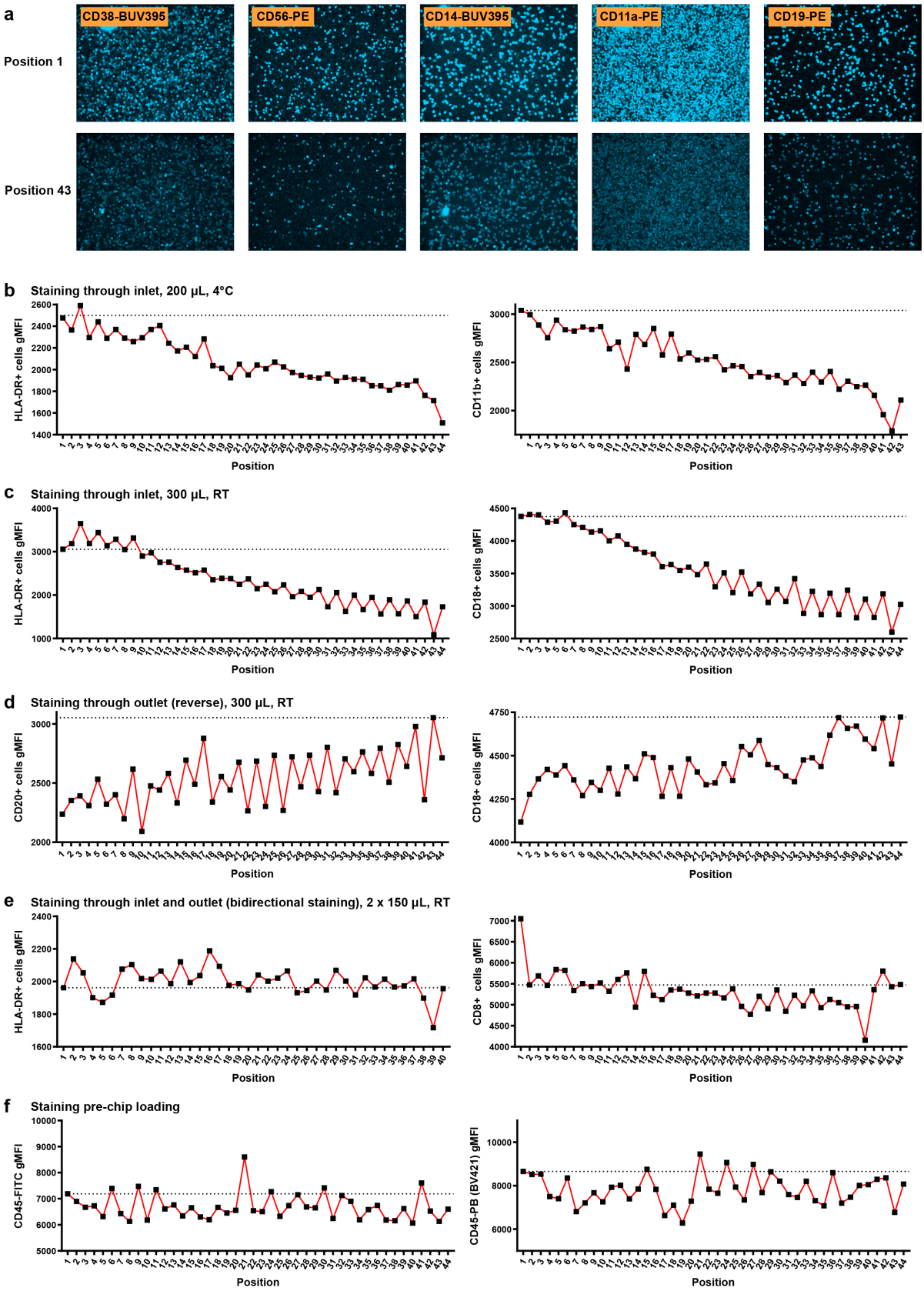


Figure 3-5. Bi-directional sample staining was required to achieve consistent staining intensities across the chip (x-direction). (a) PBMCs were loaded on microfluidic chips, stained by applying antibody mix through the chip inlet, and imaged using ChipCytometry. Images show examples of acquired chip positions 1 and 43. (b)-(e) PBMCs were stained and analysed using ChipCytometry. Graphs show the geometric mean fluorescence

intensity (gMFI) values of stained samples for each chip position. Different staining protocols were tested as indicated. To stain samples on the chips, antibody mixes were either applied through the chip inlet, through the chip outlet, or bi-directionally through the chip inlet and outlet in a sequential manner, as indicated. In addition, the staining volume and incubation temperature were varied, as indicated. (f) PBMCs were stained before they were loaded onto the chip for their analysis via ChipCytometry.

3.4.6. Inconsistent staining intensity across stained chips (y-direction)

There was a trend of positions with even numbers having lower fluorescence intensities than the following positions with odd numbers (Figure 3-6). It was found that the default setting of the ChipCytometer instrument placed the chip positions that are scanned off-centre and close to an edge of the microfluidic channel. After manipulating the software settings to place the positions of the cell suspension chip precisely centred (y-coordinate minus 500 µm), the variations of the fluorescence intensity values between odd and even positions tended to be more random. The differences between odd and even positions were most likely a result of the microfluidic properties of the chip chamber, which probably caused antibody concentrations being highest in the centre of the chip and falling off towards the edges. The off-centred placement of positions led to differences in the staining intensity between odd and even positions and could be corrected by precisely centring the positions.

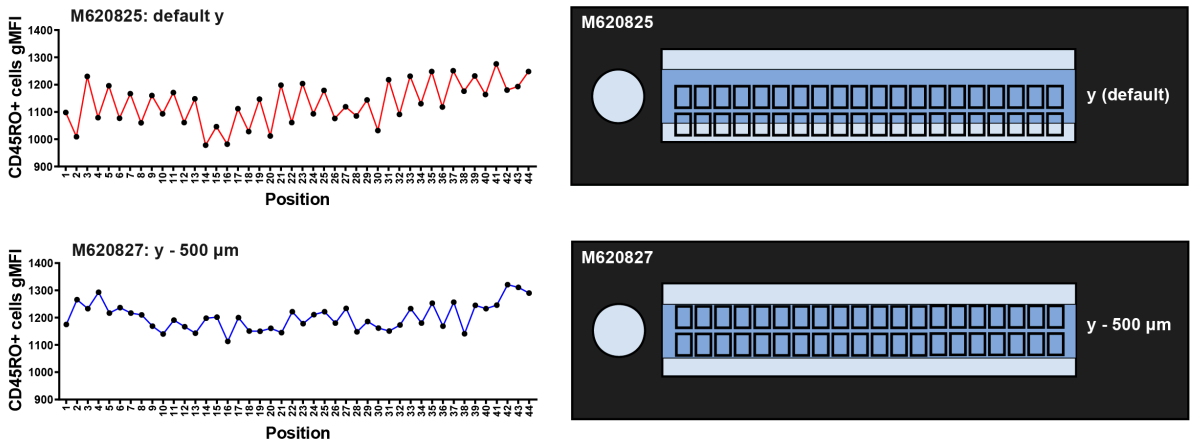


Figure 3-6. Off-centred cell suspension chips caused staining intensity bias between even and odd positions. PBMCs from one donor were loaded onto two different chips (M620825 and M620827), stained for CD45RO and analysed by ChipCytometry. M620825 was measured using the default system configuration where positions were placed off-centre and close to an edge of the microfluidic channel. M620827 was measured with adjusted y-coordinates (y - 500 µm) resulting in precisely centred positions. Left: CD45 geometric mean fluorescence intensity (gMFI) values of each chip position. Right: Illustration of how the software settings impacted the location of chip positions.

3.4.7. Fluorescence anomalies affecting ChipCytometry data

During the ChipCytometry data analysis, fluorescence anomalies were frequently observed. An example is a double-positive γδTCR^{+}Vα7.2^{+} population within the CD45^{+}CD19^{-}CD14^{-}CD56^{-}CD3^{+} cell population (Figure 3-7a). The analysis of spatial data revealed that the cells of this population were all located at chip position 43 and were clustered at a corner on this position (Figure 3-7b). The recorded transmitted light images of position 43 revealed that a foreign particle, most likely consisting of dust or debris, was located at the exact position of the anomalous cells. The foreign particle was not visible on the background images, but was fluorescent on the recorded images of the stained sample. This was most likely due to non-specific binding of staining antibodies to the foreign particle which resulted in false positive signals of all local cells.

There are many different possible causes of fluorescence anomalies, which can negatively impact the quality of ChipCytometry data, and measures should be taken to prevent them (Table 3-1). One way of eliminating fluorescence anomalies is to visually inspect each recorded image of a data set and manually delete cells that are affected by fluorescence anomalies. This is a very time-consuming process, however. Upon request, the manufacturer recommended enabling the proprietary algorithm “surrounding pixel correction” during fluorescence intensity value calculation, which can possibly mitigate the manifestation of fluorescence anomalies. For the fluorescence anomaly shown here, the recalculation of the fluorescence intensity values with this modified setting eliminated the fluorescence anomaly in the bivariate dot plot (Figure 3-7c).

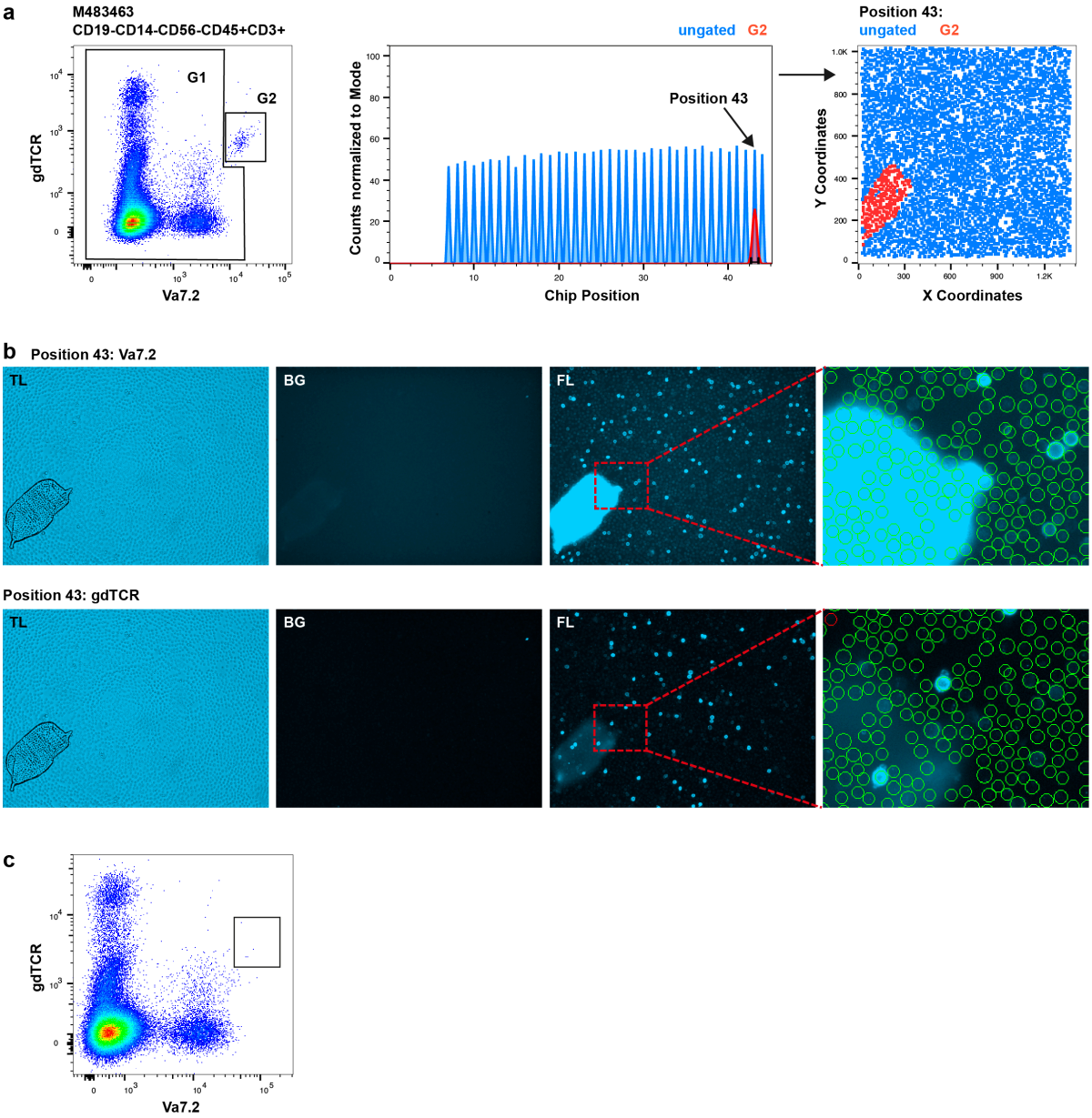


Figure 3-7. ChipCytometry data was affected by fluorescence anomalies. Isolated CD3⁺ cells were analysed by ChipCytometry with indicated markers. (a) Left: Identification of Vα7.2⁺γδTCR⁺ cells in gate G2. Middle: All events within the G2 gate were located at chip position 43. Right: Coordinate data of position 43 revealed that all cells within G2 were spatially clustered. (b) Transmitted light (TL) images of Position 43 showed that a foreign particle covered the cells from gate G2. The detritus particle caused a fluorescent spot on the fluorescence images (FL) of the stained sample, but was almost invisible on the background (BG) images, resulting in false-positive data points. Green circles in the magnified image section represent the cell segmentation. (c) Fluorescence intensity values of the data set were re-calculated using the proprietary algorithm “surrounding pixel correction”. This mitigated the manifestation of the fluorescence anomaly and the Vα7.2⁺γδTCR⁺ population was not visible any more.

Table 3-1. Causes of fluorescence anomalies in ChipCytometry data. The table summarises the various possible causes of fluorescence anomalies in ChipCytometry data. Depending on whether fluorescence anomalies affect the background image only, the image of recorded fluorescence signals of stained samples only, or both, it can increase or decrease the computed fluorescence intensity values of local cells and even cause very extreme fluorescence intensity values.

Cause	Effect	Prevention
Debris, dust particles, fibres.	Autofluorescence, non-specific binding of staining antibodies, covering of cells.	Clean work environment and work practice. Prevention of foreign particles getting into the system.
Unclean glass covers of the chip, e.g., finger prints or chemical residues of the window cleaner, which is used to clean the glass components of the chips.	Fluorescent haze on acquired images.	Avoid touching the glass cover of the chip. Ensure window cleaner does not leave smears or streaks on the cleaned glass components of the chip.
Air bubbles	Camera focussing issues, fluorescent haze on acquired images.	Use of degassed PBS for the provision of a continuous PBS flow across samples during data acquisition. Modification of the chip inlet so that trapped air can escape.
PBS spillages onto the chip surface due to blockages of the continuous PBS flow when air bubbles get trapped inside the chip.	Camera focussing issues, fluorescent haze on acquired images.	Avoid air bubbles getting into the system. Modification of chip inlet to prevent PBS from spilling onto the chip surface in case of a blockage.
Aggregates of fluorochromes or impurities of staining antibodies.	Fluorescent artefacts.	Quality control of new staining antibodies. Filtration of antibodies before their application.
Excess of staining antibody.	Due to the chip design, unbound staining antibody can get trapped at the edges of the chip. From there, it is difficult to wash out unbound antibody due to the microfluidic properties of the chip. Unbound antibody can diffuse from the edges of the chip to the centre area and become visible as fluorescent haze on acquired images.	Continuous PBS flow across samples during data acquisition prevents remaining unbound antibodies to accumulate.
Vibrations or shocks to the equipment.	Blurry images, incorrect position alignment.	Avoid shocks and vibrations in the working environment.

3.4.8. Antibody filtration with cellulose acetate filters causing granular background signals

To minimise the risk of introducing unwanted foreign particles into the chip, antibody staining mixes were filtered before their application in order to remove any contaminants that may be contained within antibody stock solutions as provided by the supplier. If cellulose acetate membrane filters were used for antibody filtration, a grainy background was observed on the recorded images of stained samples, especially in association with PE-conjugated antibodies (Figure 3-8). This could possibly be caused by wetting agents that are contained within the cellulose acetate filters. This problem was solved using polyvinylidene fluoride membrane filters instead. Their use resulted in a similar background compared to the no filter control.

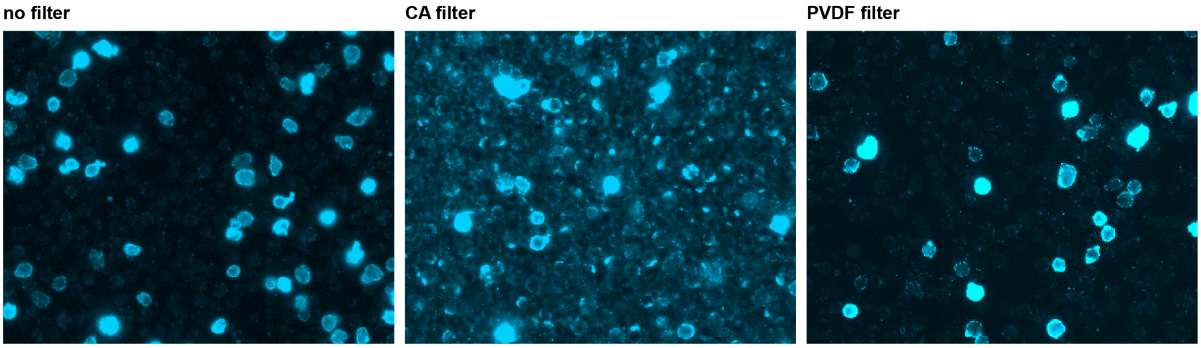


Figure 3-8. Antibody filtration using cellulose acetate membrane filters could cause a granular background. PBMCs were loaded on microfluidic chips, stained with CD56-PE and analysed by ChipCytometry. Antibody staining mixes were filtered before their application to the chip in order to remove any contaminants. Different filtering approaches were tested, including unfiltered (left), cellulose acetate (CA) membrane filter (middle) or polyvinylidene fluoride (PVDF) membrane filter (right).

3.4.9. Sample multiplexing using fluorescent barcodes to increase sample throughput

ChipCytometry has a relatively low sample throughput, as both the acquisition of the 44 chip positions and the acquisition of multiple markers on a single sample are iterative processes. Photobleaching of a single cell suspension chip took up to 80 minutes and image acquisition of a stained sample up to 40 minutes. A complete cycle including photobleaching, staining, washing and setting up the instrument took up to 3 hours. To increase sample throughput,

multiple samples were barcoded with different CD45-dye conjugates, allowing the analysis of multiple samples on a single chip. As an example, PBMCs of one donor were split into 6 different samples. The samples were stained with either CD45-BUV395, CD45-PB (BV421-channel), CD45-FITC, CD45-PE or CD45-PerCP-Cy5.5. One sample was not stained. The six samples were combined, and cells were loaded onto a microfluidic chip. After analysis on the ChipCytometer, all of the six different samples could be distinguished as shown in Figure 3-9a, demonstrating successful sample multiplexing using fluorescent barcodes.

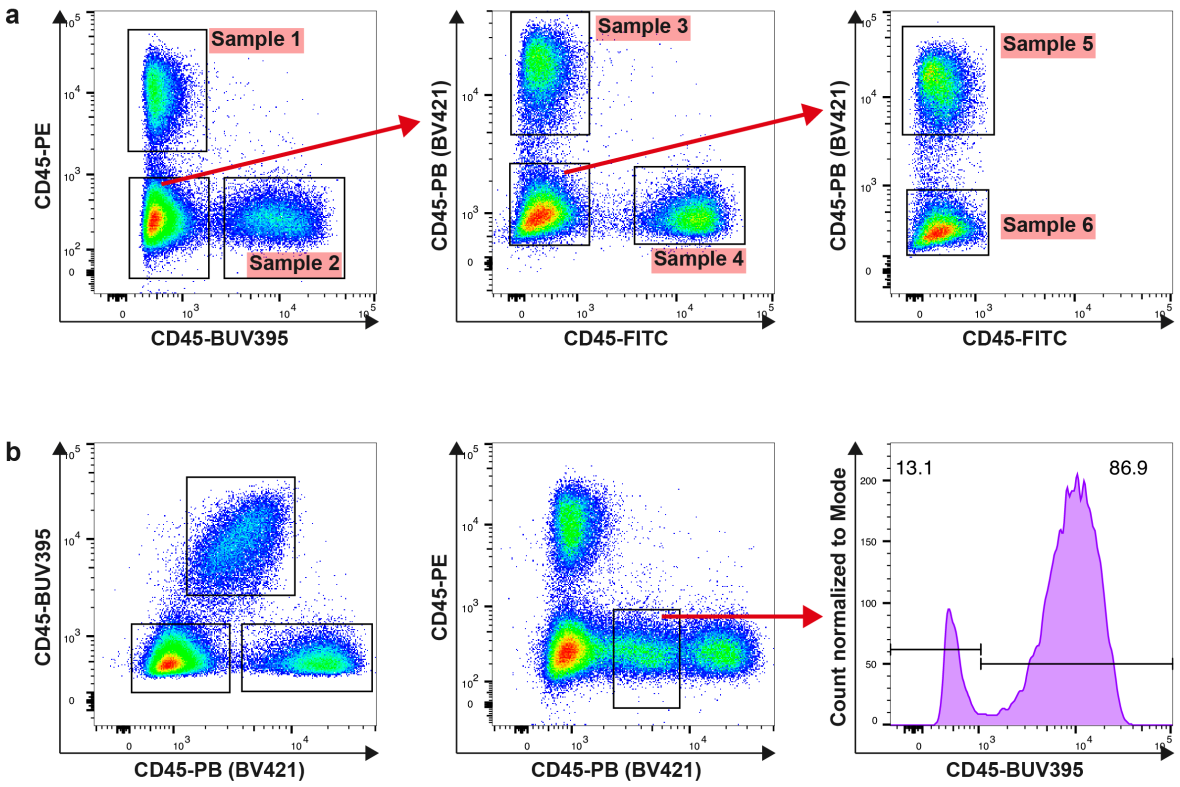


Figure 3-9. Barcoding increased sample throughput by simultaneously acquiring multiple samples on a single chip. Aliquots of PBMCs from one donor were stained with anti-CD45 antibodies coupled to either BUV395, PB (BV421-channel), FITC, PE or PerCP-Cy5.5. Unstained and stained samples were mixed, loaded into a microfluidic chip and analysed by ChipCytometry. (a) Gating strategy to distinguish 6 different samples on a single chip using barcodes: Sample 1 = CD45-PE$^+$, sample 2 = CD45-BUV395$^+$, sample 3 = CD45-BV421$^+$, sample 4 = CD45-FITC$^+$, sample 5 = CD45-PerCP-Cy5.5$^+$, sample 6 = unstained. (b) Bivariate plot of BUV395 and BV421 revealed that BUV395-positive cells could cause a signal in the BV421 channel (left). BV421 plotted against a channel different from BUV395, such as PE, demonstrated that the BUV395-stained sample could easily be misinterpreted as part of the BV421-stained sample (middle and right).

In the barcoding experiment, the BUV395 channel bled slightly into the BV421 channel (Figure 3-9b). The manufacturer's instructions of BD Horizon Brilliant Dyes state that Brilliant Violet and Ultraviolet dyes can form dye-to-dye interactions when used in combination or with dyes from other companies. Here, each of the samples was, however, stained with a single antibody-dye combination and stained cells were extensively washed before the samples were combined and loaded onto a chip. A similar spillover from the BUV395 channel to the BV421 channel was observed when using a staining mix containing both of these antibody-conjugated fluorochromes in combination with the recommended BD Horizon Brilliant Stain Buffer, which has been designed to resolve dye-to-dye interactions (data not shown). Therefore, the spillover problem is most likely not caused by dye-to-dye interactions, but is rather method-related and caution is required when using a BUV395-conjugated antibody in combination with a BV421-conjugated antibody in a ChipCytometry staining panel.

3.4.10. Excess of staining antibody causing poor distinction between positive and negative cells

Oversaturation due to excess of staining antibody during sample staining could negatively impact the separation of negative and positive populations (Figure 3-10). As an example, untreated and IL-15-, αCD3/αCD28- and IL-15+αCD3/CD28-stimulated cells were barcoded and samples were loaded onto microfluidic chips. Chips were stained with different CD71 antibody concentrations including a 1/10 and 1/40 dilution. The high antibody concentration 1/10 caused an increased background fluorescence of the negative population and a poor discrimination between positive and negative cells compared to the chip stained with a dilution of 1/40. Besides non-specific binding of antibody, the increased fluorescence intensity of negative cells can be caused by the spillover of light from oversaturated cells onto neighbouring negative cells. Therefore, precisely titrated antibody concentrations are crucial to obtain high quality ChipCytometry data. In this study, 82 markers for cell suspension analysis and 12 markers for tissue section analysis were tested and optimised to provide a

resource and establish the ChipCytometry method. The optimised markers are listed in Appendix Table I-1, Appendix Table I-2 and Appendix Table I-3.

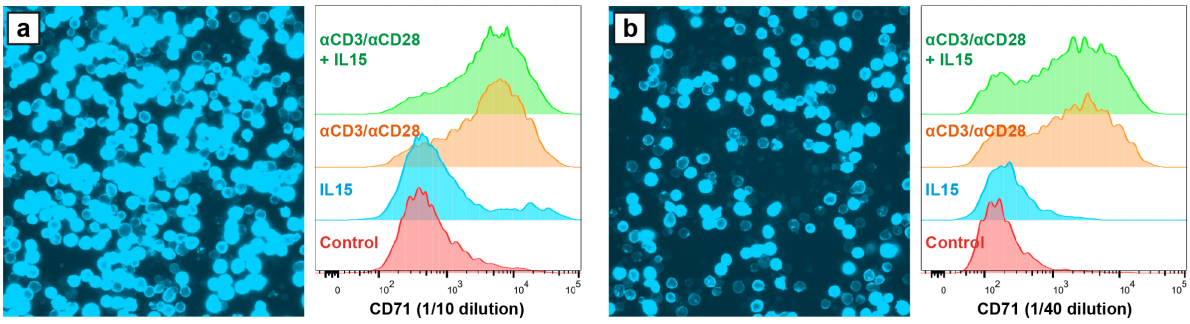


Figure 3-10. Oversaturated stains could limit the distinction between positive and negative cells. PBMCs were stimulated for 72 hours with plate-bound antibody or cytokines (untreated, IL-15, αCD3/αCD28, αCD3/αCD28+IL-15). Samples were barcoded and loaded onto microfluidic chips. Chips were stained with CD71. High antibody concentration (1/10) resulted in oversaturated stains and the signal of bright cells invaded the area of neighbouring cells, which caused relatively high fluorescence intensity values of the control (untreated) condition. A lower antibody concentration (1/40) led do reduced fluorescence intensity values of the control and a resulted in a better distinction between positive and negative cells in the stimulated samples.

3.4.11. Comparison of ChipCytometry with flow cytometry

To assess the ChipCytometry output relative to a well-established method, a cross-platform comparison of ChipCytometry and flow cytometry was performed. Human PBMCs were either stained with CD45-BUV395, -PB (BV421 channel), -FITC, -PE, or -PerCP. Stained samples were then combined and aliquots subsequently analysed by flow cytometry or ChipCytometry. The data revealed that two different ChipCytometer instruments generate cytometry data similar to a flow cytometer (Figure 3-11).

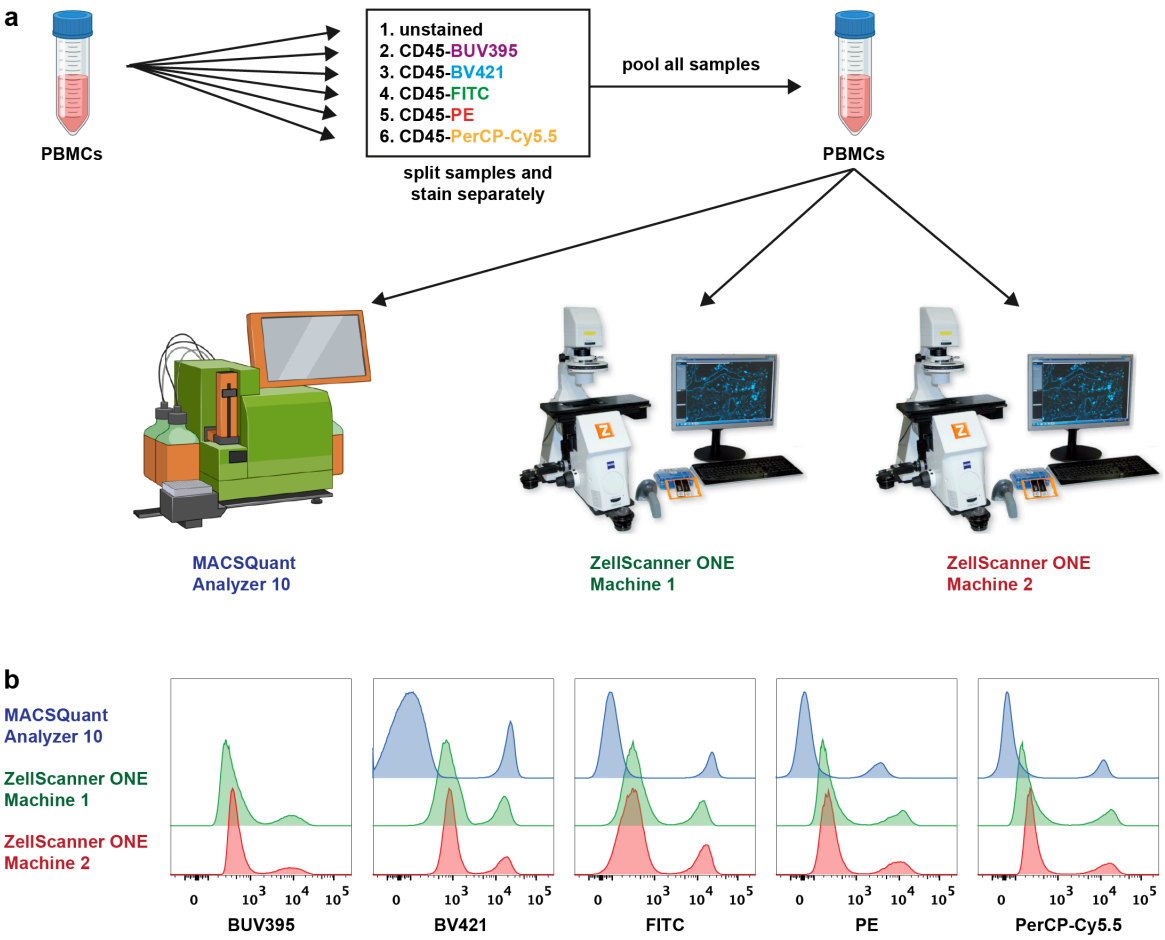


Figure 3-11. Cross-platform comparison of ChipCytometry and flow cytometry. (a) Human PBMCs were stained with either CD45-BUV395, -PB (BV421 channel), -FITC, -PE or -PerCP-Cy5.5. Unstained and stained samples were mixed and either analysed by flow cytometry (MACSQuant Analyzer 10) or by ChipCytometry (Zellscanner ONE). This comparison included two Zellscanner ONE instruments. (b) Histograms show the direct comparison of fluorescence intensities of different channels between the different platforms. Part of this figure was created with BioRender.com.

3.5. Discussion

ChipCytometry is a powerful imaging-based multiplex cytometry platform for explorative immunophenotyping and is advertised to overcome some limitations other cytometric methods have (137). ChipCytometry, for example, allows long-term storage of samples and their re-analysis even after project completion (138). When using ChipCytometry to analyse cell suspensions, several unresolved platform-specific technical problems and limitations were encountered, however. In this study, many of these problems were overcome to establish ChipCytometry as a truly viable technique.

One of the problems encountered was a fluorescent haze that appeared during the acquisition of stained samples. This haze was not observable on the background images, appeared only after sample staining and could be removed by photobleaching. Providing a continuous flow of PBS across the chip during data acquisition could prevent the appearance of the haze (Figure 3-3). A possible explanation for this issue could be the local accumulation of unbound antibodies that had been trapped in the corners and edges of the microfluidic channel. Without the continuous PBS flow, trapped antibodies probably slowly diffused towards the central acquisition area of the chip. Upon request, the manufacturer confirmed that due to the microfluidic properties of the chips, which are a result of the interior chip design, the flow of liquid inside the chip is concentrated at the centre of the microfluidic channel. Exchanges with the areas at the edges of the chip chamber are apparently mainly achieved via diffusion, which is a very slow and inefficient process to clear unbound staining antibody.

A continuous flow of PBS is required across the sample during acquisition to prevent the appearance of a fluorescent haze, but spillages of PBS can damage the ChipCytometer instrument. Therefore, the manufacturer recommended the use of an extended washing protocol after sample staining to prevent the generation of a fluorescent haze during acquisition. The extended washing protocol was, however, not successful in preventing the appearance of the haze during data acquisition (data not shown). To prevent the instrument and chip being flooded with PBS in case of a blockage within the fluidic system, an adapter was engineered. Its purpose was to permanently connect the fluidic system with the chip inlet and to allow trapped air, which can cause blockages within the fluidic system, to escape. In the rare event of air still getting trapped and causing a blockage, the adapter redirected overflowing PBS to drip into a collection device below the chip, thus preventing the sample chip and the ChipCytometer instrument from being flooded with PBS. This solution was, however, not perfect, as the fluorescent haze immediately re-appeared in case the PBS flow was blocked, making the data from that cycle unusable. The best solution to this problem would be the development of a re-designed chip with improved microfluidic properties that

allow complete removal of staining antibodies during washing prior to sample acquisition, thereby eliminating the need for a continuous flow of PBS during data acquisition.

An improved chip design with improved microfluidic properties could also benefit other issues, such as inconsistencies of fluorescence intensity values of stained cells across a chip in both x- and y-direction. The issue regarding inconsistencies of fluorescence intensity values in y-direction is most likely caused by the reverse scenario of the fluorescent haze issue. Due to the microfluidic properties of the chip chamber, the highest concentration of injected staining antibodies is probably reached at the centre of the microfluidic channel where the main flow of liquid is occurring. The staining antibody reaches the edges of the chip interior most likely mainly through slow and inefficient diffusion. This issue was solved by placing the 44 chip positions that get imaged exactly in the centre of the microfluidic channel, resulting in relative consistent fluorescence intensity values between odd and even position numbers (Figure 3-6). The issue of staining inconsistency in x-direction was solved by improving the staining protocol. The staining antibody was first applied from the chip inlet and subsequently the sample was stained a second time by applying more antibody from the chip outlet (Figure 3-5).

Besides causing blockages of the fluidic system, air bubbles that can form in the fluidic system can also pass through the chip inlet and can get imaged while passing through the microfluidic chamber. This can result in aberrant fluorescence intensity values of local cells. Similarly, foreign particles such as fibres and dust can enter the microfluidic channel during the staining cycles and can cause fluorescence anomalies, for example, by being autofluorescent or by non-specifically binding staining antibodies (Figure 3-7, Table 3-1). Air bubbles and foreign particles are often not stationary on the chip but can change their location during or between acquisition cycles. During cell segmentation, the ChipCytometry software can detect and eliminate debris and cell clumps based on a reference cycle. This tool fails, however, to remove fluorescence anomalies caused by transient foreign particles or air bubbles, as they

can change their location between different cycles. Therefore, each recorded image of a ChipCytometry experiment needs to be visually screened for fluorescence anomalies and affected cells need to be manually removed from the cell segmentation. This process can be very time consuming. In some cases, the proprietary algorithm “surrounding pixel correction” during fluorescence intensity value calculation can mitigate the manifestation of fluorescence anomalies (Figure 3-7c).

Repeated photobleaching of samples was discovered to be a destructive process that can damage epitopes, especially when multiple rounds of photobleaching and imaging were involved (Figure 3-4). This is most likely caused by the ability of proteins to absorb high-energy light in the UV region which can result in damage of the protein structure (139, 140). In this study, the cumulative photodamage was limited by the installation of longpass filters in the white light filter module to block light at the lower end of the spectrum during the photobleaching step. The higher the cut-on wavelength of the installed longpass filter, the less destructive was the photobleaching. Therefore, longpass filters with a cut-on wavelength of >420 nm were better at limiting photodamage than the 364 nm longpass filter which was eventually provided by the manufacturer.

The use of filters in the white light module had two disadvantages, however. First, the 493 nm longpass filter prevented optimal photobleaching of the BUV395 and BV421 channel through the white light filter module. Photobleaching these channels individually through corresponding filter modules instead of using the white light filter module still caused some degree of photodamage and added considerable extra time to the photobleaching procedure. Because of the issues associated with the BUV395 and BV421 channels, including the challenges of photobleaching these channels, the observation that samples can gradually acquire autofluorescence in the BV421 channel (Figure 3-2), and the fact that BUV395 can slightly bleed into BV421 (Figure 3-9), the general use of BUV395 and BV421 was abandoned except for barcoding purposes.

Secondly, the higher the cut-on wavelength of the installed longpass filter, the longer was the required time to photobleach samples. Consequently, the installation of the 493 nm longpass filter affected the sample throughput negatively. With this filter installed, PE required on average a single photobleaching cycle of 40 seconds per position to be photobleached, whereas FITC and PerCP/PerCP-Cy5.5 required on average at least 2-3 x 40 seconds of photobleaching per position. In addition, many markers only worked when conjugated to PE, which is the brightest of those fluorochromes. This resulted in an average of around 1.5 markers being used per acquisition cycle instead of the theoretically possible 5 markers.

To increase sample throughput, samples were multiplexed with fluorescent barcodes by staining different samples with CD45 antibodies that are conjugated to different fluorochromes (Figure 3-9). With combinations of 5 dyes, highly complex multiplexing strategies could be achieved to theoretically allow the analysis of up to 31 different samples on a single chip. In practice, the benefit of sample multiplexing for the increase of sample throughput is limited by the total number of cells that can be loaded onto the surface of a standard cell suspension chip (up to 250,000 cells according to the manufacturer). In this study, the optimal density for PBMCs was found to be approximately 100,000 – 150,000 cells per chip. It is possible to achieve higher cell densities, which can, however, cause cells stacking on top of each other and fluorescence signals from saturated positive cells spilling over onto adjacent cells, leading to a decrease in data quality. For experimental design, it should also be considered that samples which are to be compared with each other are placed on the same chip, as there may be significant batch effects between different chips.

ChipCytometry has a very slow acquisition speed. A hypothetical experiment in which a chip containing 125,000 cells is analysed with a 40-marker panel takes about 80 hours to execute. The resulting acquisition speed is about 0.43 events/second. This differs from the advertised acquisition speed of 2000 events/second. The advertised number of 2000 events/second might correctly reflect the time needed to take a single picture of one of the 44 chip positions

that covers an area including approximately 2000 cells. But that number does not reflect the time required to photobleach each position for at least 40 seconds and to record transmitted light, fluorescence and background images of each chip position separately for each marker in the panel. The iterative nature of both the accumulation of multiple markers on sample and the acquisition of multiple chip positions to obtain sufficient cell numbers for data analysis is the reason for the low sample throughput of single-cell suspension ChipCytometry. This is a major limitation of ChipCytometry, as other cytometry methods such as flow cytometry and mass cytometry can achieve much higher acquisition speeds of up to 5,000-35,000 and 1,000 events/second, respectively (141). In addition, advances in technology have made standard flow cytometry capable of measuring high-dimensional fluorescent antibody panels of up to 28 markers (142). Other cytometry methods such as spectral flow cytometry and mass cytometry can acquire panels between 40 and 50 markers (143, 144). Therefore, high-dimensional data acquisition of single cells is not a unique feature of ChipCytometry.

An advantage of ChipCytometry compared to other cytometry methods is, however, the option to store samples for up to 20 months without significant biomarker degradation, which allows samples that have previously already been analysed to be re-interrogated with new markers and provides the potential for biobanking (138). Therefore, ChipCytometry could have its unique utility in the analysis of rare and precious samples, as the analysis with alternative methods such as mass cytometry result in sample destruction. As rare samples are often associated with low cell quantity, the standard chip loading protocol might need to be adapted and optimised, because about up to 85 - 92.5% of cells are lost during chip loading (the standard loading protocol requires to load 100 - 200 µL of 1 x 10^7 viable cells/mL, which corresponds to a total cell number of 1 - 2 x 10^6 cells and results on average in about 1.5 x 10^5 adhered cells on the chip). To limit the loss of cells during the loading of rare samples onto the chip, smaller volumes of higher concentrated cell suspensions could be directly injected into the microfluidic chamber of the chip using a syringe.

In summary, ChipCytometry was developed as a truly viable technique in this study. Several technical problems and limitations of the ChipCytometry technique were identified and many of those issues were overcome. The relatively low sample throughput for the analysis of cell suspensions was found to be a major disadvantage of this technique. An important advantage of this technique is, however, the ability to store samples long-term providing the potential for biobanking and allowing re-analysis of samples even after project completion, which is particularly useful for the analysis of rare samples. In addition, ChipCytometry is capable of analysing tissue sections. For the analysis of tissue sections, only a small area of interest consisting of a few adjacent chip positions is usually scanned instead of 44 chip positions in the analysis of cell suspension chips. Therefore, a higher sample throughput could be achieved for the analysis of tissue sections.

3.6. Summary

1. ChipCytometry is an imaging-based multiplex immunophenotyping method
2. Several technical problems and limitations of the ChipCytometry method were identified as summarised in Table 3-2
3. Many of the problems were overcome and ChipCytometry was developed as a truly viable cytometry method (Table 3-2)

Table 3-2. Technical problems and limitations of ChipCytometry and possible solutions.

Problem	Solution
Gradually increasing auto-fluorescence in the BV421 channel over time.	Use of BV421 only for barcoding purposes or as long as a negative and positive population is clearly distinguishable.
Fluorescent haze appears during acquisition of stained samples.	Supply of a continuous flow of PBS across samples during image acquisition.
Blockages of the fluidic system flood the chip and the ChipCytometer instrument with PBS.	Engineer and 3D-print adapters that allow trapped air, which can cause blockages within the fluidic system, to escape. In the rare event that a blockage still occurs, the adapter has to be designed to divert overflowing PBS into a collection device.
Repeated photobleaching cycles (UV light exposure) render samples unstainable.	Installation of a longpass filter in the white light filter module to block damaging wavelengths in the UV range during photobleaching.
Inconsistent staining intensity across stained chips (x-direction).	Staining protocol optimization: bi-directional application of staining antibodies.
Inconsistent staining intensity across stained chips (y-direction).	Change of the default instrument settings: Acquisition area on chips has to be precisely centred.
Fluorescence anomalies.	(1) Visual inspection of all recorded images and manual removal of affected cells from the data. (2) Enable the setting “surrounding pixel correction” during fluorescence value calculation, which can mitigate the manifestation of fluorescence anomalies in certain cases.
Antibody filtration, which is performed to remove any contaminants in the stock solution, can cause a granular background on acquired images.	Use PVDF instead of CA filters for filtration.
Excess of staining antibody causes poor distinction between positive and negative cells.	Precise optimisation of antibody dilutions.

4. DEFINING T-CELL SUBSETS IN HUMAN TONSILS USING CHIPCYTOMETRY (PROOF-OF-PRINCIPLE)

4.1. Introduction

Many novel technologies have recently emerged for multi-parameter cytometry analysis of cells and tissues, offering the exciting prospect of visualising cellular phenotyping within a spatial context. These methods utilise a variety of immunostaining methodologies applied to fluorescence microscopy or mass-spectrometry imaging techniques to acquire information on the expression of multiple markers. Each method has its own advantages and disadvantages. For example, the number of markers that can be assessed on a single sample, the sample processing time and throughput, the commercial availability of reagents, operating costs and system purchasing costs are system-specific (145–149).

ChipCytometry is an imaging-based multiplex immunophenotyping method where samples, either cell suspensions or tissue sections, are immobilised on slides inside a microfluidic chip (137). Through consecutive and iterative cycles of staining with fluorochrome-labelled antibodies, imaging and subsequent photo-bleaching, a theoretically unlimited number of markers can be measured on a single sample. Advantages of ChipCytometry over other methods include that samples are preserved after analysis and can be stored for at least 20 months without significant degradation (138). This allows re-analysis with additional markers, or sample collection and storage at different sites with subsequent centralised analysis. In addition, the development of a panel of markers is relatively straightforward using standard flow cytometry antibodies. Combinations of up to five fluorochromes can be used for each cycle.

Lymphoid palatine tonsil tissue, which is very rich in immune cells and has a well-established and distinct architecture, was employed to explore the feasibility of using ChipCytometry for

immune-phenotyping. Palatine tonsils are secondary lymphoid tissues that belong to the Waldeyer's ring, which further includes the adenoids and tubal and lingual tonsils (150, 151). They are located at the transition between the mouth and oropharynx and are a part of the mucosal-associated lymphoid tissues (152, 153). The tonsils are covered by an epithelium that increases the tonsil surface by forming crypts, in which specialised cells can take up antigen and transport it to subepithelial areas where it can get in contact with immune cells (152, 154). The immune cells are organised in two major zones within the tonsils: B cell follicles and the extrafollicular region in which T cells and B cells become activated. Lymphoid follicles contain B cells and are therefore characterised by CD19 expression. Primary lymphoid follicles do not have a germinal centre (155). Secondary lymphoid follicles consist of a mantle zone including naive (IgD^+CD10^-) B cells; they also contain a germinal centre including germinal centre (IgD^-CD10^+) B cells (156, 157). Germinal centres are places of B cell proliferation, differentiation and maturation (155). Besides B cells, lymphoid follicles also contain a network of stromal-derived follicular dendritic cells, which are important for antigen presentation to B cells (158). Additionally, B cell follicles contain T cells that are critical for the humoral immune response (159). The extrafollicular region (also called the T-cell zone) contains T cells which are primarily $CD4^+$ T cells with fewer $CD8^+$ T cells. Besides T cells, the extrafollicular region includes interdigitating dendritic cells, macrophages and high-endothelial venules. The latter are specialised venules that allow circulating lymphocytes to enter the lymphoid tissue (155).

Tonsillar $CD4^+$ T-cell subsets can be divided into 3 major groups (160). Most intrafollicular T cells belong to the follicular B-helper T cell group (TFH, $CD4^+PD1^+CXCR5^+BCL6^{high}$) (159, 160). B cell and TFH cell interactions are crucial for the formation of the humoral immune response and support B cell somatic hypermutation and antibody class switching (159, 161). Other tonsillar $CD4^+$ T-cell subsets include non-TFH ($CD4^+PD1^-CXCR5^-BCL6^{low}$) and pre-TFH ($CD4^+PD1^+CXCR5^-BCL6^{mid}$). Pre-TFH cells develop from activated antigen-specific

$CD4^+$ T cells. The transcriptional program that is initiated in pre-TFH cells can induce CXCR5 expression enabling the cells to migrate towards the B-cell follicle (160, 162).

Most $CD4^+$ and $CD8^+$ T cells that enter palatine tonsils are naive cells competing for antigen in order to reach maturity (152, 155), but there are also unconventional T-cell subsets found within the tonsil, for example, innate-like T cells including MAIT and γδT cells (163–165). MAIT cells are memory-type and antigen-experienced cells with peripheral tissue homing properties (84, 87). They are characterised by their semi-invariant TCR that recognises microbial-derived riboflavin metabolites presented by a conserved MHC-Class I-like molecule called MR1 (79, 80). MAIT cells can, however, also be activated in a TCR-independent manner by cytokines such as IL-12, IL-18 and IL-15 (65, 81). Most MAIT cells are $CD8^+$ or DN in blood. They can be identified by tetramer staining or using a combination of markers including Vα7.2 and CD161 (88, 92). MAIT cells also express the innate-like marker CD218a (IL-18Rα) and the transcription factor PLZF (88). MAIT-cell selection and development begins in the thymus and MAIT cells are thought to acquire their memory antigen-experienced phenotype via contact with microbes in the periphery (166). MAIT-cell frequencies in tonsil are approximately 10 times lower than in blood (163). MAIT-cell responses play multiple roles in infection, inflammation and cancer (81, 167, 168).

In order to establish the utility of the ChipCytometry technique, using both cell suspensions and tissue sections, we aimed to depict the general tonsil architecture, showing different tonsillar regions and sub-compartments. We localised and phenotyped immune subsets including follicular $CD4^+$ T-cell subsets and rarer immune cells such as MAIT cells and finally analysed data obtained from ChipCytometry of cell suspensions for more stringent phenotyping of immune subsets.

4.2. Aims

1. Explore the feasibility and utility of using ChipCytometry to identify and phenotype cell subsets in both tissue sections and cell suspensions
2. Demonstrate the general histological architecture of human tonsils using ChipCytometry
3. Identify and characterise tonsillar immune sub-compartments and immune subsets such as the B-cell mantle and germinal centre zone and intrafollicular $CD4^+$ TFH cells
4. Identify, localise and phenotype rare tonsillar T-cell subsets such as MAIT cells

4.3. Chapter-specific materials and methods

4.3.1. Tissues and cells

Human tonsillar tissue was obtained from routine tonsillectomies collected by the Translational Gastroenterology Unit (TGU) Biobank, John Radcliffe Hospital, Oxford, following informed consent under approved study protocol 16/YH/O247. Tissue sections were prepared by snap freezing samples in OCT cutting medium (OCT embedding matrix, CellPath) and cryosectioning onto glass coverslips. Single-cell suspensions were prepared by mechanical disruption of tonsil samples.

4.3.2. ChipCytometry of cell suspensions

ChipCytometry was performed as described in GENERAL MATERIALS AND METHODS- 2.5, with the following changes: Samples were fixed (Fixation buffer, Zellkraftwerk, Leipzig, Germany) for 5 minutes at RT. For the staining of surface markers, antibody mixes were first applied through the chip inlet and incubated for 5 minutes at RT and subsequently additional staining solution was applied for 5 minutes through the chip outlet. Staining for intracellular markers was performed similar to surface staining but with prolonged incubation of 2 x 15 minutes. The applied antibody panel, including extracellular and intracellular markers, is detailed in Table 4-1 and Table 4-2, respectively.

Table 4-1. Extracellular markers for ChipCytometry cell suspension staining. Markers that are sensitive towards repeated cycles of photobleaching are indicated with an asterisk and should be stained early in the process.

	Marker	Clone	Label	Manufacturer
1	**CD3**	UCHT 1	PerCP-Cy5.5	BioLegend
2	**CD4**	RPA-T4	FITC	BioLegend
3	**CD8α**	SK1	PerCP-Cy5.5	BioLegend
4	**CD19**	LT19	PE	Miltenyi
5	**CD44**	DB105	PE	Miltenyi
6	**CD45**	HI30	FITC, PE, PerCP	BioLegend
7	**CD45RA**	HI100	PerCP-Cy5.5	BioLegend
8	**CD56***	AF12-7H3	PE	Miltenyi
9	**CD69**	FN50	PE	BioLegend
10	**CD161**	191B8	PE	Miltenyi
11	**CD178 (FAS-L)***	NOK-1	PE	BioLegend
12	**CD185 (CXCR5)**	J252D4	BV421	BioLegend
13	**CD218a (IL-18Ra)***	H44	PE	BioLegend, eBioscience
14	**CD278 (ICOS)**	C398.4A	PerCP-Cy5.5	BioLegend
15	**CD279 (PD-1)**	eBioJ105	PE	eBioscience
16	**TCR Vα7.2**	3C10	PE	BioLegend

Table 4-2. Intracellular markers for ChipCytometry cell suspension staining.

	Marker	Clone	Label	Manufacturer
1	**BCL6**	REA373	PE	Miltenyi
2	**Granzyme B**	GB11	PE	eBioscience
3	**FOXP3**	259D/C7	PE	BD Biosciences

4.3.3. ChipCytometry of tissue sections

Cryosections were cut directly onto polylysine or APES-coated coverslips (Sigma-Aldrich) and fixed immediately using freshly prepared 0.1M phosphate buffered 4% PFA (Sigma-Aldrich) or Zellkraftwerk fixation buffer (Zellkraftwerk, Leipzig, Germany) for 10 minutes at RT. After washing in PBS, sections on coverslips were assembled into tissue chips

(Zellsafe Tissue – Chips, Zellkraftwerk, Leipzig, Germany) which were immediately filled with PBS or storage buffer (Zellkraftwerk, Leipzig, Germany). Before use, the storage buffer was washed out of the chip with approximately 5 ml of PBS. Tonsil sections were initially blocked by incubating in 3% normal goat serum with 2% BSA (Thermo Fisher) in PBS for at least 1 hour at RT. Immunostaining was performed at RT for 30 minutes using 0.5 ml of diluted antibody solution per chip. Antibody cocktails were diluted in PBS alone or PBS containing 2% BSA or 2% normal goat serum. A total of 12 markers were acquired in iterative rounds of photo-bleaching, staining and imaging: CD3, CD4, CD8, CD10, CD19, CD161, γδTCR, IgD, PD1, PLZF, Vα7.2 and histone H3 (not shown). For antibody details please see Table 4-3.

Table 4-3. Markers for ChipCytometry tissue section staining.

	Marker	Clone	Label	Manufacturer
1	**CD3**	UCHT1	PerCP	BioLegend
2	**CD4**	RPA-T4	PerCP	BioLegend
3	**CD8**	SK1	FITC	BioLegend
4	**CD10**	HI10a	PE	BioLegend
5	**CD19**	LT19	PerCP	ExBio
6	**CD161**	HP-3G10	PE	eBioscience
7	**CD279 (PD-1)**	eBioJ105	PE	eBioscience
8	**IgD**	IA6-2	PerCP	BioLegend
9	**Histone-H3**	17H2L9	AF488	Invitrogen
10	**PLZF**	R17-809	PE	BD Pharmingen
11	**TCR gamma/delta (γδTCR)**	5A6.E9	FITC, PE	Life Technologies
12	**TCR Vα7.2**	3C10	PE	BioLegend

4.3.4. Data processing and statistical methods

Data analysis was performed as described in chapter 2 GENERAL MATERIALS AND METHODS with the following specifics: For supervised manual gating analysis of flow cytometry and ChipCytometry data, biexponential transformation was applied in FlowJo. For unsupervised clustering analysis, ChipCytometry cell suspension data was first transformed and pre-processed in FlowJo and then exported to R. The data was transformed using HyperLog transformation. The parameters of this transformation were adjusted and rescaling was performed so that for each marker the distribution spanned the whole dynamic range. The transformed data was binned into integer histogram channels ranging from 0 to 1023. Outliers and fluorescence anomalies outside the axis limits after transformation were assigned to either the minimum or maximum value. All datapoints with an assigned value of 0 or 1023 after the transformation were removed from further analysis. An exception was made for CXCR5, which was transformed using logarithmic transformation, because suitable rescaling could not be achieved with HyperLog in FlowJo. Data was pre-processed by excluding $CD19^+$ cells and gating on $CD3^+$ cells in FlowJo. FlowSOM R package (35) was used to identify cell clusters within the data set using all markers except for CD45 (used for barcoding), CD3 and CD19 (used for gating during pre-processing). Parameters chosen were: self-organizing map (SOM) grid = 10 x 10, seed = 1234. The resulting SOM nodes were used in the R package ConsensusClusterPlus to obtain the final optimal clusters (36). A delta area plot was created with a maximum of k = 20 metaclusters, which indicated cluster stability at a metacluster number of k = 12. Cluster information for 12 metaclusters was exported and data was further analysed in FlowJo for visualisation, including t-distributed stochastic neighbour embedding (t-SNE) analysis (settings: FIt-SNE, iteration = 3000, perplexity = 50, KNN algorithm = Exact, learning rate = Auto (opt-SNE)). For cluster characterisation, the distribution of the intensity of each marker was considered in each cluster and the median value taken [median marker expression]. This was displayed as heatmap using pheatmap package. In addition to comparing median marker expression directly, Marker Enrichment

Modeling (MEM) was performed for cluster characterisation using the R package MEM (37, 38).

4.3.5. Image processing

Images for publication were downloaded from the ChipCytometer as 16-bit uncompressed TIFF files and converted to 8-bit per channel RGB TIFF files in ImageJ/Fiji (version1.5). Scale bars were added in Adobe Photoshop CS4 according to the metadata stored with the image. Images were cropped, annotations (arrows, text etc.) were added, and brightness and contrast adjusted as necessary in Photoshop. Files were exported as flattened 300 dpi TIFF files with LZW compression. Files of each image processing stage were saved.

4.4. Results

4.4.1. Defining tonsillar architecture in humans using tissue ChipCytometry

A panel of 12 antibodies was employed to establish the anatomy of the palatine tonsil by ChipCytometry. A combination of T-cell markers (CD3, CD4, CD8) and B-cell markers (CD19, CD10, IgD) were chosen to depict general palatine tonsil architecture (Figure 4-1, Appendix Figure II-1a, Appendix Figure II-2a). Specifically, the lymphoid follicle zone (B-cell zone) was defined by CD19 expression and could be further characterised by the differential expression of IgD and CD10. Naive B cells (IgD^+CD10^-) are mainly located in the B-cell mantle zone, and germinal centre B cells (IgD^-CD10^+) are located in the B-cell germinal centre zone (156, 157). The extrafollicular zone (T-cell zone) adjacent to the B-cell zone was defined by CD3 expression. $CD3^+$ T cells included CD4-expressing and CD8-expressing cells. A few $CD3^+$ T cells could also be found within the B-cell zone.

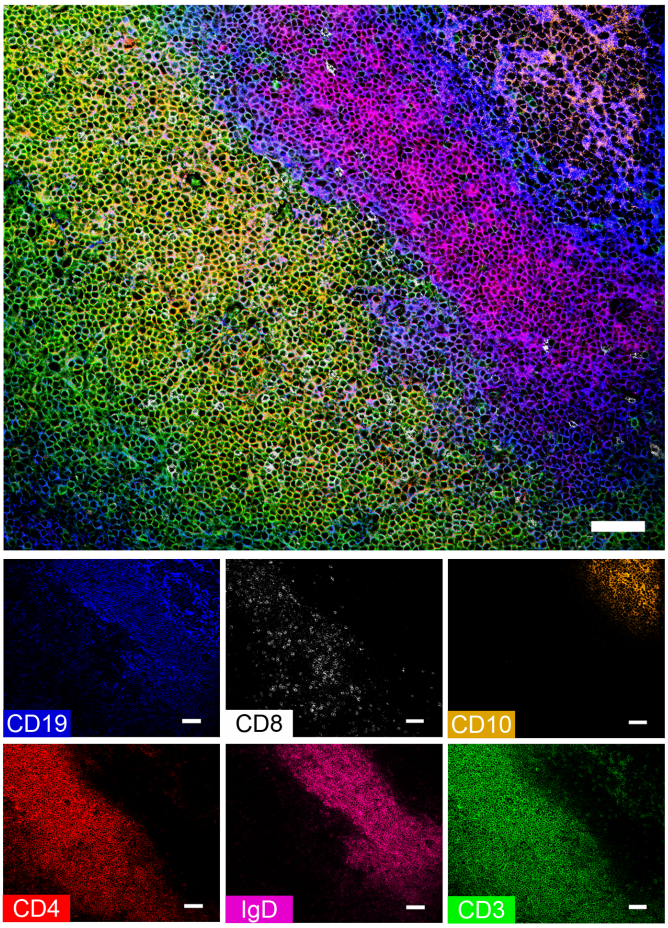


Figure 4-1. Human tonsil architecture resolved using ChipCytometry. Sections of PFA-fixed human tonsil tissue mounted in microfluidic chips were immunostained in consecutive runs using a panel of 12 fluorochrome-labelled antibodies. The top image was compiled by selecting six markers; CD19 (blue), CD8 (white), CD10 (orange), CD4 (red), IgD (magenta) and CD3 (green), assigning colours arbitrarily from the lookup table and merging to form a composite image. Expression of individual markers is shown in the small panels. The B-cell zone (B-cell follicle) is characterised by CD19 expression, in which IgD outlines the mantle zone containing IgD-expressing naive B cells, and CD10 outlines the germinal centre containing $CD10^+$ germinal centre B cells. Adjacent to the B-cell zone, CD3 expression outlines the T-cell zone (extrafollicular zone), including $CD4^+$ and $CD8^+$ T cells. Scale bars represent 50 µm.

4.4.2. Identification of CD4 T-cell subsets in human tonsils

From the full panel of 12 markers, a combination of CD3, CD4, PD1 and CD19 staining was chosen to identify palatine tonsillar T-cell subsets expressing PD1 (Figure 4-2**,** Appendix Figure II-1b, Appendix Figure II-2b). CD3 expression was concentrated within the extrafollicular T-cell zone; however, some intrafollicular $CD3^+$ T cells were identified. Many of those intrafollicular T cells were $CD4^+$ and $PD1^+$. A few rare $CD4^+PD1^+$ T cells could also be found within the extrafollicular region (T-cell zone). Tonsillar $CD3^+CD4^+PD1^+$ T cells most likely include Pre-TFH and TFH subsets (160) as opposed to $CD3^+CD4^+PD1^-$ cells that most likely include non-TFH cells. Examples of some of the many $CD3^+CD4^+PD1^+$ T cells are indicated in Figure 4-2 and Appendix Figure II-1b by white arrowheads.

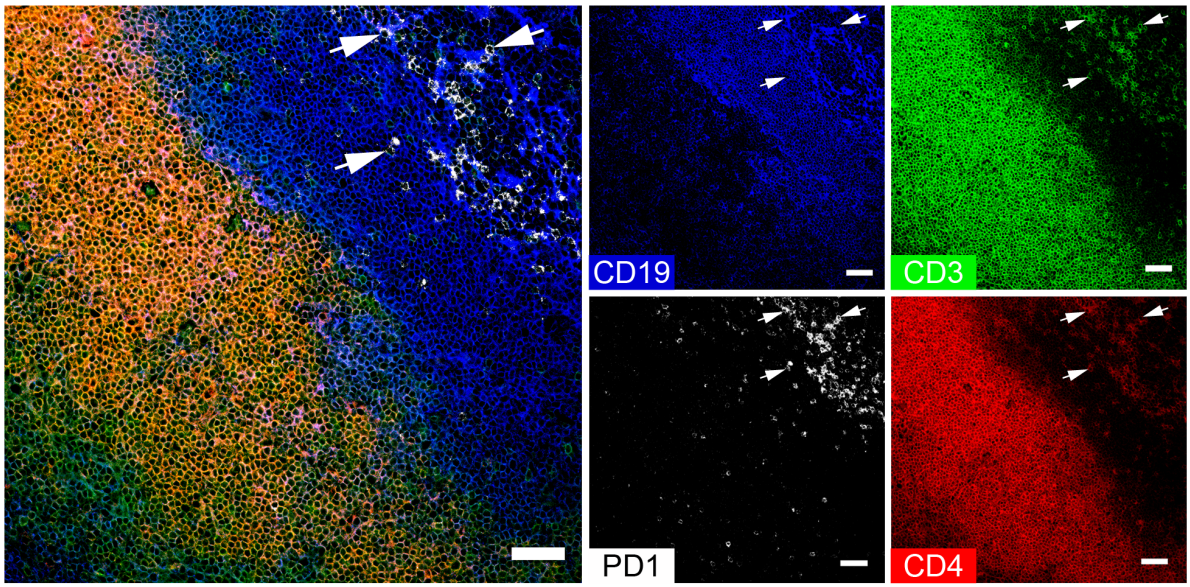


Figure 4-2. Identification of CD4⁺ T-cell subsets in human tonsils. A combination of CD4, CD19, CD3 and PD1 were chosen from the full marker panel to identify CD4⁺ T cells in the tonsil. The large multicolour composite image shows a merged image of CD19 (blue), CD3 (green), PD1 (white) and CD4 (red), while the smaller images demonstrate the expression of each marker individually. The T-cell zone is characterised by CD3 expression and includes CD4⁺ T cells; CD3⁺CD4⁺ cells appear yellow / orange in combination. PD1-expressing CD3⁺CD4⁺ are predominantly located in the B-cell zone, but a few are also located in the T-cell zone. This subset most likely includes pre-TFH and TFH cells. CD3⁺CD4⁺PD1⁻ cells are predominantly located in the extrafollicular region and include non-follicular T helper cells (non-TFH). White arrowheads indicate examples of CD3⁺CD4⁺PD1⁺ cells. Scale bars represent 50 µm.

4.4.3. Identification and phenotyping of tonsillar CD3 T-cell subsets by cell suspension ChipCytometry

To identify and phenotype tonsillar CD3 T-cell subsets, cell suspensions produced by dissociation of human palatine tonsil tissue were enriched for $CD3^+$ T cells (N=4). Cells from each donor were barcoded with CD45-antibodies coupled to different fluorochromes, allowing individual donors to be distinguished in the pooled samples. A staining panel consisting of the following 19 markers was used: BCL6, CD3, CD4, CD8, CD19, CD44, CD45, CD45RA, CD56, CD69, CD161, CXCR5, FASL, FOXP3, Granzyme B (GzmB), ICOS, IL-18Rα (CD218a), PD1 and Vα7.2. T-cell subsets were identified via unsupervised clustering using FlowSOM, a method based on Self-Organising-Map clustering (169, 170), and visualised using t-SNE (Figure 4-3a). ConsensusClusterPlus was used to estimate the optimal number of clusters within the data set, and FlowSOM clustering was performed into 12 groups (Figure

4-3b). As the process for labelling cell clusters is not established, a layered approach for cluster labelling was applied, using median marker expression together with marker enrichment modeling in a semi-supervised manner in addition to gating in FlowJo (Figure 4-3c, Appendix Figure II-3a, b). The identified $CD3^+$ T-cell subsets included various $CD4^+$ T-cell subsets, $CD8^+$ T-cell subsets and unconventional, innate-like T-cell subsets such as MAIT cells. One naive $CD4^+CD45RA^+$ T-cell subset (cluster 4) and two $CD4^+CD45RA^-$ subsets were found. The two $CD4^+CD45RA^-$ subsets differed in regard to CD44 expression (cluster 2 = $CD44^+$, cluster 9 = $CD44^-$). Each of these subsets comprised about 10% of total T cells. Additionally, three subsets were found that contained $CD4^+$ T cells expressing CD161, which is a marker generally associated with innate-like and memory cell types (68). Those were $CD161^+CXCR5^-CD69^+ICOS^+CD45RA^-$ (cluster 6, about 10% of total T cells), $CD161^+CXCR5^+IL\text{-}18R\alpha^+CD69^+PD1^+ICOS^+CD45RA^-$ (cluster 12, 0.47% of total T cells), and $CD161^+CXCR5^+IL\text{-}18R\alpha^+CD69^+PD1^+ICOS^+CD45RA^+$ (cluster 3, 1.33% of total T cells). The latter included besides $CD4^+$ T cells also a substantial fraction of DP T cells and showed lower levels of CD161, CXCR5, IL-18Rα, CD69, PD1 and ICOS expression compared to cluster 12. Other $CD4^+$ T-cell subsets included $FOXP3^+$ cells, which represent the Treg population (cluster 7, 1.69% of total T cells) and pre-follicular / follicular CD4 T helper cells (cluster 11, $CD4^+CXCR5^{+/-}PD1^+ICOS^+CD69^+$) which comprised 37.53% of total T cells. In addition to CD4 T-cell subsets, a naive $CD8^+CD45RA^+$ subset (cluster 5, approx. 10% of total T cells) and two $CD8^+CD45RA^-$ subsets were found. Of the $CD8^+CD45RA^-$ subsets, one was $GzmB^+$ (cluster 10, 1.12% of total T cells) and the other was $GzmB^-$ (cluster 8, 3.55% of total T cells), respectively. There was also a cluster that contained $CD161^{++}$ T cells including MAIT cells ($CD161^{++}V\alpha7.2^{+/-}IL\text{-}18R\alpha^+CD69^+$, cluster 1, 0.38% of total T cells), which were either $CD8^+$ or DN. The expression of the 16 phenotyping markers that were used for clustering are displayed on t-SNE plots in Figure 4-3d.

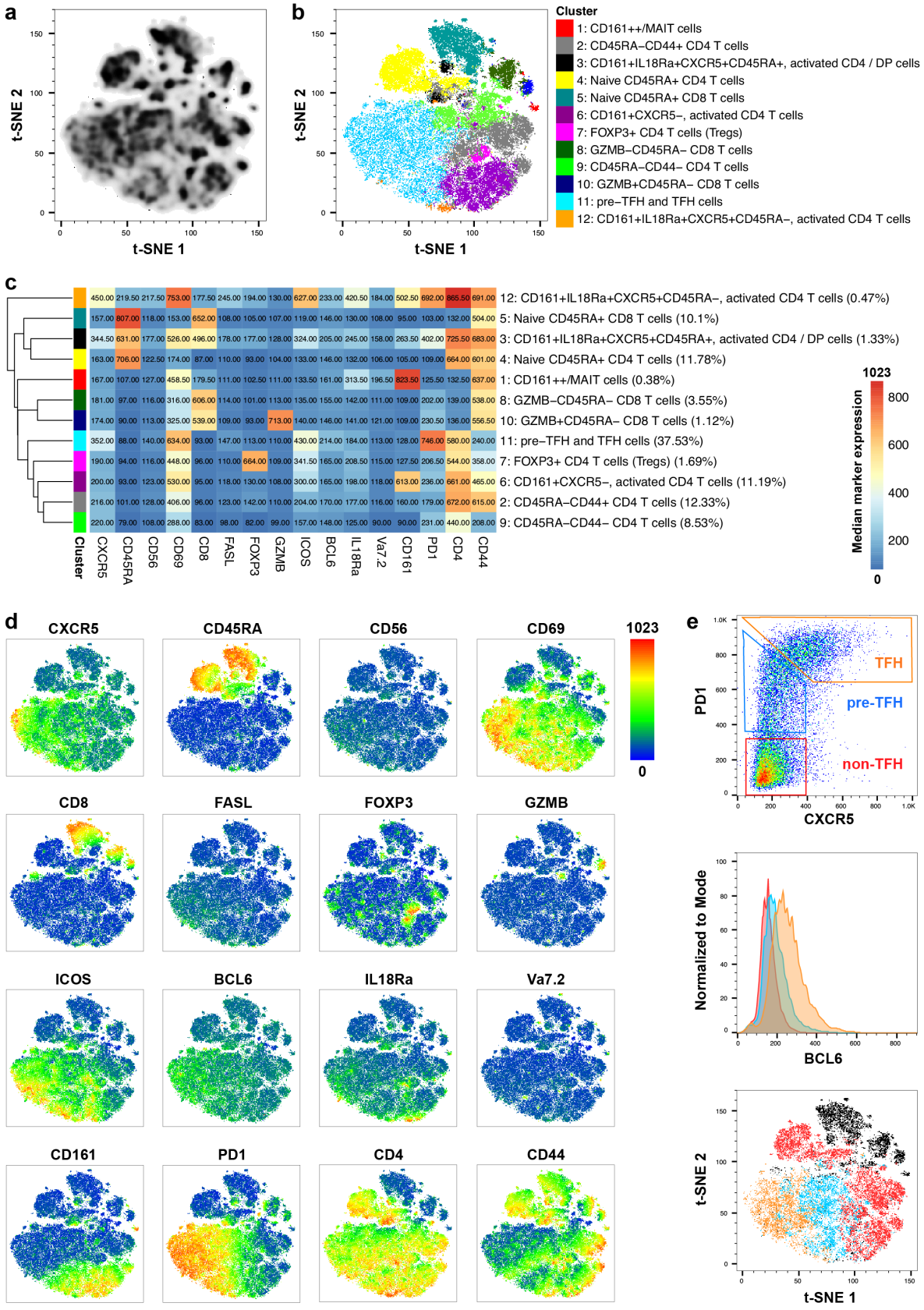


Figure 4-3. Phenotyping of tonsil-derived CD3-enriched cells by cell suspension ChipCytometry. Four human tonsils were processed to single-cell suspensions, positively enriched for CD3⁺ T cells, barcoded, loaded onto a microfluidic chip, fixed and subsequently analysed by ChipCytometry with a panel of 19 fluorochrome-labelled antibodies. (a) Density plot shows t-SNE analysis of concatenated samples including all

$CD3^+CD19^-$ cells. (b) Clusters that were identified via FlowSOM were projected onto the t-SNE coordinates and color-coded as indicated. (c) A heatmap showing median marker intensities within each cell cluster was generated to characterise cell clusters and derive cell labels. The heatmap colour represents median marker expression across all 4 aggregated samples. (d) T-SNE plots show the expression of 16 markers within the aggregated samples. (e) Top panel: Within $CD4^+$ T cells, the subsets TFH, pre-TFH and non-TFH cells were identified according to expression of CXCR5 and PD1. Centre panel: BCL6 expression is shown within non-TFH (red), pre-TFH (blue) and TFH (orange) cell subsets in human tonsils. Bottom panel: T-SNE plot shows non-TFH (red), pre-TFH (blue), TFH (orange) and non-CD4 T cells (black). Plots in (e) are derived from one donor and are representative of 4 donors.

The data set was further analysed via manual gating to elaborate on the characterisation of PD1-expressing and follicular CD4 T-cell subsets. $CD4^+$ T cells were stratified according to PD1 and CXCR5 expression (Figure 4-3e) as previously shown by Thornhill et al. (160). The subsets included $CXCR5^+PD1^+$ TFH, $CXCR5^-PD1^+$ pre-TFH and $CXCR5^-PD1^-$ non-TFH cells. These cell types differed in BCL6 expression; TFH cells had the highest levels of BCL6 expression, pre-TFH intermediate levels of BCL6 expression, and non-TFH the lowest levels of BCL6 expression. These three CD4 subsets also segregated on the t-SNE plot. The analysis of tonsil-derived CD4 T-cell subsets showed that ChipCytometry was able to replicate the characterisation of TFH cells as previously described in the literature by Thornhill et al. (160).

4.4.4. Identifying rarer T-cell subsets in tonsils by tissue ChipCytometry including MAIT cells and γδT cells

Next, we aimed to identify and phenotype rare cell subsets within palatine tonsillar tissue. MAIT cells have been described as a rare cell subset within human palatine tonsil tissue (163, 164). This was confirmed by the analysis of 8 palatine tonsils of 6 different donors using flow cytometry (Figure 4-4a-b). MAIT cells were defined as $CD3^+CD8^+V\alpha7.2^+CD161^{++}$. The frequency of MAIT cells ranged from approximately 0.1 to 1 % of total CD8 T cells. This is 10-fold lower compared to blood (90). Interestingly, palatine tonsillar MAIT cells did not show typical lymphoid tissue homing marker expression CCR7 and CD62L (Figure 4-4c-d).

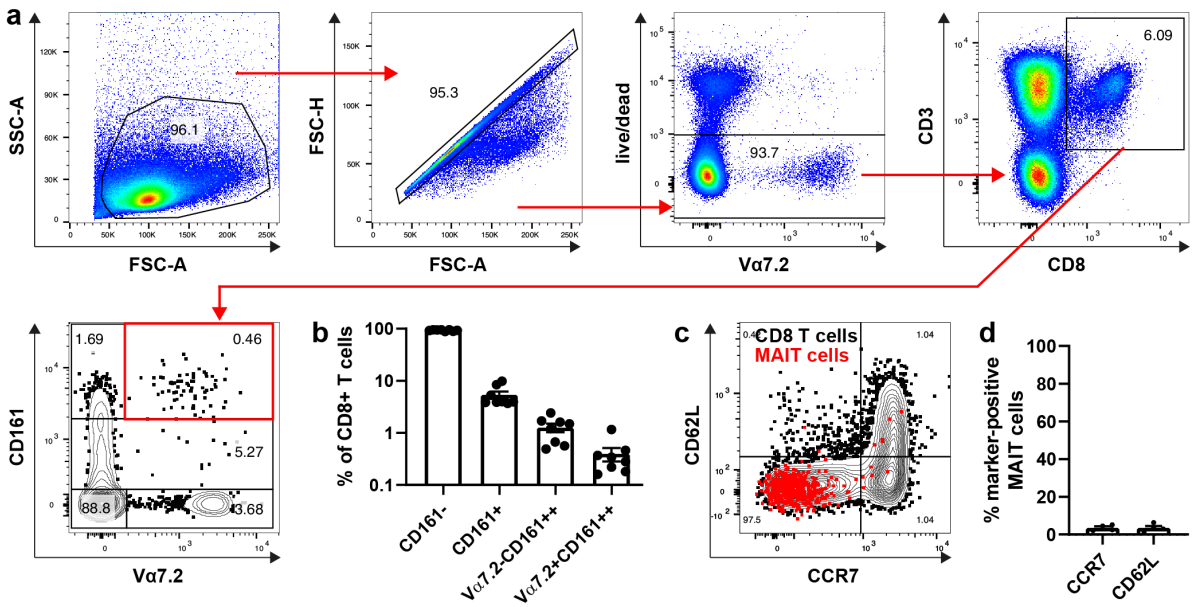


Figure 4-4. Flow cytometry identifies CD8⁺ MAIT cells as a rare subset within human tonsils. Human tonsils were processed to single-cell suspensions and analysed by flow cytometry. Stains included LIVE/DEAD™ Fixable dye, CD3, CD8, Vα7.2, CD161, CCR7 and CD62L. (a) Gating strategy is shown to identify CD8⁺ MAIT cells (Vα7.2⁺CD161⁺⁺) within tonsils. (b) Enumeration of CD8 T-cell subsets (8 tonsils from 6 donors). (c) CCR7 and CD62 expression of total CD8 T cells (black) and MAIT cells (red). The flow cytometry plot is representative of 4 biological replicates. (d) Enumeration of CCR7 and CD62L expressing MAIT cells (N=4).

MAIT cells were identified in palatine tonsil tissue sections by ChipCytometry using a combination of CD3, CD8, Vα7.2, CD161, PLZF and CD19 markers (Figure 4-5, Appendix Figure II-4). MAIT cells were defined as $CD3^{+}V\alpha7.2^{+}CD161^{+}PLZF^{+}$ cells. In Figure 4-5, all MAIT cells were $CD8^{+}$ and were located within the T-cell zone and adjacent to the B-cell zone (indicated by white arrows). In Appendix Figure II-4, $CD8^{+}$ as well as $CD8^{-}$ MAIT cells (a few examples are indicated by white arrows) were found side by side with another relatively rare tonsillar innate-like T-cell subset, the γδT cells (white arrows with asterisk). Interestingly, MAIT as well as γδT cells were not only found within the T-cell zone in the second example, but a few also adjacent and within the $CD19^{+}$ area.

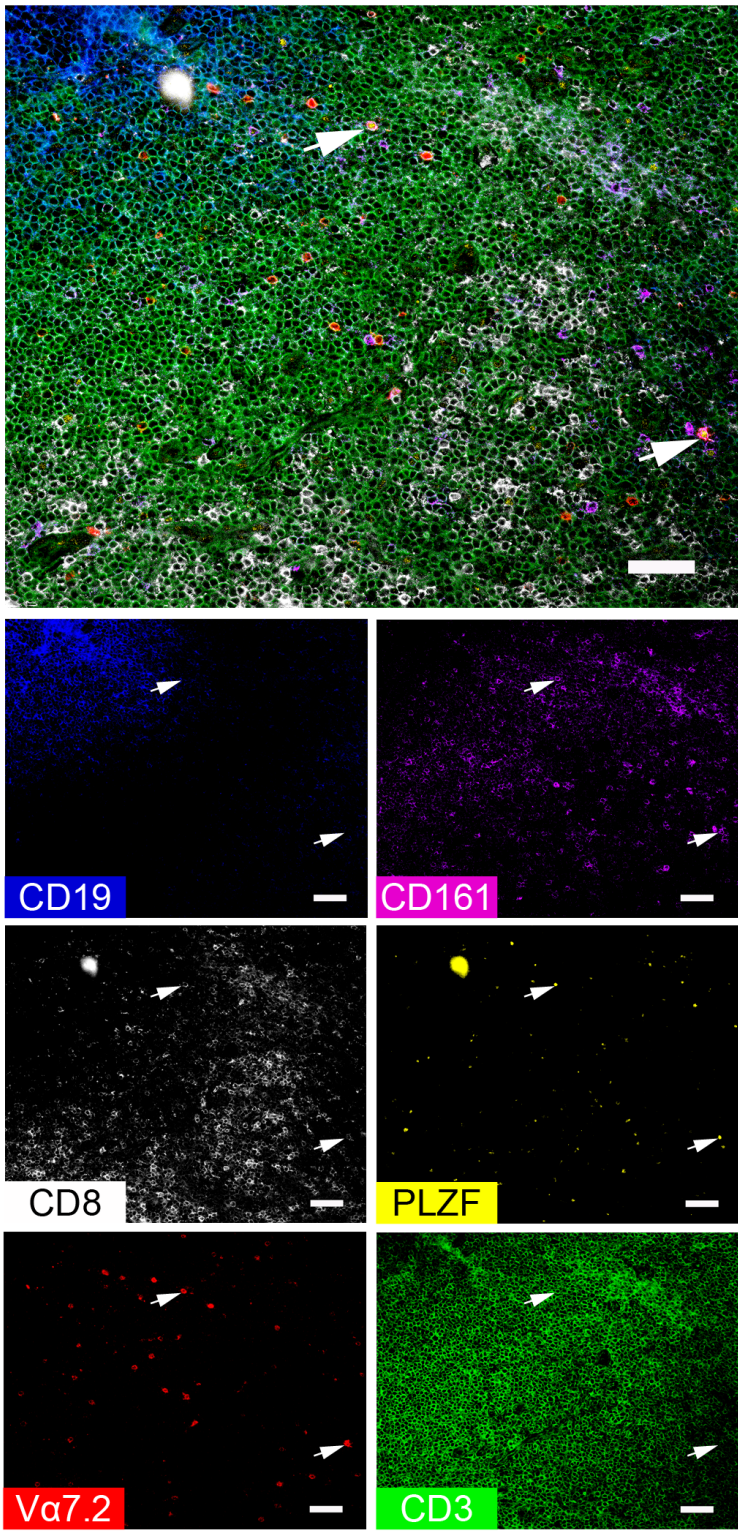


Figure 4-5. Identification of rare immune subsets in human tonsils. A combination of Vα7.2 (shown in red), CD8 (white), CD161 (magenta), PLZF (yellow), CD3 (green) and CD19 (blue) markers were selected from the available panel to illustrate the presence of MAIT cells within the tonsil. Single-colour images demonstrate the expression of each marker individually, while the larger image shows a merged composite of all six markers. White arrowheads indicate examples of cells that co-express CD3, CD8, Vα7.2, CD161 and PLZF, which represent $CD8^+$ MAIT cells. During the iterative staining process dust particles can be introduced into the microfluidic chip, generating autofluorescent artefacts such as those seen here at the top left of the CD8, PLZF and merged images. Scale bars represent 50 µm.

4.4.5. Identification and phenotyping of human tonsillar MAIT cells by cell suspension ChipCytometry

Besides the identification of $CD161^{++}$/MAIT cells within CD3-enriched tonsil-derived single-cell suspensions via unsupervised clustering (Figure 4-3b-c, Appendix Figure II-3),

4. Defining T-cell subsets in human tonsils using ChipCytometry

MAIT cells were identified and phenotyped by a traditional manual gating approach using the same data set (Figure 4-6a-f). After de-barcoding of the different donors (Figure 4-6a), MAIT cells were identified using the following gating strategy (Figure 4-6b, c): T cells were selected as $CD3^{+}CD19^{-}$ cells, and within this gate $CD4^{+}$, $CD8^{+}$ and DN T-cell subsets were identified. Within each of those subsets, MAIT cells were defined as $V\alpha7.2^{+}CD161^{++}$, and their frequencies were determined. The MAIT-cell frequencies within the $CD8^{+}$ T cells were similar to the frequencies observed in the flow cytometry experiment (Figure 4-4a-b). An approximately 6-fold higher frequency of tonsillar DN MAIT cells than tonsillar $CD8^{+}$ MAIT cells was identified using ChipCytometry (Figure 4-6d). Tonsillar $CD4^{+}$ MAIT cells numbers were negligible. The analysis of the expression of various phenotyping markers revealed that $CD8^{+}$ and DN MAIT cell subsets possess a similar phenotype (Figure 4-6e-f). Most MAIT cells were $CD69^{+}$, indicating an activated phenotype. In addition, most MAIT cells were $CD45RA^{-}CD44^{+}$, indicating a memory- and antigen-experienced phenotype. MAIT cells also expressed high levels of IL-18Rα, and about 30% of MAIT cells expressed the co-stimulatory receptor ICOS. There was only a very small fraction of $FASL^{+}$ and $GzmB^{+}$ MAIT cells. MAIT cells were considered negative for BCL6, CXCR5, PD1 and FOXP3. In summary, tonsillar MAIT cells were shown to have an activated memory phenotype ($CD44^{+}CD45RA^{-}CD69^{+}ICOS^{+}$) and to express typical innate-associated markers such as IL-18Rα. This correlates well with the generally accepted phenotype of MAIT cells described in the literature (68, 75, 90).

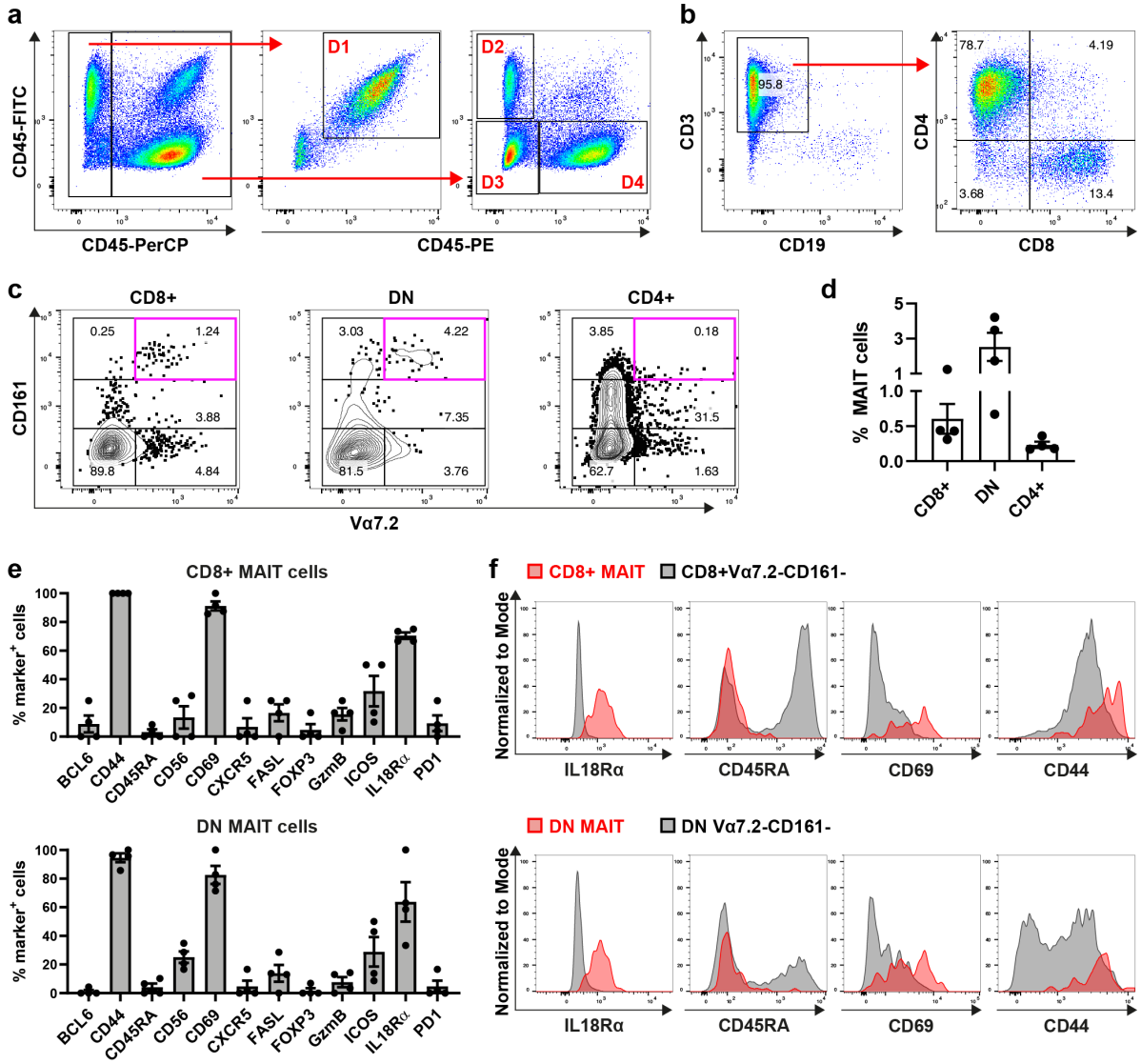


Figure 4-6. Identification and phenotyping of tonsillar MAIT cells using cell suspension ChipCytometry. Cell suspensions of four human tonsils were enriched for $CD3^+$ cells and analysed by ChipCytometry with a panel of 19 fluorochrome-labelled antibodies. (a) Pooled samples were de-barcoded to identify different donors. Barcodes consisted of combinations of CD45 antibodies that were labelled with different fluorochromes. Donor 1 (D1) = $PerCP^-FITC^+PE^+$, Donor 2 (D2) = $PerCP^+FITC^+PE^-$, Donor 3 (D3) = $PerCP^+FITC^-PE^-$, Donor 4 (D4) = $PerCP^+FITC^-PE^+$. (b) The following gating strategy was applied to identify MAIT cells: T cells were selected as $CD3^+CD19^-$ cells. Within this gate, subpopulations according to CD4 and CD8 expression were defined, including $CD4^+$, $CD8^+$ and DN T cells. (c) Within each T-cell subset, MAIT cells were identified by Vα7.2 and $CD161^{++}$ expression. (d) Enumeration of MAIT cells within T-cell subsets. (e) Phenotype of $CD8^+$ and DN MAIT cells. (f) Representative plots of IL-18Rα, CD45RA, CD69 and CD44 expression by $CD8^+$ and DN MAIT cells (red) compared to $Vα7.2^-CD161^-$ conventional T cells within $CD8^+$ and DN T cells, respectively.

4.5. Discussion

Using the palatine tonsil as a test case, it was demonstrated that ChipCytometry is a viable method which combines the power of traditional cytometry with the spatial information available from tissue sections. In this study, the immune cell compartments of the palatine

tonsil were demonstrated using tissue ChipCytometry, including the B-cell zone with its sub-compartments of naive (IgD^+CD10^-) and germinal centre (IgD^-CD10^+) B cells, and the T-cell zone (Figure 4-1, Appendix Figure II-1a, Appendix Figure II-2a). Within the $CD3^+$ T-cell compartment, multiple T-cell subsets were identified, for example $CD4^+PD1^+$ T cells, most of which were located within the $CD19^+$ B-cell zone, with a few cells present within the T-cell zone (Figure 4-2, Appendix Figure II-1b, Appendix Figure II-2b). More stringent phenotyping of tonsillar T cells was performed using cell suspension ChipCytometry, which allowed to identify two subtypes of $CD4^+PD1^+$ cells, including pre-TFH ($CD4^+PD1^+CXCR5^-BCL6^{mid}$) and TFH ($CD4^+PD1^+CXCR5^+BCL6^{high}$) cells, which were distinct from non-TFH ($CD4^+PD1^-CXCR5^-BCL6^{low}$) cells (Figure 4-3e). TFH cells are a specialised immune subset that is crucial for forming protective immunity by providing T-cell help to B cells (159, 161).

It was demonstrated that ChipCytometry is sufficiently sensitive to identify very rare palatine tonsillar immune subsets such as the innate-like T-cell subset MAIT cells. MAIT cells were identified and located in tissue sections (Figure 4-5**,** Appendix Figure II-4) and further phenotyped using single-cell suspension ChipCytometry (Figure 4-6). It was confirmed that tonsillar MAIT cells have an activated, memory-like and innate-like phenotype similar to that seen in blood-derived MAIT cells. Additionally, a second innate-like T-cell subset, the γδT cells, was identified. γδT cells were distributed alongside MAIT cells and located predominately in the T-cell zone, but with a few cells scattered within the $CD19^+$ B-cell zone (Figure 4-5**,** Appendix Figure II-4). Besides manual and supervised identification of compartments and cell types (Figure 4-3e, Figure 4-6), unsupervised clustering was performed using FlowSOM to identify different cell types that are included in the cell suspension ChipCytometry data set (Figure 4-3a-d), which is an analysis strategy similar to what has been used for similar data obtained from other methods such as mass cytometry (169, 170). Twelve cell groups were identified within the $CD3^+$ tonsillar T cells, including expected cell types such as pre-TFH/TFH cells and $CD161^{++}$/MAIT cells. The grouping of $Vα7.2^-CD161^{++}$ cells with MAIT cells in one cluster confirms that they share a similar

phenotype (68). The FlowSOM algorithm partitioned some cell types based on the heterogenous expression of a single marker (e.g., CD44 within $CD4^+CD45RA^-$ cells or GzmB within $CD8^+CD45RA^-$ cells). Clustering into fewer, but potentially biologically more meaningful cell groups can be achieved by performing manual merging of similar clusters as suggested by Nowicka et al. (170). Direct FlowSOM clustering into a smaller number of clusters can be problematic. First, cluster stability could suffer and secondly, there is the danger that not all expected and rare cell types would be detected (170).

The examples above outline the advantages of ChipCytometry where multiplex tissue cytometry data, including phenotyping and spatial information from intact tissue, can be combined with cell suspension data that includes phenotyping information on a single-cell level. Multiple adjacent positions of a tissue section can be scanned and stitched together to obtain a relatively large image for analysis (theoretically up to a limit of 1x2 cm^2) (Appendix Figure II-2). In addition, the method allows users to acquire a theoretically unlimited number of markers on a single sample (137).

The ChipCytometry technique uses directly labelled primary antibodies that are commercially widely available for flow cytometry. Panel design is straightforward as no or little compensation is required. Imaging for each fluorochrome in an antibody cocktail is performed sequentially for each fluorochrome at each position. Samples are preserved after analysis and can be stored up to 20 months without significant biomarker degradation (138). This allows re-analysis of samples even after project completion or sample collection, and processing and storage on different sites with subsequent centralised analysis.

As ChipCytometry includes two imaging steps, pre- and post-staining, some correction can be made for autofluorescence by the subtraction of the background from the post-staining image. Further advantages of ChipCytometry in comparison to alternative methods include a greater resolution limit of 500 nm as opposed to 1000 nm for imaging mass cytometry, and

wider dynamic range (9 decades vs 2-3 decades in conventional fluorescence microscopy). ChipCytometry also has a higher scannable area than imaging mass cytometry (1x2 cm^2 vs 1 mm^2) (137, 149).

There are, however, some limitations to the ChipCytometry technique. This method is a serial and iterative process, where antibodies from each subsequent round of staining are left in place and the signal is removed by photobleaching. In theory, issues due to steric hindrance could, therefore, be anticipated. Despite the highly multiplexed nature of ChipCytometry, we have not yet encountered any issues due to steric hindrance beyond any well-known antibody pairs from other applications such as flow cytometry or mass cytometry. An example is steric hindrance between the antibody pair Vδ2 clone B6 and γδTCR clone 11F2 (171).

Another factor is the negative impact of repeated photobleaching cycles on antigen integrity, most likely caused by photodamage of proteins which can absorb high-energy light in the UV region (140). A device upgrade from the manufacturer consisting of a longpass filter that blocks damaging UV in the white light filter module during the photobleaching process was provided to mitigate the destructive effect of repeated photobleaching cycles. Further mitigation can be accomplished by limiting the use of dyes to fluorochromes with a higher excitation wavelength (FITC, PE, PerCP) and photobleaching only through their respective filters instead of using the universal white light filter module for photobleaching. While these precautions generally minimise the destructive effect of repeated photobleaching, particular sensitive epitopes need to be stained early in the process. This requires, however, that each new epitope is tested to determine its relative sensitivity before its consideration in panel design. Sensitive markers applied in the panels of this study are indicated with an asterisk in Table 4-1, Table 4-2 and Table 4-3.

Due to the optimisation required, ChipCytometry has a relatively low sample throughput. In addition, each position on a sample chip is scanned one after another, and staining is

performed in a serial iterative process. Sample throughput of cell suspensions can be increased using barcodes, which allows simultaneous analysis of multiple pooled samples as shown in Figure 4-6a. This approach limits, however, the maximum cell number per sample. Alternatively, sample throughput can no doubt be increased substantially through the use of automated ChipCytometry systems.

In summary, ChipCytometry is a viable and versatile method for immunophenotyping for both tissue sections as well as cell suspensions. In this study, ChipCytometry was used to demonstrate the general palatine tonsil architecture including different immune compartments and to localise and phenotype tonsillar immune subsets, including very rare immune cell types. ChipCytometry overcomes some technical and practical method-specific limitations of other similar methods although it has a relatively low throughput and requires substantial stain-specific optimisation. This approach does lend itself to specific applications in immunology research through multi-stain imaging of specific immune subsets, which require multiple markers for definition, especially when applied in parallel with current high-content analysis of cell suspensions and scRNA-seq approaches.

4.6. Summary

1. ChipCytometry was used for multiplex-immunophenotyping of human tonsils
2. The general histological architecture of tonsils, including B-cell and T-cell zones, was demonstrated. Subcompartments such as the B-cell mantle and germinal centre zone, and intra-follicular PD1-expressing $CD4^+$ T cells were identified.
3. It was shown that $PD1^+CD4^+$ T cells are comprised of $CXCR5^+BCL6^{high}$ TFH cells and $CXCR5^-BCL6^{mid}$ pre-TFH cells
4. Rare tonsillar T-cell subsets, including MAIT and γδT cells, were identified within tonsil tissue

4. Defining T-cell subsets in human tonsils using ChipCytometry

5. It was confirmed that tonsillar MAIT cells have a phenotype similar to that of blood-derived MAIT cells
6. It was shown that ChipCytometry is a viable and versatile method for immunophenotyping for both tissue sections and cell suspensions

5. IDENTIFICATION AND PHENOTYPING OF CD161-EXPRESSING CELL TYPES IN BLOOD

5.1. Introduction

Flow cytometry has been the gold standard in the field of cytometry for the characterisation of single cells since its development in 1965. Flow cytometry is capable of quantifying protein expression on the surface or within cells, besides measuring other variables including cell count, cell size and cell granularity. Analysis of the cell cycle or proliferation can also be performed using specific assays (131–133). There has been a need for increasing panel sizes of staining antibodies included in each assay to allow the analysis of the high complexity of the immune system. Large panels allow, for example, the identification of multiple different cell types within samples and/or the identification of increasingly complex cell types that require a combination of many markers for their definition. Besides markers for cell type definition, panels are also often required to accommodate additionally a variety of markers that allow further analysis of population phenotype, function and state. As traditional flow cytometry is limited by the overlap of excitation and emission spectra of fluorochromes, various alternative cytometry methods have been developed that allow panel sizes of up to or even more than 50 markers to enable high content cytometric analysis (143). These methods include, for example, spectral flow cytometry (134, 135), mass cytometry (136), ChipCytometry (137), CODEX (CO-Detection by indexing) (172), and cytometry by sequencing such as CITE-seq (Cellular Indexing of Transcriptomes and Epitopes by sequencing) and REAP-seq (RNA expression and protein sequencing assay), with the latter accompanied by scRNA-seq analysis (173, 174). Each method has specific advantages and disadvantages, affecting for example the ease of panel design, maximal panel size, ability to measure both intracellular and extracellular markers, dynamic resolution, the number of cells that can be measured, sample throughput, sample preservation after data acquisition, and operating costs.

5. Identification and phenotyping of CD161-expressing cell types in blood

ChipCytometry is an imaging-based high-content cytometry method (137). Multiple markers are acquired in iterative cycles consisting of sample staining with a panel of up to five fluorochrome-coupled antibodies per cycle, image acquisition and subsequent photobleaching to quench the remaining fluorescence. With this serial process, an unlimited number of markers can theoretically be accumulated on a single sample (137). Advantages of ChipCytometry include the use of commercially available standard fluorochrome-coupled antibodies. Panel design is simple, as there is no or only minimal spillover between channels due to the platform design. Samples can be stored for up to 20 months without significant biomarker degradation, which provides the potential for biobanking and allows sample re-interrogation even after project completion (138), which is particularly useful for rare and precious samples. Furthermore, ChipCytometry can also be used to image intact tissue besides cell suspensions. The biggest downside of ChipCytometry is, however, its iterative nature of data acquisition, which is relatively slow and results in low sample throughput. In addition, exposure to repetitive cycles of photobleaching can damage sample epitopes. Protective longpass filters that block damaging light particularly in the UV spectrum are now provided by the manufacturer to mitigate this issue. Despite the protective filters, the staining order for antibodies that stain particularly sensitive epitopes needs to be considered especially for application in large panels (175).

Although being a very promising technique and an interesting alternative to other high-content cytometry approaches, the number of ChipCytometry publications is still limited (149) (Figure 5-1). In most ChipCytometry studies, the platform has been used applying panels of limited size, and there are no studies that explore its high-content nature and possible limits. As a test case, CD14-/CD19-depleted PBMCs were used, which are rich in different, well-defined and well-studied T-cell and NK-cell subsets. A 50-marker panel was designed to identify and deeply phenotype NK cells and innate-like T-cell subsets and to investigate their response to cytokine stimulation. Additionally, as it has not been developed before, I also aimed to create

an analysis protocol specifically for ChipCytometry data that considers platform-specific requirements, such as the identification and removal of fluorescence anomalies.

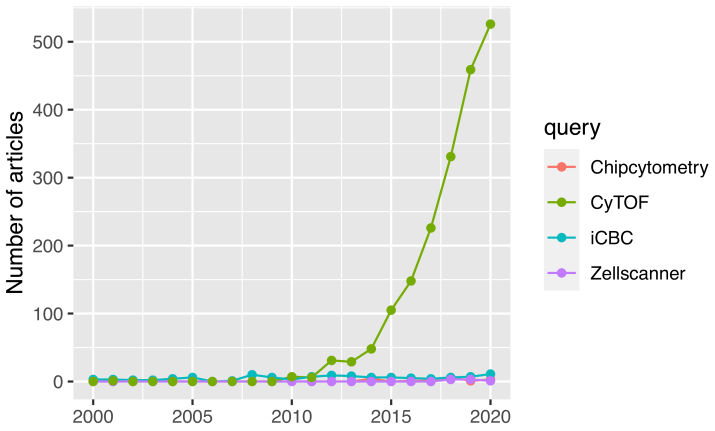


Figure 5-1. ChipCytometry publication trend. Number of ChipCytometry articles over the last two decades was queried at PubMed Central. Alternative queries included iCBC (iterative chip-based cytometry; initial ChipCytometry method description) and Zellscanner (instrument name). The query CyTOF (cytometry by time of flight) represents mass cytometry and was included for comparison.

5.2. Aims

1. Deep-phenotype CD14-/CD19-depleted PBMCs by applying a 50-marker panel using ChipCytometry
2. Develop a protocol for the analysis of high-content ChipCytometry data
3. Identify NK and innate-like T-cell subsets within CD14-/CD19-depleted PBMCs
4. Identify cell types that respond to IL-12+IL-18 stimulation within CD14-/CD19-depleted PBMCs

5.3. Chapter-specific materials and methods

5.3.1. Blood samples

Fresh blood was obtained from healthy volunteers collected at the Peter Medawar Building for Pathogen Research, University of Oxford (UK), following informed consent under approved study protocol 16/YH/O247.

5.3.2. IL-12+IL-18 stimulation

CD14-/CD19-depleted PBMCs were incubated with IL-12 (Miltenyi Biotec) and IL-18 (MBL International) at 50 ng/mL in cell culture medium for 24 hours. The control condition was incubated in R10 media only. Brefeldin A solution 1000x (eBioscience) was added with a final dilution of 1:1000 for the final 4 hours of incubation.

5.3.3. ChipCytometry

ChipCytometry was performed as described in GENERAL MATERIALS AND METHODS- 2.5, with the following specifics: Unstimulated samples were barcoded with CD45-BUV395, and cytokine-stimulated samples were barcoded with CD45-PE. Stimulated and unstimulated cells of each donor were mixed, and samples from each donor were loaded into separate cell suspension chips. Samples were fixed (fixation buffer, Zellkraftwerk, Leipzig, Germany) for 15 minutes at 4°C. The antibody panel that was applied is listed in Table 5-1. Cell segmentation and fluorescence value calculation were performed using the ZKWapp with the following settings: segmentation threshold = -1500, clump removal = 10, surrounding pixel correction = true.

Table 5-1. Staining panel. Intracellular markers are indicated with an asterisk. Antibody dilutions were optimised for the staining of samples fixed for 15 minutes.

	Marker	Clone	Manufacturer	Label	Dilution	Cycle
	anti-Biotin*	1D4-C5	BioLegend	PE	1/5000	36
1	CCR7	G043H7	BioLegend	PerCP-Cy5.5	1/25	1
2	CD134 (OX40)	Ber-ACT35	BioLegend	PE	1/20	24
3	CD137 (4-1BB)	4B4-1	BioLegend	PE	1/12.5	25
4	CD14	RMO52	Beckman Coulter	PE	1/10	26
5	CD16	3G8	BioLegend	PE	1/400	2
6	CD161	191B8	Miltenyi Biotec	PE	1/50	8
7	CD178 (FAS-L)	NOK-1	BioLegend	PE	1/5	15
8	CD19	LT19	Miltenyi Biotec	PE	1/25	11
9	CD2	RPA-2.10	BioLegend	FITC	1/25	13
10	CD218α (IL-18Rα)	H44	eBioscience	PE	1/5	12
11	CD223 (LAG3)	REA351	Miltenyi Biotec	PE	1/10	13
12	CD244 (2B4)	C1.7	BioLegend	PE	1/20	22

5. Identification and phenotyping of CD161-expressing cell types in blood

	Marker	Clone	Manufacturer	Label	Dilution	Cycle
13	CD25	3G10	Miltenyi Biotec	PE	1/100	10
14	CD26	2A6	eBioscience	PE	1/100	21
15	CD27	LG.3A10	BioLegend	PE	1/40	23
16	CD274 (PD-L1)	29E.2A3	BioLegend	PerCP-Cy5.5	1/40	13
17	CD279 (PD-1)	eBioJ105	eBioscience	PE	1/20	18
18	CD3	UCHT 1	BioLegend	PerCP	1/25	20
19	CD366 (TIM3)	7D3	BD Biosciences	PE	1/10	19
20	CD38	HIT2	BioLegend	PerCP-Cy5.5	1/20	11
21	CD39	MZ18-23C8	Miltenyi Biotec	PE	1/33	17
22	CD4	RPA-T4	BioLegend	PerCP	1/20	14
23	CD45	HI30	BioLegend	PE	1/100	1
23	CD45	HI30	BD Biosciences	BUV395	1/100	1
24	CD45RA	HI100	BioLegend	PerCP-Cy5.5	1/40	18
25	CD45RO	UCHL1	BioLegend	PerCP-Cy5.5	1/10	16
26	CD56	AF12-7H3	Miltenyi Biotec	PE	1/80	4
27	CD57	TB03	Miltenyi Biotec	PE	1/20	14
28	CD69	FN50	BioLegend	PE	1/10	16
29	CD71	CY1G4	BioLegend	PerCP-Cy5.5	1/20	25
30	CD8α	SK1	BioLegend	PerCP-Cy5.5	1/30	7
31	CD95 (FAS)	DX2	Miltenyi Biotec	PE	1/20	20
32	EOMES*	WD1928	eBioscience	PE	1/10	31
33	FOXP3*	259D/C7	BD Biosciences	PE	1/10	29
34	Granzyme A*	CB9	BioLegend	PE	1/10	34
35	Granzyme B*	GB11	eBioscience	PE	1/25	27
36	Granzyme K*	24C3	Immunotools	PE	1/10	30
37	HLA-A,B,C (HLA-Class I)	W6/32	BioLegend	FITC	1/100	9
38	HLA-DR	L243	BioLegend	PerCP	1/170	26
39	IFNγ*	4S.B3	eBioscience	PerCP-Cy5.5	1/50	28
40	IL-32αβγδ-Biotin*	KU32-52	BioLegend		1/10	36
41	Ki67*	B56	BD Pharmingen	FITC	1/10	28
42	LIVE/DEAD™ Fixable Green Dead Cell Stain		Invitrogen		$1/10^5$	1
43	PLZF*	R17-809	BD Biosciences	PE	1/10	32
44	RORγT*	Q21-559	BD Biosciences	PE	1/10	35
45	T-BET*	4B10	BioLegend	PE	1/10	33
46	TCR alpha/beta (αβTCR)	IP26	BioLegend	PE	1/50	3
47	TCR gamma/delta (γδTCR)	5A6.E9	Life Technologies	PE	1/50	6
48	TCR Vα7.2	3C10	BioLegend	PE	1/50	7

	Marker	Clone	Manufacturer	Label	Dilution	Cycle
49	TCR Vδ2	B6	BioLegend	PE	1/400	5
50	TIGIT	MBSA43	eBioscience	PE	1/10	9

5.3.4. Data transformation

Data was transformed using FlowJo-type biexponential transformation (flowjo_biexp() function from R package flowWorkspace). The parameters of this transformation were adjusted so that for each marker, the distribution spanned the whole channel range set to 0-4096. The transformation parameters for each marker are listed in Appendix Table III-1.

5.3.5. Identification and removal of fluorescence anomalies and rescaling of data

Each of the 44 chip positions were partitioned into 140 rectangles by applying a 14 x 10 grid to each position. The median of the transformed fluorescence intensity was calculated for the cells contained within each grid subunit in a marker-specific manner. For each chip, the quartiles (Q) and interquartile range (IQR) of the distribution of all subunit medians was calculated separately for each marker. If the median of a subunit was < Q1 – 3 x IQR or > Q3 + 3 x IQR, that particular subunit was flagged as an outlier and designated as a warning for a potential fluorescence anomaly at the location it is covering. Each fluorescence anomaly warning was visually investigated by inspecting the transmitted light images and the images of recorded fluorescence signals of both the background scan and the stained sample to determine whether it is a true or false positive warning. In case of a true positive warning, the particular grid subunits were not simply excluded from the data, as combinations of the rectangular grid subunits often could not perfectly accommodate the various forms of the fluorescence anomalies. Therefore, in case of a genuine positive warning, the segmentation of cells covered by the identified fluorescence anomalies were manually removed from the total segmentation using the rubber tool of the ZKWapp. Data with modified cell segmentation was re-exported and transformed for further analysis.

After the removal of fluorescence anomalies with the help of the generated warnings, the data was visually inspected for the presence of any remaining extreme values. For this purpose, a pseudo time parameter was generated and plotted against transformed marker expression of all markers in bivariate plots. For the generation of the pseudo time, all cells of the data set were ordered in an increasing manner according to the X-coordinates of their chip position, the chip position number on a chip, and the donor number. Then, each cell was assigned an integer value ranging from 1 to the total number of cells, resulting in the pseudo time parameter. A consistent pattern of marker expression is expected across the pseudo time, and outliers were identified as unexpected changes in marker fluorescence intensity over the pseudo time. Visually identified outliers at the bottom and at the top end of the marker expression range were removed via gating. Separate gates for each donor were applied in case markers were affected by strong batch effects. The upper and lower thresholds that were defined to gate out the outliers are listed in Appendix Table III-2.

The distribution of a few markers did not span the whole channel range from 0-4096 as no suitable scaling could be achieved during transformation. To make the distribution of all markers span most of the complete channel range, the data was rescaled by setting the lower threshold of the gate, which was defined to remove outliers at the bottom end of the marker intensity range, as new 0 value. For rescaling, the R package scales was used.

5.3.6. Pre-processing of data

Data was pre-processed in FlowJo (Beckton Dickinson). This included de-barcoding by identifying unstimulated samples as CD45-BUV395^{+}CD45-PE^{-} and the stimulated samples as CD45-BUV395^{-}CD45-PE^{+}. Viable cells were identified as live/dead-staining-negative cells. Any unwanted cell types, including monocytes and B cells that remained after depletion were removed by gating on CD14^{-}CD19^{-} cells.

5.3.7. Batch correction

R packages cydar and CytoNorm were used for data batch correction (176, 177). For cydar quantile-, warp- and range-normalisation, each donor and condition was provided as a separate file and each donor was specified as a separate batch. Standard settings were used with p=0.01 where applicable. For normalisation with the CytoNorm package, the two conditions of each donor were merged. The 4 donors were specified as different batches, and all of them were used for both training and validation. CytoNorm parameters were chosen as follows, if not specified otherwise: nCells = 100.000, xdim = 10, ydim = 10, nClus = 20, scale = FALSE, nQ = 101, goal = “mean”, seed = 3. QuantileNorm normalisation was used with default parameters.

5.3.8. Unsupervised clustering and dimensionality reduction

Unsupervised clustering was performed using FlowSOM R package, using all markers except those which were used for gating during data pre-processing (169). Parameters chosen were: xdim = 10, y dim = 10, rlen = 10, seed = 1234. The R package ConsensusClusterPlus was used to cluster the obtained SOM nodes to obtain the final clusters (metaclusters) (178). ConsensusClusterPlus settings were: reps = 100, pItem = 0.9. Delta area plots with a maximum of k = 20 metaclusters were generated to estimate the number of clusters within the data according to the elbow criterion. High resolution versions of the delta area plots were generated with the CATALYST R package. Although the estimated number of clusters were k = 8, a value of k = 14 was used to overcluster the data, as recommended by Nowicka et al. (170). First, only the unstimulated data was clustered to identify cell populations contained within the samples. In a second step, the data from the IL-12+IL-18-stimulated samples were mapped onto the clusters from the unstimulated data. For data visualisation, dimensionality reduction was performed using UMAP (Uniform Manifold Approximation and Projection) implementation from the uwot R package with the following settings: n_neighbors = 25, min_dist = 0.9, spread = 1, init = spectral.

5.3.9. Marker Enrichment Modeling (MEM), cluster labelling and cluster matching

Marker Enrichment Modeling (MEM) was performed for cluster characterisation using the R package MEM with default settings. Final cluster labels were created in a multi-pronged semi-supervised approach considering both MEM scores and the frequency of marker-positive cells of each marker within each cell cluster (markers that were used for gating during pre-processing were excluded). The frequency of marker-positive cells was determined by gating in FlowJo. For cluster matching, MEM scores were used to calculate the normalised root-mean-square distance (RMSD) score pairwise between populations as a measure of similarity between populations. The RMSD values were calculated using the MEM_RMSD function of the MRM R package. Regroups were defined by hierarchical clustering of RMSD scores using Euclidean distance as distance metric and cutting the obtained tree using stats R package.

5.3.10. Differential marker expression analysis

The median marker expression per marker within each donor and each condition was calculated and used for differential marker expression analysis with the limma and diffcyt R packages (179, 180). For differential expression analysis, the control and IL-12+IL-18-stimulated conditions were compared. Weights based on the cell counts of each cluster and sample were considered for differential expression analysis. Significant genes were determined by a cut-off for the p-value and the difference in median marker expression between conditions as indicated in the figure legends. Volcano plots of the results were generated with the R package EnhancedVolcano.

5.3.11. Principal component analysis (PCA)

Principal component analysis (PCA) was performed using the frequency of marker-positive cells of each marker within each cluster (markers that were used for gating during pre-processing were excluded) using the stats R package.

5.3.12. PubMed Central trend

PubMed Central publication trend was queried using the enrichplot R package.

5.4. Results

5.4.1. Experimental design

CD14-/CD19-depleted human PBMCs (N=4) were used to analyse blood-derived T cells and NK cells. This experiment included two conditions per donor; unstimulated cells (=control) and IL-12+IL-18-stimulated cells. After 24 hours of incubation, conditions were barcoded with CD45 antibodies coupled to different fluorochromes (BUV395 = control, PE = IL-12+IL-18). Conditions were mixed and samples derived from different donors were loaded on separate chips. Samples were analysed by ChipCytometry with a panel of 50 markers.

Besides the fluorescence intensity information for all markers, the acquired data also provided spatial information for each cell. The surface area of a cell suspension chip is structured into 44 positions that get imaged sequentially. Each of those positions has x- and y-coordinates. The combination of chip position and x- and y-coordinates defines a unique location for each cell on the chip.

5.4.2. ChipCytometry data transformation

Similar to other cytometry methods, the transformation function for ChipCytometry data needs to accommodate the high dynamic range of the data with fluorescence intensity values that can differ 5-6 log decades between positive and negative populations, and where the values of the positive population can be spread over multiple logarithmic decades. In addition, the transformation needs to accommodate zero and negative values that can be caused by the background correction. FlowJo-type biexponential transformation was applied, allowing the logarithmic display of high-intensity data to provide a compact visualisation of the positive populations. On the other hand, this transformation function becomes linear for low-intensity

data, for which logarithmic display is not optimal. The FlowJo-type biexponential transformation can also display zero and negative values ensuring a smooth transition between linear to logarithmic regions, thus avoiding the introduction of any visualisation artefacts (181–183). Figure 5-2a shows examples of markers pre- and post-transformation. The transformation parameters for each marker were adjusted separately so that each marker distribution spanned the whole channel range, which was set to 0 - 4096.

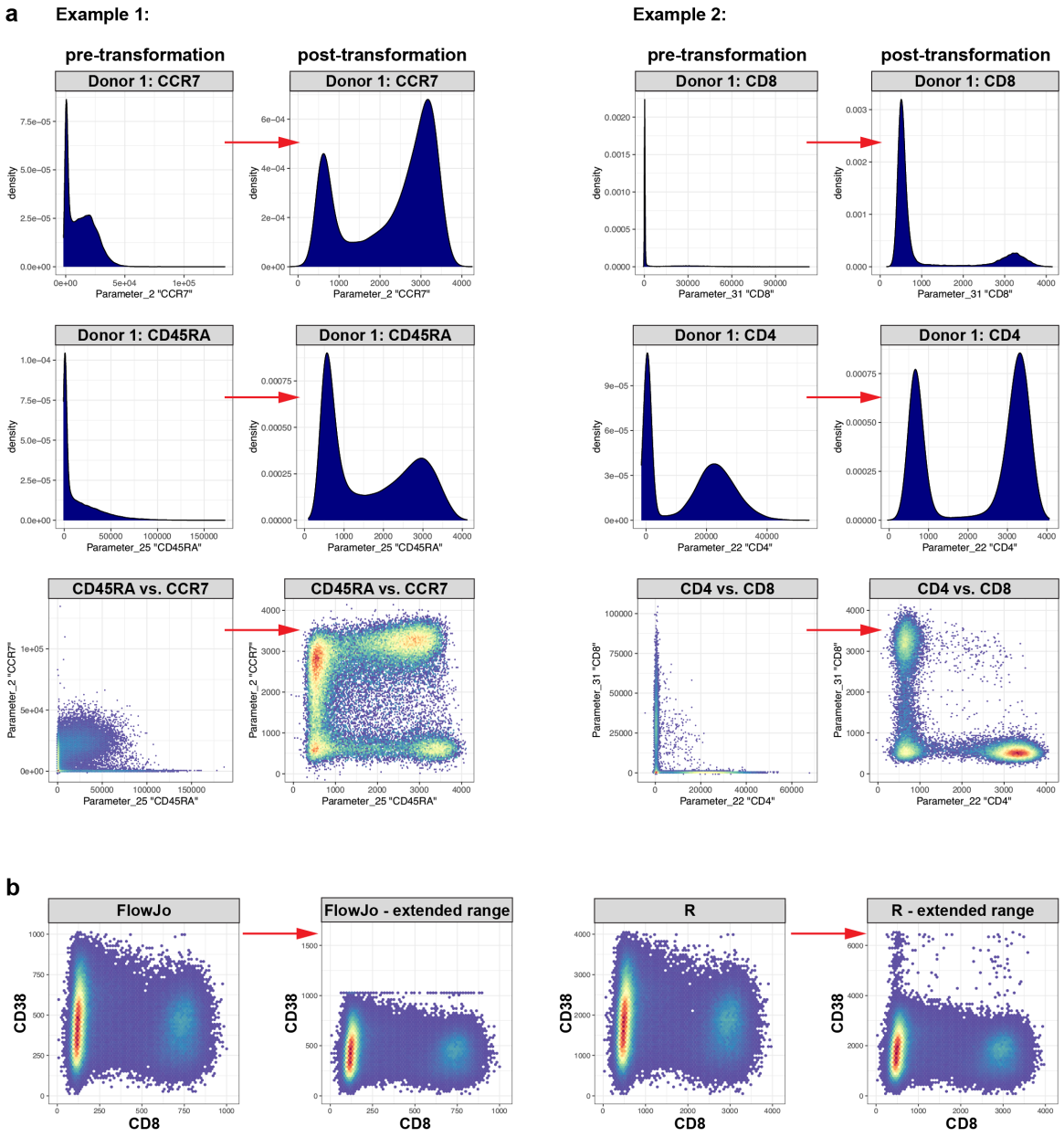


Figure 5-2. Data transformation of ChipCytometry cell suspension data. The ChipCytometry data was transformed using FlowJo-type biexponential transformation in R (flowWorkspace package). The transformation parameters were adjusted separately for each marker including maxValue, positive decades, extra negative

decades and width basis, so that the distribution of each marker spanned the whole channel range set to 0-4096. (a) The panels show two examples of data transformation with two markers each. Example 1 (left) shows histograms and scatterplots of CCR7 and CD45RA pre- and post-transformation. Example 2 (right) shows histograms and scatterplots of CD4 and CD8 pre- and post-transformation. (b) Differences in data transformation between using FlowJo (two panels most left) and FlowJo-type biexponential transformation performed with R flowWorkspace package (two panels most right) are illustrated using CD38 and CD8 as an example. The second and fourth panel show the transformation results with extended CD38 axis limits, demonstrating how FlowJo and R flowWorkspace package handle outliers outside the channel range that is defined by the transformation parameters.

FlowJo-like biexponential transformation was performed in R using an implementation provided by the flowWorkspace R package. Exporting data transformed in FlowJo instead of R resulted in outliers and fluorescence anomalies with intensity values outside the channel range being binned into either the minimum or maximum channel value. When extending the axis range beyond the standard FlowJo channel range, the binning of outliers resulted in line-shaped artefacts (Figure 5-2b). Transformation in R retained the relative intensity information of data points beyond the specified channel range.

5.4.3. Identification of fluorescence anomalies with the help of computationally generated warnings

ChipCytometry can be affected by fluorescence anomalies caused by various reasons, including dust, fibres and air bubbles that can enter the microfluidic system (Table 3-1). An example of a fluorescence anomaly affecting the marker CD38 is illustrated in Figure 5-3. A small fraction of cells from donor 2 showed some extremely high CD38 fluorescence intensity values that were much higher than the channel range specified during data transformation. Gating on these extreme values revealed that they are not evenly spread across the 44 chip positions, but are accumulated on two chip positions. The cells were also aggregated on the particular chip positions, which strongly suggests them to be fluorescence anomalies.

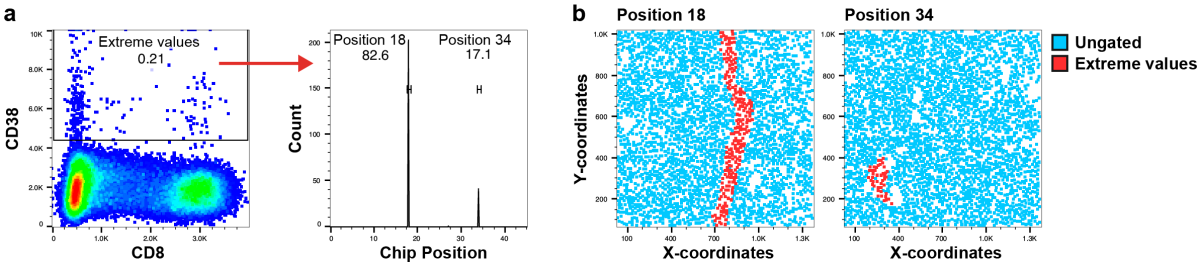


Figure 5-3. ChipCytometry data contained fluorescence anomalies. An example of fluorescence anomalies within the ChipCytometry data set is shown. (a) In order to investigate the extreme CD38 fluorescence intensity values of Donor 2, the CD38 axis limits were extended and a gate was drawn that included the extreme values. The histogram illustrates the cell count of the extreme values on chip position numbers 1 – 44. The extreme values were located on chip position numbers 18 and 34. (b) Dot plots illustrate cells on chip position numbers 18 and 34. Cells with extreme CD38 intensity values were spatially aggregated on each of the positions.

Fluorescence anomalies were observed despite performing fluorescence value computation from the raw images using the proprietary algorithm “surrounding pixel correction” in the ZKWapp as recommended by the manufacturer. The ZKWapp offers no automated option to identify and exclude fluorescence anomalies before data export, but it provides the option to manually delete individual cells from the segmentation. This allows the removal of cells that are visually identified on the recorded images as being affected by fluorescence anomalies. The number of recorded images even for a small-scale experiment can be very high. The data generated for this study contained 17,600 images of recorded fluorescence signals (4 donors x 44 positions per chip x 50 markers x 2 imaging rounds per marker, including background acquisition and stained sample acquisition). In addition to inspecting images of recorded fluorescence signals, assessing the corresponding transmitted light images can provide additional information about the cause of fluorescence anomalies, but potentially double the number of images to inspect. Considering that the ZKWapp took approximately 15 seconds to load a single image, and accounting for the time to assess individual images and to manually delete cells, the removal of fluorescence anomalies can be extremely time-consuming.

To speed up the manual fluorescence anomaly removal process, chip positions affected by fluorescence anomalies were computationally predicted, decreasing the number of images

that need to be inspected. To achieve this, each chip position was divided into 140 small rectangles by applying a 14x10 grid (Figure 5-4a). The median marker expression within each grid subunit was calculated, and the quartiles (Q) and inter quartile range (IQR) of the distribution of all grid subunit medians was determined in a marker-specific manner. If the median marker expression of a particular subunit was < Q1 – 3 x IQR or > Q3 + 3 x IQR, it was flagged as an outlier and designated as a warning for a possible fluorescence anomaly within the area covered by that grid subunit (Figure 5-4b, c). Two examples, including position 18 of CD38 and position 15 of CD8 from donor 2 are shown in Figure 5-4b. Grid subunits that were flagged as outliers on these positions are indicated by black rectangles. To determine whether a prediction was a true or false warning, the recorded images of all chip positions that contained grid subunits flagged as outliers were visually inspected. In the example of position 18 of CD38, a fibrous particle was visible on the transmitted light image, which was highly fluorescent in the fluorescence image, confirming the fluorescence anomaly warnings as true positives (Figure 5-4d). No indication of a fluorescence anomaly was visible on the CD8 images, indicating false positive warnings. From 1324 – 2227 warnings that were generated per donor, 29.42 ± 12.51 % were true positives (Figure 5-4e, f). With the settings chosen for the grid size and the cut-off that defined outliers, a relatively high frequency of false-positive warnings was allowed with the aim to minimise the number of false negatives.

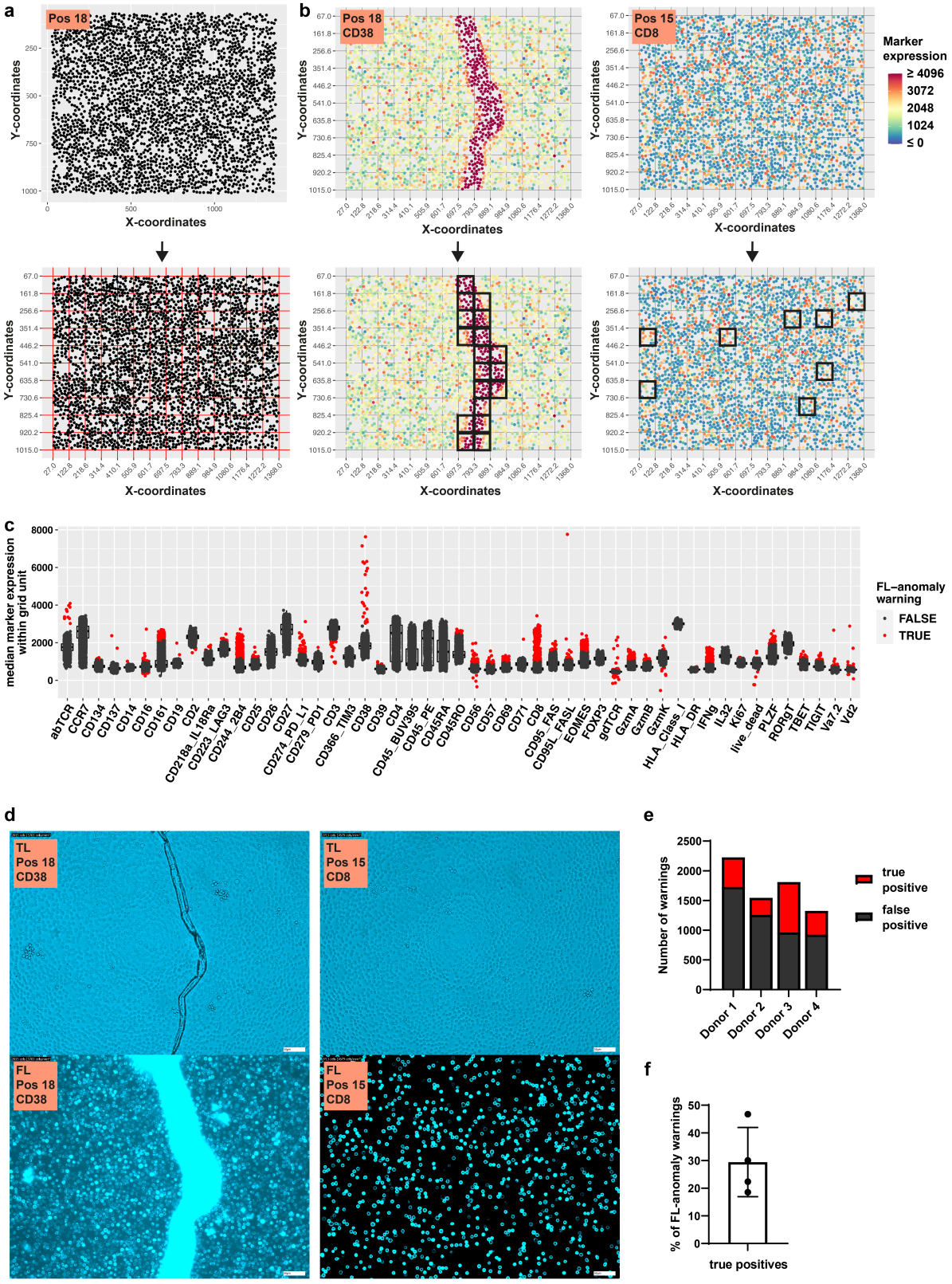


Figure 5-4. Generation of warnings for fluorescence anomalies within the ChipCytometry data set. To identify the location of possible fluorescence anomalies computationally, the surface area of each of the 44 chip positions was divided into 140 small rectangles according to a 14x10 grid. (a) As an example, a single position of a chip is shown before (top panel) and after (bottom panel) applying the grid. Each black dot represents the position of a cell defined by x- and y-coordinates. To identify grid units that were possibly affected by fluorescence anomalies, the median marker expression within each grid unit was determined in a marker-specific manner. Grid

units were defined as outliers and flagged as being possibly affected by fluorescence anomalies if the median marker expression of a grid subunit was < Q1 – 3 x IQR or > Q3 + 3 x IQR of the distribution considering the median marker expression of all grid subunits of a specific marker on a chip. (b) The expression of markers CD38 (top left) and CD8 (top right) of a single position are shown as example. Grid units flagged for possibly containing fluorescence anomalies on respective positions are indicated with black rectangles (bottom panels). (c) Box plot of the median marker expression of the individual grid units from Donor 2 is shown as an example and is representative for all other donors. Grid units that were identified as outliers and therefore constituted a warning for fluorescence anomalies are indicated in red. (d) Raw images of each position that contained warnings for fluorescence anomalies were inspected to determine true and false positive warnings. Images from the CD38 (left) and CD8 (right) acquisition cycles are shown as an example. Top panels are transmitted light images (TL) and bottom panels show the fluorescent signal acquired from the stained samples (FL). (e) Absolute quantification of true and false positive warnings of each sample across all 50 markers. (f) Relative quantification of true positive warnings.

The combination of multiple rectangular-shaped grid units did often not perfectly cover the diverse shapes of fluorescence anomalies. At the boundary of fluorescence anomalies, the grid units either covered some unaffected area in addition to the affected area, or they did not cover the affected area completely. Therefore, instead of simply excluding the cells that were covered by grid units associated with true positive warnings, the warnings were used to perform targeted manual removal of fluorescence anomalies on flagged positions. The manual removal was performed by deleting the segmentation of cells at affected areas in the raw images using the rubber tool of the ZKWapp (Figure 5-5). This allowed to outline the shape of the anomalies manually, maximising the elimination of areas truly affected by fluorescence anomalies, while minimising the elimination of the unaffected regions.

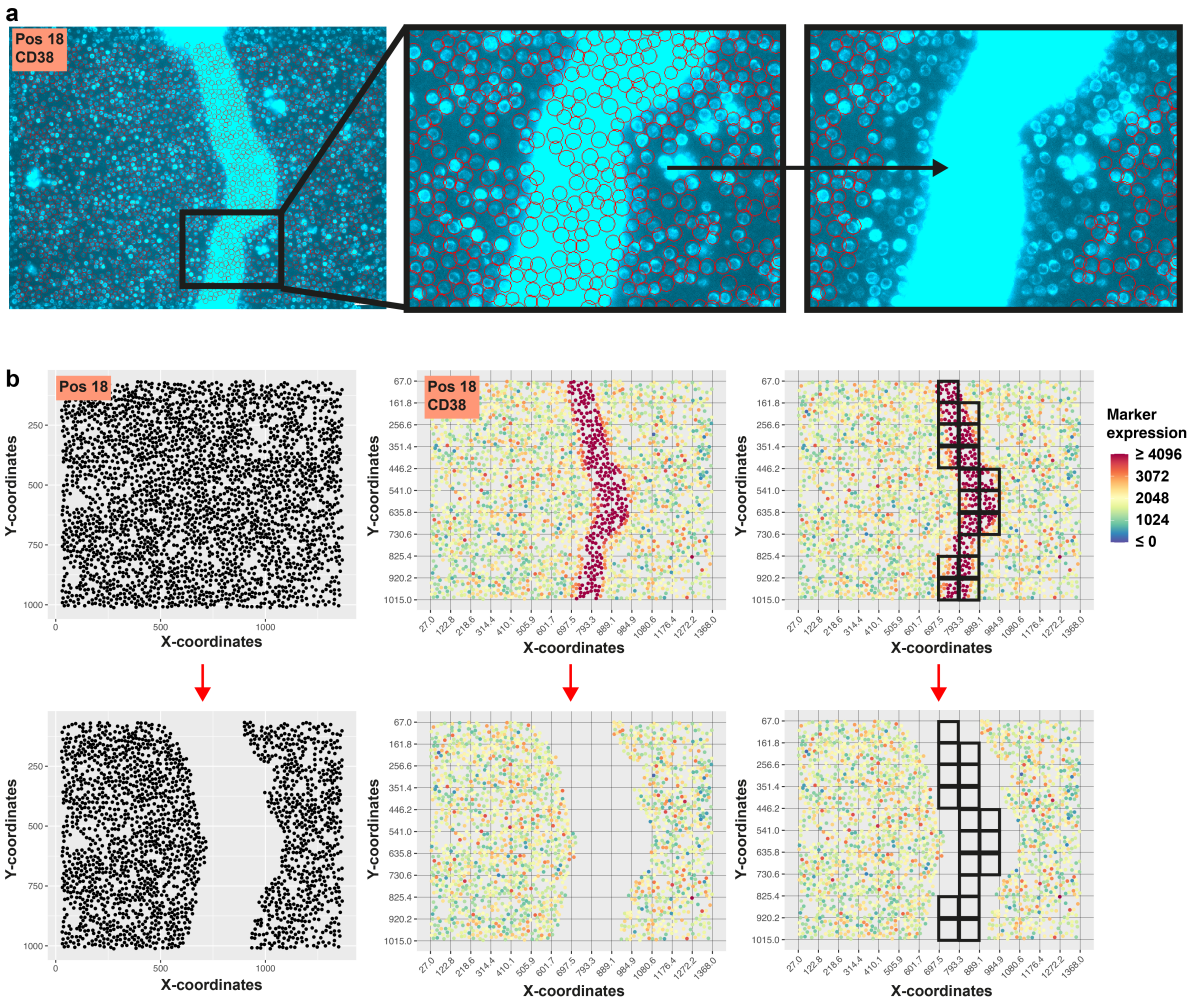


Figure 5-5. Manual removal of identified fluorescence anomalies. (a) Left panel: An example for a position containing a fluorescence anomaly is shown (Donor 2, Position 18, CD38 staining). Red circles represent segmented cells. Middle panel: Magnified section of the affected area. Right panel: Cells that were covered by the fluorescence anomaly were manually removed from the raw data using the rubber tool in the ZKWapp. (b) After manual removal of identified fluorescence anomalies, cleaned-up data was re-exported. The left panels show the comparison of the fluorescence anomaly-affected position before (top) and after the clean-up (bottom). CD38 expression is superimposed in the centre panels, and the grid units that were flagged as outliers are indicated by black rectangles in the right panels.

5.4.4. Identification and removal of any remaining extreme values by visual inspection and rescaling of data

After the removal of fluorescence anomalies, the performance of the clean-up process was investigated by comparing the data pre and post fluorescence anomaly removal. In addition, the data was screened for the presence of any remaining outliers and extreme values. A basic approach in flow cytometry to identify anomalies is the visual inspection of the fluorescence intensity of each marker plotted against time (184). As there is no inherent time parameter for

ChipCytometry data, a pseudo time parameter was created. The pseudo time was obtained by first ordering all cells according to the following parameters in an ascending manner: X-coordinates of cells within a chip position, chip position number, and donor number (= chip number). Then, each cell was assigned an integer number from 1 to the total number of cells within the data set. Cells that were recorded temporally and spatially close were represented close within the pseudo time parameter.

The pseudo time parameter allowed the visual inspection of each marker by plotting the marker expression versus pseudo time (Figure 5-6). First, it was investigated whether there were any remaining extreme values present in the data after the removal of fluorescence anomalies. It is expected that the marker expression shows a constant pattern over pseudo time. But marker CD27, for example, showed some local changes in the pattern of CD27 expression over pseudo time (Figure 5-6a). By gating on the CD27 outliers, they could be traced back to small-sized fluorescence anomalies in the recorded images, covering only a few cells. The occurrence of remaining outliers post removal of fluorescence anomalies, such as in the case of CD27, was most likely due to false-negative warnings where fluorescence anomalies were possibly too small in size to be picked up. Visually identified extreme values at the low and top end of the marker intensity range were gated out. The red lines in the plot indicate the gate thresholds of the CD27 example.

Next, all three stages of data clean-up were compared, including the data before any removal of fluorescence anomalies, the data after removal of fluorescence anomalies with the help of computationally generated warnings, and the data in which also any remaining extreme values were removed by gating (Figure 5-6b-f). This comparison revealed that most of the visually evident fluorescence anomalies were successfully removed by the manual removal of fluorescence anomalies with the help of the computationally generated warnings. The occurrence of any remaining extreme values after that step was relatively rare, as indicated by the number of cells lost during each clean-up step (Appendix Figure III-1). Relative to the

unedited data, 8.38 ± 2.82 % of cells were removed during fluorescence anomaly removal based on the computationally generated warnings. In the next step, in which remaining extreme values were removed by visual inspection and gating, a loss of only 0.24 ± 0.06 % more cells relative to the unedited data was observed. This indicates that the identification and manual removal of fluorescence anomalies with the help of computationally generated warnings successfully removed most visually evident fluorescence anomalies. The generation of a pseudo time parameter helped to identify and remove the few remaining extreme values, however. Using only visual data inspection to gate out extreme values and omitting the generation of warnings for fluorescence anomalies would likely not have been satisfactory. This visual approach alone does not allow to easily identify and remove fluorescence anomalies that do not manifest in extreme outliers but in more subtle changes of the marker distribution.

At this point, rescaling of the data was performed by setting the lower gating threshold of each marker defined during the last clean-up step as new zero. The reason is that FlowJo-like biexponential transformation did not result in suitable scaling for some markers. Disregarding the extreme values, the low-intensity values of LAG3, for example, were > 650 within the specified channel range of 0 – 4096 (Figure 5-6d). After removing extreme values and rescaling, low-intensity cells at the low end of the distribution were very close to zero for all markers.

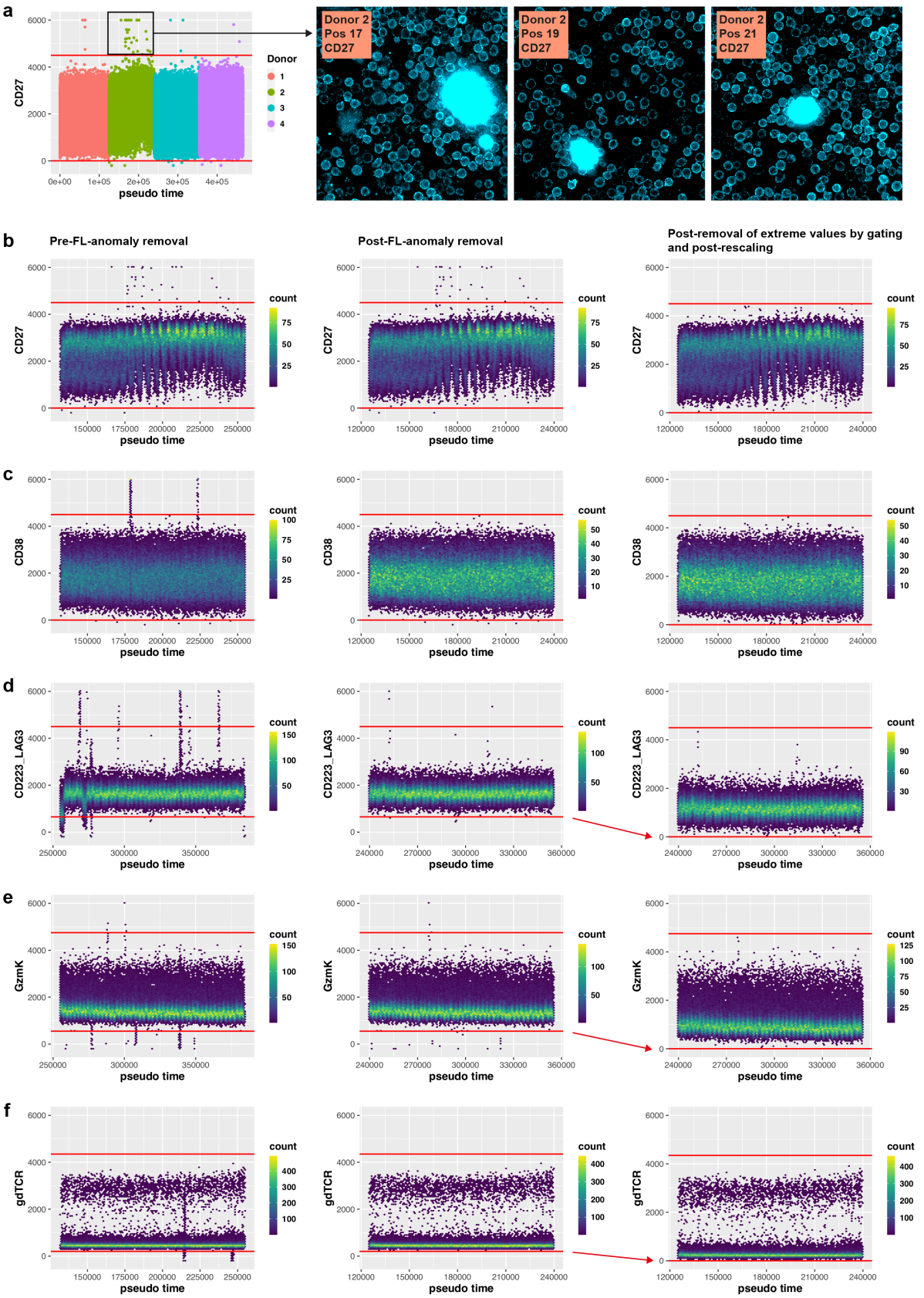


Figure 5-6. Identification and removal of remaining outliers and rescaling of data. To inspect the data visually for the presence of remaining outliers, a pseudo time parameter was generated by assigning to each cell a unique integer number from 1 to the total number of cells of the data set. The integer number was assigned to the cells after ordering the data by the following parameters in an ascending manner: x-coordinates of cells within

each position, chip position number, and donor number. Cells that were recorded spatially and temporally close appeared close in the pseudo-time parameter. (a) Outliers and remaining fluorescence anomalies were identified by inspecting marker expression versus pseudo-time. CD27 is shown as an example. An upper and lower threshold (red lines) was set to define cells outside of those limits as outliers. Tracking the outliers of donor 2 (black gate) back to the original images revealed that they were the result of several small-sized fluorescence anomalies (3 examples are shown), which were not flagged and removed during the previous fluorescence anomaly removal step as shown in Figure 5-4 and Figure 5-5. (b)-(f) Marker expression of a single donor versus pseudo-time is shown for 5 markers as examples (CD27, CD38, LAG3, GzmK, γδTCR). The left panels show the data before any fluorescence anomalies were removed. The centre panels show the data post removal of fluorescence anomalies that were identified by the computationally generated warnings. The right panels show the data after removing any remaining outliers that were defined by thresholds (red lines). The cut-off values to define outliers were determined by visual inspection in a marker-specific manner depending on the expression range of each marker. In case the expression range of a marker was very different between donors due to batch effects, the upper and lower thresholds for that marker were defined in a donor-specific manner. In addition to manually removing outliers identified by visual inspection, the data was rescaled by setting the defined lower threshold as new zero (indicated by red arrows between centre and right panels).

5.4.5. Pre-processing of data

Next, data was pre-processed in FlowJo (Figure 5-7). First, data was de-barcoded to distinguish the different conditions of each donor that were mixed and analysed on a single chip. The barcodes consisted of CD45 antibodies coupled to different fluorochromes. The unstimulated samples were identified as $BUV395^{+}PE^{-}$ cells and the IL-12+IL-18-stimulated samples were identified as $BUV395^{-}PE^{+}$ cells. Next, dead cells were excluded by gating on cells negative for the viability dye. Finally, unwanted cell types were excluded by gating $CD14^{-}CD19^{-}$ cells to remove any remaining monocytes or B cells.

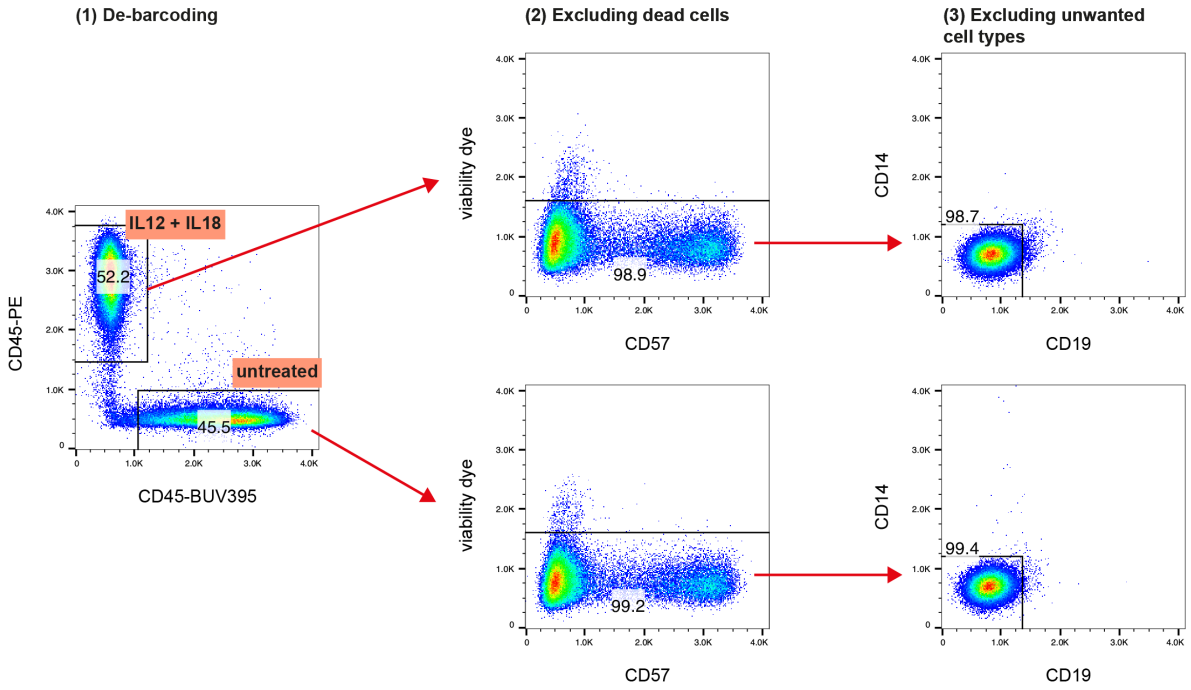


Figure 5-7. Pre-processing of data in FlowJo. Each chip contained both the untreated (control) and IL-12+IL-18-stimulated samples of a single donor. The cells of the two conditions were barcoded prior to chip-loading using the pan-leucocyte marker CD45 coupled to different fluorochromes, either PE or BUV395. De-barcoding of conditions was performed by gating on BUV395^{+}PE^{-} cells (untreated) and BUV395^{-}PE^{+} cells (IL-12+IL-18-stimulated). Next, dead cells were excluded by gating on viability dye-negative cells. Finally, unwanted cell types, including any remaining monocytes or B cells, were excluded from the CD14-/CD19-depleted PBMCs by gating on CD14^{-}CD19^{-} cells.

5.4.6. Batch correction of ChipCytometry data

The cells of each donor were analysed on separate chips. This resulted in each donor representing a different batch. Due to the iterative staining process, the trend of batch effects between different donors can vary with each round of staining (Figure 5-8a). This includes differences in the expression range and/or differences in the position of the histogram peaks of markers. It was observed, for example, that the fluorescence intensity of markers with relatively weak staining can decrease from the first sample measured to the last sample measured, such as in the case of FASL for which the fluorescence intensity decreased from donor 1 to donor 4. For IL-18Rα, the order of acquisition was intentionally reversed, which resulted in the inversed trend, and the fluorescence intensity decreased from donor 4 to donor 1. While the batch effect of FASL is represented mainly by differences of the marker range, the batch effects of GzmB, PD-L1, RORγT, CD27 and IL-18Rα are represented by misaligned

histogram peaks alone or in combination with differences in the marker range. The batch effects are an issue for directly comparing fluorescence intensities between samples and for defining common gates across samples.

Therefore, ChipCytometry data was batch-corrected using different tools and methods, including quantile, warp and range correction from the cydar R package (176), and QuantileNorm and CytoNorm correction from the CytoNorm R package (177). Figure 5-8b shows the batch correction results of GzmB as an example, which was one of the markers that showed the largest differences between donors. While cydar quantile and QuantileNorm seemed to align the GzmB histograms perfectly, they performed very poorly for more than half of all other markers, as they added artefacts to the data (Figure 5-9). For this reason, cydar quantile normalisation and QuantileNorm were not further considered. Warp normalisation perfectly aligned the GzmB histogram peaks, but the resulting expression range was very different between batches (Figure 5-8b). The range normalisation resulted in equal expression ranges between batches, but the histogram peaks were misaligned. In addition, range correction performed very poorly for the three markers γδTCR, Vδ2 and CD39, as this method added differences between batches much larger than those observed before correction (Figure 5-10). For this reason, the three affected markers were excluded from correction during range normalisation (Appendix Table III-3). CytoNorm correction aligned the GzmB histogram peaks and resulted in similar intensity ranges between batches. But CytoNorm added artefacts to some of the markers including, for example, CD161, Vα7.2, γδTCR, Vδ2, CD4 and CD3 (Figure 5-11a). Using CytoNorm, fewer markers were affected by artefacts compared to cydar quantile and QuantileNorm correction, however. As CytoNorm performed extremely well in aligning histogram peaks and in matching expression ranges across batches, and caused artefacts only in a relatively low number of markers (Figure 5-8c), it was explored whether the CytoNorm parameters could be further tweaked to minimize or avoid the generation of artefacts.

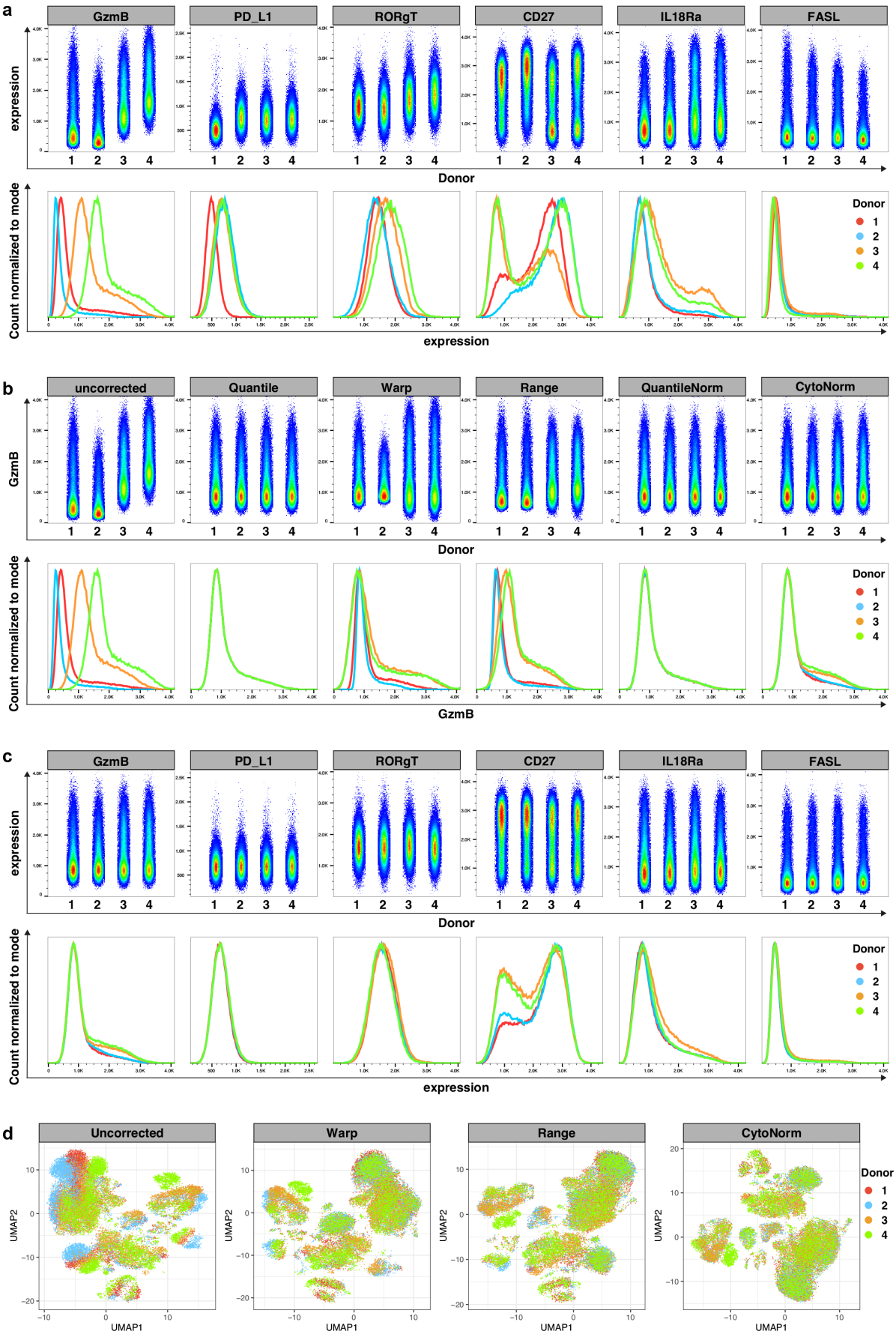

a
GzmB
PD_L1
RORgT
CD27
IL18Ra
FASL
expression
Donor
Count normalized to mode
Donor
1
2
3
4
b
uncorrected
Quantile
Warp
Range
QuantileNorm
CytoNorm
GzmB
c
d
Uncorrected
Warp
Range
CytoNorm
UMAP1
UMAP2

Figure 5-8. Batch correction of ChipCytometry data. Each donor of the data set comprises a different batch. (a) Examples of markers for which batch effects between donors were observed. Top panels show the expression of 6 markers (GzmB, PD_L1, RORγT, CD27, IL-18Rα, FASL) versus donor number. Bottom panels show histograms of those markers and the different donors are color-coded as indicated. (b) Different tools to correct the batch effects between the donors were compared, including quantile-, warp- and range-normalisation from the cydar R package and the QuantileNorm- and CytoNorm-normalisation from the CytoNorm R package. As an example, the results of the batch-corrected GzmB marker are depicted. Top panels show GzmB expression versus donor number. Bottom panels show histograms of GzmB expression of all four batches. (c) Panels show the expression of the six example markers after batch correction using CytoNorm. Top panels show marker expression versus donor number, and bottom panels show marker histograms. (d) Visual representation of the ChipCytometry data set using UMAP. Plots show uncorrected and batch-corrected data, including warp-, range- and CytoNorm-corrected data. Cells are coloured by donor number.

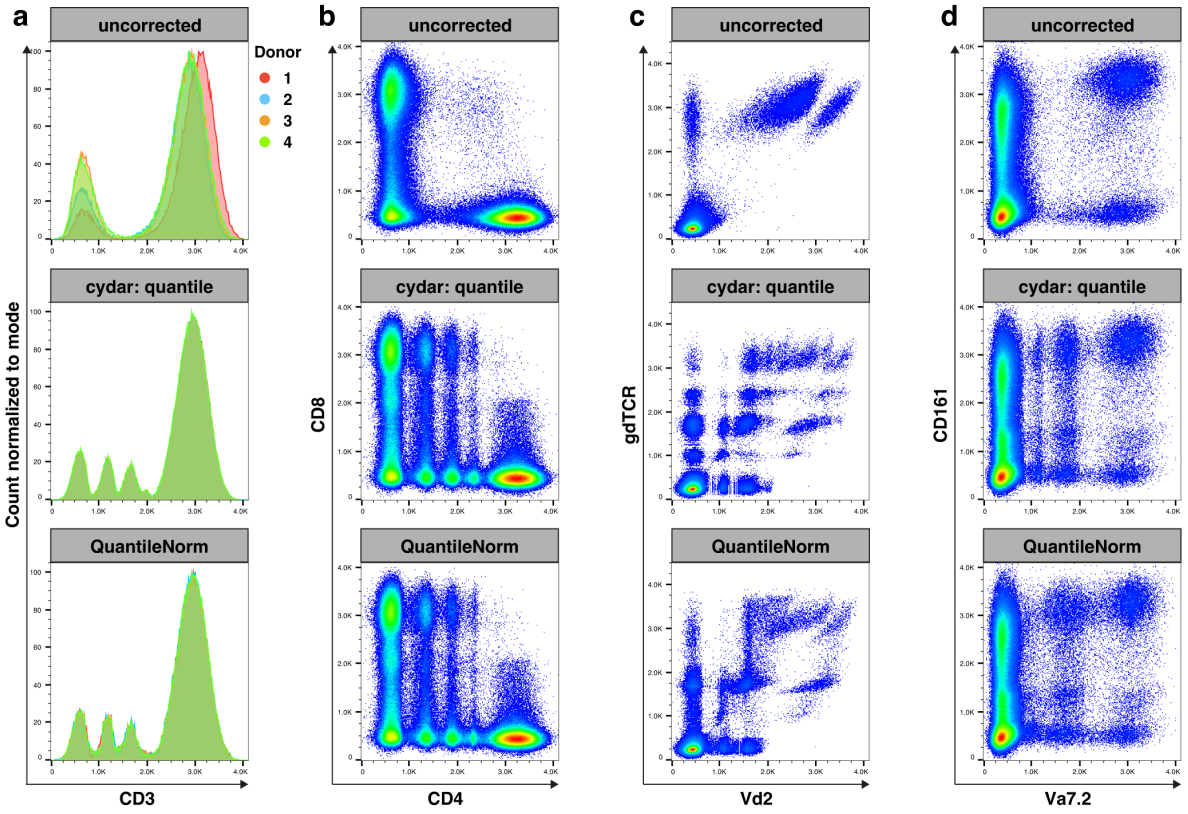


Figure 5-9. Examples of artefacts induced by quantile normalisation. (a)-(d) ChipCytometry data was batch-corrected by applying quantile normalisation using either the R package cydar or the QuantileNorm function from the CytoNorm R package. Examples of markers that were affected by artefacts after batch correction are shown. The uncorrected data is shown for reference.

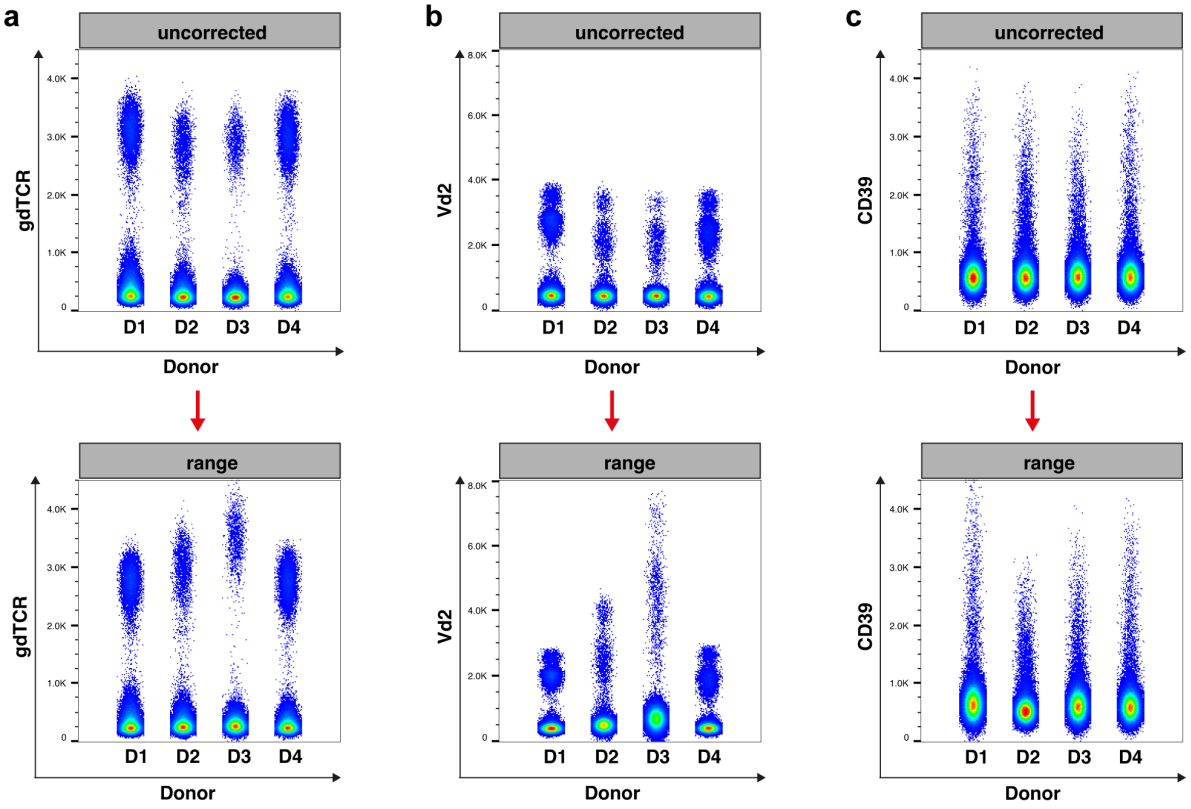


Figure 5-10. Examples of markers for which batch correction using range normalisation failed. (a)-(c) ChipCytometry data was batch-corrected applying range normalisation using the R package cydar. The plots show the markers for which the range normalisation with the setting p = 0.01 failed. The marker expression was plotted against donor number (Donor 1 = D1, Donor 2 = D2, Donor 3 = D3, Donor 4 = D4). Plots from the uncorrected data are shown for reference.

CytoNorm correction was used to perform unsupervised data clustering during a training step, after which batch correction was performed separately within each cluster on a marker-by-marker basis. The effect of different clustering settings on the appearance of artefacts was tested by varying the number of clusters (nClus = 3, 5, 10, 15, 20, 25) while adjusting the batches to the mean distribution of all donors. Increasing the cluster number could eliminate artefacts of some markers, including CD3 and CD4 for nClus > 10, but artefacts of other markers were still visible for all tested clusters settings, including Vα7.2 and Vδ2. Next, each donor was tested as goal distribution for normalisation (Figure 5-11b). When normalising to the distribution from a single donor, the manifestation of artefacts within affected markers could be reduced to a minimum or be completely avoided.

Normalising to a goal distribution derived from a single donor was problematic, however. Complete populations could appear or disappear, depending on their presence within the chosen reference donor. Examples are shown in Figure 5-12, tracking a few selected populations within donor 2 before and after CytoNorm correction using different reference distributions, including reference distributions from single donors and the mean distribution of all donors. Distinct $CD56^{++}CD137^{+}$ and $CD56^{++}CD134^{+}$ populations were visible when donor 1 was used as reference, but they were essentially absent when donor 3 was set as reference. Another example is a $CD161^{++}2B4^{+}$ population. With donor 1 as reference, this population is 2B4-intermediate while with donor 4 as reference the population is 2B4-high. Finally, with donor 2 or 3 as a reference, there were almost no $TBET^{+}$ cells visible within $CD161^{++}$ and $CD161^{-}$ populations. With donor 4 as reference, however, there was a large $TBET^{+}$ population in both $CD161^{++}$ and $CD161^{-}$ populations observable.

As CytoNorm normalisation can induce an extreme bias with a single donor as a reference, the mean distribution of all donors was chosen as goal distribution for further analysis. The settings for the clustering step during CytoNorm normalisation were optimised so that as few markers as possible were affected by artefacts (nClust = 20, SOM dimensions: 10x10) (Figure 5-11a). With the optimised settings, CytoNorm added artefacts to four markers, including CD161, Vα7.2, Vδ2 and PLZF (Figure 5-13). Therefore, these four markers were only used for clustering during CytoNorm normalisation, but excluded from the normalisation step, as their batch effects were relatively minor (Appendix Table III-3).

To visualise the batch effects pre- and post-batch-correction, including warp, range and CytoNorm correction, UMAP dimensionality reduction was performed and samples were coloured according to batches. Although all batch correction tools resulted in better alignment of populations and minimized batch-specific regions, CytoNorm performed best (Figure 5-8d). Compared to warp- and range-normalisation, CytoNorm was the superior tool, as it could both align histogram peaks and match the expression range across donors.

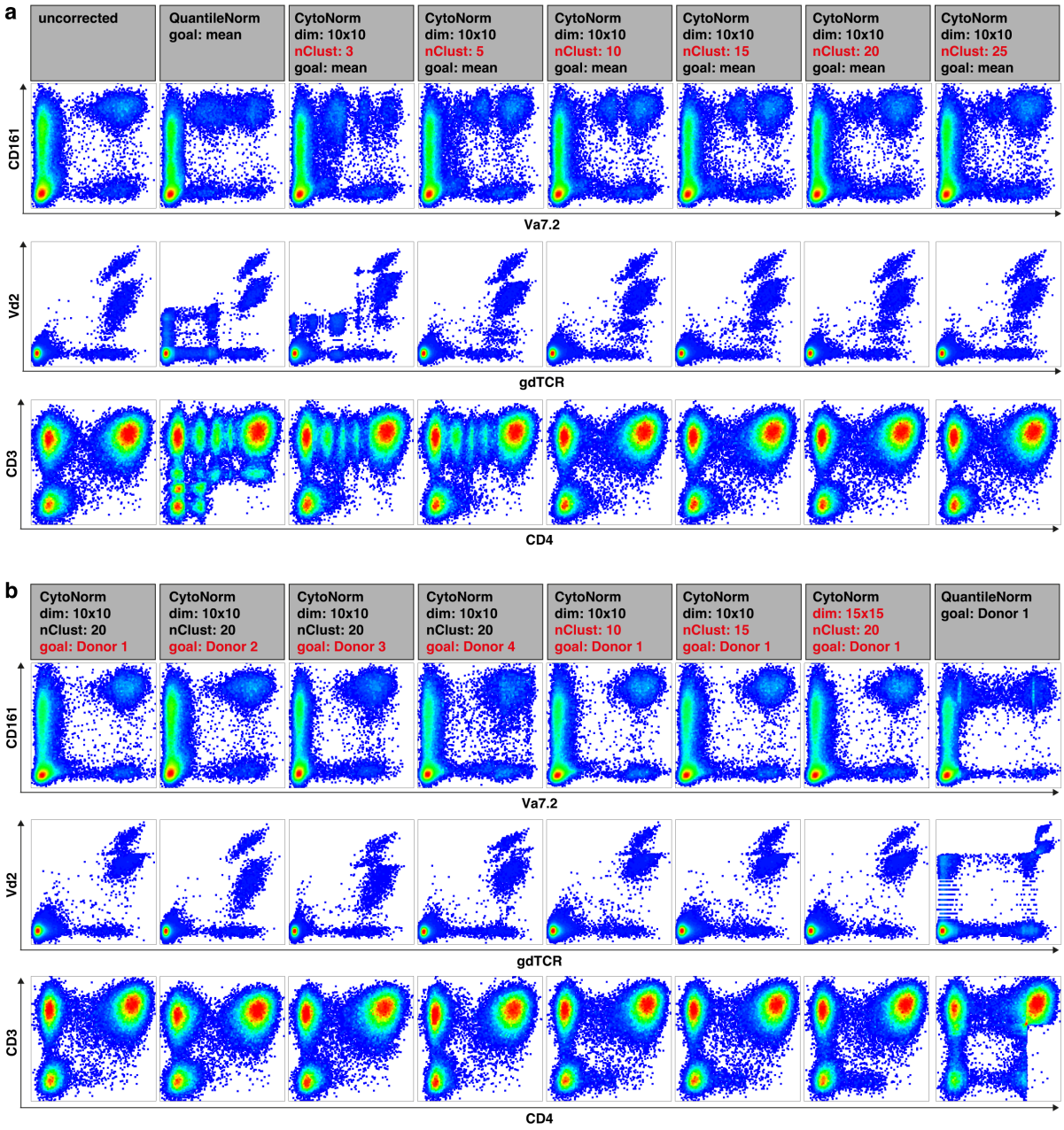


Figure 5-11. Optimisation of CytoNorm batch correction parameters. Different CytoNorm-normalisation settings were tested to minimise the number of markers affected by artefacts post correction. (a) The number of clusters (nClust) was varied from 3 to 25 in increments as indicated (highlighted in red) while the grid dimension (dim = 10x10) and the normalisation goal (goal = mean) were kept constant. The expression of some markers that were most affected by CytoNorm-induced artefacts are shown as an example, including Vα7.2, CD161, γδTCR, Vδ2, CD4 and CD3. The uncorrected and QuantileNorm-corrected data (goal = mean) is shown for reference. The plots are derived from a single donor and are representative for all four donors. (b) Similar analysis as in (a), but the CytoNorm normalisation goal, nClust and dim setting were varied as indicated (highlighted in red). The last column shows QuantileNorm results with normalisation goal = Donor 1 for comparative purposes.

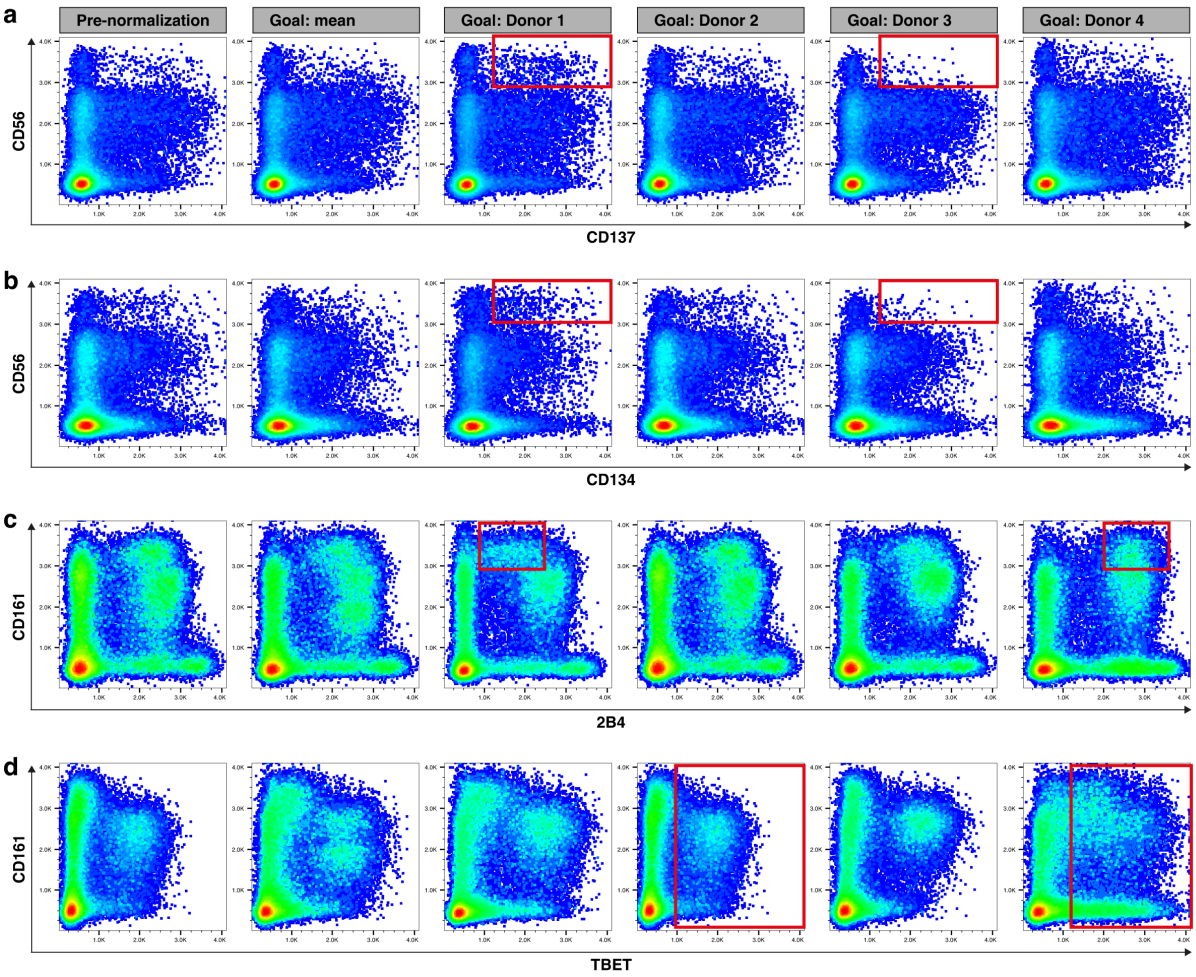


Figure 5-12. Limitations of CytoNorm batch correction using only a single donor as reference. Examples show marker expression before (column 1) and after CytoNorm batch correction (columns 2-6). Markers include (a) CD137 vs. CD56, (b) CD134 vs. CD56, (c) 2B4 vs. CD161, and (d) TBET vs. CD161. The panels are derived from donor 2 and are representative for all four donors. CytoNorm settings used were nClust = 20 and dim = 10x10, while the normalisation goal was varied as indicated. The red rectangles highlight obvious differences in the appearance of populations when different donors were chosen as a normalisation reference.

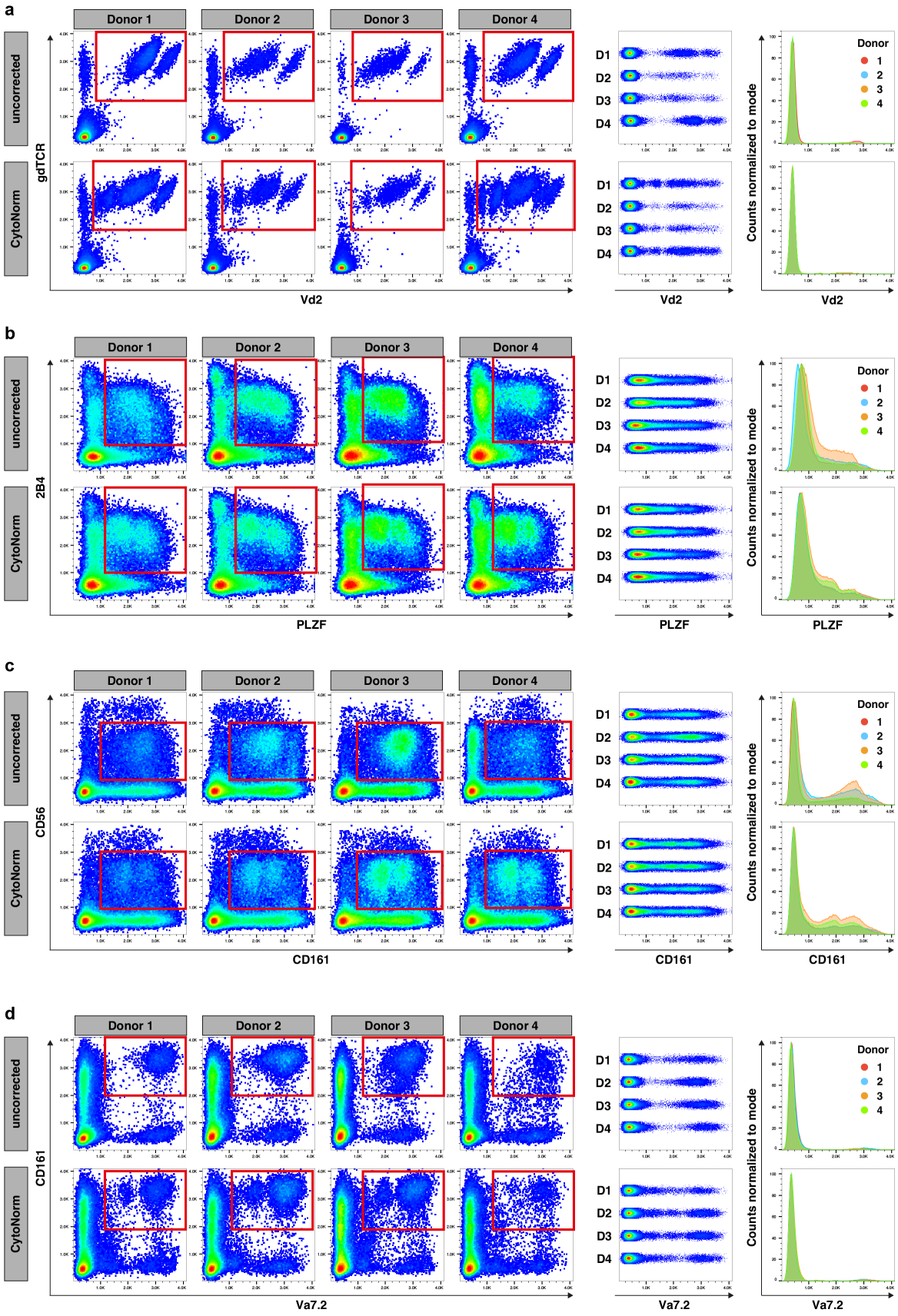


Figure 5-13. Some markers are affected by CytoNorm-induced artefacts despite the optimisation of normalisation settings. The ChipCytometry data was batch-corrected using CytoNorm batch correction with optimised settings: nClust = 20, dim = 10x10, goal = mean. Four of the 50 markers were negatively affected by

the batch correction, including Vδ2, PLZF, CD161 and Vα7.2. Each marker was plotted against a suitable second marker to illustrate the artefacts that were introduced, including (a) Vδ2 vs. γδTCR, (b) PLZF vs. 2B4, (c) CD161 vs. CD56 and (d) Vα7.2 vs. CD161. The plots show uncorrected and CytoNorm-corrected data as indicated. On the right side, the expression of affected markers is plotted against donor number (Donor 1 = D1, Donor 2 = D2, Donor 3 = D3, Donor 4 = D4) and additionally depicted as histograms with each donor coloured differently as indicated.

5.4.7. Unsupervised clustering of ChipCytometry data

Data from the unstimulated condition was clustered in an unsupervised manner to identify cell populations within the CD14-/CD19-depleted PBMCs. To compare the impact of the batch correction on clustering, the data from all four differently corrected data files was clustered, including non-batch-corrected data and warp-, range- and CytoNorm-corrected data. Clustering was performed using FlowSOM R package in a two-step approach (169). First, data was clustered using self-organizing map (SOM) clustering, which is a specific type of artificial neural network (185, 186). For this purpose, unstimulated data from all donors was aggregated and cells were assigned to 100 nodes of a 10 x 10 SOM grid according to their similarity. Secondly, the 100 SOM nodes were clustered using ConsensusClusterPlus R package to obtain the final clusters (metaclusters) by applying hierarchical clustering (178). One hundred iterations of hierarchical clustering of the SOM nodes were performed on random subsamples of the data (proportion of cells to sample = 0.9) for k= 2-20 metaclusters. Consensus matrices were created for each k, in which the consensus index value (ranging from 0 to 1) describes in a pairwise manner how often SOM nodes from all iterations were in the same cluster. Delta area plots were generated to determine the minimum number for k to reach high stability of metaclusters. The plots show the relative change in the area under the cumulative distribution function (CDF) curve of the consensus index value distribution comparing k with k-1. According to the elbow criterion, cluster stability was reached at k=8 for both the uncorrected and corrected data, including warp-, range- and CytoNorm-normalised data. (Figure 5-14).

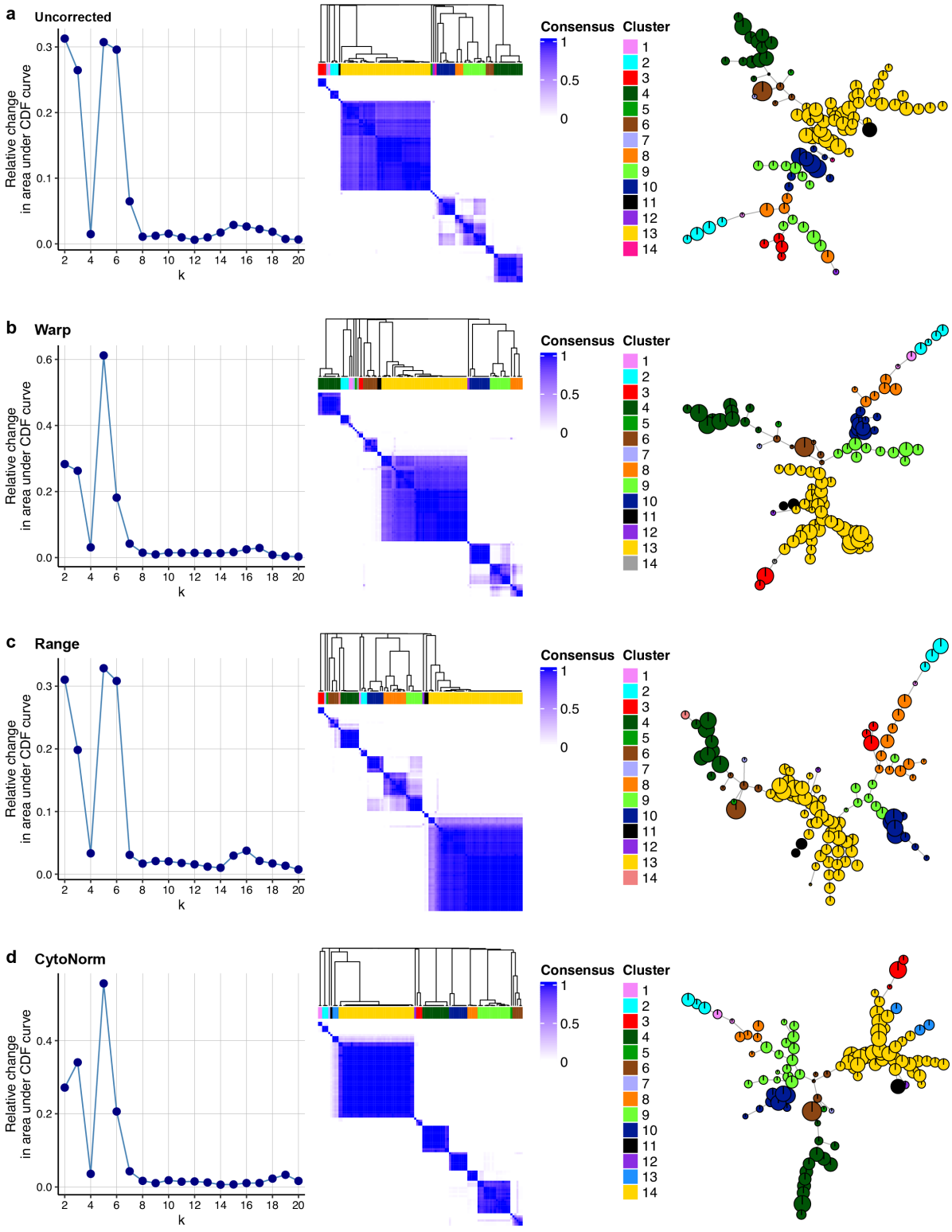


Figure 5-14. Unsupervised cluster identification using FlowSOM and ConsensusClusterPlus. (a) Uncorrected and batch-corrected ChipCytometry data, including (b) warp-, (c) range-, and (d) CytoNorm-normalised data, were clustered in a two-step process. First, a SOM with a dimension of 10x10 was created using the R package FlowSOM. In the second step, ConsensusClusterPlus was used to cluster the 100 SOM nodes to obtain the final number of clusters (metaclusters). For each of the data sets in (a) to (d), a delta area plot (left plots) was created, showing the relative change in area under the consensus CDF curve comparing k and k-1 clusters. The curve indicates the relative increase in cluster stability from k to k-1 clusters and provides an indication of the minimum number of clusters required to reach cluster stability when metaclustering the 100

SOM nodes. Metaclustering was then performed by overclustering, resulting in 14 final clusters for each of the data sets in (a) to (d). The centre plots show consensus matrices for k = 14, in which the SOM nodes are represented in both the rows and columns. Consensus values range from 0 to 1. A value of 0 indicates that a pair of SOM nodes never clustered together and a value of 1 indicates that a pair of SOM nodes always clustered together. On the right side, the SOM nodes are represented in a minimum spanning tree in which the 14 metaclusters are indicated by different colours. For unsupervised clustering, 46 markers were used that were not previously used for gating during pre-processing. The clustering illustrated in this figure was performed using only cells from the untreated (control) condition. The clustering of cells from the IL-12+IL-18-stimulated samples was performed afterwards by mapping the cells from the stimulated samples to the SOM nodes of the untreated condition. Matching clusters between the uncorrected and warp-, range-, and CytoNorm-corrected data were assigned identical colours based on the cluster matching shown in Figure 5-15.

To ensure detection of small and rare clusters, k = 14 metaclusters was chosen to overcluster the data as recommended by Nowicka et al. (170). The consensus matrices for k=14 for each of the four differently normalised data files are shown in Figure 5-14. While ambivalent clustering of the SOM nodes was low for all four data files with k=14, the CytoNorm-normalised data showed the highest cluster stability. Metaclustering of the data with k=14 was visualized by representing the SOM nodes connected in a minimal spanning tree and the 14 metaclusters indicated by coloured nodes.

5.4.8. Cluster matching and cluster characterisation

To match the 4 x 14 clusters that were identified in the unstimulated samples from the uncorrected and batch-corrected data, including warp, range and CytoNorm-normalised data, a two-step approach was applied. First, the 14 clusters within each of the four differently normalised data files were characterised using Marker Enrichment Modeling (MEM) (187, 188). Quantitative MEM identity labels in form of enrichment scores ranging from -10 to +10 were created, based on features enriched in a cluster relative to all cells not in that cluster (Figure 5-15a, Appendix Figure III-2). In the second step, the MEM label similarity between the 56 clusters from the four normalisation approaches was quantified. As a measure of similarity, the normalised root-mean-squared distance (RMSD) of the MEM scores was calculated pairwise between the 56. The normalised RMSD scores were clustered using hierarchical clustering with the Euclidean distance as the distance metric, and the

dendrogram tree was cut to obtain 17 regroups that include the matching clusters (Figure 5-15b).

The uncorrected data and the warp-, range- and CytoNorm-corrected data had only 1 unique cluster each, while all the other clusters had matching clusters in all four data files. This indicates that batch correction did not change the data in a way to have a major impact on unsupervised clustering. The data of each of the normalisation approaches was visualised using UMAP dimensionality reduction, and matching clusters were indicated by matching colours (Figure 5-15c).

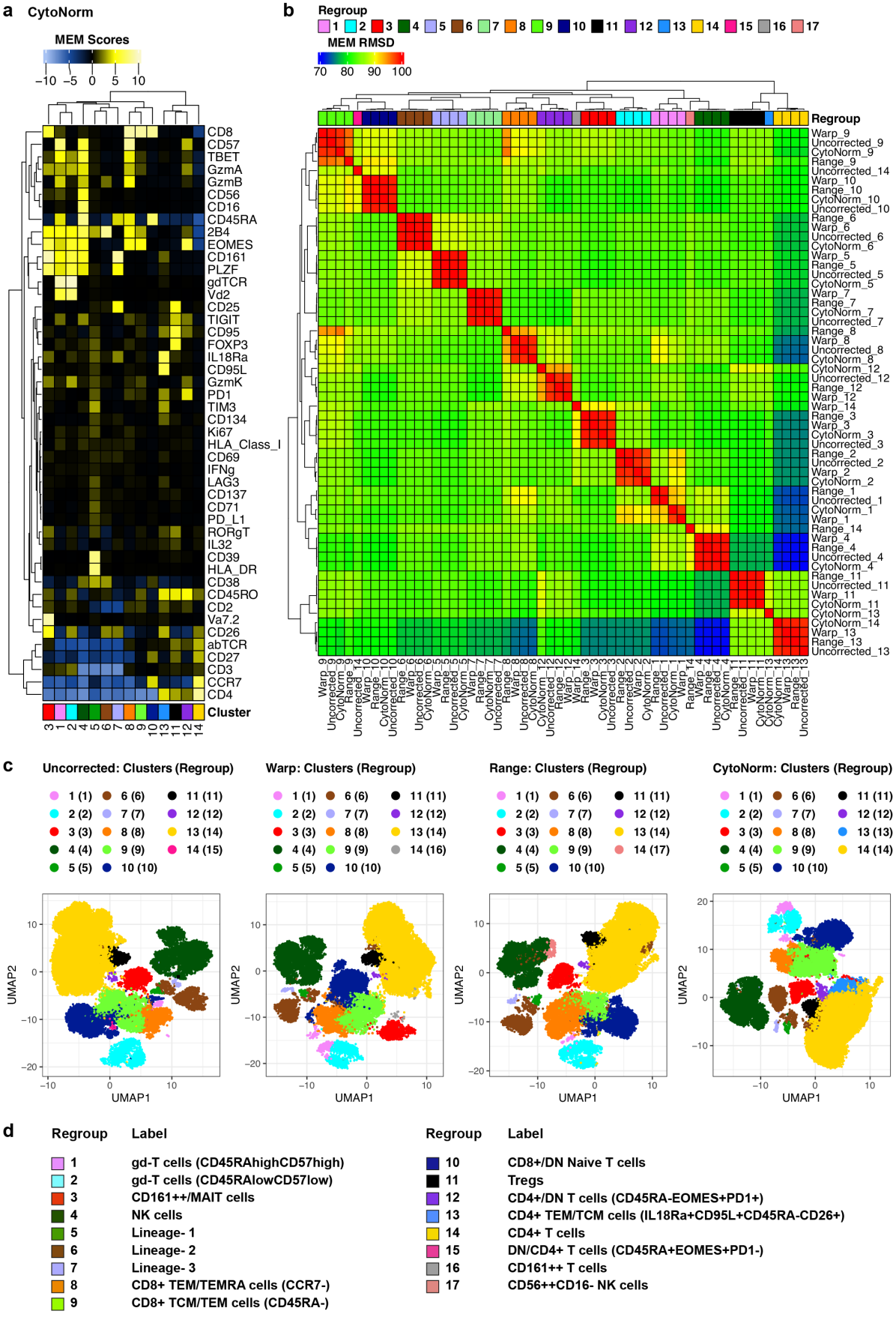


Figure 5-15. Cluster matching of clusters identified in non-batch-corrected and batch-corrected ChipCytometry data. Cluster matching of clusters that were identified in the uncorrected and batch-corrected

data, including warp, range and CytoNorm-normalised data, was performed in two steps. First, Marker Enrichment Modeling (MEM) was used to generate quantitative identity labels for each of the 14 clusters within each of the four differently normalised data files. MEM labels consist of enrichment scores ranging from -10 to +10, which are based on features enriched in a cluster relative to all cells not in that cluster. (a) As an example, the CytoNorm-normalised data results are shown as heatmap, which displays MEM scores for each of the 14 clusters and each of the 46 markers that were not previously used for gating during pre-processing. This analysis was based on unstimulated (control) samples only. (b) Secondly, MEM label similarity between the 56 clusters from all four different normalisation approaches was quantified by the pairwise calculation of the root-mean-square distance (RMSD) of the MEM scores as measure of similarity. The heatmap shows normalised MEM RMSD scores that were clustered using hierarchical clustering with the Euclidean distance as the distance metric. The dendrogram tree was cut to obtain 17 regroups that include the matching clusters. For the cluster matching process only unstimulated (control) samples were considered. (c) Clusters within the uncorrected and warp-, range-, and CytoNorm-corrected data are displayed using UMAP, including unstimulated (control) and IL-12+IL-18-stimulated samples (the cells from the stimulated condition were mapped onto the clusters from the unstimulated condition as further described in 5.4.9). Cells are coloured by cluster membership and matching clusters between normalisation approaches are displayed with identical colours. The figure legend includes the normalisation approach-specific cluster number followed by the regroup number in parentheses. (d) Labels were assigned to regroups using a multi-pronged approach, including MEM identity labels and the frequency of marker-positive cells as detailed in Figure 5-16.

Cluster labels indicated in Figure 5-15d were derived in a multi-pronged semi-supervised approach using MEM scores and gating in FlowJo, which is shown for the CytoNorm-corrected data as an example in Figure 5-15a and Figure 5-16. For instance, besides having positive MEM scores for PLZF, EOMES, TBET, IL-18Rα, CD26, GzmA and GzmK, cluster 3 of the CytoNorm-normalized data had highly positive enrichment scores for both CD161 and Vα7.2 (CD161 = +9.36, Vα7.2 = +9.08). This could lead to the conclusion that cluster 3 consists of CD161- and Vα7.2-expressing MAIT cells (Figure 5-15a). FlowJo was used to determine the frequency of marker-positive cells within each cluster for all of the 46 different markers. In addition, uni- and bivariate displays of markers were assessed (Figure 5-16a, b). FlowJo analysis revealed that all cells in cluster 3 expressed CD161, but only about 90% expressed Vα7.2. This indicated that cluster 3 also contained $CD161^{++}V\alpha7.2^{-}$ cells besides MAIT cells (Figure 5-16a). The presence of both $V\alpha7.2^{+}$ and $V\alpha7.2^{-}$ populations in this cluster was also evident from the bivariate display of CD161 vs Vα7.2 (Figure 5-16b). This was, however, not obvious from assessing MEM scores alone. $CD161^{++}V\alpha7.2^{-}$ T cells are phenotypically and functionally very similar to MAIT cells, which is probably the reason why these cells clustered together (68). Another example is Cluster 8, which contained $CD8^{+}$ T cells and had MEM scores of CD45RA = +4.53 and CCR7 = -6.00. This indicated that the

cells of this cluster belonged to the $CD45^{+}CCR7^{-}$ TEMRA subset. The FlowJo analysis revealed that about 22% of the cells were CD45RA-negative (Figure 5-16a), however, indicating that this cluster also contained TEM cells besides TEMRA cells, which was visualised in the dot plot of Figure 5-16b.

The final labels assigned to the 14 clusters from the CytoNorm-corrected data by assessing both MEM scores as well as gating in FlowJo are as follows: Cluster 1 and cluster 2 contained both γδT-cell subsets. Cluster 1 were $\gamma\delta TCR^{+}CD45RA^{high}CD57^{high}$ cells, whereas cluster 2 were $\gamma\delta TCR^{+}CD45RA^{low}CD57^{low}$ cells. In addition, cluster 1 had a higher frequency of $TIGIT^{+}$ cells, whereas cluster 2 had a higher frequency of $CD26^{+}$ and $GzmK^{+}$ cells. Cluster 3 comprised $CD161^{++}$/MAIT cells that were $CD3^{+}V\alpha7.2^{+/-}CD161^{++}$. Cluster 3 included both $CD8^{+}$ and DN T cells which expressed the transcription factors PLZF, RORγT, EOMES and TBET, had a relatively high frequency of $GzmK^{+}$ and IL-18Rα^{+} cells, and expressed high levels of GzmA, CD26 and 2B4. Cluster 4 were NK cells that were $CD3^{-}CD56^{+}$ and expressed the transcription factor EOMES, high levels of TBET and had a high frequency of $PLZF^{+}$ cells. NK cells also had a relatively high frequency of $CD16^{+}$, $GzmB^{+}$, $TIGIT^{+}$, $CD57^{+}$ and $CD161^{+}$ cells, and expressed high levels of GzmA and 2B4. The clusters 5, 6 and 7 were linage-negative cells that were $CD3^{-}CD56^{-}$. These clusters contained most likely ILCs, but were not further specified as the panel did not include necessary markers to categorise ILCs. Clusters 8, 9 and 10 contained $CD8^{+}$ T cells, from which cluster 10 also contained a small fraction of DN T cells. Cluster 8 contained $CCR7^{-}$ TEM/TEMRA cells, cluster 9 $CD45RA^{-}$ TCM/TEM cells, and cluster 10 $CD45RA^{+}CCR7^{+}$ naive T cells. Cluster 8 was positive for 2B4, TBET, EOMES, GzmA, and GzmB and expressed relatively high levels of CD57 and TIGIT, but low levels of CD27. Cluster 9 had a high fraction of $EOMES^{+}$ cells, but a relatively low fraction of $TBET^{+}$, $CD57^{+}$ and $GzmB^{+}$ cells and expressed intermediate levels of CD27. The naive T cells in cluster 10 were $CD27^{high}TBET^{-}EOMES^{-}GzmA^{-}GzmB^{-}CD57^{-}TIGIT^{-}2B4^{-}$.

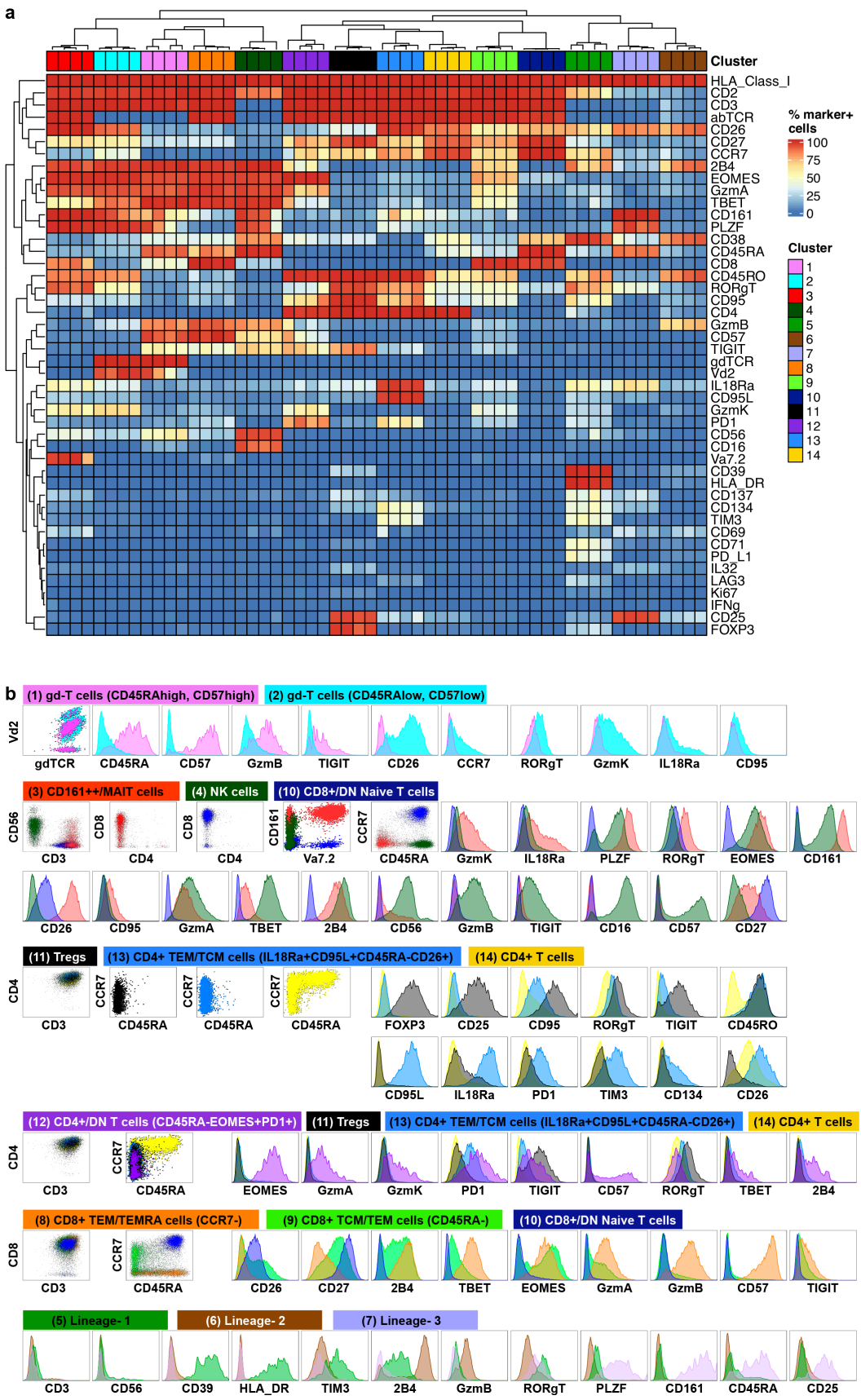


Figure 5-16. Characterisation of clusters from the CytoNorm-normalised data by analysing the frequency of marker-positive cells in each cluster.(a) To characterise the clusters identified in the CytoNorm-normalised data, the frequency of marker-positive cells for each marker in each cluster was determined by gating in FlowJo.

A threshold to define positive and negative cells was defined in a marker-specific manner. The heatmap shows the frequency of marker-positive cells for each of the four of the biological replicates. Hierarchical clustering with Euclidean distance as the distance metric was performed for both rows and columns. (b) Histograms and dot plots of selected markers that illustrate the differences between clusters are shown. The plots were generated using the aggregated data of all four donors. The cluster characterisation analysis was based on the unstimulated (control) samples.

Clusters 11, 12, 13 and 14 contained various $CD4^+$ T-cell subsets. Cluster 11 were Tregs, which were $CD3^+CD4^+FOXP3^+CD25^+CD95^+CD45RO^+$ and expressed relatively high levels of TIGIT. Cluster 12 comprised $CD4^+$ and very few DN T cells that were $CD45RA^-EOMES^+PD1^+$ and contained a relatively high frequency of $GzmA^+$, $CD57^+$ and $TIGIT^+$ cells. Cluster 13 contained $CD4^+CD45RA^-$ TEM/TCM cells that were $CD95L^+$IL-18Rα^+CD26^+ and had relatively high levels of PD1, TIM3 and CD134 expression. Cluster 14 contained the general $CD4^+$ T cell population.

In most cases, there was a relatively high agreement between matching clusters of uncorrected, warp-, range- and CytoNorm-normalized data. The detailed MEM and FlowJo gating analysis of the uncorrected data is shown in Appendix Figure III-2 and Appendix Figure III-3, and the results are very similar to the results obtained from the CytoNorm data analysis. There were, however, also some differences between matching clusters of the differently normalised data files (Appendix Figure III-4a). For example, within the uncorrected and range-normalised data, the γδT-cell subset 1 ($CD45RA^{high}CD57^{high}$) was $V\delta2^-$ and $PLZF^-$, and most cells of subset 2 ($CD45RA^{low}CD57^{low}$) were $V\delta2^+$ and $PLZF^+$. The expression of Vδ2 and PLZF was more heterogenous in subset 1 and 2 within warp- and CytoNorm-normalised data, however.

For each of the different normalisation approaches, including non-batch-corrected and warp-, range- and CytoNorm-corrected data, a unique cluster was observed. Cluster 13 ($CD4^+$ TEM/TEM cells, IL-$18RA^+CD95L^+CD45RA^-CD26^+$) within the CytoNorm-normalised file was a unique CD4 T cell cluster. Cluster 14 within the uncorrected data was a unique DN/$CD4^+$ T

cell cluster that was CD45RA^{+}EOMES^{+}PD1^{-} (Appendix Figure III-3). Within the warp-normalised data, the CD161^{++}/MAIT cells split into two clusters, where CD161^{++}Vα7.2^{-} T cells formed a separate cluster (Appendix Figure III-4b). Within the range-normalised data, NK cells were split into two clusters, including CD56^{++}CD16^{-} NK cells and the rest of the NK cells (Appendix Figure III-4c).

As CytoNorm performed best to correct for batch effects and CytoNorm-corrected data showed the highest cluster stability for the chosen cluster settings, CytoNorm-corrected data was used for all following analyses.

5.4.9. Clustering of the IL-12+IL-18-stimulated condition and comparison to clusters from the unstimulated condition

After identifying clusters within the unstimulated condition, the data of the stimulated samples were clustered by mapping the data from the stimulated sample to the SOM nodes of the unstimulated data, to allow comparison between conditions within each identified cluster.

The similarity of clusters from control and stimulated conditions was assessed by performing MEM and calculating the normalised MEM RMSD scores in a pairwise manner (Figure 5-17a, Appendix Figure III-2, Appendix Figure III-5, Appendix Figure III-6). Matching clusters showed very high similarity according to MEM RMSD scores. Only one cluster, cluster 2, had relatively low similarity between control and stimulated conditions, potentially due to a phenotype change upon stimulation.

The similarity of matching clusters from the two different conditions was further investigated. First, the proportions of the control and stimulated cells within each of the 14 clusters was analysed. In all of the 14 clusters, the conditions had almost equal proportions, resembling the proportions from the total data (Figure 5-17b, Appendix Figure III-1b). Secondly, the proportions of each of the 14 clusters were determined within each donor and each condition.

The cluster proportions were very similar between conditions (Figure 5-17c). Thirdly, the data was visualised using UMAP. The cells were coloured according to the cluster they belonged to and the analysis was stratified by condition. This showed that matching clusters of the control and stimulated condition were located in the same UMAP clusters (Figure 5-17d), although there were some condition-specific regions visible within clusters (Figure 5-17d, e).

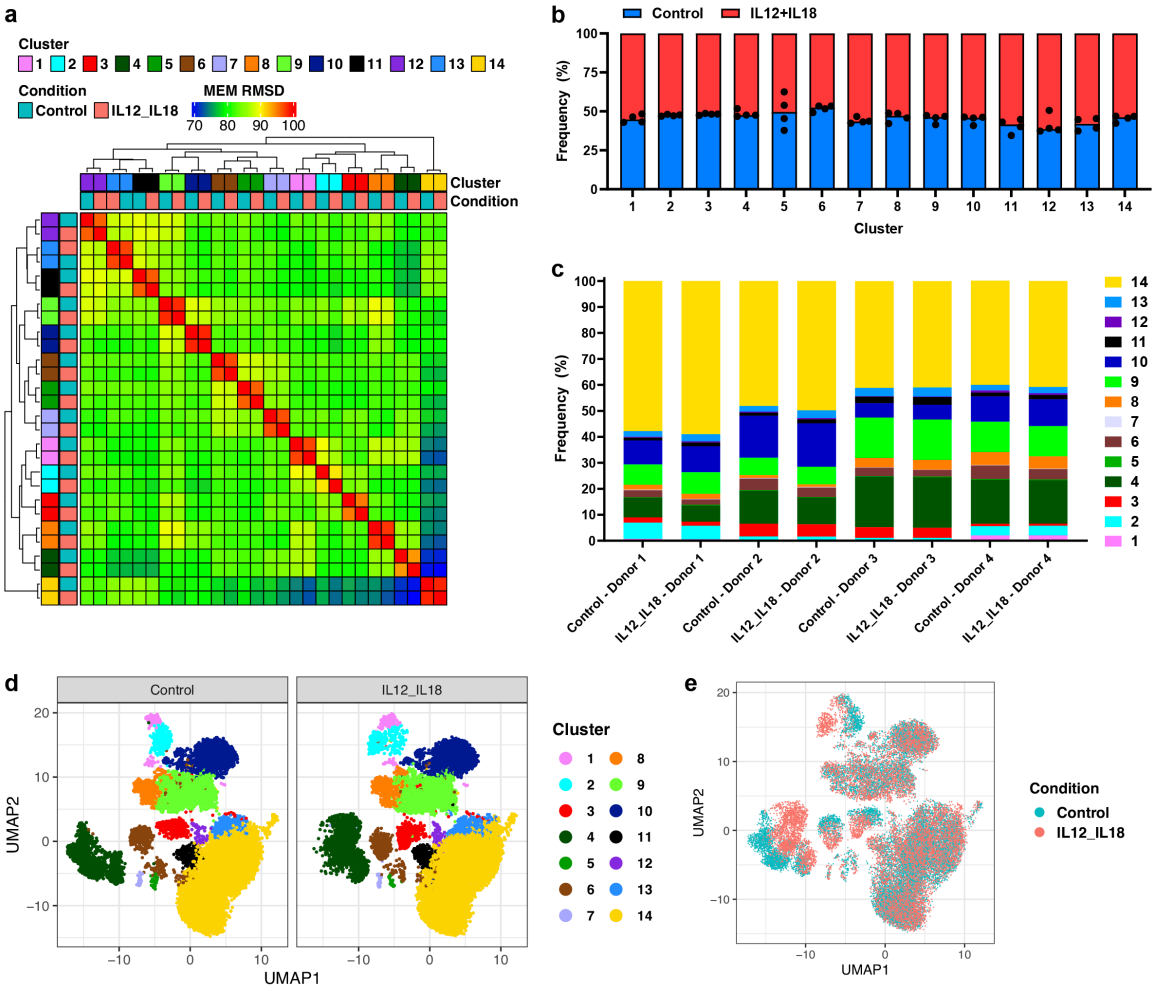


Figure 5-17. Comparison of cluster properties between stimulated and unstimulated conditions from the CytoNorm-corrected data. (a) As a measure of similarity between all 28 clusters of the unstimulated (control) and IL-12+IL-18-stimulated samples, the normalised RMSD scores were calculated in a pairwise manner, using MEM scores as input. The results are displayed in a heatmap, in which both rows and columns were hierarchically clustered using Euclidean distance as distance metric. (b) Bar plot shows relative abundance of the unstimulated (control) and IL-12+IL-18-stimulated cells within each cluster. Each dot represents a different donor. (c) Bar plot shows the relative abundance of clusters within samples stratified by donor (Donor 1-4) and condition (unstimulated = Control, stimulated = IL-12_IL-18). (d) CytoNorm-normalised data, stratified by condition, is displayed using UMAP. Cells are coloured by cluster membership. (e) CytoNorm-normalised data is displayed using UMAP. Cells coloured by condition.

In summary, these observations indicate that mapping the data from the stimulated samples to the clusters identified within the unstimulated samples resulted in similar clustering of conditions despite the possible phenotype differences between conditions. This was confirmed by analysing the frequency of marker-positive cells within each donor, condition and cluster for each of the 46 markers that were not previously used for gating during pre-processing (Figure 5-18). Hierarchical clustering resulted in the grouping of matching clusters from different conditions. In addition, there was no major difference observable between matching clusters from different conditions in regard to the expression of markers that defined the clusters and were used for cluster labelling. Similar results were obtained for the analysis of the uncorrected data (Appendix Figure III-7, Appendix Figure III-8).

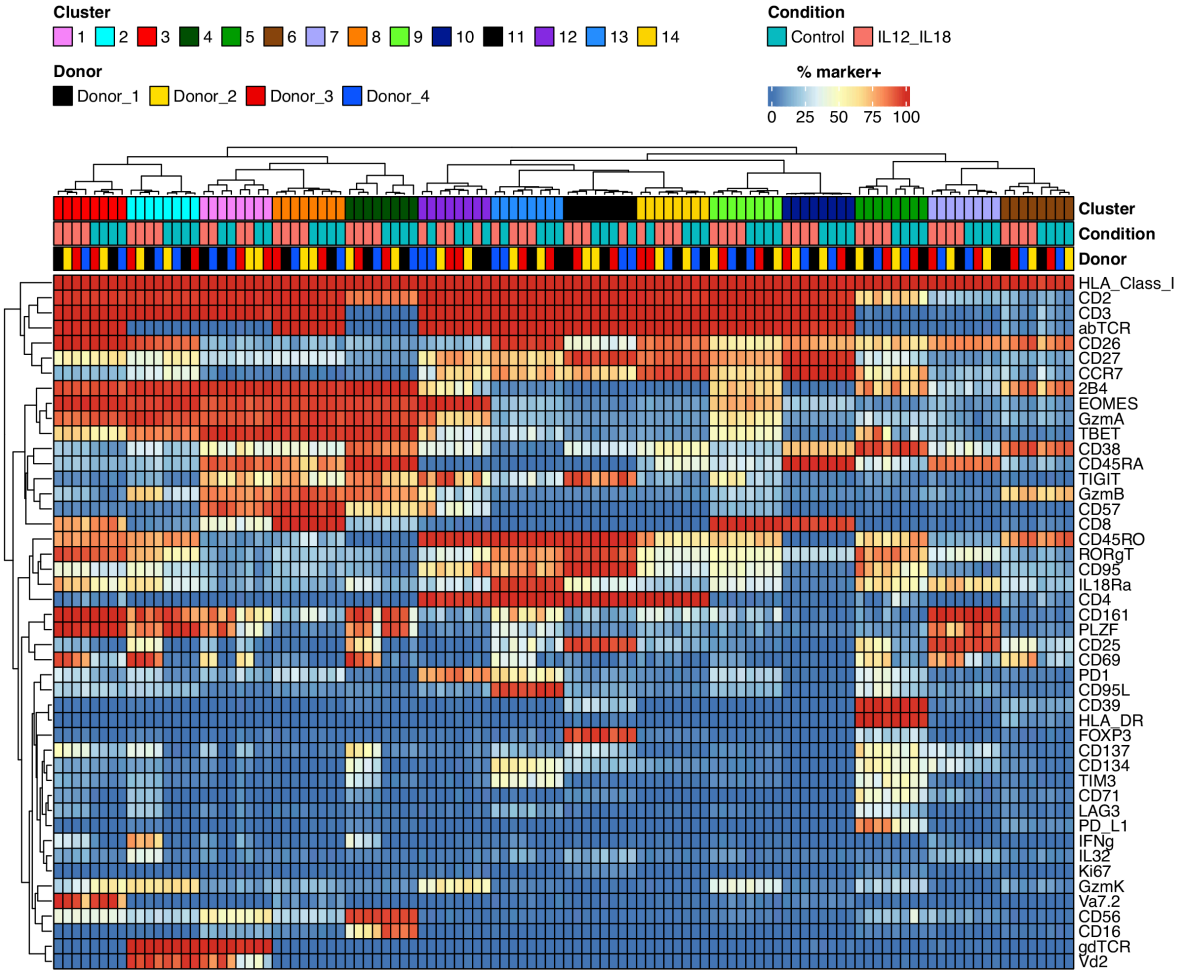


Figure 5-18. Comparison of the unstimulated and IL-12+IL-18-stimulated conditions from the CytoNorm-corrected data by analysing the frequency of marker-positive cells. The heatmap shows the frequency of marker-positive cells of each of the 46 markers that were not previously used for gating within each

of the 14 clusters. The threshold to define the frequency of positive and negative cells was defined in a marker-specific manner using FlowJo.

5.4.10. Statistical analysis of differences between unstimulated and IL-12+IL-18-stimulated cells within clusters identified by FlowSOM

Differences between the control and IL-12+IL-18-stimulated condition regarding the frequency of marker-positive cells of 24 selected markers were statistically analysed within each of the 14 clusters of the CytoNorm-normalised data (Figure 5-19, Appendix Figure III-9).

The difference in the expression of five activation markers was investigated between control and IL-12+IL-18-stimulated samples, including CD69, CD25, CD71, CD38, HLA-DR. The γδT cell cluster 2, $CD161^{++}$/MAIT and NK cells responded to IL-12+IL-18 stimulation with a significant increase in the fraction of cells expressing the activation markers CD69, CD25, CD71 and CD38. An exception was the CD38-response of the NK cells, which was lower compared to the other subsets and not statistically significant. The magnitude of these $CD161^{++}$/MAIT cell responses were consistently lower compared to the responses of γδT cell cluster 2. Cytokine-stimulated cells of the γδT cell cluster 1 had a significantly higher fractions of $CD69^{+}$, $CD25^{+}$ and $CD38^{+}$ cells than the control, but no significant CD71 response was observed. The responses of γδT cell cluster 1 were smaller in magnitude compared to γδT cell cluster 2 and similar in their magnitude to the $CD161^{++}$/MAIT cell responses. $Lineage^{-}$ clusters also responded to IL-12+18 stimulation with a significant increase in the frequency of $CD69^{+}$ cells. At least one or more $lineage^{-}$ clusters also showed a significant increase in $CD25^{+}$ and $CD38^{+}$ cells. The magnitude of the responding $lineage^{-}$ clusters was similar to $CD161^{++}$/MAIT cells and γδT cell cluster 1. $Lineage^{-}$ cluster 6 was the only cluster that showed a significant increase in the frequency of HLA-DR^{+} cells upon stimulation. The IL-18$R\alpha^{+}CD4^{+}$ T cell cluster number 13 showed significant CD69 and CD25 responses, which were lower compared to the responses of other subsets, however.

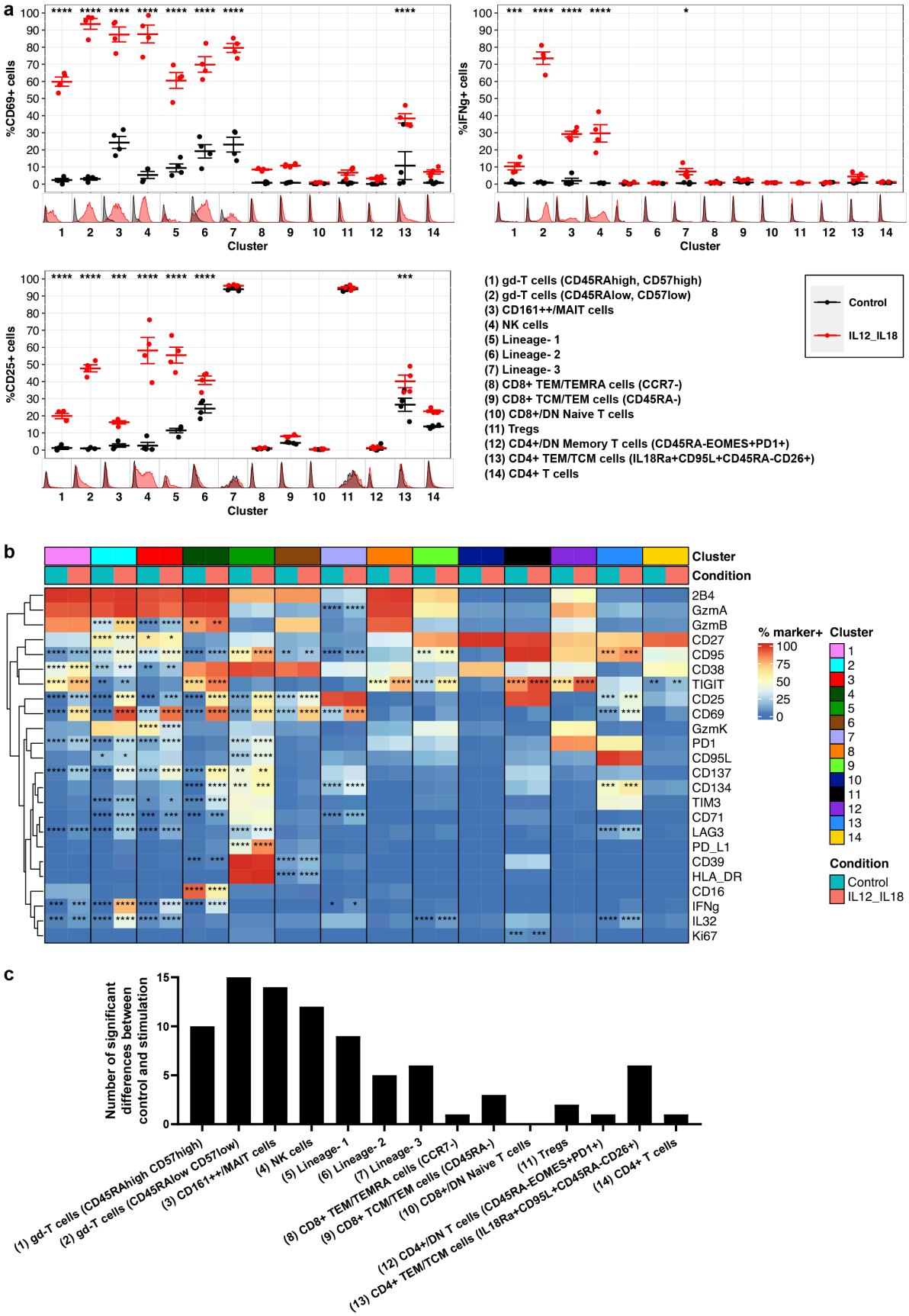


Figure 5-19. Statistical analysis comparing unstimulated and IL-12+IL-18-stimulated conditions within the clusters that were identified by FlowSOM in the CytoNorm-corrected data. Twenty-four markers that potentially change expression upon stimulation were statistically analysed. (a) As an example, the statistical

analyses of three markers, including CD69, IFNγ and CD25 are shown. The strip charts show the frequency of marker-positive cells of untreated and IL-12+IL-18-stimulated samples within each of the 14 identified clusters. The mean of each condition is indicated ± standard error of the mean (SEM). Two-way repeated measures ANOVA with Bonferroni's multiple comparisons test was performed. Representative histograms of marker expression are shown below the strip charts. (b) Summary of the results from all 24 markers that were analysed. The heatmap shows the mean frequency of marker-positive cells from 4 donors. Asterisks indicate a statistically significant difference between control and IL-12+IL-18-stimulated condition. (c) Bar chart illustrates the quantification of significant changes in the frequency of marker-positive cells between the control and stimulated condition for each cell population. ****p<0.0001, ***p<0.001, **p<0.01, *p<0.05

The expression of eight immune checkpoint receptors, including the costimulatory receptors CD134 (OX40) and CD137 (4-1BB), the inhibitory receptors PD1, TIM3, LAG3, TIGIT and CD39, and the both costimulatory and inhibitory receptor 2B4 (CD244) was compared between control and stimulated samples. Additionally, the expression of PD-L1, a ligand for PD1 was analysed. The γδT cell cluster 2 and the $CD161^{++}$/MAIT cell cluster had a significantly increased frequency of $CD137^{+}$, $PD1^{+}$, $TIM3^{+}$ and $LAG3^{+}$ cells upon stimulation compared to the control. The γδT cell cluster 1 and $lineage^{-}$ cells showed a significant upregulation of CD137, PD1 and LAG3 upon stimulation, but not of TIM3. NK cells had significant CD137 and TIM3 responses. In addition, NK cells and one of the $lineage^{-}$ clusters showed a significant increase in the frequency of $CD134^{+}$ and $CD39^{+}$ cells upon stimulation. The increase in $CD39^{+}$ cells was relatively low (3-5%), however. CD4 memory T-cell subset cluster 13 also showed a significant CD134 upregulation. A significant increase in the fraction of $TIGIT^{+}$ cells was observed for many clusters, including both of the γδT-cell subsets, NK cells, both of the CD8 memory T-cell subsets, CD4 T cells, T regs and the CD4 memory T-cell subset cluster 12. There were no significant changes observed for 2B4. The frequency of $PD\text{-}L1^{+}$ cells was significantly increased in the $lineage^{-}$ cluster 5. Overall, NK cells had the highest CD134, CD137 and TIM3 responses. The immune checkpoint upregulation of $CD161^{++}$/MAIT cells was overall lower than of the γδT cell cluster 2, and the γδT cell cluster 1 and $lineage^{-}$ cells showed even lower upregulation than $CD161^{++}$/MAIT cells.

In addition, the expression of effector cytokines and granzymes was analysed, including IFNγ, IL-32, GzmA, GzmK and GzmB. Both the γδT cell cluster 2 and the $CD161^{++}$/MAIT cell cluster

showed a significant increase in the frequency of IFNγ^{+}, IL-32^{+} and GzmB^{+} cells. In addition, CD161^{++}/MAIT cells showed a significant decrease in GzmK^{+} cells upon stimulation. The CD161^{++}/MAIT cell responses were than those of the γδT cell cluster 2. The γδT cell cluster 1 showed a significant increase in the fraction of IFNγ^{+} and IL-32^{+} cells, which was smaller in magnitude than that of γδT cell cluster 2, however. NK cells showed significant IFNγ and GzmB responses. Lineage^{-} cells showed significant IFNγ and GzmA responses, which were relatively small in magnitude.

The analysis of the expression of the death receptor FAS (CD95) and its ligand FASL (CD95L) showed that many cell types had a significantly increased frequency of CD95^{+} cells upon cytokine stimulation, including both of the γδT-cell subsets, CD161^{++}/MAIT cells, NK cells, lineage^{-} clusters, CD8^{+}CD45RA^{-} TCM/TEM cells and the IL-18Rα^{+}CD4^{+} T cell cluster number 13. CD95L-responses were observed in the γδT cell cluster 2 and in one of the lineage^{-} clusters. Further differences between the control and stimulated samples were observed for CD27, a marker associated with maturation. There was a significant decrease in CD27^{+} cells in the γδT cell cluster 2 and CD161^{++}/MAIT cells upon stimulation. A statistically significant decrease in the frequency of CD16^{+} NK cells was observed upon stimulation. For the proliferation marker Ki67, there was a very small statistically significant decrease within Tregs of about -2% upon stimulation.

In summary, the γδT cell cluster 2 (CD45RA^{low}CD57^{low}), CD161^{++}/MAIT cells and NK cells were the most responsive cell types in both the overall magnitude of the responses and the number of parameters that had a significant difference between the control and stimulated condition. Within the γδT cells, the CD45RA^{low}CD57^{low} subset (cluster 2) was overall more responsive than the CD45RA^{high}CD57^{high} subset (cluster 1) in both magnitude and number of parameters with a significant difference. There were also some significant responses observed within linage^{-} clusters depending on the marker. These responses were often smaller in their magnitude than those of the other responding cell types. The total number of

significant changes per cluster was also lower for linage^{-} cells compared to the γδT, CD161^{++}/MAIT and NK cells. The CD4 T-cell subset cluster 13, which was defined by a couple of innate-associated markers, including IL-18Rα and CD26, also responded to IL-12+IL-18 stimulation. This cell subset had significant responses within about half as many markers as the γδT, CD161^{++}/MAIT and NK cells, but the magnitude of the responses was lower overall. The analysis of the non-batch-corrected data showed similar results (Appendix Figure III-10, Appendix Figure III-11).

Next, the two different conditions were compared by performing differential expression analysis using the median marker expression as input, which provided similar results compared to the previous analysis of changes in the frequency of marker-positive cells. The median marker expression was calculated per donor, condition, cluster and marker for 24 selected markers. The medians for each cluster-marker combination were used to perform differential marker expression analysis using limma and diffcyt R packages (179, 180). Weights based on the cell count per cluster were calculated for the differential expression analysis to accommodate for the uncertainty which increases with decreasing cell numbers of clusters (170). The markers IFNγ, CD69 and TIGIT showed significant increases in median expression upon stimulation with the overall highest magnitude compared to other markers (Figure 5-20a-c). IFNγ and CD69 were particularly upregulated within the innate-like T cell populations, including γδT-cell subsets and CD161^{++}/MAIT cells, and NK cells. The largest upregulation was observed within CD45RA^{low}CD57^{low} γδT cells (cluster 2). Lineage^{-} clusters also showed a significant upregulation of CD69.

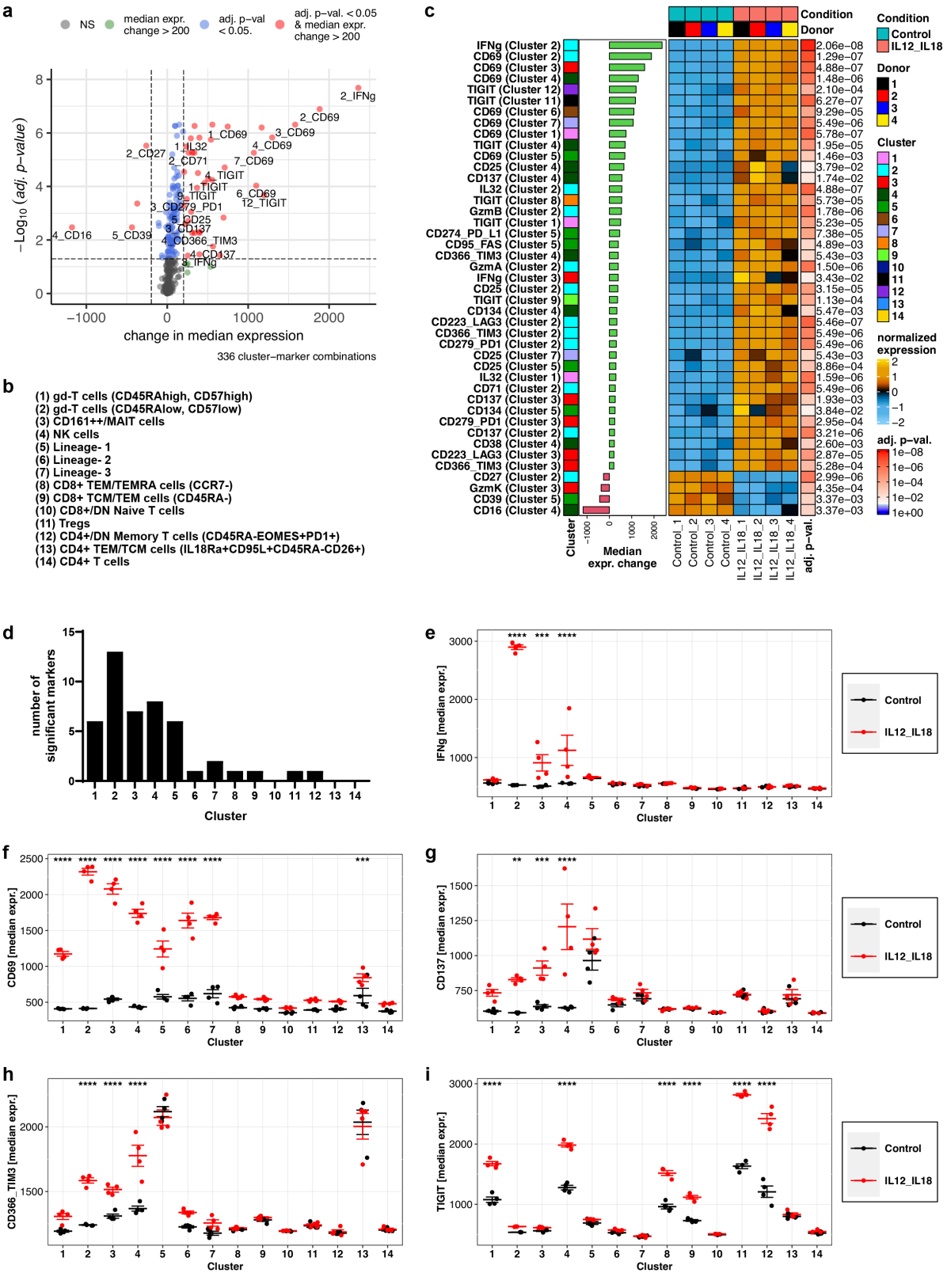


Figure 5-20. Differential marker expression analysis between control and IL-12+IL-18-stimulated conditions within FlowSOM clusters. The median marker expression was calculated per donor, condition, cluster and marker for 24 selected markers. The medians of all cluster-marker combinations were used to perform differential expression analysis between the control and IL-12+IL-18-stimulated conditions using limma and diffcyt R packages. (a) Volcano plot shows up- and down-regulated cluster-marker pairs in the IL-12+IL-18-stimulated samples compared to the control samples. Significant cluster-marker combinations were defined having both an

increase of >200 in absolute median marker expression and an adjusted p-value of < 0.05 (indicated in red). The names of some significant cluster-marker pairs are indicated by the cluster number followed by the marker name. Blue: p-value < 0.05; green: change in median marker expression > 200; NS: non-significant. (b) Cluster labels. (c) Heatmap shows z-score-normalised median expression of all significant cluster-marker pairs. The cluster-marker combinations were ordered by the change in median marker expression between conditions, which is depicted on the left side of the heatmap as a bar plot. (d) Quantification of statistically significant median marker expression changes within each cluster. (e)-(i) Strip charts show the median expression of five significantly upregulated markers in the differential expression analysis. The mean of each condition is indicated ± SEM. Two-way repeated measures ANOVA with Bonferroni's multiple comparisons test was performed, ****p<0.0001, ***p<0.001, **p<0.01, *p<0.05.

Other markers that were significantly upregulated include CD25, CD71, CD134, CD137, PD1, TIM3, LAG3, GzmB and IL-32, for example. The significant upregulation of those markers was associated with cell types from clusters 1-7 which include γδT-cell subsets, $CD161^{++}$/MAIT cells, NK cells and $lineage^{-}$ cells. Significant upregulation of TIGIT was observed in many subsets, including $CD45RA^{high}CD57^{high}$ γδT cells, NK cells, Tregs, $CD4^{+}$/DN Memory T cells cluster 12 and $CD8^{+}$ memory T-cell subsets cluster 8 and 9. The highest number of markers with a significant change in expression upon stimulation were found within the γδT-cell subsets, $CD161^{++}$/MAIT cells, NK cells and $lineage^{-}$ cells cluster 5 (Figure 5-20d). As examples, the strip charts in Figure 5-20e-i show the median marker expression of five markers that were significantly upregulated in some of the clusters, including IFNγ, CD69, TIGIT, CD137 and TIM3. In summary, differential expression analysis confirmed results from the statistical analysis using the frequency of marker-positive cells, showing that the most IL-12+IL-18-responsive subsets were γδT, $CD161^{++}$/MAIT, NK and some $linage^{-}$ cells.

5.4.11. ChipCytometry data analysis using traditional manual gating

Besides the identification of cell subsets using unsupervised clustering, bivariate manual gating was performed as an alternative analysis approach. The gating strategy is shown in Figure 5-21 for the CytoNorm-normalized data. Within the $CD45^{+}CD14^{-}CD19^{-}live/dead^{-}$ cells, three subsets including $CD3^{+}$ T cells, $CD3^{-}CD56^{+}$ NK cells and $CD3^{-}CD56^{-}$ $lineage^{-}$ cells were identified. NK cells were further stratified according to CD56 and CD161 expression levels

($CD56^{+}CD161^{-}$, $CD56^{+}CD161^{+}$, $CD56^{++}CD161^{-}$, $CD56^{++}CD161^{+}$). Within T cells, γδT cells and αβT cells were identified. γδT-cell subsets were defined by Vδ2 and CD161 expression ($Vδ2^{-}CD161^{-}$, $Vδ2^{-}CD161^{+}$, $Vδ2^{+}CD161^{-}$, $Vδ2^{+}CD161^{+}$). Within αβT cells, MAIT cells were defined as $CD161^{++}Vα7.2^{+}$. In the non-MAIT cell gate, T-cell subsets were identified according to CD4 and CD8 expression, including single-positive $CD4^{+}$ T cells, $CD8^{+}$ T cells, DP $CD4^{+}CD8^{+}$ T cells and DN $CD4^{-}CD8^{-}$ T cells. In the $CD4^{+}$ T cells, Tregs were defined as $FOXP3^{+}CD25^{+}$. Within all non-Treg $CD4^{+}$ T cells and $CD8^{+}$ T cells, memory subsets were identified (T Naive = $CCR7^{+}CD45RA^{+}$, TCM = $CCR7^{+}CD45RA^{-}$, TEM = $CCR7^{-}CD45RA^{-}$, TEMRA = $CCR7^{-}CD45RA^{+}$).

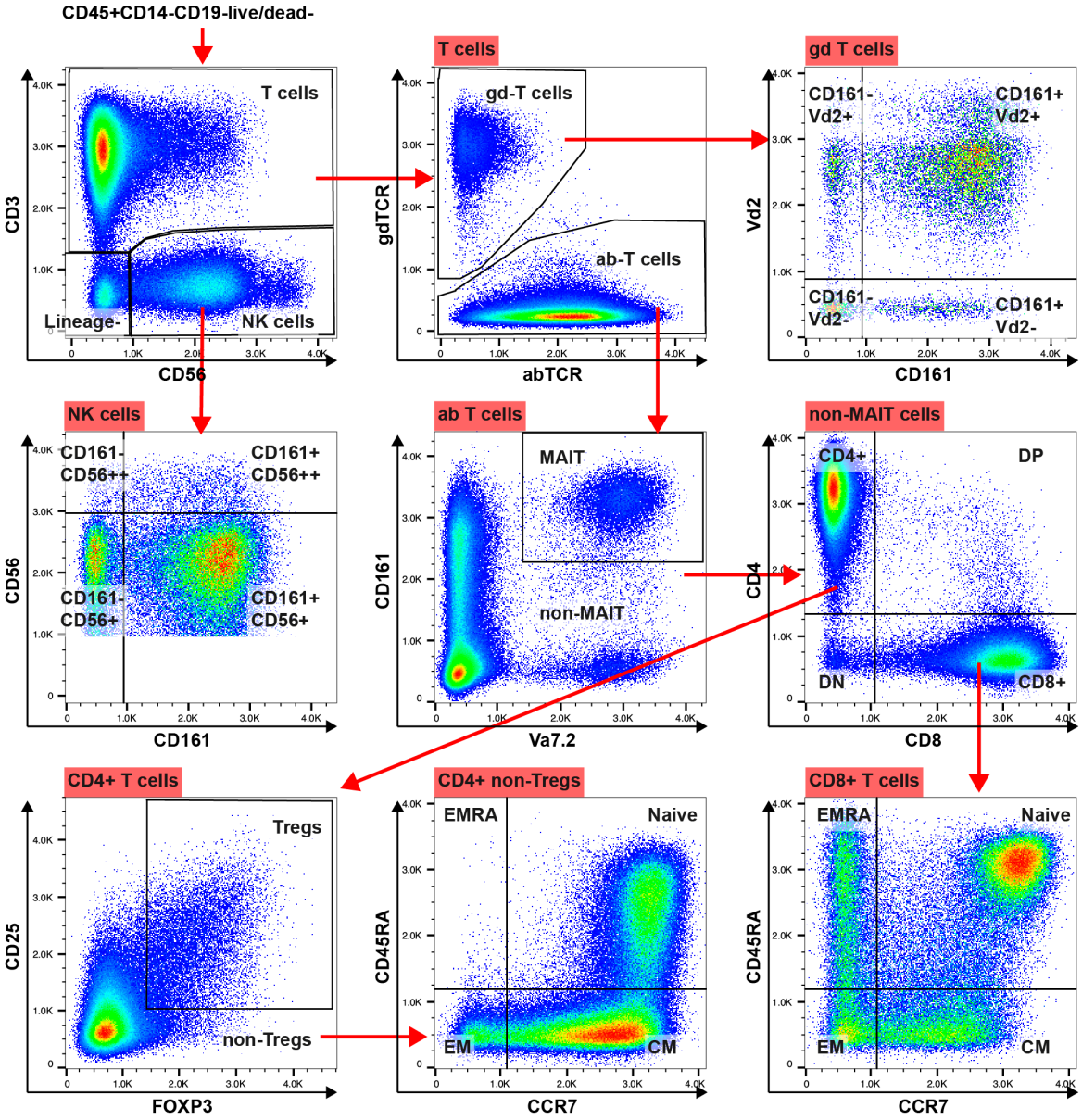


Figure 5-21. Gating strategy for manual identification of cell populations within the ChipCytometry data set. CD45$^+$CD14$^-$CD19$^-$live/dead$^-$ cells, which were gated during pre-processing in FlowJo, were used for further manual gating to define different cell populations within the data. First, CD3 and CD56 expression defined T cells (CD3$^+$), NK cells (CD3$^-$CD56$^+$) and lineage$^-$ cells (CD3$^-$CD56$^-$). NK cells were further stratified according to CD56 expression (CD56$^+$/CD56^{++}) and CD161 expression (CD161$^-$/CD161$^+$). T cells were further divided into γδT cells (γδTCR$^+$αβTCR$^-$) and αβT cells (γδTCR$^-$αβTCR$^+$). γδT cells were further stratified according to Vδ2 expression (Vδ2$^-$/Vδ2$^+$) and CD161 expression (CD161$^+$/CD161$^-$). Within αβT cells, MAIT cells were defined as CD161^{++}Vα7.2$^+$. Four subsets were defined within all non-MAIT cells according to CD4 and CD8 expression, including CD4$^+$, CD8$^+$, DN (double-negative) and DP (double-positive) cells. Within the CD8$^+$ T cells, different memory subsets were identified via differential CD45RA and CCR7 expression, including naive, TCM, TEM and TEMRA cells. Within CD4$^+$ T cells, Tregs were identified as FOXP3$^+$CD25$^+$ cells. Within the CD4$^+$ non-Treg cells, four subsets were defined according to differential CD45RA and CCR7 expression, including naive, TCM, TEM and TEMRA subsets.

5.4.12. Phenotype of cell populations that were identified by manual gating

To investigate the phenotype of the 21 cell populations identified by manual gating, the frequency of marker-positive cells for 46 markers that were not used during pre-processing was determined within each cell population of the unstimulated samples (Figure 5-22a, b).

MAIT cells expressed the transcription factors PLZF, EOMES, RORγT and intermediate levels of TBET. MAIT cells were positive for CD45RO, CD26, 2B4 and GzmA, but lacked GzmB, CD45RA and CCR7 expression. In addition, MAIT cells expressed relatively high levels of GzmK and IL-18Rα, and intermediate levels of CD27 (Figure 5-22a-b, Appendix Figure III-12, Appendix Figure III-13).

γδT-cell subsets showed a trend of increasing marker expression in the order from $CD161^{-}V\delta2^{-}$ < $CD161^{+}V\delta2^{-}$ < $CD161^{-}V\delta2^{+}$ < $CD161^{+}V\delta2^{+}$ cells for a group of markers including 2B4, CD26, EOMES, PLZF, RORγT, TBET, GzmA, GzmK, IL-18Rα and CD45RO. $CD161^{+}V\delta2^{+}$ cells showed the highest fraction of cells expressing these markers and therefore demonstrated a phenotype very similar to that of MAIT cells. An opposite trend compared to this group of markers was observed for CD45RA expression. $CD161^{-}V\delta2^{-}$ cells had the highest fraction of $CD45RA^{+}$ cells and $CD161^{+}V\delta2^{+}$ cells had the lowest fraction. In addition, the $CD161^{-}V\delta2^{-}$ population had a relatively high fraction of $CCR7^{+}$ cells compared to the other γδT-cell subsets (Figure 5-22a-b, Appendix Figure III-12).

All NK cells subsets expressed EOMES and TBET, but lacked RORγT expression. PLZF expression varied between subsets. $CD161^{+}$ NK cells had a higher frequency of $PLZF^{+}$ cells compared to $CD161^{-}$ NK cells. $CD56^{+}$ NK cells had a higher frequency of $CD16^{+}$, $CD57^{+}$, $TIGIT^{+}$ and $GzmB^{+}$ cells compared to $CD56^{++}$ NK cells, whereas $CD56^{++}$ NK cells had a higher frequency of $CD27^{+}$, $GzmK^{+}$ and $IL\text{-}18Ra^{+}$ cells compared to the $CD56^{+}$ subset. All NK-cell subsets showed relatively high numbers of $GzmA^{+}$ cells, but the fraction of $GzmA^{+}$ cells was

5. Identification and phenotyping of CD161-expressing cell types in blood

higher in CD56^{+} cells than in CD56^{++} cells. Most NK cells expressed CD45RA and CD38 (Figure 5-22a-b, Appendix Figure III-13).

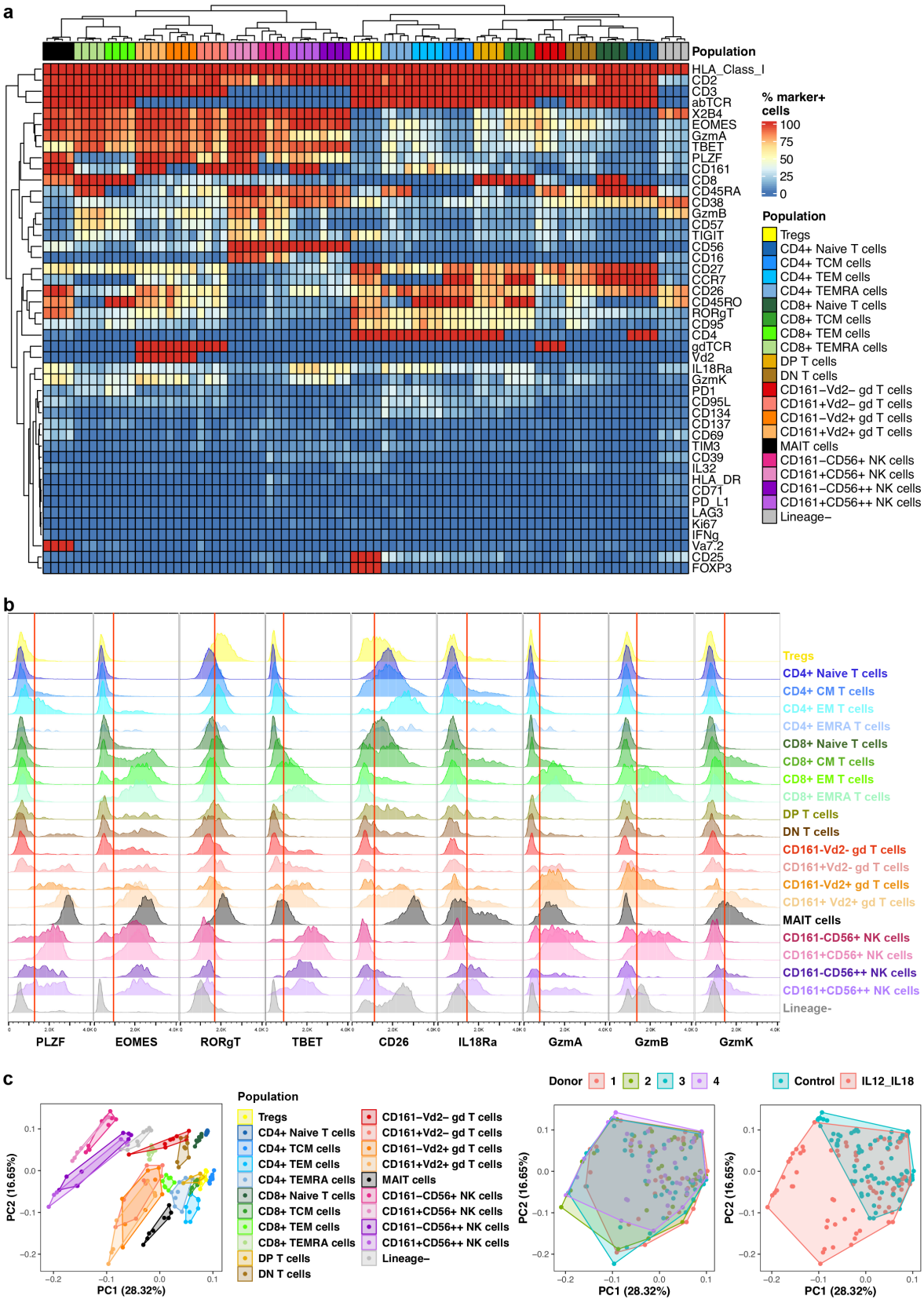


Figure 5-22. Phenotype of cell populations identified via manual gating within the CytoNorm-corrected data set. (a) To characterise the cell populations that were defined by manual gating in the CytoNorm-corrected data, the frequency of marker-positive cells for all markers was determined within each cell population using FlowJo. The results of all four biological replicates are shown in the heatmap. (b) Representative histograms of a selection of phenotyping markers are shown, including some transcription factors and innate-associated markers. Phenotyping analysis was performed using data from the unstimulated (control) samples. (c) PCA was performed using the frequency of marker-positive cells from 46 markers of all 21 cell populations and both conditions as input. The results show PC1 (principal component 1) and PC2 (principal component 2). The populations were either coloured according to their population membership (left), according to the donor number (middle) or the condition (right).

$CD4^+$ Tregs expressed CD27 and a majority of Tregs were $ROR\gamma T^+$ and $CD95^+$. A relatively high fraction of $TIGIT^+$ and $CD38^+$ Tregs (about 50% of Tregs each) were found. In addition, a small subset of $CD39^+$ Tregs (about 12%) was identified. Within $CD4^+$ memory T cells, there were $EOMES^+$, $TBET^+$ and $ROR\gamma T^+$ subsets. The fraction of $EOMES^+$ and $TBET^+$ cells was higher in TEM/TEMRA subsets compared to TCM cells. The fraction of $ROR\gamma T^+$ cells was similar between different $CD4^+$ memory T cells subsets. Naive $CD4^+$ T cells were $CD27^+$, whereas the frequency of $CD27^+$ cells was decreased in memory subsets, with TEM/TEMRA having the lowest frequency. The same trend was observed for CD38, for which memory T-cell subsets had a lower frequency of positive cells compared to naive T cells. In contrast to naive $CD4^+$ T cells, fractions of memory T cells expressed CD161 (about 50%), IL-18Rα (about 30-50%) and CD95 (about 50-70%). Naive $CD4^+$ T cells were negative for CD134, PD1, TIGIT and TIM3 in contrast to memory T cells, which showed a trend of increasing marker expression in the order from TCM < TEM < TEMRA cells. About 25% of TEM/TEMRA cells expressed CD134, PD1 or TIGIT, and about 15% expressed TIM3. In addition, about 30-35% of the TEM/TEMRA expressed CD95L (Figure 5-22a-b, Appendix Figure III-14).

Within $CD8^+$ T cell memory populations, $EOMES^+$ and $TBET^+$ subsets were found. The fraction of $EOMES^+$ and $TBET^+$ cells increased in the order from TCM < TEM < TEMRA cells. Almost all TEMRA cells were $EOMES^+$ and $TBET^+$. Fractions of $CD8^+$ T-cell subsets expressed RORγT. The fraction of $CD38^+$ cells in naive CD8 T cells was higher compared to memory subsets. Naive T cells were also $CD27^+$, and the fraction of positive cells decreased

in the order from naive T cells > TCM > TEM > TREMA cells, where TEMRA had the lowest fraction of $CD27^+$ cells. CD57 and 2B4 expression followed exactly the opposite trend compared to CD27. Memory CD8 T-cell subsets had also higher frequencies of GzmA-, GzmB-, GzmK-, CD161-, IL-18Rα-, TIGIT-, PD1- and CD95-expressing cells compared to naive cells (Figure 5-22a-b, Appendix Figure III-15).

Within both DP and DN T-cell subsets, fractions of $EOMES^+$, $TBET^+$ and $ROR\gamma T^+$ cells were observed. A large fraction of DP and DN T cells (about 70-80%) expressed CD27. A relative high fraction of $lineage^-$ cells expressed 2B4, CD38, GzmB, CD26 and CD45RO. $Lineage^-$ cells most likely comprised ILCs, but were not further specified as the panel did not include necessary markers to properly define ILCs.

PCA was performed using the frequency of marker-positive cells of 46 markers and the 21 cell populations, including both control and stimulated samples, in order to visualise the similarity between cell populations (Figure 5-22c). No difference between donors was observed according to PCA1 and PCA2, indicating that there were no batch effects. In contrast to that, control and stimulated samples did not completely overlap, indicating differences between conditions.

Similar results were obtained analysing non-batch-corrected data (Appendix Figure III-16).

5.4.13. Comparison of unstimulated and IL-12+IL-18-stimulated immune subsets that were identified by manual gating

The heatmap in Figure 5-23 shows the frequency of marker-positive cells for 46 markers within each of the 21 populations that were identified by manual gating, including both control and IL-12+IL-18-stimulated samples. The differences between conditions were statistically analysed for 24 selected markers that were not used for gating and potentially change expression within populations upon stimulation (Figure 5-24, Appendix Figure III-18).

5. Identification and phenotyping of CD161-expressing cell types in blood

The activation marker analysis revealed a significant increase in the frequency of $CD69^+$ and $CD25^+$ cells within MAIT cells, γδT-cell subsets, NK-cell subsets, $lineage^-$ cells and $CD4^+$ TEM/TEMRA subsets. Only the $CD161^-Vδ2^-$ γδT-cell subset showed no significant CD25 response. CD71 was significantly upregulated in γδT-cells and $CD56^{++}$ NK-cell subsets. MAIT cells also showed a small increase in the fraction of $CD71^+$ cells, which was, however, not statistically significant. CD38 was significantly upregulated in γδT-cells, MAIT cells and $CD161^-$ NK cells. $Lineage^-$ cells were the only subset that had a significant increase in the frequency of $HLA\text{-}DR^+$ cells upon stimulation. Overall, the largest responses were observed within γδT cells, MAIT cells and NK cells. Within γδT-cell subsets, there was a trend of increasing response magnitude with increasing Vδ2 and CD161 expression levels. Similarly, there was a trend of increasing response magnitude within NK cells with increasing CD161 and CD56 expression levels.

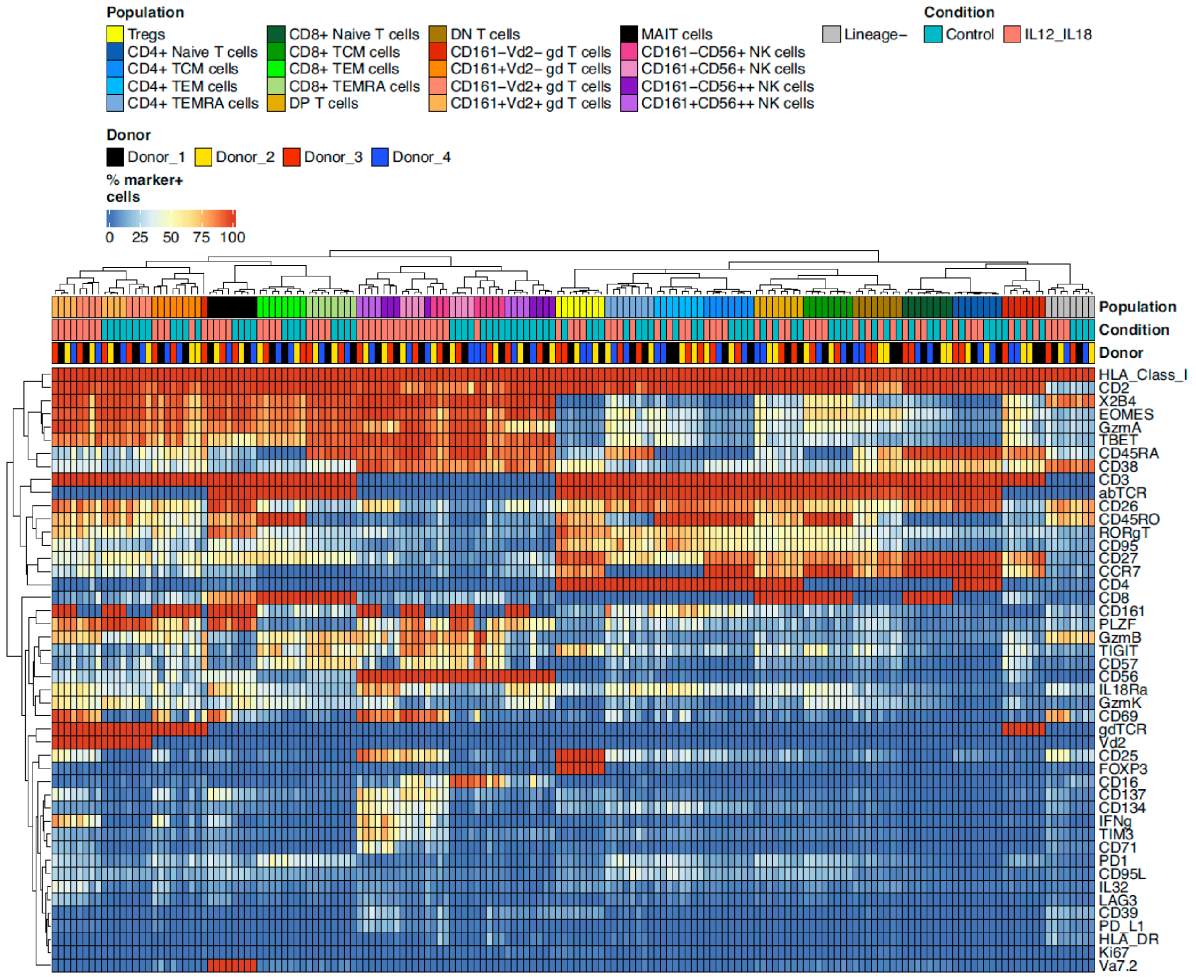


Figure 5-23. Phenotype comparison of unstimulated and IL-12+IL-18-stimulated samples. The heatmap shows the frequency of marker-positive cells of each of the 46 markers, each of the 21 populations, two conditions and four donors. The frequency of marker-positive cells was determined in FlowJo.

The upregulation of costimulatory and inhibitory checkpoint receptors and ligands varied between populations depending on the marker. MAIT cells significantly upregulated CD137, PD1 and LAG3. All γδT-cell subsets significantly upregulated PD1, CD137 and LAG3, except for the $CD161^{-}V\delta2^{-}$ subset. PD-L1 was significantly upregulated in $CD161^{+}$ γδT-cell subsets, and CD134 and TIM3 were significantly upregulated in the $CD161^{+}V\delta2^{+}$ γδT-cell subset. In contrast to that, TIGIT and 2B4 were significantly upregulated in the $CD161^{-}V\delta2^{-}$ γδT-cell subset only. Stimulated NK cells showed significantly higher frequencies of $CD134^{+}$, $CD137^{+}$, $LAG3^{+}$, $TIGIT^{+}$ and $PD\text{-}L1^{+}$ cells than the control condition. In addition, $CD56^{++}$ cells showed significant TIGIT and CD39 upregulation. Significant upregulation of CD134, CD39 and PD-L1 was observed for $lineage^{-}$ cells. $CD4^{+}$ TEMRA cells showed significant CD134, PD1 and 2B4 upregulation, and the frequency of $TIGIT^{+}$ cells was significantly increased within Tregs, $CD4^{+}$ TCM/TEMRA cells and all $CD8^{+}$ memory subsets. The response magnitude regarding immune checkpoint receptor upregulation varied between different subsets depending on the marker. Overall, NK cells showed some of the largest changes upon stimulation.

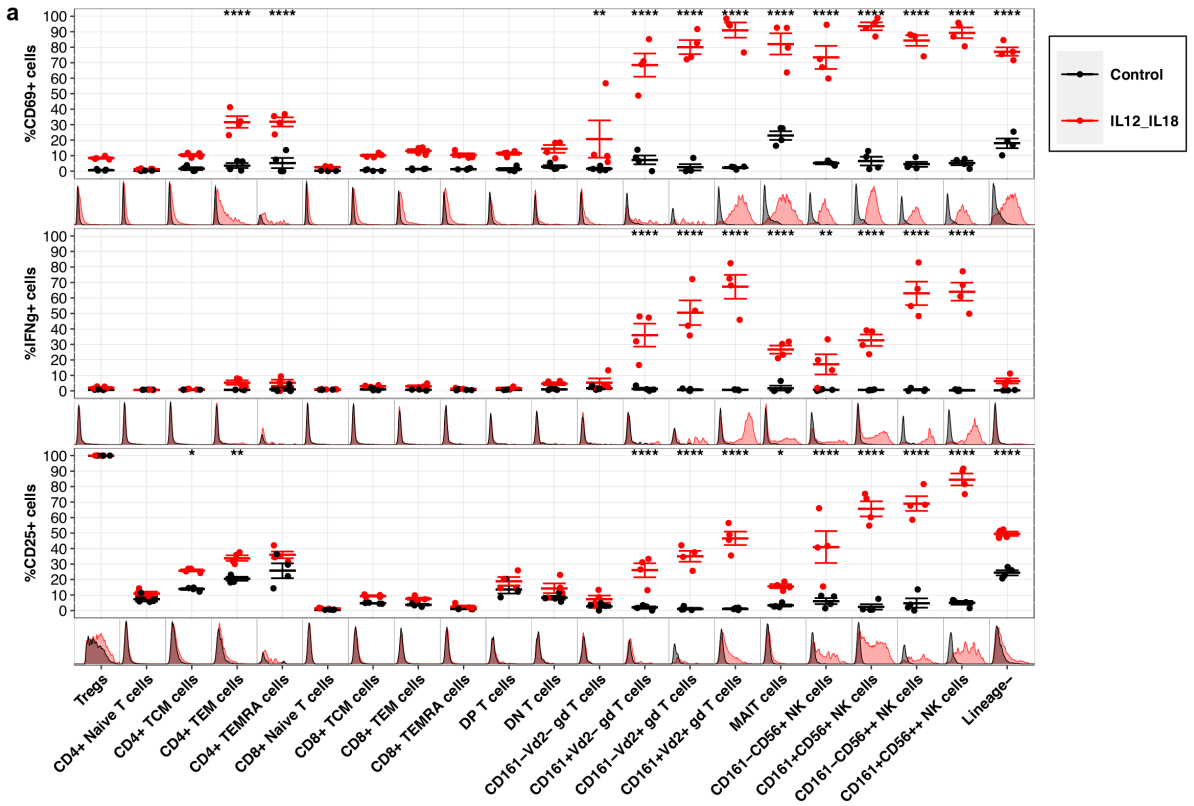
Upon stimulation, MAIT cells had a significantly increased frequency of $IFN\gamma^{+}$ cells compared to the control condition. There was also an increased frequency of $GzmB^{+}$ cells, which was, however, not statistically significant. But there was a statistically significant decrease in the frequency of $GzmK^{+}$ MAIT cells. γδT-cells, except for the $CD161^{-}V\delta2^{-}$ subset, showed significant IFNγ and IL-32 responses. There was also a significant upregulation of GzmB in all γδT-cells, except for $CD161^{+}V\delta2^{-}$ cells. Overall, there was a trend of increased responses of Vδ2- and CD161-expressing γδT-cells compared to non-expressing cells. All NK-cell subsets responded to cytokine stimulation by upregulating IFNγ. There was a trend of increasing IFNγ upregulation within NK cells with increasing levels of CD56 and CD161 expression. In addition, $CD56^{++}$ NK-cell subsets significantly upregulated IL-32, GzmA and

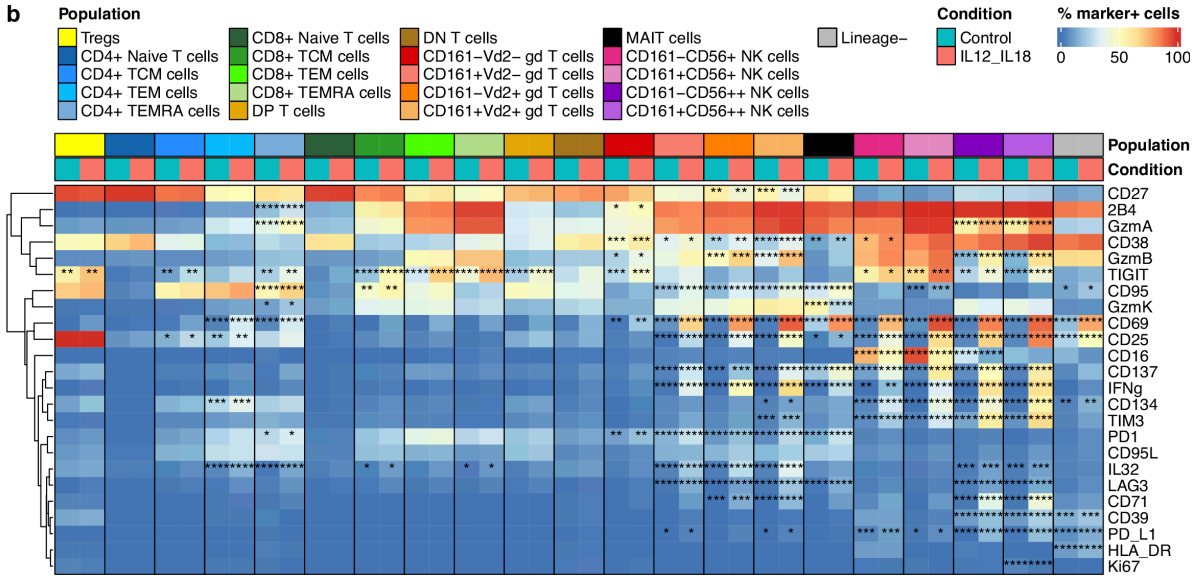
GzmB. Besides the responses of NK cells and innate-like T cells, $CD4^+$ TEMRA cells significantly upregulated GzmA and GzmK. In addition, $CD4^+$ TEM/TEMRA cells and $CD8^+$ TCM/TEMRA cells upregulated IL-32 upon stimulation. IL-32 expression was particularly associated with $CD161^{+/++}$ subsets within conventional T cells (Appendix Figure III-17).

Cytokine stimulation also induced a significant increase in the frequency of $CD95^+$ cells within all γδT-cell subsets, $CD161^+CD56^+$ NK cells, $CD4^+$ TEMRA cells, $CD8^+$ TCM cells and $lineage^-$ cells. There was no statistically significant change in the fraction of $CD95L^+$ cells observable. In contrast, the fraction of $CD27^+$ cells was significantly decreased in $Vδ2^+$ γδT-cell subsets upon stimulation. The frequency of $CD16^+$ cells was significantly decreased within NK-cell subsets except for the $CD161^+CD56^{++}$ subset. The latter subset showed, however, a significant decrease of $Ki67^+$ cells of about 2.5% upon stimulation.

In summary, the overall most responsive subsets were γδT cells, MAIT cells and NK cells, which showed the highest number of markers with a significant difference between the control and stimulated condition. Overall, the magnitude of the responses within γδT cells often increased with Vδ2 and CD161 expression. Similarly, the magnitude of NK cell responses increased often with CD56 and CD161 expression. The MAIT cell responses were often weaker compared to γδT and NK cell responses. In addition, there were also relatively many significant responses within the $CD4^+$ TEMRA subset and $lineage^-$ cells. The magnitude of those responses was, however, often smaller than those of γδT cell, NK cell and MAIT cells.

Similar results were obtained in the analysis of non-batch-corrected data (Appendix Figure III-19, Appendix Figure III-20).


a
%CD69+ cells
%IFNg+ cells
%CD25+ cells
Control
IL12_IL18
Tregs
CD4+ Naive T cells
CD4+ TCM cells
CD4+ TEM cells
CD4+ TEMRA cells
CD8+ Naive T cells
CD8+ TCM cells
CD8+ TEM cells
CD8+ TEMRA cells
DP T cells
DN T cells
CD161−Vd2− gd T cells
CD161+Vd2− gd T cells
CD161−Vd2+ gd T cells
CD161+Vd2+ gd T cells
MAIT cells
CD161−CD56+ NK cells
CD161+CD56+ NK cells
CD161−CD56++ NK cells
CD161+CD56++ NK cells
Lineage−


b
Population
Tregs
CD4+ Naive T cells
CD4+ TCM cells
CD4+ TEM cells
CD4+ TEMRA cells
CD8+ Naive T cells
CD8+ TCM cells
CD8+ TEM cells
CD8+ TEMRA cells
DP T cells
DN T cells
CD161−Vd2− gd T cells
CD161+Vd2− gd T cells
CD161−Vd2+ gd T cells
CD161+Vd2+ gd T cells
MAIT cells
CD161−CD56+ NK cells
CD161+CD56+ NK cells
CD161−CD56++ NK cells
CD161+CD56++ NK cells
Lineage−
Condition
Control
IL12_IL18
% marker+ cells
0
50
100
Population
Condition
CD27
2B4
GzmA
CD38
GzmB
TIGIT
CD95
GzmK
CD69
CD25
CD16
CD137
IFNg
CD134
TIM3
PD1
CD95L
IL32
LAG3
CD71
CD39
PD_L1
HLA_DR
Ki67

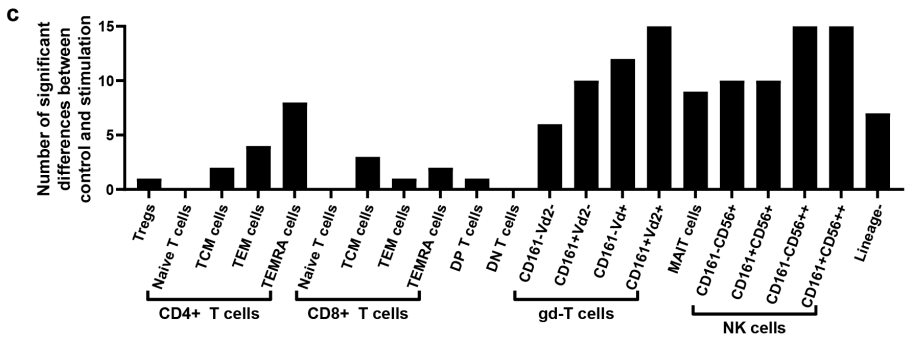

c
Number of significant differences between control and stimulation
Tregs
Naive T cells
TCM cells
TEM cells
TEMRA cells
Naive T cells
TCM cells
TEM cells
TEMRA cells
DP T cells
DN T cells
CD161-Vd2-
CD161+Vd2-
CD161-Vd+
CD161+Vd2+
MAIT cells
CD161-CD56+
CD161+CD56+
CD161-CD56++
CD161+CD56++
Lineage-
CD4+ T cells
CD8+ T cells
gd-T cells
NK cells

Figure 5-24. Statistical analysis comparing unstimulated and IL-12+IL-18-stimulated conditions within populations identified by manual gating. Twenty-four markers that potentially change expression upon stimulation were statistically analysed. (a) As an example, the statistical analyses of three markers, including CD69, IFNγ and CD25 are shown. The strip charts show the frequency of marker-positive cells of untreated and IL-12+IL-18-stimulated samples within each of the 21 populations that were identified via manual gating. The mean of each condition is indicated ± SEM. Two-way repeated measures ANOVA with Bonferroni's multiple comparisons test was performed. Representative histograms of marker expression are shown below the strip charts. (b) Summary of the results from all 24 markers that were analysed. The heatmap shows the mean frequency of marker-positive cells from 4 donors. Mean values for each condition within each of the 21 populations are shown. Asterisks indicate a statistically significant difference between the control and IL-12+IL-18-stimulated condition. (c) Bar chart illustrates the quantification of significant changes in the frequency of marker-positive cells between the control and stimulated condition within each cell population. ****p<0.0001, ***p<0.001, **p<0.01, *p<0.05.

Besides the comparison of conditions using the frequency of marker-positive cells, differential marker expression analysis was performed based on the median marker expression of 24 selected markers within the 21 cell populations (Figure 5-25a-c). Statistically significantly upregulated markers in the IL-12+IL-18-stimulated cells with the highest increase in median marker expression included IFNγ and CD69. Those markers were significantly upregulated in γδT-cell subsets, except the $CD161^{-}V\delta2^{-}$ subset, NK-cell subsets and MAIT cells. The highest CD69 and IFNγ responses were observed within $CD56^{++}$ NK cells and $V\delta2^{+}$ γδT cells. MAIT cells showed a similarly high CD69 but a lower IFNγ upregulation. Other markers that showed significant changes in median marker expression were also associated with innate-like cell types including γδT cells, NK cells and MAIT cells. Those markers include CD25, CD137, CD134, GzmA, GzmB, TIM3, PD1, LAG3 and IL-32. Some conventional T-cell subsets, including Tregs and $CD4^{+}$ and $CD8^{+}$ memory T cells showed significant upregulation of TIGIT. Furthermore, $lineage^{-}$ cells showed a relatively high CD69 and CD25 upregulation. The median expression of three of the significant markers that showed changes in median marker expression of relatively high magnitude, including CD69, IFNγ and CD137, are depicted in Figure 5-25d in form of strip charts.

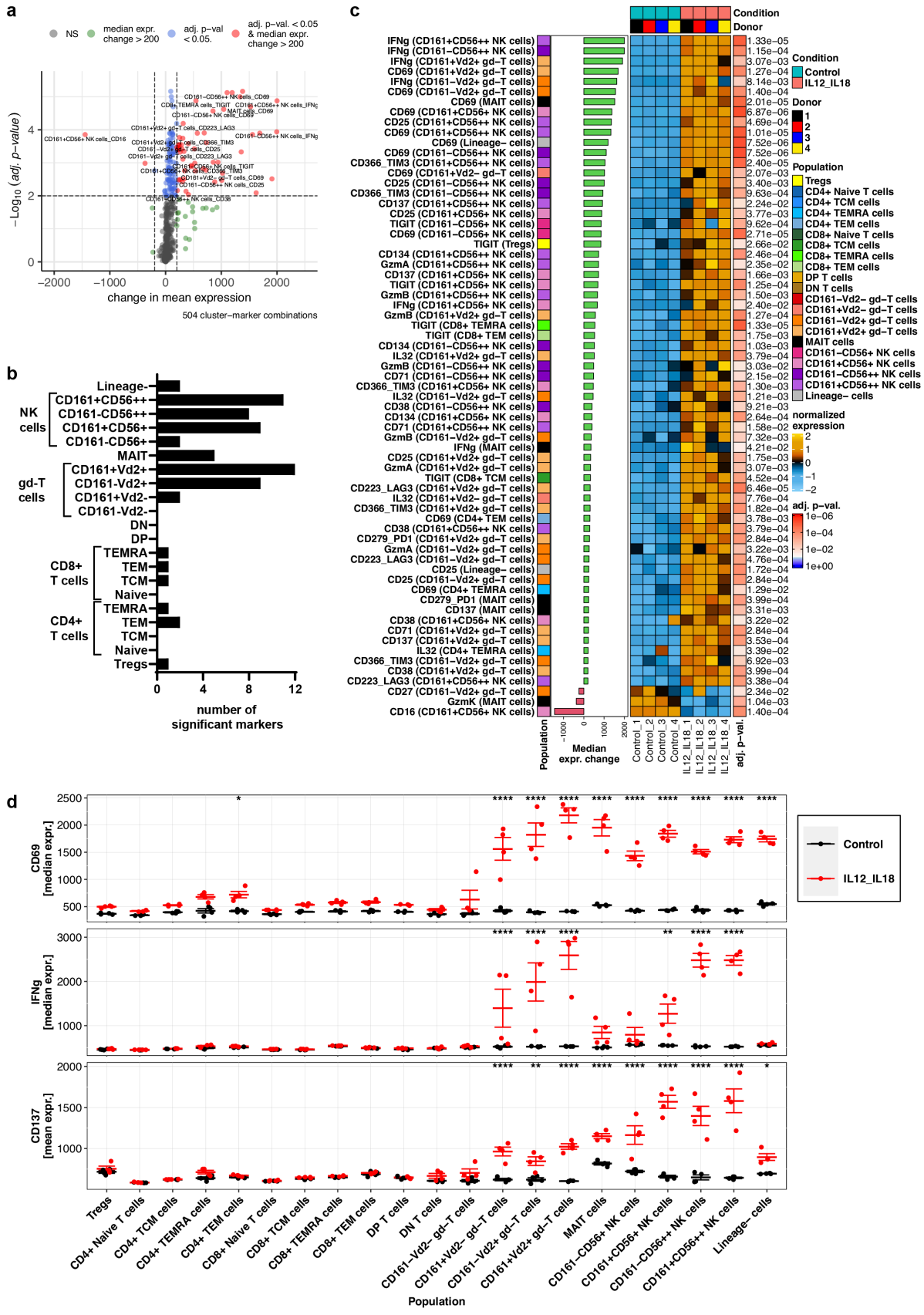


Figure 5-25. Differential marker expression analysis of manually gated data. The median marker expression was calculated per donor, condition, population and per marker for 24 selected markers. The medians of all population-marker combinations were used to perform differential expression analysis between the control and

IL-12+IL-18-stimulated conditions. (a) Volcano plot shows up- and down-regulated population-marker pairs in the IL-12+IL-18-stimulated samples compared to the control samples. Significant population-marker combinations were defined having both an increase of >200 in absolute median marker expression and an adjusted p-value of < 0.05 (indicated in red). The names of some significant population-marker pairs are indicated by the cluster number followed by the marker name. Blue: p-value < 0.05; green: change in median marker expression > 200; NS: non-significant. (b) Quantification of statistically significant median marker expression changes within each population. (c) Heatmap shows z-score-normalised median expression of all significant population-marker pairs. The population-marker combinations were ordered by the change in median marker expression between conditions, which is depicted on the left side of the heatmap as a bar plot. (d) Strip charts show the median expression of three markers that were significantly upregulated in the differential expression analysis. The mean of each condition is indicated ± SEM. Two-way repeated measures ANOVA with Bonferroni's multiple comparisons test was performed, ****p<0.0001, ***p<0.001, **p<0.01, *p<0.05.

5.5. Discussion

5.5.1. Development of an analysis protocol for cell suspension ChipCytometry data

In this study, a panel of 50 markers was applied on cell suspension samples using the ChipCytometry technique for the first time. In addition, an analysis protocol for high content ChipCytometry data was developed. There are analysis protocols for high content cytometry data from similar methods such as mass cytometry (170), but these protocols lack some technique-relevant steps for the analysis of ChipCytometry data, for example the identification and removal of fluorescence anomalies. Finally, the phenotype of blood-derived innate-like T cells and NK cells was determined, and it was shown that innate-like T cells and NK cells are the primary responders to IL-12+IL-18 stimulation.

For data transformation, FlowJo-type biexponential transformation was applied (181–183), which performed well in terms of compressing the positive populations, keeping compact negative populations while adjusting the data in a way that it spans the whole channel range set from 0 to 4096 (Figure 5-2). For a few markers, a suitable transformation to obtain a marker distribution that spans the whole channel range could not be achieved, leading to the introduction of a rescaling step later on (Figure 5-6). Other transformation functions could be applied that might result in a more suitable transformation of problematic markers without requiring a rescaling step, for example hyperlog or inverse hyperbolic sine (arcsinh) transformation (189).

A problem that was encountered is that ChipCytometry data is affected by fluorescence anomalies (Figure 5-3). The reasons are manifold, including detritus, dust, fibres and air bubbles entering the microfluidic channel of the sample chips. The foreign particles or air bubbles can impact the fluorescence intensity values of covered cells, resulting in fluorescence anomalies. The particles causing the fluorescence anomalies are often not stationary and can move across the chip during and between staining cycles. The image processing pipeline of the company that is implemented in the ZKWapp fails to remove fluorescence anomalies. The app is capable of removing cell clumps during cell segmentation calculation based on a reference acquisition cycle. Still, it fails to remove non-stationary fluorescence anomalies which are spread over different acquisition cycles. The proprietary algorithm “surrounding pixel correction” of the company can improve the impact of fluorescence anomalies in some cases (Figure 3-7). However, despite using “surrounding pixel correction”, 5-11% of the data in this study was still affected by obvious fluorescence anomalies (Figure 5-3, Figure 5-4, Figure 5-5, Figure 5-6, Appendix Figure II-1).

Current approaches to eliminate fluorescence anomalies within cytometry data include the manual removal by visual inspection for changes in fluorescence intensity over acquisition time on a marker-by-marker basis and more sophisticated tools such as flowClean, flowAI and flowCut (184, 190, 191). The tool flowClean tracks fluctuations of cell populations, which represent a summary of all parameters in centred log ratio space over time (184). FlowAI is a three-pronged approach that removes suspected anomalies based on changes in the flow rate (number of acquired cells per time unit), instabilities of signal intensity over time, and margin data points in the upper limit of the dynamic range and outliers in the lower limit (190). FlowCut removes time segments with a low flow rate and eliminates conspicuous time segments based on 8 measures calculated from the marker intensity values (191). ChipCytometry does not contain a time parameter, making ChipCytometry FCS data files incompatible with any of these fluorescence anomaly removal tools. Instead of being

associated with time, fluorescence anomalies in ChipCytometry data are conspicuous within a spatial context.

An option to identify ChipCytometry fluorescence anomalies was the visual inspection of recorded raw images. This can be very time consuming even for small-scale experiments such as the data generated in this study, which consisted of samples from only 4 donors each located on a separate chip. The data set of this study comprised a total of 17,600 images of acquired fluorescence signals (44 positions/chip x 4 chips x 50 markers x 2 acquired images/position - pre and post staining). In case the transmitted light images are checked in addition to the fluorescence images in order to obtain further information about the cause of the fluorescence anomalies, the number of images that need to be checked could potentially be doubled. Examining such a high number of images and manually deleting cells affected by fluorescence anomalies from the segmentation is extremely time consuming, particularly considering the responsiveness of the ZKWapp that took up to 15 seconds to load a single image. For the data of this study, the total loading time for the images can sum up to about 73-147 hours without accounting for the time required to inspect for and correct anomalies.

To speed up the process of manual inspection, a strategy was developed to predict the chip positions that contain fluorescence anomalies and the affected area within flagged chip positions. This was achieved by dividing each chip position in smaller units by applying a 14x10 grid and by comparing the median marker expression of each grid subunit to the overall median of all grid subunits in a marker-specific manner. Grid subunits that were identified as outliers were flagged for potentially containing a fluorescence anomaly (Figure 5-4). Therefore, only positions containing flagged grid units were visually inspected. In the case of true positive warnings, the cells within the flagged grid subunits were not simply excluded from the data, but cells affected by fluorescence anomalies were manually removed from the cell segmentation. The reason is that the rectangular grid subunits could not accommodate the various shapes of fluorescence anomalies. This is not too much of a concern if the grid

unit also covers some unaffected area in addition to an affected area, besides losing good data. But the flagged grid units often only covered parts and not the complete area of a fluorescence anomaly, which was most evident at the border regions of fluorescence anomalies (Figure 5-5). The manual elimination of identified fluorescence anomalies allowed a more accurate outline of affected areas and data clean-up. For the generation fluorescence anomaly warnings, non-stringent values for parameters such as grid size and the threshold for flagging grid subunits as outliers were chosen to allow a relatively high number of false positives (approx. 70% on average) with the aim to minimise false negatives. Any potential false negative warnings were not quantified due to the vast number of total grid subunits to check manually (more than 1.23 million in total).

This approach of fluorescence anomaly removal performed very well when comparing the data before and after fluorescence anomaly removal (Figure 5-6c-f). There were, however some rare cases of remaining outliers that were not picked in the process of computationally predicting fluorescence anomalies (Figure 5-6a, b). The remaining outliers, identified via visual inspection, were therefore manually removed via gating.

In order to automate the process of fluorescence anomaly detection, a small subsample of the data could be further annotated and indexed for false and true positive and false and true negative warnings. This could be used to train a neural network to predict fluorescence anomalies in an automated manner. If it is possible to train a neural network to identify fluorescence anomalies missed by the warnings generated in this study, the second additional data clean-up step of visual inspection for remaining outliers and their manual removal by gating would be rendered redundant.

Another issue encountered is that ChipCytometry data is affected by batch effects (Figure 5-8). Batch effects consisted of misaligned marker histogram peaks, obvious differences in the expression range or of combinations of both. One could avoid batch effects by placing

multiple samples that are to be compared with each other on a single chip using barcodes. The downside is, however, that this limits the maximal number of cells that can be acquired per sample. In addition, the antibodies required for barcodes also limit the number of other markers that can be applied during the first acquisition round in which markers can be acquired that require staining before sample fixation.

Several different tools are available to correct for batch effects within cytometry data, including quantile-, range- and warp-normalisation from the cydar R package, and QuantileNorm and CytoNorm from the Cytonorm package (176, 177). The cydar quantile correction coerces the quantiles of each batch to the quantiles of a reference, which was the mean of all batches in this study. Range-correction equalises the range of each batch to the range of the pooled distribution of all batches at percentiles p and 1-p. Warp-correction identifies high-density regions (landmarks) of each marker and aligns landmarks by computing warping functions (192). Similar to the cydar quantile function, QuantileNorm adjusts the quantiles of each batch to the quantiles of the defined reference. CytoNorm correction, on the other hand, is a two-step process. First, batch effects are learned based on reference control samples that are shared across batches. Training includes unsupervised clustering to identify cell populations within control samples. Within each cluster, quantiles of each marker are computed for each control sample and a goal distribution is generated. Spline functions are computed that allow the translation of the old values to the new values from the goal distribution. In the second step, other samples are mapped to the clusters identified within reference samples and quantiles of the other samples are aligned to the goal distribution for each cluster and each marker using the splines. The reason to perform batch correction separately within each cluster is to remove any dependencies between markers (177).

In ChipCytometry, each sample located on a different chip constitutes a different batch. In addition, the trend of the differences between batches can vary between separate acquisition

cycles, resulting in each cycle representing essentially a different batch. The use of control samples in ChipCytometry could be achieved by mixing experimental samples with control samples applying barcodes. There are several issues to consider, however. First, cell numbers on a chip are limited and space is scarce even for experimental samples. Rare sample chips can fit more cells due to an increased surface compared to standard chips. But as ChipCytometry is a sequential process regarding both marker acquisition and acquisition of multiple positions, this would significantly decrease sample throughput. In addition, the impact of increased exposure periods of samples to the interior of the ChipCytometer, encountering heat and scattered light during image acquisition and photobleaching, needs to be investigated. Secondly, the antibodies required for barcoding, which can allow reference control samples to be added onto the chip, limit the number of markers that can be stained prior to sample fixation and acquired in the first round of image acquisition. As no reference control samples were included in the experiment of this study, all batches were used for the CytoNorm training step. In the second step, normalization was performed with the mean distribution specified as goal distribution. With this approach, potentially biologically relevant differences in the distribution could be removed, similar to the use of other batch correction approaches. If reference controls are available, CytoNorm was designed to specifically identify and normalise technical variations and retain biological variations (177). The setup of the present study has, however, still the benefit of cluster-specific normalisation on a marker-by-marker basis where dependencies between markers are removed.

Many of the batch correction tools can induce artefacts in cytometry data. QuantileNorm and cydar quantile induced artefacts in more than half of the markers (Figure 5-9). CytoNorm caused artefacts only in about 10% of the markers after optimising normalisation settings (Figure 5-13). In contrast to previously published observations (193), warp normalisation did not cause any artefacts in the present study. Cydar range normalization can induce distortions due to outliers, which is why the range of each distribution is computed at percentiles p and 1-p (192). With the default setting of p=0.1 for all markers, distortions were observed for 3

markers within the data set of this study (Figure 5-10). Changing the percentile setting might prevent the distortions in the affected markers, but could lead to distortions in other markers. Optimising the parameter p separately for each marker might allow the generation of distortion-free range-normalised data.

In this study, the best performing tool for correcting batch effects of ChipCytometry data was CytoNorm. CytoNorm-normalisation caused artefacts in relatively few markers and resulted in both aligned histogram peaks and aligned intensity ranges (Figure 5-8). Optimisation of CytoNorm clustering parameters was crucial, however, to minimise the number of markers affected by artefacts. Normalising to one of the batches as a reference instead of the mean distribution of all batches could remove distortion artefacts almost completely (Figure 5-11). But coercing all batches to resemble the distribution of a single batch most likely did not reflect the data properly (Figure 5-12). When normalising to the mean, careful screening is required to see whether distortion artefacts affect markers. If the batch effects of artefact-affected markers are minor, those markers can be left uncorrected. Alternatively, the use of other batch correction tools specifically for the artefact-affected markers could be considered.

FlowSOM was used to identify cell populations within the unstimulated samples of CD14-/CD19-depleted PBMCs via unsupervised clustering (169). Studies benchmarking different clustering tools for single-cell data showed that FlowSOM is one of the best performing clustering tools in regard to accurately reproducing populations defined by expert manual gating, while having one of the fastest runtimes (194, 195). Besides FlowSOM, Phenograph clustering tool performs relatively well and is widely used. The Phenograph runtimes are, however, much longer compared to FlowSOM and the number of detected clusters increases with sample size while the precision decreases (195, 196). In contrast to Phenograph, FlowSOM requires the user to specify the number of clusters to obtain. A delta area plot can be generated using ConsensusClusterPlus to test a range for the number of final clusters. According to the “elbow criterion” assessment, this method can give some idea

about the minimal number of clusters required to reach cluster stability for FlowSOM clustering (170, 178). The elbow criterion is relatively subjective, however, and according to Liu et al. consistently provides a too small number of final clusters and worsens the performance of FlowSOM (195). Nowicka et al. suggest overclustering when using FlowSOM to ensure detection of rare and all expected cell types (170). In a subsequent step, clusters could be merged in a reproducible fashion, given the expert knowledge of markers and cell types of the researcher, to obtain a more biologically meaningful cell stratification (170).

Besides FlowSOM and Phenograph, PARC and FastPG are two recently published clustering tools, based on similar principles as Phenograph. First, k-nearest neighbour network is created. Secondly, weights are added to the network. Finally, cells are partitioned into clusters by community detection (196–198). Both new tools have improved run times compared to Phenograph, which are similar to those of FlowSOM. And while PARC and FastPG are shown to have a similar or better accuracy than Phenograph, both the two new methods and Phenograph are shown to outperform FlowSOM overall (197, 198). This contradicts previous benchmark publications, although the same data sets were used in some of the benchmark tests of these studies. Liu et al. showed, for example, that FlowSOM outperformed Phenograph in the majority of analysed data sets and Weber et al. showed that FlowSOM outperformed Phenograph consistently (194, 195). In addition, in the publication of PARC, the authors show consistently more accurate cell assignment of PARC compared to FlowSOM (197), but in the FastPG publication, FlowSOM and PARC seem to perform similarly, using the same data sets for some of the benchmarks (198). Further studies are required to confirm the performance of PARC and FastPG, which might be interesting clustering alternatives to FlowSOM for ChipCytometry data analysis.

Unsupervised FlowSOM clustering of the unstimulated data was performed with both the non-batch-corrected data and batch-corrected data in order to see whether batch correction changed the data in a way to have a major impact on clustering. The clustering results of the

uncorrected and warp-, range- and CytoNorm-corrected data were very similar. Each of the four data files had 13 matching clusters in the other files (Figure 5-15). CytoNorm-normalised data showed, however, most stable clustering compared to the other files, which might be due to the fact that it had the best performance regarding batch effect elimination between donors (Figure 5-14).

For cluster characterisation, a multi-pronged approach was used combining information obtained by MEM and gating in FlowJo, in which the frequency of marker-positive cells for each marker and each cluster was determined (Figure 5-15, Figure 5-16, Appendix Figure II-1). MEM generates quantitative cluster identity labels indicating enrichment of features in a cluster relative to a reference. Therefore, MEM labels are highly dependent on the reference population (187, 188). In the present study, the reference for each cluster was chosen to be all other cells excluding the current cluster. MEM has some advantages compared to other traditional cluster labelling approaches that define the identity of a cluster based on features with the highest magnitude or based on features with the highest variability across groups. MEM accounts for both feature magnitude differences as well as intra- and inter-population feature heterogeneity. Most importantly, MEM also quantifies negative feature enrichment relative to the reference population, which can be overlooked when searching for the most highly expressed features for cluster labelling (187, 188). The relative nature of MEM labels with regard to the reference population can lead to some unclarity in the field of cytometry where cell labels are usually considered absolute. In this study, for example, the MEM scores of Vα7.2 and CD161 of cluster 3 from the CytoNorm-normalised data were both >9 (Figure 5-15). As the combination of Vα7.2 and CD161 define MAIT cells, it is suggested that cluster 3 consisted of MAIT cells. Gating in FlowJo revealed, however, that a small fraction of the cells in this cluster were not MAIT cells but Vα7.2^{-}CD161^{++} T cells (Figure 5-16). Therefore, the information from both MEM scores and FlowJo gating were considered to label the cell clusters.

The MEM scores can also be utilised for cluster matching, as the pairwise calculated and normalised RMSD of MEM labels between clusters can serve as a measure of similarity. In addition, this method for cluster comparison can be even applied across studies and platforms (187, 188). In this study, MEM RMSD values were used to match clusters identified in differently normalised data (non-batch-corrected, warp-, range- and CytoNorm-normalised) and for intra-donor cluster matching to compare clusters from unstimulated and stimulated samples (Figure 5-15b, Figure 5-17a, Appendix Figure III-6). This method could also be used for inter-donor cluster matching in the case each donor is clustered separately. The trend of batch effects between ChipCytometry samples is not consistent across all markers, but can vary between the markers of each acquisition cycle. Therefore, it is best to perform inter donor cluster matching using MEM RMSD values from batch-corrected data. Alternatively, inter-donor cluster matching with non-batch-corrected data could be performed by binarizing MEM scores and using the scRNA-seq tool ClusterMap for cluster matching, which is based on hierarchical clustering (199).

To allow for comparison of the control and stimulated condition within each of the detected cell clusters, the stimulated data was mapped onto the clusters identified within the unstimulated data. Matching clusters from the control and stimulated condition were confirmed to be similar, demonstrated by a similar phenotype (analysed using MEM scores and frequency of marker-positive cells), similar relative abundances of clusters and conditions, and clustering on the UMAP plot. (Figure 5-17, Figure 5-18, Appendix Figure III-7). An alternative approach to cluster control and stimulated data is the aggregation of control and stimulated samples before clustering. With this approach, intra-cluster comparisons of conditions could be more difficult, however, as unstimulated and stimulated cells could be grouped in separate clusters. As an alternative approach to unsupervised clustering, traditional manual gating was applied, using bivariate scatter plots to define cell populations in a separate analysis (Figure 5-21).

5.5.2. Identification of cell types within CD14-/CD19-depleted PBMCs and their response to lIL-12+IL-18 stimulation

The differences between control and IL-12+IL-18-stimualted conditions within each cluster and population was investigated by the statistical analysis of the frequency of marker-positive cells of 24 selected markers, including activation markers, effector cytokines, and costimulatory and inhibitory checkpoint receptors and ligands (Figure 5-19, Figure 5-24). In addition, differential expression analysis based on the diffcyt R package and limma was performed (Figure 5-20, Figure 5-25) (179, 180). Alternative tools for differential expression analysis of cytometry data, including both marginal and multiple regression approaches, are available and include cydar (176), a classic regression-based approach (170), Citrus (200), CellCnn (201) and CytoGLMM (202).

Two different γδT cell populations were identified by unsupervised clustering, including. $CD45RA^{high}CD57^{high}$ (cluster1), and $CD45RA^{low}CD57^{low}$ (cluster 2) subsets (Figure 5-15, Figure 5-16). CD57 is a marker for proliferative senescence and is expressed by terminally differentiated T cells, including γδT cells (203, 204). In line with this, the $CD45RA^{high}CD57^{high}$ γδT-cell subset showed low expression of the maturation marker CD27, indicating a terminal effector phenotype (203, 204). While both γδT-cell clusters responded to IL-12+IL-18 stimulation, for example, by upregulating IFNγ and CD69, the responses of the $CD45RA^{high}CD57^{high}$ subset were overall lower compared to the $CD45RA^{low}CD57^{low}$ subset (Figure 5-19, Figure 5-20). In addition, some markers, such as CD71, were only significantly upregulated in the $CD45RA^{low}CD57^{low}$ and not in the $CD45RA^{high}CD57^{high}$ subset upon stimulation. CD57 has previously been described as a marker expressed by less responsive immune cells. $CD57^{+}$ NK cells, for example, are less responsive to IL-12+IL-18 stimulation than $CD57^{-}$ NK-cell subsets, resulting in lower IFNγ expression by $CD57^{+}$ NK cells (46, 52). In addition, $CD57^{+}$ antigen-specific CD8 T cells showed impaired IFNγ-responses after stimulation with specific antigen (205). Similar to these examples, CD57 might mark a less

responsive γδT-cell subset in the present study. Further studies are required to confirm this observation.

Within manually gated γδT-cells, the expression of innate-associated markers such as IL-18Rα, PLZF and CD26 was lowest in the $Vδ2^{-}CD161^{-}$ subset, followed by the $Vδ2^{-}CD161^{+}$ subset and highest in the $Vδ2^{+}CD161^{-}$ and $Vδ2^{+}CD161^{+}$ subsets, which corresponds to previous reports (66, 68). In addition, it was confirmed that a fraction of γδT cells express EOMES and TBET, GzmA and GzmK (206, 207) (Figure 5-22). The responsiveness to IL-12+IL-18 stimulation, measured by the increase in the expression of various effector cytokines, activation markers and checkpoint receptors, followed a similar trend as observed for the innate-associated markers. The magnitude of responses increased with CD161 and Vδ2 expression, being lowest or non-significant in the $Vδ2^{-}CD161^{-}$ subset and highest within the $Vδ2^{+}VD161^{+}$ subset, which is in line with previous reports (66, 68) (Figure 5-24, Figure 5-25).

The phenotype of $CD161^{++}$/MAIT cell cluster (cluster 3) and the manually gated MAIT cell population was similar and included typical MAIT cell markers such as CD161, CD26, IL-18Rα, 2B4, PLZF, EOMES, TBET, RORγT, GzmA and GzmK as described in the literature (68, 84, 87–89) (Figure 5-15, Figure 5-16, Figure 5-22). The grouping of $CD161^{++}Vα7.2^{-}$ cells and $CD161^{++}Vα7.2^{+}$ cells in cluster 3 is most likely due to the fact that these cell types share a very similar phenotype and have similar functional properties (68). $CD161^{++}$/MAIT cells responded to IL-12+IL-18-stimulating by upregulating, for example, IFNγ, CD69 and PD1 expression, while downregulating GzmK expression. This data corresponds to previous observations (64, 65, 86). The magnitude of the most responsive γδT-cell subsets was higher compared to MAIT cells, both in the unsupervised clustering analysis and in the analysis using manual gating, which confirms observations from previous reports (66, 68) (Figure 5-19, Figure 5-20, Figure 5-24, Figure 5-25).

5. Identification and phenotyping of CD161-expressing cell types in blood

A single NK-cell subset was identified using unsupervised clustering, whereas four different NK-cell subsets were defined according to CD161 and CD56 expression levels using manual gating (Figure 5-15, Figure 5-16, Figure 5-22). NK cells expressed 2B4, EOMES, TBET and PLZF, which confirms the phenotype described in the literature (46, 206, 208). The fraction of $PLZF^+$ cells was higher in $CD161^+$ compared to $CD161^-$ NK cells as previously described (46). It was also confirmed that the frequency of $CD16^+$ and $GzmB^+$ cells is higher in $CD56^+$ than in $CD56^{++}$ NK cells, and that GzmK is almost exclusively expressed within $CD56^{++}$ and not in $CD56^+$ NK cells (48, 209, 210). The maturation marker CD57 was mainly expressed on the mature $CD56^+$ NK-cell subset. The maturation marker CD27 showed the opposite trend and was mainly associated with the immature $CD56^{++}$ subset (46, 51, 52). Similar to MAIT and γδT cells, NK cells responded to IL-12+IL-18 stimulation by upregulating, for example, IFNγ and CD69 (Figure 5-19, Figure 5-20, Figure 5-24, Figure 5-25). NK cells showed particular high upregulation of the markers CD71, CD134, CD137 and TIM3 compared to other subsets. The magnitude of the responses within NK-cell subsets increased with CD161 expression and CD56 expression levels, confirming what is known from the literature (46). The observations of this study are also in line with the reports of $CD57^+$, $CD27^-$ and $CD56^{mid}$ NK-cell subsets being associated with lower responsiveness to IL-12+IL-18 stimulation compared to subsets that are $CD57^-$, $CD27^+$ and $CD56^{++}$ (46, 51, 52). In addition, it was confirmed that NK cells downregulate CD16 upon stimulation (211).

The three $lineage^-$ cell clusters were identified via unsupervised clustering and a single $lineage^-$ cell population defined by manual gating, which lacked CD14, CD19, CD3 and CD56 expression (Figure 5-15, Figure 5-16, Figure 5-22). Therefore, $lineage^-$ cells most likely included ILCs, but were not further characterised as crucial markers for ILC definition and characterisation were not included in the panel of this study, such as CD34, CD127, CRTH2, CD117, NKp46 and NKp44 (212). $Lineage^-$ cells responded, however, to IL-12+IL-18 similar as other responding subsets, for example, by upregulating CD69. The magnitude of the $lineage^-$ cell responses was overall lower compared to other responding clusters and

populations, with exceptions such as CD69 responses that were similar in magnitude (Figure 5-19, Figure 5-20, Figure 5-24, Figure 5-25).

Besides NK and innate-like T cells, subsets of $CD4^+$ T cells showed responses to IL-12+IL-18 stimulation, for example by upregulation of CD69. This includes cluster 12 identified in the CytoNorm-normalised data and $CD4^+$ TEM/TEMRA subsets identified via manual gating (Figure 5-19, Figure 5-20, Figure 5-24, Figure 5-25). Compared to other responding subsets, the responses of both cluster 12 and $CD4^+$ TEM/TEMRA subsets were lower in magnitude and the number of parameters changing significantly upon stimulation was lower. Cluster 12 contained IL-18Rα^+CD26$^+$CD45RA$^-$ memory cells with about half of the cells expressing CD161. Further investigations are required to confirm whether this cluster represents an innate-like $CD4^+$ T-cell subset or a conventional memory T-cell subset with an activated phenotype. The responding $CD4^+$ TEM/TEMRA cells could include TH1 cells that can respond to IL-12+IL-18 in a TCR-independent manner (213). Similarly, Munk et al. showed that subsets of both $CD45RO^+$ and $CD45RA^+CD4^+$ T cells can respond to IL-12+IL-18 in an antigen-independent matter. The fraction of responding $CD45RA^+$ cells in the study of Munk et al. was very low compared to the $CD45RO^+$ cells, and it was not distinguished between naive and TEMRA subsets within $CD45RA^+$ cells (214). In our study, naive cells did not show any significant responses in contrast to the TEMRA subset, indicating that the latter is actually the cytokine-responsive $CD45RA^+$ subset. The frequency of the $CD4^+$ TEMRA subset was very low in the present study, however, and only comprised about 45-65 cells per donor. Further studies with higher cell numbers should be conducted to confirm the results regarding this subset.

As expected, other conventional T-cell subsets and Tregs did not show any major responses to IL-12+IL-18 stimulation. An exception was TIGIT which was significantly increased after IL-12+IL-18-treatment in many conventional memory T-cell subsets and Tregs (Figure 5-19, Figure 5-20, Figure 5-24, Figure 5-25). The determined phenotype of conventional T cells

and Tregs agreed with what is known from the literature. For example, Tregs were identified via unsupervised clustering and manual gating as $CD4^+CD45RO^+FOXP3^+CD25^+$ with a fraction of the cells expressing RORγT, CD95, TIGIT, CD38 and CD39 (215–220) (Figure 5-15, Figure 5-16, Figure 5-22). It was also confirmed that a higher fraction of memory T cells expressed transcription factors such as EOMES and TBET than the naive subsets (206).

It was also observed that a fraction of γδT-cell subsets, $CD161^{++}$/MAIT cells, NK-cell subsets and some conventional memory T-cell subsets expressed IL-32 after IL-12+IL-18 stimulation (Figure 5-19, Figure 5-20, Figure 5-24, Figure 5-25). IL-32 is a novel cytokine with a dual role having both pro- and anti-inflammatory functions. Many immune and non-immune cells can express IL-32 upon stimulation and under inflammatory conditions (221). IL-12+IL-18 can induce IL-32 expression in both NK cells and $CD4^+$ T cells (109, 110). The results of this study expand on these observations, demonstrating that CD4 memory cell types, particularly the $CD161^{++/+}$ subsets of CD4 memory cell types, $CD161^{++}$ conventional CD8 T cells, and $CD56^{++}$ NK-cell subsets can express IL-32 upon IL-12+IL-18 stimulation (Appendix Figure III-17). It has not been shown before that MAIT cells express IL-32 in response to IL-12+IL-18-stimulation alone, but in response to *E. coli*+IL-12+IL-18 stimulation. Inhibiting MR1 interaction partially blocked the IL-32 response, indicating a role for IL-12+IL-18 (222). Another study has shown that MAIT cells downregulate *IL32* gene expression upon TCR stimulation using 5-OP-RU (223). Similar to MAIT cells, the ability of γδT cells to express IL-32 is also underexplored. Phosphoantigen-specific γδT cells were shown to upregulate IL-32 after antigen stimulation in a microarray experiment, but results were inconsistent when confirming the observation via RT-qPCR, for which the description or figure of the crucial time point seems erroneous (224). The ability of $CD161^{++/+}$ T-cell subsets, including innate-like T cells, to express IL-32 upon cytokine stimulation in a TCR-independent manner should be confirmed and further explored.

In summary, an analysis protocol for ChipCytometry cell suspension data analysis was developed, which includes steps similar to protocols from other high content cytometry methods. Still, I added some platform-specific requirements, such as a two-step approach to eliminate fluorescence anomalies. Future work could automate the proposed manual and relatively labour-intensive approach of fluorescence anomaly removal by training a neuronal network, which could possibly also be further adapted to clean-up tissue ChipCytometry data. The phenotype of T- and NK-cell subsets within PBMCs was analysed, and their response to IL-12+IL-18 stimulation was investigated by applying for the first time a panel of 50-markers using ChipCytometry. Therefore, it was shown that ChipCytometry is a competitive method compared to other high-content cytometry techniques. The biggest challenges of ChipCytometry include the occurrence of batch effects between sample chips and the relatively low sample throughput. Its strengths include the ability to analyse both cell suspension and tissue sections, the use of standard fluorochrome-labelled antibodies, high dynamic and spatial resolution, long-term sample storage, and the ability to re-interrogate analysed samples. Thus, ChipCytometry will be of particular use for the analysis of rare and precious samples.

5.6. Summary

1. For the first time, a panel consisting of 50 markers was applied on single-cell suspension samples using the ChipCytometry technique.
2. A protocol for the analysis of high-content single-cell ChipCytometry data was developed, including data transformation, identification and removal of fluorescence anomalies and extreme values, rescaling, batch correction, pre-processing (de-barcoding, gating), unsupervised clustering, dimensionality reduction, cluster characterisation and labelling, cluster matching, and quantitative and statistical analysis (differential expression analysis).

5. Identification and phenotyping of CD161-expressing cell types in blood

3. CD14-/CD19-depleted PBMCs were shown to contain NK cells, innate-like T-cell subsets including MAIT cells and different γδT-cell subsets, Tregs, conventional T-cell subsets and linage- cells.
4. NK cells, $CD161^{+}$ and $V\delta2^{+}$ γδT-cell subsets and MAIT cells were shown to be the major responders to IL-12+IL-18 cytokine stimulation, for example, by upregulating IFNγ and CD69.
5. Lineage- cells and conventional memory T-cell subsets could also respond to IL-12+IL-18 stimulation, for example, by upregulating CD69. The magnitude of the responses was lower compared to NK and innate-like T-cell subsets.

6. ROLE OF IL-32 IN INNATE-LIKE T-CELL ACTIVATION

6.1. Introduction

6.1.1. IL-32 is a novel pluripotent cytokine

The cytokine IL-32 was first described by Dahl et al. and named NK4, because its expression was increased after mitogen stimulation of T cells or IL-2 stimulation of NK cells (225). Kim et al. demonstrated the biological effects of IL-32 on cells, particularly the induction of TNFα and IL-8 in a human monocytic cell line (109), which is the reason why NK4 was renamed IL-32. This cytokine is encoded by 8 exons and through alternative splicing multiple different isoforms can be generated. Nine IL-32 isoforms have been described so far, including α, β, γ, δ, ε, ζ, η, θ and small (226). IL-32α, -β, -γ and -δ are the best studied and IL-32γ is the largest and biologically most active isoform (227). IL-32 isoforms can interact with each other and various heterodimeric interactions have been described (226). In addition, IL-32 isoforms can promote or inhibit each other's activity, which makes it difficult to dissect the functions of each isoform (228).

There is no sequence homology of IL-32 with any known cytokine families (109). Equine, swine, ovine and bovine, but no murine IL-32 homologs have been found (109). Murine cells can respond to recombinant human IL-32, however (109, 229). IL-32 can be expressed intracellularly, secreted or attached to cell membranes. Although only the γ-isoform contains a signal peptide, the other isoforms can also be secreted, most likely via non-classical secretion pathways or via release from apoptotic cells upon cell death (109, 230–232).

6.1.2. IL-32 is expressed by non-immune and immune cells

IL-32 can be expressed by immune and non-immune cells (Figure 6-1). Epithelial cells express IL-32 upon stimulation with cytokines such as IL-1β, IFNγ, TNFα and IL-18 (109, 230, 233), but also in response to microbial components such as double-stranded RNA and Influenza A protein (234–236). Endothelial cells express IL-32α/γ constitutively and switch to

β/ε upon IL-1β stimulation (237). Similar to epithelial cells, synovial fibroblast and myofibroblasts express IL-32 in response to certain cytokines (238, 239).

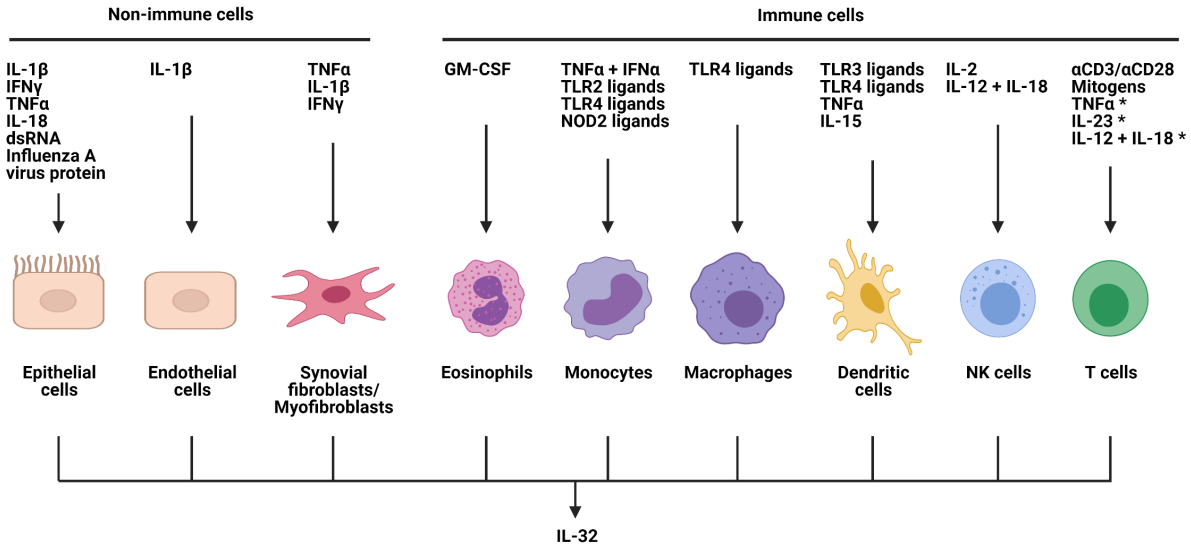


Figure 6-1. Inducers of IL-32 expression. Illustration showing cytokines and receptors for microbial-derived substances that can induce IL-32 expression in non-immune and immune cells (108–110, 221, 225, 230, 233–246). The asterisk indicates cytokines that induced IL-32 expression in the $CD4^+$ T-cell subset. This figure was created with BioRender.com.

Many immune cell subsets, including eosinophils, monocytes and DCs can express IL-32 upon cytokine stimulation. Additionally, monocytes, macrophages and DCs can express IL-32 in response to microbial-derived products. Depending on the cell type, stimuli include GM-CSF, TNFα, IFNα, IL-15, TLR2/3/4 ligands and NOD2 ligands (108, 110, 240–246). Besides eosinophils and myeloid immune cell types, NK and T lymphocytes possess the ability to express IL-32. NK cells can express IL-32 upon stimulation with IL-12+IL-18 (109), and T cells upon activation via anti-CD3/anti-CD28 antibodies or mitogens such as ConA (110). $CD4^+$ T-cell subset can express IL-32 upon stimulation with IL-23, TNFα, or IL-12+IL-18, similar to NK cells (110). IL-32 expression has also been observed by stimulated innate-like T-cell subsets, including phosphoantigen-specific γδT cells upon antigen stimulation (224) and MAIT cells upon stimulation with *E. coli*+IL-12+IL-18 (222). TCR

stimulation with the synthetic ligand 5-OP-RU, however, downregulates *IL32* gene expression in MAIT cells (223).

6.1.3. Effects of IL-32 on non-immune and immune cells

A specific receptor for IL-32 that mediates the response to stimulation has not yet been identified, but interactions between IL-32 and other proteins have been described. IL-32α can, for example, be bound by Proteinase-3 (PR3), and cleavage of IL-32α by PR3 increases its activity (247, 248). IL-32 can also bind to integrins via its RGD-motif, including αVβ3 and αVβ6, but not αVβ8n (249). These integrins may mediate signalling from extracellular IL-32. In addition, IL-32 interacts with intracellular proteins which are involved in intracellular signalling of integrin and focal adhesion pathways, particularly FAK (focal adhesion kinase) and paxillin. Inhibition of FAK can modulate IL-32-mediated effects, which indicates that IL-32 may play a dual role in integrin signalling (249). Various signalling molecules have been reported to be involved in IL-32 signal transduction, including p38, NFκB, caspase-1, PLC, JNK, ERK1/2, PI3K, Akt, p300, DAPK-1, STAT3, PKCε, PU.1, PKCδ, C/EBPα and STAT5 (108, 109, 221, 241, 250–254). IL-32 can also synergise with NOD1/2 receptor activation (255, 256). The signalling molecules involved in IL-32 signal transduction are to some extent tissue-specific and depend on the isoform involved (257).

Many different cell types can respond to IL-32, including non-immune cells, such as endothelial cells, epithelial cells and fibroblasts, but also various immune cells, such as eosinophils, monocytes, macrophages, DCs, NK cells and T cells (221, 258) (Figure 6-2). A dual-role of IL-32 has been described, having both pro- and anti-inflammatory properties (221, 258). IL-32 can induce the expression of different pro-inflammatory cytokines and chemokines, including IL-1β, IL-6, IL-8 and TNFα (109, 221, 258). IL-32 can also promote the differentiation of monocytes into macrophages and DCs (241, 243, 254, 259). The isoform IL-32θ has the opposite effect, however, inhibiting the differentiation of monocytes into macrophages (260). Moreover, IL-32 can induce the antiviral and anti-microbial activity of

macrophages (261–264), promote TH1 and TH17 responses by inducing IL-12 and IL-6 expression in DCs (254), and enhance NK-cell mediated cytotoxicity via DR3, FAS and ULBP2 (265, 266). On the other hand, IL-32α inhibits NK-cell cytotoxicity by supressing IL-15 mediated GzmB and perforin expression (108). Other immune-inhibitory functions of IL-32 include the induction of various anti-inflammatory cytokines such as IL-10, IDO and ILT4, expressed by different cell types including monocytes, macrophages, DCs and T cells (244, 267). In addition, IL-32 can promote apoptosis in epithelial cells and T cells (232, 268). In summary, IL-32 has different effects depending on the context, particularly the cell type, and is involved in immune responses in infection, inflammatory diseases and cancer (229, 246, 263, 267, 269, 270).

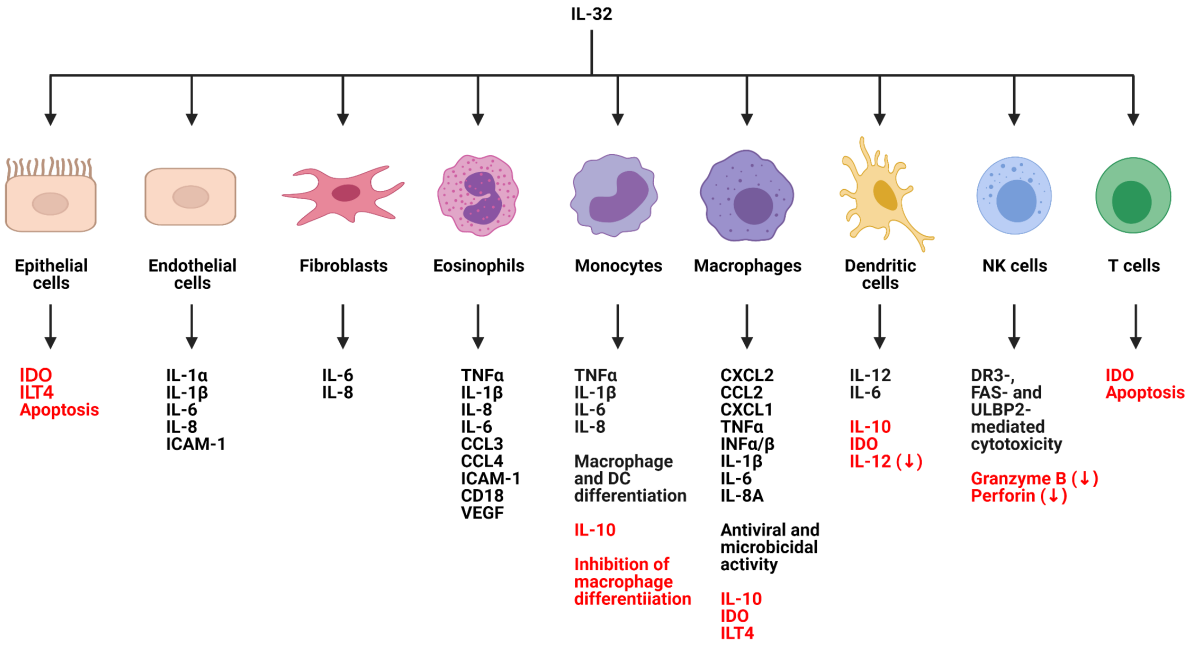


Figure 6-2. Effects of IL-32 on non-immune and immune cells. Illustration showing the effects of IL-32 on various non-immune and immune cells (108, 109, 221, 232, 241, 243, 244, 254, 258–268). This figure was created with BioRender.com.

6.1.4. The role of IL-32 in cancer

IL-32 expression has been described in many different cancers, including both haematological and solid tumours, for example breast cancer, colorectal cancer, cervical cancer, gastric cancer, lung cancer, head and neck squamous cell carcinoma, renal clear cell

carcinoma, thyroid carcinoma, myelodysplastic syndrome, chronic myelomonocytic leukaemia, cutaneous lymphoma, oesophageal cancer, gastric lymphoma, hepatocellular cancer and pancreatic cancer. Overall, IL-32 expression in these cancers is often positively correlated with clinical stage, tumour size, metastasis and poor prognosis (257, 269, 271–285) (Table 6-1). In melanoma, however, IL-32 expression is associated with increased overall survival (286).

The link between IL-32 expression and carcinogenesis and tumour progression is supported by the fact that the IL-32 germ-line encoded single nucleotide polymorphism rs28372698, which leads to increased IL-32γ expression, is associated with a higher risk of developing various different cancers, including thyroid carcinoma, endometrial cancer and ovarian cancer (271, 287–289). In addition, this polymorphism is associated with therapy resistance in thyroid carcinoma, and clinical stage and cervical invasion in endometrial cancer (271, 287).

Mechanistically, IL-32 has a dual role in cancer with both pro- and anti-cancer effects. IL-32 can promote cancer cell apoptosis, for example, via caspase 3 or 8 (249, 257, 268). There is some conflicting evidence, however, indicating that certain isoforms can both promote and inhibit cancer cell apoptosis (257, 290). On the other hand, IL-32 can promote epithelial-mesenchymal transition, invasion, migration and angiogenesis. These processes are mediated, for example, by the IL-32-induced upregulation of VEGF and matrix metalloproteinases (257, 281, 284, 291, 292).

Table 6-1. IL-32 expression in cancer and its association with clinical parameters. Table modified from (257). HC, healthy control. int, intermediate. LN, lymph node.

Cancer Type	Frequency of positive cancers	Association with clinical parameters
Cervical cancer (278)	55% (n=40)	
Gastric cancer (279)	45.86% (n=181)	Associated with tumour depth, LN metastasis, lymphatic and venous invasion and poorer survival.
Lung cancer (280)	16% of squamous-cell carcinomas (n=49), 73% of adenocarcinomas (n=64), 77% of small-cell lung cancers (n=13) and 64% of large-cell carcinomas (n=22).	Associated with clinical stage and metastasis
Cancer Type	**High/intermediate expression according to expression scores**	**Association with clinical parameters**
Breast cancer (281)	High: 8%, int: 24%, (n=137)	Correlation with tumour size, LN metastasis and tumour stage
Colorectal cancer (282)	High/int: 51.42% (n=70)	Associated with LN and organic metastasis
Head and neck squamous cell carcinoma (283)	High: 58,46% (n=65)	Associated with decreased disease-free periods and decreased overall survival
Lung cancer (284)	High: 48.3% of lung adenocarcinomas (n=60, of which 85% are positive)	Associated with LN and distant metastasis, negatively associated with survival time
Renal clear cell carcinoma (285)	High: 10.7%, int: 27.7% (n=112)	Associated with high recurrence rates, low recurrence free survival, low overall survival and low disease-specific survival.
Thyroid carcinoma (271)	High: 15%, int: 41% (n=27)	Germ-line polymorphism that leads to increased IL-32 expression is associated with higher thyroid cancer risk and treatment resistance
Cancer Type	**Relative expression in cancer compared to control samples**	**Association with clinical parameters**
Colon cancer (272)	Colon cancer (61.67% positive) > non-cancerous colon (n=60)	Associated with tumour stage, tumour size and shorter overall survival time
Chronic myelomonocytic leukaemia (269)	Primary marrow stroma cells from cancer patient < HC (n=6)	
Cutaneous T cell lymphoma (273)	Cancerous skin samples (n=26) > HC skin samples (n=6)	
Oesophageal cancer (274)	Cancer (n=65) > HC (n=35)	
Gastric lymphoma (275)	Primary gastric lymphoma tissue (n=31) > gastritis tissue (n=19)	Associated with LN metastasis and advanced stage
Hepatocellular carcinoma (276)	Cancer > adjacent non-tumour tissues (n=25)	Increased IL-32 expression with progression of liver disease
Myelodysplastic syndrome (269)	Primary marrow stroma cells from cancer patient (n=13) > HC (n=6)	
Pancreatic cancer (277)	Pancreatic cancer cells (high) > pancreatic duct, inflamed lesions (int) > pancreatic duct, normal (low) (n= 5)	

Apart from its direct effect on cancer cells, IL-32 can also affect the anti-cancer immune response. Evidence comes from the observation that NK cells from myelodysplastic syndrome and chronic myelomonocytic leukaemia patients that express lower levels of IL-32 than healthy controls show reduced cytotoxic capacity (269). In addition, IL-32α-overexpressing chronic myelomonocytic leukaemia cell lines showed increased susceptibility to NK cell-mediated killing by upregulating FAS and ULBP2 (265). Moreover, IL-32 promotes NK cell-mediated colon cancer cell killing via DR3 (266). In Melanoma, IL-32 expression was associated with myeloid markers, DC maturation, T-cell activation markers and a positive prognosis (286). Similarly, IL-32 expression was associated with inflammation- and T-cell response-associated genes in breast cancer (293). Conversely, IL-32 can promote the differentiation of DCs and macrophages that express the immunosuppressive IDO in cutaneous T-cell lymphoma, and IL-32 expression was observed to correlate with the immunosuppressive cytokine IL-10 (294). IL-32 was also associated with Tregs in oesophageal cancer and linked to an adverse prognosis (295, 296). Overall, IL-32 can both promote and inhibit an anti-cancer immune response, dependent on the cancer type, but further investigation is required to elucidate the precise role of IL-32 in anti-cancer immunity.

6.2. Aims

IL-32 is involved in regulating carcinogenesis, tumour progression and the anti-cancer immune response (257). Therefore, it is an interesting target for immunotherapy whose manipulation could facilitate an improvement to the quality of life of cancer patients. The biology of IL-32 is relatively complex, however, and its use as a novel therapeutic tool requires a better understanding of its expression, function and role.

T cells, the most potent effector cells in the antitumour immune response (297, 298), can express IL-32 upon TCR stimulation (110, 224). In addition, IL-12+IL-18 cytokine stimulation

can induce IL-32 expression in $CD4^+$ T cells, similar to NK cells (109, 110). Within T cells, CD161-expressing T-cell subsets, including innate-like T-cell subsets such as MAIT and γδT cells, are in general the responsive cell types towards cytokines such as IL-12, IL-18 or IL-15 (68, 81). Therefore, it was hypothesized that CD161-expressing T cells, in contrast to $CD161^-$ subsets, could express IL-32 in response to cytokine stimulation. In fact, MAIT cells were shown to express IL-32 upon stimulation with *E. coli*+IL-12+IL-18, which was partially blocked by an anti-MR1 antibody, indicating a role for IL-12+IL-18 in IL-32 induction (222). The ability of cytokines to induce IL-32 expression in T cells is, however, underexplored.

Furthermore, IL-32α was shown to directly inhibit NK cell function. As CD161-expressing T-cell subsets can respond to cytokines similar to NK cells (68), it was hypothesized that IL-32α and possibly other isoforms can directly regulate T cell function of CD161-expressing subsets.

As the role of IL-32 in the antitumour immune response is very poorly understood (257), I also aimed to generate a pan-cancer *IL32* gene signature to explore which biological processes IL-32 is associated with in cancer, and which immune cell types are associated with the expression of IL-32 and the IL-32 signature genes. In addition, I aimed to explore the association of *IL32* gene expression with patient survival across different cancers.

Summary of aims:

1. Investigate the ability of various cytokines to induce IL-32 expression in T-cell subsets
2. Investigate the effect of IL-32 on the activation and function of T-cell subsets
3. Generate a pan-cancer *IL32* gene signature to investigate which biological processes IL-32 is associated with in cancer
4. Investigate which immune subsets are associated with the expression of *IL32* and the expression of *IL32* signature genes in cancer
5. Investigate the association of *IL32* expression with cancer patient survival

6.3. Chapter-specific materials and methods

6.3.1. IL-32 ELISA

IL-32 concentration in the supernatant of stimulated PBMCs was measured using IL-32 DuoSet ELISA and DuoSet ELISA Ancillary Reagent Kit 2 (R&D Systems) following manufacturer's instructions.

6.3.2. TCGA samples and clinical information

TCGA (The Cancer Genome Atlas) data was obtained from multiple different repositories and used as further detailed in the results section. TCGA data, generated by the TCGA Research Network (https://www.cancer.gov/tcga) was obtained from the National Cancer Institute (NCI) Genomic Data Commons (GDC) harmonized data portal and GDC Legacy Archive using TCGAbiolinks R package (299–301). Broad Institute TCGA Genome Data Analysis Center (GDAC) data was obtained from https://gdac.broadinstitute.org/ (Broad Institute TCGA Genome Data Analysis Center (2016): Firehose stddata__2016_01_28 run. Broad Institute of MIT and Harvard. doi:10.7908/C11G0KM9). Recount2 TCGA data was obtained from https://jhubiostatistics.shinyapps.io/recount/ (302). Batch-corrected PanCan Atlas TCGA data and TCGA Pan-Cancer Clinical Data Resource (TCGA-CDR) data was obtained from https://gdc.cancer.gov/about-data/publications/pancanatlas (303, 304). Study abbreviations are listed in Table 6-2.

Table 6-2. TCGA study abbreviations.

Study name	Study abbreviation
ACC	Adrenocortical carcinoma
BLCA	Bladder Urothelial Carcinoma
BRCA	Breast invasive carcinoma
CESC	Cervical squamous cell carcinoma and endocervical adenocarcinoma
CHOL	Cholangiocarcinoma
COAD	Colon adenocarcinoma
DLBC	Lymphoid Neoplasm Diffuse Large B-cell Lymphoma
ESCA	Oesophageal carcinoma
GBM	Glioblastoma multiforme
HNSC	Head and Neck squamous cell carcinoma
KICH	Kidney Chromophobe
KIRC	Kidney renal clear cell carcinoma
KIRP	Kidney renal papillary cell carcinoma
LAML	Acute Myeloid Leukaemia
LGG	Brain Lower Grade Glioma
LIHC	Liver hepatocellular carcinoma
LUAD	Lung adenocarcinoma
LUSC	Lung squamous cell carcinoma
MESO	Mesothelioma
OV	Ovarian serous cystadenocarcinoma
PAAD	Pancreatic adenocarcinoma
PCPG	Pheochromocytoma and Paraganglioma
PRAD	Prostate adenocarcinoma
READ	Rectum adenocarcinoma
SARC	Sarcoma
SKCM	Skin Cutaneous Melanoma
STAD	Stomach adenocarcinoma
TGCT	Testicular Germ Cell Tumours
THCA	Thyroid carcinoma
THYM	Thymoma
UCEC	Uterine Corpus Endometrial Carcinoma
UCS	Uterine Carcinosarcoma
UVM	Uveal Melanoma

6.3.3. Generation of an *IL32* gene signature

The workflow of generating a pan-cancer *IL32* gene signature is illustrated in Figure 6-3. The unpublished RENOIR R package, which was developed and kindly provided by Dr.

Alessandro Barberis and Prof. Francesca Buffa, Department of Oncology, University of Oxford, was used in this workflow. Further details are explained in the results section.

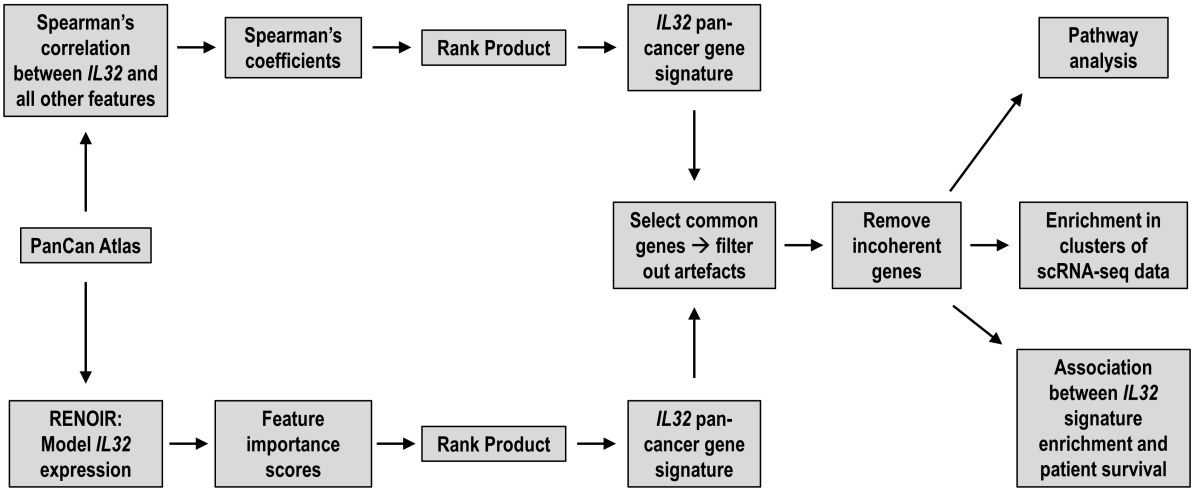


Figure 6-3. Generation of the pan-caner *IL32* gene signature. Flowchart illustrating the workflow for the generation of the pan-cancer *IL32* gene signature using PanCan Atlas TCGA data.

6.3.4. Pathway analysis

Pathway analysis was performed using clusterProfiler R package. Over-representation analysis was performed using GO (Gene Ontology) Biological Processes, KEGG (Kyoto Encyclopedia of Genes and Genomes) and WikiPathways annotation databases. Redundancy of enriched GO terms was removed using the clusterProfiler simplify function with a cut-off value of 0.55.

6.3.5. scRNA-seq data analysis

Pre-processed CITE-seq data from PBMCs of 8 healthy volunteers was obtained from Hao et al. (305). The volunteers had been part of a phase 1a HIV vaccine trial testing a DNA vaccine administered via intramuscular electroporation with or without coadministration of IL-12 in form of a plasmid at months 0, 1 and 3. At month 6, a booster vaccination had followed with a VSV-vectored HIV *gag* vaccine (305–307). Blood samples for CITE-seq had been collected at day 0 before administration of the VSV-vectored HIV booster vaccine and at day

3 and 7 post vaccination. In the present study, only data from day 0, which includes 53364 PBMCs, was used. Reference cell types were aggregated to 12 cell types as indicated in the results section.

Pre-processed breast cancer scRNA-seq data including 21253 immune cells from 8 treatment naive patients were obtained from Azizi et al. (308). To identify different immune cell types in the breast cancer data, reference mapping using Seurat R package was performed with the PBMC CITE-seq data from Hao et al. as reference. Reference cell types in the breast cancer data were aggregated to 11 cell types as indicated in the results section.

Differential gene expression analysis was performed using presto R package. Differential gene expression was tested between each cell type and all other cells. LogFC (log-fold change) was considered being significant if it was between the minimum and maximum logFC obtained from performing differential gene expression analysis 100 times with randomly permutated cell labels.

6.4. Results

6.4.1. IL-12-, IL-18- and IL-15-induced IL-32 expression in T cells within PBMCs

To investigate the ability of cytokines to induce IL-32 expression in T cells, human PBMCs from healthy donors were stimulated with IL-12, IL-18, IL-15, or combinations of two of these cytokines for 24 hours. To analyse IL-32 expression by flow cytometry, a two-step staining protocol was applied, including primary staining with a biotin-labelled anti-IL-32 antibody that recognises the α, β, γ and δ isoform and secondary staining with fluorochrome-labelled streptavidin or anti-biotin antibodies. Figure 6-4a and Appendix Figure IV-1 show staining examples including staining controls.

6. Role of IL-32 in innate-like T-cell activation

IL-15 alone and in combination with IL-12 or IL-18 induced significant IL-32 expression in all analysed T-cell subsets compared to the untreated control, including $CD161^-$, $CD161^+$ and $CD161^{++}$ cells within $CD8^+$ and $CD8^-$ T cells, and $V\delta2^-$ and $V\delta2^+$ γδT cells (Figure 6-4b-d). Stimulation with IL-12 or IL-12+IL-18 caused a significant increase in IL-32 expression in CD161-expressing T-cell subsets and γδT cells, with the exceptions that IL-12 did not induce a significant IL-32 response in $CD161^+CD8^+$ cells and IL-12+IL-18 did not induce a significant IL-32 response in the $V\delta2^-$ γδT-cell subset. The highest IL-12- and IL-12+IL-18-mediated responses were observed within $CD161^{++}$ and $V\delta2^+$ subsets. IL-18 alone induced significant IL-32 expression in CD161-expressing $CD8^+$ T cells and $V\delta2^+$ γδT cells. IL-18-induced IL-32 responses were, however, relatively small compared to other cytokine-induced IL-32 responses. Overall, there was a trend of increasing IL-32 expression with increasing levels of CD161 expression with up to about 70% IL-32-expressing $CD161^{++}$ T cells upon IL-15+IL-12 stimulation. Within γδT cells there was a trend of increased IL-32 expression in $V\delta2^+$ cells compared to $V\delta2^-$ cells. IL-32 expression was not observed within $CD161^-CD3^-$ cells (Figure 6-4e). In $CD161^+CD3^-$ cells, which most likely contain NK cells and ILCs, significant IL-32 expression was observed upon stimulation with any of the tested cytokines or cytokine combinations. The magnitude of these responses was relatively low compared to the cytokine-induced IL-32 responses in T cells, however, with only up to approximately 11% of NK cells expressing IL-32. In summary, IL-15 alone and in combination with other cytokines can induce IL-32 expression in all T-cell subsets. IL-12-, IL-18- and IL-12+IL-18-mediated IL-32 expression was particularly associated with CD161-expressing and innate-like T cells. Overall, innate-like T cells showed the highest frequencies of $IL\text{-}32^+$ cells upon cytokine stimulation compared to other subsets.

IFNγ expression was analysed in addition to IL-32 expression to confirm cytokine-mediated T- and NK-cell activation (Appendix Figure IV-2a). As expected, $CD161^{++}\gamma\delta TCR^-$ T cells, $\gamma\delta TCR^+V\delta2^+$ T cells and $CD3^-CD161^+$ cells were the major responders to cytokine stimulation in terms of IFNγ expression, particularly in response to stimulation with the combination of

two cytokines. Smaller but significant responses were observed by $CD161^{+}\gamma\delta TCR^{-}$ and $\gamma\delta TCR^{+}V\delta2^{-}$ γδT cells. In addition, a very small fraction of $CD161^{-}CD8^{+}$ T cells responded to IL-15+IL-18 and IL-15+IL-12 stimulation by expressing IFNγ (Appendix Figure IV-2a).

Parallel to the use of flow cytometry, cytokine-induced IL-32 expression of PBMCs was also confirmed using a sandwich ELISA based on polyclonal IL-32 capture and detection antibodies (Figure 6-4f). The IL-32 concentration in the supernatants of IL-12- and IL-12+IL-15-stimulated PBMCs was analysed. After 24 hours, a statistically significant increase in IL-32 concentration compared to the untreated control was only observed for the positive control PMA+Ionomycin. After 48 hours, however, IL-12+IL-15 stimulation resulted in significantly increased IL-32 levels in the supernatant in comparison to the untreated condition, similar to the positive control. There was also an increase in the IL-32 concentration after IL-12 stimulation, but it was not statistically significant.

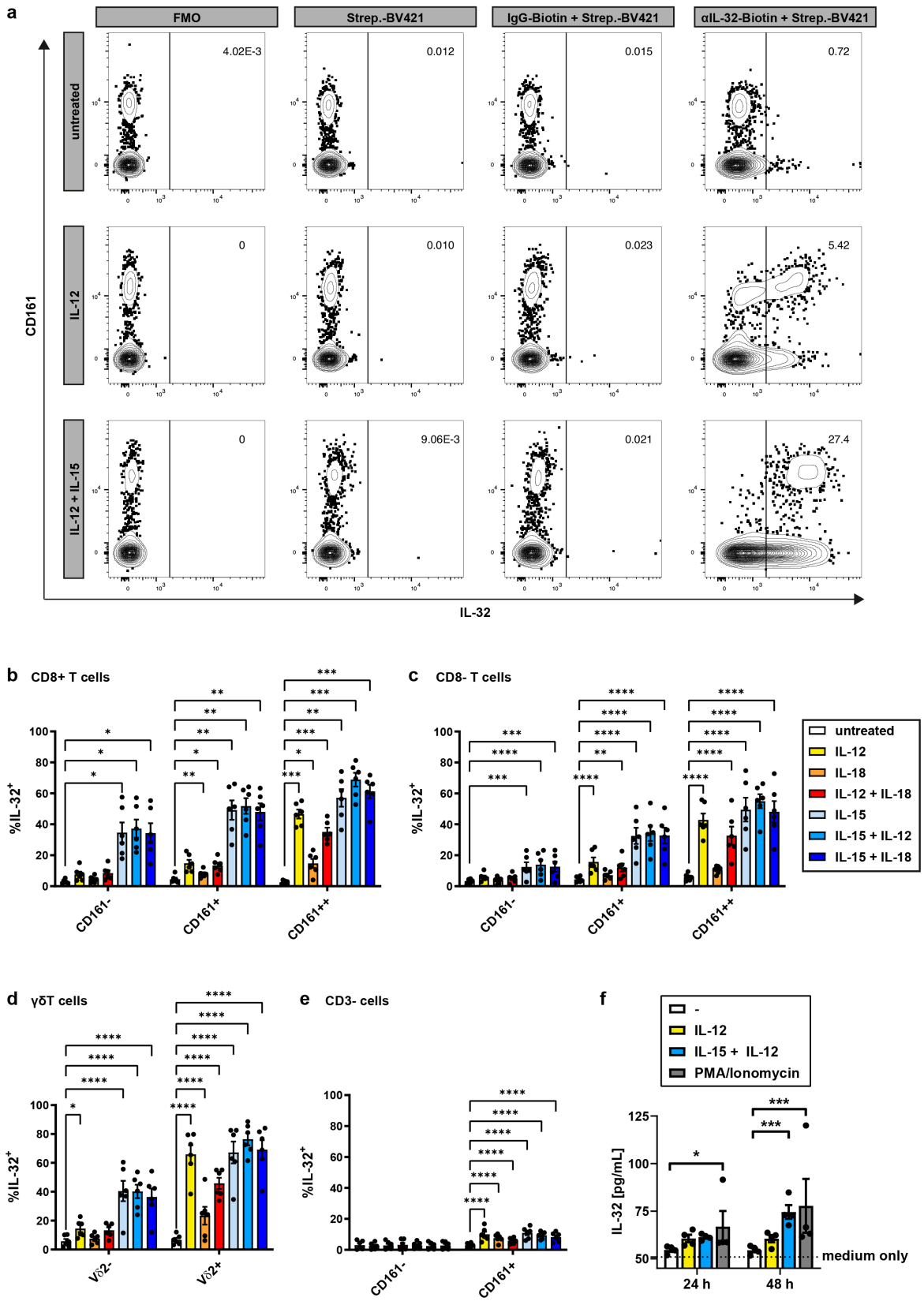


Figure 6-4. Cytokine-induced IL-32 expression in PBMCs. (a) PBMCs were stimulated with IL-12 or IL-12+IL-15 for 24 hours. Medium only served as a negative control (-). IL-32 expression was analysed by flow cytometry using a biotin-labelled anti-IL-32 antibody in combination with fluorochrome-labelled Streptavidin. Staining controls included fluorescence minus one (FMO), Streptavidin-BV421 only, and IgG-Biotin + Streptavidin-BV421. Representative plots are shown, illustrating IL-32-expression within $CD8^+$ T cells. (b)-(e)

IL-32 expression of indicated T cell and $CD3^-$ subsets within PBMCs (N=6, pooled from two independent experiments) was analysed using flow cytometry after stimulation for 24 hours with different cytokines and cytokine combinations, including IL-12, IL-18, IL-15, IL-12+IL-18, IL-12+IL-15 and IL-18+IL-15. (f) IL-32 concentration in the supernatant of stimulated PBMCs (N=4) was analysed using ELISA. Conditions included medium only control (-) and IL-12, IL-12+IL-15 and PMA/Ionomycin stimulation. Bar plots indicate mean ± SEM. Two-way repeated measures ANOVA with Bonferroni's multiple comparisons test was performed. ****p<0.0001, ***p<0.001, **p<0.01, *p<0.05.

6.4.2. IL-12-, IL-18- and IL-15-induced IL-32 expression in enriched T cells

Next, cytokine-induced IL-32 expression was analysed using enriched and untouched T and NK cells that were obtained by CD14- and CD19-depletion of PBMCs in order to exclude the possibility that cytokine-induced IL-32 expression is solely a result of indirect T- and NK-cell stimulation by other cytokine-activated cell types within PBMCs. After 24 hours of stimulation with IL-12, IL-15, IL-18 or combinations of two of these cytokines, IL-32 expression was measured using flow cytometry (Figure 6-5a-e).

Similar to the results from total PBMCs, IL-15 alone and in combination with IL-12 or IL-18 induced significant IL-32 expression in all T-cell subsets compared to the untreated control, including subsets of CD8, CD4 and DN T cells, stratified by CD161 and Vα7.2 expression, and γδT-cell subsets, stratified by Vδ2 and CD161 expression. An exception to this was the $CD161^-CD4^+$ T cell population which did not show a significant response. Stimulation with IL-15 in combination with other cytokines induced higher frequencies of $IL\text{-}32^+$ cells compared to IL-15 alone, particularly within $Vα7.2^-CD161^{++}$, MAIT, $CD161^+Vδ2^-$ γδT and $Vδ2^+$ γδT cells. IL-12 alone and IL-12+IL-18 induced significant IL-32 expression in $Vα7.2^-CD161^{++}$ cells, MAIT cells and all γδT-cell subsets except for $CD161^-Vδ2^-$ γδT cells. In addition, a small fraction of $CD161^+$ DN T cells expressed IL-32 upon IL-12+IL-18 stimulation. In contrast to the analysis of bulk PBMCs, IL-18 alone did not induce any significant IL-32 expression in any T-cell subsets within CD14-/CD19-depleted PBMCs. A trend of increasing IL-32 expression of cytokine-stimulated T cells was observed with increasing levels of CD161 expression and with Vδ2 expression. The highest IL-32 responses were seen in IL-15+IL-18- and IL-15+IL-12-stimulated MAIT and $CD161^+Vδ2^+$ γδT cells, of which

approximately 70% were IL-32-positive. Within NK-cell subsets, both $CD161^-$ and $CD161^+$ cells showed significant IL-32 expression after stimulation with almost any of the tested cytokines or cytokine combinations. An exception was the $CD161^+$ NK-cell subset that showed no significant IL-32 response after IL-18 stimulation. Cytokine-induced IL-32 responses in NK cells were relatively low with only about 13% positive cells upon IL-15+IL-18 stimulation. In addition to IL-32 expression, IFNγ expression was analysed to confirm cytokine-mediated T- and NK-cell activation, shown in Appendix Figure IV-2b.

Overall, IL-32 expression of cytokine-stimulated T- and NK-cell subsets within CD14-/CD19-depleted PBMCs was similar to the expression observed using total PBMCs, indicating that cytokines can directly induce IL-32 expression by T and NK cells. IL-15 could induce IL-32 expression in almost all T-cell subsets, whereas IL-12- and IL-12+IL-18-mediated responses were particularly associated with CD161-expressing and innate-like T-cell subsets including MAIT and $Vδ2^+$ γδT cells. MAIT and $Vδ2^+$ γδT cells also showed the highest frequencies of $IL\text{-}32^+$ cells upon stimulation compared to other subsets. A difference compared to stimulation of bulk PBMCs was observed for IL-18, which did not induce significant IL-32 expression in T cells within CD14-/CD19-depleted PBMCs.

The MAIT-cell subset was chosen to further dissect cytokine-induced IL-32 responses. This population responded to most of the tested cytokines and cytokine combinations and showed some of the highest IL-32 responses observed. In blood, the majority of MAIT cells are $CD8^+$ (88, 91), which is why CD8-enriched PBMCs were used to study the kinetics of cytokine-induced IL-32 expression in MAIT cells. CD8-enriched PBMCs were stimulated with IL-12, IL-15, IL-12+IL-18 or IL-15+IL-12 for different periods of time up to 72 hours (Figure 6-5f-g). The highest frequency of $IL\text{-}32^+$ MAIT cells was observed after 48 hours of stimulation, with about 60% $IL\text{-}32^+$ cells upon IL-12 stimulation, about 80% $IL\text{-}32^+$ cells upon IL-12+IL-18 stimulation, and about 95% $IL\text{-}32^+$ cells upon IL-15 or IL-15+IL-12 stimulation. Cytokine-induced IFNγ expression showed similar kinetics with the highest responses after

48 hours of stimulation. The kinetics of cytokine-mediated CD69 expression reached a maximum after 48-72 hours.

Co-expression of IL-32 and CD69 or IFNγ by MAIT cells was analysed after 48 hours of cytokine stimulation. This analysis revealed that IL-32 and CD69 is highly co-expressed upon stimulation with almost any of the tested cytokines and cytokine combinations (Figure 6-5h). Only IL-12 alone and IL-12+IL-18 resulted in IL-32 single-positive MAIT cells. CD69 single-positive MAIT cells were observed in the medium only control and in the IL-18 only condition, but their frequency was relatively low. By contrast, analysis of IL-32 and IFNγ co-expression revealed that a fraction of cytokine-stimulated MAIT cells were IL-32^{+}IFNγ^{+}, while another fraction was IL-32 single-positive. Stimulation with IL-12 or IL-15 alone resulted in more IL-32 single-positive than IL-32^{+}IFNγ^{+} cells, while for stimulation with combinations of two cytokines the opposite was true. Stimulation with IL-18 alone did not induce relevant IL-32 or IFNγ responses.

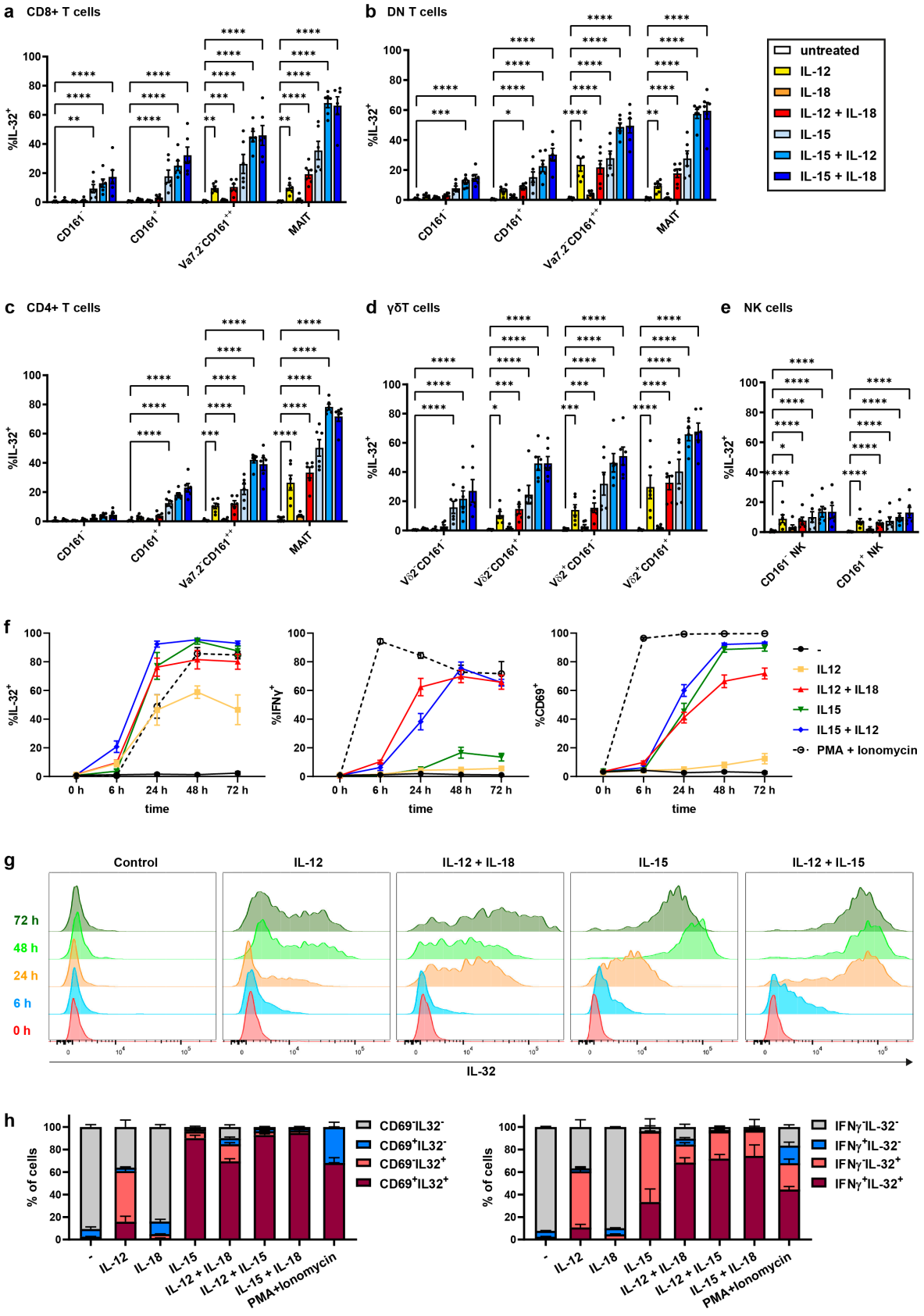


Figure 6-5. Cytokine-induced IL-32 expression in CD14-/CD19-depleted PBMCs and enriched CD8⁺ T cells. (a)-(e) IL-32 expression of indicated T cell and CD3⁻ subsets within CD14-/CD19-depleted PBMCs (N=6, pooled from two independent experiments) was analysed using flow cytometry after stimulation for 24 hours with individual cytokines and cytokine combinations, including IL-12, IL-18, IL-15, IL-12+IL-18, IL-12+IL-15 and

IL-18+IL-15. (f) Kinetics of IL-32, IFNγ and CD69 expression of cytokine-stimulated MAIT cells within CD8-enriched cells (N= 4) was analysed using flow cytometry. Controls included medium only (-) and PMA+Ionomycin stimulation. (g) Representative histograms showing IL-32 expression in MAIT cells within CD8-enriched cells upon stimulation with cytokines at indicated time points. Medium only condition served as a negative control. (h) CD8-enriched T cells (N=5) were stimulated with indicated cytokines for 48 hours. Controls included medium only (-) and PMA+Ionomycin. The frequency of MAIT cells that co-express IL-32 with CD69 or IFNγ was determined using flow cytometry. Graphs show mean ± SEM. For statistical analysis, two-way repeated measures ANOVA with Bonferroni's multiple comparisons test was performed. ****p<0.0001, ***p<0.001, **p<0.01, *p<0.05.

6.4.3. Common γ-chain cytokine-induced IL-32 expression in T cells

IL-15, a member of the common γ-chain cytokine family, could induce IL-32 expression in almost all T-cell subsets (Figure 6-4, Figure 6-5). Therefore, the ability of the other common γ-chain cytokine family members to induce IL-32 expression in T-cell subsets was tested. To see whether common γ-chain cytokines can indirectly or directly induce IL-32 expression in T cells, both total PBMCs and CD8-enriched PBMCs were stimulated. Cells were incubated in the presence of IL-2, IL-4, IL-7, IL-9, IL-15 or IL-21 for 48 hours (Figure 6-6). From the tested cytokines, IL-2, IL-7 and IL-15 induced significant IL-32 expression in all CD8 T-cell subsets, including MAIT, $CD161^{++}V\alpha7.2^{-}$, $CD161^{+}$ and $CD161^{-}$ cells. There was a trend of increasing frequencies of $IL\text{-}32^{+}$ cells with increasing levels of CD161 expression. $V\alpha7.2^{-}CD161^{++}$ and MAIT cells showed the highest frequencies of $IL\text{-}32^{+}$ cells. The results from bulk PBMCs and CD8-enriched PBMCs were very similar.

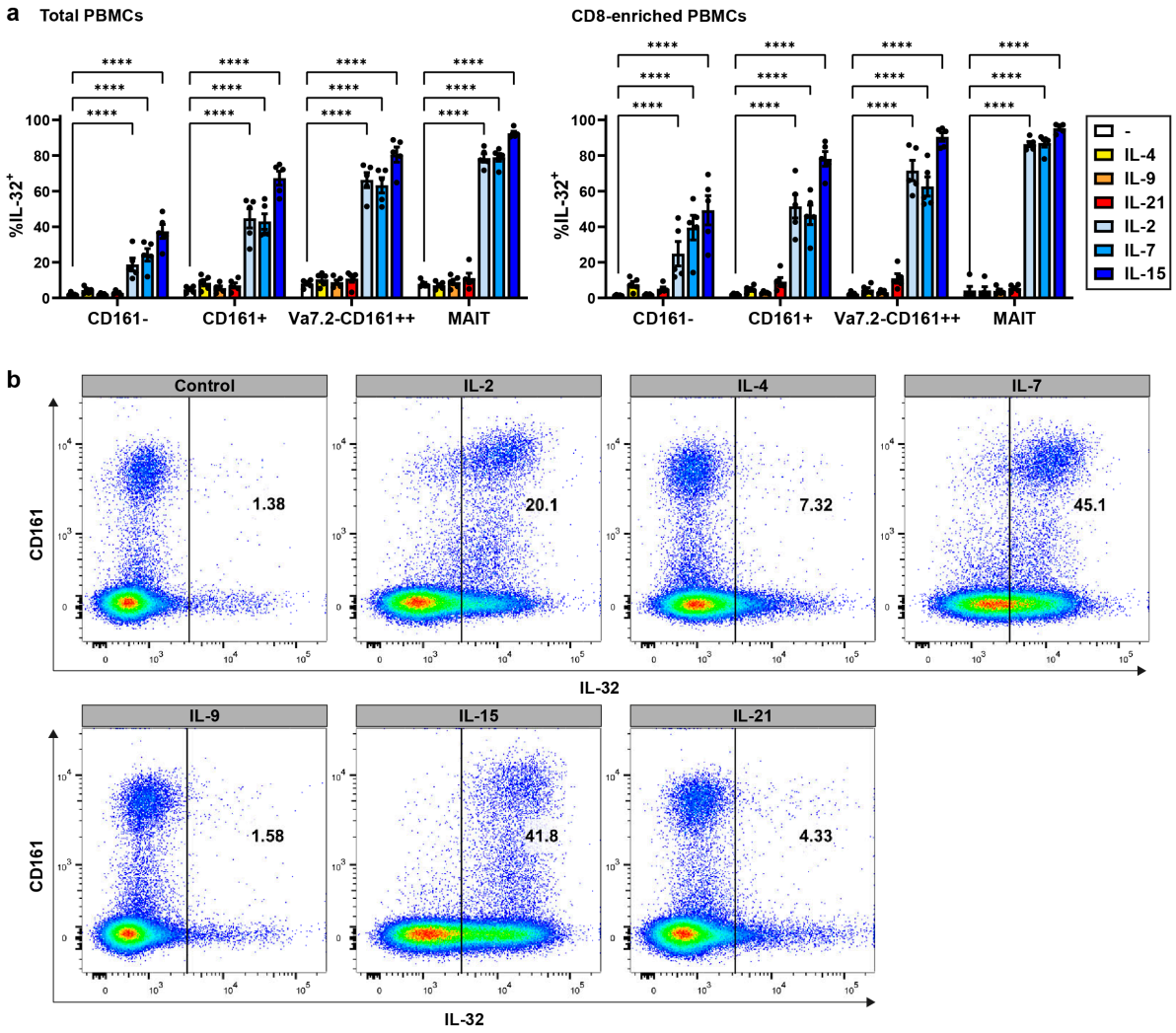


Figure 6-6. Common γ-chain cytokine-induced IL-32 expression in T cells. (a) PBMCs or CD8-enriched PBMCs (N=5) were stimulated by common γ-chain cytokines IL-2, IL-4, IL-7, IL-9, IL-15 or IL-21 for 48 hours. Medium only (-) was used as a negative control. After stimulation, IL-32 expression was measured in different $CD8^+$ T-cell subsets as indicated using flow-cytometry. (b) Representative pseudocolour plots showing IL-32 expression in CD8-enriched PBMCs plotted versus CD161. Bar plots indicate mean ± SEM. Two-way repeated measures ANOVA with Bonferroni's multiple comparisons test was performed. ****p<0.0001, ***p<0.001, **p<0.01, *p<0.05.

6.4.4. Comparison of IL-32 expression in memory T and MAIT cells

Apart from being expressed by NK and innate-like T lymphocytes, CD161 expression has also been associated with memory T cells (73). To test whether cytokine-induced IL-32 expression is particularly associated with the MAIT-cell subset as a representative of CD161-expressing innate-like cell types, or whether cytokine-induced IL-32 expression is a feature of memory T cells, CD8-enriched PBMCs were stimulated with individual cytokines and cytokine combinations for 48 hours (Appendix Figure IV-3). All CD8 T-cell subsets,

including naive T, TCM, TEM, TEMRA and MAIT cells, showed a significant IL-32 response upon stimulation with IL-2, IL-7, IL-15, IL-15+IL-18 and IL-15+IL-12. There was a trend of increasing IL-32 expression in the order from naive T < TCM < TEM/TEMRA < MAIT cells. MAIT cells were the only cell type to show significant IL-32 responses to IL-12, IL-18 and IL-12+IL-18 stimulation. The $CD8^+$ TEMRA cell subset was the only cell type with a significant IL-32 response upon IL-21 stimulation.

6.4.5. E. coli- and TCR-induced IL-32 expression in T cells

To investigate if MAIT cells can also express IL-32 in response to microbes, an experimental model in which PFA-fixed *E. coli* were added to total PBMCs was used. APCs within the PBMCs process PFA-fixed *E. coli* and activate MAIT cells in an MR1-dependent manner through presentation of bacterial-derived riboflavin metabolites. In addition, activated APCs produce cytokines including IL-12 and IL-18 which activate MAIT cells (65, 309). After stimulation of PBMCs with *E. coli* for 48 hours, approximately 70% of $CD8^+$ MAIT cells expressed IL-32 measured by flow cytometry (Figure 6-7a-b). $V\alpha7.2^+CD161^{++}$ and $CD161^+$ CD8 T cells also showed significant, but smaller *E. coli*-induced IL-32 responses. $CD161^-$ cells did not respond to *E. coli.* Like $CD161^{++}$/MAIT cells, $V\delta2^+$ T cells also expressed IL-32 upon *E. coli* stimulation of PBMCs (Figure 6-7c). The magnitude of *E. coli*-induced IL-32 responses was similar to IL-12+IL-18-mediated IL-32 responses (Figure 6-7a-c). In addition to IL-32 expression, IFNγ and CD69 expression was analysed to confirm T-cell activation (Appendix Figure IV-4a-b).

To further dissect the contribution of TCR and cytokine stimulation on *E. coli*-induced IL-32 expression in $CD161^{++}$/MAIT cells, anti-IL-12, anti-IL-18 and anti-MR1 blocking antibodies were applied. To test for additional factors that could contribute to the induction of IL-32 expression in MAIT cells in response to *E. coli*, anti-TNFα, anti-IFNγ and anti-IL-15 blocking antibodies, as well as B18R, a soluble vaccinia virus-encoded receptor that binds type I IFNs, were applied (Figure 6-7d-e). Anti-IL-12, anti-IL-18, anti-MR1 and the combination of

anti-IL-12 + anti-IL-18 could partially block *E. coli*-induced IL-32 expression. The combination of all three blocking antibodies reduced IL-32 expression by about 85%. From the other blocking antibodies tested and B18R, only anti-TNFα showed a significant effect and reduced IL-32 expression by approximately 18%. In summary, *E. coli*-induced IL-32 expression in CD161^{++}/MAIT cells is mediated via multiple factors including both TCR and IL-12+IL-18 stimulation, but blocking these factors did not completely abrogate IL-32 expression. Other factors such as TNFα could also contribute to induce the expression of IL-32. By comparison, *E. coli*-induced IL-32 expression in CD161-intermediate T cells was partially blocked by anti-IL-12 and anti-TNFα antibodies, but anti-IL-18 and anti-MR1 did not seem to have a noticeable effect (Appendix Figure IV-4c).

In contrast to IL-32, *E. coli*-induced IFNγ expression in CD161^{++}/MAIT cells was almost completely blocked by anti-IL-12 + anti-IL-18. Blocking MR1 did not have a significant effect on IFNγ expression, most likely due to the fact that TCR-mediated IFNγ-induction plays an early role in the response against *E. coli* (up to about 6 hours), whereas later IFNγ-induction is mainly cytokine-mediated (89). In addition, a reduction in IFNγ expression was observed when anti-TNFα and anti-IFNγ antibodies were added, and B18R reduced the IFNγ response by about 85%. Similar results were observed for CD161-intermediate T cells in which IFNγ expression was reduced when cytokines were blocked (Appendix Figure IV-4d).

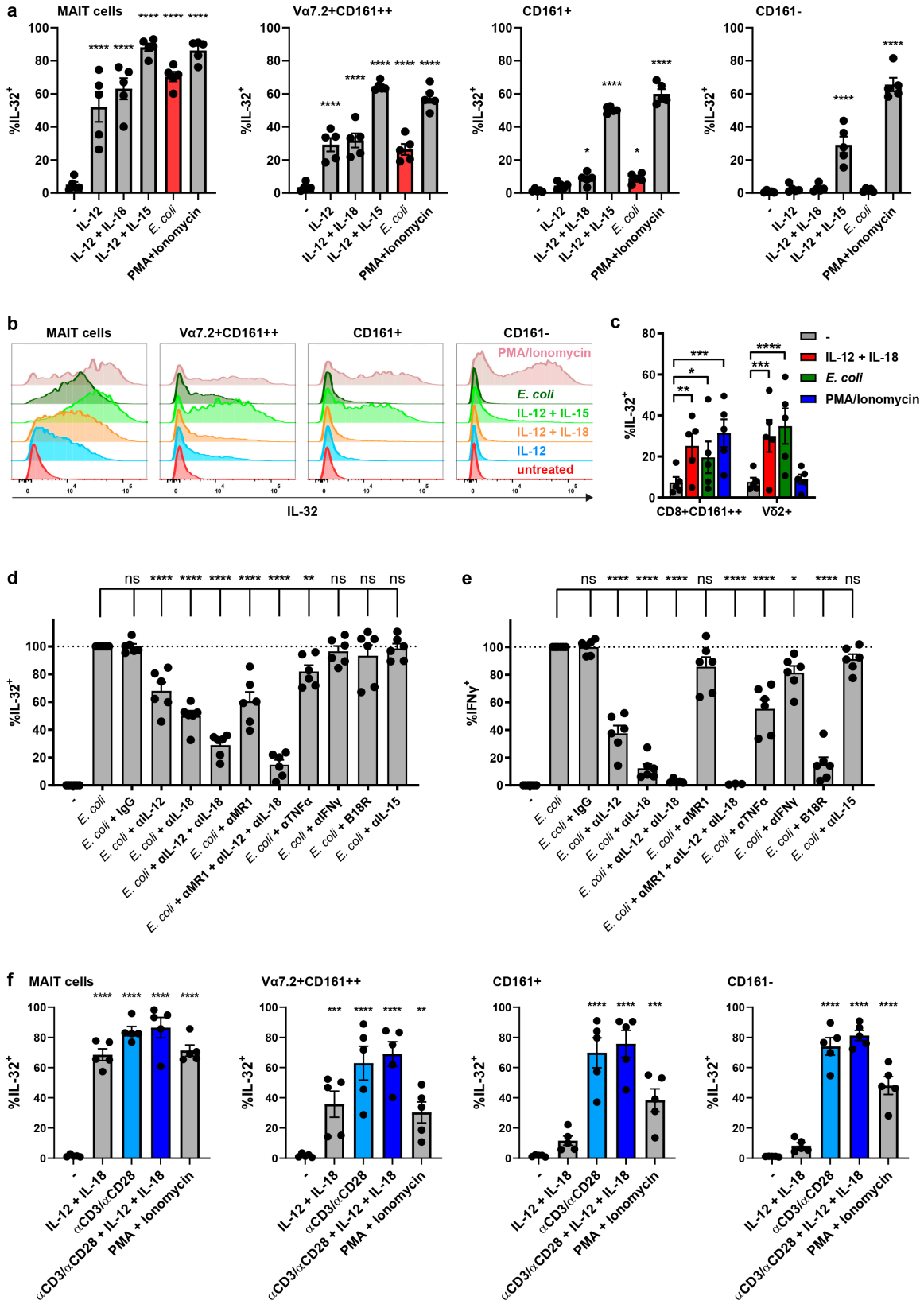


Figure 6-7. *E. coli*- and TCR-induced IL-32 expression in T cells. (a) PBMCs (N=5) were incubated with PFA-fixed *E. coli* for 48 hours. Controls included medium only (-), cytokines (IL-12, IL-12+IL-18 or IL-12+IL-15), and PMA+Ionomycin. IL-32 expression in indicated $CD8^+$ T-cell subsets was analysed using flow-cytometry. (b) Representative histograms show IL-32 expression within different T-cell subsets upon stimulation. (c) After stimulation of PBMCs (N=5) with IL-12+IL-18, *E. coli* or PMA+Ionomycin for 24 hours, IL-32 expression was

analysed in Vδ2^{+} T cells and CD8^{+}CD161^{++} T cells using flow cytometry. CD8^{+}CD161^{++} T cells include MAIT and Vα7.2^{-}CD161^{++} T cells. (d)-(e) PBMCs (N=6) were incubated for 48 hours with *E. coli* in the presence or absence of blocking antibodies as indicated. Controls included medium only (-) and IgG isotype control. IL-32 and IFNγ expression in Vα7.2^{-}CD161^{++}/MAIT cells was analysed using flow cytometry. (f) CD8-enriched T cells (N=5) were stimulated with IL-12+IL-18, plate-bound anti-CD3 and soluble anti-CD28 antibodies, or the combination of anti-CD3/anti-CD28 and IL-12+IL-18 cytokines for 48 hours. Controls included medium only (-) and PMA+Ionomycin. IL-32-expression was analysed in indicated T-cell subsets using flow cytometry. Bar plots indicate mean ± SEM. For statistical testing, one-way repeated measures ANOVA (in a, d, e and f) or two-way repeated measures ANOVA (in c) with Bonferroni's multiple comparisons test was performed. ****p<0.0001, ***p<0.001, **p<0.01, *p<0.05.

The ability of different T-cell subsets to express IL-32 upon TCR stimulation instead of cytokine stimulation was analysed by stimulating CD8-enriched PBMCs via plate-bound anti-CD3 and soluble anti-CD28 antibodies for 48 hours (Figure 6-7f). IL-32 expression was analysed using flow cytometry. All CD8 T-cell subsets, including CD161^{-}, CD161^{+}, Vα7.2^{-}CD161^{++} and MAIT cells expressed IL-32 upon TCR stimulation. The combination of anti-CD3/anti-CD28 with IL-12+IL-18 did not result in a noticeable difference as anti-CD3/anti-CD28-induced IL-32 responses appeared close to saturation. In addition to IL-32, IFNγ and CD69 expression was analysed to confirm T-cell activation (Appendix Figure IV-5).

6.4.6. Regulation and modulation of cytokine-mediated responses of CD161-expressing T cells by IL-32

The α-isoform of IL-32 has recently been reported to inhibit NK cell function directly (108). As NK cells share several features of their responses with innate-like T cells (65, 167), the effect of the three commercially available IL-32 isoforms α, β and γ on CD161-expressing cells was tested. First, PBMCs were incubated in the presence or absence of cytokines or combinations of cytokines at suboptimal concentrations, including IL-15, IL-12 and IL-18. To each condition, diluted IL-32α, IL-32β, IL-32γ or pure medium (control) was added. After 24 hours, IFNγ and GzmB expression of different CD8 T-cell subsets was analysed using flow cytometry (Figure 6-8a).

6. Role of IL-32 in innate-like T-cell activation

Within $CD161^{++}CD8^{+}$ T cells, none of the IL-32 isoforms had a significant effect on IFNγ or GzmB expression on their own compared to the untreated condition. But IL-32β and IL-32γ could enhance GzmB and IFNγ responses of $CD161^{++}CD8^{+}$ T cells in presence of other cytokines compared to the control condition. The largest IL-32β/γ-mediated increases of IFNγ responses were observed in the IL-12, IL-15 and IL-15+IL-18 conditions. The largest IL-32β/γ-mediated increases of GzmB responses were observed in the IL-15, IL-15+IL-12 and IL-15+IL-18 conditions. No significant effect of IL-32β/γ was observed in the IL-18 only condition. IL-32α did not show any significant effects on IFNγ and GzmB responses. The effect of IL-32α/β/γ on $CD161^{+}CD8^{+}$ T cells was similar to the effect on $CD161^{++}CD8^{+}$ T cells, but the magnitude of IL-32β/γ-mediated responses were smaller (Appendix Figure IV-6a, b). The effect of IL-32β/γ on $CD161^{-}CD8^{+}$ T cells was negligible (Appendix Figure IV-6c, d). The effects of IL-32 isoforms on IFNγ and GzmB responses of $CD8^{-}$ T-cell subsets were similar to what was observed for $CD8^{+}$ T-cell subsets (Appendix Figure IV-6e-j).

The greatest response to IL-32β/γ was observed within the $CD161^{++}CD8^{+}$ T cell population, which mainly consists of $CD8^{+}Vα7.2^{+}CD161^{++}$ MAIT cells (65, 68). For that reason, the effect of IL-32α, β and γ on enriched, cytokine-stimulated $CD8^{+}$ cells was tested next, to specifically investigate the effect of IL-32 on MAIT cells in the absence of APCs. By repeating the experiment above with enriched $CD8^{+}$ T cells, IL-32β and IL-32γ could enhance MAIT cell IFNγ and GzmB responses to IL-15 and to combinations of IL-15 with IL-12 or IL-18 (Figure 6-8b-c). Both isoforms also increased the IFNγ responses to IL-12+IL-18, but not GzmB. None of the IL-32 isoforms had a significant effect on their own or could promote IFNγ or GzmB responses in combination with IL-12 or IL-18. In contrast, IL-32β/γ could promote IL-12-mediated MAIT cell responses within PBMCs. Similar results to those from MAIT cells were observed when analysing $Vα7.2^{-}CD161^{++}$ and $CD161^{+}CD8^{+}$ T cells, although responses were reduced or completely absent for certain conditions within $CD161^{+}CD8^{+}$ T cells (Appendix Figure IV-7). The effects of IL-32β/γ on $CD161^{-}CD8^{+}$ T cells were negligible.

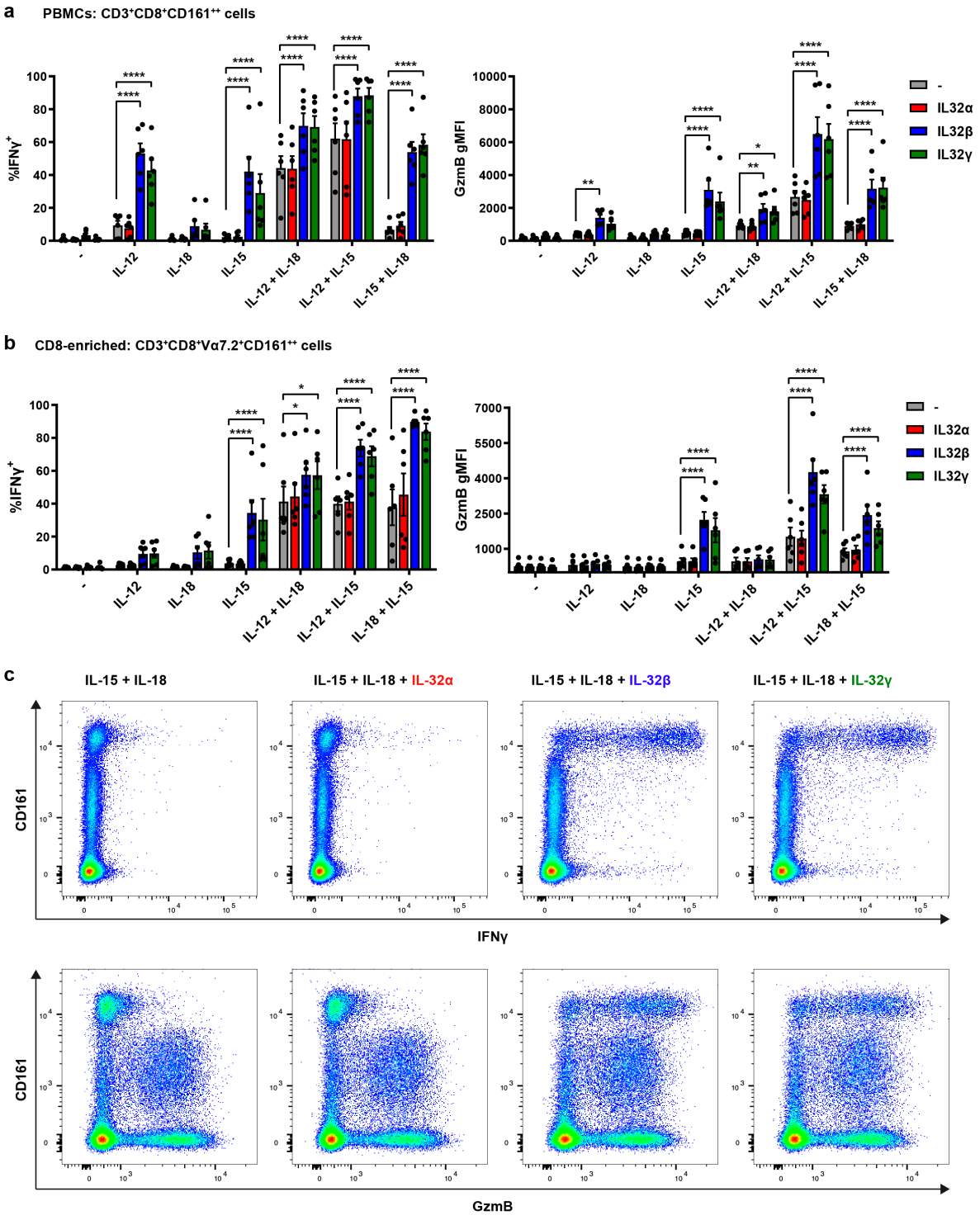


Figure 6-8. IL-32 enhances cytokine-mediated responses of CD8⁺CD161⁺⁺ T cells. (a)-(b) PBMCs or CD8-enriched PBMCs (N=6, pooled from two independent experiments with N=3) were incubated in the presence or absence of cytokines or combinations of cytokines at suboptimal concentrations, including IL-15, IL-12 and IL-18. To each condition, diluted IL-32α, IL-32β, IL-32γ or pure medium (-) was added. After 24 hours, IFNγ and GzmB expression in CD8⁺CD161⁺⁺ T cells (within PBMCs) or MAIT cells (within CD8-enriched PBMCs) was analysed using flow cytometry. Columns with error bars represent mean ± SEM. Geometric mean fluorescence intensity, gMFI. Two-way repeated measures ANOVA with Bonferroni's multiple comparisons test was performed. ****p<0.0001, ***p<0.001, **p<0.01, *p<0.05. (c) Representative pseudocolour plots show IL-32 versus CD161 expression of CD8⁺ T cells in CD8-enriched PBMCs after stimulation with IL-15+IL-18 in the absence or presence of IL-32α, β or γ.

6. Role of IL-32 in innate-like T-cell activation

Cytokine-stimulation of Vδ2$^+$ and Vδ2$^-$ γδT-cell subsets within PBMCs revealed that IL-32β/γ had similar effects on Vδ2$^+$ γδT cells as on MAIT cells (Appendix Figure IV-8). An effect of IL-32 on Vδ2$^-$ γδT cells was only seen in a few conditions, particularly when IL-15 was present. IL-32-mediated responses in Vδ2$^-$ cells were lower in magnitude compared to those in Vδ2$^+$ cells.

As some of the largest effects of IL-32β/γ on cytokine-mediated MAIT-cell activation were observed in combination with suboptimal levels of IL-15+IL-18, this cytokine combination was chosen to further investigate the role of IL-32 in regulating MAIT cell effector functions. Enriched CD8$^+$ cells were stimulated with suboptimal levels of IL-15+IL-18 in the presence of increasing concentrations of IL-32α, β or γ to determine the dose-response relationship of IL-32. Cytokine-induced IFNγ and GzmB responses of MAIT cells were assessed using flow cytometry (Figure 6-9a). IL-32β and IL-32γ enhanced IFNγ and GzmB responses in a dose-dependent manner, with EC_{50} values ranging from about 30 – 180 ng/mL, depending on the measured response and the IL-32 isoform. No significant IL-32α-mediated responses were observed.

Next, the effect of IL-32 on the responsiveness towards cytokine stimulation was investigated. CD8-enriched PBMCs were stimulated with optimal levels of IL-32β/γ in combination with increasing concentrations of IL-15+IL-18 (Figure 6-9b). The presence of both IL-32β and γ decreased EC_{50} values of IL-15+IL-18-mediated IFNγ and GzmB responses of MAIT cells. In addition, IL-32β/γ increased the magnitude of IL-15+IL-18-induced IFNγ and GzmB responses under saturated conditions.

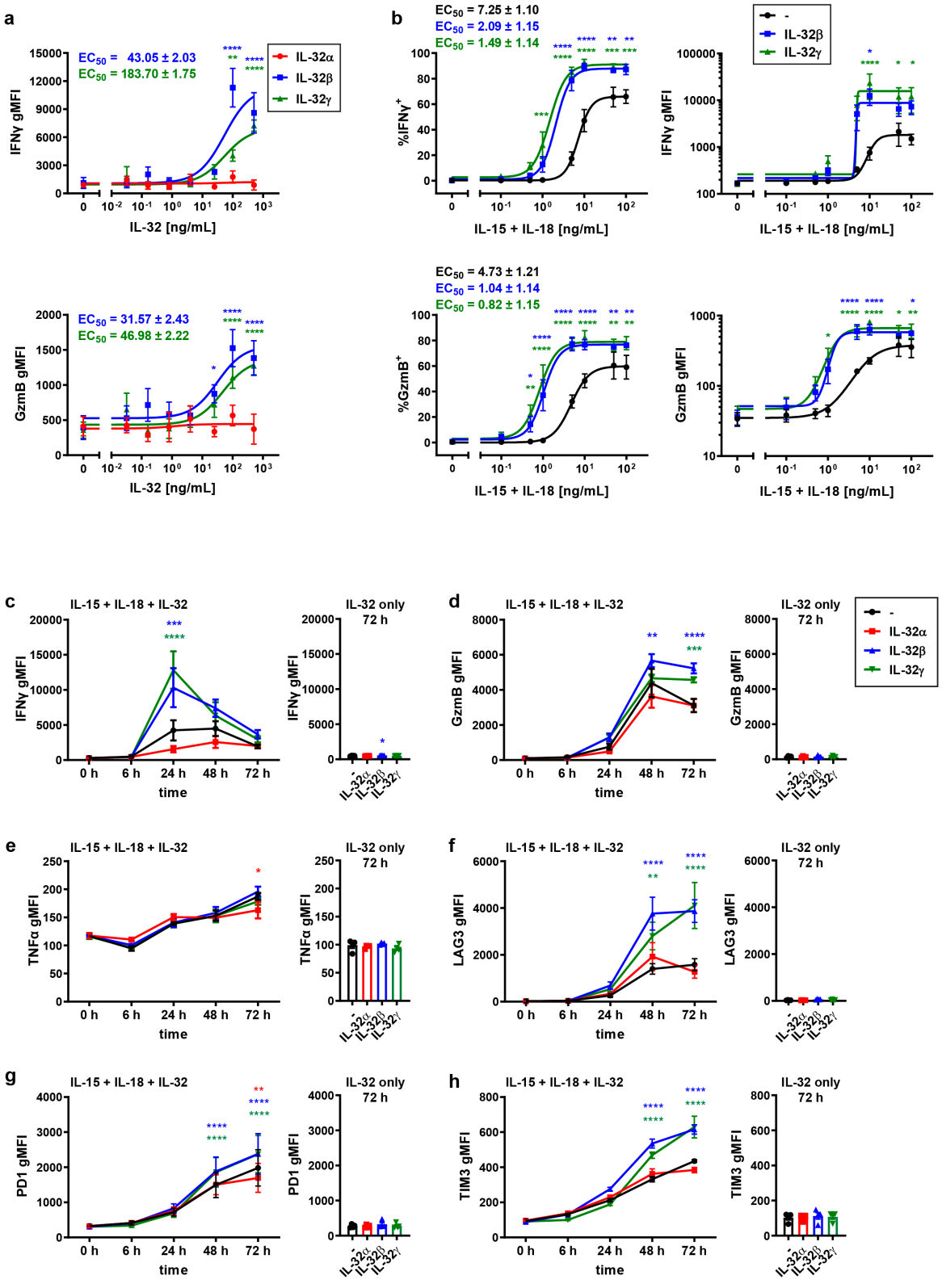


Figure 6-9. Dose-response and kinetics of IL-32-mediated MAIT-cell activation. (a) CD8-enriched PBMCs were stimulated with suboptimal levels of IL-15+IL-18 in the presence of increasing concentrations of IL-32α, IL-32β or IL-32γ as indicated. IFNγ and GzmB expression levels of MAIT cells were determined by flow cytometry. Data analysis of dose response curves and calculation of EC_{50} values was performed using a three-parameter non-linear fit model integrated into GraphPad Prism. Two-way repeated measures ANOVA with Bonferroni's multiple comparisons test was performed with the medium only condition (0 ng/mL) as reference group. (b)

CD8-enriched PBMCs were stimulated with increasing concentrations of IL-15+IL-18 as indicated in presence or absence of IL-32β or IL-32γ at constant concentrations. IFNγ and GzmB expression levels of MAIT cells were determined by flow cytometry. Data analysis of dose response curves and calculation of EC_{50} values was performed using a four-parameter non-linear fit model integrated into GraphPad Prism. Two-way repeated measures ANOVA with Bonferroni's multiple comparisons test was performed with the no-IL-32 condition (-) as reference group. (c)-(h) Left graphs: CD8-enriched PBMCs were stimulated with suboptimal levels of IL-15+IL-18 in presence or absence of IL-32α, IL-32β or IL-32γ for different periods of time as indicated. Right graphs: CD8-enriched PBMCs were stimulated with IL-32α, IL-32β or IL-32γ in the absence of IL-15+IL-18 for 72 hours. IFNγ, GzmB, TNFα, LAG3, PD1 and TIM3 expression levels of MAIT cells were determined by flow cytometry. Geometric mean fluorescence intensity, gMFI. Two-way repeated measures ANOVA with Bonferroni's multiple comparisons test was performed with the no-IL-32 condition as reference group. ****p<0.0001, ***p<0.001, **p<0.01, *p<0.05.

The kinetics of IL-32-mediated MAIT cell stimulation were analysed by stimulating enriched $CD8^+$ cells with suboptimal concentrations of IL-15+IL-18 in the presence of IL-32 for different periods of time up to 72 hours (Figure 6-9c). IL-32β and IL-32γ had the biggest impact on IFNγ expression after 24 hours and on the GzmB expression after 48 – 72 hours. IL-32α had no significant effect on IFNγ or GzmB responses. TNFα expression was not affected by IL-32, except for a minimal decrease after 72 hours in the presence of IL-32α. Additionally, there was a significant increase in LAG3, PD1 and TIM3 expression in presence of IL-32β and IL-32γ after 48 and 72 hours of stimulation compared to the control.

6.4.7. Generation of a pan-cancer *IL32* gene signature

IL-32 has both a tumour promoting and suppressive effect by directly acting on cancer cells and is a regulator and effector cytokine of immune responses. The role of IL-32 in the anti-cancer immune response is, however, underexplored (257, 310).

To generate a pan-cancer *IL32* gene signature that allows one to study the role of IL-32 in cancer, the TCGA data repository was used, which contains bulk RNA-seq data of more than 11,000 samples from 33 different cancer types. Hoadley et al. generated the PanCan Atlas which is a batch-corrected TCGA version (303). The batch-corrected data contains some slightly negative values, which are problematic for the downstream analysis including log-transformation. Due to the large range of RSEM (RNA-Seq by Expectation Maximization)

expression values from -0.99 to 9.92*10^6, all negative values were replaced with 0 without drastically impacting the overall distribution. After batch correction, the authors also replaced genes with mostly zero reads or genes with residual batch effects with missing data values (NAs) (303). NAs were found in 8/33 cancer types and affected between 0.42 – 18.34% of total data values depending on the cancer type (Figure 6-10a). The fraction of affected samples ranged from 6 – 100 % and the fraction of affected genes ranged from 7.03 – 18.34%, depending on the cancer type (Appendix Table IV-1). In total, a relatively high proportion of genes (4196/20531 = 20.44%) contained missing data. As only 8/33 cancer types were affected, genes with missing data were not simply excluded from further analysis. Missing value imputation was not an option as missing data values were not random. Therefore, the feasibility of replacing NAs with 0 was investigated, which requires confirmation of these genes as being absent or lowly expressed.

For this purpose, processed TCGA data was obtained from other sources including Recount2, GDC harmonized data portal, GDC Legacy Archive and Broad Institute GDAC Firehose. The suitability of TCGA data sets sourced from different repositories for the investigation of the original expression levels of the PanCan Atlas NAs was analysed by assessing the overlap of samples and gene IDs with PanCan Atlas data (Figure 6-10b-e). Depending on the TCGA repository, about 0.80 – 5.47% samples from the PanCan Atlas data were missing. Gene IDs between PanCan Atlas, Broad Institute Firehose and GDC Legacy TCGA data matched exactly as they were all annotated with Entrez IDs. In contrast, about 3.54 – 3.57% of PanCan Atlas Entrez IDs had no match in Recount2 and GDC harmonized TCGA data sets, which were annotated with Ensembl gene IDs. For further analysis, Recount2, GDC harmonized and Broad Institute Firehose TCGA data sets were chosen to cover as many PanCan NAs as possible (Figure 6-10f).

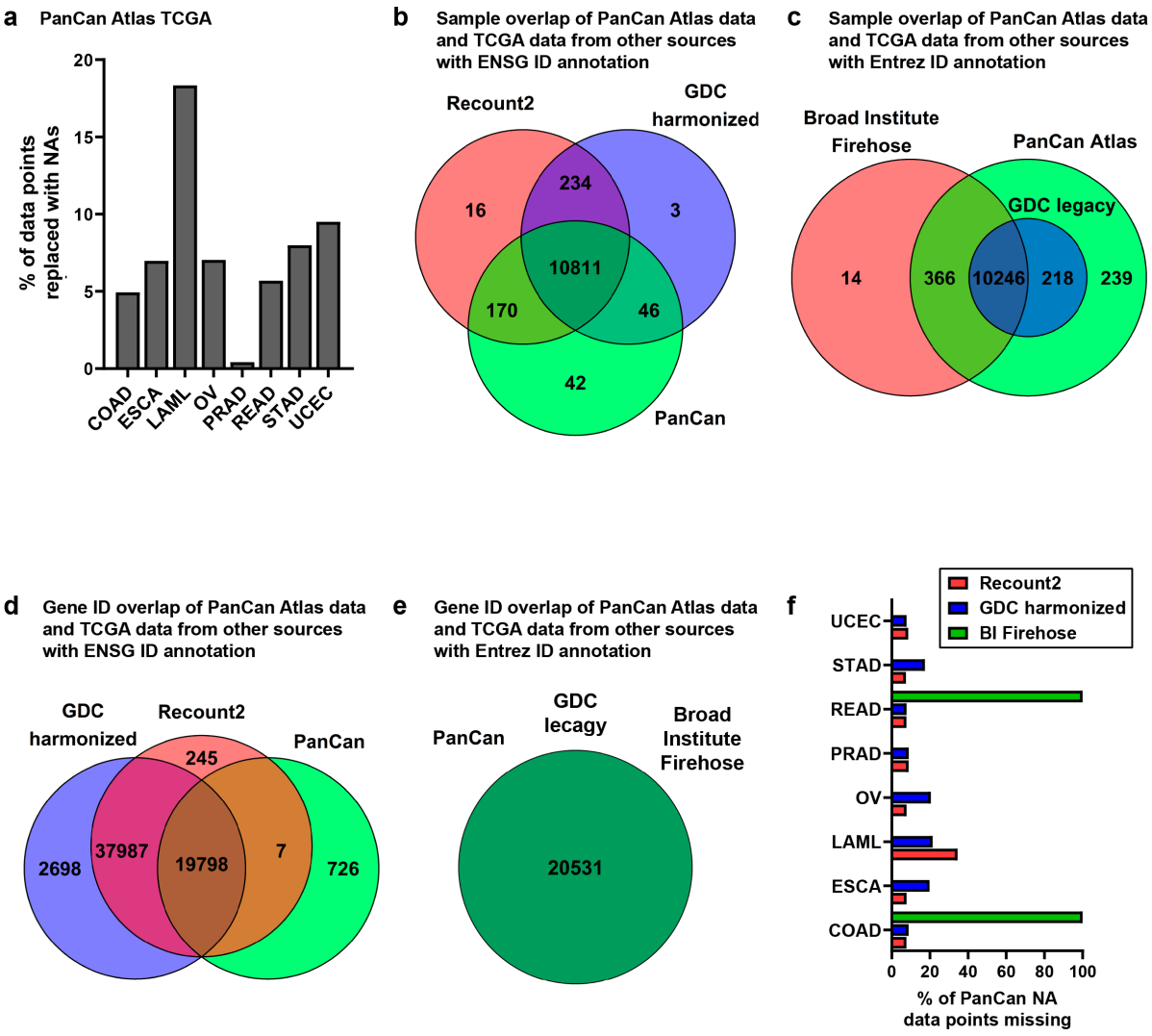


Figure 6-10. PanCan Atlas TCGA data set contains missing values. (a) Frequency of missing data values (NAs) within the 8 cancer types that are affected by missing data in the PanCan Atlas data. Non-batch-corrected TCGA data from different repositories were assessed for their use to investigate the original expression values of missing data in the PanCan Atlas TCGA data. (b)-(c) Sample overlap between PanCan Atlas data with TCGA data obtained from sources with (b) Ensembl Gene ID annotation, including Recount2 and GDC harmonized data portal, or with (c) Entrez Gene ID annotation, including GDC Legacy Archive and Broad Institute TCGA GDAC Firehose data. (d)-(e) Gene ID overlap between PanCan Atlas data with TCGA data obtained from sources with (d) Ensembl Gene ID annotation, including Recount2 and GDC harmonized data portal, or with (e) Entrez Gene ID annotation, including GDC Legacy Archive and Broad Institute TCGA GDAC Firehose data. (f) Relative number of PanCan Atlas TCGA NAs that are not covered by TCGA data from Recount2, GDC harmonized data portal and Broad Institute GDAC Firehose, stratified by cancer type.

These three TCGA data sets were filtered for samples and genes common to PanCan Atlas data. The global distribution of gene expression of all genes was assessed, and the 40th percentile of the global gene expression distribution was chosen as the cut-off for relevant gene expression (Figure 6-11a). Then, for each of the three TCGA data sets sourced from

different repositories, the distribution of data values that were replaced with NAs in the PanCan Atlas data was assessed separately for each gene, obtaining the NA gene distributions. The 90^{th} and 95^{th} percentiles of the NA gene distributions were calculated. Next, the frequency of the 90^{th}/95^{th} percentiles of NA gene distributions being smaller than P_i of the global TCGA gene expression distribution was calculated, where P_i stands for percentiles ranging from the 5^{th}-95^{th} in steps of 5 (Figure 6-11b). The results showed that for 85-91% of NA-affected genes, the 90^{th} percentile of NA gene distribution was below the 40^{th} percentile of the global gene expression distribution, depending on the TCGA data set used. Similarly, for 91-95% of NA-affected genes, the 95^{th} percentile of the NA gene distributions was below the 40^{th} percentile of the global gene expression distribution. This indicates that most of the genes that were replaced with NAs in certain samples were not or only lowly expressed.

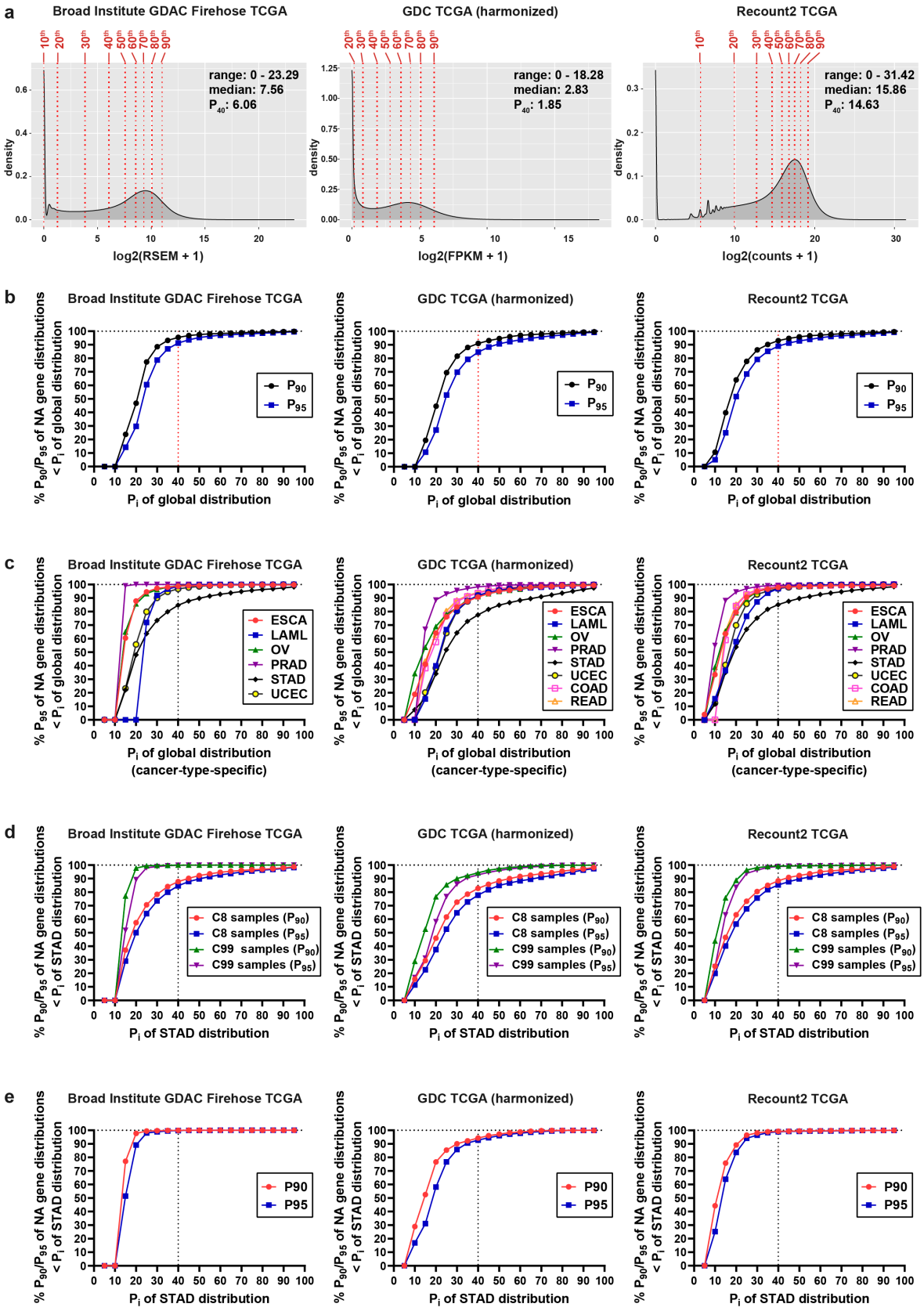


Figure 6-11. Investigation of the original expression values of PanCan TCGA NAs with the help TCGA data obtained from other repositories. To investigate the original expression values of PanCan TCGA NAs and to compare them to the overall global and cancer type-specific global gene expression, TCGA data was obtained from alternative repositories, including Broad Institute GDAC Firehose, GDC harmonized data portal and

Recount2. (a) Density plots show global gene expression distribution from TCGA data obtained from the three different repositories. Only samples and genes common with PanCan Atlas data were analysed. Red lines indicate percentiles. (b) For each of the three TCGA data sets obtained from the different repositories, the distribution of data points that were replaced with NAs within the PanCan Atlas TCGA data was assessed, separately for each affected gene (NA gene distribution). The 90^{th} and 95^{th} percentiles (P_{90}, P_{95}) for the NA distributions of each affected gene were calculated. The graphs display the frequency for the fulfilled condition of P_{90}/P_{95} of NA gene distributions < P_i of the global TCGA gene expression distribution, where i stands for percentiles from 5-95 in steps of 5. (c) Same as in (b), but analysis was stratified by cancer type that is affected by NAs in the PanCan Atlas data. Both the calculation of P_{95} of NA gene distribution and the percentiles of global gene expression distribution was performed in a cancer-specific manner. (d) Same as in (c), but only STAD cancer was analysed. STAD cancer analysis was stratified by C8 and C99 samples. C8 samples are a fraction of STAD patient samples (8.44%) of which 3766 genes were replaced with NAs in the PanCan Atlas data. C99 samples comprise a fraction of STAD samples (90.89%) of which only 1455 genes were replaced with NAs in the PanCan Atlas data. (e) Same as in (c), but only STAD samples were analysed. C8 samples were excluded in this analysis.

As there could be cancer-type specific differences in gene expression, this analysis was repeated in a cancer type-specific manner where similar results were obtained (Figure 6-11c, Appendix Figure IV-9). For about 90-100% of NA-affected genes, the $90^{th}/95^{th}$ percentiles of the NA gene distribution were below the 40^{th} percentile of cancer type-specific global gene distribution. An exception was STAD, for which this condition was only fulfilled in about 77-88%. Therefore, STAD analysis was repeated and stratified by C8 and C99 samples (Figure 6-11d). C8 samples comprised a fraction of 8.44% of STAD samples in which 3766 genes had been replaced with NAs, whereas C99 samples comprised a fraction of 90.89% STAD samples in which only 1455 genes had been replaced with NAs. Analysis revealed that for about 93-99.99% of NA-affected genes in C99 samples, the condition of $90^{th}/95^{th}$ percentile of the NA gene distribution < 40^{th} percentile of STAD global gene distribution was fulfilled. In contrast, this condition was fulfilled only for about 77-88% of NA-affected genes in C8 samples. C8 samples were excluded from further analysis, resulting in about 93-99.7% of NA-affected genes fulfilling the above-mentioned condition in STAD samples (Figure 6-11e). Overall, this analysis confirmed that most genes that were replaced with NAs in certain samples of PanCan Atlas data were absent or poorly expressed, justifying the replacement of PanCan Atlas NAs with 0.

6. Role of IL-32 in innate-like T-cell activation

In cancers from the PanCan Atlas, a range of *IL32* expression levels could be observed that differed between cancer types (Figure 6-12a). In order to generate an *IL32* gene signature containing genes associated with *IL32* expression, RENOIR R package (REsampliNg methOds for machIne learning, unpublished, developed and kindly provided by Dr. Alessandro Barberis and Prof. Francesca Buffa, Department of Oncology, University of Oxford) was used. RENOIR was employed to model Y=MX where Y=*IL32* gene expression and M=expression of all other genes within PanCan Atlas data (Figure 6-12b-c). Only data from primary cancers was considered. RENOIR fits generalised linear models via penalized maximum likelihood based on elastic net regression. In this process, RENOIR considers 5 different training-set sizes, creates 50 training-validation sets for each training-set size from the total data set by random sampling, and uses cross-validation for parameter estimation. The cross-validation procedure produces two models from two sets of hyperparameter values each time, one set (min) resulting in a model with the mean cross-validated error being minimised, the other set (1SE) resulting in the mean cross-validated error being within 1SE of the minimum. RENOIR assessed the performance of fitted models using the mean squared error as accuracy measure, which was calculated on the training, testing and the whole data set. RENOIR chose the best model across all the considered training set sizes by using an automated internal procedure.

RENOIR also generated an importance score for each feature across all models of all different training set sizes separately for the min and 1SE results. The importance scores represent weighted coefficients of the models where the weights consider the prediction accuracy of the models. The importance scores of each cancer type were used as input for rank product analysis to generate a pan-cancer signature containing genes that are positively associated with *IL32* expression. Using 21 different pfp (percentage of false positives) cut-offs ranging from 1E-1 to 1E-20, 21 different signatures were generated for both the min and 1SE results (Figure 6-12d).

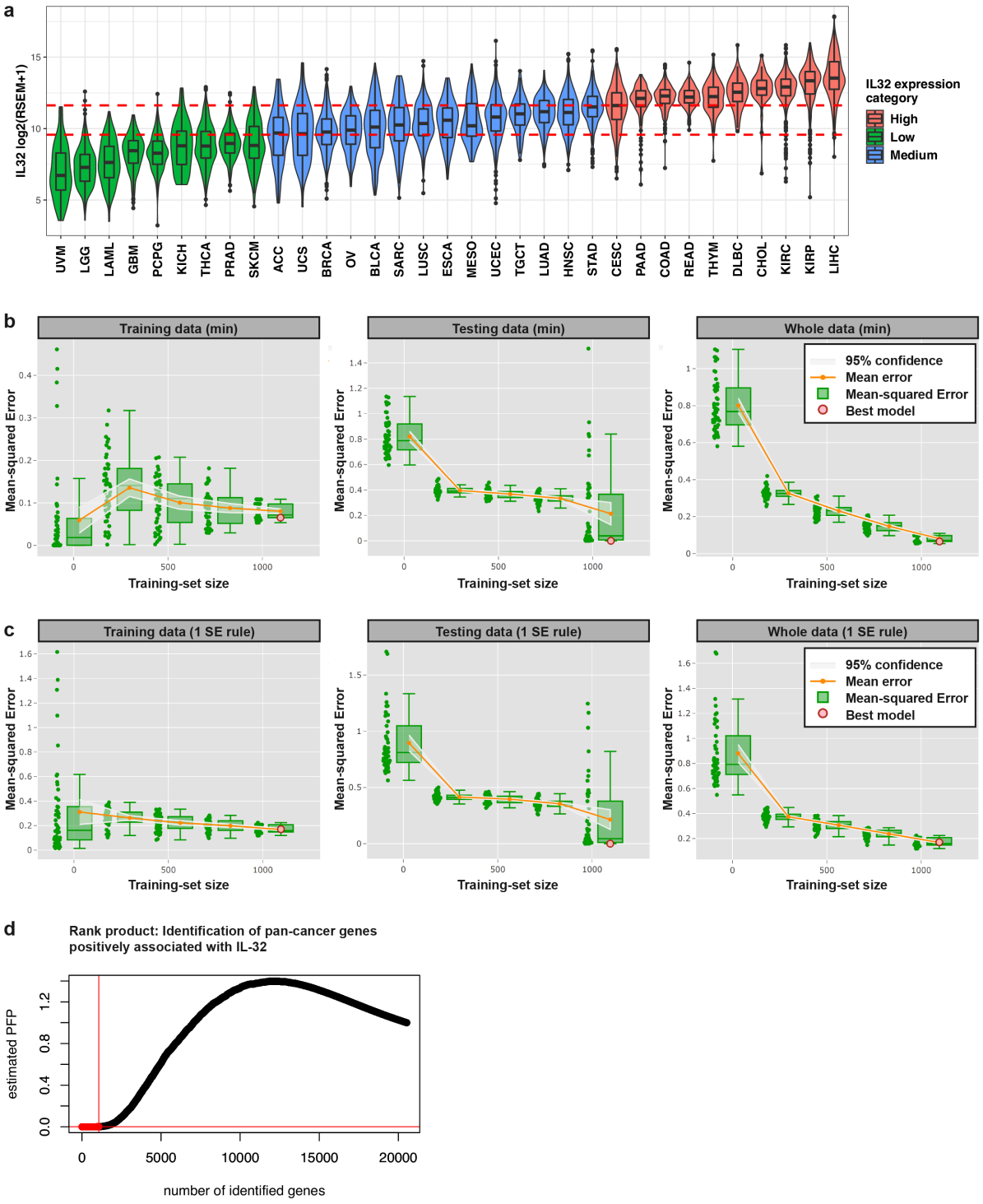


Figure 6-12. Generation of an *IL32* gene signature using RENOIR. (a) Violin plot shows *IL32* gene expression within 33 cancer types of PanCan Atlas TCGA data. Only data from primary cancers was considered. Red lines indicate tertiles of global *IL32* gene expression distribution. Cancer types were categorised into low, medium and high *IL32* expression, depending on whether the median of their *IL32* distribution was below the first tertile, between the first and second tertile or above the second tertile, respectively. (b)-(c) *IL32* gene expression was modeled for 33 cancer types from the PanCan Atlas data using RENOIR R package (unpublished, developed by Dr. Alessandro Barberis and Prof. Francesca Buffa, Department of Oncology, University of Oxford). RENOIR was employed to model Y=MX, where Y=*IL32* gene expression and M= expression of all other genes, by fitting generalised linear models via penalized maximum likelihood based on elastic net regression. Only data from primary cancers were considered. RENOIR considers 5 different training-set sizes and creates 50

training-validation sets for each training-set size from the total data set by random sampling. In addition, RENOIR uses cross-validation for parameter estimation. Graphs show performance overview of fitted models across the training-set sizes using BRCA as an example. Performance was assessed using the mean squared error as accuracy measure, which was calculated on the training, testing and the whole data. Each trained model is represented as a green dot. The mean error and confidence intervals are indicated for each training-set size. RENOIR automatically selects the best model (red dot) using an automated internal procedure. In (b), the best model is chosen according to a set of hyperparameter values so that the mean cross-validated error is minimised (min). In (c), the best model is chosen according to a set of hyperparameter values, so that the mean cross-validated error is within one standard error of the minimum (1SE). (d) RENOIR generates an importance score for each feature across all models of all different training set sizes. The importance scores represent weighted feature coefficients, where the weights consider the prediction accuracy of each model. The feature importance scores for each cancer type were used as input for rank product analysis to generate a pan-cancer signature of genes positively associated with *IL32* expression. Twenty-one signatures for both the min and 1SE results were generated using different pfp (percentage of false positives) cut-offs ranging from 1E-1 to 1E-20. As an example, the graph shows the rank product results (pfp=0.001) using feature importance scores of models generated with the 1SE rule as the input.

Besides using RENOIR, additional *IL32* gene signatures were generated by performing simple correlation analysis using the Spearman method. For this purpose, data was pre-processed by filtering for highly variable genes and excluding lowly expressed genes (Figure 6-13a-b). Only data from primary cancers was considered. Next, the correlation of *IL32* with all other genes within the pre-processed data was analysed using Spearman's correlation (Figure 6-13c). The analysis was performed separately for each gene and each cancer type. The calculation of Spearman's correlation coefficients was repeated using bootstrapping with 1000 bootstrap replicates to test whether the limited sample size of some of the cancer types had impacted the results (Figure 6-13d). Differences between the standard Spearman's coefficients and bootstrapped Spearman's coefficients were very small ranging from -0.02 to 0.02. To generate a pan-cancer *IL32* signature of genes positively associated with *IL32* expression, Spearman's correlation coefficients of the 33 cancer types were used as input for rank product analysis. Using 21 different pfp cut-offs ranging from 1E-1 to 1E-20, 21 different signatures were created (Figure 6-13e).

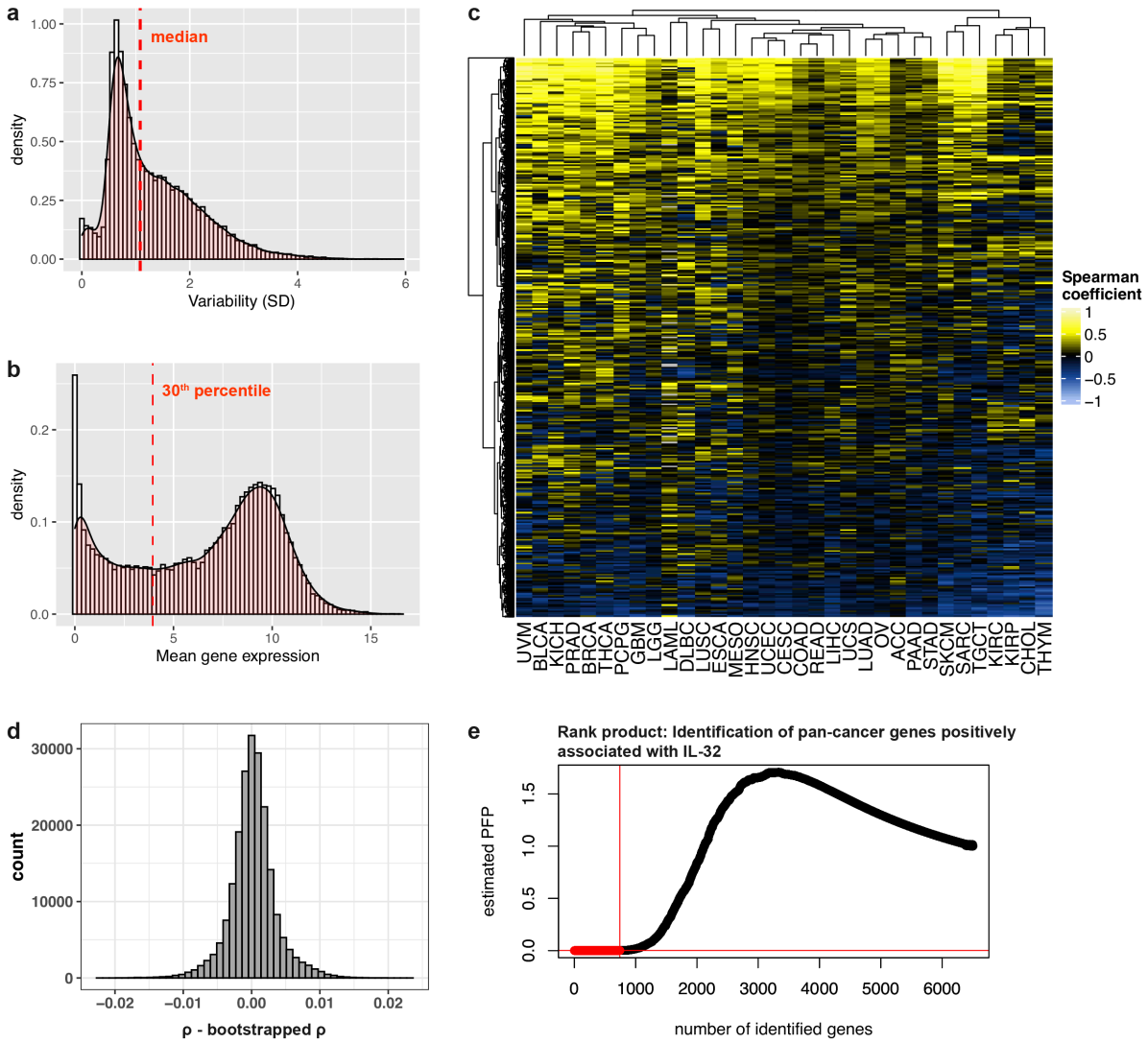


Figure 6-13. Generation of an *IL32* gene signature using Spearman's correlation analysis. PanCan Atlas data was pre-processed by (a) filtering for the 50% most highly variable genes using standard deviation (SD) as variability measure and by (b) removing the 30% most lowly expressed genes considering mean gene expression. Only data from primary cancers was considered. (c) The correlation of *IL32* gene expression with all other features in the pre-processed PanCan Atlas data was calculated using the Spearman method. The correlation analysis was performed separately for each gene and for each cancer type. Genes for which the correlation coefficient analysis resulted in NA in any of the cancers were excluded from further analysis. The obtained correlation coefficients are displayed in a heat map. (d) To test if the limited sample size in any of the cancer types negatively impacted the correlation results, the correlation analysis was repeated by estimating the Spearman's correlation coefficient (ρ) using bootstrapping with 1000 bootstrap replicates. The histogram shows the differences between all standard ρ and all bootstrapped ρ. (e) The Spearman's coefficients from all 33 cancer types were used as input for rank product analysis to generate a pan-cancer signature of genes positively associated with *IL32* expression. Using different pfp (percentage of false positives) cut-offs ranging from 1E-1 to 1E-20, 21 different signatures were generated. As an example, graph shows rank product results for pfp=0.001.

In total, 63 *IL32* gene signatures were obtained, including RENOIR min-, RENOIR 1SE- and simple correlation-derived signatures with 21 signatures each. The number of signature genes differed between signatures, depending on the pfp cut-off chosen for rank product

analysis (Figure 6-14a). To assess the performance of signatures obtained with different pfp cut-offs, three scores were calculated for each of the 63 signatures, including mean and median expression across all signature genes and PC1 (principal component 1) for each primary cancer sample within PanCan Atlas data (Figure 6-14b). As a negative control, the mean and median expression scores were calculated across all 20531 PanCan Atlas genes. Pearson's and Spearman's correlation between each of the three scores and *IL32* gene expression levels in primary cancer samples within PanCan Atlas data was calculated. For all 63 signatures relatively high correlation coefficients ranging from 0.53 – 0.8 were observed. At this point, there was no reason to exclude any signatures from further analysis.

Next, the overlap of *IL32* signature genes between RENOIR min- and RENOIR 1SE-derived signatures with matching pfp cut-offs was investigated (Figure 6-14c). The results showed that the RENOIR min signatures comprised essentially a subset of RENOIR 1SE signatures with a few unique RENOIR min genes observable particularly for non-stringent pfp cut-offs. RENOIR 1SE signatures were chosen for further analysis.

Due to multicollinearity (intercorrelation among two or more explanatory variables), linear regression methods, such as those employed by RENOIR, can recruit genes that become associated with the response variable (= *IL32* expression) only in the model, but which are not directly correlated with *IL32* expression (311). Therefore, only common genes between RENOIR 1SE- and simple correlation-derived signatures with matching pfp cut-offs were chosen for further analysis (Figure 6-14d). This step excluded artefacts caused by multicollinearity, as the signature genes from the simple correlation signature are directly correlated with *IL32* gene expression. This approach is also superior to considering simple correlation alone, as the latter can only consider bivariate correlations and not the complicated relationship between different predictor features themselves and predictor features and *IL32* expression (311). To obtain the final *IL32* signatures, another filtering step was performed excluding non-coherent genes, which were defined as genes that have a

Spearman's correlation coefficient < 0 in at least 1 of 33 cancer types with a p value < 0.05 (Figure 6-14e, Appendix Table IV-2, Appendix Table IV-3).

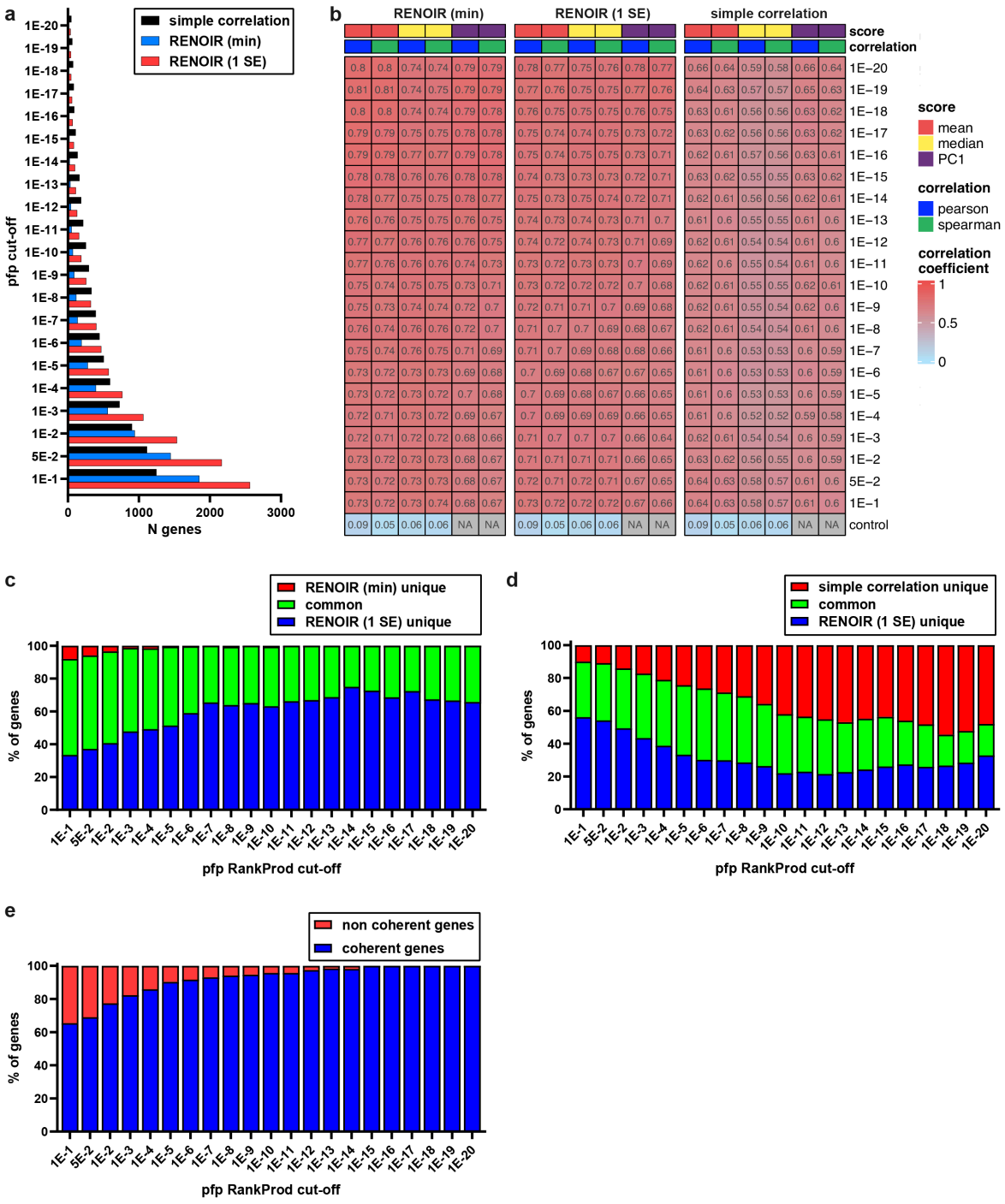


Figure 6-14. Assessment of IL32 gene signatures created by using RENOIR and Spearman's correlation. (a) Quantification of the number of genes within the different pan-cancer *IL32* gene signatures obtained by rank product analysis with different pfp (percentage of false positives) cut-offs, including signatures derived by using Spearman's correlation (simple correlation), RENOIR min and RENOIR 1SE results. (b) To assess the performance of the different signatures, three different scores were calculated for each signature using PanCan Atlas data, including mean expression, median expression and PC1 of all signature genes. As a negative control, scores were calculated across all 20531 PanCan Atlas genes. Pearson's and Spearman's correlation of each

score with *IL32* gene expression was calculated. Heatmap shows obtained correlation coefficients. (c) Bar plot shows quantification of signature genes common and unique for RENOIR min and RENOIR 1SE signatures relative to the total number of signature genes obtained by the respective pfp (percentage of false positives) cut-off. RENOIR 1SE signatures were chosen for further analysis. (d) Bar plot shows quantification of signature genes common and unique for signatures obtained by RENOIR 1SE and Spearman's correlation (simple correlation) relative to the total number of signature genes obtained by the respective pfp cut-off. Only common genes were chosen for further analysis, as linear regression methods, as applied in RENOIR, can recruit genes that are associated with *IL32* expression only in the model due to multicollinearity, but which are not directly correlated with *IL32* expression. Filtering for common genes ensures that such artefacts are excluded and all signature genes are directly correlated with *IL32* expression. (e) Bar plot shows the quantification of coherent and non-coherent genes relative to the total number of common signature genes from RENOIR 1SE and simple correlation (Spearman's correlation) signatures. Non-coherent genes were defined as genes that have a Spearman's correlation < 0 and a p-value < 0.05 in any of the 33 cancer types. Non-coherent genes were excluded to obtain the final *IL32* signatures.

6.4.8. Pathway analysis of *IL32* signature genes

To investigate which processes the *IL32* signature genes are associated with, pathway analysis was performed (Figure 6-15a-c). For this purpose, the 1E-3 *IL32* gene signature was chosen, which has a relatively stringent pfp cut-off and yet contains a relatively large number of genes for comprehensive pathway analysis. Over-representation analysis was performed querying GO Biological Processes, KEGG and WikiPathways annotation databases. The top 17 results from each annotation database consisted mainly of immune-related pathways. Examples of GO results included T-cell activation, immune response – activating signal transduction, positive regulation of cytokine production, response to interferon-gamma and response to tumour necrosis factor. Significant KEGG pathways included cytokine-cytokine receptor interaction, cell adhesion molecules, and antigen processing and presentation. Similar to the results obtained using GO or KEGG pathway databases, the top 17 results using WikiPathways included type II interferon signalling (IFNG) pathway and T-cell activation- and TCR-signalling-related pathways (T-cell activation SARS-CoV-2, T-cell receptor (TCR) signalling pathway, Modulators of TCR signalling and T cell activation, T-cell antigen receptor (TCR) pathway during Staphylococcus aureus infection). In addition, pathways related to immune responses in cancer were observed, including cancer immunotherapy by PD-1 blockade and interactions of natural killer cells in pancreatic cancer.

6. Role of IL-32 in innate-like T-cell activation

Screening of the top 56 genes associated with *IL32* expression (1E-14 *IL32* signature), genes associated with the immunoproteasome, including *PSMB8*, *PSMB9* and *PSMB10*, and many genes associated with antigen presentation, including *HLA-A*, *HLA-B*, *HLA-C*, *HLA-F*, *HLA-DMA*, *CD74* and *TAP1*, were found (Figure 6-15d). Considering additional genes from the 1E-3 *IL32* signature, 20 HLA-encoding genes were found in total in addition to other genes associated with antigen presentation such as *CIIA*.

Another group of 1E-14 *IL32* signature genes, associated particularly with T and NK cells, were found, including, for example, *CD2*, *CD3E*, *CD3D*, *CD6*, *CD7*, *CD247*, *CCL5*, *CXCR3*, *NKG7*, *GZMA*, *GzmB*, *GZMH*, *PRF1* and *ZNF683*. Considering additional genes from the 1E-3 *IL32* signature, further T and NK cell-associated genes were found, such as *CD3G*, *CD4*, *CD8A*, *CD8B*, *CD28*, *GZMK*, *GZMM*, *GNLY*, *CXCR6* and *KLRB1*. *CXCR6* and *KLRB1* are particularly highly expressed by MAIT cells.

In addition, a group of genes encoding for cytokines and cytokine receptors were found in the 1E-14 *IL32* signature, including cytokines and receptors of the common γ-chain cytokine family, for example, *IL2RB*, *IL2RG*, *IL15RA*. Also considering the genes from the 1E-3 *IL32* signature, further cytokine- and cytokine receptor-encoding genes were found, for example, *IL15*, *IL21R*, *IL12RB1* and *IL27RA*.

On the other hand, genes associated with immunosuppression such as *IDO* and *FOXP3*, and genes encoding for inhibitory immune checkpoint receptors or ligands, including PD1, PD-L2, CTLA4, LAG3, TIM3 and TIGIT were identified within the signature genes of the 1E-3 *IL32* signature.

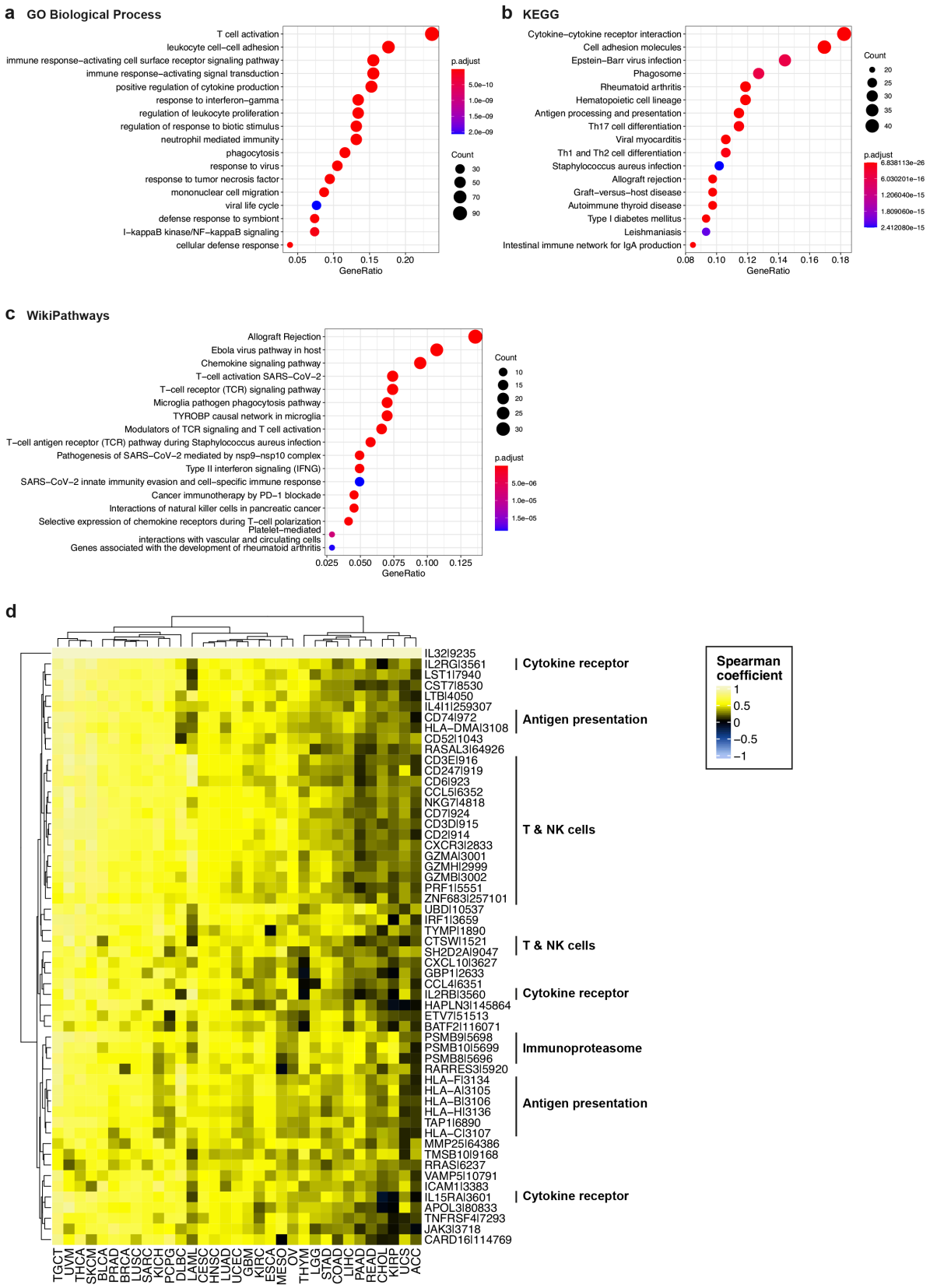


Figure 6-15. Pathway analysis reveals association of *IL32* with immunological processes in cancer. (a)-(d) Pathway analysis of *IL32* signature genes (1E-3 signature). Over-representation analysis was performed using (a) GO Biological Processes, (b) KEGG and (c) WikiPathways pathway databases. (d) Heat map shows Spearman's correlation coefficient of the 56 most significant signature genes (1E-14 signature genes) with *IL32* expression.

In summary, *IL32* signature genes were mainly associated with immune-related pathways including many T cell-associated pathways. Within the most highly *IL32*-associated signature genes, many genes associated with T and NK cells and genes linked to antigen presentation and cytokine signalling were found.

6.4.9. *IL32* expression and *IL32* signature enrichment in immune subsets from breast cancer tissue

Before investigating which immune cell subsets are associated with *IL32* expression and *IL32* signature enrichment in cancer scRNA-seq data, CITE-seq data from healthy PBMCs was analysed. The purpose of this was to establish an analysis workflow for single-cell data including cell type labelling of rare cell subsets such as MAIT and γδT cells, and to assess *IL32* expression and signature enrichment in PBMCs as a reference for the analysis of immune cells derived from cancer.

The CITE-seq data from healthy PBMCs was obtained from Hao et al. (305), comprising 53364 cells from 8 healthy donors which were participants in a phase 1a HIV vaccine trial (305–307). Samples had been collected at day 0 just before administration of the booster vaccination (305). Cell types that had been identified by Hao et al. by integrating both protein and RNA expression were aggregated to 12 immune cell subsets for the present study (Figure 6-16a). *IL32* was most highly expressed in MAIT, γδT and $CD4^+$ and $CD8^+$ memory T cells (Figure 6-16b). These cell types also showed significant *IL32* logFCs ranging from 1.06 to 1.42 compared to other cell types, obtained by differential gene expression analysis (Figure 6-16c). NK cells, Tregs, $CD4^+$ and $CD8^+$ naive T cells also expressed *IL32*, but at lower levels with logFCs ranging from 0.29 to 0.69. B cells, DCs and monocytes had negligible *IL32* expression levels and negative logFCs ranging from -0.78 to -1.34.

In addition, ssGSEA was performed to determine *IL32* signature enrichment scores for the different cell types (Figure 6-16d-e). *IL32* signatures with less stringent pfp cut-offs such as

5E-2 were most highly enriched in monocytes. With a relatively large difference, DCs scored second highest. Tregs, naive T cells and B cells had the lowest enrichment scores and the enrichment scores of other cells were located in-between. Whilst enrichment scores of NK and T cells increased continuously with increasing stringency of *IL32* signature pfp cut-off, the enrichment scores of DCs, B cells and monocytes stagnated or even decreased slightly after a cut-off of 1E-7. Analysis of *IL32* signatures with a highly stringent cut-off such as the 1E-16 signature showed the highest enrichment within MAIT, γδT, NK and $CD8^+$ memory T cells, whereas the lowest enrichment scores were observed for DCs, B cells and Monocytes.

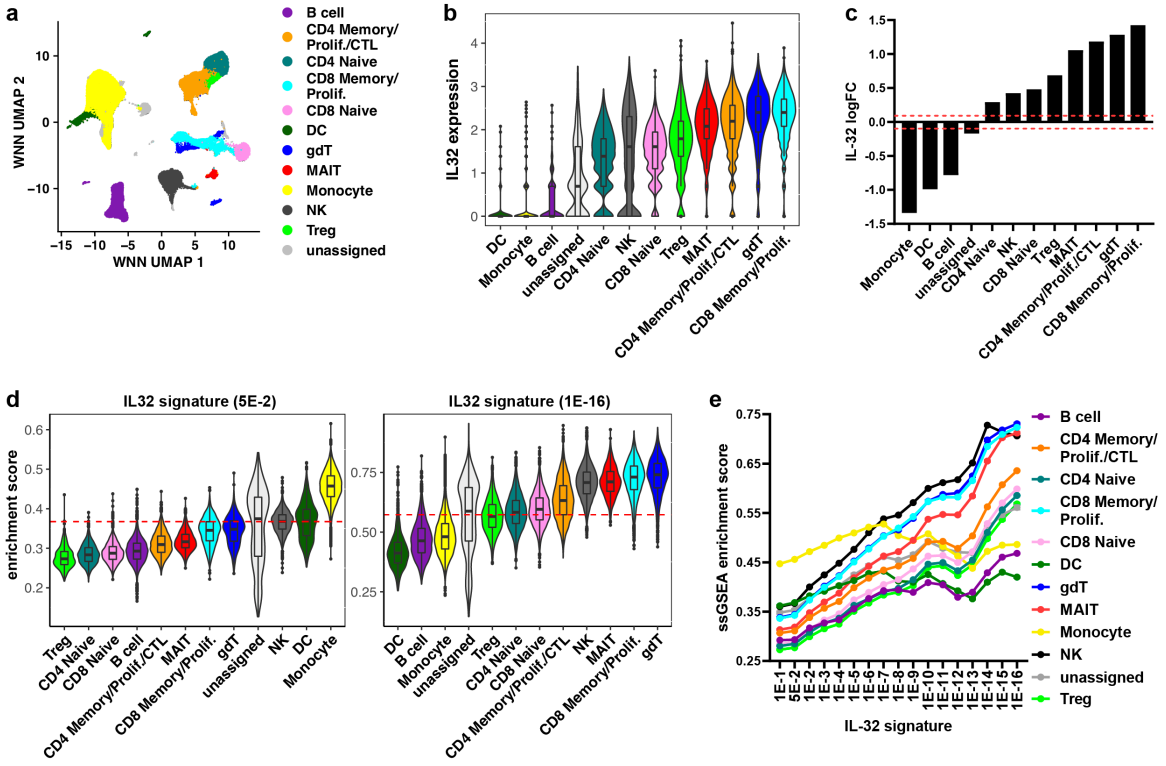


Figure 6-16. *IL32* gene expression and *IL32* signature enrichment in immune subsets from healthy blood. CITE-seq data including 53364 PBMCs from 8 healthy donors was obtained from Hao et al. (305). The volunteers had been part of a phase 1a HIV vaccine trial. The samples used for this analysis had been obtained at day 0 just before administration of the booster vaccination. (a) WNN (weighted nearest neighbour) UMAP visualization shows 12 aggregated cell types derived from the original clustering and annotation. (b) Violin plot shows SCTransform-normalized (312) *IL32* gene expression within the 12 immune cell types. (c) Presto R package (313) was used to perform differential gene expression analysis between each cell type and all other cells. Bar plot depicts log-fold change (logFC). Red lines indicate bottom and top threshold beyond which results are considered significant. Thresholds represent minimum and maximum logFC obtained from performing differential gene expression analysis 100 times with randomly permutated cell labels. (d) Violin plots show ssGSEA enrichment scores of 5E-2 and 1E-16 *IL32* signatures for each of the 12 immune cell types. As reference point, 95% confidence intervals (red lines) are indicated, derived from the distribution of cell type-specific mean ssGSEA enrichment scores that were obtained by 100 times randomly permutating cell labels of ssGSEA scores. (e) Graph

shows mean ssGSEA enrichment scores ± SEM for each of the 12 immune cell types and indicated *IL32* signatures.

As *IL32* expression in breast cancer has previously been linked with immune response-related genes including T cell-associated genes (293), *IL32* was studied next in the context of breast cancer. For this purpose, scRNA-seq data comprising 21253 immune cells from breast cancer was obtained from Azizi et al. (308). Cells were annotated using reference mapping implemented in Seurat v4 R package with the PBMC CITE-seq data from Hao et al. as a reference (305). The reference cell types were aggregated to 11 cell types for this analysis (Figure 6-17a). In contrast to the PBMC analysis, $CD4^+$ and $CD8^+$ T cells in breast cancer were not stratified into naive and memory subsets as the vast majority of cells were memory cells. In addition, ILCs were defined as separate subset due to their increased frequency in the breast cancer data compared to the PBMC data. The identity of annotated cell types was confirmed by investigating the expression of a selection of lineage markers and other cell-type specific markers (Figure 6-17b). For example, MAIT cells were confirmed to express *CD3D*, *CD3E*, *CD8A* and high levels of *KLRB1* and *CXCR6*. The expression of the 10 most differentially expressed genes of each cell type compared to all other cells is shown in Appendix Figure IV-10.

Similar to the observations from healthy PBMCs, *IL32* was most highly expressed in MAIT, γδT, memory $CD8^+$ and memory $CD4^+$ T cells and Tregs, confirmed by significant logFCs compared to the other cells ranging from 0.46 to 1.29 (Figure 6-17c-d). These cell types also showed the highest frequencies of *IL32*-expressing cells (Figure 6-17e). NK cells and ILCs had no significant logFCs. Monocytes, B cells and DCs showed negligible *IL32* expression with negative logFCs ranging from -0.91 to -1.17.

The analysis of *IL32* signature enrichment in breast cancer immune subsets based on ssGSEA gave similar results to those obtained from healthy PBMCs. *IL32* signatures with a

less stringent pfp cut-off, such as the 5E-2 *IL32* signature, were most highly enriched in monocytes and DCs. B cells showed by far the lowest enrichment scores, followed by $CD4^+$ T cells and T regs. There was an increase in *IL32* signature enrichment scores in all immune subsets with increasing stringency of signature pfp cut-off values. ILCs, NK cells and all T-cell subsets overtook monocytes and DCs in terms of *IL32* signature enrichment scores and showed the highest enrichment scores for signatures with very stringent pfp cut-offs, such as for the 1E-16 *IL32* signature. Conversely, unassigned cells, DCs, B cells and monocytes had the lowest 1E-16 *IL32* signature enrichment scores.

In summary, highest *IL32* expression was observed within memory T-cell subsets, Tregs and innate-like T cells such as MAIT and γδT cells. These cell types were also amongst those with the highest enrichment of *IL32* signature genes, in addition to ILCs and NK cells.

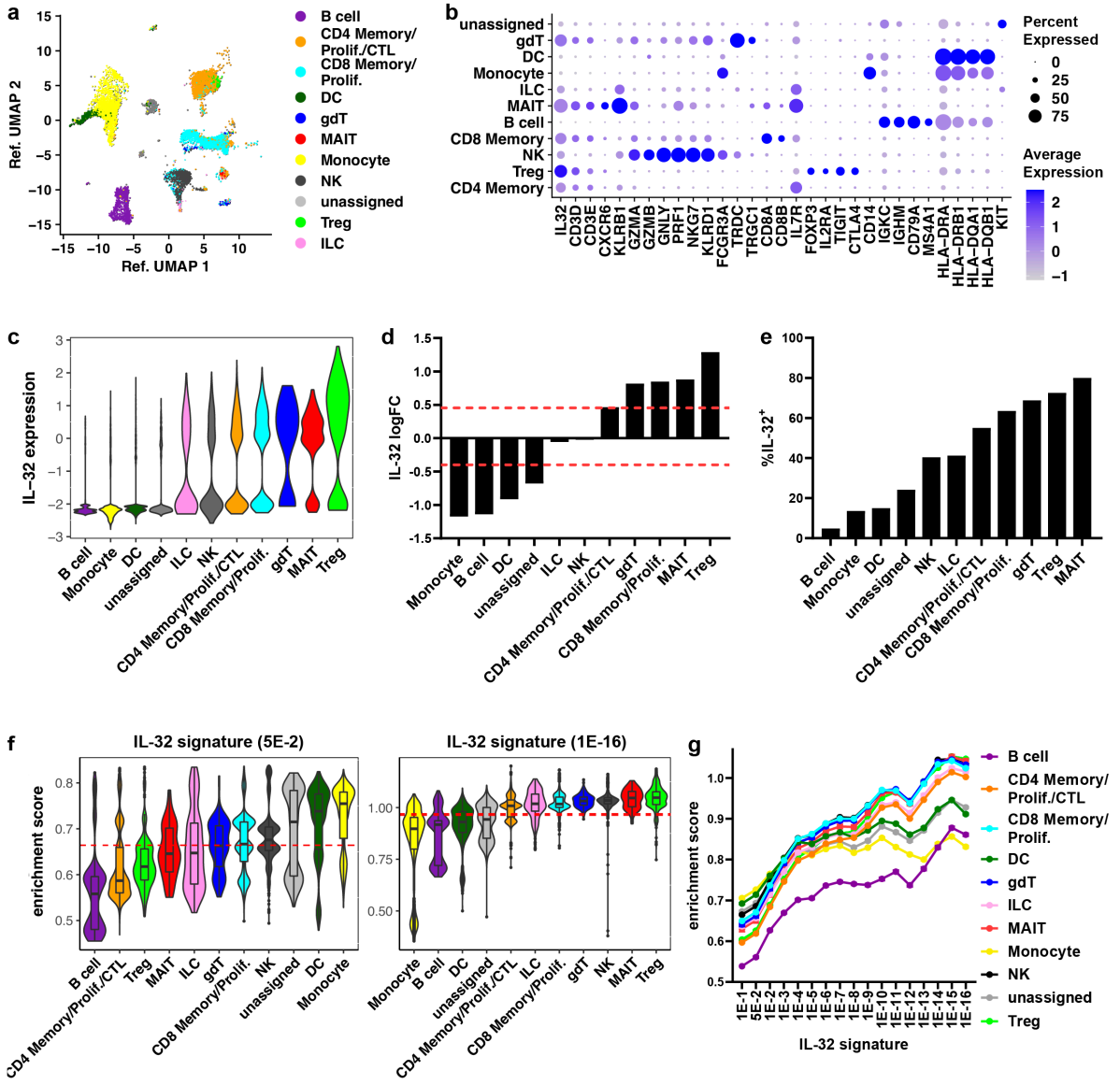


Figure 6-17. IL32 gene expression and IL32 signature enrichment in breast cancer-derived immune cells. Breast cancer scRNA-seq data including 21253 immune cells from 8 treatment naive patients was obtained from Azizi et al. (308). (a) In order to identify different immune cell types in the breast cancer scRNA-seq data, reference mapping using Seurat v4 R package was performed with the PBMC CITE-seq data from Hao et al. as reference (305). Graph shows the breast cancer data projected onto the reference UMAP including the annotation of 11 aggregated cell types derived from the reference mapping. (b) To confirm the identity of annotated cell types, the expression of a selection of genes, including lineage markers and other cell type-specific markers was analysed. Dot plot shows average gene expression and the percentage of cells expressing a particular gene. (c) Violin plot shows Biscuit-normalized *IL32* gene expression within the 11 immune cell types. (d) Presto R package (313) was used to perform differential gene expression analysis between each cell type and all other cells. Bar plot depicts log-fold change (logFC). Red lines indicate bottom and top thresholds beyond which results are considered significant. Thresholds represent minimum and maximum logFC obtained from performing differential gene expression analysis 100 times with randomly permutated cell labels. (e) Percentage of cells expressing *IL32*. (f) Violin plots show ssGSEA enrichment scores of 5E-2 and 1E-16 *IL32* signatures for each of the 11 immune cell types. As reference point, 95% confidence intervals (red lines) are indicated, derived from the distribution of cell type-specific mean ssGSEA enrichment scores that were obtained by 100 times randomly permutating cell labels of ssGSEA scores. (g) Graph shows mean ssGSEA enrichment scores ± SEM for each of the 11 immune cell types and indicated *IL32* signatures.

6.4.10. Association of *IL32* gene expression with cancer patient survival

To investigate the association of *IL32* gene expression with cancer patient survival, PanCan Atlas gene expression data was used in combination with overall survival outcome data from TCGA-CDR (304). Univariate Cox regression was performed analysing 26 different cancer types. *IL32* expression was associated with a favourable prognosis in two cancers, including SARC and UCEC, whereas an adverse prognosis was observed in 5 cancers, including LGG, PAAD, MESO, ACC and UVM (Figure 6-18a). Enrichment of *IL32* signature genes was associated with favourable prognosis in 6 cancers, including SKCM, SARC, CESCA, UCEC, BRCA and HNSC, whereas an adverse prognosis was observed for 3 cancers, including KIRC, LGG, and UVM (Figure 6-18b). The association of *IL32* signature enrichment and outcome was similar across different *IL32* signatures (Figure 6-18c). A correlation between the hazard ratio (HR) of *IL32* gene expression and HR of *IL32* signature gene enrichment was observed across the analysed cancers (Figure 6-18d).

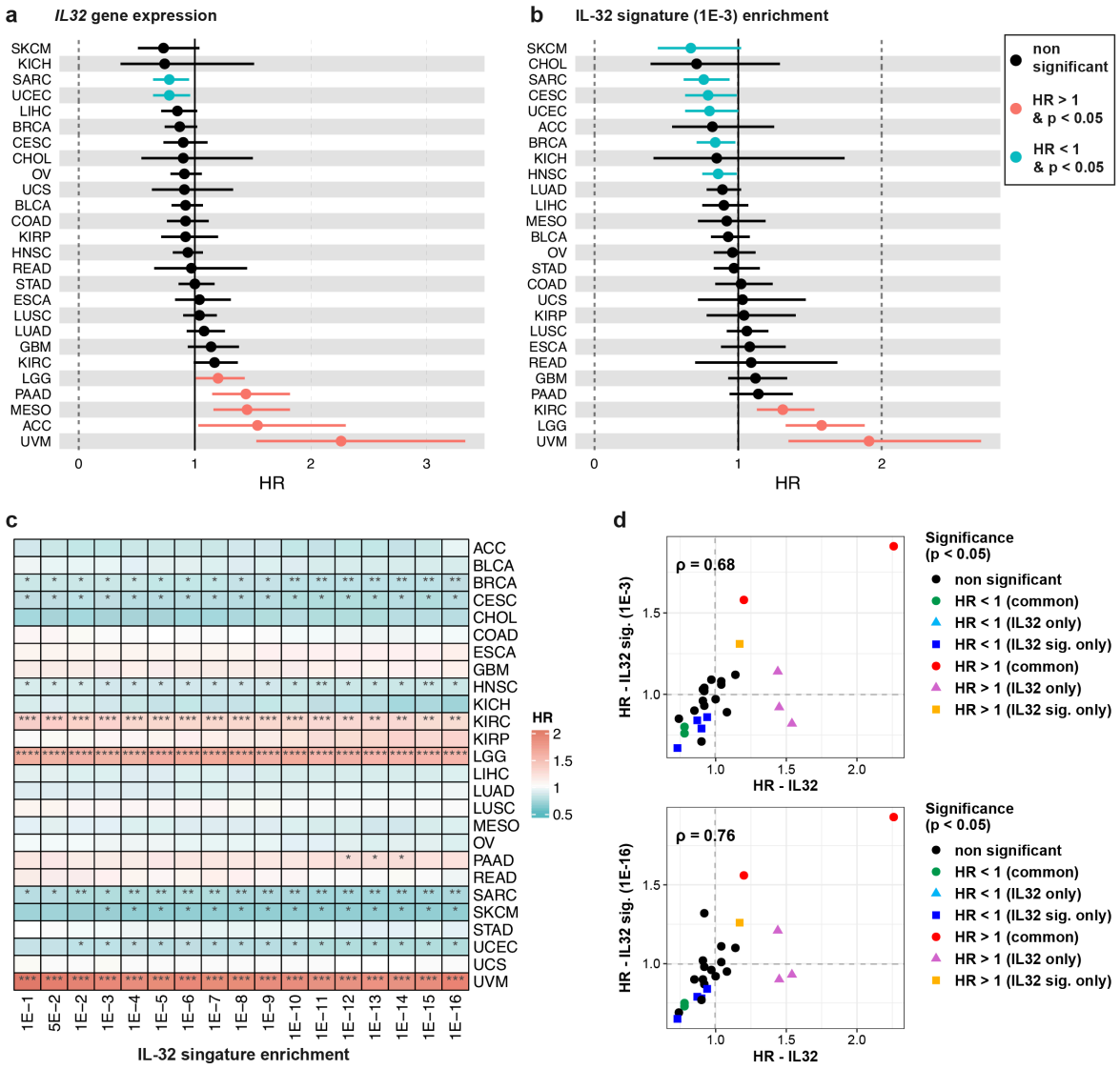


Figure 6-18. Association of *IL32* gene expression and *IL32* signature enrichment with cancer patient survival. Univariate Cox regression analysis was performed to investigate the association between the survival time (overall survival) of PanCan Atlas cancer patients and *IL32* gene expression or *IL32* signature enrichment. (a) Forest plot shows prognostic value of *IL32* gene expression for 26 cancer types. (b)-(c) Prognostic value of *IL32* signature enrichment for 26 cancer types. Enrichment scores were calculated using ssGSEA. In (b), forest plot for 1E-3 *IL32* signature enrichment is shown as an example. Heatmap in (c) summarises the results from 1E-1 to 1E-16 *IL32* signatures. ****p<0.0001, ***p<0.001, **p<0.01, *p<0.05. (d) Spearman's correlation between the HR of *IL32* gene expression and HR of *IL32* signature enrichment was analysed considering the results of 26 PanCan Atlas cancer types. Each dot in the graphs represents a different cancer type. ρ, Spearman's correlation coefficient.

6.5. Discussion

6.5.1. IL-32 expression by activated T cells

Non-immune and immune cells can express IL-32, although IL-32 expression is most prominent in immune tissues (109, 110). It was shown that eosinophils, monocytes,

macrophages, DCs, NK and T cells can express IL-32 upon stimulation (108–110, 221, 240–246). T cells express IL-32 upon mitogen or TCR stimulation (110), which was confirmed in this study (Figure 6-7f). In addition, $CD4^+$ T cells can express IL-32 upon stimulation with IL-12+IL-18, TNFα and IL-23 (110).

As CD161-expressing subsets are the T cells that respond to cytokines such as IL-12+IL-18 in a TCR-independent manner (66, 68, 73), it was hypothesized that these subsets would show the largest IL-32 responses upon cytokine stimulation. Indeed, IL-12 alone or IL-12+IL-18 could induce IL-32 in CD161-expressing T-cell subsets. The highest IL-12- or IL-12+IL-18-induced IL-32 expression was observed in $CD4^+$, $CD8^+$ and DN $CD161^{++}$/MAIT subsets, as well as $CD161^+V\delta2^-$ and $CD161^{+/-}V\delta2^+$ cells (Figure 6-4, Figure 6-5). These subsets are generally considered the most IL-12/IL-18-responsive T cells, measured, for example, by IFNγ expression (66, 68). Small but significant IL-18-induced IL-32 responses were observed in CD161-expressing T-cell subsets in PBMCs, but not in CD14-/CD19-depleted PBMCs, indicating that IL-18 might activate monocytes and/or B-cells, which in combination with IL-18 can induce IL-32 expression in CD161-positive T cells (Figure 6-4). By contrast, neither IL-12 nor IL-18 alone are potent inducers of the expression of effector cytokines such as IFNγ in T cells, including $CD161^{++}$/MAIT cells (Appendix Figure IV-2) (65, 213, 314). Further investigation of cytokine-induced IL-32 expression in MAIT cells revealed that there are IFNγ and IL-32 co-expressing MAIT cells, but the concordance was not as good as for co-expression of IL-32 with CD69. This indicates that the expression of cytokine-induced IFNγ and IL-32 effector molecules are regulated differently (Figure 6-5h).

MAIT cells can express IL-32 also in response to *E.coli*+IL-12+IL-18 (222). In the present study, it was found that MAIT cells can express IL-32 in response to *E. coli* alone, which can be partially blocked using blocking antibodies specific for MR1, IL-12, IL-18 or other factors such as TNFα (Figure 6-7a-e). This indicates that both TCR- and cytokine-mediated signals play a role in IL-32 induction after 48h of stimulation. This is different to *E. coli*-induced IFNγ

expression, where TCR signals play a crucial role in inducing IFNγ early in the response (approximately 6 hours post stimulation), but later becomes mainly cytokine-dependent (approximately 20 hours post stimulation) (89). The results of the present study confirm that blocking MR1 does not have a significant impact on IFNγ responses at 48 hours of stimulation (Figure 6-7e). In addition, IL-32 expression was not impacted by B18R, indicating that type I IFNs do not induce IL-32 expression in contrast to IFNγ expression. Overall, *E. coli*-mediated IL-32 expression seems to be differentially regulated compared to IFNγ expression, similar to what was observed from cytokine-stimulation *in vitro*. In contrast to *E. coli* stimulation, tetramer stimulation of MAIT cells downregulates IL-32 expression, measured using RNA-seq (89). This might be a result of the use of different experimental models or different methods of measuring IL-32 expression, and needs to be further explored. *E. coli*-induced IL-32 expression in other CD161-expressing cells and γδT cells is most likely mediated via cytokines such as IL-12 and IL-18 and is not TCR-mediated (Appendix Figure IV-4c).

In this study, it was also demonstrated that besides TCR stimulation, the common γ-chain cytokines IL-2, IL-7 and IL-15 are potent inducers of IL-32 expression in T cells in a TCR-independent manner (Figure 6-6). Despite the fact that conventional T-cell activation is usually dependent on TCR signals, the common γ-chain cytokine IL-15 can induce certain effector functions in memory T cells such as IFNγ expression (315). Similarly, there was a trend of higher common γ-chain-induced IL-32 expression in memory T-cell subsets compared to naive T cells (Appendix Figure IV-3).

IL-2 and IL-12+IL-18 can induce IL-32 expression in NK cells (109, 225). In the present study, it was found that NK cells also express IL-32 in response to stimulation with IL-12 alone, IL-15 alone or IL-15 in combination with IL-12 or IL-18. The frequency of IL-32 expressing NK cells was much lower compared to the frequency of IL-32 expressing T cells upon cytokine stimulation, however. This indicates that cytokine-activated T cells and particularly

cytokine-responsive CD161-expressing T cells are a major source of IL-32 instead of NK cells (Figure 6-4, Figure 6-5).

There are, however, several unanswered questions. First, it needs to be investigated which particular isoforms are expressed by T cells and innate-like T cells, and whether different isoforms are expressed upon activation with different stimuli. It also needs to be investigated whether IL-32 is only expressed intracellularly in T cells or whether it is secreted and can act on other cells. The ELISA performed in this study indicated that cytokine-stimulation results in IL-32 being secreted by PBMCs (Figure 6-4f). In addition, another study found IL-32 in the supernatant of TCR-stimulated T cells (232).

6.5.2. IL-32 can increase cytokine-mediated responses of CD161-expressing T cells

CD161-expressing subsets, including $CD161^{++}$/MAIT cells can be activated in a TCR-independent manner via cytokine stimulation. These cytokines include IL-12, IL-18, IL-15, type I IFNs and TL1A (64–66, 81–83).

In the present study, IL-32β/γ was identified as another cytokine that contributes to $CD161^{++}$/MAIT-cell activation (Figure 6-8, Figure 6-9). Similar to TL1A, IL-32β/γ alone did not show a demonstrable effect on IFNγ and GzmB expression of T cells, but could increase cytokine-mediated responses of $CD161^{++}$/MAIT cells (82). A particularly large increase in IFNγ and GzmB expression was observed with suboptimal concentrations of IL-15 alone or in combination with IL-12 or IL-18. Results from stimulated PBMCs or enriched $CD8^{+}$ T cells were similar, with the exception that only in total PBMCs $CD161^{++}$/MAIT cells showed a response to IL-32β/γ in combination with IL-12, indicating an indirect mechanism of MAIT cell stimulation involving a non-CD8 PBMC cell type. IL-32β/γ made MAIT cells more responsive to lower cytokine concentrations and increased the maximum IFNγ and GzmB responses in saturated conditions. In addition to enhancing IFNγ and GzmB expression, IL-32β/γ increased the expression of inhibitory checkpoint receptors such as PD1, LAG3, and TIM3. The latter

could represent a negative regulatory mechanism to maintain self-tolerance and to terminate immune responses upon IL-32 stimulation (128, 316, 317). No significant effect of IL-32 on TNFα expression was observed, except for a small decrease in the mean fluorescence intensity induced by IL-32α after 72 hours of stimulation. IL-32β/γ-mediated effects were relatively specific for CD161-expressing T-cell subsets, and the largest responses were observed in CD161^{++}/MAIT subsets. Vδ2^{+} γδT cells showed similar responses to IL-32 as MAIT cells (Appendix Figure IV-8). By contrast, Vδ2^{-} γδT cells showed greatly reduced or non-detectable responses to IL-32. This indicates that IL-32 responsiveness within T cells might be particularly associated with innate-like T cells, similar to IL-12+IL-18-mediated T cell responses (66, 68).

IL-32α influences NK cell activity by affecting IL-15 signalling via inhibition of STAT5 phosphorylation (108). As IL-32β/γ can enhance T-cell activation particularly in combination with IL-15 (Figure 6-8, Figure 6-9), IL-32β/γ might similarly modulate IL-15-mediated STAT5 phosphorylation in CD161-expressing T cells. IL-32α did not show an inhibitory effect on the activity on CD161-expressing T cells as demonstrated for NK cell activity, however (108). An exception to this was slightly decreased TNFα expression of MAIT cells after 72 hours of IL-32α stimulation (Figure 6-9e). This indicates that IL-32α might have different effects on NK and CD161-expressing T cells. As IL-32 seems to modulate cytokine-mediated CD161^{++}/MAIT and NK cell responses in the presence of IL-15, it needs to be determined whether IL-32 can also oppose or synergise with other cytokines of the common γ-chain family such as IL-2 or IL-7.

Further questions which need to be addressed include whether IL-32 can also affect TCR-mediated T-cell activation of CD161-expressing and conventional T cells. In addition, there might be a positive feedback loop of activation as IL-32 can increase CD161^{++}/MAIT-cell activation, and activated CD161^{++}/MAIT cells can express IL-32. The use of an IL-32 blocking antibody would be helpful to dissect this mechanism. The ability of different monoclonal and

polyclonal anti-IL-32 antibodies to block IL-32β/γ-mediated effects was tested, but none showed blocking ability (data now shown). The generation of pan-IL-32 and isoform-specific blocking antibodies would also be helpful to further dissect the mechanism of IL-32 in different clinically relevant contexts, such as infection, inflammation and cancer.

6.5.3. The role of IL-32 in the anti-cancer immune response

IL-32 can have both stimulatory and inhibitory effects on immune responses, but the role of IL-32 in the anti-cancer immune response is poorly understood (257).

To find pathways associated with *IL32* expression in cancer, pan-cancer *IL32* gene signatures, derived from 33 cancer types, were created (Figure 6-12, Figure 6-13, Figure 6-14). *IL32* signature genes were associated with immune response-related pathways, including T-cell activation-associated pathways (Figure 6-15). In addition, many of the most significant IL-32 signature genes were associated with T and NK cells and antigen presentation. These results expand on the observations that IL-32 is associated with inflammation and T-cell response-associated genes in breast cancer (293) and T-cell activation markers in melanoma (286). In the present study, *IL32* expression was most highly associated with memory T cells, Tregs, MAIT and γδT cells in scRNA-seq data from both blood-derived PBMCs of healthy donors and breast cancer-derived immune cells (Figure 6-17). Furthermore, the most significant *IL32* signature genes from signatures with a relatively stringent significance cut-off were most highly enriched within breast cancer-derived Tregs, memory T, MAIT, γδT and NK cells. In contrast, IL-32 signature genes of signatures with a non-stringent significance cut-off were most highly enriched within monocytes and DCs (Figure 6-17f-g). A similar observation was made in melanoma, where *IL32* expression is associated with myeloid and DC maturation markers (286). The results from the present study suggest that the *IL32* signatures generated could contain multiple groups of genes associated with different immune subsets.

6. Role of IL-32 in innate-like T-cell activation

While *IL32* signatures contained many genes associated with immune response activation and genes encoding for effector molecules that could target cancer cells, such as granzymes, granulysin and perforin, they also contained genes encoding for immunoregulatory proteins, such as IDO, and genes associated with immunoinhibitory cell types, such as *FOXP3*. This indicates that IL-32 could also have an inhibitory role in the anti-cancer immune response, as described for cutaneous T-cell lymphoma, in which IL-32 was associated with immunosuppressive DCs, macrophages, IDO and IL-10 (294). Similarly, IL-32 was associated with Tregs and linked to an adverse prognosis in oesophageal cancer (295, 296). More studies are required to elucidate the exact mechanism and function of IL-32 in cancer, which is made more difficult by the fact that there is no murine IL-32 homolog and by the complexity posed by the high number of different IL-32 splice variants that can interact and modulate the activity of each other (109, 226, 228).

A limitation of this study is using TCGA-derived *IL32* gene signatures for studying the role of *IL32* in the anti-cancer immune response. TCGA RNA-seq data is generated from bulk cancer samples containing cancer and immune cells. In order to identify immune response-specific *IL32* signature genes, one could exclude cancer cell-specific *IL32* signature genes by deriving a cancer cell-specific *IL32* gene signature using RNA-seq data from cancer cell lines from the Cancer Cell Line Encyclopedia (318).

In addition, a discrepancy between IL-32 protein and mRNA expression levels was observed. Measuring IL-32 protein expression by flow cytometry in resting PBMCs from healthy donors indicated minimal steady-state IL-32 expression (Figure 6-4a, Appendix Figure IV-1). In contrast, scRNA-seq data from PBMCs of healthy donors indicated relatively high steady state *IL32* gene expression in certain cell populations (Figure 6-16). This discrepancy could be explained by the fact that the donors from scRNA-seq data were participants in a HIV vaccination study and the primary vaccination might have induced long lasting changes in *IL32* mRNA expression. Alternatively, there could be a regulatory mechanism that prevents

IL-32 protein expression from *IL32* mRNA expression in resting immune cells and IL-32 protein is only expressed upon stimulation. It was shown, however, that relative changes in IL-32 protein and *IL32* mRNA expression are similar using stimulated PBMCs, monocytic or lymphocytic cell lines (319). This indicates that it is possible to draw conclusions about changes in IL32 protein expression levels from relative changes in the mRNA levels.

6.5.4. The association of IL-32 with patient survival

IL32 was significantly associated with outcome in 7/26 analysed cancers, 5 of which were associated with adverse outcome (Figure 6-18). Previously reported associations of *IL32* expression and patient survival in cancer, such as in head and neck squamous cell carcinoma, gastric, colon and kidney cancer (Table 6-1), could not be confirmed. The discrepancy might be explained by the limitations of TCGA clinical data. The TCGA data resource was not created with the purpose of acquiring complete patient outcome data and is therefore limited by relatively short follow-up intervals (304). For this reason, overall survival data of only 26 of 33 cancer types is recommended for use. There are some reservations using the outcome data for even these 26 cancer types due to short follow-up intervals, small number of events and small sample sizes (304). In addition, the use of disease-specific survival data would be more appropriate than overall survival data for the type of analysis of this study. But there is only estimated disease-specific survival data available, whose use is even less recommended than overall survival data (304). Better outcome data without these limitations could allow the generation of more specific and significant results.

IL32 signature gene enrichment was associated with outcome in 9/26 analysed cancers, 6 of which were associated with favourable prognosis (Figure 6-18). While *IL32* signature gene enrichment was associated with favourable prognosis in more cancer types than *IL32* gene expression, *IL32* expression and signature enrichment showed a similar trend regarding outcome across all analysed cancers, as expected. For two cancer types, however, ACC and MESO, the HR of *IL32* signature gene enrichment did not match the trend of the HR of *IL32*

expression across cancers. Why *IL32* expression is associated with a different prognosis in certain cancers compared to *IL32*-associated genes could be explained by the dual role of *IL32* in both immune responses and its direct effects on cancer cells. In addition, different IL-32 isoforms could be expressed in different cancers and therefore mediate different biological functions (226, 228). Further studies are required to dissect the effects of IL-32 and its isoforms on cancer cells and on the anti-cancer immune response.

6.5.5. Relevance of the findings of this study

In this study, T cells were discovered as potent producers of IL-32 upon activation, either upon TCR-stimulation or upon IL-2, IL-7 or IL-15 cytokine stimulation in a TCR-independent manner. In addition, innate-like T cells including $CD161^{++}$/MAIT and γδT cells express high levels of IL-32 upon cytokine stimulation such as with IL-12+IL-18. Moreover, IL-32 was found to be a novel mediator enhancing the activation of $CD161^{++}$/MAIT and $V\delta2^{+}$ γδT cells. The better understanding of IL-32 expression and its biological activity could potentially allow for the manipulation of this activity towards desirable therapeutic outcomes in various disease contexts where IL-32 is implicated.

IL-32 is a pro- and anti-inflammatory cytokine and plays a role in inflammation, infection, autoimmunity and cancer (221, 257, 320). There is evidence, for example, that IL-32 is involved in the pathogenesis of various inflammatory and autoimmune conditions such as rheumatoid arthritis and inflammatory bowel disease. In these conditions, IL-32 is strongly associated with inflammatory cytokines such IL-6, IL-1β, IL-18 and TNFα (229, 321). There is also ample evidence that IL-32 expression is associated with clinicopathological parameters and adverse outcomes in cancer (Table 6-1). In line with this, IL-32 was found to be associated with an adverse outcome in 5 cancer types in this study, including LGG, PAAD, MESO, ACC and UVM (Figure 6-18). In-depth analysis of breast cancer showed that *IL32* is particularly highly expressed by various T-cell subsets, including Tregs, MAIT, γδT and memory T cells (Figure 6-17). Further studies are required to investigate whether blocking

IL-32 expression in these cell types could be used as a therapeutic intervention to promote a favourable prognosis in cancer patients or to decrease inflammation in autoimmune disease.

On the other hand, IL-32 has a direct impact on cancer cells preventing tumour cell growth and inducing cancer cell apoptosis (322–324). IL-32 can also promote immune responses (221). In line with this, pathway analysis of *IL32*-associated genes in cancer showed associations with immune response and T-cell activation-related biological processes in this study. These IL-32 functions could contribute to a favourable prognosis in cancer. An association of IL-32 expression with favourable prognosis was reported for melanoma (286). In the present study, *IL32* expression was also found to be associated with favourable prognosis in SARC and UCEC. Mechanisms that induce IL-32 expression in T cells could therefore be exploited as a therapeutic intervention in cancer types in which IL-32 is implicated to play a beneficial role.

6.6. Summary

1. T cells can express IL-32 in response to anti-CD3/anti-CD28 stimulation or in response to IL-2, IL-7 or IL-15 in a TCR-independent manner.
2. Innate-like T cells, including $CD161^{++}$/MAIT and $V\delta2^{+}$ γδT cells can express IL-32 in response to IL-12 or IL-12+IL-18 stimulation.
3. IL-32β/γ can enhance cytokine-mediated IFNγ and GzmB responses of innate-like T cells, including $CD161^{++}$/MAIT and Vδ2+ γδT cells.
4. *IL32* expression and genes positively associated with *IL32* expression are linked to immune response- and T-cell activation-related pathways in cancer.
5. T-cell subsets, including Tregs, MAIT, γδT and memory T cells, express high levels of *IL32* in breast cancer.
6. The most significant *IL32* signature genes are enriched in ILCs, NK cells and T-cell subsets, including Tregs, MAIT, γδT and memory T cells in breast cancer.

6. Role of IL-32 in innate-like T-cell activation

7. *IL32* gene expression and *IL32* signature enrichment is associated with clinical outcome in certain cancer types. Depending on the cancer type, there is an association with favourable or adverse prognosis.

7. ROLE OF CD161 IN CANCER

7.1. Introduction

7.1.1. *KLRB1* is one of the most favourable prognostic pan-cancer genes

In a meta-analysis, which included the transcriptomic analysis of about 18,000 tumours across 39 different cancer types, Gentles et al. identified *KLRB1* as one of the most favourable prognostic pan-cancer genes (130). Another study confirmed the association of *KLRB1* with favourable outcome in non-small cell lung cancer (325). *KLRB1* encodes for the C-type lectin CD161, which is expressed by various subsets of NK- and T-cells, including MAIT, γδT, iNKT, TH17 and TRM cells (46, 67–69, 73, 75). In addition, subsets of the relatively rare ILCs can express CD161 (58). Estimating immune cell type abundances using the CIBERSORT immune deconvolution method suggested that γδT and CD8 T cells might be the relevant *KLRB1*-expressing immune subsets leading to favourable prognosis (130). The study of Gentles et al. only included a few cell subsets that can express *KLRB1*, such as γδT, CD8 T and NK cells, but lacked signatures of, for example, MAIT and TH17 cells. In addition, the CD8 T-cell subset is a very broadly defined cell type and unhelpful as determinant to attribute the favourable prognostic association of *KLRB1* across cancers to a specific cell type. Therefore, there is a need to further investigate which *KLRB1*-expressing immune cell type contributes most to a favourable prognosis in cancer. The relevant immune subset could be exploited for novel therapeutic interventions to improve the quality of life of cancer patients.

7.1.2. The role of CD161-expressing immune cell types in cancer

7.1.2.1. MAIT cells

MAIT cell TCRs recognise microbial-derived products presented by MR1 (80). Endogenous or tumour antigens that can be presented by MR1 have not yet been identified (326). Microbes have been found within various cancers, however, including breast, lung, colon, ovarian, pancreatic, cholangiocarcinoma and prostate cancers. In fact, microbes of the host

microbiome can confer susceptibility for certain malignancies and can impact therapeutic responses, for example, towards immunotherapies (327). High expression of TCR-driven CD39 by tumour-infiltrating MAIT cells was demonstrated in colorectal cancer, where bacterial infiltration was confirmed. One of the most enriched species *Fusobacteria nucleatum* induced TCR-mediated MAIT-cell activation *in vitro* (328). Besides TCR stimulation, MAIT cells could potentially also be activated by cytokines such as IL-12 and IL-18 in the inflammatory tumour-microenvironment (329). Upon activation, MAIT cell-derived IL-17 could promote tumours by recruiting immune-suppressive myeloid cells, promoting epithelial-mesenchymal transition and mitogenic signalling, or through pro-angiogenic effects (330, 331). On the other hand, MAIT cells could have protective effects by killing cancer cells via the release of cytotoxic effector molecules such as GzmB and perforin. NK receptors such as NKG2D or CD16, which can bind antibody-coated targets, could contribute to target cell recognition and induce cancer cell lysis. In addition, MAIT cell-derived effector cytokines such as IFNγ may enhance antigen presentation, FAS upregulation and activate other cell types such as M1 macrophages, NK and CD8 T cells (329).

It was shown that MAIT cells have direct antitumour activity *in vitro*, either by arresting the cell cycle of cancer cell lines or showing direct killing activity against cancer cell lines upon activation (332, 333). MAIT cells were also shown to infiltrate tumours, including kidney, liver, brain, colorectal, lung and gastric cancers, lesions of Langerhans cell histiocytosis and colorectal cancer liver metastases (332–339). Circulating MAIT cell frequencies are often decreased in cancer, including cervical, colorectal, lung and gastric cancer, and multiple myeloma. It is suggested that MAIT cells are recruited into the tumour site, particularly in colorectal, lung and gastric cancer (332, 333, 340, 341). In Langerhans cell histiocytosis, however, MAIT cell frequencies were decreased in both blood and lesions compared to healthy controls (338). Tumour-derived MAIT cells were functionally impaired. In particular, MAIT cells from colorectal cancer and liver metastasis expressed lower levels of IFNγ, but increased levels of IL-17 (332, 335, 337). Blood-derived MAIT cells from multiple myeloma

patients were also functionally impaired compared to healthy controls (341). Conversely, circulating MAIT cells from mucosal-associated cancers did not show any functional impairment (333). In colorectal carcinoma, high MAIT cell frequencies in the tumour were associated with poor outcome (336). In addition, low MAIT cell frequencies in circulation were associated with low progression-free survival in cervical cancer or N staging in mucosal-associated cancers (333, 340). If circulating MAIT cells are recruited into cancer tissue, this suggests cancer-infiltrating MAIT cells are associated with adverse prognosis. In hepatocellular carcinoma, however, low MAIT cell frequencies in cancer tissue were associated with poor prognosis (339).

7.1.2.2. γδT cells

In the study of Gentles et al., γδT cells were one of the most favourable prognostic immune subsets across cancers (130). The TCRs of γδT cells can be triggered via endogenous ligands in cancer. For example, Vδ2$^+$ cells can recognise over-expressed endogenous ligand isopentenyl pyrophosphate from transformed cells (342). Like MAIT cells, γδT cells can also be activated by cytokines, such as IL-12, IL-18 and IL-15. It is proposed that upon activation, γδT cells can either promote tumours, for example via IL-17, or mediate anticancer effects involving cytotoxic effector molecules, NK receptors such as NKG2D, death receptor ligands such as FASL, and effector cytokines such as IFNγ (343, 344).

Numerous studies demonstrated antitumour activity of human Vδ1$^+$ and Vδ2$^+$ γδT cells *in vitro* (345). *In vivo*, increased frequencies of γδT cells were associated with favourable prognosis in leukaemia after bone marrow transplantation (346, 347). In addition, tumour-infiltrating Vδ1$^+$ cells were associated with prolonged survival in necrotic choroidal melanoma (348). Similarly, Vδ2$^+$ cells were associated with lower relapse and mortality rate in melanoma. In breast cancer, however, Vδ1$^+$ but not Vδ2$^+$ γδT cells were shown to be associated with increased progression-free and overall survival (349). Conversely, there is also evidence that tumour-infiltrating γδT cells can be associated with tumour stage and

adverse outcome in breast cancer (350, 351). Particularly the Vδ1$^+$ subset was shown to be immunosuppressive, negatively impacting T cells and DCs in breast cancer (352). Similarly, Vδ1$^+$ cells were enriched in rectal cancer tissue and show inhibitory functions, and positively correlated with T stage. The opposite trend has been reported for Vδ2$^+$ cells, however, with decreased numbers in rectal cancer tissue, cytolytic function and negative correlation with T stage (353). Ovarian cancer is another example where high numbers of γδT cells were associated with advanced clinicopathological features. Moreover, blood- and tumour-derived γδT cells from ovarian cancer patients showed increased expression of IL-17, but decreased IFNγ expression (354). IL-17 producing γδT cells seem to have a particular negative impact on cancer patients. They were shown to be immunosuppressive in colorectal cancer, for example, by recruiting myeloid-derived suppressor cells, and were associated with tumour stage and unfavourable clinicopathological features (355, 356). Similarly, IL-17-producing γδT cells promoted angiogenesis and were associated with adverse prognosis in gallbladder cancer (357).

7.1.2.3. iNKT cells

The iNKT-cell subset can recognise lipid antigens presented by CD1d. In the context of cancer, iNKT cells could be activated by exogenous ligands from tumour-infiltrating microbes or by overrepresented endogenous ligand generated due to dysregulated lipid metabolism in transformed cells (345). The proposed role of iNKT cells in cancer includes direct tumour cell killing induced via TCR-mediated recognition of cancer cells or mediated via NKG2D or FASL. iNKT cells may also transactivate other immune cells, including B, NK, CD4 T and CD8 T cells via cytokines such as IFNγ or direct interaction via CD40-CD40L, and inhibit suppressive cells in the tumour microenvironment, for example, by killing tumour-associated macrophages (358–360). On the other hand, iNKT cells may also be involved in immunosuppressive processes mediated via cytokines such as IL-4, IL-10, IL-13 or IL-17 (102, 103, 359, 360).

7. Role of CD161 in cancer

It was shown that the iNKT-cell subset has lytic ability against cancer cells *in vitro* (361–363), and that iNKT cells can infiltrate tumours, including kidney, brain and colorectal cancers, neuroblastoma and cervical neoplastic tissues (334, 364–366). Infiltration of iNKT cells in cancerous tissue in colorectal carcinoma and neuroblastoma was associated with favourable prognosis (364, 365). In numerous solid and hematologic cancers, low frequencies of circulating iNKT cells were observed (367–370). Low frequencies of circulating iNKT cells in cancer, including myeloid leukaemia, CLL, head and neck squamous cell carcinoma and neuroblastoma, were generally associated with poor prognosis (371–375). Blood-derived iNKT cells from prostate cancer and myelodysplastic syndrome patients showed impaired IFNγ expression capacity, while IL-4 expression was unaffected (367, 370). In contrast, another study reported no altered of IFNγ expression capacity of blood-derived iNKT cells from cancer patients across various solid cancer types (368).

7.1.2.4. TH17 cells

TH17 cells could have a dual function in cancer. On the one hand, IL-17 could support tumours by promoting mitogenic signalling, angiogenesis, EMT and the recruitment of immune-suppressive myeloid cells (330, 331, 376). On the other hand, IL-17 could recruit neutrophils and NK cells, and mediate the antitumour immune response by inducing IL-6 and IL-12 expression by other cells (376). In addition, TH17 cells show high plasticity and can convert to produce cytokines from other TH cell subsets, such as IFNγ, which could promote the anti-tumour response (377).

TH17 cells were shown to infiltrate tumours, including melanoma, primary intraocular lymphoma, colorectal, breast, prostate, gastric, liver and lung cancer (378–385). There is some conflicting evidence about the effect of TH17 cells on patient survival. The abundance of intratumoural TH17 cells and/or high IL-17 levels were associated with disease progression and poor prognosis in colorectal, gastric, prostate, liver and lung cancer (378–381, 384, 385). Intratumoural TH17 cell abundance also correlated with micro vessel density in hepatocellular

carcinoma, suggesting a role of TH17 cells in the promotion of angiogenesis most likely via IL-17 (379). In contrast, TH17 cells and IL-17A were associated with less advanced clinical stage in CLL (386). Similarly, IL-17 levels in ascites from ovarian cancer patients were positively associated with patient survival, and IL-17A expression by T cells negatively correlated with tumour burden in primary intraocular lymphoma (382, 387). A meta-analysis from Punt et al., which includes 56 different studies, indicated that serum IL-17 levels are associated with adverse prognosis, but circulating, tumour-associated fluid-derived and tumour tissue-derived TH17 cells are associated with favourable prognosis (388).

7.1.2.5. TRM cells

The TRM cell subset that expresses intermediate levels of CD161 is probably the least studied CD161-expressing cell type in cancer, particularly as studies often do not specifically distinguish between intermediate and high CD161-expressing T-cell subsets. The polyclonal $CD161^{int}CD8^{+}$ T-cell subset was shown to be highly polyfunctional and to express increased levels of cytotoxic mediators *in vitro*. This subset also expresses markers associated with tissue migration and tissue residence (73, 74, 87, 389). These features could make $CD161^{int}CD8^{+}$ T cells highly potent effector cells in the antitumour immune response. A recent study identified *KLRB1*-expressing $CD4^{+}$ and $CD8^{+}$ T-cell subsets in diffuse glioma, which are not MAIT, NKT or γδT cells and most likely comprise $CD161^{int}$ T cells. Their presence was confirmed in other tumours, including hepatocellular carcinoma, melanoma, non-small cell lung and colorectal cancer. In addition, it was shown that genetic inactivation of *KLRB1* or blocking CD161 with monoclonal antibodies can increase the function of these T cells, including cytokine expression and cytotoxicity (77).

7.1.2.6. NK cells and other ILCs

NK cells are a subtype of group 1 ILCs (390). NK cells express a stochastic combination of germline encoded stimulatory and inhibitory receptors, which include various killer cell immunoglobulin-like receptors and other receptors such as NKG2D (8, 391). These receptors

allow NK cells to detect altered or downregulated MHC molecule expression or induced stress ligands on tumour cells. Depending on the balance between inhibitory and stimulatory signals, NK cells can kill target cells (392). Antibody-dependent cellular cytotoxicity, mediated via CD16, could also contribute to cancer cell lysis (393). For optimal effector capacity, NK cells need priming through cytokines, such as IL-15, IL-12 and IL-18 (391, 394–396). Besides their cytotoxic capacity, activated NK cells can also produce cytokines such as IFNγ, which could support the anti-tumour response by promoting antigen presentation and activation of other immune cells (391). In addition, NK cells could also induce target cell apoptosis by the engagement of death receptors via FASL or TRAIL (397).

In comparison to other CD161-expressing cell types, the role of NK cells in tumour immunosurveillance has been relatively well established. Besides the ability of human NK cells to kill cancer cells *in vitro* (398), it has also been shown that natural NK-cell deficiencies are associated with increased risk of developing haematopoietic malignancies and virus-induced cancers (399–401). In line with this, two large meta studies, analysing 56 and 53 studies, respectively, concluded that NK cells are overall associated with favourable prognosis in solid cancers (402, 403). In addition, NK cells are also involved in immune responses against hematologic malignancies (404, 405).

It is proposed that ILCs other than NK cells can both promote and protect against cancer. IL-15 activated ILC1s could directly lyse cancer cells and mediate anti-cancer immune response via cytokines such as IFNγ. IL-33 activated ILC2s could recruit eosinophils via IL-5, which in turn could recruit T cells to mediate anti-tumour response. ILC2s could also promote tumours via cytokines such as IL-4, IL-9 and IL-13. IL-13, for example, can recruit myeloid-derived suppressor cells. ILC3s could promote the anti-tumour response by inducing the formation of local tertiary lymphoid organs. On the other hand, IL-23-activated ILC3s could promote tumours via production of IL-17 and IL-22 (406–408).

7. Role of CD161 in cancer

Direct antitumour responses of ILCs against cancer cells were shown *in vitro*. This includes IFNγ and TNFα production measured in total ILCs and direct KIR-independent cancer cell killing activity observed from CD56+ ILC1-like cells (408, 409). Circulating ILCs from haematological cancers such as AML and CLL showed impaired cytokine expression, affecting IFNγ, TNFα, IL-5 and IL-13 (409, 410). While in AML total circulating ILC counts were decreased, with a decrease in ILC3 numbers but an increase of ILC1s (410, 411), circulating ILCs in CLL were increased, including both ILC1s and NCR^- ILC3s (409). Similarly, circulating ILC3s are increased in pancreatic cancer (412) and circulating ILC2s in both gastric cancer and AML (410, 412).

An increased count of circulating ILCs in CLL was associated with disease progression (409). Increased ILC frequencies have also been observed in malignant tissue of solid tumours, including ILC1s in gastrointestinal tumours (413), ILC2s in breast, bladder and pancreatic cancer (413–415), and ILC3s in lung and breast cancer (416–418). ILC1 cells were, however, decreased in pulmonary squamous cell carcinoma (418). Studies on the effect of tumour-infiltrating ILCs on patient survival revealed that ILC2s were associated with favourable prognosis in pancreatic cancer (415, 419). In contrast, ILC2s are suggested to have a tumour-promoting role in AML and bladder cancer, mediated, for example, by the expression of IL-13, which in turn has been associated with the recruitment and induction of monocytic myeloid-derived suppressor cells (411, 414). ILC3s were generally associated with adverse clinical features such as lymph node metastasis in breast cancer, distant metastasis and vascular invasion in pancreatic cancer and adverse prognosis in lung cancer (412, 417, 418). Mechanistically, ILC3s were shown to promote tumour progression by producing IL-17 (418). In addition, ILC3s can promote cancer cell proliferation, invasion and migration via IL-22 expression (412, 416). Cancers were also shown to exploit the plasticity of ILCs by producing IL-23, which can convert ILC1s into ILC3s to support tumour progression (418). On the other hand, ILC3s were shown to have lymphoid tissue-inducing properties and the

potential to express IL-2, IL-8 and TNFα and to activate endothelial cells, which can potentially mediate the local tumour inflammation and infiltration (416).

7.2. Aims

1. Investigate the association of different immune cell populations with patient survival across 26 different cancer types
2. Identify immune cell types to which the prognostic association of *KLRB1* across cancers is attributable to

7.3. Chapter-specific materials and methods

7.3.1. Data used in this study

RNA-seq data from 29 sorted, blood-derived immune cell types was obtained from Monaco et al. (420). Pre-processed CITE-seq data of PBMCs from 8 healthy volunteers, who were part of a phase 1a HIV vaccine trial, was obtained from Hao et al. (305). Only samples that had been taken before administration of the booster vaccination were analysed. Pre-processed scRNA-seq data from breast cancer-derived immune cells was obtained from Azizi et al. (308). PanCan Atlas TCGA data and TCGA Pan-Cancer Clinical Data Resource (TCGA-CDR) data was obtained from https://gdc.cancer.gov/about-data/publications/pancanatlas (303, 304). Estimated immune cell abundances within TCGA data, generated by Miao et al. using ImmuCellAI, were obtained from http://bioinfo.life.hust.edu.cn/ImmuCellAI#!/ (421). ImmuCellAI cell types are represented in Figure 7-1. Ten different TRM signatures were obtained from FitzPatrick et al. (422), Savas et al. (423) and Kumar et al. (424).

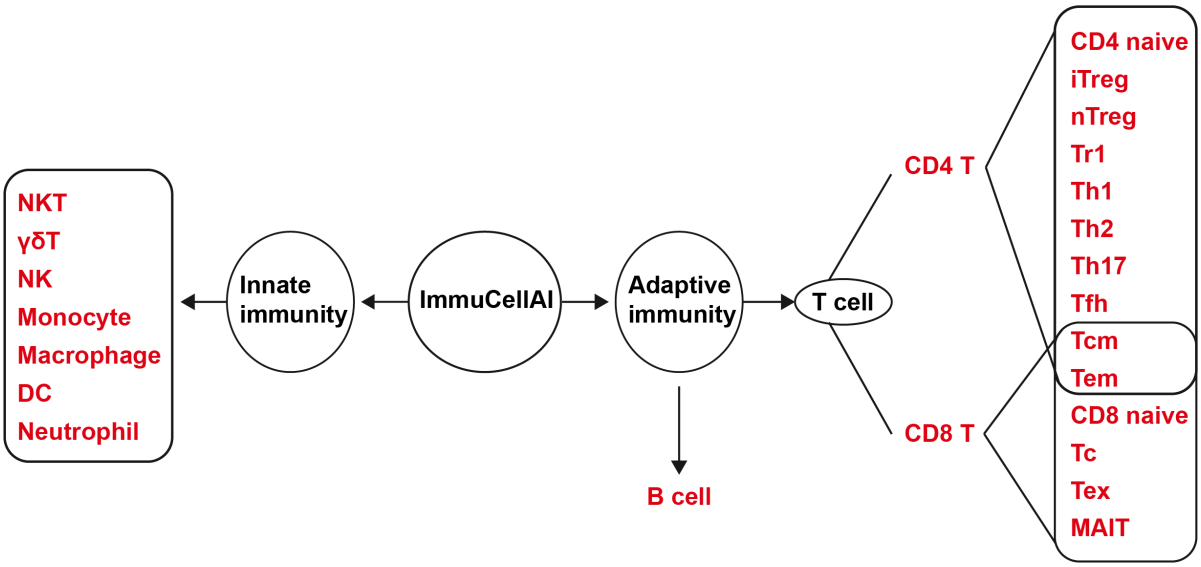


Figure 7-1. ImmuCellAI cell types. Graph shows the 24 cell types that have been estimated within TCGA data by ImmuCellAI (highlighted in red) (421). Tr1, T regulatory type 1. iTreg, induced regulatory T cell. nTreg, natural regulatory T cell. Th1, type 1 T helper. Th2, type 2 T helper. Th17, type 17 T helper. Tfh, T follicular helper. Tcm, T central memory. Tem, T effector memory. Tc, cytotoxic T cell. Tex, exhausted T cell. MAIT, mucosal-associated invariant T cell. NKT, natural killer T cell. NK, natural killer cell. DC, dendritic cell.

7.4. Results

7.4.1. Identification of *KLRB1*-expressing cell types

To confirm which immune subsets can express *KLRB1*, bulk RNA-seq data from 29 sorted, blood-derived immune cell types, obtained from Monaco et al. was analysed (420) (Figure 7-2a). Highest levels of *KLRB1* expression were observed in MAIT and Vδ2^{+} γδT cells, followed by NK, TH17, TH1/TH17 and TFH cells. Lower levels of KLRB1 expression were observed in Vδ2^{-} γδT, TH1 and CD8 effector memory and terminal effector T cells. These results confirm what is known from the literature, although TFH cells have previously not been particularly associated with CD161 expression in the literature due to low CD161 expression levels and low frequencies of CD161-expressing TFH cells (325, 425, 426). The data from Monaco et al. lacks the rare human iNKT-cell subset and non-NK ILC subsets, which can also express CD161 (56, 58, 67, 69, 427). CITE-seq data of PBMCs from 8 healthy volunteers, obtained from Hao et al. (305), showed that *KLRB1* mRNA and CD161 surface protein expression correspond. High CD161 and *KLRB1* expression levels were observed by ILCs, CD4 TEM, NK, CD56bright NK, proliferating NK, MAIT and γδT cells (Figure 7-2b-d),

similar to the results obtained from the analysis of bulk RNA-seq data. Analysis of scRNA-seq data from breast cancer-derived immune cells obtained from Azizi et al. (308) showed that *KLRB1* is highly expressed in the same immune subsets as in blood, including ILCs, NK, CD56bright NK, CD4 TEM, γδT and MAIT cells (Figure 7-2e). Some immune subsets from the breast cancer data were excluded, however, due to very low cell numbers ($n < 40$).

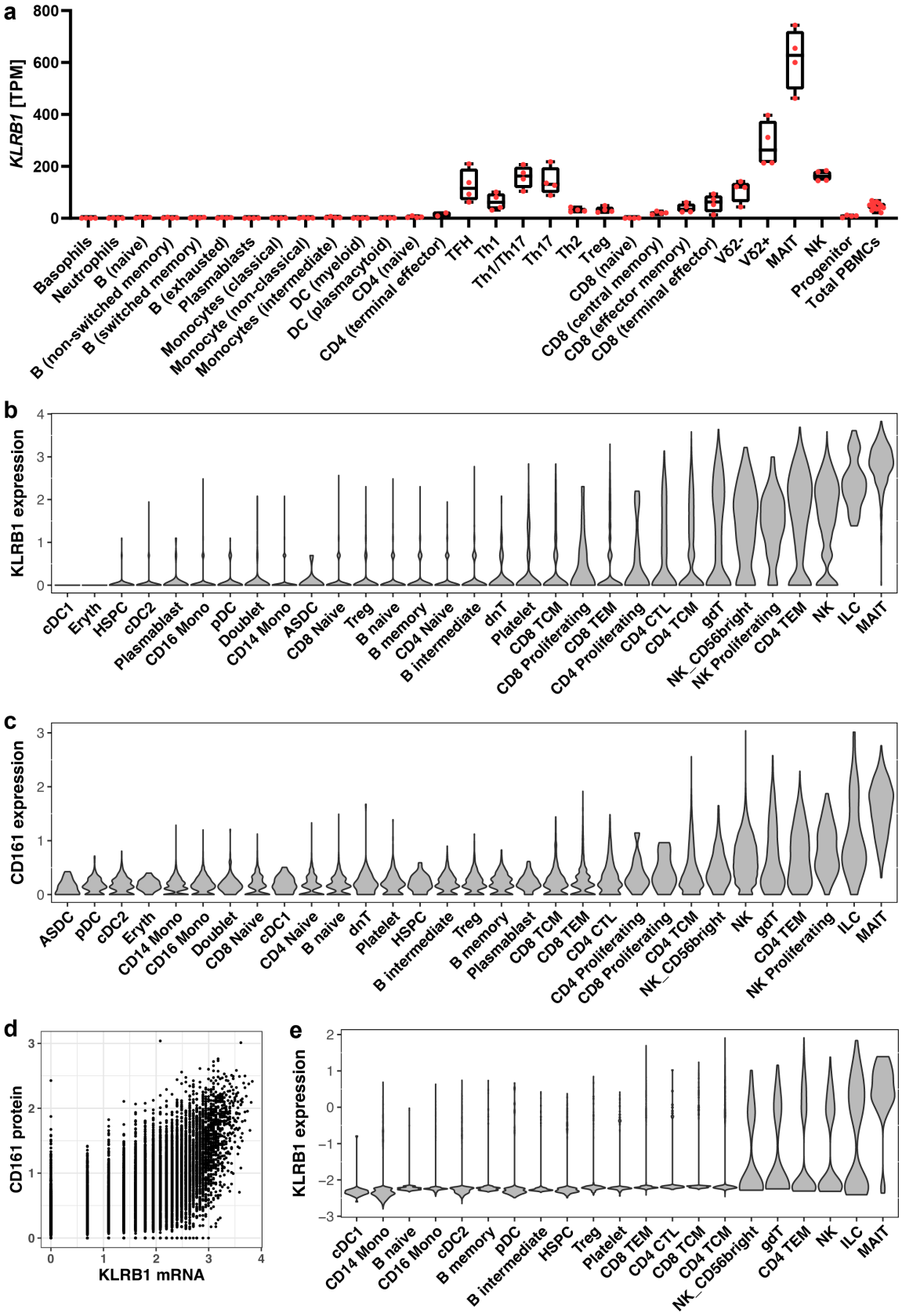


Figure 7-2. *KLRB1* gene expression in 29 different immune cell types. (a) Bulk RNA-seq data from 29 sorted, blood-derived immune cell types (N=4) and total PBMCs (N=13) was obtained from Monaco et al. (420). Box plot shows KLRB1 expression values (TPM, transcripts per million). (b)-(c) CITE-seq data of PBMCs from 8 healthy

volunteers, who were part of a phase 1a HIV vaccine trial, was obtained from Hao et al. (305). Samples that had been taken before administration of the booster vaccination were analysed here. Violin plots show SCTransform-normalized *KLRB1* mRNA and centred-log ratio-transformed CD161 surface protein expression of different cell types. (d) Scatter plot shows *KLRB1* mRNA and CD161 surface protein expression of all cells from PBMC CITE-seq data set. (e) scRNA-seq data from breast cancer-derived immune cells was obtained from Azizi et al. (308). Immune cell types were identified using reference mapping implemented in Seurat R package. The PCMB CITE-seq data set from Hao et al. served as a reference. Violin plot shows Biscuit-normalized *KLRB1* expression of cell types with a cell number of > 40.

7.4.2. The association of *KLRB1* expression and immune cell types that can express *KLRB1* with cancer patient survival

First, the association of *KLRB1* expression with cancer patient survival was investigated within 26 cancer types of the PanCan Atlas using univariate Cox regression (Figure 7-3a). For this purpose, overall survival outcome data was obtained from the TCGA-CDR (304). Only primary cancers were considered for survival analysis. *KLRB1* was significantly associated with a favourable prognosis in 10 cancer types including ACC, CHOL, UCEC, CESC, SARC, BRCA, LIHC, LUAD, MESO and HNSC. In addition, a significant adverse prognostic association was found in 3 cancer types including ESCA, LGG and UVM.

Next, the association between various immune cell types and cancer patient survival was investigated. For this purpose, estimated immune cell abundances within TCGA data were obtained, which were generated by Miao et al. using ImmuCellAI (421). Enrichment scores for 24 different immune cell types and a general infiltration score were available, including 5 cell types that are known to express *KLRB1*, namely MAIT, γδT, NKT, TH17 and TFH cells. The association of ImmuCellAI immune cell types with cancer patient survival within 26 cancer types was analysed using univariate Cox regression (Figure 7-3b-d). In BRCA, for example, NK cells and several T-cell subsets, including TFH, TCM, $CD8^+$ T, $CD4^+$ T, MAIT, NK, TH2, and γδT cells were associated with favourable prognosis (Figure 7-3b). In contrast, nTregs, neutrophils, monocytes and macrophages were associated with adverse prognosis.

7. Role of CD161 in cancer

Considering the association of the analysed immune subsets with cancer patient survival within all 26 cancer types, hierarchical clustering identified 3 different groups of cancers and 3 different groups of immune cells (Figure 7-3c). For immune cell group 1, particularly $CD4^+$ T, $CD8^+$ T, TH1, TH2, TCM, TFH, TC, MAIT and γδT cells, a trend of a generally positive association with survival was observed in cancer group 1, including HNSC, CESC, LUAD, BRCA, BLCA, KICH, PAAD, SARC, LIHC, AAC, and MESO. In contrast, most immune cell subsets in cancer group 3, including KIRC, LGG and UVM were associated with adverse prognosis. Interestingly, for cell types of immune cell group 2, including monocytes, neutrophils, NKT, TH17, naive $CD4^+$ T and naive $CD8^+$ T cells, a trend of an overall positive association with survival was observed in group 3 cancers and an overall negative association with survival was observed in group 1 cancers.

The analysed immune subsets were ranked according to their positive association with patient survival across cancers (Figure 7-3d). For each cancer an immune subset showed a HR < 1 and $p < 0.05$, the score was raised by 1, whereas for each cancer with a HR > 1 and $p < 0.05$, the score was decreased by 1. In case of a tie between the rank of immune subsets, the immune subset that had fewer results with HR > 1 and $p < 0.05$ ranked higher. Cell types that ranked highest and above the general infiltration score included $CD8^+$ T, γδT, TFH, TCM, CD4+ T, B, TC, NK, TH17 and TH1 cells. Cell types ranked at the bottom of the list included neutrophils, macrophages, nTregs, NKT cells and monocytes.

In order to gather more evidence to which particular *KLRB1*-expressing cell type the favourable prognostic association of *KLRB1* across cancers is attributable to, the correlation between *KLRB1* and estimated immune cell abundances in TCGA data was investigated (Figure 7-3e). Most T-cell subsets, NK cells and the general infiltration score showed a relatively high correlation with *KLRB1* across cancers. Amongst the cells that can express CD161, TFH and NK cells showed the highest and most coherent correlation with *KLRB1* across cancers, followed by MAIT and γδT cells. In contrast, NKT cells correlated with *KLRB1*

only in a few cancers, and for both NKT and TH17 cells inverse correlation with *KLRB1* expression was observed in certain cancers.

In addition, the correlation between HR of *KLRB1* gene expression and HR of different immune subsets across the 26 cancer types was analysed (Figure 7-3g, Appendix Figure V-1). From the cell types that can express *KLRB1*, TFH cells showed the highest correlation, followed by NK, MAIT and γδT cells. NKT and TH17 cells showed no or inverse correlation. Besides immune subsets that can express *KLRB1*, a high correlation was observed for TC, $CD8^+$ T, TH2 and $CD4^+$ T cells, as well as for the general immune infiltration score.

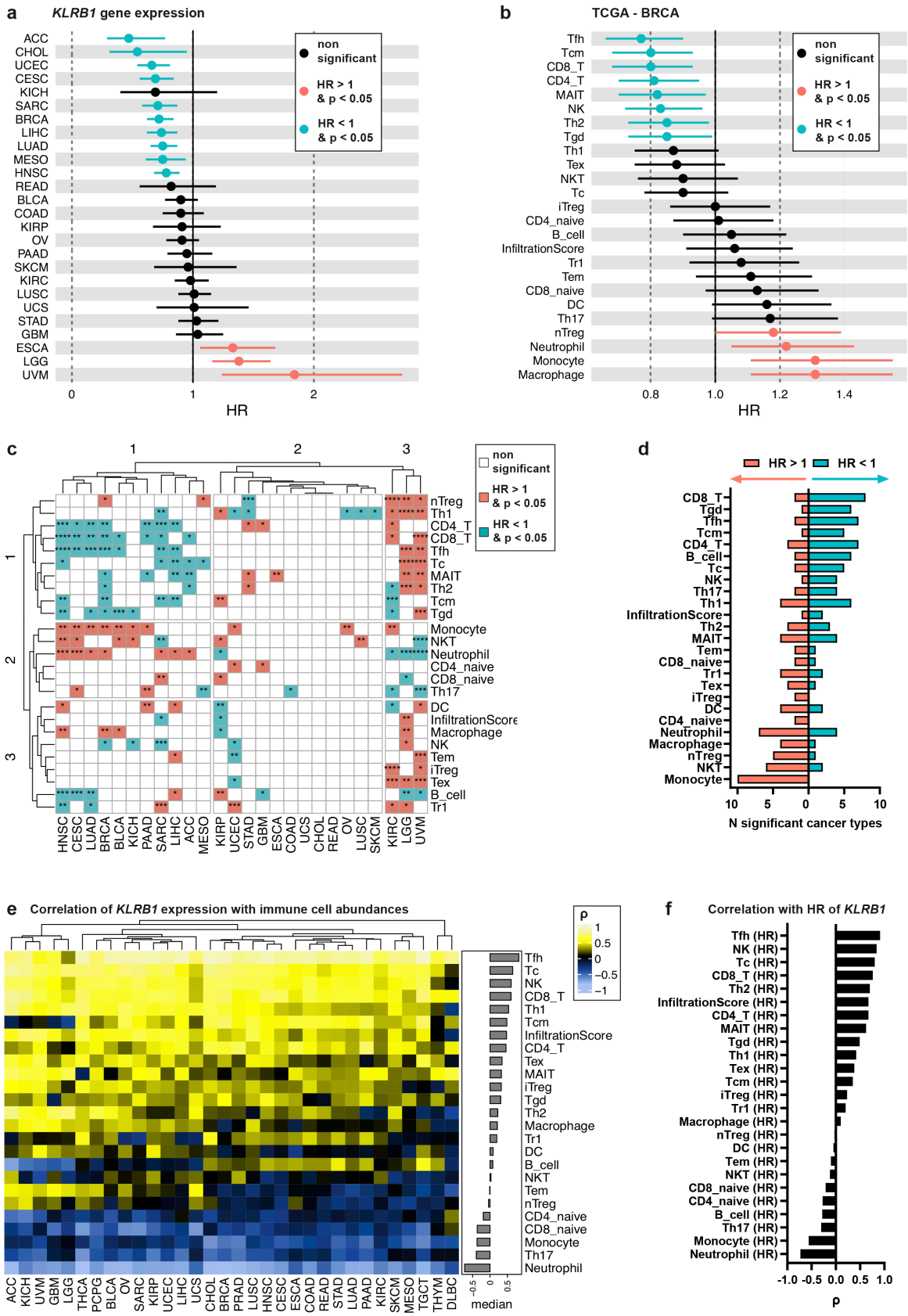


Figure 7-3. Association of immune cell subsets that can express *KLRB1* with patient survival in cancer. (a) The prognostic value of *KLRB1* gene expression in cancer was investigated by univariate Cox regression within 26 cancer types. (b)-(c) Immune cell abundances of 25 different cell types within TCGA patient samples, estimated by ImmuCellAI, were obtained from Miao et al. (421). The association of the 25 immune subsets with

patient survival was analysed within the 26 cancer types using univariate Cox regression. As an example, the forest plot in (b) shows the association of the different immune cell subsets with BRCA patient survival. In (c), results from all analysed cancer types are summarised. ****p<0.0001, ***p<0.001, **p<0.01, *p<0.05. (d) Ranking of immune subsets according to their association with patient survival across cancers. The ranking score for each subset was increased by 1 for each cancer with HR<1 and p<0.05, and decreased by 1 for each cancer with HR>1 and p<0.05. In case of equal ranking scores, the cell type with less cancers having HR>1 and p<0.05 ranked higher. (e) Heatmap shows Spearman's correlation of *KLRB1* expression with ImmuCellAI immune cell types stratified by cancer type. Bar plot on the right shows median Spearman's coefficient across all analysed cancer types. (f) Spearman's correlation between the HR of KLRB1 expression and HR of ImmuCellAI immune subset enrichment was analysed considering 26 TCGA cancer types. For all analyses, only primary cancers were considered. ρ, Spearman's coefficient.

7.4.3. The association of TRM cells with cancer patient survival

CD161 is also expressed by a subset of TRM cells (73). As the ImmuCellAI immune subsets do not include TRM cells, 10 different TRM-cell signatures were obtained from FitzPatrick et al. (422), Savas et al. (423) and Kumar et al. (424). Of these signatures, only FitzPatrick CD8 TRM1 signature included *KLRB1*, however. Signature enrichment within PanCan Atlas data was analysed using ssGSEA. Enrichment scores served as input for survival analysis using univariate Cox regression (Figure 7-4a-c). From the analysed signatures, FitzPatrick CD8 TRM1 and TRM2 signatures showed overall the strongest association with cancer patient survival compared to the other TRM-cell signatures. Enrichment of the FitzPatrick CD8 TRM1 and TRM2 signatures was associated with a favourable prognosis in 6 cancer types each and an adverse prognosis in 3 cancer types each.

Most of the TRM signatures showed relatively high correlation with *KLRB1* (Figure 7-4d), except for CD4 TRM signatures and Kumar Lung CD8 signature, which showed relatively low correlation. The highest and most coherent correlation with *KLRB1* across cancer types was observed for FitzPatrick CD8 TRM1 and TRM 2 signatures. Similarly, a relatively high correlation between the HR of *KLRB1* gene expression and HR of TRM signature enrichment across the 26 analysed cancer types was observed for many of the TRM-cell signatures (Figure 7-4e-f). The highest correlation was observed for the FitzPatrick CD8 TRM1 signature.

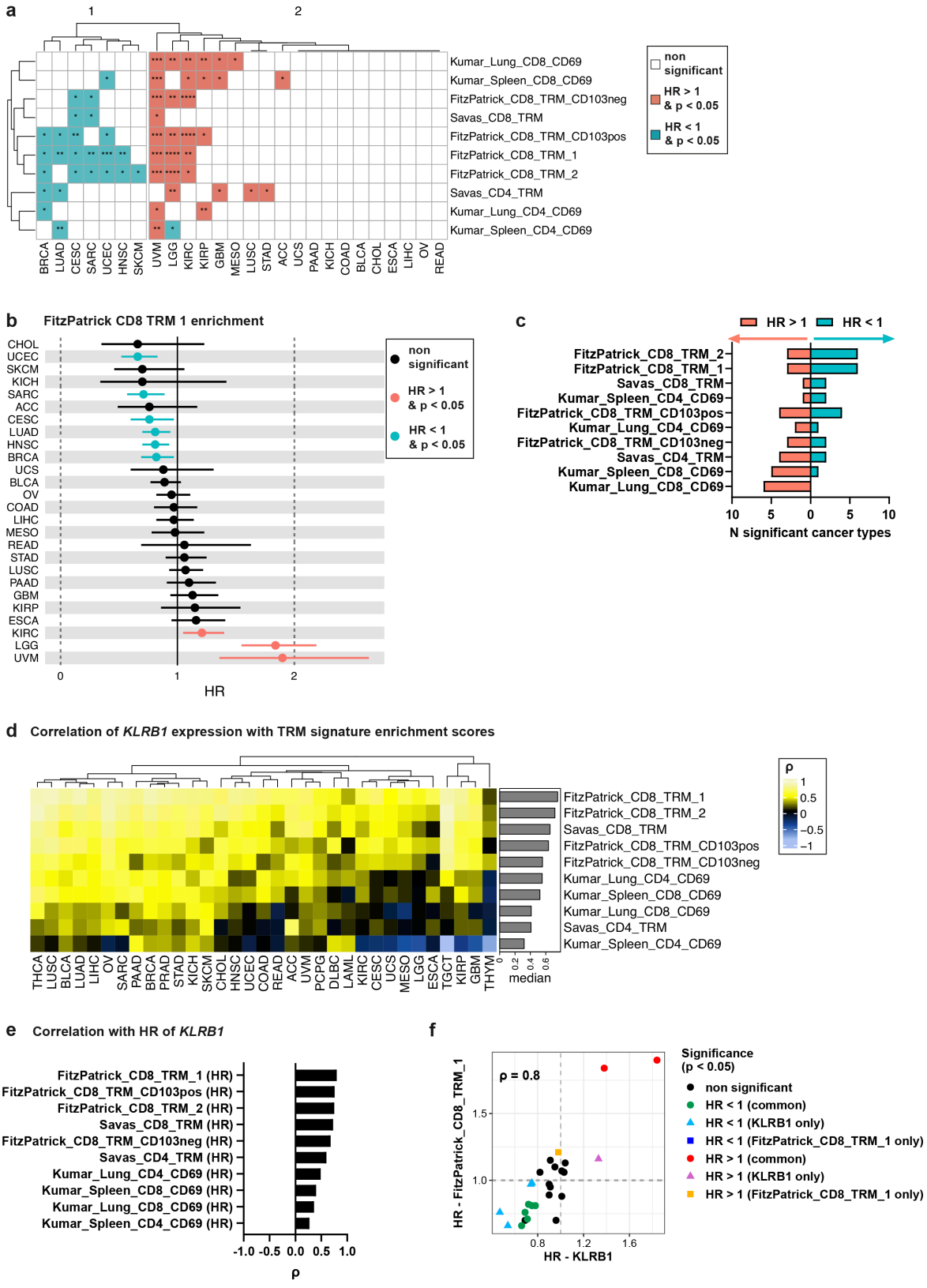


Figure 7-4. Association of TRM cells with cancer patient survival. Different TRM signatures were obtained from FitzPatrick et al. (422), Savas et al. (423) and Kumar et al. (424). (a) The association of TRM signature enrichment and PanCan Atlas cancer patient survival was analysed using univariate Cox regression analysis. Graph summarizes the significant results from the survival analysis of all analysed TRM signatures. ****p<0.0001, ***p<0.001, **p<0.01, *p<0.05. (b) Forest plot shows the association of FitzPatrick TRM1 signatures enrichment

with patient survival. (c) Ranking of TRM signatures according to the association of their enrichment with patient survival across cancers. The ranking score for each subset was increased by 1 for each cancer with HR<1 and p<0.05, and decreased by 1 for each cancer with HR>1 and p<0.05. In case of equal ranking scores, the cell type with less cancers having HR>1 and p<0.05 ranked higher. (d) Heatmap shows Spearman's correlation of *KLRB1* expression with enrichment scores of TRM signatures within TCGA data. Bar plot on the right shows median Spearman's coefficient across all analysed cancer types. (e) Correlation between the HR of *KLRB1* gene expression and HR of TRM signature enrichment was analysed considering the results of 26 cancer types from TCGA. (f) Dot plot shows HR of *KLRB1* gene expression and HR of Fitzpatrick CD8 TRM1 signature enrichment of 26 PanCan Atlas cancer types. Each dot in the graphs represents a different cancer type. For all analyses, only primary cancers were considered. ρ, Spearman's correlation coefficient.

Overall, the results obtained from the different TRM signatures were relatively similar, which can be explained by the relatively high intercorrelation between the ssGSEA enrichment scores of the different signatures (Appendix Figure V-2). Differences were mainly observed between CD4 and CD8 TRM signatures. CD8 signatures, particularly from FitzPatrick et al. and Savas et al. showed the highest correlation with *KLRB1* expression and their association with patient survival was most similar to the trend of the prognostic association of *KLRB1* across cancers. Altogether, FitzPatrick CD8 TRM1 signature performed best and was used for further analysis.

7.4.4. Association between *KLRB1*, ImmuCellAI immune subsets and FitzPatrick TRM1 signature

Correlation between *KLRB1* expression, estimated immune cell type abundances and FitzPatrick CD8 TRM signature enrichment was investigated within TCGA data, separately for each cancer type (Figure 7-5). A correlation matrix showing the median Spearman's correlation coefficient across all analysed cancers was generated. Cell types that correlated highly with *KLRB1*, including TFH, FitzPatrick CD8 TRM1, TC, NK, CD8 T, TH1 and TCM cells, showed also high correlation among each other. Due to the high degree of intercorrelation among the abundance scores of different immune subsets, it was not possible to attribute the prognostic association of *KLRB1* across cancers to a single immune cell type and disentangle the issue. There is also the possibility that the prognostic association of *KLRB1* across cancers is attributable to multiple immune subsets that can express *KLRB1*.

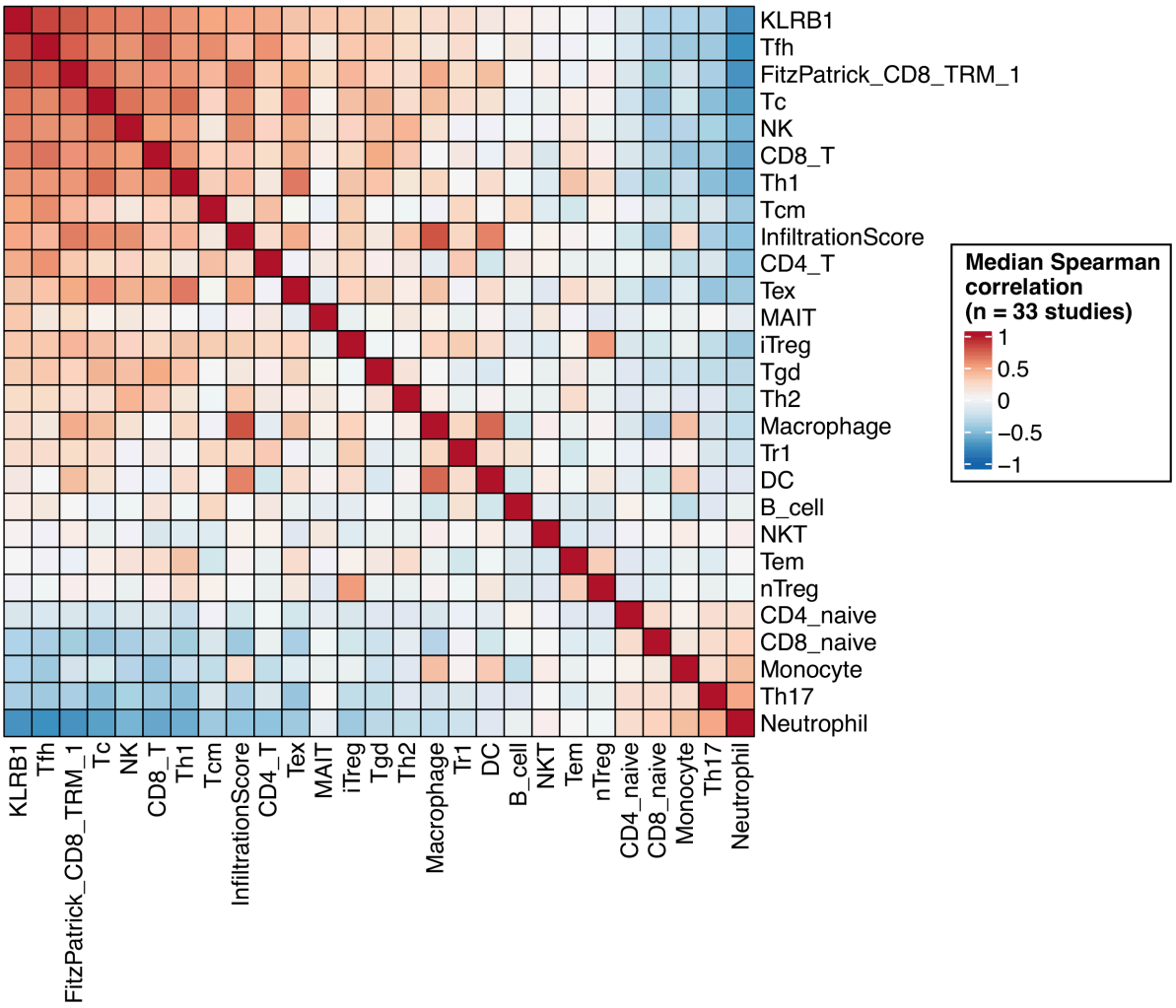


Figure 7-5. Dependence between *KLRB1*, ImmuCellAI immune cell types and FitzPatrick TRM1 signature. Heatmap shows the median Spearman's correlation across 33 analysed TCGA cancer types between *KLRB1* expression and immune cell abundance scores. Immune cell abundance scores include ImmuCellAI immune cell type abundance scores and FitzPatrick CD8 TRM1 ssGSEA enrichment scores. Rows and columns are ordered according to decreasing correlation with *KRLB1*.

7.5. Discussion

In this study it was confirmed that innate-like T cells, including MAIT- and γδT-cell subsets, particularly Vδ2$^+$ T cells, can express high levels of *KLRB1*. Other cell types that expressed *KLRB1* included ILCs, NK, TH1, TH17 and CD8$^+$ memory/effector T cells (Figure 7-2). Interestingly, TFH cells were also found to express *KLRB1*. Incidentally, TFH cells and Monocytes are the only cell types whose ImmuCellAI signatures contain *KLRB1* (421). A previous publication reported monocytes and DCs to express CD161 (428), but neither

7. Role of CD161 in cancer

CD161 surface protein expression nor *KLRB1* mRNA expression of monocytes or DCs was confirmed in the present study (Figure 7-2). There is some literature confirming CD161 expression of TFH cells, however (325, 425, 426). CD161-expressing TFH cells were identified in human tonsils, but the expression levels of CD161 were lower compared to non-TFH $CD4^+$ T cells (426, 429). Llibre et al. reported relatively low frequencies of CD161-expressing cells within TFH cells compared to non-TFH $CD4^+$ T cells (429), whereas Germain et al. found similar proportions of CD161-expressing cells in TFH and non-TFH $CD4^+$ T cells (426). In addition, a *KLRB1*-expressing subset of circulating TFH cells with TH17-like properties was identified (430). Braud et al. demonstrated the presence of CD161-expressing TFH cells in tertiary lymphoid structures within lung cancer and lymph nodes of lung cancer patients, but the proportions of CD161-expressing cells in the TFH-cell subset were significantly lower compared to non-TFH $CD4^+$ T cells (325).

TFH cells were one of the most favourable prognostic cell types in the present study and their abundance scores showed the highest correlation with *KLRB1* expression compared to other cell types (Figure 7-3). Consequently, the HR of TFH cells correlated well with the HR of *KLRB1* expression across 26 analysed cancers. This suggests that the favourable prognostic association of *KLRB1* could be largely attributed to TFH cells. The relatively high correlation of *KLRB1* with TFH cells compared to other cell types could, however, be the result of a bias, as the TFH-cell subset is the only cell type besides monocytes which contains *KLRB1* in its ImmuCellAI signature (421).

Similar to the results of the present study, Gentles et al. reported TFH cells as one of the most favourable prognostic cell types across cancers of the PRECOG (PREdiction of Clinical Outcomes from Genomic profiles) data base. In that study, the median correlation between *KLRB1* expression and inferred levels of TFH cells was relatively low, however (130). This discrepancy could be explained by the use of different cell type signatures and the analysis of different cancer studies. In addition, different methods for estimating cell type abundances

were applied. In the present study, cellular composition was estimated using ImmuCellAI which is a marker gene-based method computing the enrichment of signature genes. In contrast, Gentles et al. used CIBERSORT, which is a deconvolution-based method (130, 431).

Further evidence for the beneficial impact of TFH cells on patient survival was demonstrated in colorectal cancer, where TFH cells provided B cell help and inversely correlated with cancer progression and recurrence (432). Another study showed an association of $CXCL13^{+}CXCR5^{-}$ TFH cells with favourable prognosis in breast cancer (433). Tumour-infiltrating $CXCL13^{+}CXCR5^{-}$ TFH-like subsets, which provide $CD8^{+}$ T cell help and show enrichment of a cytotoxicity-related gene signature that contains *KLRB1*, were described in lung cancer (434). Further investigation is required, however, to confirm the association of TFH cells with *KLRB1* expression and to dissect their precise role in cancer.

The γδT-cell subset is another cell type that can express *KLRB1* and is one of the most favourable prognostic cell types in both the present study and the study from Gentles et al. (130). In the present study, γδT cells correlated with *KLRB1* expression, but the correlation was relatively low compared to other cell types. Consequently, the correlation between the HR of γδT cells and the HR of *KLRB1* expression across cancers was lower compared to other subsets such as TFH cells. In contrast, γδT cells showed the highest correlation with *KLRB1* of all analysed cells across cancers in the study from Gentles et al. (130). This difference may be due to the methodological differences between the studies as outlined above. In addition, there are many different γδT-cell subsets, from which $Vδ2^{+}$ γδT cells have a higher proportion of CD161-expressing cells and are functionally more similar to other CD161-expressing innate-like T cells than other γδT-cell subsets such as $Vδ1^{+}$ cells (66). Separate signatures for the functionally different γδT-cell subsets might be required to properly assess their role in cancer survival.

NK cells were also correlated with *KLRB1* expression and therefore a high correlation between the HR of NK cells and the HR of KLRB1 across cancers was observed. In addition, NK cells were amongst the most favourable prognostic cell types, although they scored lower than TFH cells. This makes NK cells another candidate to which the favourable prognostic value of *KLRB1* could be attributed to. Similar to γδT cells, NK cells consist of functionally different subsets, including CD161-negative and CD161-positive subsets (46). Subset-specific analysis would allow a more precise assessment of the role of NK cells in cancer.

CD8 T and TC cells were also amongst the highest-ranking cell types in terms of favourable prognosis and correlation with *KLRB1* across cancers. Thus, the HR of both cell types correlated well with HR of *KLRB1* expression across analysed cancers. These two subsets most likely contain the tissue-resident $CD161^{int}CD8^{+}$ T-cell subset, which is highly polyfunctional and expresses increased levels of cytotoxic mediators (73, 74, 87, 389). As the ImmuCellAI signatures do not include a separate signature for TRM cells to investigate their role in cancer, 10 published TRM signatures were obtained and the association of their enrichment with patient survival in cancer was analysed (Figure 7-4). The analysis was performed separately from the ImmuCellAI immune cell type analysis, as the TRM signature ssGSEA scores were not directly comparable with the ImmuCellAI immune cell scores. The latter is based on ssGSEA, but includes correction of the bias that results from shared genes in the signatures of different immune cell types (421). From all analysed TRM signatures, the FitzPatrick CD8 TRM1 signature was the only signature containing *KLRB1*. This signature ranked highest considering both the association with favourable prognosis across cancers and the correlation with *KLRB1* expression. The correlation with *KLRB1* was similarly high as observed for TFH cells. Consequently, there was also a high correlation between the HR of this TRM signature and the HR of *KLRB1* across cancers.

MAIT, TH17 and TH1 cells showed correlation with *KLRB1* and/or showed association with favourable prognosis in some cancers, but ranked lower compared to other cell types. Interestingly, NKT cells were associated with adverse prognosis across cancers. This is surprising, as iNKT cells have been associated with favourable prognosis in cancer such as colorectal carcinoma and neuroblastoma (364, 365), and low frequencies of circulating iNKTs have been associated with poor outcome in various malignancies (371–375). It needs to be confirmed whether the ImmuCellAI NKT signature is truly specific for iNKT cells or also estimates the abundance of type II NKT cells. The latter T-cell subset has CD1d-restricted variable αβTCRs, and is thought to inhibit the anti-cancer immune response in contrast to iNKT cells (345).

In summary, several immune cell subsets that can express *KLRB1* ranked relatively high regarding their association with a favourable prognosis across cancers, including NK, TFH, γδT, and Fitzpatrick CD8 TRM1 cells. These cell types also showed a relatively high correlation with *KLRB1* expression, except for γδT cells, which showed only a moderate correlation. These observations expand on the results from Gentles et al., in which immune subsets that showed relevant correlation with *KLRB1* and were amongst the most favourable prognostic cell types in cancer included γδT, $CD8^+$ T, and memory $CD4^+$ T cells (130). Except for γδT cells, these are relatively broadly defined cell subsets, however, and therefore not very useful as determinants to investigate the link of the prognostic association of *KLRB1* and different *KLRB1*-expressing immune cell types. Another limitation of the study from Gentles et al. is the poor performance of CIBERSORT in estimating γδT cell abundances from bulk transcriptomic data. The validation of the signature used by Gentles et al. showed no significant correlation between estimated γδT cell abundances and the ground truth consisting of frequencies determined by flow cytometry (431). This is the reason why there were some doubts regarding the γδT cell-related results from the study of Gentles et al.

Due to strong correlation among immune subsets that were analysed in the present study (Figure 7-5), it was not possible to disentangle to which particular immune subset the favourable prognostic association of *KLRB1* across cancers can be attributed to. None of the analysed immune subsets exactly matched the pattern of all cancer types in which KLRB1 showed a significant association with favourable prognosis. It is possible, that the favourable prognosis of *KLRB1* is attributable to multiple *KLRB1*-expressing cell types.

On the other hand, the reason that none of analysed cell types exactly matched the prognostic association of *KLRB1* across cancers could be due to limitations of the applied methods. The results of the present study are dependent on the performance of the ImmuCellAI method, which was used to estimate immune cell abundances within TCGA data (421). Therefore, the results of the present study should be validated and the performance of ImmuCellAI compared to other immune cell signatures in combination with other marker gene- or deconvolution-based methods for the analysis of cellular composition. Unfortunately, other well-validated signatures, such as the LM22 signature matrix, which was used by Gentles et al. in combination with CIBERSORT, do not contain most of the major *KLRB1*-expressing cell types (431). The LM22 signature matrix, for example, lacks the MAIT-cell subset, which expresses the highest levels of *KLRB1* compared to other cell types (Figure 7-2). A signature matrix developed by Monaco et al., which can be used in combination with robust linear modeling or CIBERSORT, contains many of major CD161-expressing cell types, including NK, Vδ2^{+} γδT and MAIT cells. Thus, the Monaco et al. signature matrix presents an interesting alternative to ImmuCellAI. Its use for deconvolution of bulk transcriptomic data of tissue samples, containing both immune and non-immune cells, has not been investigated and validated, yet (420). Another limitation of the present study is the use of TCGA data for survival analysis. The TCGA data resource was not created with the purpose of acquiring complete patient outcome data and is therefore limited by short follow-up intervals (304), as discussed in 6.5.4. Other repositories of cancer transcriptomic data accompanied with

survival data such as PRECOG could be used to confirm the results of the present study (130).

Taken together, the present study showed that NK, TFH, CD8 T, TC and *KLRB1*-expressing TRM cells are highly associated with *KLRB1* expression and are amongst the most favourable prognostic cell types across cancers. *KLRB1* is one of the most favourable prognostic pan-cancer biomarkers (130), and understanding to which cell subset this favourable prognostic association can be attributed to sets the stage for the development of strategies for their manipulation *in vivo* towards desirable therapeutic outcomes. This is particularly relevant as CD161 has recently been described as a novel inhibitory immune checkpoint in cancer and its genetic inactivation or blockage can, for example, unleash the cytotoxic capacity of tumour infiltrating CD161-expressing T cells (77). Due to the high correlation among immune subsets, it was not possible to disentangle whether the prognostic association of *KLRB1* across cancers is linked to one or multiple immune subsets, however. Further studies are required to confirm the results of this study and to explore the specific anti-tumour mechanisms of the relevant CD161-expressing immune subset.

7.6. Summary

1. NK, TFH, CD8 T, TC and *KLRB1*-expressing TRM cells were highly associated with *KLRB1* expression and were amongst the most favourable prognostic cell types across cancers.
2. γδT cells were amongst the most favourable prognostic cell types across cancers but showed only moderate correlation with *KLRB1.*
3. MAIT, TH17 and TH1 cells showed correlation with *KLRB1* and/or showed association with favourable prognosis in some cancers, but ranked lower compared to other cell types.

4. NKT cells showed inverse correlation with *KLRB1* and were associated with adverse prognosis across cancers.
5. Different immune subsets were highly correlated among each other, which did not allow to attribute the prognostic association of *KLRB1* across cancers to a specific immune subset.
6. The prognostic association of *KLRB1* across cancers might be attributable to multiple immune subsets.

8. DISCUSSION

8.1. ChipCytometry

8.1.1. Key findings

ChipCytometry is an emerging imaging-based multiplex immunophenotyping method. In the present study, several technical problems and limitations of the ChipCytometry method were identified. Many of the issues were overcome and ChipCytometry was developed as a truly viable cytometry method for high-content profiling of cell suspension and tissue sections. In a proof-of-principle study, the general histological architecture of tonsils, including T-cell and B-cell zones and subcompartments, was demonstrated. In addition, ChipCytometry could identify and localize tonsillar cell populations including rare cell types, such as tonsillar MAIT cells, which were phenotypically similar to blood-derived MAIT cells.

Despite ChipCytometry being a highly promising technique, the number of publications and applied panel sizes of staining antibodies are still limited for this method. Here, ChipCytometry was used to identify and deeply phenotype cytokine-responsive T- and NK-cell subsets in human blood with a panel of 50 markers. An analysis protocol for single-cell ChipCytometry data was developed, including platform-required steps such as identification and removal of fluorescence anomalies (Figure 8-1). Unsupervised clustering identified NK- and T-cell subsets in the data, including innate-like T cells such as MAIT and γδT cells. NK and innate-like T cells were found to be the major responders to IL-12+IL-18 stimulation. A trend of increased cytokine responsiveness of CD161-expressing subsets compared to CD161-negative subsets was observed. ChipCytometry was demonstrated as a viable and competitive high-content cytometry technique, and an interesting alternative to similar methods such as mass cytometry.

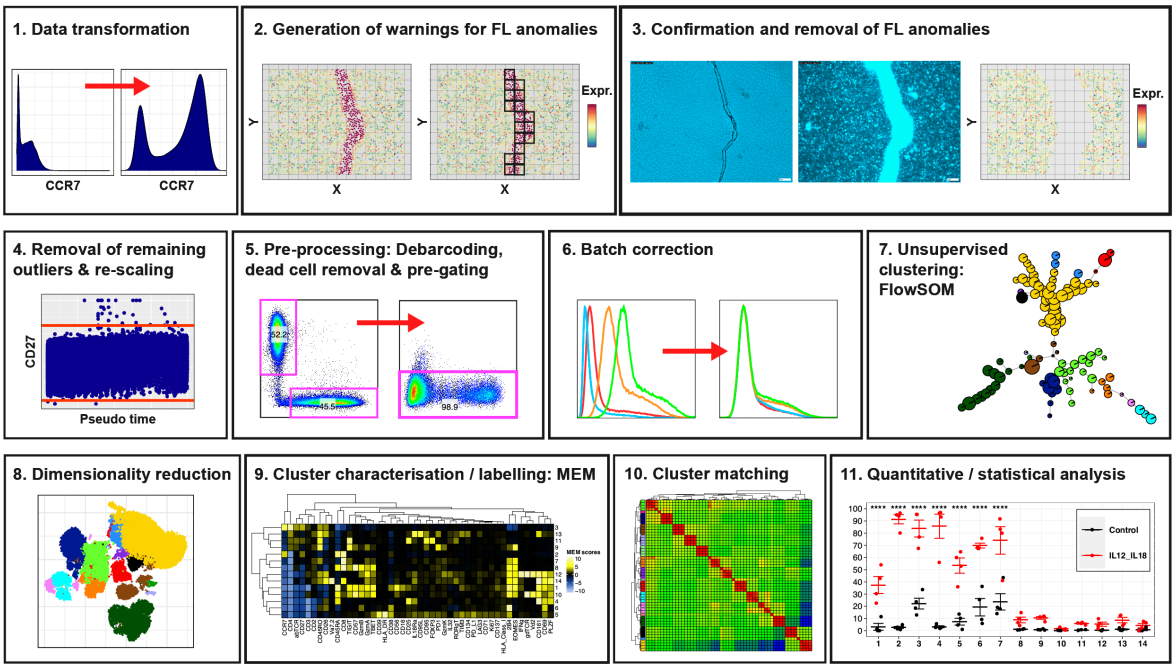


Figure 8-1. Analysis protocol for high-content single-cell ChipCytometry data. Panels summarise the steps of the analysis protocol developed in this study for single-cell ChipCytometry data. FL anomalies, fluorescence anomalies.

8.1.2. Strengths and challenges of ChipCytometry

High content cytometry methods allow the application of a large number of lineage and phenotyping markers to identify a large number of different cell types, including complex cell types that require a large number of markers for their definition, and allow to additionally allocate a high number of parameters for functional markers. High-content cytometry methods other than ChipCytometry include mass cytometry (136), spectral flow cytometry (134, 135), CODEX (172), and cytometry by sequencing such as CITE-seq and REAP-seq. The latter are techniques accompanied by scRNA-seq (173, 174). Although panels with far more than 50 markers can theoretically be acquired with any of those techniques, it is still challenging to develop panels with more than 40 markers for most of these methods. For example, the Aurora spectral flow cytometer from Cytek Biosciences can detect up to 64 fluorescent channels, but panel development is limited by the availability of dyes that have distinct fluorescent spectra (135). A 43 colour panel for spectral flow cytometry has been developed

which pushed the limits of that method (143). Panel development for mass cytometry is limited by the availability of suitable isotopes to tag antibodies. One of the largest mass cytometry panels applied has 48 markers (144). CODEX has mainly been used for tissue cytometry and a recently published CODEX panel to stain formalin-fixed, paraffin-embedded tissue sections consisted of 56 markers plus nuclear stains (435). In the present study it was shown that ChipCytometry is highly competitive to these methods by applying a panel consisting of 50 markers. Panels consisting of significantly more than 50 markers in cytometry have been applied using methods based on sequencing of oligonucleotide-tagged antibodies. CITE-seq, for example, was used to analyse the expression of more than 200 proteins on single cells (305).

Panel design for ChipCytometry is more straightforward than for other methods, combining up to 5 commercially available standard fluorochrome-labelled antibodies per acquisition round. No or only minimal spillover compensation is required, as the five ChipCytometry channels are equipped with very narrow filter sets, and different fluorochromes are excited and their emission is captured in a serial manner. ChipCytometry requires, however, very careful consideration of the order of antibody staining. Despite protective longpass filters that block damaging UV light, repeated photobleaching cycles can damage particularly sensitive epitopes, which must be stained early in the protocol. Another advantage of ChipCytometry is the potential for biobanking. Samples can be stored at least 20 months without significant biomarker degradation (138), enabling re-interrogation of samples long after project completion. This also allows for samples being collected at different locations with subsequent centralised analysis. Mass cytometry, in contrast, is a destructive process in which samples are vaporised during analysis (436), thus less useful for the analysis of rare or precious samples. The methods ChipCytometry, mass cytometry and CODEX also allow the analysis of tissue sections, whereas spectral flow cytometry and cytometry by sequencing, such as CITE-seq and REAP-seq, require the dissociation of cells and the loss of spatial information (437). Finally, although CITE-seq and REAP-seq are capable of

acquiring much larger panels than other cytometry methods, they are limited to surface targets and incapable of staining intracellular markers (438).

A further advantage of ChipCytometry is the use of 32 bit per colour high dynamic resolution imaging (≈ 4.29 billion intensity values per pixel ≈ 9 logarithmic decades dynamic resolution) achieved by exposure fusion. By comparison, mass cytometry has 4-5 decades dynamic resolution and the dynamic range of standard fluorescence microscopy is about 3 decades. ChipCytometry images every cell twice for acquired each marker, pre- and post-staining. Automatic subtraction of the background fluorescence allows corrections for autofluorescence and optical artefacts, resulting in a net-fluorescence HDR image with a dynamic range of 5-6 decades (149). ChipCytometry also has a higher spatial resolution of 500 nm per pixel compared to 1000 nm per pixel resolution of mass cytometry (439). CODEX can resolve 600 nm or 250 nm depending on the selected objective. The fluorescence microscope instrumentation that is combined with the CODEX platform determines its dynamic resolution (16 bit output supported) (440).

Challenges of ChipCytometry include the occurrence of batch effects between samples that are located on separate chips and the need for manual and time-consuming identification and removal of fluorescence anomalies. The biggest challenge of ChipCytometry is the low sample throughput because of the sequential nature of data acquisition, both for the acquisition of individual positions on a sample chip and the accumulation of multiple markers through staining rounds of up to 5 markers each. This particularly impacts the sample throughput of cell suspension ChipCytometry. In order to obtain sufficient cell numbers for data analysis, as many chip positions as possible need to be acquired, each of which can accommodate about 3400 PBMCs on average. In contrast to that, only a relatively small area of interest consisting of a few adjacent chip positions is usually scanned for the analysis tissue sections, allowing a higher sample throughput. Therefore, ChipCytometry could show its utility particularly in the high-content analysis of tissue sections, especially with added advantages

in dynamic and spatial resolution. The use of automated versions of the ChipCytometer (CYTOBOT) could increase sample throughput for both cell suspension and tissue section ChipCytometry and allow the routine application of >50 marker panels by default.

8.1.3. Future work

ChipCytometry could benefit from further work addressing the following aspects:

- Train a neuronal network to automate fluorescence anomaly detection and removal.
- Strengthen the utility of this technique by applying 50-marker panels to tissue sections and expanding the panel beyond immune profiling markers by staining for additional non-immune markers such as stromal cell markers.
- Development of an analysis protocol for high-content tissue ChipCytometry-derived spatial data, including neighbourhood and cellular interaction network analysis.

8.2. Expression and function of IL-32

8.2.1. Key findings and their relevance

Innate-like T cells are characterised by TCRs with low diversity, CD161 expression and the ability to respond to cytokines in a TCR-independent manner similar to NK cells (18, 64–67). In the present study, the poorly studied cytokine IL-32 was found to be a novel mediator of innate-like T-cell activation, acting on $CD161^{++}$/MAIT and $V\delta2^{+}$ γδT cells (Figure 8-2). In particular, IL-32 β and γ isoforms enhanced cytokine-mediated responses, for example, by augmenting IFNγ and GzmB expression.

IL-32 is expressed by both non-immune and immune cells, although the highest expression has been linked to immune-related tissues (109, 110). In the present study, it was found that CD161-expressing cells, particularly innate-like T cells including $CD161^{++}$/MAIT and $V\delta2^{+}$ γδT

cells can express IL-32 upon stimulation with IL-12, IL-12+IL-18 and *E. coli* (Figure 8-2). In addition, both innate-like and conventional T cells expressed IL-32 in response to IL-2, IL-7 or IL-15 stimulation in a TCR-independent manner or upon anti-CD3/anti-CD28 stimulation. After stimulation, there was a trend of higher IL-32-expression in innate-like T cells compared to conventional T cells. Cytokine-stimulated CD161-expressing T cells, particularly CD161^{++}/MAIT and Vδ2^{+} γδT cells, also showed up to 4-8-fold higher frequencies of IL-32 expressing cells compared to stimulated NK cells, the cells in which IL-32 expression was first discovered. This suggests that innate-like T cells could be a major source of IL-32.

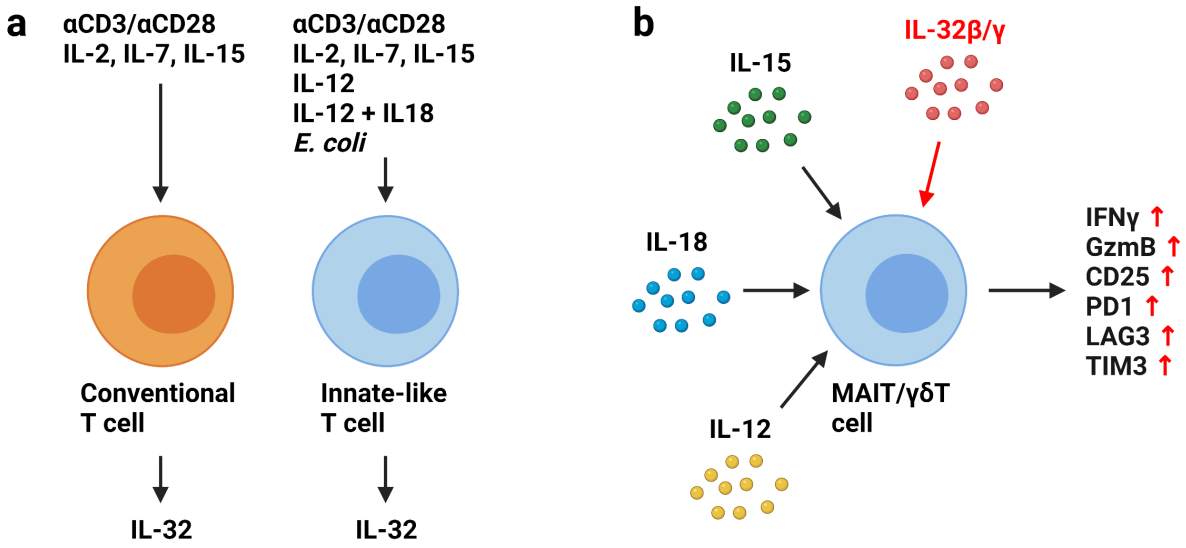


Figure 8-2. IL-32 expression and function associated with T cells. Illustration summarising the key findings of this study. (a) All T-cell subsets, including conventional and innate-like T cells, can express IL-32 upon stimulation with common γ-chain cytokines IL-2, IL-7 and IL-15 in a TCR-independent manner. In addition, T cells can express IL-32 upon TCR-stimulation using anti-CD3/anti-CD28 antibodies. Innate-like T cells can express IL-32 specifically in response to stimulation with IL-12, IL-12 + IL-18 or *E. coli*. Overall, the proportion of IL-32-expressing innate-like T cells upon stimulation is higher than that of stimulated conventional T cells. (b) IL-32β or -γ can enhance cytokine-mediated responses of innate-like T cells including MAIT and γδT cells, particularly in combination with IL-15 alone, IL-15+IL-12, IL-15+IL-18 or IL-12+IL-18. This includes the increase of IFNγ and GzmB expression, but also the upregulation of CD25, PD1, LAG3 and TIM3. This figure was created with BioRender.com.

These results provide a better understanding of IL-32 expression and function, which can be translated to advanced treatments of diseases where IL-32 has been implicated, including infection, autoimmune disease and cancer (221, 257, 320). For example, IL-32 is overexpressed and suggested to be associated with pathogenesis in rheumatoid arthritis,

inflammatory bowel disease, Chron's disease, and atherosclerotic arterial vessel tissue. (229, 255, 321, 441). In addition, IL-32 can have detrimental effects in infection by contributing to the immunopathology in HBV and HCV infection (242, 442, 443), or by mediating immunosuppression in HIV infection (267). Detrimental IL-32 activity could be neutralised using monoclonal antibodies or its expression reduced with agents such as COX-2 inhibitors (235) or caproic acid (444).

Conversely, IL-32-mediated protection has been reported against various pathogens, including bacteria such as *Mycobacterium tuberculosis* (263, 264, 445, 446) and *Mycobacterium leprae* (243), and both RNA and DNA viruses such as HSV-2, HBV and HIV by inducing antiviral pathways (261, 319, 447, 448). In addition, IL-32 has an anti-inflammatory role in a murine model of allergic asthma (449). Where beneficial, IL-32 could be administered or its expression could be promoted by mechanisms demonstrated in the present study.

In this study, the role of IL-32 in the anti-cancer immune response was investigated, as little research has been done on it before. Similar to the results obtained from analysing *in vitro*-stimulated PBMCs, *IL32* was highly expressed by innate-like T-cell subsets (MAIT and γδT cells) in addition to Tregs and conventional memory T cells in breast cancer. The pan-cancer *IL32* gene signature generated in this study was associated with pro-inflammatory processes including immune response activating signal transduction, antigen presentation, cytokine signalling and T-cell activation. These results expand on the observation that IL-32 is associated with myeloid markers and DC maturation in melanoma and with T-cell response genes in both melanoma and breast cancer (286, 293). Cell types that were associated with the most significant *IL32* signature genes included NK cells, other ILCs, MAIT, γδT, Tregs and memory T cells in breast cancer, suggesting their involvement in IL-32-mediated immune responses in cancer.

The pan-cancer *IL32* signature included genes encoding for mediators of the anti-cancer immune response, such as granzymes, perforin, granulysin, various chemokines and cytokines, but it also contained genes associated with immunosuppression such as *IDO* and *FOXP3*, and genes encoding for inhibitory immune checkpoint receptors. Similar observations have been made specifically in oesophageal cancer, where IL-32 is associated with GzmB and IFNγ expression, but also correlated with Tregs and *FOXP3* expression. It has been suggested that IL-32 can even promote Treg development in cancer (295, 296). Further associations of IL-32 with anti-inflammatory processes were described in cutaneous T-cell lymphoma, where it promotes the differentiation of IDO-expressing DCs and macrophages and correlates with IL-10 (294). These results indicate that IL-32 could have both tumour-enhancing and -inhibiting effects, similar to the dual roles observed in infection and autoimmunity.

The dichotomy of IL-32 is also reflected in the results of the survival analysis across 26 cancer types. Both *IL32* gene expression and *IL32* signature enrichment was associated with clinical outcome in certain cancer types. Depending on the cancer type, associations with prognosis were either favourable or adverse, suggesting tumour-specific pathways.

The dual role of IL-32 in different diseases needs to be further addressed. The role of IL-32 in cancer is even more complex than in other diseases, as besides its role in regulating and mediating the anti-cancer immune response, it can directly act on cancer cells, mediating both anti- and pro-cancer effects (257). The dual nature of IL-32 could be explained by the existence of different splice variants with different roles and complex interactions (226, 228). A precise understanding of the role of IL-32 isoforms could allow targeted disruption of immunosuppressive and tumour-promoting functions while maintaining beneficial anti-cancer cytotoxic effects and immune-activating functions.

8.2.2. Future work

The study of IL-32 could benefit from further work addressing the following aspects:

- Investigate the effect of IL-32 on TCR-mediated activation of conventional and innate-like T cells
- Investigate whether IL-32 can activate innate-like T cells in combination with other common γ-chain cytokines in a similar manner to that observed with IL-15
- Investigate potential positive feedback loops consisting of IL-32 expression by activated innate-like T cells and subsequent augmentation of innate-like T cells activation by IL-32
- Investigate the mechanisms through which IL-32 expression is induced in conventional and innate-like T cells in cancer
- Investigate the impact of conventional and innate-like T cell-derived IL-32 on cancer cells and other tumour-infiltrating immune cells
- Investigate the role of IL-32 in cancer in an isoform-specific manner

8.3. The role of CD161 in cancer

8.3.1. Key findings and their relevance

KLRB1, encoding for CD161, has recently been described as the most favourable prognostic pan-cancer biomarker by Gentles et al. (130). The association of *KLRB1* with estimated abundances of different immune subsets was also investigated. It was shown that *KLRB1* expression is most correlated with γδT, CD8 T and CD4 memory T-cell subsets, which were all amongst the most favourable prognostic cell types across cancers. The study had some limitations, however, as the analysis lacked various *KLRB1*-expressing subsets such as MAIT cells (130). In addition, the estimation of γδT-cell abundances showed very poor performance during method validation (431). Lastly, CD8 T and CD4 memory T-cell subsets were too broadly defined subsets and therefore unhelpful as determinants to attribute the favourable prognostic association of *KLRB1* across cancers to a specific cell type (130). The question of

which of the CD161-expressing immune cell subsets contribute to a positive outcome in cancer patients is highly relevant, however, as CD161-expressing immune subsets are attractive targets for immunotherapy (329, 345). For example, MAIT cells and γδT cells, particularly $V\delta2^+$ γδT cells, comprise relatively large populations in blood (88, 329), can home to various tissues that are frequent sites of cancer development such as the mucosa of the gut (329, 450–452), can infiltrate primary tumours and metastases (329, 332–339, 349, 353, 453), are capable of producing anti-cancer effector cytokines such as IFNγ very rapidly upon activation and possess cytotoxic capacity (65, 66, 86, 329, 333, 345). Importantly, both cell types are not MHC-restricted, eliminating the risk of graft-versus-host-disease which opens the door for donor-unrestricted therapeutics with adoptive transfer (79, 80, 97, 329, 345, 454, 455). MAIT cells also express the multidrug receptor ABCB1 (also called MDR1), which equips them with some resistance against certain chemotherapeutic agents (84, 329, 456, 457). Moreover, genetic inactivation of *KLRB1* or blocking CD161 with monoclonal antibodies has been shown to enhance tumour-killing ability of CD161-expressing T cells (77), which could potentially be exploited in cancer therapies to unleash the full potential of CD161-expressing cells.

To investigate to which immune cell subsets the favourable prognostic association of *KLRB1* can be attributed to, ImmuCellAI-inferred immune cell type abundances within TCGA data were used in this study (421). NK, TFH, CD8 T, TC, γδT and TRM cells were highly correlated with *KLRB1* expression and were amongst the most favourable prognostic cell types across cancers (Figure 8-3). An exception was the γδT-cell subset, which showed only moderate correlation with *KLRB1*, most likely due to the fact that its signature covers total γδT cells, including both CD161-positive and CD161-negative γδT-cell subsets. The association of CD8 T, TC, and TRM signatures with *KLRB1* expression is most likely attributable to the highly polyfunctional and cytotoxic $CD161^{int}CD8^+$ T-cell subset (73). MAIT, TH17 and TH1 cells showed correlation with *KLRB1* and/or showed association with favourable prognosis in some cancers, but ranked overall lower compared to other cell types. NKT cells showed inverse

correlation with *KLRB1* and were associated with adverse prognosis across cancers. Many of the analysed immune subsets were highly correlated among each other, which made linking the prognostic association of *KLRB1* across cancers with a specific immune subset challenging. The prognostic association of *KLRB1* across cancers might be attributable to multiple immune subsets, however.

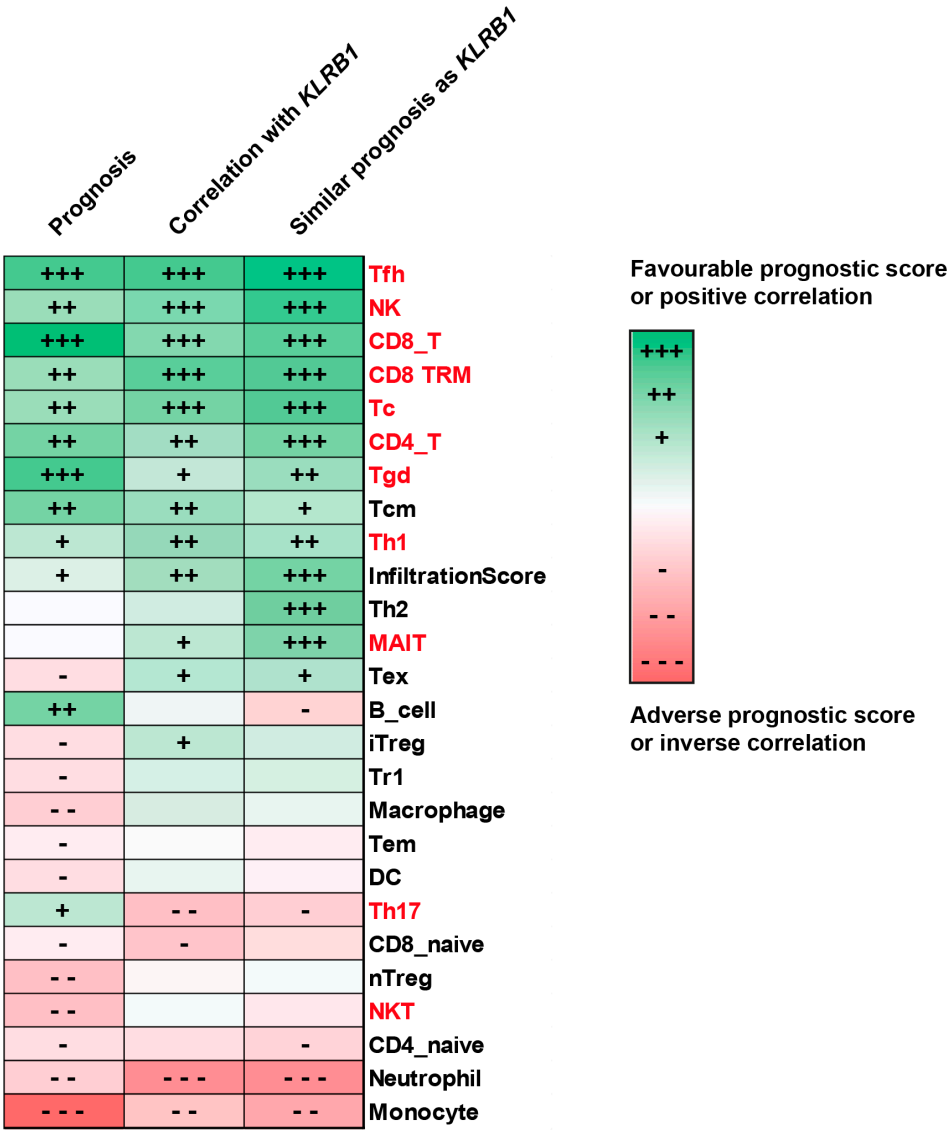


Figure 8-3. Association of various immune cell types with outcome and *KLRB1* in cancer. Scores for the prognostic association of immune cell types across cancers (left column), the correlation of cell types with *KLRB1* across cancers (centre column) and the correlation between the HR of cell types and the HR of *KLRB1* across cancers (right column) are shown. Colours and symbols indicate the direction and magnitude of prognostic scores or correlation coefficients (green/plus symbol = favourable prognosis or high correlation, red/minus symbol = adverse prognosis or inverse correlation). Cell types are ordered according to the rank product of the columns. Labels of cell types which are known to express CD161/*KLRB1* are highlighted in red. The general CD8 and CD4 T-cell populations are also highlighted as they contain other CD161-expressing subsets.

In order to exploit the mechanisms that are linked to the favourable prognostic association of *KLRB1* across cancers for therapeutic purposes, it is crucial to understand which cell types *KLRB1* is associated with in cancer. Although this is challenging to completely disentangle due to intercorrelation among different immune subsets, a group of cells that are associated with *KLRB1* and are amongst the most favourable prognostic cell types across cancers were identified in this study, including NK, TFH, γδT, CD8 T, TC and *KLRB1*-expressing TRM cells. In addition, it is important to understand the function and regulation of CD161-expressing cell types for their exploitation in cancer therapies. In this study, IL-32 was discovered to be a novel regulator the activity of CD161-expressing T-cell subsets. Moreover, IL-32 expression was identified as a novel function of CD161-expressing T cells upon both cytokine stimulation in a TCR-independent manner and TCR stimulation. These results expand the knowledge of the regulation and function of CD161-expressing immune subsets and their role in cancer, which could potentially allow the development of strategies for their manipulation towards desirable therapeutic outcomes, or their use as clinical biomarkers.

8.3.2. Future work

The study of the role of CD161 in cancer could benefit from further work addressing the following aspects:

- Generate immune cell type signatures for the estimation of cellular composition in cancer that include more and better defined CD161-expressing immune cell subsets such as $CD161^{+}$ILCs, $CD161^{+}V\delta2^{+}$ γδT, $CD161^{+}V\delta2^{-}$ γδT, $CD161^{int}CD8^{+}$ TRM and $CD161^{+}$ NK cells
- Confirm the results of this study using alternative methods for estimating cellular composition in cancer
- Confirm the results of this study using an alternative repository of cancer studies with accompanying survival data such as PRECOG

8.4. Major limitations

A major limitation of this study is the analysis of total *IL32* expression in cancer, which did not allow me to shed light on dual role of IL-32. Isoform-specific studies could allow the dissection of the precise mechanisms contributing to the pro- and anti-inflammatory effects of IL-32 in the anti-cancer immune response. In addition, in the study investigating to which cell type the favourable prognostic association of *KLRB1* is attributable to, TFH cells and monocytes were the only immune subsets that contained *KLRB1* in their gene signature which might have skewed the results. Alternative signatures and methods for estimating cellular composition in cancer transcriptomics data should be used to confirm the results of this study. Immune cell signatures with more and better defined CD161-expressing immune subsets may provide further insights. Follow-up studies are required to elucidate the function of the poorly studied CD161-expressing TFH cells in cancer.

Another complication was the observation that several immune subsets that can express CD161 were highly correlated with each other. This makes it difficult to determine which immune subsets truly contribute to promote a positive outcome for cancer patients and which subsets are correlated with a favourable prognosis merely due to co-infiltration of tumours without a functional role. It needs to be determined if the correlation is caused by methodological limitations, or whether there is a true correlation among several tumour-infiltrating CD161-expressing immune subsets. If the correlation is a result of methodological limitations, improved signatures and tools for the estimation of cellular composition could allow disentangling of this matter further. Generating a TCGA-like repository based on scRNA-seq or CITE-seq data rather than bulk RNA-seq data may provide a better basis for investigating the question of which CD161-expressing immune subset is most crucial in promoting a favourable outcome in cancer. If there is a true correlation between different tumour-infiltrating CD161-expressing cell types, mechanistic experiments may provide more insight. The use of animal models, such as mouse models, to answer the

outstanding questions has some major limitations. For some human CD161-expressing immune subsets, such as such as $V\delta2^{+}V\gamma9^{+}$ γδT cells, there is no direct counterpart in mice (458). For other cell types that show a high degree of conservation across species, such as iNKT and MAIT cells, there are still interspecies differences observable, including cell numbers, molecular mechanisms facilitating their interactions, coreceptor expression, functional and tissue homing properties (459–463). Therefore, mouse models are suboptimal in studying the complicated interplay and redundancy of a group of highly correlated cell types. Mouse models additionally have more general limitations, failing to reflect environmental and genetic variation present in human cohorts (459, 464). To gain mechanistic insight by means other than animal models, genetic experiments of nature and the results of interventions of various kinds, such as the administration of blocking antibodies or effectors, can be studied. As long as the knowledge about the prognostic role of CD161-expressing cell types and information about their regulation and function can be harnessed in a way sufficient for the development of an intervention or their use as a prognostic marker, there may not be a need to dissect the full mechanism.

8.5. Summary and conclusion

The purpose of this study was to investigate the regulation and function of CD161-expressing T cells and to study their role in cancer. ChipCytometry, a novel method for high-content biomarker analysis, was developed as a truly viable technique in order to identify and deeply phenotype immune cell types that express CD161 in blood and tissue, which included subsets of NK and T cells, particularly innate-like T-cell subsets such as MAIT and γδT cells. In addition, novel mechanisms of CD161-expressing innate-like T-cell regulation and activation by the relatively obscure cytokine IL-32 were discovered in this study. Moreover, the ability of CD161-expressing T-cell subsets to express IL-32 was demonstrated. Studying the role of IL-32 in cancer revealed that it is linked to genes associated with immune response activation and T-cell responses but also to genes associated with immune inhibition. Cell types most

highly associated with IL-32 in cancer included CD161-expressing subsets such as MAIT and γδT cells in addition to memory T cells and Tregs. The association of CD161 with favourable prognosis in cancer was not attributable to a single cell type, but linked to multiple CD161-expressing cell types. The poorly studied TFH cell subset that can express CD161 was particularly highly associated with a favourable prognosis in cancer. A speculative model illustrating the role of CD161-expressing cells and IL-32 in cancer, based on the findings of this study and the knowledge from the literature, is shown in Figure 8-4.

Taken all together, the results of this study expand the current understanding of the regulation and function of CD161-expressing immune subsets and their role in cancer, setting the stage for their use as novel therapeutic mechanism or as clinical biomarkers.

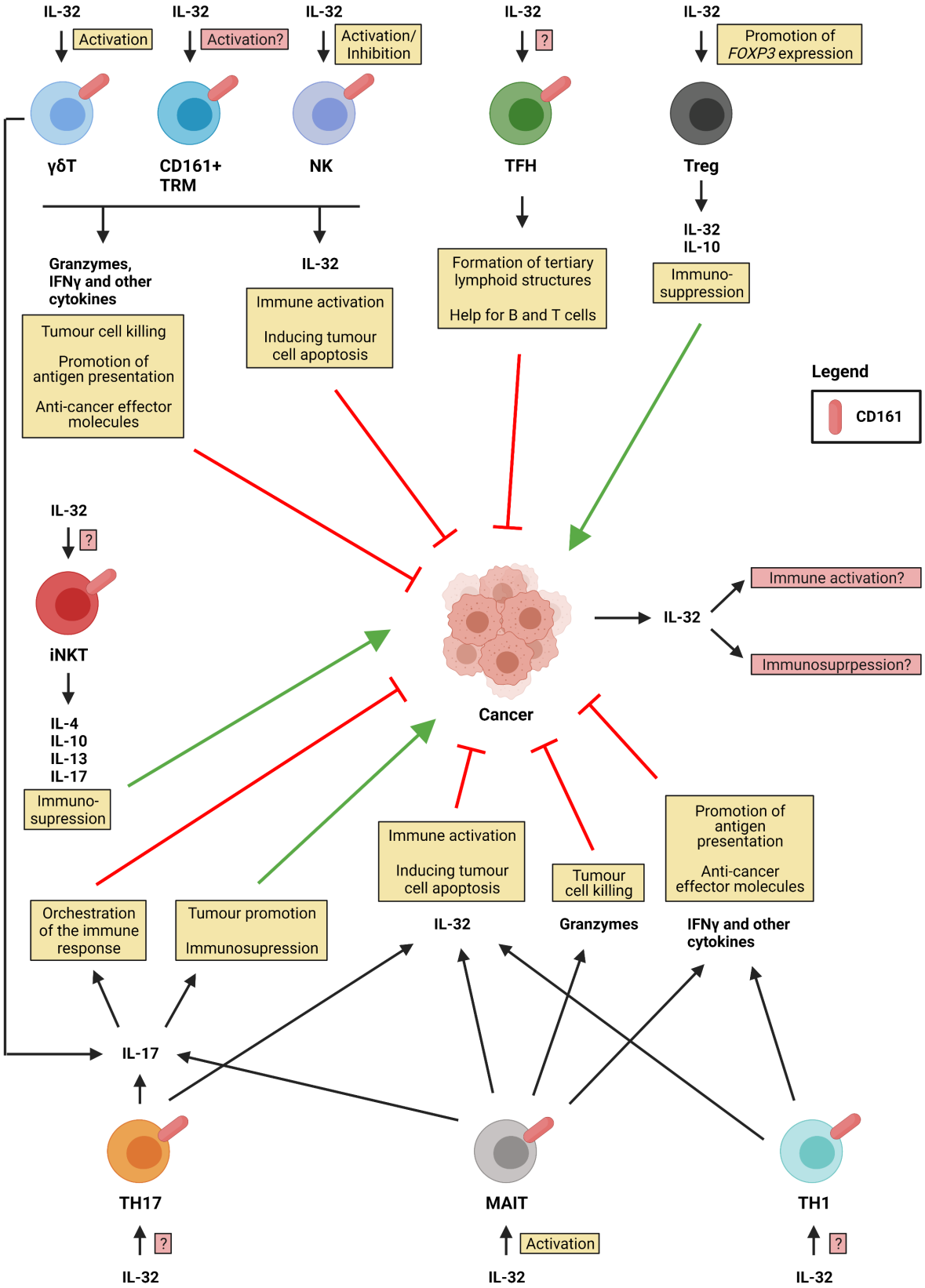


Figure 8-4. The role of CD161-expressing cells and IL-32 in cancer. A speculative model illustrating the role of CD161-expressing cells and IL-32 in cancer was created, based on the findings of this study and the knowledge from the literature. IL-32 can promote Treg development by promoting *FOXP3* expression. Tregs can promote tumour progression by suppressing the anti-cancer immune response, for example via immunosuppressive

cytokines such as IL-10. Tregs can also express IL-32, and given the immunoinhibitory role of Tregs, Treg-derived IL-32 is probably an isoform involved in immunoinhibitory pathways. IL-32β/γ can promote the activation of γδT cells and most likely also of CD161-intermediate cytotoxic TRM cells. The responsiveness of CD161-intermediate TRM cells is most likely lower compared to innate-like T cells such as γδT cells. IL-32 can both promote and inhibit NK cell effector functions, most likely a mediated by different isoforms. γδT, CD161^{+} TRM and NK cells are associated with favourable prognosis across cancers due to inhibition of tumour progression by various mechanisms, including direct tumour cell killing and secretion of various effector cytokines such as IFNγ. In addition, γδT, CD161^{+} TRM and NK cells can express high levels of IL-32. In this context, IL-32 may have an immune-stimulating role and the ability to directly induce tumour cell apoptosis. TFH cells are highly associated with favourable prognosis across cancers, most likely due to their role in the formation of tertiary lymphoid structures in cancer, where adaptive immune responses of B and T cells are orchestrated. In contrast, iNKT cells are associated with adverse prognosis, most likely due their polarisation to subsets that express immunoinhibitory cytokines, such as IL-4, IL-10, IL-13 and IL-17. The effect of IL-32 on TFH, iNKT, TH1 and TH17 cells is unexplored. IL-32β/γ can enhance the activation of MAIT cells, however. MAIT, TH1 and TH17 have overall a less beneficial association with cancer patient survival compared to other cell types such as γδT, CD161^{+} TRM, NK and TFH cells. TH1 cell responses, mediated via cytokines such as IFNγ, are generally considered to inhibit tumour progression. There is a dual role of TH17 cell responses, mediated via cytokines such as IL-17, which can either supress the anti-cancer immune response and promote tumour progression or orchestrate and promote the anti-cancer immune response. MAIT cells can express both type 1 and type 17 cytokines and have cytotoxic capacity to kill tumour cells. MAIT, TH1 and TH17 cells can express IL-32, which can promote immune responses and directly induce tumour cell apoptosis. It is unknown whether cancer cell-derived IL-32 activates or inhibits anti-cancer immune responses. CD161-expressing cell types are indicated. This figure was created with BioRender.com.

APPENDICES

I. Appendices I

Appendix Table I-1. Antibodies to stain for extracellular markers using cell suspension ChipCytometry. Antibodies were optimised to stain samples that were fixed for 5 minutes.

Marker	Clone	BUV395	BV421	FITC	PE	PerCP-Cy5.5	Manufacturer	Order number
CD2	RPA-2.10			1:50	1:80			300207, 300206
CD3	UCHT 1	1:25		1:25		1:50	BD Biosciences; BioLegend	563546; 300406, 300428
CD4	RPA-T4			1:20	1:20	1:20	BD Biosciences; BioLegend	555347; 300506, 300530
CD5	UCHT2				1:25		BioLegend	300607
CD7	M-T701	1:10					BD BioSciences	565979
CD8α	SK1					1:30	BioLegend	301032
CD8β	REA715				1:20		Miltenyi	130-110-568
CD10	HI10a						BioLegend	312203
CD11a	REA378				1:20		Miltenyi	130-105-479
CD11b	ICRF44				1:20		eBioscience	12-0118-71
CD11c	S-HCL-3				1:20		BioLegend	371503
CD14	MφP9, RMO52, M5E2	1:20			1:20	1:20	BD Biosciences, Beckman Coulter, BioLegend	563561, IM0650U, 301806, 301848
CD16	3G8				1:1,200 - 1:400		BioLegend	302007
CD18	TS1/18					1:50	BioLegend	302120
CD19	LT19				1:100		Miltenyi	130-091-247
CD20	2H7	1in20					BD Biosciences	563782
CD24	32D12				1:25		Miltenyi	130-098-861
CD25	3G10				1:20 (1:100)		Miltenyi	130-101-428 , 130-117-381
CD26	2A6				1:100		eBiosciences	12-0269-42
CD27	LG.3A10				1:200		BioLegend	124210
CD28	CD28.2				1:25		BioLegend	302908
CD31	WM59					1:40	BioLegend	303132
CD32	FUN-2				1:80		BioLegend	303205
CD38	HIT2	1:20				1:20	BD Biosciences, BioLegend	563811, 303522
CD39	MZ18-23C8				1:25		Miltenyi	130-099-926
CD40	5C3	1:10					BD Biosciences	565202
CD44	DB105				1:300		Miltenyi	130-095-108
CD45	HI30	1:50	1:50	1:40	1:50	1:25	BD Biosciences, BioLegend	563792; 304029, 304028, 304039, 304038
CD45RA	HI100					1:25	BioLegend	304122

Marker	Clone	BUV395	BV421	FITC	PE	PerCP-Cy5.5	Manufacturer	Order number
CD45RO	UCHL1	1:10				1:20	BD Biosciences	564292
CD49a	TS2/7				1:20		BioLegend	328303
CD54	HA58				1:80		eBioscience	12-0549-41
CD56	AF12-7H3				1:100 - 1:20		Miltenyi	130-098-137
CD57	TB03				1:20		Miltenyi	130-099-185
CD69	FN50				1:20		BioLegend	310906
CD71	CY1G4					1:40	BioLegend	334114
CD79a	HM47					1:20	BioLegend	333508
CD95 (FAS)	DX2				1:20		Miltenyi	130-099-094
CD97	VIM3b				1:40		BioLegend	336307
CD123	9F5				1:20		BD Biosciences	340545
CD134 (OX40)	Ber-ACT35				1:25		BioLegend	350004
CD137 (4BB1)	4B4-1				1:20		BioLegend	309804
CD154	5C8				1:20		Miltenyi	130-098-884
CD161	191B8				1:50		Miltenyi	130-092-677
CD178 (FAS-L)	NOK-1				1:20		BioLegend	306407
CD183 (CXCR3)	G025H7, 1C6/CXCR3			1:20		1:10	BioLegend, BD Biosciences	353704, 560832
CD184 (CXCR4)	REA649				1:25		Miltenyi	130-109-885
CD185 (CXCR5)	J252D4		1:25				BioLegend	353919
CD196 (CCR6)	11A9					1:20	BD Biosciences	560467
CD197 (CCR7)	150503, G043H7	1:10		1:40		1:25	BD Biosciences, BioLegend	563977, 353216, 353219
CD218a (IL-18Ra)	H44				1:20		BioLegend, eBioscience	313808, 12-7183-42
CD223 (LAG3)	REA351				1:20		Miltenyi	130-105-495
CD244 (2B4)	C1.7				1:20		BioLegend	329507
CD273 (PD-L2)	24F.10C12				1:20		BioLegend	329606
CD274 (PD-L1)	29E.2A3				1:40	1:20	BioLegend	329737, 329738
CD278 (ICOS)	C398.4A					1:40	BioLegend	313518
CD279 (PD-1)	eBioJ105				1:25		eBioscience	12-2799-42
TIM3	REA635, 7D3				1:20, 1:30		Miltenyi, BD Biosciences	130-109-761, 563422
HLA-A,B,C (HLA-Class I)	W6/32			1:100			BioLegend	311404
HLA-DR	L243			1:100	1:300		BioLegend	307604, 307628
IgA	IS11-8E10				1:10		Miltenyi	130-099-108
IgD	IA6-2				1:50		BioLegend	348203
IgE	MHE-18					1:20	BioLegend	325511
IgG	G18-145	1:25					BD Biosciences	564229
IgM	MHM-88				1:20		BioLegend	314508
LIVE/DEAD™ Fixable Green Dead Cell Stain				1:100, 000			ThermoFisher Scientific	L34969

Marker	Clone	BUV395	BV421	FITC	PE	PerCP-Cy5.5	Manufacturer	Order number
TCR alpha/beta (αβTCR)	IP26				1:100 - 1:50		BioLegend	306707
TCR gamma/delta (γδTCR)	5A6.E9, MBSA43				1:20		Life Technologies, Miltenyi	MHGD04, 130-100-081
TCR Vα7.2	3C10				1:20	1:20	BioLegend	351706, 351710
TCR Vδ2	B6				1:400		BioLegend	331407

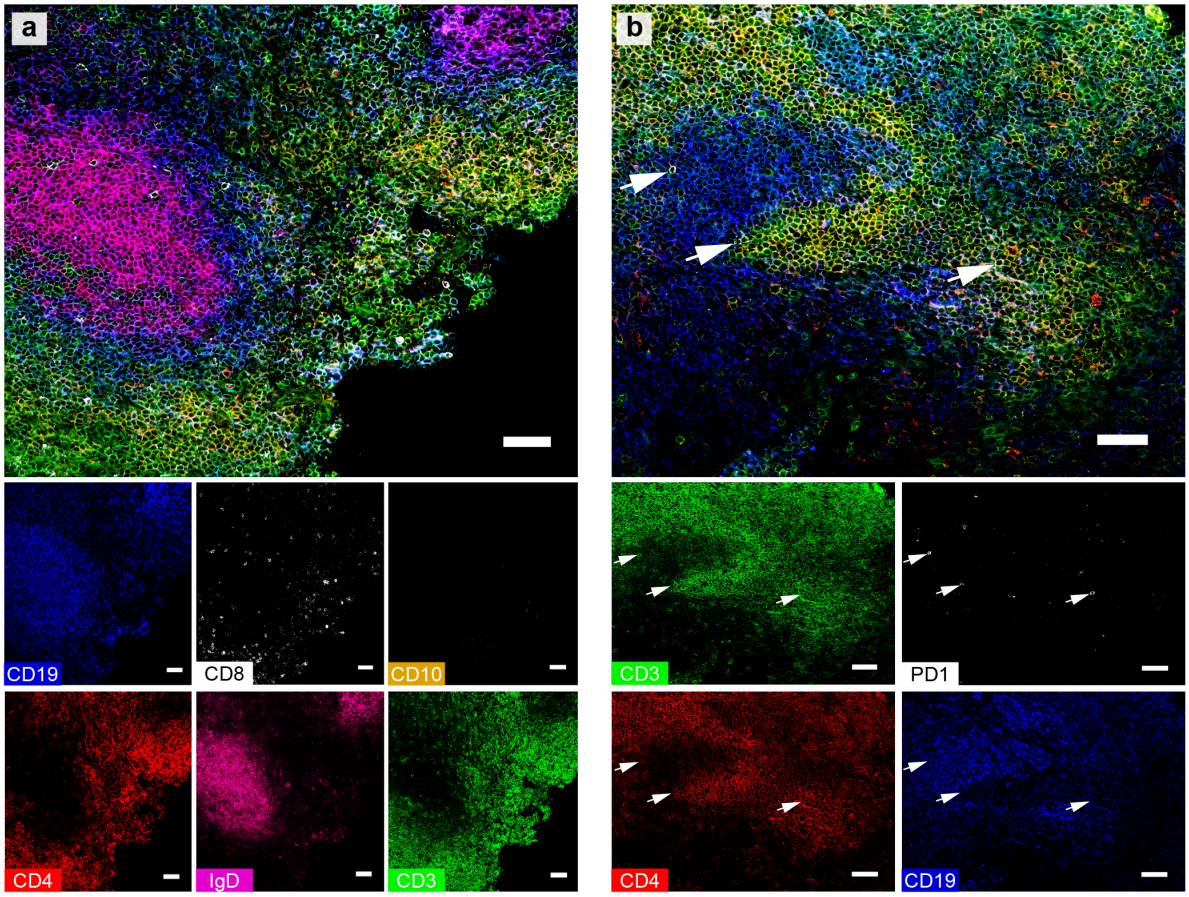
Appendix Table I-2. Antibodies to stain for intracellular markers using cell suspension ChipCytometry. Antibodies were optimised to stain samples that were fixed for 5 minutes.

Marker	Clone	BUV 395	BV 421	FITC	PE	PerCP-Cy5.5	Manufacturer	Order number
BCL6	REA373				1:10		Miltenyi	130-105-486
Eomes	WD1928				1:10		eBioscience	12-4877-42
FoxP3	259D/C7, 236A/E7, 3G3				1:10		BD Biosciences, eBioscience, Miltenyi	560046, 12-4777-41, 130-093-014
Granzyme A	CB9				1:10		BioLegend	507206
Granzyme B	GB11, GB12				1:25		eBioscience, Life Technologies	12-8899-41, MHGB04
Granzyme K	24C3				1:10		Immunotools	21144054
IL32 (-Biotin + αBiotin -PE)	KU32-52, 1D4-C5				1:10, 1:5,000		BioLegend	513501, 409004
IFNγ	4S.B3					1:100	eBioscience	45-7319-41
KI67	B56			1:40			BD Pharmigen	51-36524X
PLZF	Mags.21F7				1:10		eBioscience	12-9320-82
RORγT	Q21-559, AFKJS-9				1:10		BD Biosciences, eBioscience	563081, 12-6988-82
T-bet	4B10				1:10		BioLegend	644810

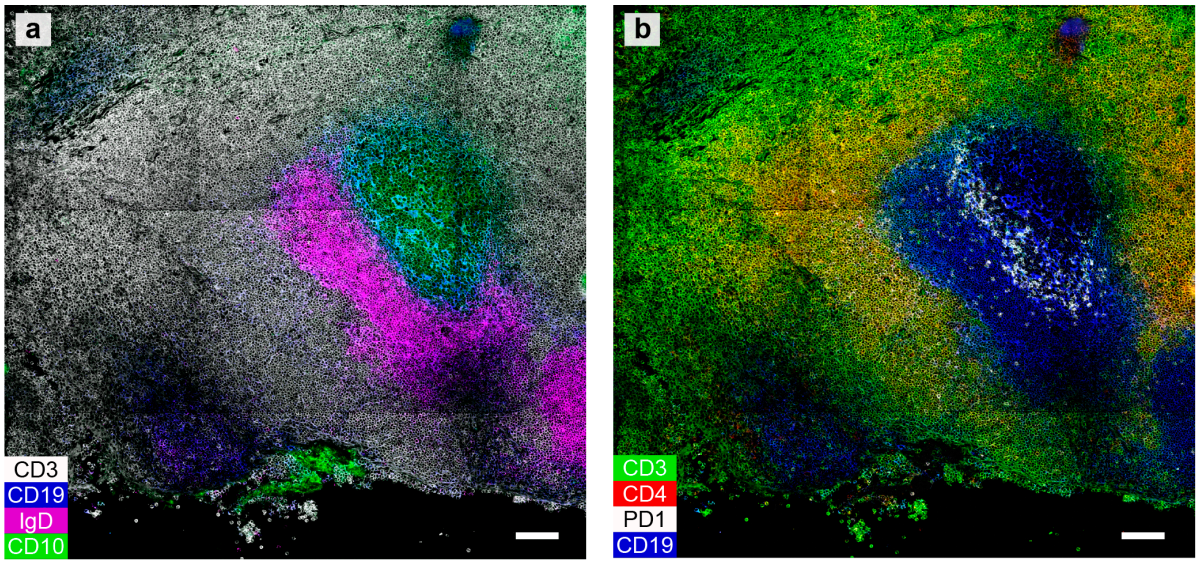
Appendix Table I-3. Antibodies to stain tissue sections using ChipCytometry. Antibodies were optimised to stain samples that were fixed for 5 minutes.

Marker	Clone	BUV395	BV421	FITC	PE	PerCP-Cy5.5	Manufacturer	Order number
DAPI			1:30M					
CD3	UCHT 1					1:500	BioLegend	300428
CD4	RPA-T4			1:25			BioLegend	300506
CD8	SK1					1:100	BioLegend	301032
CD10	HI10a				1:100		BioLegend	312203
CD19	LT19				1:1000		Miltenyi	130-091-247
CD32	FUN-2				1:1600		BioLegend	303205
CD38	HIT2					1:250	BioLegend	303522
IgD	IA6-2				1:500		BioLegend	348203

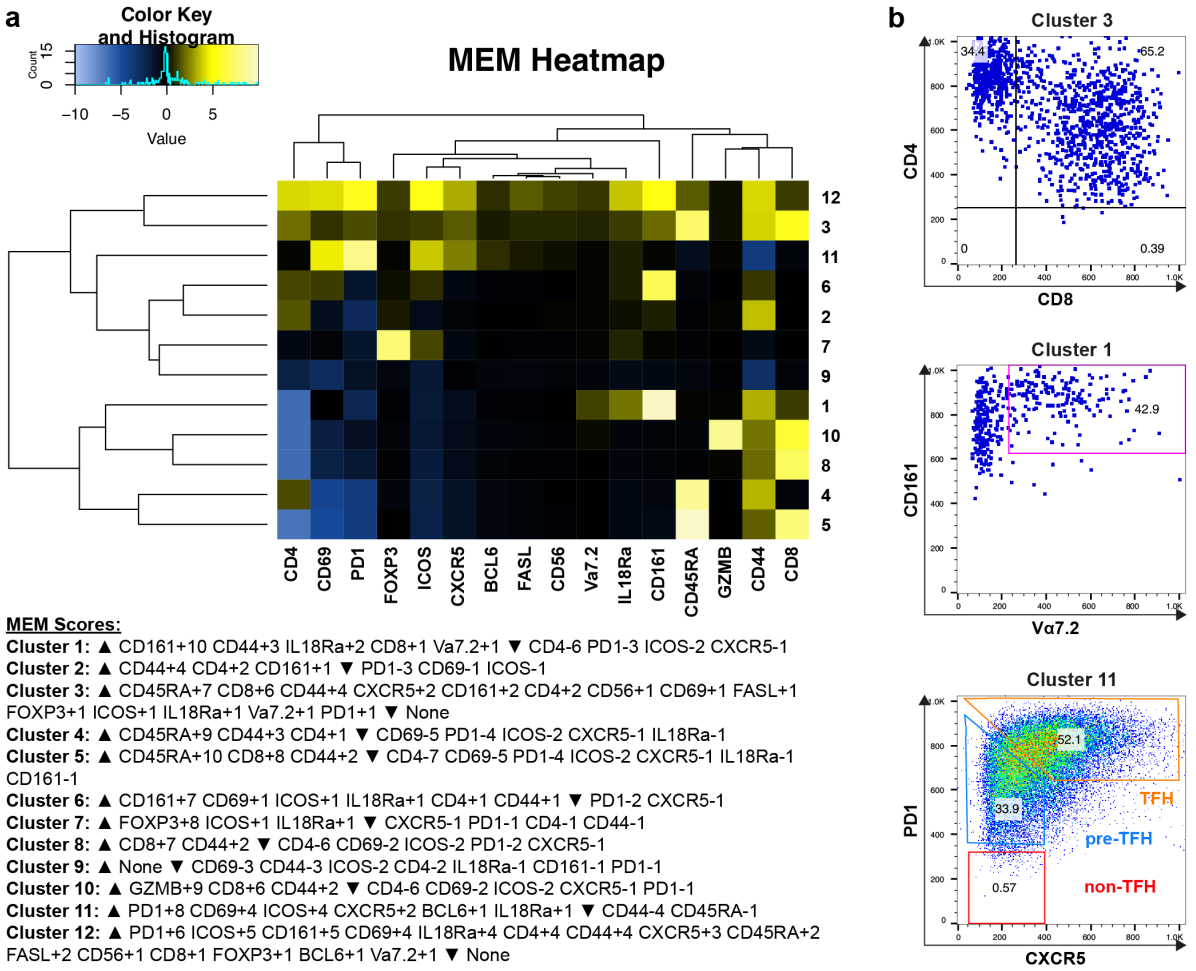
II. Appendices II



Appendix Figure II-1. Identification of the general human tonsil architecture and tonsillar CD4⁺ T-cell subsets using ChipCytometry (second example). Sections of PFA-fixed human tonsil tissue mounted in microfluidic chips were immunostained in consecutive runs using a panel of 12 fluorochrome-labelled antibodies. (a) Six markers were selected to depict the general human tonsil architecture: CD19 (blue), CD8 (white), CD10 (orange), CD4 (red), IgD (magenta) and CD3 (green). The large multicolour image shows a composite image of all the 6 markers, whereas the expression of individual markers is shown in the small panels. The B-cell zone (B-cell follicle) is characterised by CD19 expression, in which IgD outlines the mantle zone containing IgD-expressing naive B cells, and CD10 outlines the germinal centre containing CD10⁺ germinal centre B cells. Adjacent to the B-cell zone, CD3 expression outlines the T-cell zone (extrafollicular zone), including CD4⁺ and CD8⁺ T cells. Scale bars represent 50 µm. (b) A combination of CD4, CD19, CD3 and PD1 was chosen from the full marker panel to identify tonsillar CD4⁺ T cells and their subsets according to PD1 expression. The large multicolour composite image shows a merged image of CD19 (blue), CD3 (green), PD1 (white) and CD4 (red), while the smaller images demonstrate the expression of each marker individually. The T-cell zone is characterised by CD3 expression and includes CD4⁺ T cells; CD3⁺CD4⁺ cells appear yellow / orange in combination. PD1-expressing CD3⁺CD4⁺ are predominantly located in the B-cell zone, but a few are also located in the T-cell zone. This subset most likely includes pre-follicular (pre-TFH) and follicular T helper cells (TFH). CD3⁺CD4⁺PD1⁻ cells are predominantly located in the extrafollicular region and include non-follicular T helper cells (non-TFH). White arrowheads indicate examples of CD3⁺CD4⁺PD1⁺ cells. Scale bars represent 50 µm.

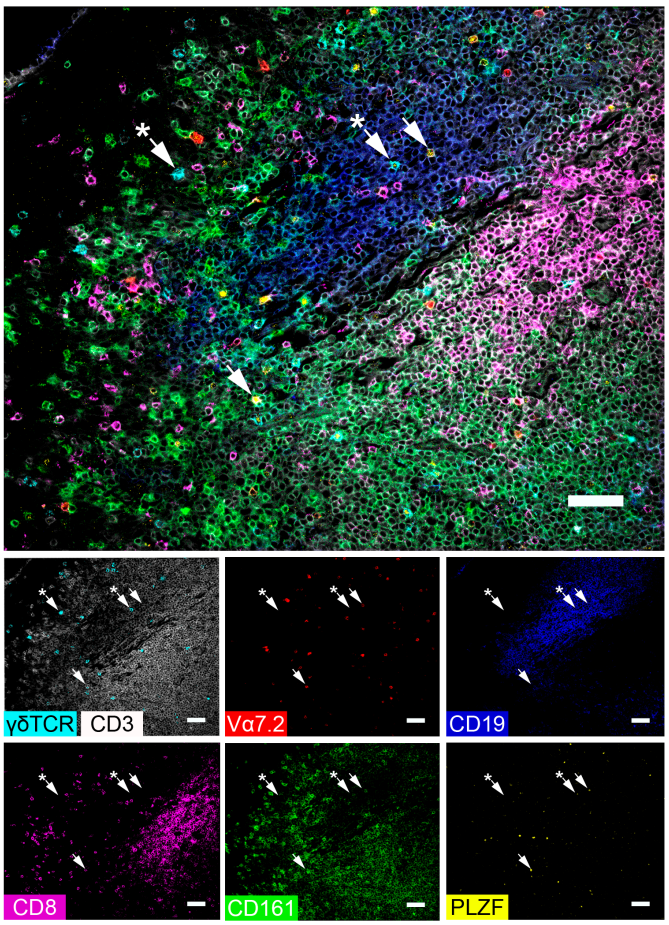


Appendix Figure II-2. ChipCytometry allows the acquisition of multiple adjacent positions of a tissue section that can be tiled to obtain a larger field of view. Human tonsil tissue was fixed, mounted on microfluidic chips and analysed by ChipCytometry with panel of 12 fluorochrome-labelled antibodies. Multiple adjacent positions were recorded and stitched together to obtain an overview over a larger tissue area. Different combinations of markers were chosen to illustrate different immune compartments in the tissue. (a) CD19 (blue), CD10 (green), IgD (purple) and CD3 (white) were chosen to illustrate different tonsil regions including extrafollicular T-cell zone ($CD3^+$), B cell follicle ($CD19^+$) and B cell sub-compartments including mantle zone (IgD^+CD10^-) and germinal centre zone (IgD^-CD10^+). For further information please refer to Figure 4-1 and Appendix Figure II-1a. (b) CD3 (green), CD4 (red), CD19 (blue) and PD1 (white) was chosen to depict PD1-expressing CD4 T cells and their location relative to B cell and T-cell zones. For further information refer to Figure 4-2 and Appendix Figure II-1b. Scale bars represent 100 µm.



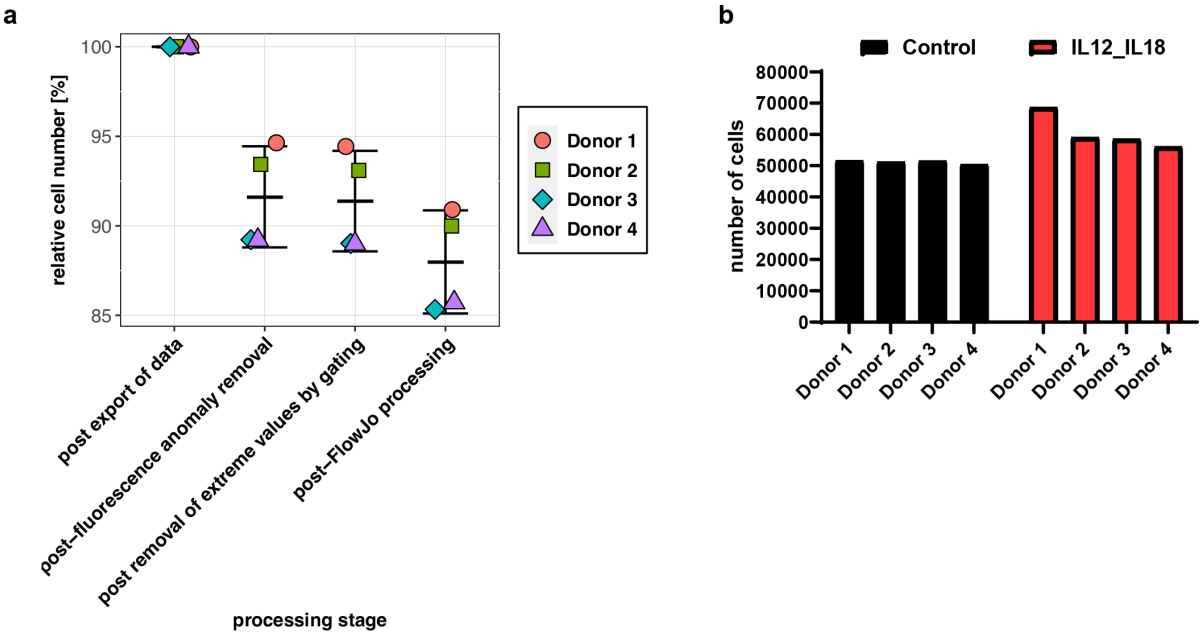
MEM Scores:
Cluster 1: ▲ CD161+10 CD44+3 IL18Ra+2 CD8+1 Va7.2+1 ▼ CD4-6 PD1-3 ICOS-2 CXCR5-1
Cluster 2: ▲ CD44+4 CD4+2 CD161+1 ▼ PD1-3 CD69-1 ICOS-1
Cluster 3: ▲ CD45RA+7 CD8+6 CD44+4 CXCR5+2 CD161+2 CD4+2 CD56+1 CD69+1 FASL+1 FOXP3+1 ICOS+1 IL18Ra+1 Va7.2+1 PD1+1 ▼ None
Cluster 4: ▲ CD45RA+9 CD44+3 CD4+1 ▼ CD69-5 PD1-4 ICOS-2 CXCR5-1 IL18Ra-1
Cluster 5: ▲ CD45RA+10 CD8+8 CD44+2 ▼ CD4-7 CD69-5 PD1-4 ICOS-2 CXCR5-1 IL18Ra-1 CD161-1
Cluster 6: ▲ CD161+7 CD69+1 ICOS+1 IL18Ra+1 CD4+1 CD44+1 ▼ PD1-2 CXCR5-1
Cluster 7: ▲ FOXP3+8 ICOS+1 IL18Ra+1 ▼ CXCR5-1 PD1-1 CD4-1 CD44-1
Cluster 8: ▲ CD8+7 CD44+2 ▼ CD4-6 CD69-2 ICOS-2 PD1-2 CXCR5-1
Cluster 9: ▲ None ▼ CD69-3 CD44-3 ICOS-2 CD4-2 IL18Ra-1 CD161-1 PD1-1
Cluster 10: ▲ GZMB+9 CD8+6 CD44+2 ▼ CD4-6 CD69-2 ICOS-2 CXCR5-1 PD1-1
Cluster 11: ▲ PD1+8 CD69+4 ICOS+4 CXCR5+2 BCL6+1 IL18Ra+1 ▼ CD44-4 CD45RA-1
Cluster 12: ▲ PD1+6 ICOS+5 CD161+5 CD69+4 IL18Ra+4 CD4+4 CD44+4 CXCR5+3 CD45RA+2 FASL+2 CD56+1 CD8+1 FOXP3+1 BCL6+1 Va7.2+1 ▼ None

Appendix Figure II-3. Cluster characterisation using Marker Enrichment Modeling (MEM) and FlowJo gating. (a) Cell clusters that were identified using FlowSOM as shown in Figure 4-3b were characterised with the help of MEM in R as described by Diggins et al. (37, 38). MEM scores ranging from -10 to +10 indicate positive or negative enrichment of each marker within a population compared to the average of all other populations. (b) Examples of using FlowJo gating for cluster characterisation. Median marker expression (Figure 4-3c) and MEM scores (Appendix Figure II-3a) provided in certain cases ambiguous information for cell cluster labelling. An example is cluster 3, which showed increased median marker expression values and positive MEM scores for both CD8 and CD4 compared to the other clusters. To determine whether the cluster contained CD4 SP and CD8 SP T cells or DP T cells, CD4 and CD8 expression was inspected within cluster 3 using FlowJo as shown in the top panel. This revealed that cluster 3 contained both CD4 SP T cells and DP T cells, but no CD8 SP T cells. Another example is cluster 1, for which FlowJo inspection (middle panel) revealed that it contained CD161^{++} T cells including both Vα7.2^{+} MAIT cells (pink gate) and Vα7.2^{-} non-MAIT cells. The dichotomy of Vα7.2 expression in this cluster was not obvious from evaluating Vα7.2 median marker expression or MEM score. The last example of FlowJo cluster inspection (bottom panel) showed that cluster 11 contained both pre-TFH (CXCR5^{-}PD1^{+}) as well as TFH (CXCR5^{+}PD1^{+}) cells. Final labels for all cell clusters were determined in a multi-pronged approach considering median marker expression of each marker, MEM Scores and manual inspection of clusters in FlowJo.

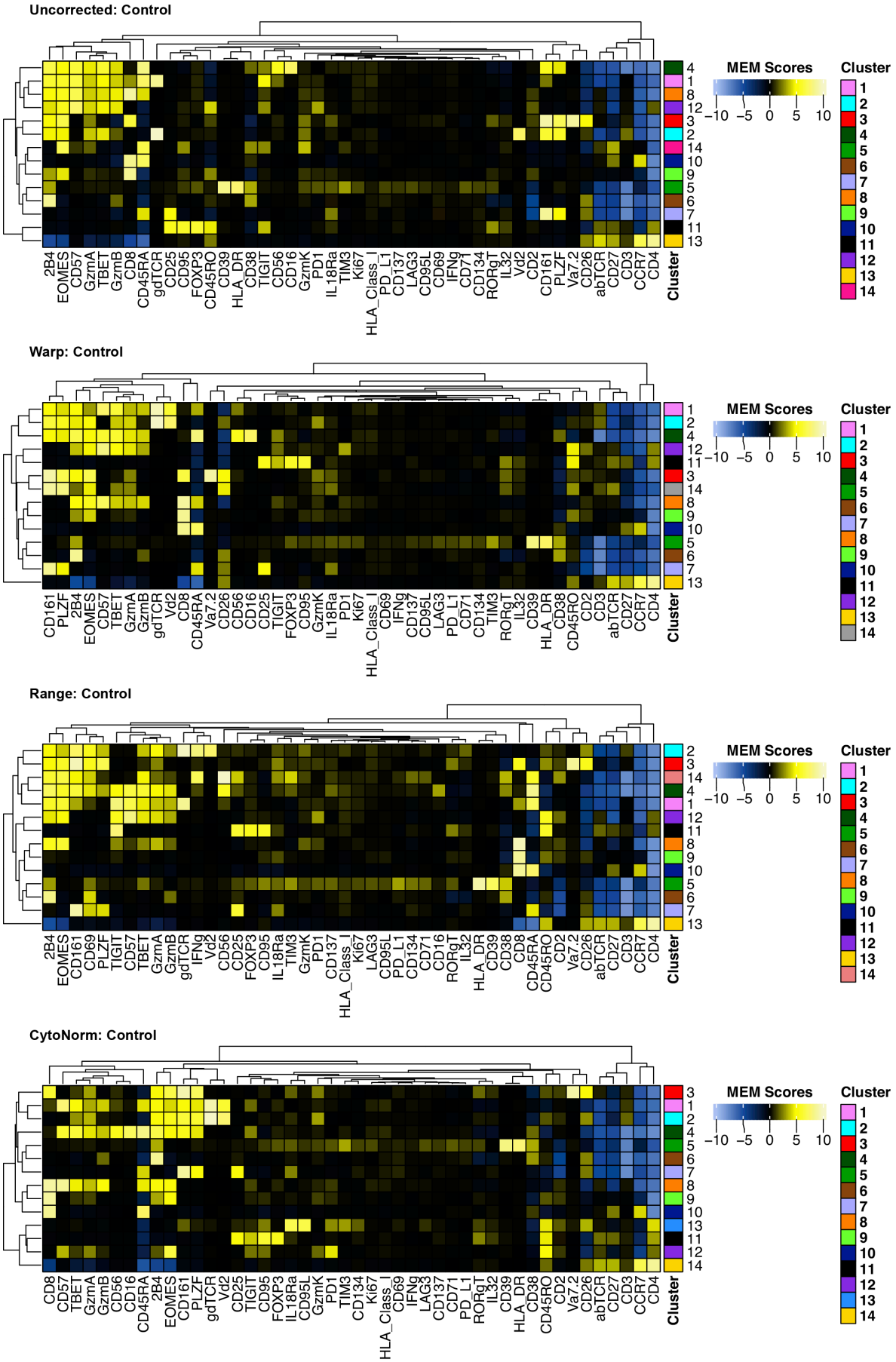


Appendix Figure II-4. Identification of rare immune subsets in human tonsils including MAIT and γδT cells. A combination of the markers γδTCR (cyan), CD3 (white), Vα7.2 (red), CD19 (blue), CD8 (magenta), CD161 (green) and PLZF (yellow) were selected from the available panel to illustrate the presence of MAIT cells and γδT cells within the tonsil. The large panel shows a merged multicolour composite image with all seven markers and the smaller panels show single- and dual-colour images as indicated. A few examples of MAIT cells ($CD3^+Vα7.2^+CD161^+PLZF^+$) are indicated by white arrowheads without an asterisk. CD8 was co-expressed in some of the MAIT cells, but there were also $CD8^-$ MAIT cells. γδT cells can be recognised side by side with MAIT cells in the T-cell zone ($CD3^+$, white) but also adjacent and within the B cell zone ($CD19^+$, blue). A few examples of many γδT cells are indicated by white arrows with an asterisk. Scale bars represent 50 µm.

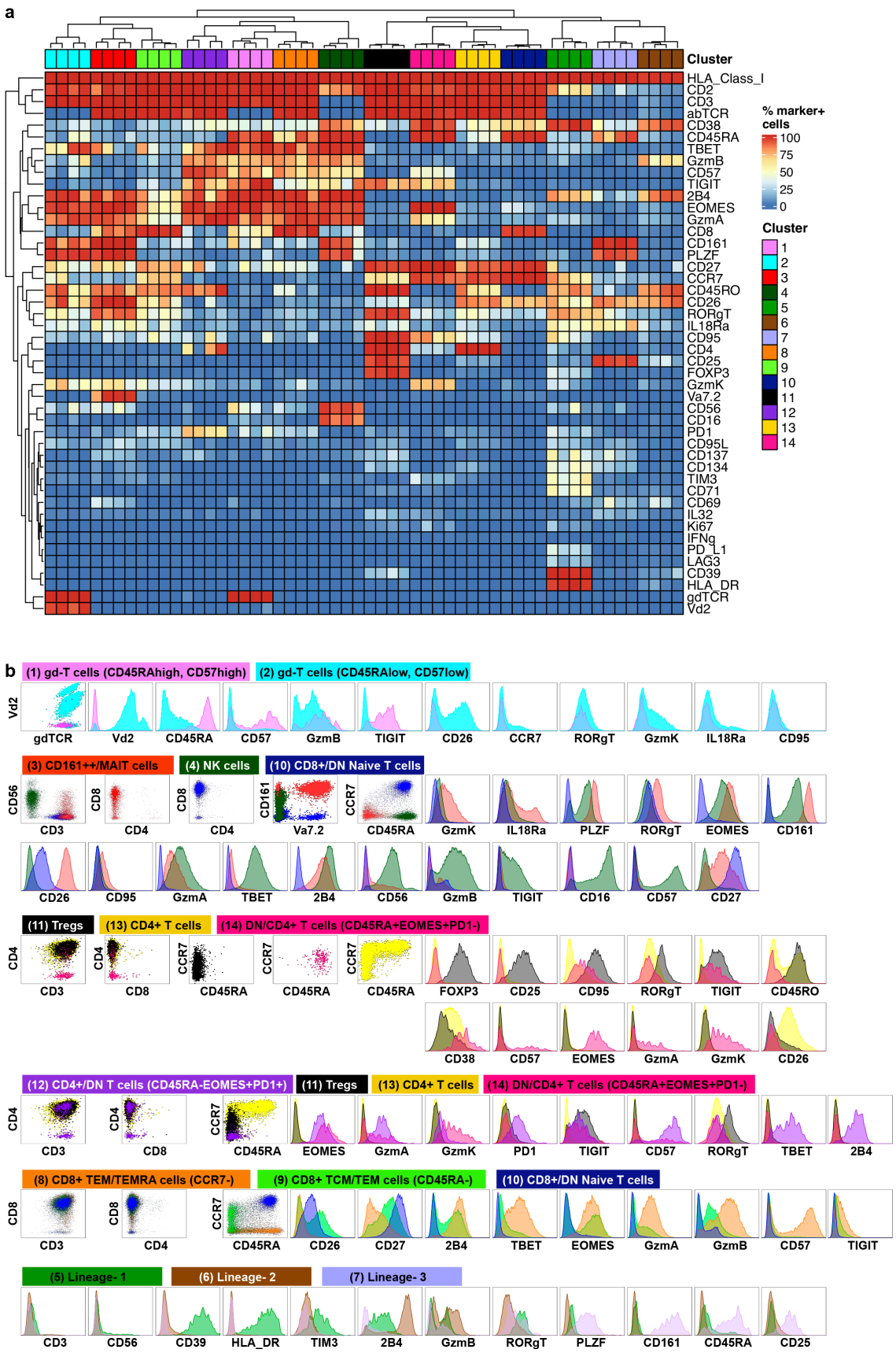
III. Appendices III



Appendix Figure III-1. Quantification of cell numbers at different stages of ChipCytometry data processing. (a) The number of cells within each donor was determined at different stages of data processing as indicated and was normalised to the number of cells of the exported raw data (= post export of data). The mean ± SD is indicated. (b) Quantification of number of cells post-FlowJo processing within each donor stratified by condition.

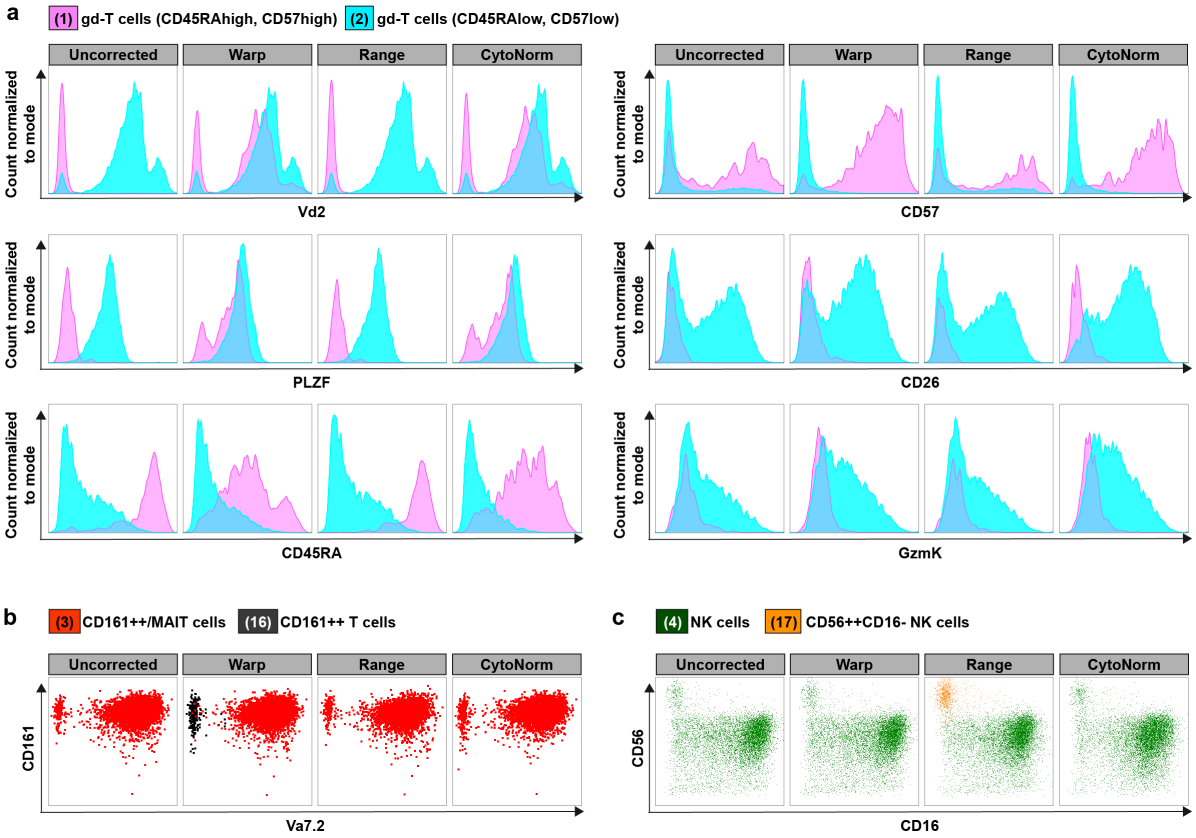

Uncorrected: Control
Warp: Control
Range: Control
CytoNorm: Control
MEM Scores
−10 −5 0 5 10
Cluster
1 2 3 4 5 6 7 8 9 10 11 12 13 14

Appendix Figure III-2. MEM results of control samples of the ChipCytometry data set. Marker enrichment modeling was performed using the unstimulated samples from the ChipCytometry data set. Uncorrected and batch-corrected data was analysed, including warp-, range-, and CytoNorm-corrected data. MEM labels are reported as heatmap.

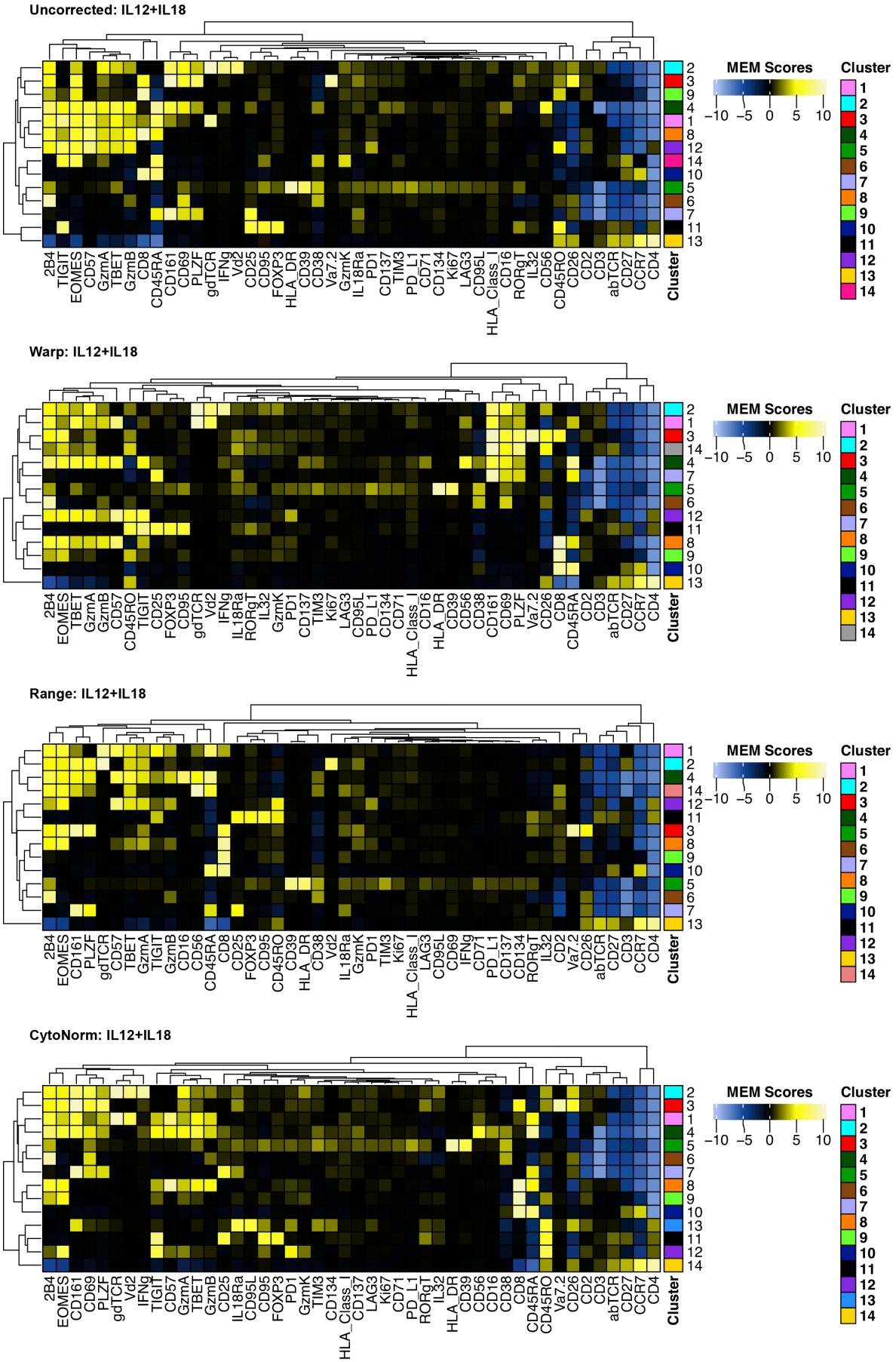


Appendix Figure III-3. Characterisation of clusters from the non-batch-corrected data by analysing the frequency of marker-positive cells in each cluster. (a) To characterise the clusters identified in the non-batch-corrected data, the frequency of marker-positive cells for each marker in each cluster was determined

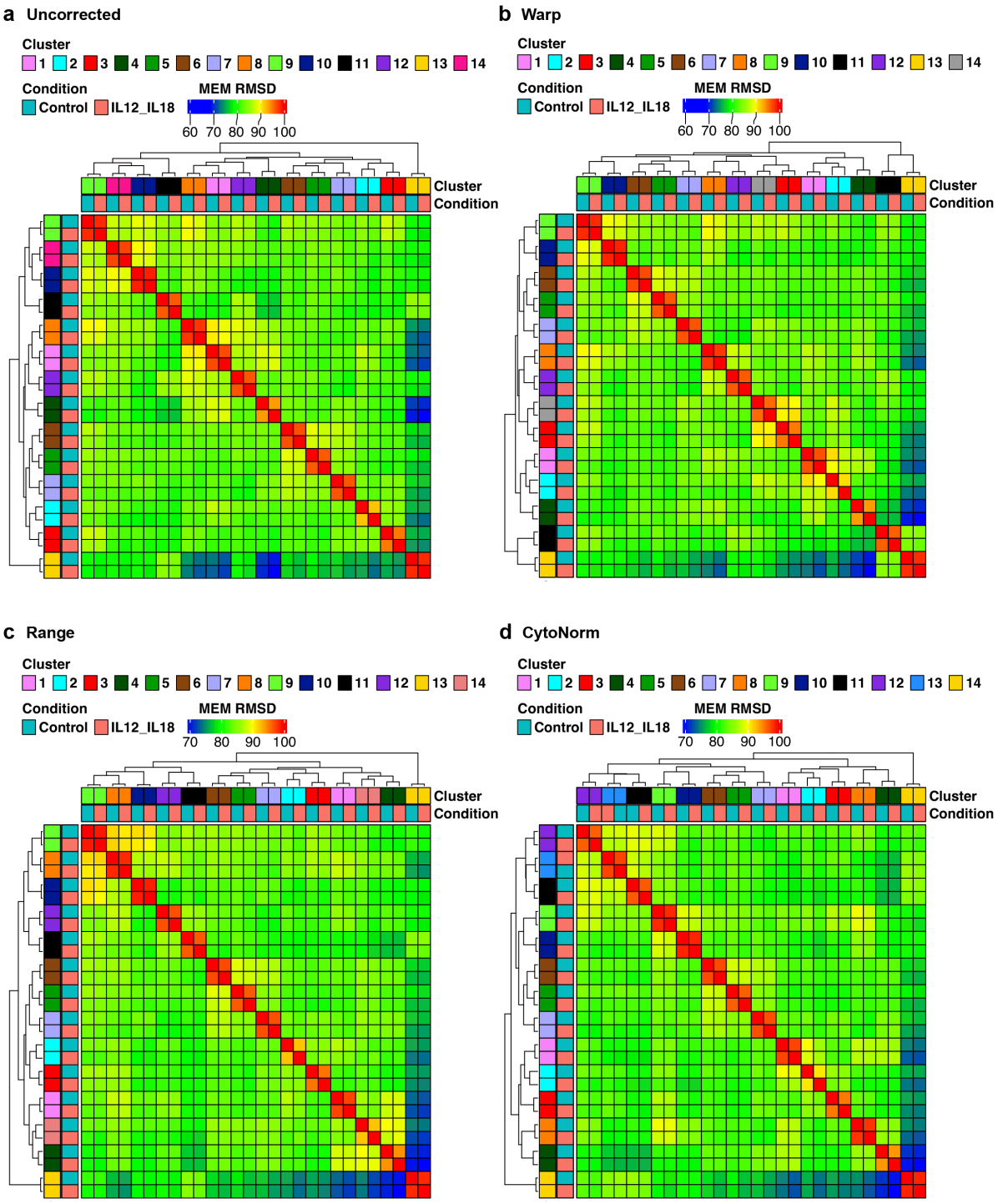
by gating in FlowJo. A threshold to define positive and negative cells was defined in a marker-specific manner. The heatmap shows the frequency of marker-positive cells for each of the four biological replicates. Hierarchical clustering with Euclidean distance as the distance metric was performed for both rows and columns. (b) Histograms and dot plots of selected markers that illustrate the differences between clusters are shown. The plots were generated using the aggregated data of all four donors. The cluster characterisation analysis was based on the unstimulated (control) samples.



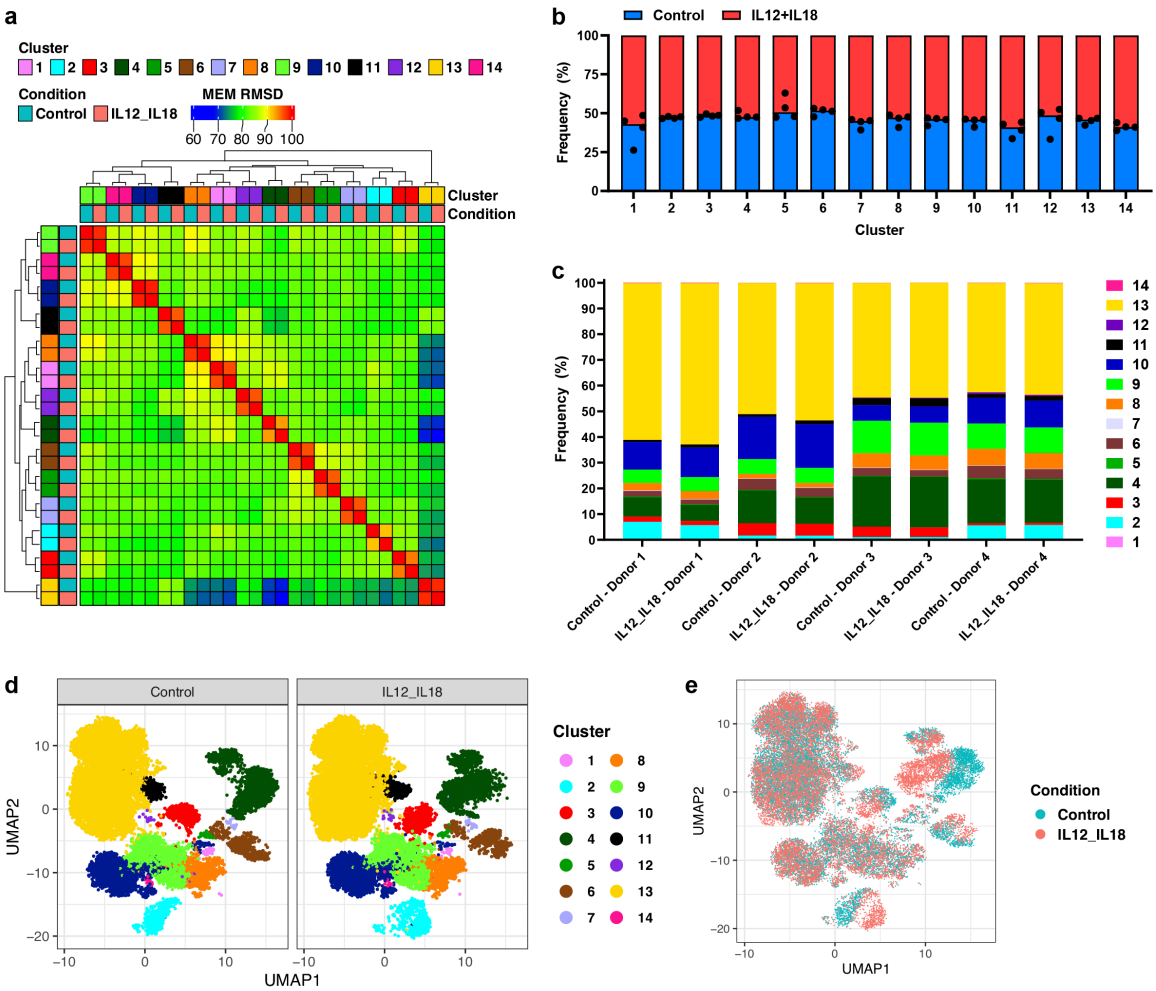
Appendix Figure III-4. Differences between matched clusters from uncorrected and warp-, range-, and CytoNorm-corrected data. (a) Histograms of markers that highlight differences and similarities of clusters 1 and 2 between the non-batch-corrected and warp-, range- and CytoNorm-corrected data are shown. (b) Dot plots illustrate the difference of cluster 3 between non-batch-corrected and warp-, range- and CytoNorm-corrected data. In the Warp-normalised data, CD161^{++}/MAIT cells were split into two clusters, including MAIT cells and CD161^{++} non-MAIT cells. The CD161^{++} T cells were defined as regroup 16 during cluster matching. (c) Dot plots illustrate the difference of cluster 4 between non-batch-corrected and warp-, range- and CytoNorm-corrected data. In the range-normalised data, CD56^{++}CD16^{-} NK cells were clustered separately from the rest of NK cells. During cluster matching, the CD56^{++}CD16^{-} NK cells were assigned regroup 17.


Uncorrected: IL12+IL18
2B4 TIGIT EOMES CD57 GzmA TBET GzmB CD8 CD45RA CD161 CD69 PLZF gdTCR IFNg Vd2 CD25 CD95 FOXP3 HLA_DR CD39 CD38 Va7.2 GzmK IL18Ra PD1 CD137 TIM3 PD_L1 CD71 CD134 Ki67 LAG3 CD95L HLA_Class_I CD16 RORgT IL32 CD56 CD45RO CD26 CD2 CD3 abTCR CD27 CCR7 CD4 Cluster
2 3 9 4 1 8 12 14 10 5 6 7 11 13
MEM Scores
−10 −5 0 5 10
Cluster
1 2 3 4 5 6 7 8 9 10 11 12 13 14
Warp: IL12+IL18
2B4 EOMES TBET GzmA GzmB CD57 CD45RO TIGIT CD25 FOXP3 CD95 gdTCR Vd2 IFNg IL18Ra RORgT IL32 GzmK PD1 CD137 TIM3 Ki67 LAG3 CD95L PD_L1 CD134 CD71 HLA_Class_I CD16 HLA_DR CD39 CD56 CD38 CD161 CD69 PLZF Va7.2 CD26 CD8 CD45RA CD2 CD3 abTCR CD27 CCR7 CD4 Cluster
2 1 3 14 4 7 5 6 12 11 8 9 10 13
MEM Scores
−10 −5 0 5 10
Cluster
1 2 3 4 5 6 7 8 9 10 11 12 13 14
Range: IL12+IL18
2B4 EOMES CD161 PLZF gdTCR CD57 TBET GzmA TIGIT GzmB CD16 CD56 CD45RA CD8 CD25 FOXP3 CD95 CD45RO CD39 HLA_DR CD38 Vd2 IL18Ra GzmK PD1 TIM3 Ki67 HLA_Class_I LAG3 CD95L CD69 IFNg CD71 PD_L1 CD137 CD134 RORgT IL32 CD2 Va7.2 CD26 abTCR CD27 CD3 CCR7 CD4 Cluster
1 2 4 14 12 11 3 8 9 10 5 6 7 13
MEM Scores
−10 −5 0 5 10
Cluster
1 2 3 4 5 6 7 8 9 10 11 12 13 14
CytoNorm: IL12+IL18
2B4 EOMES CD161 CD69 PLZF gdTCR Vd2 IFNg TIGIT CD57 GzmA TBET GzmB CD25 IL18Ra CD95L CD95 FOXP3 PD1 GzmK TIM3 CD134 HLA_Class_I CD137 LAG3 Ki67 CD71 PD_L1 RORgT IL32 HLA_DR CD39 CD56 CD16 CD38 CD8 CD45RA CD45RO Va7.2 CD26 CD2 CD3 abTCR CD27 CCR7 CD4 Cluster
2 3 1 4 5 6 7 8 9 10 13 11 12 14
MEM Scores
−10 −5 0 5 10
Cluster
1 2 3 4 5 6 7 8 9 10 11 12 13 14

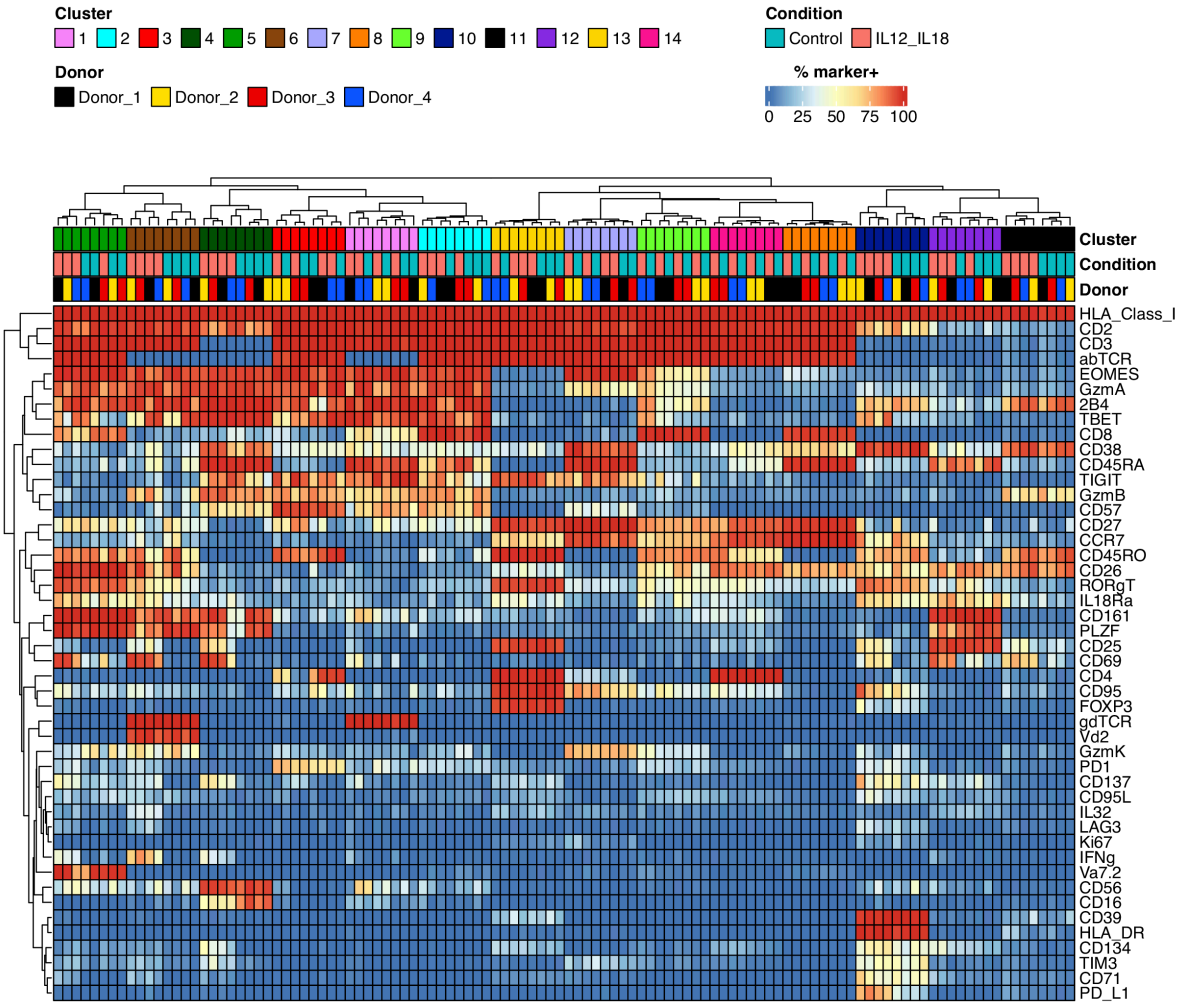
Appendix Figure III-5. MEM results of IL-12+IL-18-stimulated samples of the ChipCytometry data set. Marker enrichment modeling was performed using the IL-12+IL-18-stimulated samples from the ChipCytometry data set. Uncorrected and batch-corrected data was analysed, including warp-, range-, and CytoNorm-corrected data. MEM labels are reported as heatmap.



Appendix Figure III-6. Quantification of MEM label similarity between unstimulated and IL-12+IL-18-stimulated samples. (a)-(d) As a measure of similarity between the clusters of the unstimulated (control) and IL-12+IL-18-stimulated samples, the normalised RMSD scores were calculated in a pairwise manner, using MEM scores as input. Heatmaps illustrate the results of the uncorrected data and batch-corrected data, including warp-, range-, and CytoNorm-corrected data.



Appendix Figure III-7. Comparison of cluster properties between stimulated and unstimulated conditions within the non-batch-corrected data. (a) As a measure of similarity between all 28 clusters of the unstimulated (control) and IL-12+IL-18-stimulated samples, the normalised RMSD scores were calculated in a pairwise manner, using MEM scores as input. The results are displayed in a heatmap, in which both rows and columns were hierarchically clustered using Euclidean distance as the distance metric. (b) Bar plot shows relative abundance of the unstimulated (control) and IL-12+IL-18-stimulated cells within each cluster. Each dot represents a different donor. (c) Bar plot shows the relative abundance of clusters within samples stratified by donor (Donor 1-4) and condition (unstimulated = Control, stimulated = IL-12_IL-18). (d) Non-batch-corrected data, stratified by condition, is displayed using UMAP. Cells are coloured by cluster membership. (e) Non-batch-corrected data is displayed using UMAP. Cells are coloured by condition.



Appendix Figure III-8. Comparison of unstimulated and IL-12+IL-18-stimulated conditions from the non-batch-corrected data by analysing the frequency of marker-positive cells. The heatmap shows the frequency of marker-positive cells of each of the 46 markers that were not previously used for gating within each of the 14 clusters. The threshold to define the frequency of positive and negative cells was defined in a marker-specific manner using FlowJo.

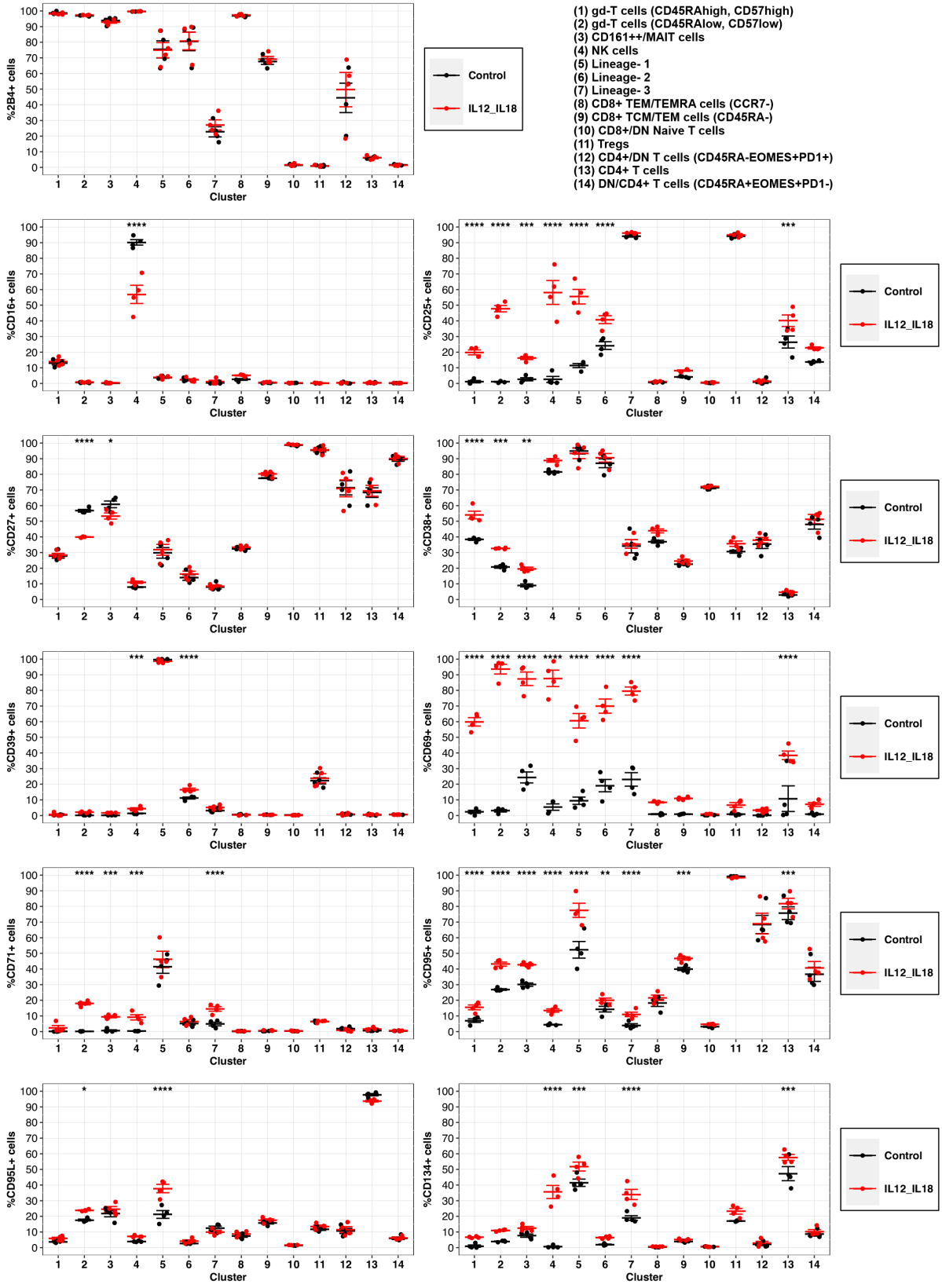


Figure continues on the next page

Appendix Figure III-9. Comparison of the expression of 24 markers between unstimulated and IL-12+IL-18-stimulated conditions in the clusters of the CytoNorm-corrected data set. The expression of twenty-four markers that potentially change expression upon stimulation was analysed. The strip charts show the frequency of marker-positive cells of untreated and IL-12+IL-18-stimulated samples within each of the 14 clusters that were identified via FlowSOM clustering in the CytoNorm-corrected data. The mean of each condition is

indicated ± SEM. Two-way repeated measures ANOVA with Bonferroni's multiple comparisons test was performed, ****p<0.0001, ***p<0.001, **p<0.01, *p<0.05.

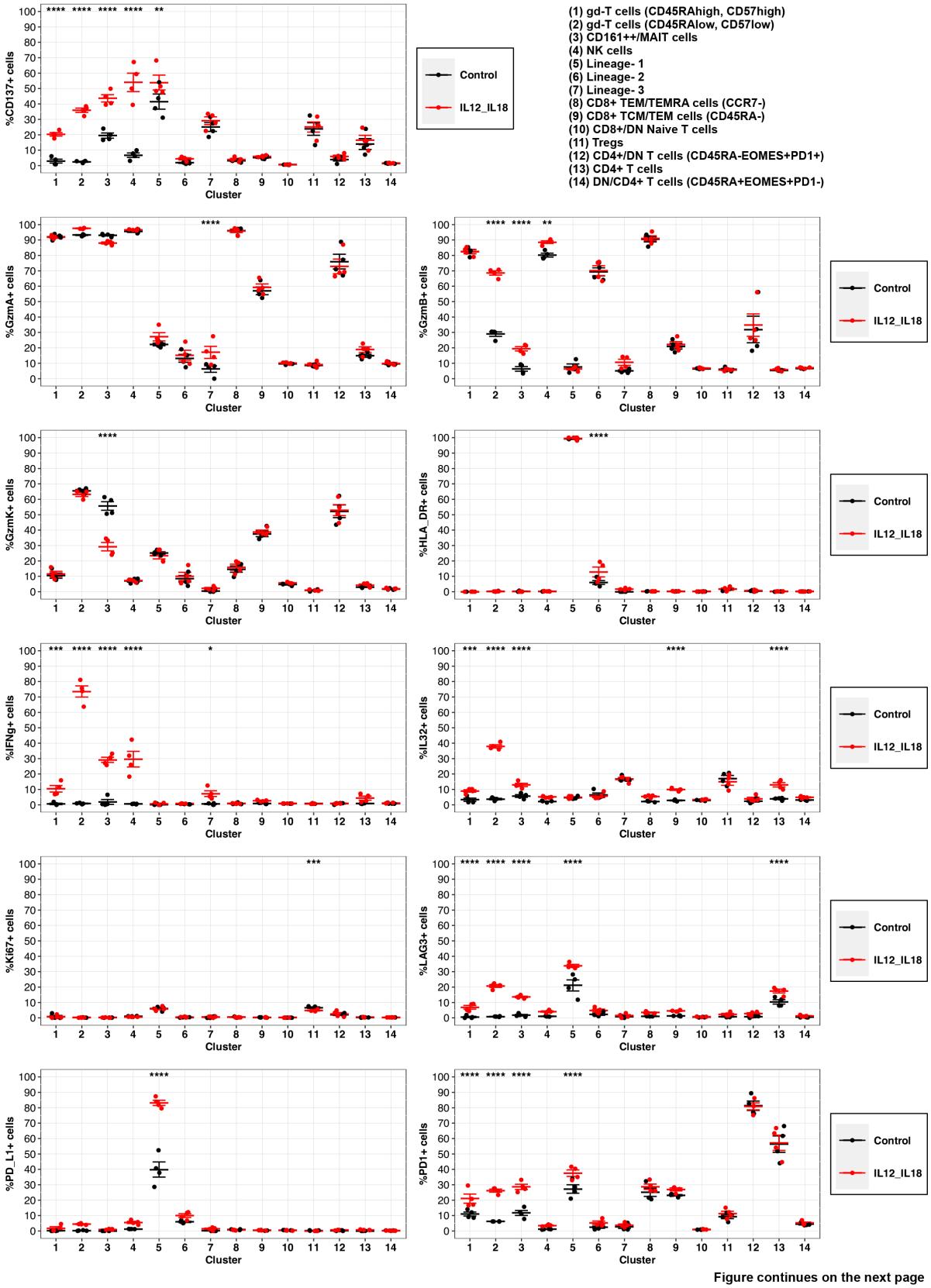
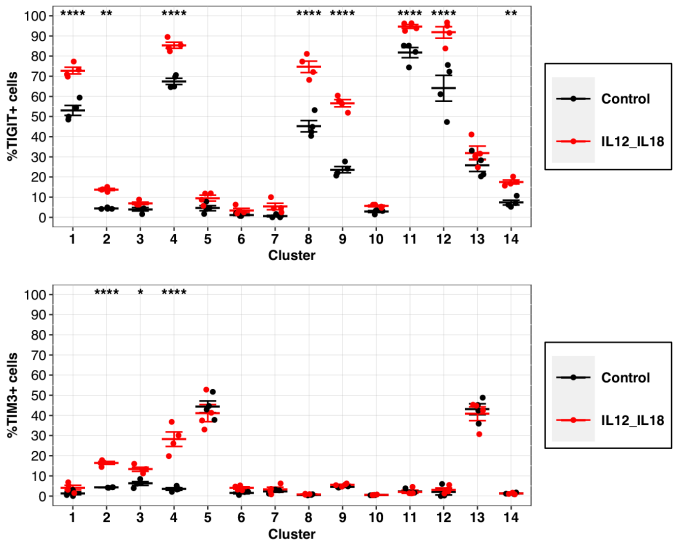


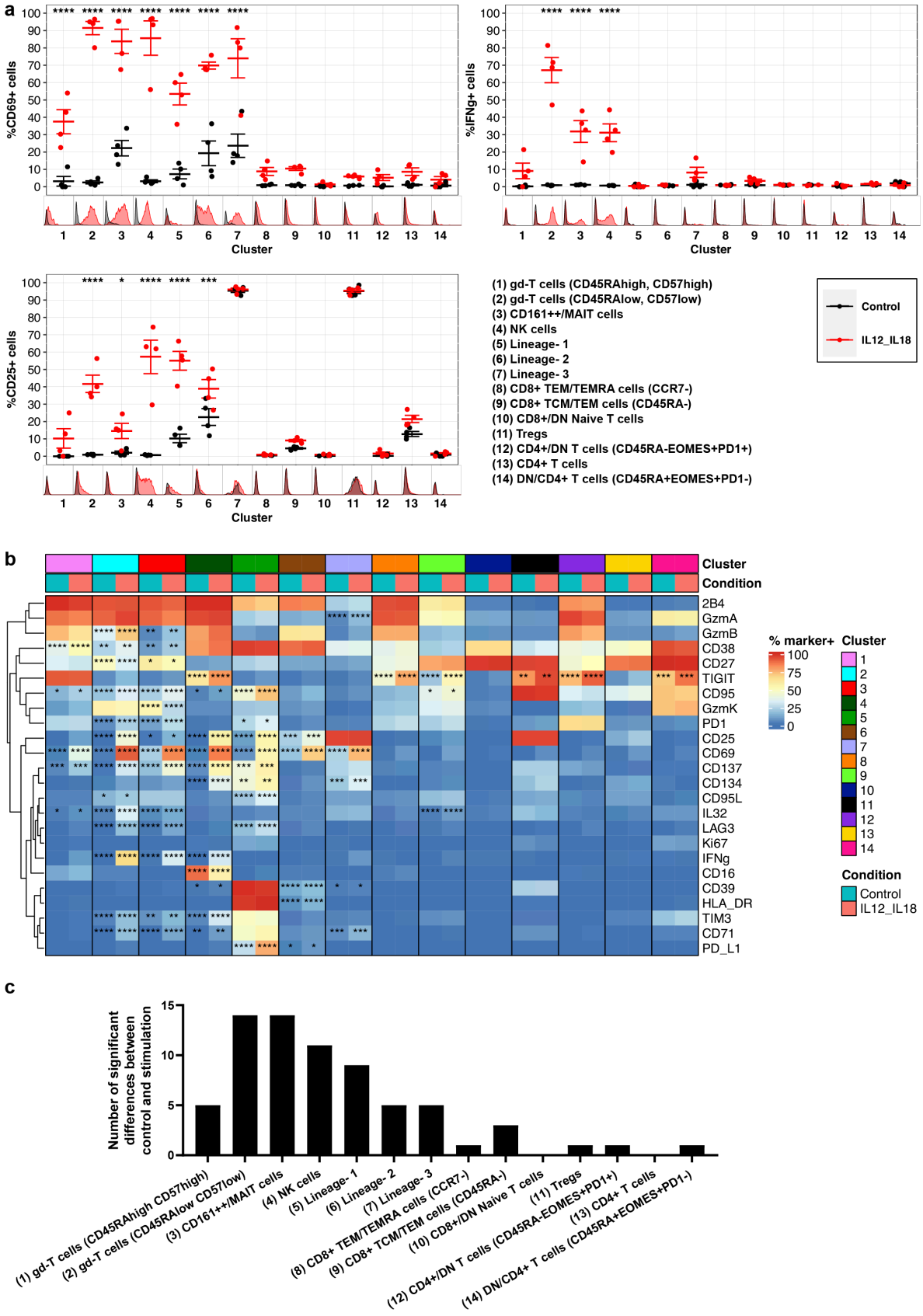
Figure continues on the next page

Appendix Figure III-9 continued.



(1) gd-T cells (CD45RAhigh, CD57high)
(2) gd-T cells (CD45RAlow, CD57low)
(3) CD161++/MAIT cells
(4) NK cells
(5) Lineage- 1
(6) Lineage- 2
(7) Lineage- 3
(8) CD8+ TEM/TEMRA cells (CCR7-)
(9) CD8+ TCM/TEM cells (CD45RA-)
(10) CD8+/DN Naive T cells
(11) Tregs
(12) CD4+/DN T cells (CD45RA-EOMES+PD1+)
(13) CD4+ T cells
(14) DN/CD4+ T cells (CD45RA+EOMES+PD1-)

Appendix Figure III-9 continued.



Appendix Figure III-10. Statistical analysis comparing unstimulated and IL-12+IL-18-stimulated conditions within the clusters that were identified by FlowSOM in the non-batch-corrected data. Twenty-four markers that potentially change expression upon stimulation were statistically analysed. (a) As an example, the statistical analyses of three markers, including CD69, IFNγ and CD25 are shown. The strip charts show the frequency of

marker-positive cells of untreated and IL-12+IL-18-stimulated samples within each of the 14 identified clusters. The mean of each condition is indicated ± standard error of the mean (SEM). Two-way repeated measures ANOVA with Bonferroni's multiple comparisons test was performed. Representative histograms of marker expression are shown below the strip charts. (b) Summary of the results from all 24 markers that were analysed. The heatmap shows the mean frequency of marker-positive cells from 4 donors. Asterisks indicate a statistically significant difference between control and IL-12+IL-18-stimulated condition. (c) Bar chart illustrates the quantification of significant changes in the frequency of marker-positive cells between the control and stimulated condition for each cell population. ****p<0.0001, ***p<0.001, **p<0.01, *p<0.05

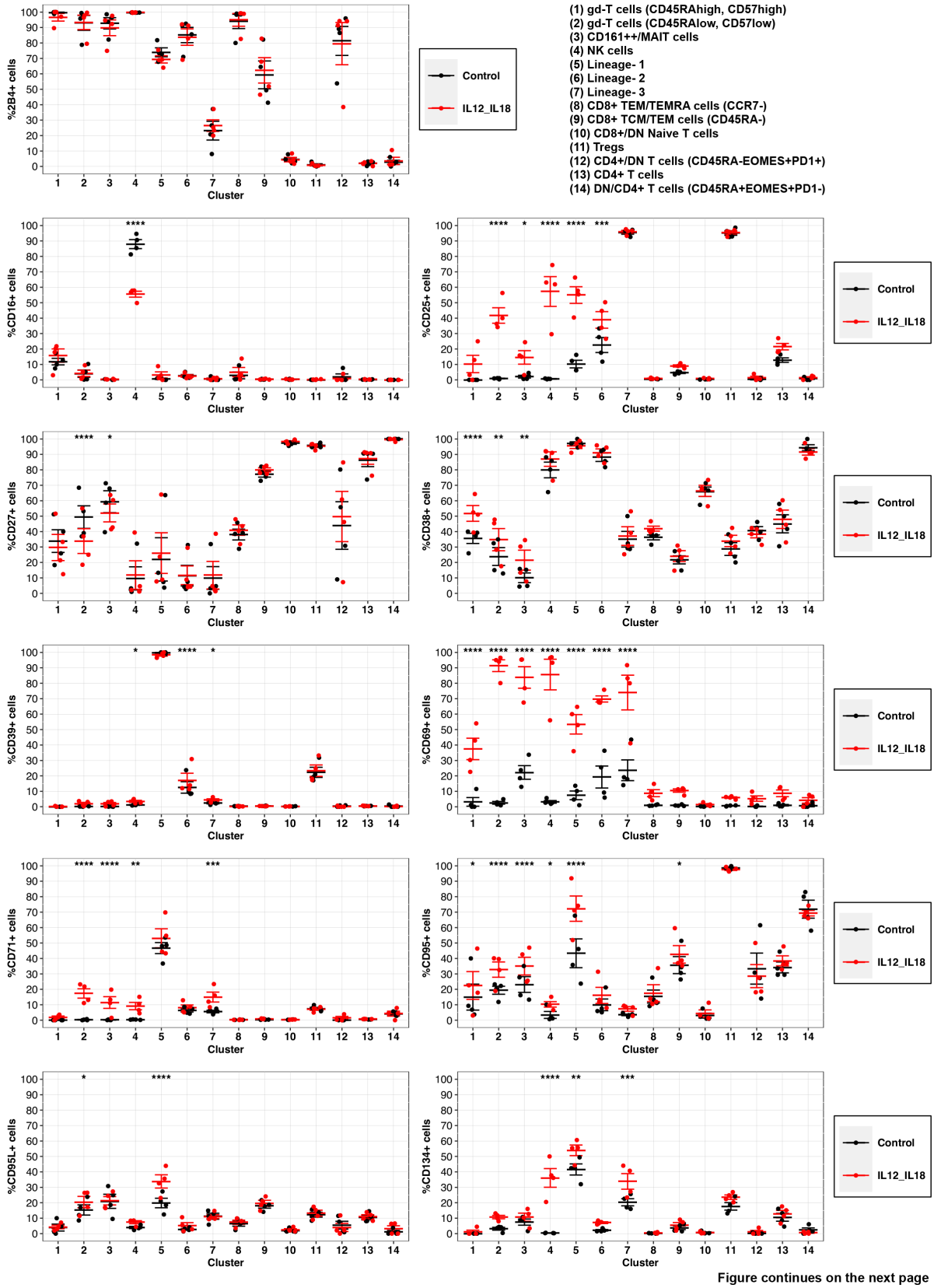


Figure continues on the next page

Appendix Figure III-11 Comparison of the expression of 24 markers between unstimulated and IL-12+IL-18-stimulated conditions in the clusters of the non-batch-corrected data set. The expression of twenty-four markers that potentially change expression upon stimulation was analysed. The strip charts show the frequency of marker-positive cells of untreated and IL-12+IL-18-stimulated samples within each of the 14 clusters that were identified via FlowSOM clustering in the non-batch-corrected data. The mean of each condition is

indicated ± SEM. Two-way repeated measures ANOVA with Bonferroni's multiple comparisons test was performed, ****p<0.0001, ***p<0.001, **p<0.01, *p<0.05.

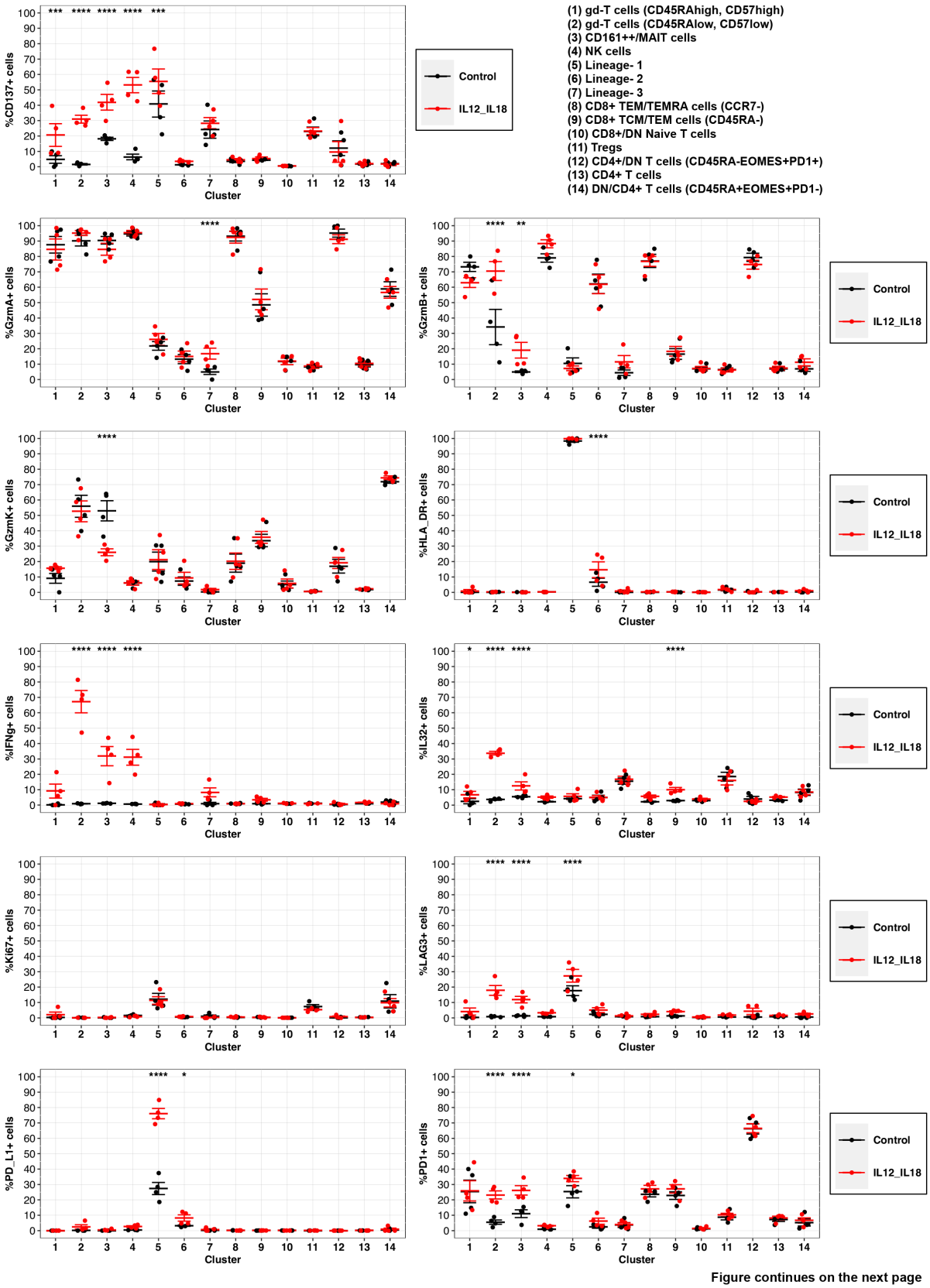
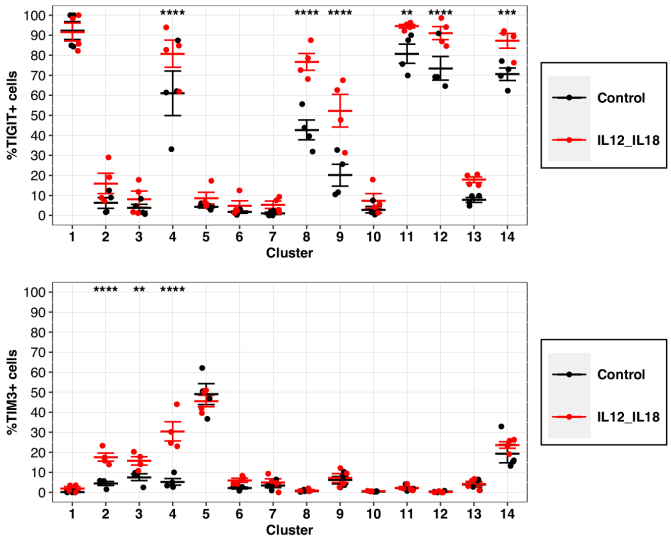


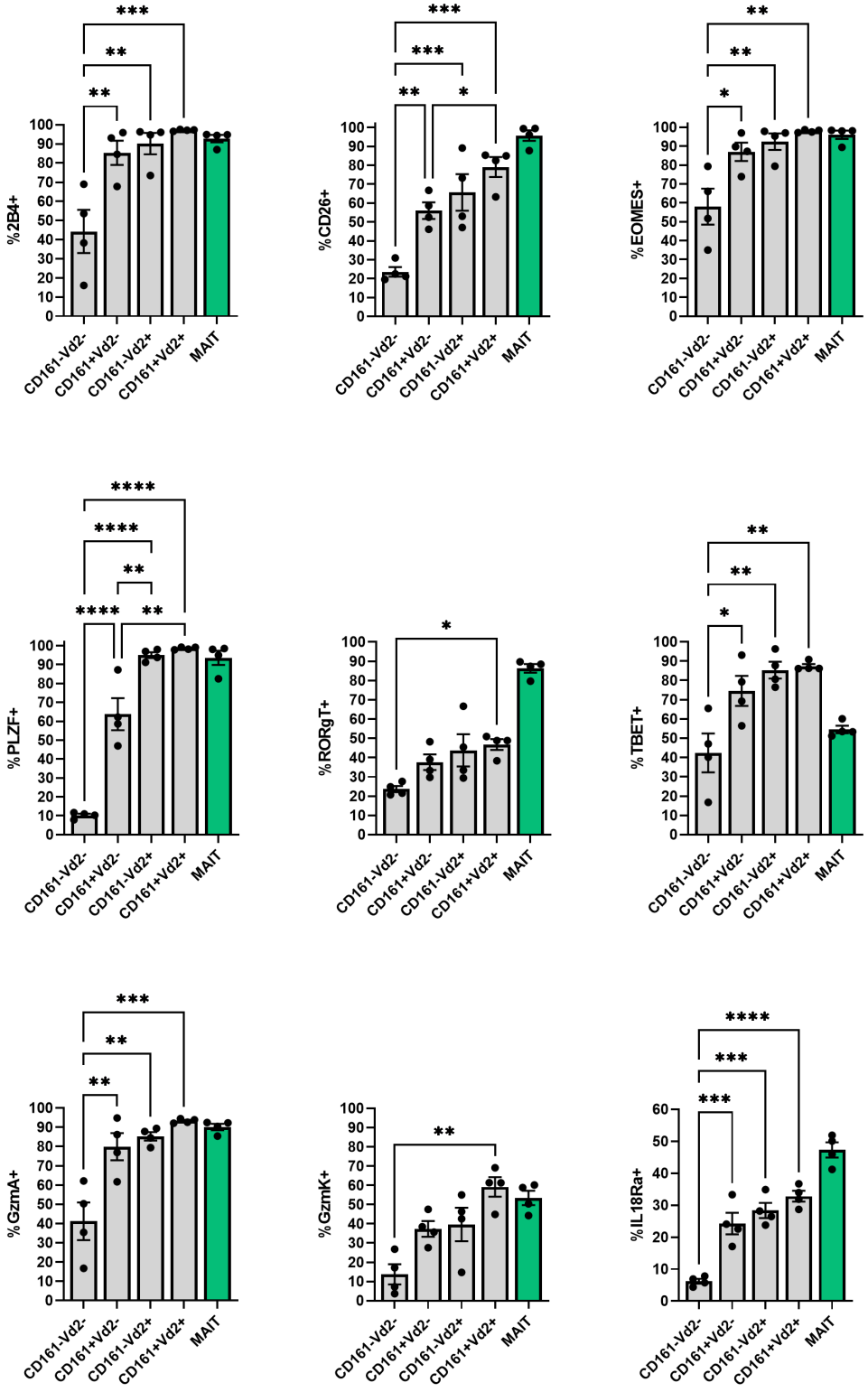
Figure continues on the next page

Appendix Figure III-11 continued.

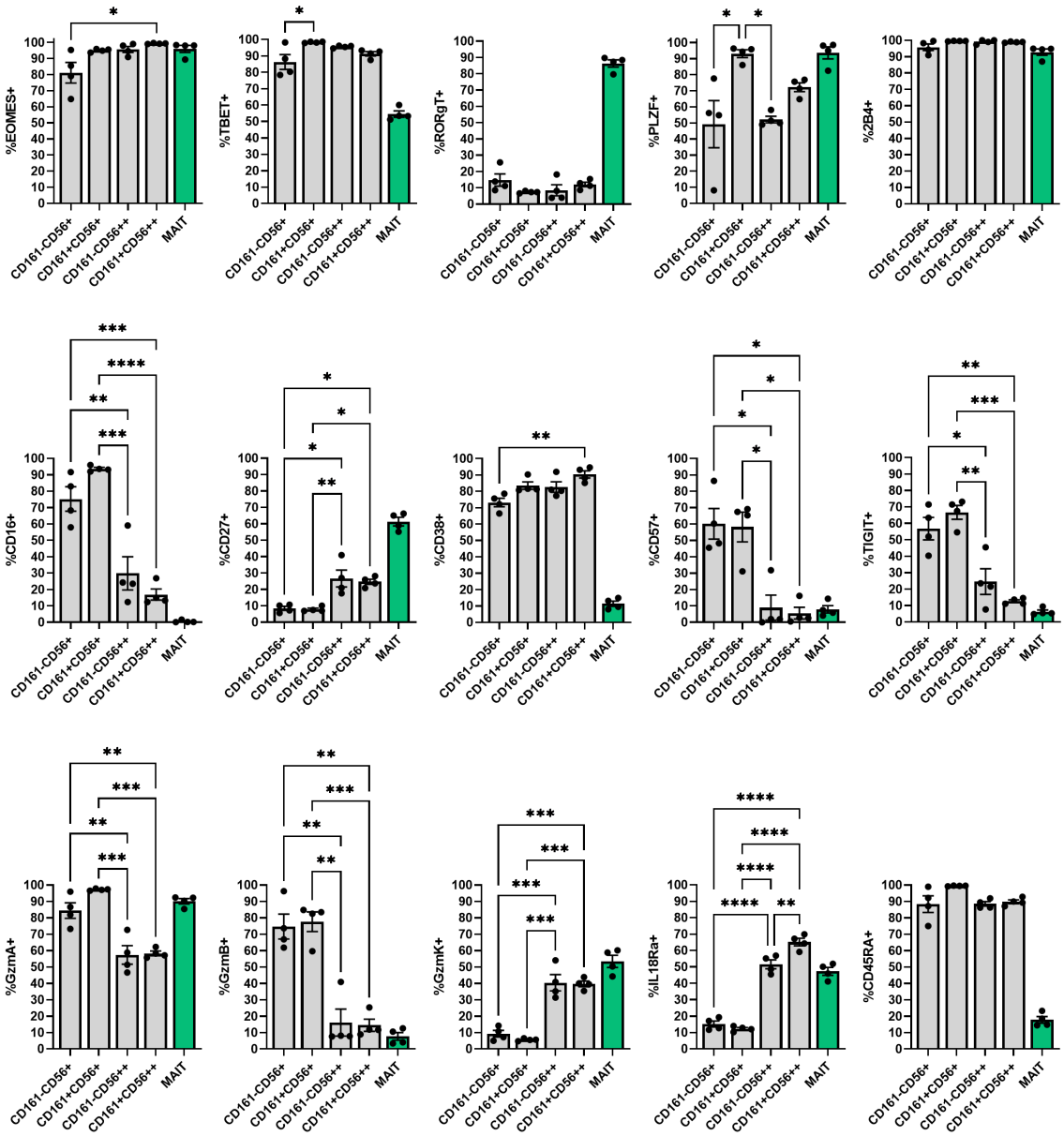


(1) gd-T cells (CD45RAhigh, CD57high)
(2) gd-T cells (CD45RAlow, CD57low)
(3) CD161++/MAIT cells
(4) NK cells
(5) Lineage- 1
(6) Lineage- 2
(7) Lineage- 3
(8) CD8+ TEM/TEMRA cells (CCR7-)
(9) CD8+ TCM/TEM cells (CD45RA-)
(10) CD8+/DN Naive T cells
(11) Tregs
(12) CD4+/DN T cells (CD45RA-EOMES+PD1+)
(13) CD4+ T cells
(14) DN/CD4+ T cells (CD45RA+EOMES+PD1-)

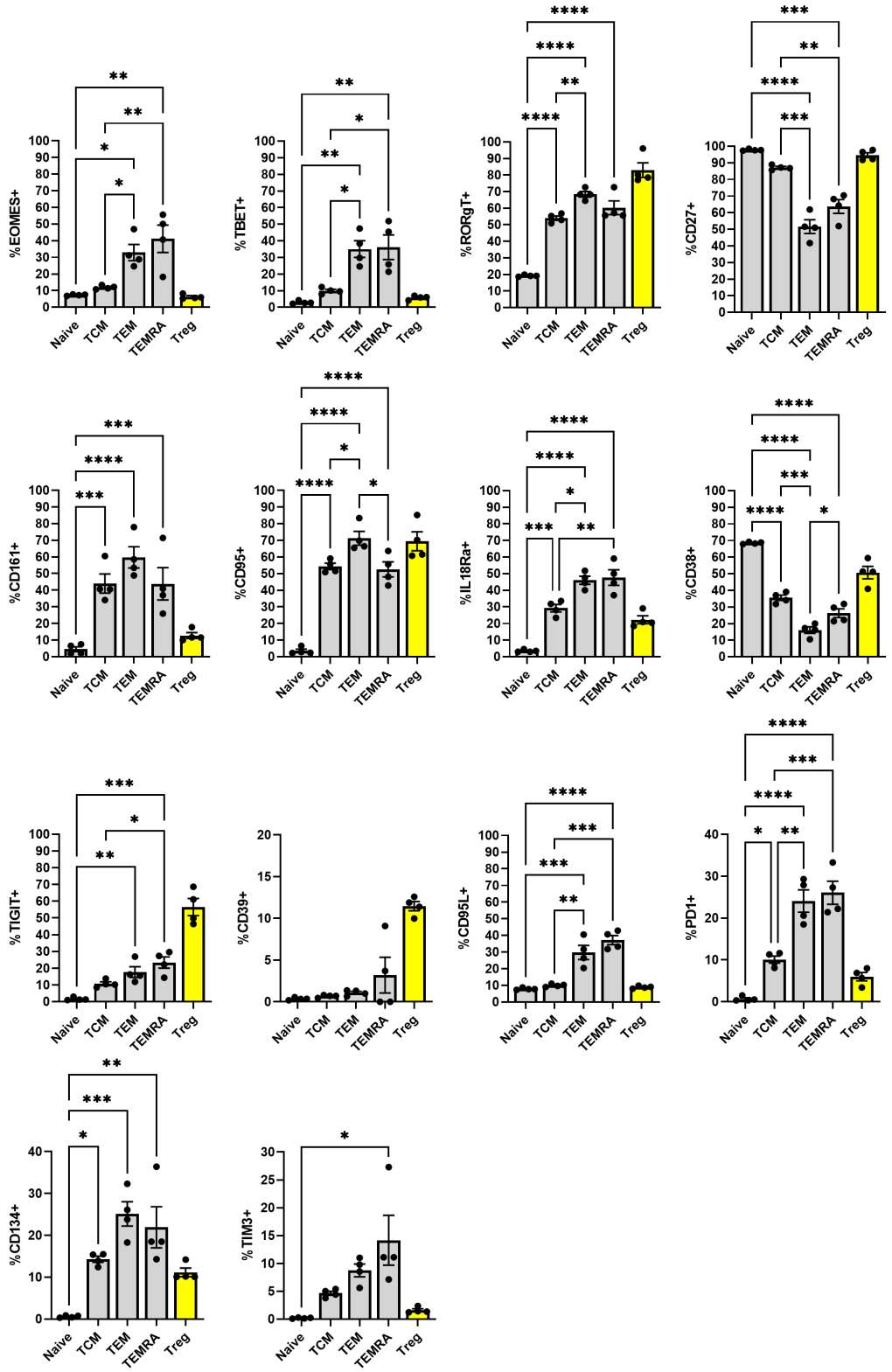
Appendix Figure III-11 continued.



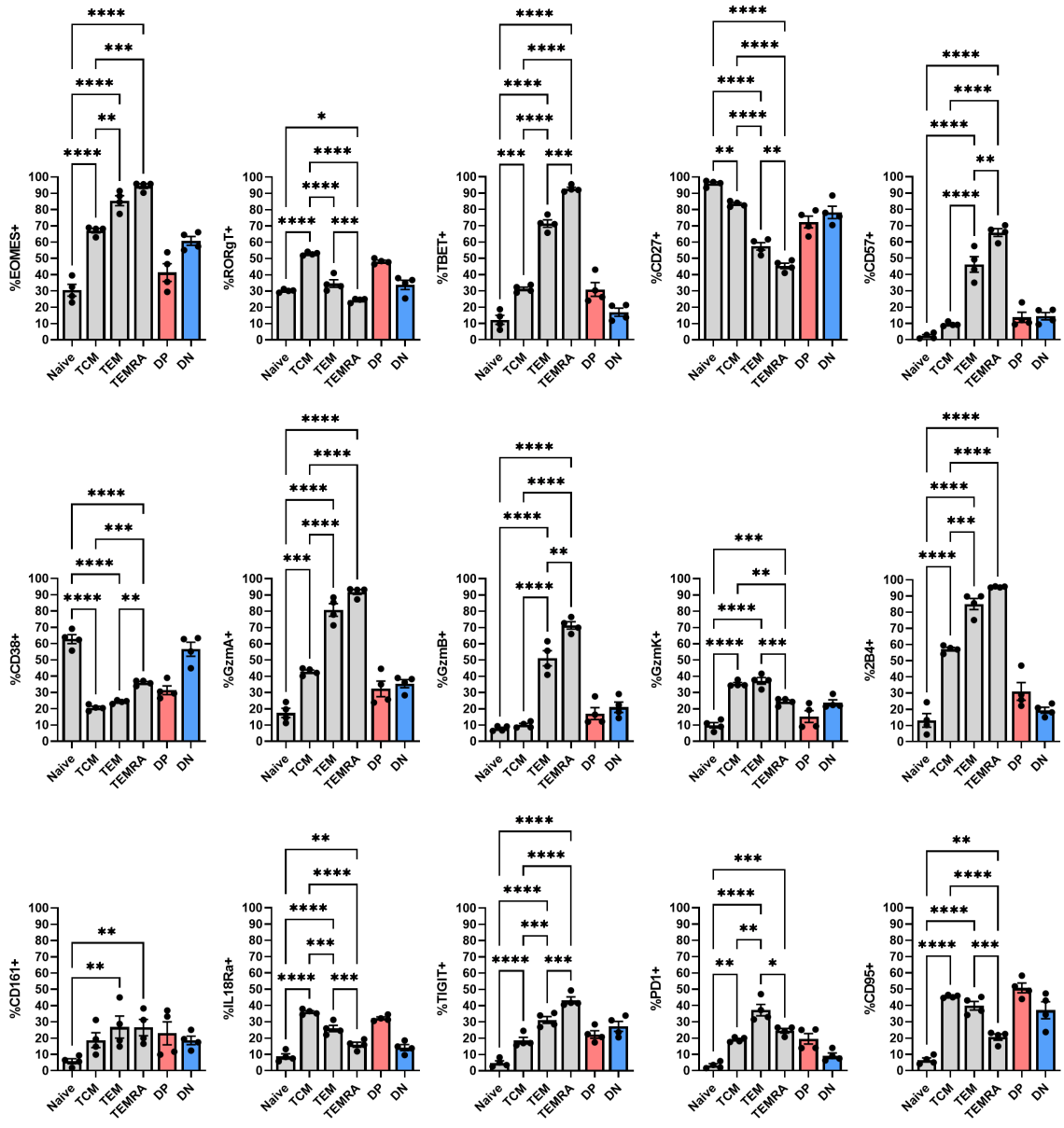
Appendix Figure III-12. Phenotyping of γδT cells and comparison to MAIT cells. The frequency of marker-positive cells of a selection of markers that illustrate the differences between populations is shown. The mean for each population is indicated ± SEM. One-way repeated measures ANOVA with Bonferroni's multiple comparisons test was performed for all γδT-cell subsets, excluding MAIT cells. ****p<0.0001, ***p<0.001, **p<0.01, *p<0.05.



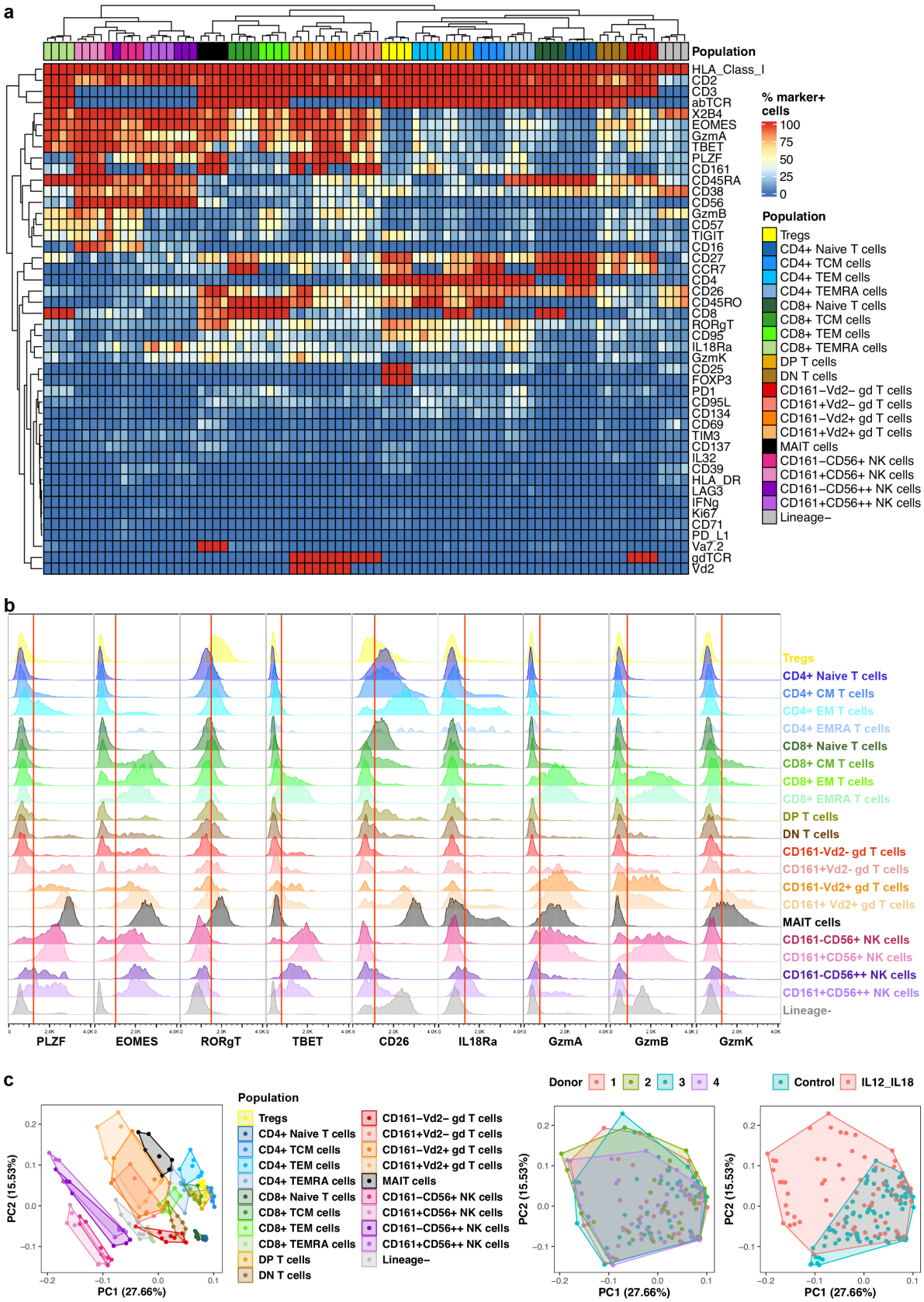
Appendix Figure III-13. Phenotyping of NK cells and comparison to MAIT cells. The frequency of marker-positive cells of a selection of markers that illustrate the differences between populations is shown. The mean for each population is indicated ± SEM. One-way repeated measures ANOVA with Bonferroni's multiple comparisons test was performed for all NK-cell subsets, excluding MAIT cells. ****p<0.0001, ***p<0.001, **p<0.01, *p<0.05.



Appendix Figure III-14 Phenotyping of CD4⁺ T cells and comparison to Tregs. The frequency of marker-positive cells of a selection of markers that illustrate the differences between populations is shown. The mean for each population is indicated ± SEM. One-way repeated measures ANOVA with Bonferroni's multiple comparisons test was performed for all CD4⁺ T-cell subsets, excluding Tregs. ****p<0.0001, ***p<0.001, **p<0.01, *p<0.05.

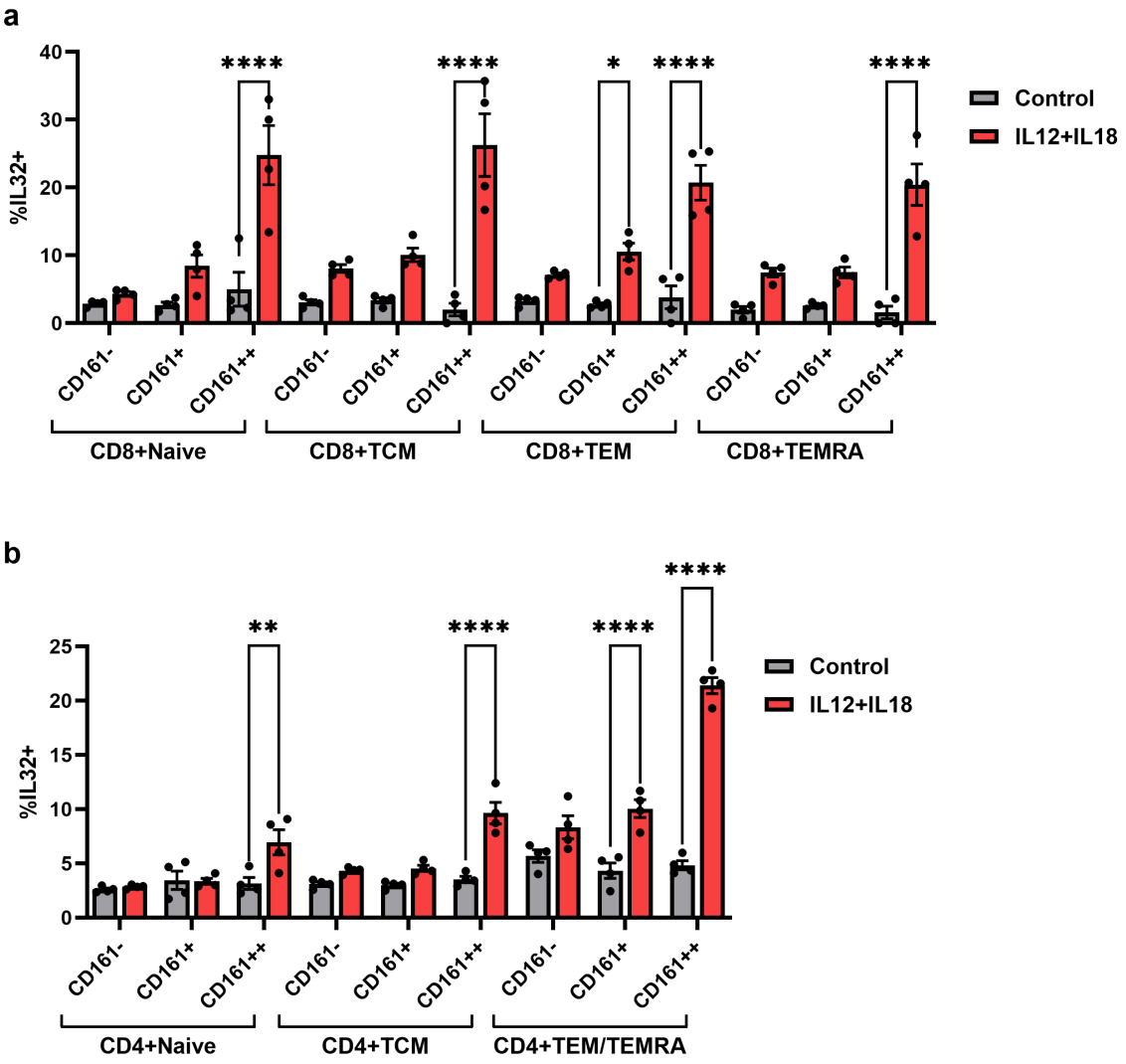


Appendix Figure III-15. Phenotyping of CD8⁺ T cells and comparison to DN/DP T cells. The frequency of marker-positive cells of a selection of markers that illustrate the differences between populations is shown. The mean for each population is indicated ± SEM. One-way repeated measures ANOVA with Bonferroni's multiple comparisons test was performed for all CD8⁺ T-cell subsets, excluding DN/DP T cells. ****p<0.0001, ***p<0.001, **p<0.01, *p<0.05.



Appendix Figure III-16. Phenotype of cell populations identified via manual gating within the non-batch-corrected data set. (a) To characterise the cell populations that were defined by manual gating in the non-batch-corrected data, the frequency of marker-positive cells for all markers was determined within each cell population using FlowJo. The results of all four biological replicates are shown in the heatmap. (b) Representative

histograms of a selection of phenotyping markers are shown, including some transcription factors and innate-associated markers. Phenotyping analysis was performed using data from the unstimulated (control) samples. (c) PCA was performed using the frequency of marker-positive cells from 46 markers of all 21 cell populations and both conditions as input. The results show PC1 (principal component 1) and PC2 (principal component 2). The populations were either coloured according to their population membership (left), according to the donor number (middle) or the condition (right).



Appendix Figure III-17. IL-32 expression by conventional CD8⁺ and CD4⁺ T-cell subsets upon IL-12+IL-18 stimulation. The frequency of IL-32⁺ cells of conventional (a) CD8⁺ and (b) CD4⁺ T-cell subsets is shown for control and IL-12+IL-18-stimulated conditions. The mean frequency of IL-32⁺ cells is indicated ± SEM. Two-way repeated measures ANOVA with Bonferroni's multiple comparisons test was performed, ****p<0.0001, ***p<0.001, **p<0.01, *p<0.05.

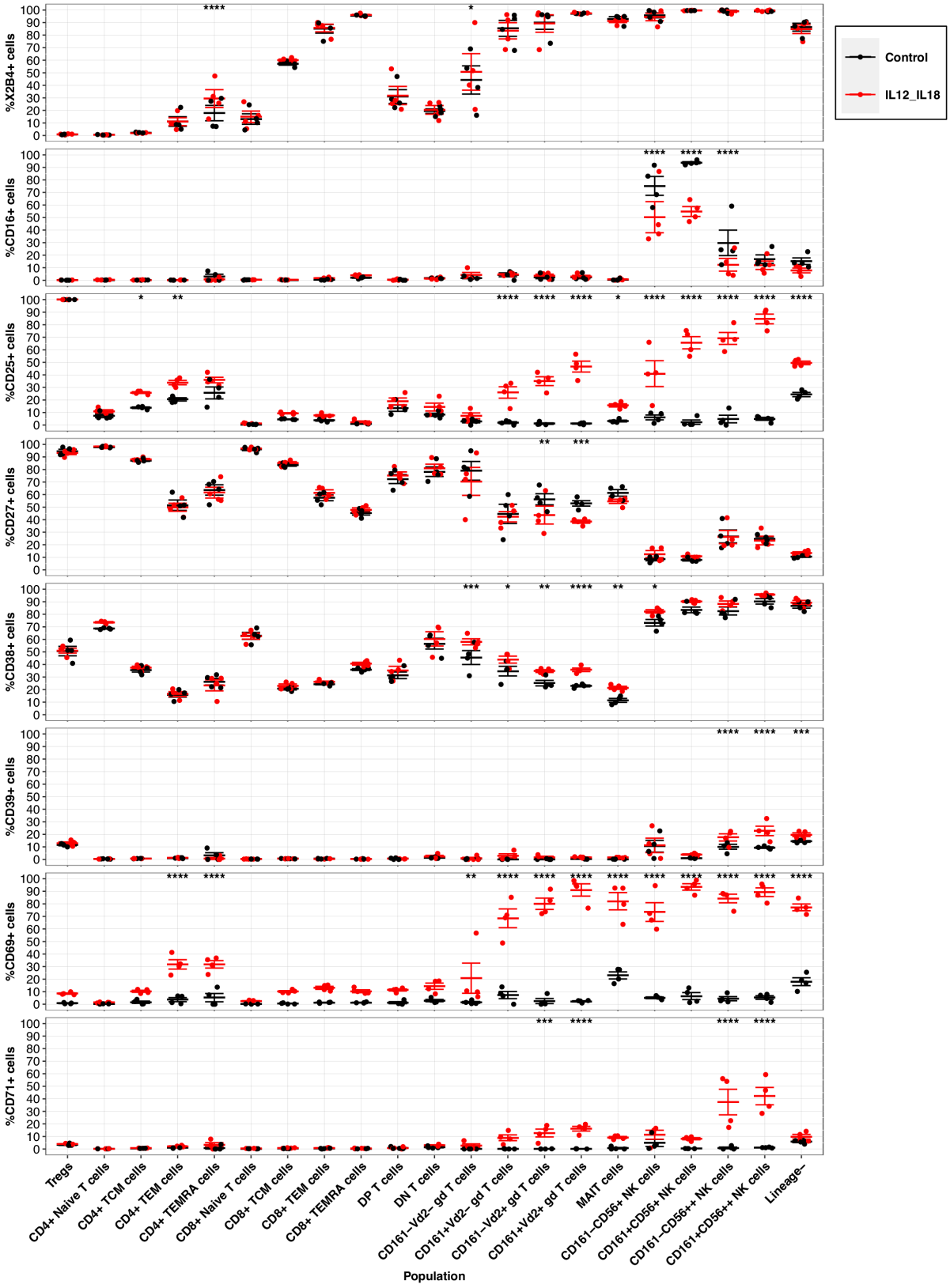


Figure continues on the next page

Appendix Figure III-18. Comparison of the expression of 24 markers between unstimulated and IL-12+IL-18-stimulated conditions in the manually-gated populations of the CytoNorm-corrected data set. The expression of twenty-four markers that potentially change expression upon stimulation was analysed. The strip charts show the frequency of marker-positive cells of untreated and IL-12+IL-18-stimulated samples within each of the 21 cell populations that were identified via manual gating in the CytoNorm-corrected data. The mean

of each condition is indicated ± SEM. Two-way repeated measures ANOVA with Bonferroni's multiple comparisons test was performed, ****p<0.0001, ***p<0.001, **p<0.01, *p<0.05.

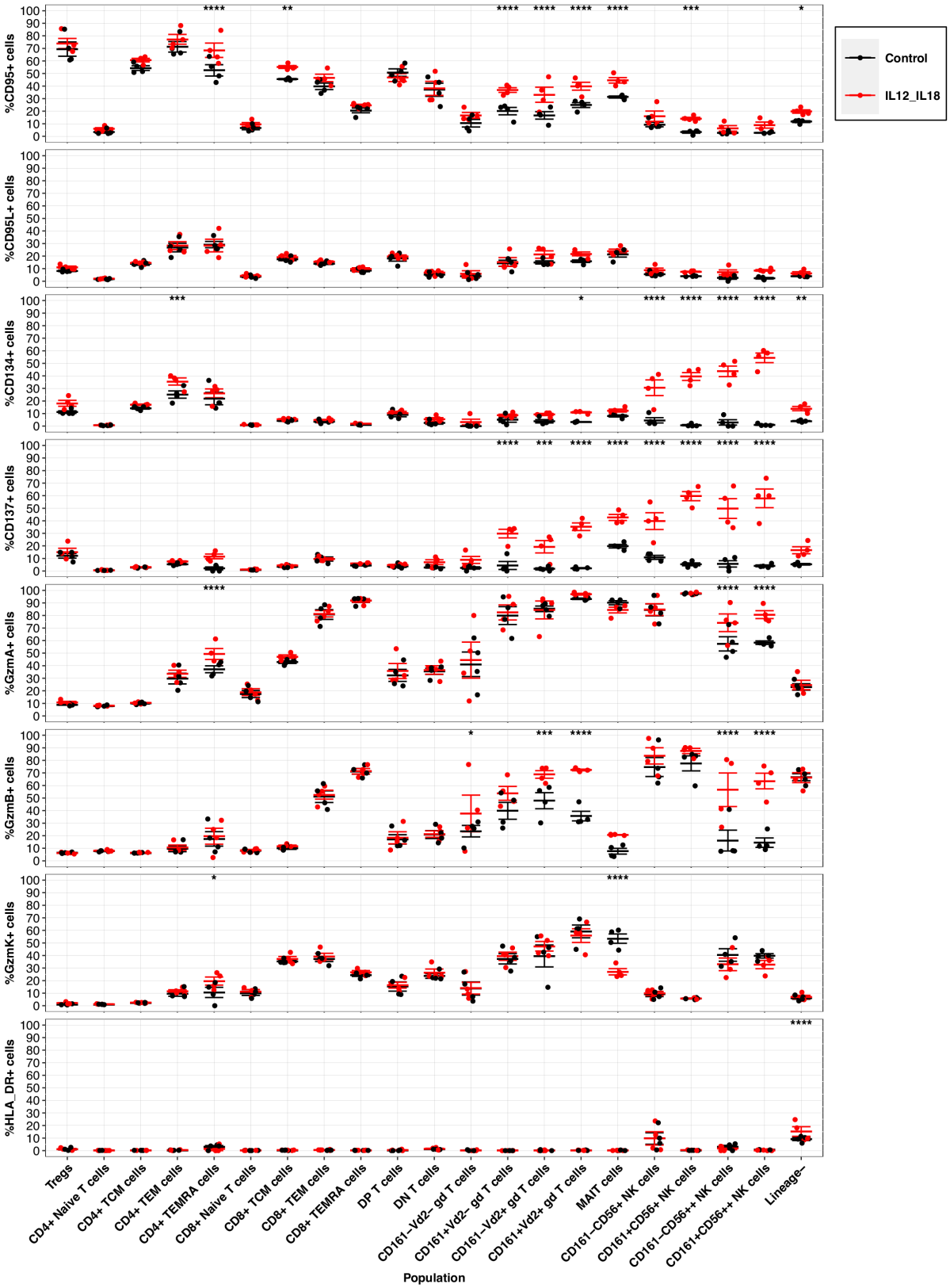
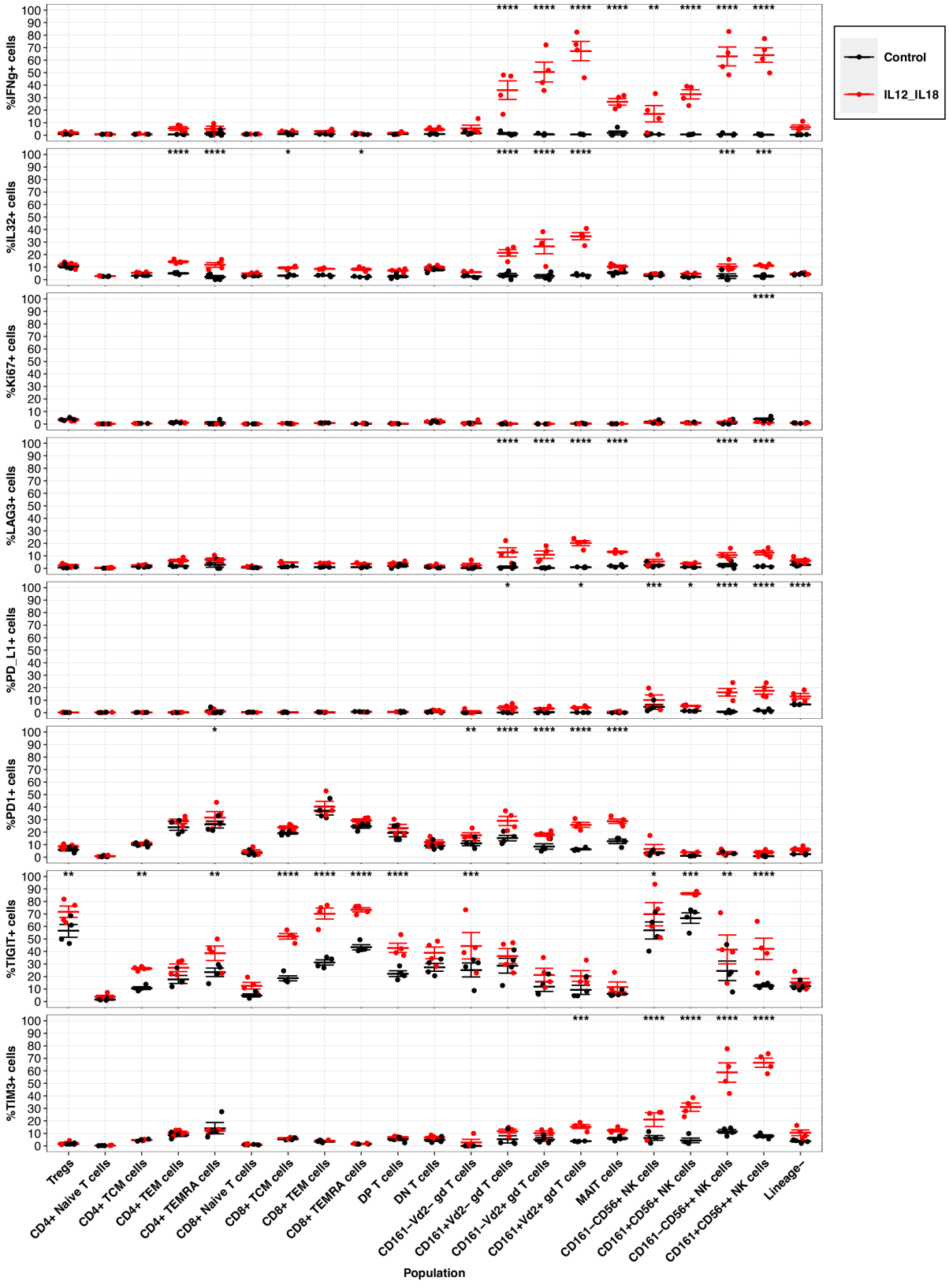
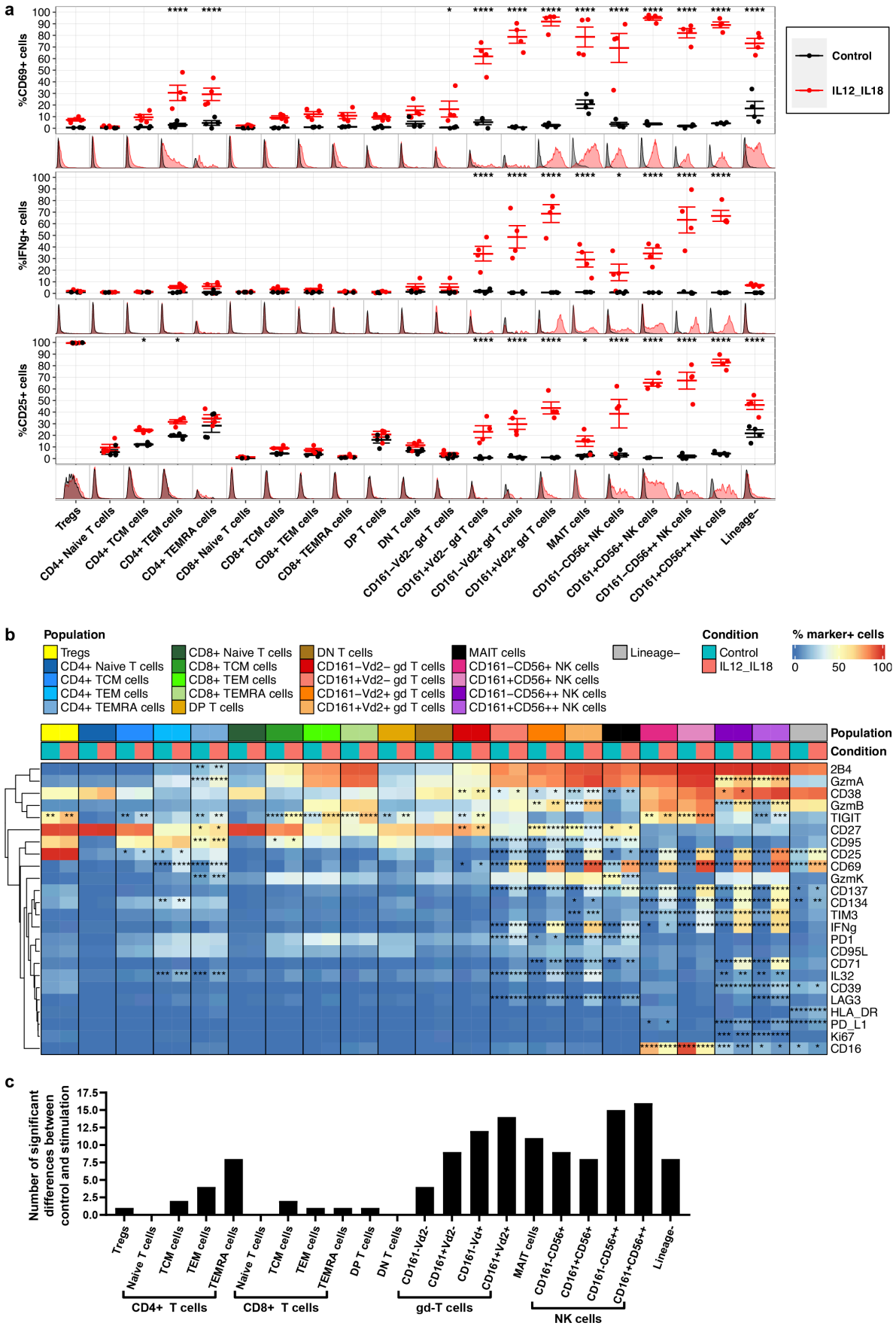


Figure continues on the next page

Appendix Figure III-18 continued.



Appendix Figure III-18 continued.



Appendix Figure III-19. Statistical analysis comparing unstimulated and IL-12+IL-18-stimulated conditions within populations identified by manual gating in the non-batch-corrected data. Twenty-four markers that

potentially change expression upon stimulation were statistically analysed. (a) As an example, the statistical analyses of three markers, including CD69, IFNγ and CD25 are shown. The strip charts show the frequency of marker-positive cells of untreated and IL-12+IL-18-stimulated samples within each of the 21 populations that were identified via manual gating. The mean of each condition is indicated ± SEM. Two-way repeated measures ANOVA with Bonferroni's multiple comparisons test was performed. Representative histograms of marker expression are shown below the strip charts. (b) Summary of the results from all 24 markers that were analysed. The heatmap shows the mean frequency of marker-positive cells from 4 donors. Mean values for each condition within each of the 21 populations are shown. Asterisks indicate a statistically significant difference between the control and IL-12+IL-18-stimulated condition. (c) Bar chart illustrates the quantification of significant changes in the frequency of marker-positive cells between the control and stimulated condition within each cell population. ****$p<0.0001$, ***$p<0.001$, **$p<0.01$, *$p<0.05$.

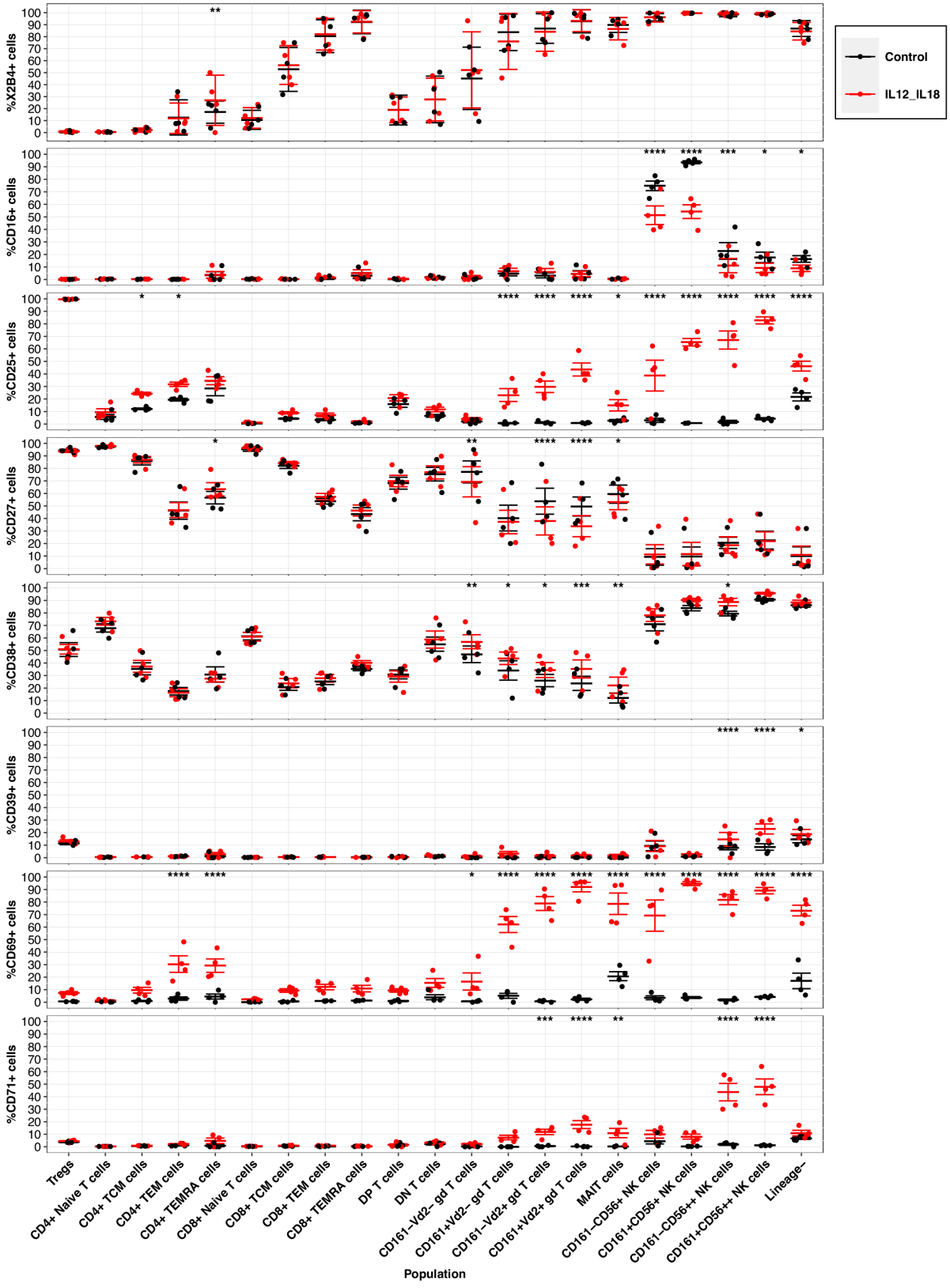


Figure continues on the next page

Appendix Figure III-20. Comparison of the expression of 24 markers between unstimulated and IL-12+IL-18-stimulated conditions in the manually-gated populations of the non-batch-corrected data set. The expression of twenty-four markers that potentially change expression upon stimulation was analysed. The strip charts show the frequency of marker-positive cells of untreated and IL-12+IL-18-stimulated samples within each of the 21 cell populations that were identified via manual gating in the non-batch-corrected data. The mean

of each condition is indicated ± SEM. Two-way repeated measures ANOVA with Bonferroni's multiple comparisons test was performed, ****p<0.0001, ***p<0.001, **p<0.01, *p<0.05.

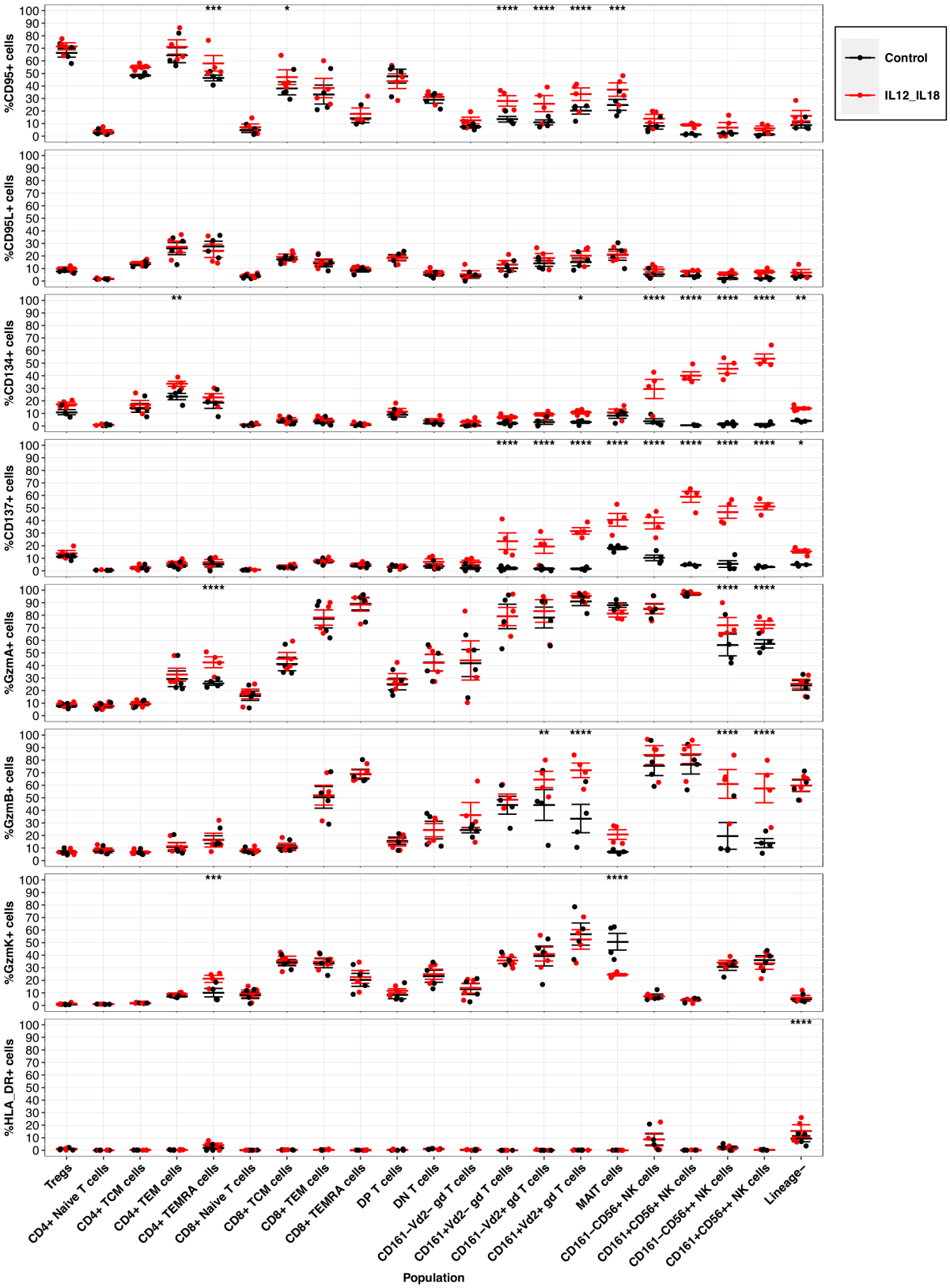
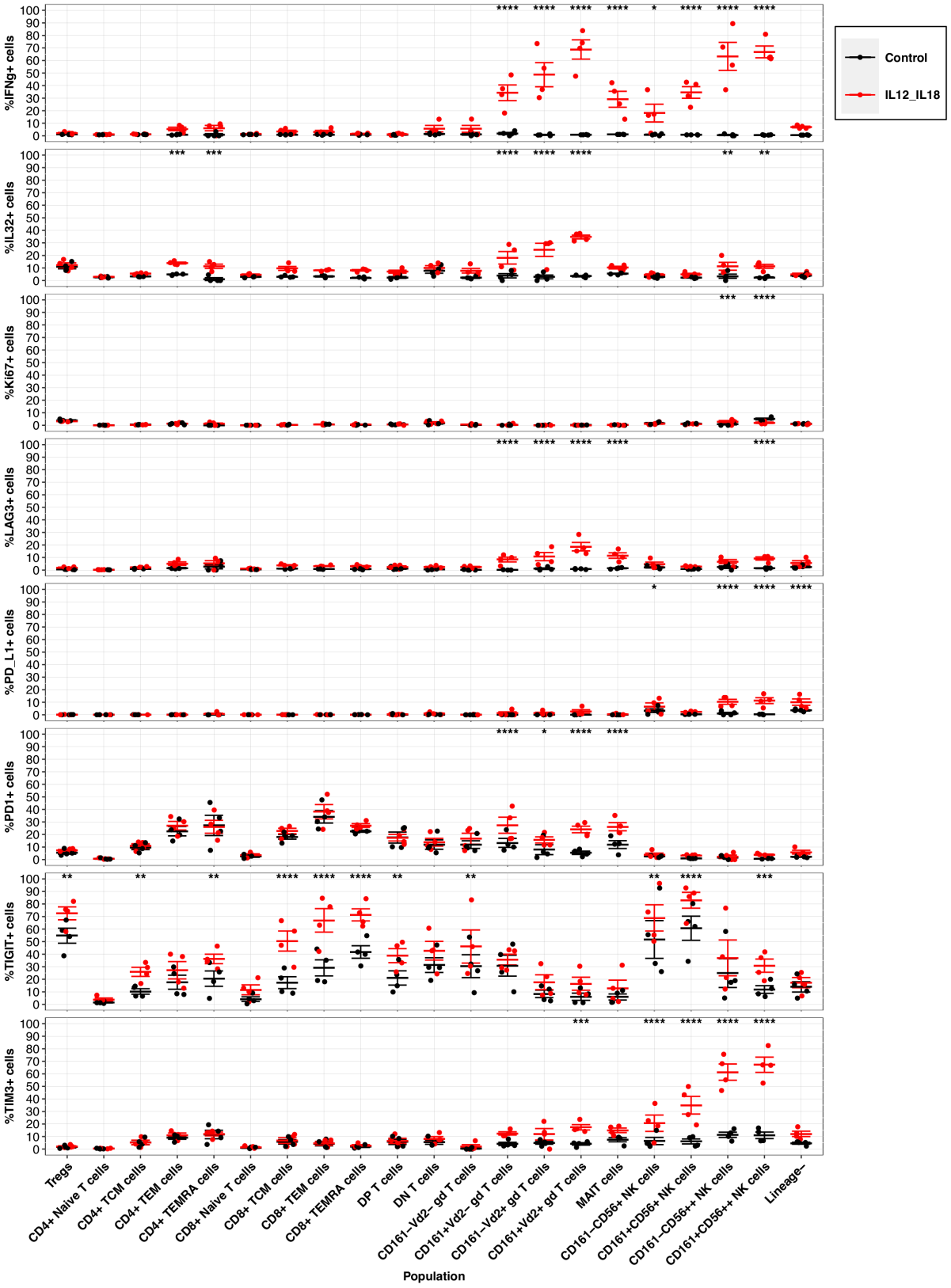


Figure continues on the next page

Appendix Figure III-20 continued.



Appendix Figure III-20 continued.

Appendix Table III-1. Data transformation settings for FlowJo-type biexponential transformation.

marker	channelRange	maxValue	pos	neg	widthBasis	inverse
αβTCR	4096	115000	2.4	0	-3.98	FALSE
CCR7	4096	75000	2.4	0	-1	FALSE
CD134	4096	20000	2	0	-1	FALSE
CD137	4096	175000	3.1	0	-3.98	FALSE
CD14	4096	20000	2	0	-3.98	FALSE
CD16	4096	50000	2.9	0	-6.31	FALSE
CD161	4096	115000	2.8	0	-1	FALSE
CD19	4096	15000	2	0	-1	FALSE
CD2	4096	65000	2.2	0	-1	FALSE
IL-18Rα	4096	37000	2	0	-1	FALSE
LAG3	4096	6200	2	0	-10	FALSE
2B4	4096	70000	2.4	0	-1	FALSE
CD25	4096	30000	2.3	0	-1	FALSE
CD26	4096	95000	2.6	0	-1	FALSE
CD27	4096	20000	2	0	-1	FALSE
PD_L1	4096	75000	2	0	-1	FALSE
PD1	4096	17000	2	0	-1	FALSE
CD3	4096	70000	2.3	0	-1	FALSE
TIM3	4096	7000	2	0	-6.31	FALSE
CD38	4096	19000	2	0	-1	FALSE
CD39	4096	120000	2.8	0	-3.98	FALSE
CD4	4096	55000	2	0	-1	FALSE
CD45-BUV395	4096	165000	2.3	0	-6.31	FALSE
CD45-PE	4096	130000	2.1	0	-2	FALSE
CD45RA	4096	160000	2.6	0	-1	FALSE
CD45RO	4096	135000	2	0	-1	FALSE
CD56	4096	230000	3.4	0	-6.31	FALSE
CD57	4096	3.00E+05	3.1	0	-1	FALSE
CD69	4096	270000	2.9	0	-1	FALSE
CD71	4096	30000	2	0	-1	FALSE
CD8	4096	105000	2.5	0	-1	FALSE
CD95	4096	40000	2.3	0	-1	FALSE
FASL	4096	80000	2.3	0	-1	FALSE
EOMES	4096	175000	2.1	0	-1	FALSE
FOXP3	4096	46000	2	0	-1	FALSE
γδTCR	4096	140000	2.6	0	-1	FALSE
GzmA	4096	320000	2.6	0	-1	FALSE
GzmB	4096	280000	2.5	0	-1	FALSE
GzmK	4096	42000	2	0	-1	FALSE
HLA_Class_I	4096	150000	4.2	0	-1	FALSE
HLA_DR	4096	70000	2.7	0	-5.01	FALSE
IFNγ	4096	2.00E+05	2.8	0	-1	FALSE
IL-32	4096	190000	2	0	-1	FALSE
Ki67	4096	250000	2	0	-1	FALSE

marker	channelRange	maxValue	pos	neg	widthBasis	inverse
live/dead	4096	30000	2	0	-1	FALSE
PLZF	4096	75000	2	0	-1	FALSE
RORγT	4096	90000	2	0	-1	FALSE
TBET	4096	135000	2	0	-1	FALSE
TIGIT	4096	37000	2.2	0	-1	FALSE
Vα7.2	4096	105000	2.7	0	-1	FALSE
Vδ2	4096	140000	3.2	0	-6.31	FALSE

Appendix Table III-2. Upper and lower thresholds that were defined to gate out any remaining outliers after the removal of fluorescence anomalies.

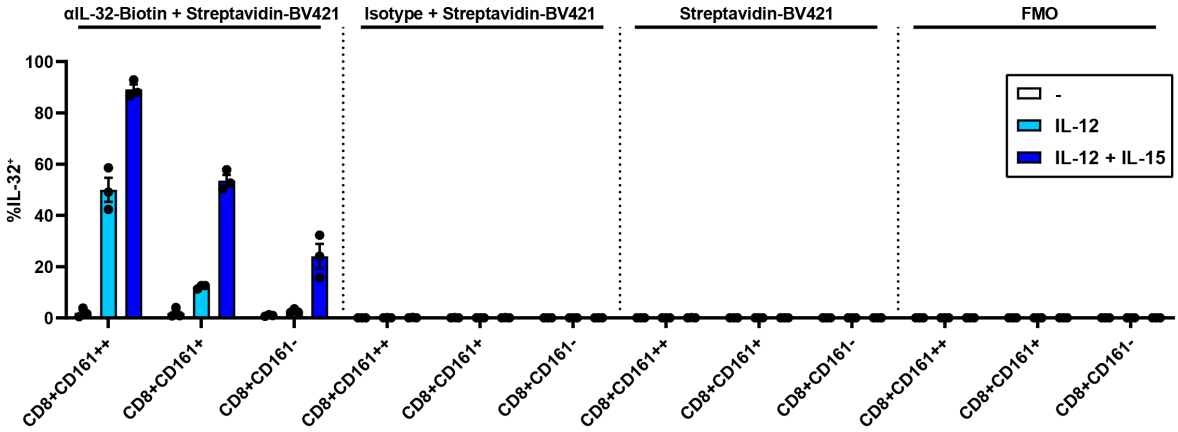
marker	upper threshold	lower threshold
αβTCR	4500	250
CCR7	4250	0
CD134	5000	0
CD137	5000	0
CD14	5000	0
CD16	4250	50
CD161	4750	75
CD19	5000	125
CD2	4250	325
CD218a_IL-18Rα	4500	350
CD223_LAG3	4500	650
CD244_2B4	4500	0
CD25	5000	125
CD26	4500	0
CD27	4500	0
CD274_PD_L1	3750	375
CD279_PD1	5000	-50
CD3	4500	75
CD366_TIM3	5000	0
CD38	4500	0
CD39	4500	0
CD4	4250	0
CD45_BUV395	4125	100
CD45_PE	4125	125
CD45RA	4500	50
CD45RO	4500	375
CD56	4500	50
CD57	4500	50
CD69	4500	175
CD71	4500	125
CD8	4500	50
CD95_FAS	5000	0
CD95L_FASL	4750	300

marker	upper threshold	lower threshold
EOMES	5000	500
FOXP3	4750	500
γδTCR	4350	200
GzmA	4750	375
GzmB	5000	375 (Donor 1 and 2), 600 (Donor 3), 850 (Donor 4)
GzmK	4750	550
HLA_Class_I	5000	0
HLA_DR	4500	0
IFNγ	4500	125
IL-32	4750	625
Ki67	4000	500
live_dead	4000	125
PLZF	5500	500
RORγT	4500	750
TBET	5000	500
TIGIT	5000	200
Vα7.2	4500	100
Vδ2	4500	125

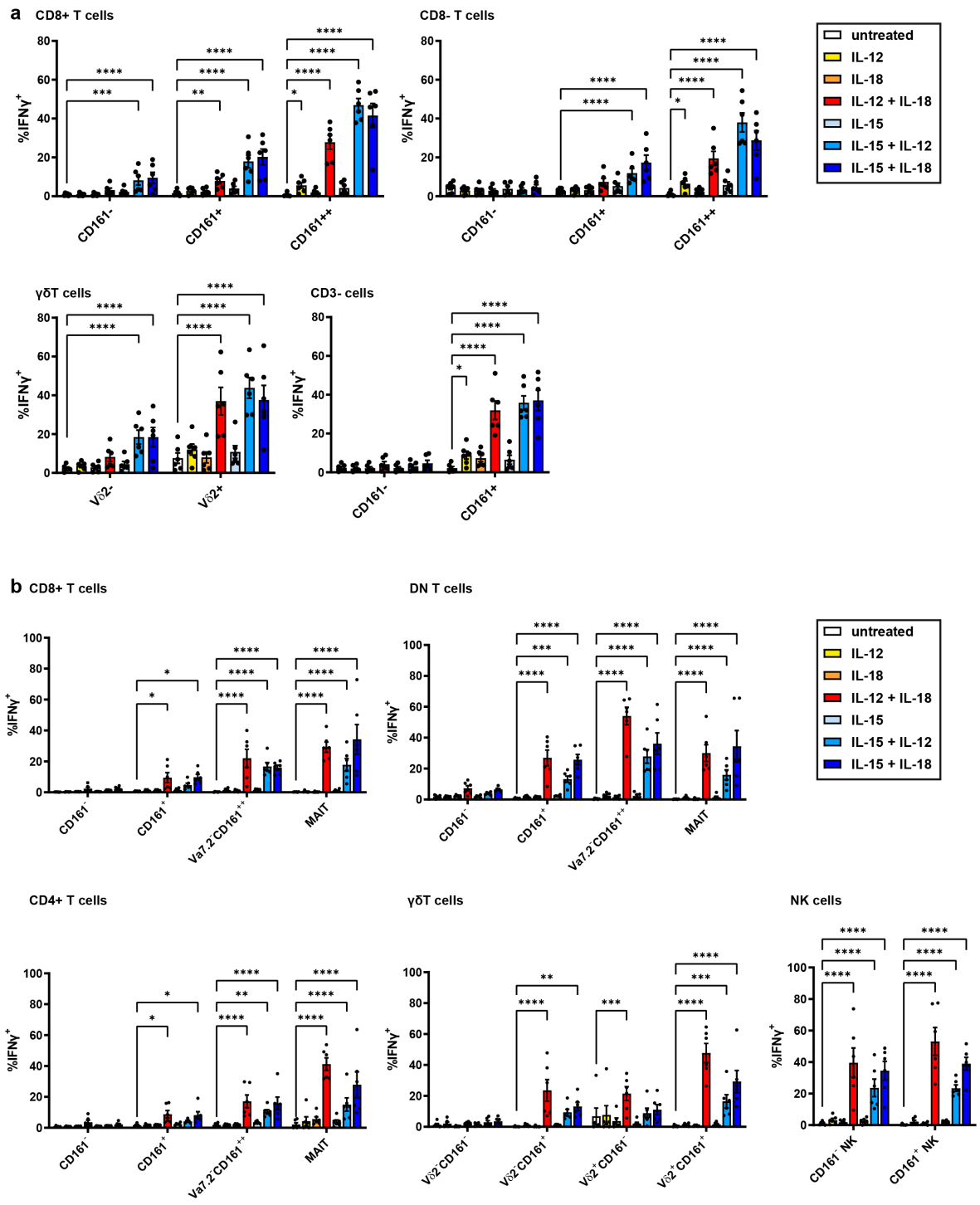
Appendix Table III-3. Details for batch correction of ChipCytometry data using different approaches. Markers that were negatively impacted by range or CytoNorm correction were left uncorrected as indicated in the table.

Marker	Uncorrected	Warp	Range	CytoNorm
2B4	uncorrected	warp	range	CytoNorm
αβTCR	uncorrected	warp	range	CytoNorm
CCR7	uncorrected	warp	range	CytoNorm
CD134	uncorrected	warp	range	CytoNorm
CD137	uncorrected	warp	range	CytoNorm
CD16	uncorrected	warp	range	CytoNorm
CD161	uncorrected	warp	range	uncorrected
CD2	uncorrected	warp	range	CytoNorm
CD25	uncorrected	warp	range	CytoNorm
CD26	uncorrected	warp	range	CytoNorm
CD27	uncorrected	warp	range	CytoNorm
CD3	uncorrected	warp	range	CytoNorm
CD38	uncorrected	warp	range	CytoNorm
CD39	uncorrected	warp	uncorrected	CytoNorm
CD4	uncorrected	warp	range	CytoNorm
CD45RA	uncorrected	warp	range	CytoNorm
CD45RO	uncorrected	warp	range	CytoNorm
CD56	uncorrected	warp	range	CytoNorm
CD57	uncorrected	warp	range	CytoNorm
CD69	uncorrected	warp	range	CytoNorm
CD71	uncorrected	warp	range	CytoNorm
CD8	uncorrected	warp	range	CytoNorm
CD95	uncorrected	warp	range	CytoNorm
Eomes	uncorrected	warp	range	CytoNorm
FASL	uncorrected	warp	range	CytoNorm
FOXP3	uncorrected	warp	range	CytoNorm
γδTCR	uncorrected	warp	uncorrected	CytoNorm
Granzyme A	uncorrected	warp	range	CytoNorm
Granzyme B	uncorrected	warp	range	CytoNorm
Granzyme K	uncorrected	warp	range	CytoNorm
HLA Class I	uncorrected	warp	range	CytoNorm
HLA-DR	uncorrected	warp	range	CytoNorm
IFNγ	uncorrected	warp	range	CytoNorm
IL-18RA	uncorrected	warp	range	CytoNorm
IL-32	uncorrected	warp	range	CytoNorm
Ki67	uncorrected	warp	range	CytoNorm
LAG3	uncorrected	warp	range	CytoNorm
PD1	uncorrected	warp	range	CytoNorm
PD-L1	uncorrected	warp	range	CytoNorm
PLZF	uncorrected	warp	range	uncorrected
RORγT	uncorrected	warp	range	CytoNorm
Tbet	uncorrected	warp	range	CytoNorm
TIGIT	uncorrected	warp	range	CytoNorm
TIM3	uncorrected	warp	range	CytoNorm
VA7.2	uncorrected	warp	range	uncorrected
Vδ2	uncorrected	warp	uncorrected	uncorrected

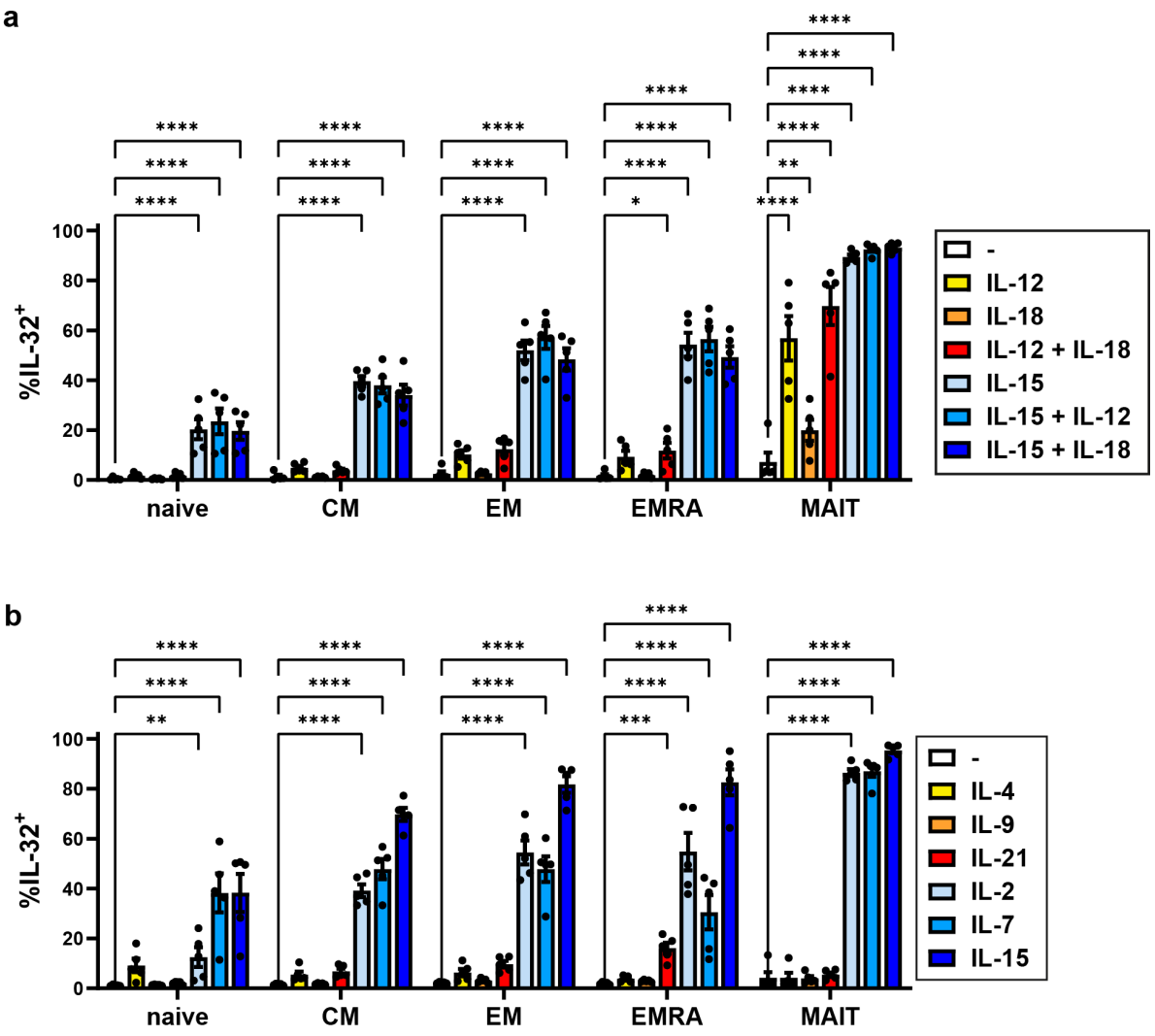
IV. Appendices IV



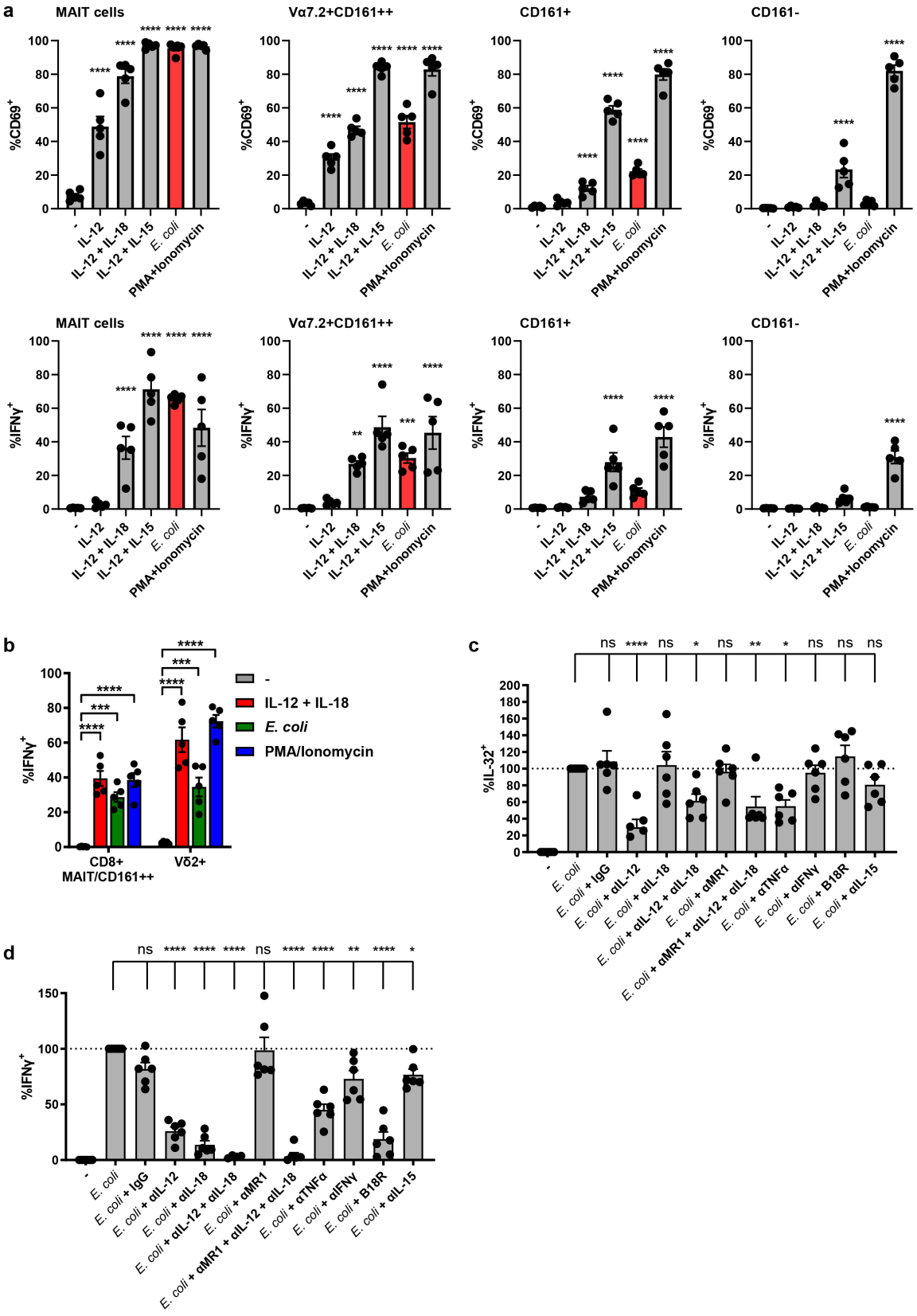
Appendix Figure IV-1. Quantification of the frequency of IL-32$^+$ cells using flow cytometry. PBMCs were stimulated with IL-12 or IL-12+IL-15 for 24 hours. Medium only served as a negative control (-). IL-32 expression was analysed by flow cytometry using a biotin-labelled anti-IL-32 antibody in combination with fluorochrome-labelled Streptavidin. Staining controls included fluorescence minus one (FMO), Streptavidin-BV421 only, and IgG-Biotin + Streptavidin-BV421. Bar chart shows the quantification of IL-32$^+$ cells within CD8$^+$ T cells subsets.



Appendix Figure IV-2. Cytokine-induced IFNγ expression in PBMCs and CD14-/CD19-depleted PBMCs. IFNγ expression of indicated T cell and CD3$^-$ subsets within CD14-/CD19-depleted PBMCs (N=6, pooled from two independent experiments) was analysed using flow cytometry after stimulation for 24 hours with individual cytokines and cytokine combinations, including IL-12, IL-18, IL-15, IL-12+IL-18, IL-12+IL-15 and IL-18+IL-15. In (a), total PBMCs were used. In (b), T and NK cells were enriched by CD14- and CD19-depletion. Bar plots indicate mean ± SEM. Two-way repeated measures ANOVA with Bonferroni's multiple comparisons test was performed. ****p<0.0001, ***p<0.001, **p<0.01, *p<0.05.

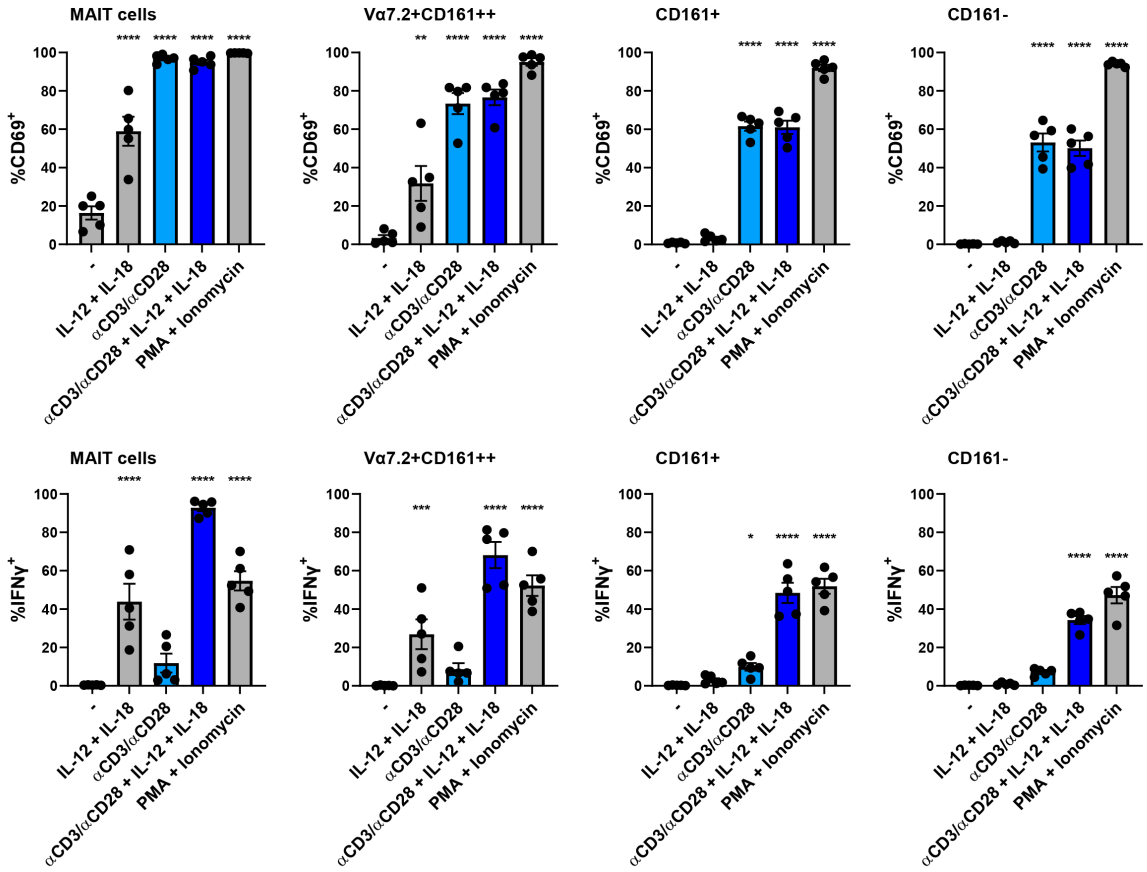


Appendix Figure IV-3. Comparison of cytokine-induced IL-32 expression between MAIT cells and memory T-cell subsets. (a)-(b) PBMCs (N=5) were stimulated with indicated cytokines for 48 hours. IL-32 expression in indicated $CD8^+$ T-cell subsets was analysed using flow cytometry. Bar plots indicate mean ± SEM. Two-way repeated measures ANOVA with Bonferroni's multiple comparisons test was performed. ****p<0.0001, ***p<0.001, **p<0.01, *p<0.05.

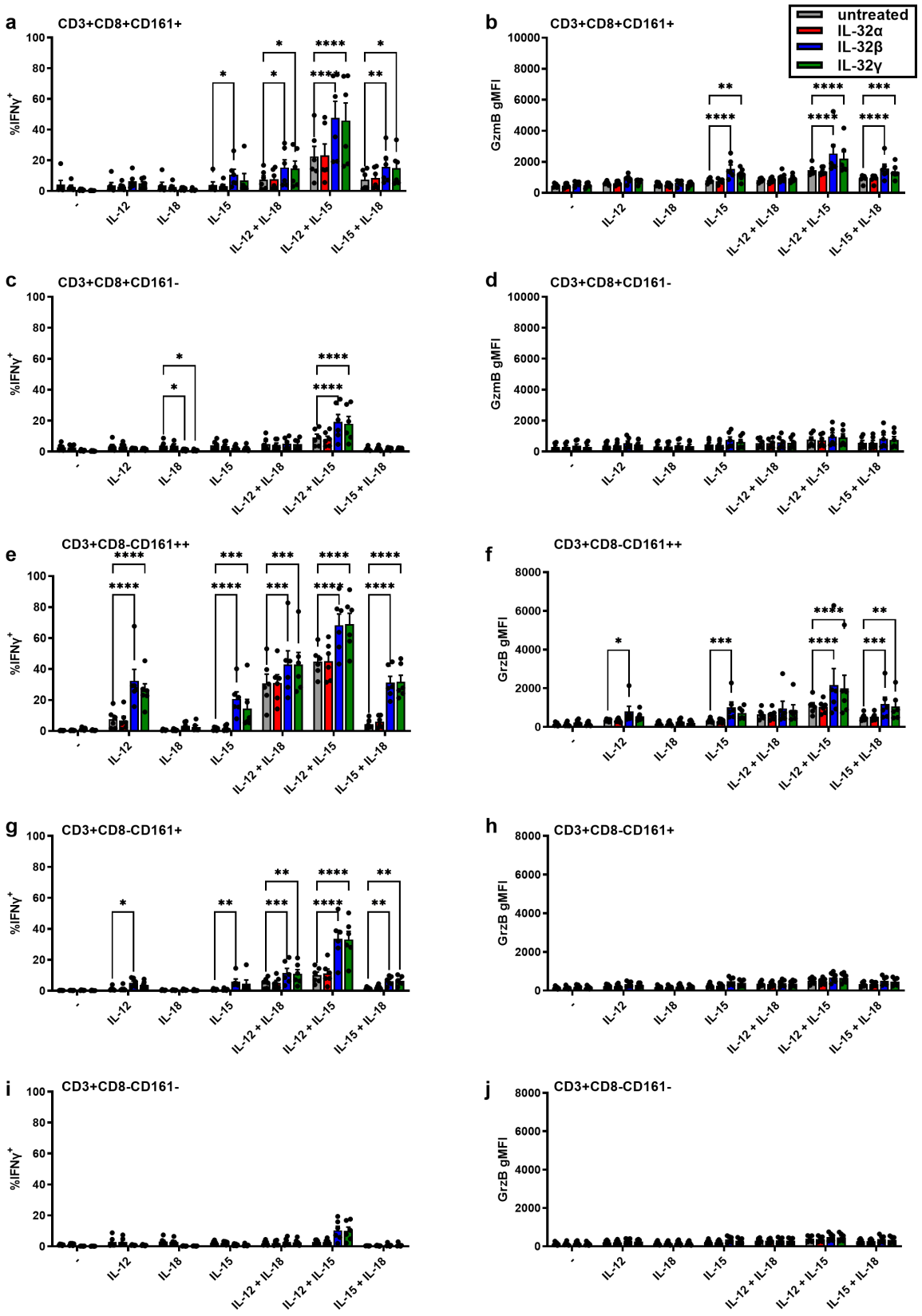


Appendix Figure IV-4. *E. coli*-induced CD69 and IFNγ expression in T cells. (a) PBMCs (N=5) were incubated with PFA-fixed *E. coli* for 48 hours. Controls included medium only (-), cytokines (IL-12, IL-12+IL-18 or IL-12+IL-15) and PMA+Ionomycin. CD69 and IFNγ expression was analysed in indicated T-cell subsets using flow-cytometry. Bar plots indicate mean ± SEM. One-way repeated measures ANOVA with Bonferroni's multiple comparisons test was performed. (b) After stimulation of PBMCs (N=5) with IL-12+IL-18, *E. coli* or

PMA+Ionomycin for 24 hours, IFNγ expression was analysed in Vδ2⁺ T cells and CD8⁺CD161⁺⁺ T cells using flow cytometry. CD8⁺CD161⁺⁺ T cells include MAIT and Vα7.2⁻CD161⁺⁺ T cells. Bar plots indicate mean ± SEM. Two-way repeated measures ANOVA with Bonferroni's multiple comparisons test was performed. (c)-(d) PBMCs (N=6) were incubated for 48 hours with *E. coli* in presence or absence of blocking antibodies as indicated. Controls included medium only (-) and IgG isotype control. IL-32 and IFNγ expression in CD8⁺ T cells that express intermediate CD161 levels was analysed using flow cytometry. Bar plots indicate mean ± SEM. One-way repeated measures ANOVA with Bonferroni's multiple comparisons test was performed. ****p<0.0001, ***p<0.001, **p<0.01, *p<0.05.

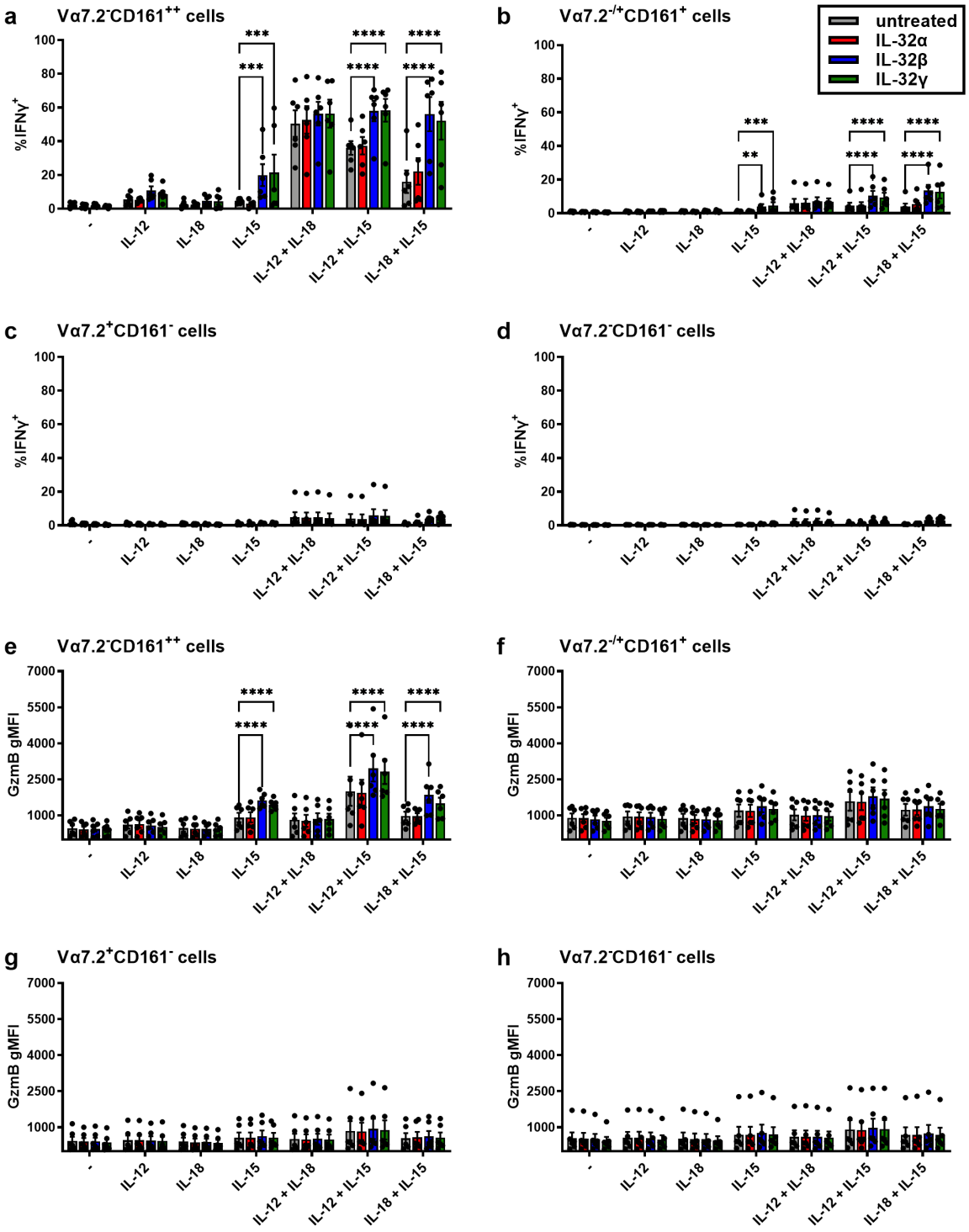


Appendix Figure IV-5. TCR-induced IL-32 expression in T cells. CD8-enriched T cells (N=5) were stimulated with IL-12+IL-18, plate-bound anti-CD3 and soluble anti-CD28 antibodies, or the combination of anti-CD3/anti-CD28 and IL-12+IL-18 cytokines for 48 hours. Controls included medium only (-) and PMA+Ionomycin. CD69 and IFNγ expression was analysed in indicated T-cell subsets using flow cytometry. Bar plots indicate mean ± SEM. For statistical testing, one-way repeated measures ANOVA with Bonferroni's multiple comparisons test was performed. ****p<0.0001, ***p<0.001, **p<0.01, *p<0.05.



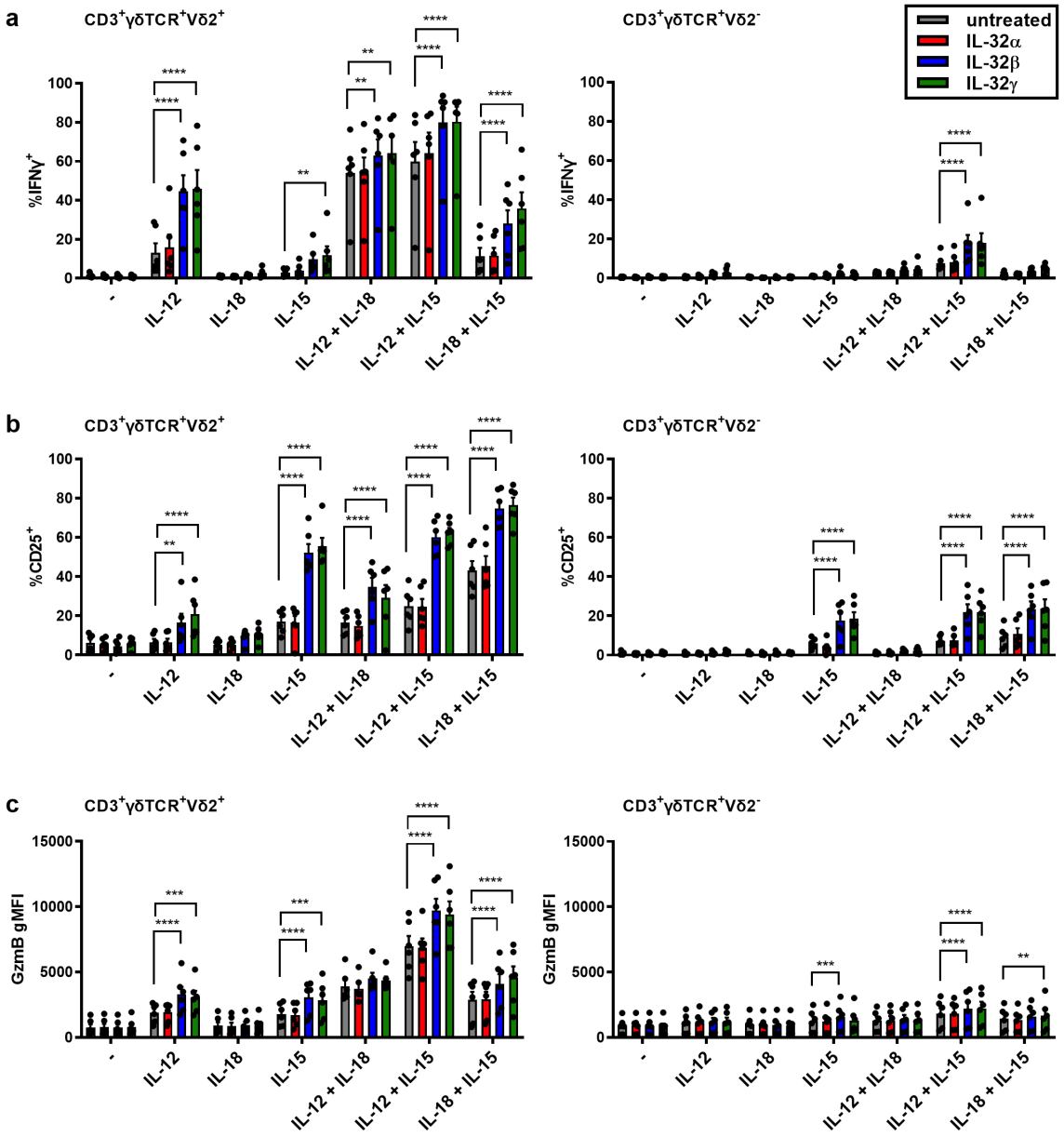
Appendix Figure IV-6. Effect of IL-32 on cytokine-stimulated T cells within PBMCs. (a)-(j) PBMCs (N=6, pooled from two independent experiments with N=3) were incubated in the presence or absence of cytokines or combinations of cytokines at suboptimal concentrations, including IL-15, IL-12 and IL-18. To each condition, diluted IL-32α, IL-32β, IL-32γ or pure medium (-) was added. After 24 hours, IFNγ and GzmB expression in

indicated T-cell subsets was analysed using flow cytometry. Columns with error bars represent mean ± SEM. Geometric mean fluorescence intensity, gMFI. Two-way repeated measures ANOVA with Bonferroni's multiple comparisons test was performed. ****p<0.0001, ***p<0.001, **p<0.01, *p<0.05.

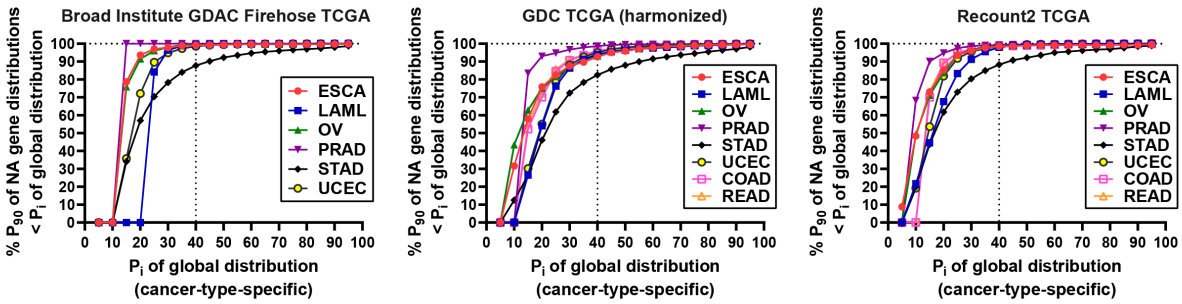


Appendix Figure IV-7. Effect of IL-32 on cytokine-stimulated T cells within CD8-enriched PBMCs. (a)-(h) CD8-enriched PBMCs (N=6, pooled from two independent experiments with N=3) were incubated in the presence or absence of cytokines or combinations of cytokines at suboptimal concentrations, including IL-15, IL-12 and IL-18. To each condition, diluted IL-32α, IL-32β, IL-32γ or pure medium (-) was added. After 24 hours, IFNγ and GzmB expression in indicated T-cell subsets was analysed using flow cytometry. Columns with error bars

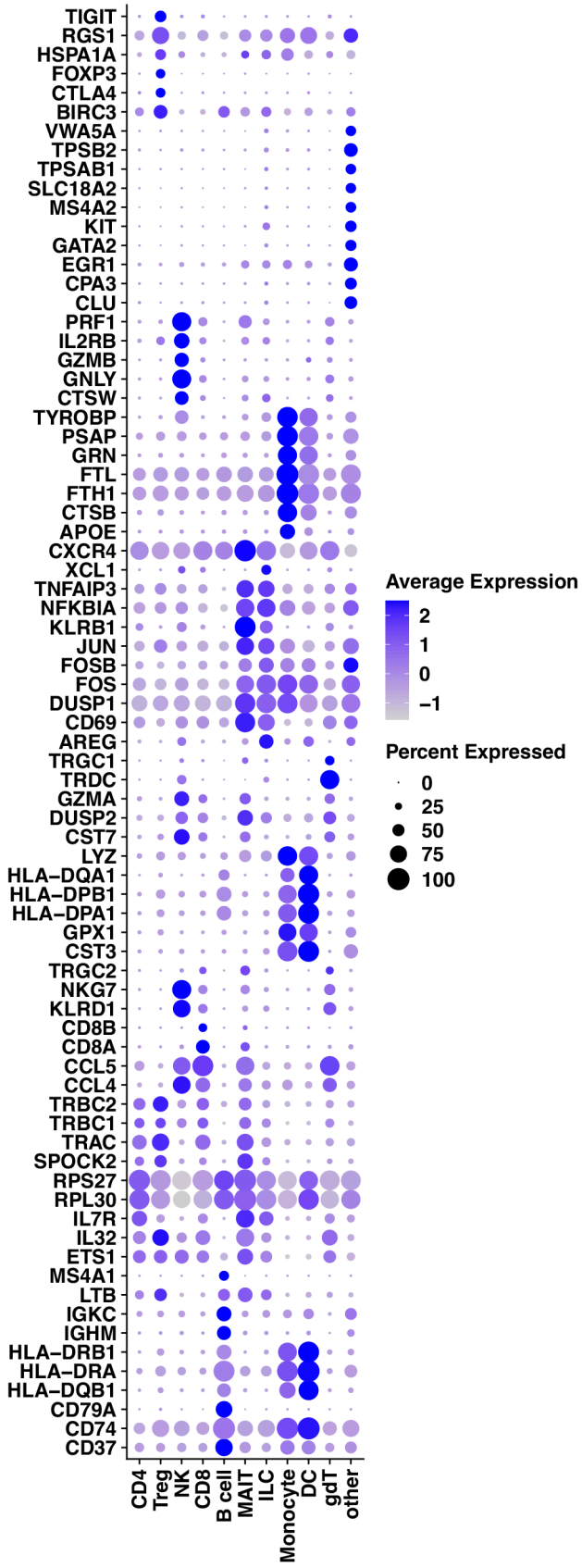
represent mean ± SEM. Geometric mean fluorescence intensity, gMFI. Two-way repeated measures ANOVA with Bonferroni's multiple comparisons test was performed. ****p<0.0001, ***p<0.001, **p<0.01, *p<0.05.



Appendix Figure IV-8. Effect of IL-32 on cytokine-stimulated γδT cells within PBMCs. (a)-(c) PBMCs (N=6, pooled from two independent experiments with N=3) were incubated in the presence or absence of cytokines or combinations of cytokines at suboptimal concentrations, including IL-15, IL-12 and IL-18. To each condition, diluted IL-32α, IL-32β, IL-32γ or pure medium (-) was added. After 24 hours, IFNγ, CD25 and GzmB expression in indicated γδT-cell subsets was analysed using flow cytometry. Columns with error bars represent mean ± SEM. Geometric mean fluorescence intensity, gMFI. Two-way repeated measures ANOVA with Bonferroni's multiple comparisons test was performed. ****p<0.0001, ***p<0.001, **p<0.01, *p<0.05.



Appendix Figure IV-9. Analysis of expression levels of genes that were replaced with NAs in PanCan Atlas data utilising TCGA data obtained from different repositories. To investigate the original expression values of PanCan TCGA NAs and to compare them to the overall global and cancer type-specific global gene expression, TCGA data was obtained from alternative repositories, including Broad Institute GDAC Firehose, GDC harmonized data portal and Recount2. For each of three TCGA data sets obtained from different repositories, the distribution of data points that were replaced with NAs within the PanCan Atlas TCGA data was assessed, separately for each affected gene (NA gene distribution). The 90th percentiles (P_{90}) for the NA distributions of each affected gene were calculated. The graphs display the frequency for the fulfilled condition P_{90} of NA gene distributions < P_i of the global gene expression distribution of the respective cancer type, where i stands for percentiles from 5-95 in steps of 5.



Appendix Figure IV-10. Expression of top 10 differentially expressed genes of cell types identified in Azizi et al. breast cancer scRNA-seq data. Breast cancer scRNA-seq data including 21253 immune cells from 8 treatment naive patients were obtained from Azizi et al. (308). In order to identify different immune cell types in the breast cancer scRNA-seq data, reference mapping using Seurat v4 R package was performed using the

PBMC CITE-seq data from Hao et al. as a reference (305). Reference cell types were aggregated to obtain the final 11 aggregated cell types analysed in the present study. To confirm the identity of annotated cell types, the top 10 differentially expressed genes of each cell type compared to all other cells were determined using presto R package (313). Dot plot shows average expression and the percentage of positive cells of the top 10 differentially expressed genes of all 11 cell types.

Appendix Table IV-1. Quantification of samples and genes containing NAs stratified by cancer type. *STAD: 1455 genes were replaced with NAs in 99.33% of samples. 2311 additional genes were replaced with NAs in 8.44% of samples.

	Fraction of samples containing NAs [%]	Number of genes containing NAs
COAD	33.54	3024 (14.73%)
ESCA	98.47	1455 (7.09%)
LAML	100.00	3766 (18.34%)
OV	99.35	1455 (7.09%)
PRAD	6.00	1443 (7.03%)
READ	38.60	3024 (14.73%)
STAD*	8.44 / 99.33	3766 / 1455 (18.34% / 7.09%)
UCEC	64.55	3024 (14.73%)

Appendix Table IV-2. List of *IL32* signature genes, including 1E-1, 5E-2, 1E-2, 1E-3, 1E-4, 1E-5, 1E-6, 1E-7, 1E-8 and 1E-9 *IL32* signatures.

1.E-01	5.E-02	1.E-02	1.E-03	1.E-04	1.E-05	1.E-06	1.E-07	1.E-08	1.E-09
IL32	IL32	IL32	IL32	IL32	IL32	IL32	IL32	IL32	IL32
MMP25	MMP25	MMP25	MMP25	MMP25	MMP25	MMP25	MMP25	MMP25	MMP25
UBD	UBD	UBD	UBD	UBD	UBD	UBD	UBD	UBD	UBD
IRF1	IRF1	IRF1	IRF1	IRF1	IRF1	IRF1	IRF1	IRF1	IRF1
IL2RG	IL2RG	IL2RG	IL2RG	IL2RG	IL2RG	IL2RG	IL2RG	IL2RG	IL2RG
ICAM1	ICAM1	ICAM1	ICAM1	ICAM1	ICAM1	ICAM1	ICAM1	ICAM1	ICAM1
CCL5	CCL5	CCL5	CCL5	CCL5	CCL5	CCL5	CCL5	CCL5	CCL5
PSMB9	PSMB9	PSMB9	PSMB9	PSMB9	PSMB9	PSMB9	PSMB9	PSMB9	PSMB9
RRAS	RRAS	RRAS	RRAS	RRAS	RRAS	RRAS	RRAS	RRAS	RRAS
LTB	LTB	LTB	LTB	LTB	LTB	LTB	LTB	LTB	LTB
IL4I1	IL4I1	IL4I1	IL4I1	IL4I1	IL4I1	IL4I1	IL4I1	IL4I1	IL4I1
HLA-A	HLA-A	HLA-A	HLA-A	HLA-A	HLA-A	HLA-A	HLA-A	HLA-A	HLA-A
IL15RA	IL15RA	IL15RA	IL15RA	IL15RA	IL15RA	IL15RA	IL15RA	IL15RA	IL15RA
PSMB10	PSMB10	PSMB10	PSMB10	PSMB10	PSMB10	PSMB10	PSMB10	PSMB10	PSMB10
TAP1	TAP1	TAP1	TAP1	TAP1	TAP1	TAP1	TAP1	TAP1	TAP1
SOD2	SOD2	SOD2	SOD2	SOD2	SOD2	SOD2	SOD2	SOD2	SOD2
CD74	CD74	CD74	CD74	CD74	CD74	CD74	CD74	CD74	CD74
GBP2	GBP2	GBP2	GBP2	GBP2	GBP2	GBP2	GBP2	GBP2	GBP2
SLC2A6	SLC2A6	SLC2A6	SLC2A6	SLC2A6	SLC2A6	SLC2A6	SLC2A6	SLC2A6	SLC2A6
HLA-F	HLA-F	HLA-F	HLA-F	HLA-F	HLA-F	HLA-F	HLA-F	HLA-F	HLA-F

DRAM1	DRAM1	DRAM1	DRAM1	DRAM1	DRAM1	DRAM1	DRAM1	DRAM1	TNFRSF4
TNFRSF4	TNFRSF4	TNFRSF4	TNFRSF4	TNFRSF4	TNFRSF4	TNFRSF4	TNFRSF4	TNFRSF4	APOL3
APOL3	APOL3	APOL3	APOL3	APOL3	APOL3	APOL3	APOL3	APOL3	SH2D2A
SH2D2A	SH2D2A	SH2D2A	SH2D2A	SH2D2A	SH2D2A	SH2D2A	SH2D2A	SH2D2A	BIRC3
BIRC3	BIRC3	BIRC3	BIRC3	BIRC3	BIRC3	BIRC3	BIRC3	BIRC3	HLA-H
HLA-H	HLA-H	HLA-H	HLA-H	HLA-H	HLA-H	HLA-H	HLA-H	HLA-H	HLA-B
HLA-B	HLA-B	HLA-B	HLA-B	HLA-B	HLA-B	HLA-B	HLA-B	HLA-B	TYMP
TYMP	TYMP	TYMP	TYMP	TYMP	TYMP	TYMP	TYMP	TYMP	GBP1
GBP1	GBP1	GBP1	GBP1	GBP1	GBP1	GBP1	GBP1	GBP1	TMSB10
TMSB10	TMSB10	TMSB10	TMSB10	TMSB10	TMSB10	TMSB10	TMSB10	TMSB10	GZMH
GZMH	GZMH	GZMH	GZMH	GZMH	GZMH	GZMH	GZMH	GZMH	CD3E
CD3E	CD3E	CD3E	CD3E	CD3E	CD3E	CD3E	CD3E	CD3E	ETV7
ETV7	ETV7	ETV7	ETV7	ETV7	ETV7	ETV7	ETV7	ETV7	HAPLN3
HAPLN3	HAPLN3	HAPLN3	HAPLN3	HAPLN3	HAPLN3	HAPLN3	HAPLN3	HAPLN3	JAK3
JAK3	JAK3	JAK3	JAK3	JAK3	JAK3	JAK3	JAK3	JAK3	CD7
CD7	CD7	CD7	CD7	CD7	CD7	CD7	CD7	CD7	GZMA
GZMA	GZMA	GZMA	GZMA	GZMA	GZMA	GZMA	GZMA	GZMA	ICAM2
ICAM2	ICAM2	ICAM2	ICAM2	ICAM2	ICAM2	ICAM2	ICAM2	ICAM2	CD247
CD247	CD247	CD247	CD247	CD247	CD247	CD247	CD247	CD247	NKG7
NKG7	NKG7	NKG7	NKG7	NKG7	NKG7	NKG7	NKG7	NKG7	IL15
IL15	IL15	IL15	IL15	IL15	IL15	IL15	IL15	IL15	CXCL10
CXCL10	CXCL10	CXCL10	CXCL10	CXCL10	CXCL10	CXCL10	CXCL10	CXCL10	CD2
CD2	CD2	CD2	CD2	CD2	CD2	CD2	CD2	CD2	CD6
CD6	CD6	CD6	CD6	CD6	CD6	CD6	CD6	CD6	CD3D
CD3D	CD3D	CD3D	CD3D	CD3D	CD3D	CD3D	CD3D	CD3D	APOL1
APOL1	APOL1	APOL1	APOL1	APOL1	APOL1	APOL1	APOL1	APOL1	PSMB8
PSMB8	PSMB8	PSMB8	PSMB8	PSMB8	PSMB8	PSMB8	PSMB8	PSMB8	CD52
CD52	CD52	CD52	CD52	CD52	CD52	CD52	CD52	CD52	IL2RB
IL2RB	IL2RB	IL2RB	IL2RB	IL2RB	IL2RB	IL2RB	IL2RB	IL2RB	LST1
TNFAIP3	TNFAIP3	TNFAIP3	TNFAIP3	TNFAIP3	TNFAIP3	TNFAIP3	LST1	LST1	RARRES3
LST1	LST1	LST1	LST1	LST1	LST1	LST1	RARRES3	RARRES3	CCL2
RARRES3	RARRES3	RARRES3	RARRES3	RARRES3	RARRES3	RARRES3	CCL2	CCL2	CST7
CCL2	CCL2	CCL2	CCL2	CCL2	CCL2	CCL2	CST7	CST7	ZNF683
CST7	CST7	CST7	CST7	CST7	CST7	CST7	ZNF683	ZNF683	VAMP5
ZNF683	ZNF683	ZNF683	ZNF683	ZNF683	ZNF683	ZNF683	VAMP5	VAMP5	MVP
VAMP5	VAMP5	VAMP5	VAMP5	VAMP5	VAMP5	VAMP5	MVP	MVP	CXCR3
MVP	MVP	MVP	MVP	MVP	MVP	MVP	CXCR3	CXCR3	BATF2
CXCR3	CXCR3	CXCR3	CXCR3	CXCR3	CXCR3	CXCR3	BATF2	BATF2	PRF1
BATF2	BATF2	BATF2	BATF2	BATF2	BATF2	BATF2	NEURL3	NEURL3	RASAL3
NEURL3	NEURL3	NEURL3	NEURL3	NEURL3	NEURL3	NEURL3	PRF1	PRF1	HLA-DMA
PRF1	PRF1	PRF1	PRF1	PRF1	PRF1	PRF1	RASAL3	RASAL3	CXCL9

RASAL3	RASAL3	RASAL3	RASAL3	RASAL3	RASAL3	RASAL3	HLA-DMA	HLA-DMA	CARD16
HLA-DMA	HLA-DMA	HLA-DMA	HLA-DMA	HLA-DMA	HLA-DMA	HLA-DMA	CXCL9	CXCL9	EBI3
CXCL9	CXCL9	CXCL9	CXCL9	CXCL9	CXCL9	CXCL9	CARD16	CARD16	HLA-C
CARD16	CARD16	CARD16	CARD16	CARD16	CARD16	CARD16	EBI3	EBI3	CCL4
EBI3	EBI3	EBI3	EBI3	EBI3	EBI3	EBI3	HLA-C	HLA-C	CTSW
HLA-C	HLA-C	HLA-C	HLA-C	HLA-C	HLA-C	HLA-C	CCL4	CCL4	HSD3B7
CCL4	CCL4	CCL4	CCL4	CCL4	CCL4	CCL4	CTSW	CTSW	GzmB
CTSW	CTSW	CTSW	CTSW	CTSW	CTSW	CTSW	HSD3B7	HSD3B7	CXCL11
HSD3B7	HSD3B7	HSD3B7	HSD3B7	HSD3B7	HSD3B7	HSD3B7	GzmB	GzmB	PTPN7
GzmB	GzmB	GzmB	GzmB	GzmB	GzmB	GzmB	CXCL11	CXCL11	BATF
FSTL3	FSTL3	FSTL3	FSTL3	CXCL11	CXCL11	CXCL11	PTPN7	PTPN7	ODF3B
CXCL11	CXCL11	CXCL11	CXCL11	PTPN7	PTPN7	PTPN7	BATF	BATF	HLA-DPA1
PTPN7	PTPN7	PTPN7	PTPN7	BATF	BATF	BATF	ODF3B	ODF3B	SIRPG
BATF	BATF	BATF	BATF	ODF3B	ODF3B	ODF3B	HLA-DPA1	HLA-DPA1	CASP4
ODF3B	ODF3B	ODF3B	ODF3B	HLA-DPA1	HLA-DPA1	HLA-DPA1	SIRPG	SIRPG	CD5
HLA-DPA1	HLA-DPA1	HLA-DPA1	HLA-DPA1	SIRPG	SIRPG	SIRPG	CASP4	CASP4	IFITM3
SIRPG	SIRPG	SIRPG	SIRPG	CASP4	CASP4	CASP4	TNF	CD5	HCST
CASP4	CASP4	CASP4	CASP4	TNF	TNF	TNF	CD5	IFITM3	SLAMF8
TNF	TNF	TNF	TNF	PLA2G4C	PLA2G4C	CD5	IFITM3	HCST	HLA-DRA
PLA2G4C	PLA2G4C	PLA2G4C	PLA2G4C	CD5	CD5	IFITM3	HCST	SLAMF8	IFI30
CD5	CD5	CD5	CD5	IFITM3	IFITM3	HCST	SLAMF8	HLA-DRA	DOK2
IFITM3	IFITM3	IFITM3	IFITM3	HCST	HCST	SLAMF8	HLA-DRA	IFI30	STAT4
HCST	HCST	HCST	HCST	SLAMF8	SLAMF8	HLA-DRA	TNFRSF12A	DOK2	HLA-DPB1
SLAMF8	SLAMF8	SLAMF8	SLAMF8	DENND1C	DENND1C	TNFRSF12A	IFI30	STAT4	AMICA1
DENND1C	DENND1C	DENND1C	DENND1C	HLA-DRA	HLA-DRA	IFI30	DOK2	HLA-DPB1	NCR00152
HLA-DRA	HLA-DRA	HLA-DRA	HLA-DRA	TNFRSF12A	TNFRSF12A	DOK2	STAT4	AMICA1	ACAP1
TNFRSF12A	TNFRSF12A	TNFRSF12A	TNFRSF12A	IFI30	IFI30	STAT4	HLA-DPB1	NCR00152	LCP2
IFI30	IFI30	IFI30	IFI30	DOK2	DOK2	HLA-DPB1	AMICA1	ACAP1	ZAP70
DOK2	DOK2	DOK2	DOK2	LDLRAD2	LDLRAD2	AMICA1	NCR00152	LCP2	CD48
LDLRAD2	LDLRAD2	LDLRAD2	LDLRAD2	STAT4	STAT4	NCR00152	ACAP1	ZAP70	CTSS
STAT4	STAT4	STAT4	STAT4	HLA-DPB1	HLA-DPB1	CXCL16	LCP2	CD48	IL21R
HLA-DPB1	HLA-DPB1	HLA-DPB1	HLA-DPB1	AMICA1	AMICA1	ACAP1	ZAP70	CTSS	TMEM176A
AMICA1	AMICA1	AMICA1	AMICA1	NCR00152	NCR00152	LCP2	CD48	IL21R	PSTPIP1
NCR00152	NCR00152	NCR00152	NCR00152	CXCL16	CXCL16	ZAP70	CTSS	TMEM176A	FLT3LG
CXCL16	CXCL16	CXCL16	CXCL16	ACAP1	ACAP1	CD48	IL21R	PSTPIP1	HMHA1
ACAP1	ACAP1	ACAP1	ACAP1	LCP2	LCP2	CTSS	TMEM176A	FLT3LG	HLA-DRB1
LCP2	LCP2	LCP2	LCP2	ZAP70	ZAP70	IL21R	PSTPIP1	HMHA1	FCER1G

ZAP70	ZAP70	ZAP70	ZAP70	CD48	CD48	TMEM176A	FLT3LG	HLA-DRB1	CCRL2
CD48	CD48	CD48	CD48	CTSS	CTSS	PSTPIP1	HMHA1	FCER1G	PLEKHO1
CTSS	CTSS	CTSS	CTSS	IL21R	IL21R	FLT3LG	HLA-DRB1	NMI	GMFG
IL21R	IL21R	IL21R	IL21R	TMEM176A	TMEM176A	HMHA1	FCER1G	CCRL2	RAC2
TMEM176A	TMEM176A	TMEM176A	TMEM176A	PSTPIP1	PSTPIP1	HLA-DRB1	NMI	PLEKHO1	LSP1
PSTPIP1	PSTPIP1	PSTPIP1	PSTPIP1	FLT3LG	FLT3LG	FCER1G	WARS	GMFG	TMEM176B
FLT3LG	FLT3LG	FLT3LG	FLT3LG	HMHA1	HMHA1	NMI	CCRL2	RAC2	PLAUR
HMHA1	HMHA1	HMHA1	HMHA1	HLA-DRB1	HLA-DRB1	WARS	PLEKHO1	LSP1	CCR5
HLA-DRB1	HLA-DRB1	HLA-DRB1	HLA-DRB1	FCER1G	FCER1G	CCRL2	BCL3	TMEM176B	PTPRCAP
BBC3	BBC3	BBC3	BBC3	NMI	NMI	PLEKHO1	GMFG	PLAUR	LOC606724
FCER1G	FCER1G	FCER1G	FCER1G	WARS	WARS	BCL3	RAC2	CCR5	GSDMD
NMI	NMI	NMI	NMI	CCRL2	CCRL2	GMFG	LSP1	PTPRCAP	KLHDC7B
WARS	WARS	WARS	WARS	PLEKHO1	PLEKHO1	RAC2	TMEM176B	LOC606724	TRPV2
CCRL2	CCRL2	CCRL2	CCRL2	BCL3	BCL3	LSP1	PLAUR	GSDMD	SLA2
PLEKHO1	PLEKHO1	PLEKHO1	PLEKHO1	GMFG	GMFG	TMEM176B	CCR5	KLHDC7B	CD8A
BCL3	BCL3	BCL3	BCL3	RAC2	RAC2	PLAUR	PTPRCAP	TRPV2	IFITM2
GMFG	GMFG	GMFG	GMFG	LSP1	LSP1	CCR5	LOC606724	SLA2	CXCR6
RAC2	RAC2	RAC2	RAC2	TMEM176B	TMEM176B	PTPRCAP	GSDMD	CD8A	SERPING1
LSP1	LSP1	LSP1	LSP1	PLAUR	PLAUR	LOC606724	KLHDC7B	IFITM2	MYO1F
TMEM176B	TMEM176B	TMEM176B	TMEM176B	CCR5	CCR5	GSDMD	TRPV2	CXCR6	SIT1
PLAUR	PLAUR	PLAUR	PLAUR	PTPRCAP	PTPRCAP	KLHDC7B	SLA2	SERPING1	C10orf125
CCR5	CCR5	CCR5	CCR5	LOC606724	LOC606724	TRPV2	CD8A	MYO1F	CIITA
PTPRCAP	PTPRCAP	PTPRCAP	PTPRCAP	GSDMD	GSDMD	SLA2	IFITM2	SIT1	APOB48R
LOC606724	LOC606724	LOC606724	LOC606724	KLHDC7B	KLHDC7B	CD8A	CXCR6	C10orf125	SAMD3
GSDMD	GSDMD	GSDMD	GSDMD	TRPV2	TRPV2	TRAF1	SERPING1	CIITA	GZMM
KLHDC7B	KLHDC7B	KLHDC7B	KLHDC7B	SLA2	SLA2	IFITM2	MYO1F	APOB48R	GBP5
TRPV2	TRPV2	TRPV2	TRPV2	CD8A	CD8A	CXCR6	SIT1	SAMD3	TIGIT
SLA2	SLA2	SLA2	SLA2	TRAF1	TRAF1	SERPING1	C10orf125	GZMM	TNFRSF1B
CD8A	CD8A	CD8A	CD8A	NLRC3	IFITM2	MYO1F	CIITA	GBP5	CLEC2B
TRAF1	TRAF1	TRAF1	TRAF1	IFITM2	CXCR6	SIT1	APOB48R	TIGIT	GPR84
NLRC3	NLRC3	NLRC3	NLRC3	CXCR6	SERPING1	C10orf125	SAMD3	TNFRSF1B	AIF1
IFITM2	IFITM2	IFITM2	IFITM2	SERPING1	MYO1F	CIITA	GZMM	HLA-DQB1	Sep-01
CXCR6	CXCR6	CXCR6	CXCR6	MYO1F	SIT1	APOB48R	GBP5	CLEC2B	TBC1D10C
SERPING1	SERPING1	SERPING1	SERPING1	SIT1	RFTN1	SAMD3	TIGIT	GPR84	CCL3
MYO1F	MYO1F	MYO1F	MYO1F	RFTN1	C10orf125	GZMM	TNFRSF1B	AIF1	ITGAL
SIT1	SIT1	SIT1	SIT1	C10orf125	CIITA	GBP5	HLA-DQB1	Sep-01	MYO1G
RFTN1	RFTN1	RFTN1	RFTN1	CIITA	APOB48R	TIGIT	CLEC2B	CAPG	HLA-DQA1

C10orf125	C10orf125	C10orf125	C10orf125	APOB48R	SAMD3	TNFRSF1B	GPR84	TBC1D10C	CD8B
CIITA	CIITA	CIITA	CIITA	SAMD3	GZMM	HLA-DQB1	AIF1	CCL3	COTL1
APOB48R	APOB48R	APOB48R	APOB48R	GZMM	GBP5	CLEC2B	Sep-01	ITGAL	GNGT2
SAMD3	SAMD3	SAMD3	SAMD3	GBP5	TIGIT	GPR84	CAPG	MYO1G	IDO1
GZMM	GZMM	GZMM	GZMM	TIGIT	TNFRSF1B	AIF1	TBC1D10C	HLA-DQA1	FAM26F
GBP5	GBP5	GBP5	GBP5	TNFRSF1B	HLA-DQB1	Sep-01	CCL3	CD8B	SECTM1
TIGIT	TIGIT	TIGIT	TIGIT	HLA-DQB1	CLEC2B	CAPG	ITGAL	COTL1	NNMT
TNFRSF1B	TNFRSF1B	TNFRSF1B	TNFRSF1B	CLEC2B	GPR84	TBC1D10C	MYO1G	CD40	ABI3
HLA-DQB1	HLA-DQB1	HLA-DQB1	HLA-DQB1	GPR84	AIF1	VCAM1	HLA-DQA1	GNGT2	FGR
CLEC2B	CLEC2B	CLEC2B	CLEC2B	AIF1	Sep-01	CCL3	CD8B	IDO1	C14orf73
ACHE	ACHE	ACHE	ACHE	Sep-01	CAPG	ITGAL	ITGAM	FAM26F	
ATHL1	ATHL1	ATHL1	GPR84	CAPG	TBC1D10C	MYO1G	COTL1	SECTM1	
GPR84	GPR84	GPR84	AIF1	TBC1D10C	VCAM1	HLA-DQA1	CD40	NNMT	
AIF1	AIF1	AIF1	Sep-01	VCAM1	CCL3	CD8B	GNGT2	ABI3	
Sep-01	Sep-01	Sep-01	CAPG	CCL3	ITGAL	TRIM47	IDO1	FGR	
CAPG	CAPG	CAPG	TBC1D10C	ITGAL	MYO1G	ITGAM	FAM26F	FAM113B	
TBC1D10C	TBC1D10C	TBC1D10C	VCAM1	MYO1G	HLA-DQA1	COTL1	SECTM1	C14orf73	
VCAM1	VCAM1	VCAM1	CCL3	HLA-DQA1	CD8B	CD40	NNMT	BCL2A1	
CCL3	CCL3	CCL3	ITGAL	CD8B	TRIM47	GNGT2	ABI3	CD96	
ITGAL	ITGAL	ITGAL	MYO1G	TRIM47	ITGAM	IDO1	FGR	TNFRSF14	
MYO1G	MYO1G	MYO1G	HLA-DQA1	ITGAM	COTL1	FAM26F	FAM113B	LGALS1	
HLA-DQA1	HLA-DQA1	HLA-DQA1	CD8B	COTL1	CD40	NLRC5	C14orf73	CD244	
CD8B	CD8B	CD8B	TRIM47	CD40	GNGT2	SECTM1	BCL2A1	S1PR4	
TRIM47	TRIM47	TRIM47	ITGAM	GNGT2	IDO1	NNMT	CD96	SLC7A7	
ITGAM	ITGAM	ITGAM	COTL1	IDO1	FAM26F	ABI3	TNFRSF14	ARHGAP9	
COTL1	COTL1	COTL1	CD40	FAM26F	NLRC5	FGR	LGALS1	ICOS	
CD40	CD40	CD40	GNGT2	NLRC5	SECTM1	FAM113B	CD244	GPR132	
LOC650368	LOC650368	LOC650368	IDO1	SECTM1	NNMT	C14orf73	S1PR4	EMP3	
GNGT2	GNGT2	GNGT2	FAM26F	NNMT	ABI3	BCL2A1	SLC7A7	GNLY	
IDO1	IDO1	IDO1	NLRC5	ABI3	FGR	CD96	ARHGAP9	LILRB3	
FAM26F	FAM26F	FAM26F	SECTM1	FGR	FAM113B	HCP5	ICOS	KLRD1	
NLRC5	NLRC5	NLRC5	NNMT	FAM113B	C14orf73	HCG26	GPR132	GZMK	
SECTM1	SECTM1	SECTM1	PDLIM1	C14orf73	BCL2A1	TNFRSF14	EMP3	GRAP	
NNMT	NNMT	NNMT	ABI3	ADA	CD96	LGALS1	GNLY	HLA-DOB	
PDLIM1	PDLIM1	PDLIM1	FGR	BCL2A1	HCP5	TMEM140	LILRB3	MEI1	
ABI3	ABI3	ABI3	FAM113B	CD96	HCG26	CD244	KLRD1	S100A4	
FGR	FGR	FGR	C14orf73	HCP5	TNFRSF14	S1PR4	GZMK	HLA-DRB6	

FAM113B	FAM113B	FAM113B	ADA	SP140L	LGALS1	SLC7A7	GRAP	MLKL	
C14orf73	C14orf73	C14orf73	BCL2A1	TNFSF10	TMEM140	ARHGAP9	HLA-DOB	PYCARD	
ADA	ADA	ADA	CD96	HCG26	CD244	ICOS	MEI1	TNFAIP8L2	
BCL2A1	BCL2A1	BCL2A1	HCP5	TNFRSF14	S1PR4	GPR132	S100A4	SLC15A3	
CD96	CD96	CD96	SP140L	LGALS1	SLC7A7	EMP3	HLA-DRB6	EPSTI1	
HCP5	HCP5	HCP5	TNFSF10	TMEM140	ARHGAP9	GNLY	TAGLN2	BATF3	
SP140L	SP140L	SP140L	HCG26	CD244	ICOS	LILRB3	PIK3R6	ISG20	
TNFSF10	TNFSF10	TNFSF10	TNFRSF14	S1PR4	RRAD	KLRD1	MLKL		
HCG26	HCG26	HCG26	LGALS1	SLC7A7	GPR132	GZMK	PYCARD		
TNFRSF14	TNFRSF14	TNFRSF14	TMEM140	ARHGAP9	EMP3	GRAP	TNFAIP8L2		
LGALS1	LGALS1	LGALS1	CD244	ICOS	GNLY	HLA-DOB	SLC15A3		
TMEM140	TMEM140	TMEM140	S1PR4	RRAD	LILRB3	MEI1	EPSTI1		
CD244	CD244	CD244	TNFAIP8	GPR132	KLRD1	S100A4	HLA-DQB2		
S1PR4	S1PR4	S1PR4	SLC7A7	EMP3	GZMK	HLA-DRB6	BATF3		
TNFAIP8	TNFAIP8	TNFAIP8	ARHGAP9	GNLY	GRAP	TAGLN2	ISG20		
SLC7A7	SLC7A7	SLC7A7	ICOS	LILRB3	RAB32	PIK3R6	ITK		
ARHGAP9	ARHGAP9	ARHGAP9	RRAD	KLRD1	HLA-DOB	MLKL	CCL4L2		
ICOS	ICOS	ICOS	GPR132	GZMK	MEI1	PYCARD	HLA-DQA2		
RRAD	RRAD	RRAD	IKBKE	CMTM3	S100A4	TNFAIP8L2	GIMAP4		
GPR132	GPR132	GPR132	EMP3	GRAP	HLA-DRB6	SLC15A3	WAS		
IKBKE	IKBKE	IKBKE	GNLY	RAB32	TAGLN2	EPSTI1	FOXP3		
EMP3	EMP3	EMP3	LILRB3	HLA-DOB	PIK3R6	HLA-DQB2	FERMT3		
GNLY	GNLY	GNLY	KLRD1	MEI1	MLKL	BATF3	CYTIP		
LILRB3	LILRB3	LILRB3	GZMK	S100A4	PYCARD	ISG20	LAG3		
KLRD1	KLRD1	KLRD1	CMTM3	HLA-DRB6	TNFAIP8L2	ITK	BST2		
GZMK	GZMK	GZMK	GRAP	TAGLN2	SLC15A3	CCL4L2	CORO1A		
CMTM3	CMTM3	CMTM3	RAB32	PIK3R6	EPSTI1	HLA-DQA2	SPI1		
GRAP	GRAP	GRAP	HLA-DOB	MLKL	HLA-DQB2	GIMAP4	CLEC4E		
RAB32	RAB32	RAB32	MEI1	PYCARD	BATF3	WAS	GPR171		
HLA-DOB	HLA-DOB	HLA-DOB	S100A4	TNFAIP8L2	ISG20	FOXP3	NCF2		
MEI1	MEI1	MEI1	HLA-DRB6	SLC15A3	ITK	FERMT3	ADAM8		
S100A4	S100A4	S100A4	TAGLN2	EPSTI1	CCL4L2	CYTIP	CASP1		
HLA-DRB6	HLA-DRB6	HLA-DRB6	PIK3R6	HLA-DQB2	HLA-DQA2	LAG3	C1QA		
TAGLN2	TAGLN2	TAGLN2	MLKL	BATF3	GIMAP4	BST2	SELPLG		
PIK3R6	PIK3R6	PIK3R6	PYCARD	ISG20	WAS	CORO1A	ARHGDIB		
MLKL	MLKL	MLKL	TNFAIP8L2	ITK	FOXP3	SPI1	LGALS9		
PYCARD	PYCARD	PYCARD	SLC15A3	CCL4L2	FERMT3	CLEC4E	CD97		

TNFAIP8L2	TNFAIP8L2	TNFAIP8L2	EPSTI1	HLA-DQA2	CYTIP	GPR171	KLRB1		
SLC15A3	SLC15A3	SLC15A3	HLA-DQB2	GIMAP4	LAG3	NCF2	NCF1		
EPSTI1	EPSTI1	EPSTI1	BATF3	WAS	BST2	ADAM8	C1orf54		
PRR5L	PRR5L	PRR5L	ISG20	FOXP3	CORO1A	CASP1	BIN2		
HLA-DQB2	HLA-DQB2	HLA-DQB2	ITK	FERMT3	SPI1	C1QA	SLAMF1		
BATF3	BATF3	BATF3	CCL4L2	CYTIP	CLEC4E	SELPLG	SLAMF7		
ISG20	ISG20	ISG20	HLA-DQA2	LAG3	GPR171	ARHGDIB	HLA-DRB5		
ITK	ITK	ITK	GIMAP4	BST2	NCF2	LGALS9	TYROBP		
CCL4L2	CCL4L2	CCL4L2	WAS	CORO1A	ADAM8	CD97			
HLA-DQA2	HLA-DQA2	HLA-DQA2	FOXP3	SPI1	HAAO	KLRB1			
GIMAP4	GIMAP4	GIMAP4	FERMT3	CLEC4E	CASP1	NCF1			
WAS	WAS	WAS	CYTIP	GPR171	C1QA	C1orf54			
FOXP3	FOXP3	FOXP3	LAG3	NCF2	SELPLG	BIN2			
FERMT3	FERMT3	FERMT3	BST2	ADAM8	ARHGDIB	SLAMF1			
CYTIP	CYTIP	CYTIP	CORO1A	HAAO	LGALS9	SLAMF7			
LAG3	LAG3	LAG3	SPI1	CASP1	CD97	HLA-DRB5			
BST2	BST2	BST2	CLEC4E	C10orf10	KLRB1	TYROBP			
CORO1A	CORO1A	CORO1A	GPR171	C1QA	NCF1	IL12RB1			
SPI1	SPI1	SPI1	NCF2	SELPLG	C1orf54	ICAM3			
CLEC4E	CLEC4E	CLEC4E	ADAM8	ARHGDIB	BIN2	TRAF3IP3			
GPR171	GPR171	GPR171	HAAO	LGALS9	SLAMF1	LOC541471			
NCF2	NCF2	NCF2	CASP1	CD97	SLAMF7	CD27			
ADAM8	ADAM8	ADAM8	C1QTNF1	KLRB1	HLA-DRB5	PTGIR			
HAAO	HAAO	HAAO	C10orf10	NCF1	TYROBP	LAPTM5			
CASP1	CASP1	CASP1	C1QA	LOC151534	IL12RB1	LIMD2			
C1QTNF1	C1QTNF1	C1QTNF1	SELPLG	C1orf54	ICAM3	XAF1			
C10orf10	C10orf10	C10orf10	ARHGDIB	BIN2	TRAF3IP3	GLIPR2			
C1QA	C1QA	C1QA	LGALS9	SLAMF1	LOC541471	RAB20			
SELPLG	SELPLG	SELPLG	CD97	SLAMF7	CD27	LCP1			
ARHGDIB	ARHGDIB	ARHGDIB	KLRB1	ADORA2A	PTGIR	ALOX5AP			
LGALS9	LGALS9	LGALS9	NCF1	HLA-DRB5	LAPTM5	C1orf162			
CD97	CD97	CD97	LOC151534	TYROBP	LIMD2	CD300LF			
KLRB1	KLRB1	KLRB1	C1orf54	IL12RB1	XAF1	CCR2			
NCF1	NCF1	NCF1	BIN2	ICAM3	GLIPR2	LAT			
LOC151534	LOC151534	LOC151534	SLAMF1	TRAF3IP3	FAIM3	GPSM3			
C1orf54	C1orf54	C1orf54	SLAMF7	LOC541471	RAB20	ANKRD58			
BIN2	BIN2	BIN2	ADORA2A	CD27	LCP1	CLEC10A			

SLAMF1	SLAMF1	SLAMF1	HLA-DRB5	PTGIR	ALOX5AP	PDCD1			
SLAMF7	SLAMF7	SLAMF7	TYROBP	LAPTM5	C1orf162	CHI3L2			
ADORA2A	ADORA2A	ADORA2A	CLIC2	LIMD2	CD300LF	NCF4			
HLA-DRB5	HLA-DRB5	HLA-DRB5	FADS3	XAF1	GPR68	LGALS2			
TYROBP	TYROBP	TYROBP	IL12RB1	GLIPR2	CCR2	CYBA			
CLIC2	CLIC2	CLIC2	ICAM3	FAIM3	LAT	PLEKHF1			
FADS3	FADS3	FADS3	TRAF3IP3	RAB20	GPSM3	C19orf38			
IL12RB1	IL12RB1	IL12RB1	LOC541471	LCP1	ANKRD58	HCK			
ICAM3	ICAM3	ICAM3	CD27	ALOX5AP	CLEC10A	RUNX3			
TRAF3IP3	TRAF3IP3	TRAF3IP3	PTGIR	C1orf162	PDCD1				
LOC541471	LOC541471	LOC541471	LAPTM5	CD300LF	CHI3L2				
CD27	CD27	CD27	LIMD2	GPR68	NCF4				
PTGIR	PTGIR	PTGIR	XAF1	CCR2	GGTLC2				
LAPTM5	LAPTM5	LAPTM5	GLIPR2	LAT	LGALS2				
LIMD2	LIMD2	LIMD2	FAIM3	GPSM3	CYBA				
XAF1	XAF1	XAF1	RAB20	ANKRD58	PLEKHF1				
GLIPR2	GLIPR2	GLIPR2	LCP1	CLEC10A	C19orf38				
FAIM3	FAIM3	FAIM3	ALOX5AP	PDCD1	HCK				
RAB20	RAB20	RAB20	C1orf162	CHI3L2	RUNX3				
LCP1	LCP1	LCP1	ANXA2	NCF4	CD3G				
ALOX5AP	ALOX5AP	ALOX5AP	S100A10	GGTLC2	OSCAR				
C1orf162	C1orf162	C1orf162	CD300LF	LGALS2	GIMAP1				
ANXA2	ANXA2	ANXA2	GPR68	CYBA	CD69				
S100A10	S100A10	S100A10	CCR2	PLEKHF1	HLA-DMB				
CD300LF	CD300LF	CD300LF	LAT	C19orf38	IFI27				
GPR68	GPR68	GPR68	GPSM3	HCK	SERPI1				
CCR2	CCR2	CCR2	ANKRD58	RUNX3	VAMP8				
LAT	LAT	LAT	CLEC10A	CD3G	SOCS1				
GPSM3	GPSM3	GPSM3	PDCD1	OSCAR	SH2D1A				
ANKRD58	ANKRD58	ANKRD58	CHI3L2	RHBDF2	CD53				
CLEC10A	CLEC10A	CLEC10A	NCF4	GIMAP1	NCF1C				
PDCD1	PDCD1	PDCD1	GGTLC2	CD69	CD4				
CHI3L2	CHI3L2	CHI3L2	MICB	HLA-DMB	TNFRSF6B				
NCF4	NCF4	NCF4	LGALS2	IFI27	GIMAP5				
GGTLC2	GGTLC2	GGTLC2	CYBA	SERPI1	CYTH4				
DJC15	DJC15	MICB	PLEKHF1	VAMP8	CTLA4				
MICB	MICB	LGALS2	C19orf38	SOCS1	TNFSF13B				
LGALS2	LGALS2	CYBA	HCK	SH2D1A	LILRB2				

CYBA	CYBA	PLEKHF1	RUNX3	CCL22	STX11				
PLEKHF1	PLEKHF1	C19orf38	CD3G	CD53	APOBEC3G				
C19orf38	C19orf38	HCK	OSCAR	NCF1C	THEMIS				
HCK	HCK	RUNX3	RHBDF2	CD4	CCR7				
RUNX3	RUNX3	GBP3	GIMAP1	TNFRSF6B	PLAU				
GBP3	GBP3	CD3G	IL27RA	GIMAP5	IL3RA				
CD3G	CD3G	OSCAR	CD69	CYTH4	PARVG				
OSCAR	OSCAR	RHBDF2	HLA-DMB	CTLA4	PECAM1				
RHBDF2	RHBDF2	GIMAP1	IFI27	TNFSF13B					
GIMAP1	GIMAP1	IL27RA	SERPI1	LILRB2					
IL27RA	IL27RA	CD69	VAMP8	STX11					
CD69	CD69	HLA-DMB	SOCS1	CST3					
HLA-DMB	HLA-DMB	IFI27	SH2D1A	APOBEC3G					
IFI27	IFI27	SERPI1	CCL22	THEMIS					
SERPI1	SERPI1	VAMP8	CD53	CCR7					
VAMP8	VAMP8	SOCS1	CD101	PLAU					
SOCS1	SOCS1	SH2D1A	NCF1C	IL3RA					
SH2D1A	SH2D1A	CCL22	CD4	PARVG					
CCL22	CCL22	CD53	TNFRSF6B	PECAM1					
CD53	CD53	CD101	GIMAP5	NFAM1					
CD101	CD101	NCF1C	CYTH4	APOC1					
NCF1C	NCF1C	CD4	CTLA4	FCGR1B					
LOC728855	LOC728855	TNFRSF6B	CXCR4	IRF8					
CD4	CD4	GIMAP5	TNFSF13B	CCDC88B					
TNFRSF6B	TNFRSF6B	CYTH4	LILRB2	GIMAP2					
GIMAP5	GIMAP5	CTLA4	STX11	LIME1					
CYTH4	CYTH4	FTHL3	CST3	ZMYND15					
CTLA4	CTLA4	CXCR4	APOBEC3G	MFNG					
FTHL3	FTHL3	TNFSF13B	THEMIS	CXCL2					
CX3CL1	CX3CL1	LILRB2	CCR7	HLA-DOA					
CXCR4	CXCR4	STX11	PLAU	APOBEC3D					
TNFSF13B	TNFSF13B	CST3	IL34	PILRA					
LILRB2	LILRB2	APOBEC3G	IL3RA	SASH3					
STX11	STX11	THEMIS	PARVG	C1orf38					
CST3	CST3	CCR7	PECAM1	GIMAP7					
APOBEC3G	APOBEC3G	PLAU	NFAM1	HAVCR2					
THEMIS	THEMIS	IL34	APOC1	SLAMF6					
CCR7	CCR7	IL3RA	FCGR1B	LILRB1					
PLAU	PLAU	PARVG	IRF8	FAM78A					
IL34	IL34	PECAM1	CCDC88B	ITGB2					

IL3RA	IL3RA	NFAM1	GIMAP 2	CD86					
PARVG	PARVG	APOC1	LIME1	PLEK					
PECAM1	PECAM1	FCGR1B	ZMYND 15	GLIPR1					
NFAM1	NFAM1	IRF8	MFNG	MICAL1					
APOC1	APOC1	CCDC88B	SH2D3 C	FCN1					
FCGR1B	FCGR1B	GIMAP2	CXCL2	SI3					
IRF8	IRF8	LIME1	HLA-D OA	C1QB					
CCDC88B	CCDC88B	ZMYND15	ALPK2	MFRP					
GIMAP2	GIMAP2	MFNG	APOBE C3D	LRRC2 5					
LIME1	LIME1	SH2D3C	PILRA	MAP4K 1					
ZMYND15	ZMYND15	CXCL2	ANKRD 22	AOAH					
MFNG	MFNG	HLA-DOA	SASH3						
SH2D3C	SH2D3C	TEAD4	LOC11 5110						
CXCL2	CXCL2	ALPK2	C1orf38						
HLA-DOA	HLA-DOA	APOBEC3D	GIMAP 7						
TEAD4	TEAD4	PILRA	HAVCR 2						
ALPK2	ALPK2	ANKRD22	SLAMF 6						
APOBEC3D	APOBEC3D	SASH3	LILRB1						
PILRA	PILRA	CLEC5A	FAM78 A						
ANKRD22	ANKRD22	LOC115110	ITGB2						
SASH3	SASH3	C1orf38	CD86						
CLEC5A	CLEC5A	GIMAP7	PLEK						
CCDC28B	LOC115110	HAVCR2	SLC38 A5						
LOC115110	C1orf38	SLAMF6	TLR2						
C1orf38	GIMAP7	LILRB1	HLA-G						
GIMAP7	HAVCR2	FAM78A	GLIPR1						
HAVCR2	SLAMF6	ITGB2	MICAL1						
SLAMF6	LILRB1	CD86	FCN1						
LILRB1	FAM78A	PLEK	SI3						
FAM78A	ITGB2	SLC38A5	C1QB						
ITGB2	CD86	TLR2	OAF						
CD86	PLEK	HLA-G	MFRP						
PLEK	SLC38A5	GLIPR1	LRRC2 5						
SLC38A5	TLR2	MICAL1	MAP4K 1						
TLR2	HLA-G	FCN1	AOAH						
HLA-G	GLIPR1	SI3	PIK3CD						
GLIPR1	MICAL1	C1QB	TMC8						
MICAL1	FCN1	OAF	C15orf4 8						
FCN1	SI3	MFRP	GADD4 5B						
SI3	C1QB	LRRC25	FCGR1 A						
C1QB	IL23A	MAP4K1	C2						

IL23A	OAF	AOAH	FCGR1C						
OAF	MFRP	PIK3CD	C1QC						
MFRP	LRRC25	TMC8	HK3						
LRRC25	MAP4K1	C15orf48	CLEC4A						
MAP4K1	AOAH	GADD45B	STOM						
AOAH	PIK3CD	FCGR1A	MYL9						
PIK3CD	TMC8	C2	FXYD5						
TMC8	C15orf48	FCGR1C	KCNMB1						
C15orf48	GADD45B	BCL2L14	SOX18						
GADD45B	FCGR1A	C1QC	PTPRC						
FCGR1A	C2	HK3	RGS10						
C2	FCGR1C	CLEC4A	FYB						
FCGR1C	BCL2L14	STOM	RHOH						
BCL2L14	C1QC	MYL9	CD300A						
C1QC	HK3	FXYD5	RCN3						
HK3	ICOSLG	KCNMB1	SLC16A3						
ICOSLG	CLEC4A	SOX18	ARHGAP25						
CLEC4A	STOM	PTPRC	HVCN1						
STOM	MYL9	ATF5	OCIAD2						
MYL9	FXYD5	MSRA	ASB2						
AK1	KCNMB1	RGS10	CD37						
FXYD5	SOX18	FYB	FCGR3A						
KCNMB1	PTPRC	RHOH	IKZF1						
SOX18	ATF5	CD300A	CD28						
PTPRC	MSRA	SLC17A9	ZBP1						
ATF5	RGS10	DENND3	GPBAR1						
MSRA	FYB	RCN3	G0S2						
RGS10	RHOH	SLC16A3	IGFBP7						
FYB	CD300A	ARHGAP25	LY9						
RHOH	SLC17A9	HVCN1	UNC13D						
CD300A	DENND3	OCIAD2	AIM2						
SLC17A9	RCN3	ASB2	ECSCR						
DENND3	SLC16A3	CD37	LILRA6						
RCN3	GGT1	FCGR3A	RBP5						
SLC16A3	ARHGAP25	IKZF1	CCL3L1						
GGT1	GPR35	CD28	LAT2						
ARHGAP25	HVCN1	ZBP1	SAT1						
GPR35	OCIAD2	GPBAR1	CD14						
HVCN1	ASB2	TRIP10	FPR3						
OCIAD2	CD37	MMP7	PDCD1LG2						
ASB2	FCGR3A	G0S2	DOK3						
CD37	IKZF1	IGFBP7	C5orf39						
FCGR3A	CD28	LY9	CCDC109B						

IKZF1	ZBP1	UNC13D	ARHGAP15						
CD28	GPBAR1	AIM2	CARD9						
ZBP1	TRIP10	ECSCR	FMNL1						
GPBAR1	LTBR	ASGR1	S100A3						
TRIP10	MMP7	IL18R1	GLRX						
LTBR	G0S2	LILRA6	RELT						
MMP7	IGFBP7	RBP5	CTSC						
G0S2	LY9	CCL3L1	CXCL13						
IGFBP7	UNC13D	LAT2	IGSF6						
LY9	AIM2	SAT1							
UNC13D	LAMP3	CD14							
AIM2	ECSCR	FPR3							
LAMP3	ASGR1	PDCD1LG2							
ECSCR	IL18R1	DOK3							
ASGR1	LILRA6	C5orf39							
IL18R1	RBP5	CCDC109B							
LILRA6	CCL3L1	ARHGAP15							
RBP5	LAT2	CARD9							
CCL3L1	SAT1	FMNL1							
LAT2	CD14	S100A3							
SAT1	FPR3	GLRX							
CD14	PDCD1LG2	PARVB							
FPR3	DOK3	RELT							
PDCD1LG2	C5orf39	CTSC							
DOK3	CCDC109B	CXCL13							
C5orf39	ARHGAP15	IGSF6							
CCDC109B	CARD9	RARRES2							
ARHGAP15	FMNL1	RIPK3							
CARD9	S100A3	TIMP1							
FMNL1	GLRX	SIGLEC10							
S100A3	PARVB	CXCL3							
GLRX	RELT	RSET2							
PARVB	CTSC	LILRB4							
CD99	CXCL13	HSPA6							
RELT	IGSF6	RAB42							
CTSC	RARRES2	SLA							
CXCL13	CENPW	HLA-L							
IGSF6	RIPK3	PTPN22							
RARRES2	TIMP1	CD72							
CENPW	SIGLEC10	HSH2D							
RIPK3	CXCL3	FCGR2A							
TIMP1	RSET2	NUPR1							
SIGLEC10	LILRB4	ADAM6							
CXCL3	HSPA6	FABP3							
RSET2	RAB42	UCP2							
LILRB4	SLA	IL10RA							

HSPA6	HLA-L	GPR65							
RAB42	PTPN22	LOC96610							
SLA	CD72	SELM							
HLA-L	HSH2D	FAM167B							
PTPN22	FCGR2A	CD79B							
CD72	NUPR1	ARPC1B							
HSH2D	ADAM6	FLVCR2							
FCGR2A	SLC12A7	NCF1B							
NUPR1	FABP3	TRIM69							
ADAM6	UCP2	PSB							
SLC12A7	IL10RA	TBXAS1							
FABP3	GPR65	HCLS1							
UCP2	LOC96610	GPR114							
IL10RA	SELM	FKBP11							
GPR65	FAM167B	S100A13							
LOC96610	CD79B	C13orf18							
SELM	ARPC1B	RAB3IL1							
PTGES	FLVCR2	SNX20							
FAM167B	NCF1B	IRF4							
CD79B	TRIM69	SIGLEC9							
ARPC1B	PLEK2	TCIRG1							
FLVCR2	PSB	FTL							
NCF1B	TBXAS1	PRKCDBP							
TRIM69	HCLS1	EVI2B							
PLEK2	GPR114	NPC2							
PSB	FKBP11	TNFSF12-TNFSF13							
TBXAS1	S100A13	CLEC12A							
HCLS1	HES4	KMO							
GPR114	C13orf18	CLIC3							
FKBP11	RAB3IL1	FCGR2B							
S100A13	SNX20	TAGLN							
HES4	IRF4	TNFSF12							
C13orf18	SIGLEC9	TLR8							
RAB3IL1	MT1F	FGD3							
SNX20	LOC100270710	SQRDL							
IRF4	TCIRG1	CTSB							
SIGLEC9	ADAT3	AQP9							
MT1F	FTL	SIGLEC7							
LOC100270710	PRKCDBP	FAM176B							
TCIRG1	EVI2B	CLDN5							
ADAT3	NPC2	KYNU							
FTL	TNFSF12-TNFSF13	CCL18							
PRKCDBP	CLEC12A	IFFO1							
EVI2B	KMO	LGALS3BP							
NPC2	CLIC3	PIM2							

TNFSF12-TNFSF13	FCGR2B	VAV1							
CLEC12A	TAGLN	MARCO							
KMO	TNFSF12	NCKAP1L							
CLIC3	TLR8	DTX2							
FCGR2B	SLC9A3R2	CFP							
TAGLN	FGD3	CD1C							
TNFSF12	SQRDL								
GK	CTSB								
TLR8	AQP9								
SLC9A3R2	SIGLEC7								
FGD3	FAM176B								
SQRDL	PLA1A								
CTSB	CLDN5								
AQP9	KYNU								
SIGLEC7	CCL18								
FAM176B	IFFO1								
EFEMP2	LGALS3BP								
PLA1A	PIM2								
CLDN5	VAV1								
KYNU	MARCO								
CCL18	FAM18A								
IFFO1	NCKAP1L								
LGALS3BP	DTX2								
PIM2	CFP								
VAV1	CD1C								
MARCO	CSF1R								
FAM18A	FCGRT								
NCKAP1L	CSF2RA								
DTX2	APOBEC3F								
CFP	LY86								
KDELR3	HSPB2								
CD1C	COX7A1								
C8orf73	IRF7								
CSF1R	BST1								
FCGRT	TNFRSF8								
CSF2RA	HMOX1								
APOBEC3F	PLCB2								
LY86	CEBPD								
HSPB2	LGALS9C								
RPLP0P2	PIK3R5								
COX7A1	SERPINF1								
IRF7	IGJ								
BST1	ARHGAP4								
TNFRSF8	ITGAX								
HMOX1	TGFBI								
CP	GAB3								

PLCB2	SELL								
CEBPD	C3AR1								
LGALS9C	LILRA5								
PIK3R5	ACADS								
SERPINF1	CD1D								
IGJ	SAMSN1								
ARHGAP4	MS4A6A								
ITGAX	ACP5								
TGFBI	IL16								
GAB3	HSPA7								
SELL	PHLDA2								
C3AR1	RHEBL1								
LILRA5	NINJ2								
ACADS	SLC6A12								
CD1D	NCR00116								
SAMSN1	SIGLEC5								
MS4A6A	CD300C								
ACP5	PCOLCE								
IL16	LOXL1								
HSPA7	PLA2G2D								
PHLDA2	THY1								
RHEBL1	DEF6								
NINJ2	CEBPB								
SLC6A12	TRPM2								
NCR00116	TPM2								
SIGLEC5	CMTM7								
CD300C	PVRIG								
PCOLCE	APOE								
LOXL1	ADAMDEC1								
PLA2G2D	C17orf60								
THY1	LY96								
DEF6	CLEC1A								
CEBPB	RGS1								
TRPM2	OASL								
TPM2	CHI3L1								
CMTM7	EMILIN2								
PVRIG	CSF3R								
APOE	ADAP2								
ADAMDEC1	C6orf105								
C17orf60	SYNC								
LY96	TMEM119								
CLEC1A	RENBP								
RGS1	WIPF1								
MT1E									
ADAP1									
OASL									

SARDH									
CHI3L1									
EMILIN2									
CSF3R									
ADAP2									
C6orf105									
SYNC									
TMEM119									
RENBP									
WIPF1									
OLR1									
RGS14									
CD79A									
TAGAP									
CECR1									
CHIT1									
TNFAIP6									
AGPAT2									
DAB2									
GPR183									
MT2A									
PLAC8									
OXER1									
TNFSF9									
CD68									
SLC22A18AS									
LILRA2									
TMEM171									
COX4I2									
ANGPTL4									
FBLN5									
LOC388242									
LCAT									
PLEKHA4									
METRNL									
LTF									
TMEM156									
TREM2									
MGMT									
ISG15									

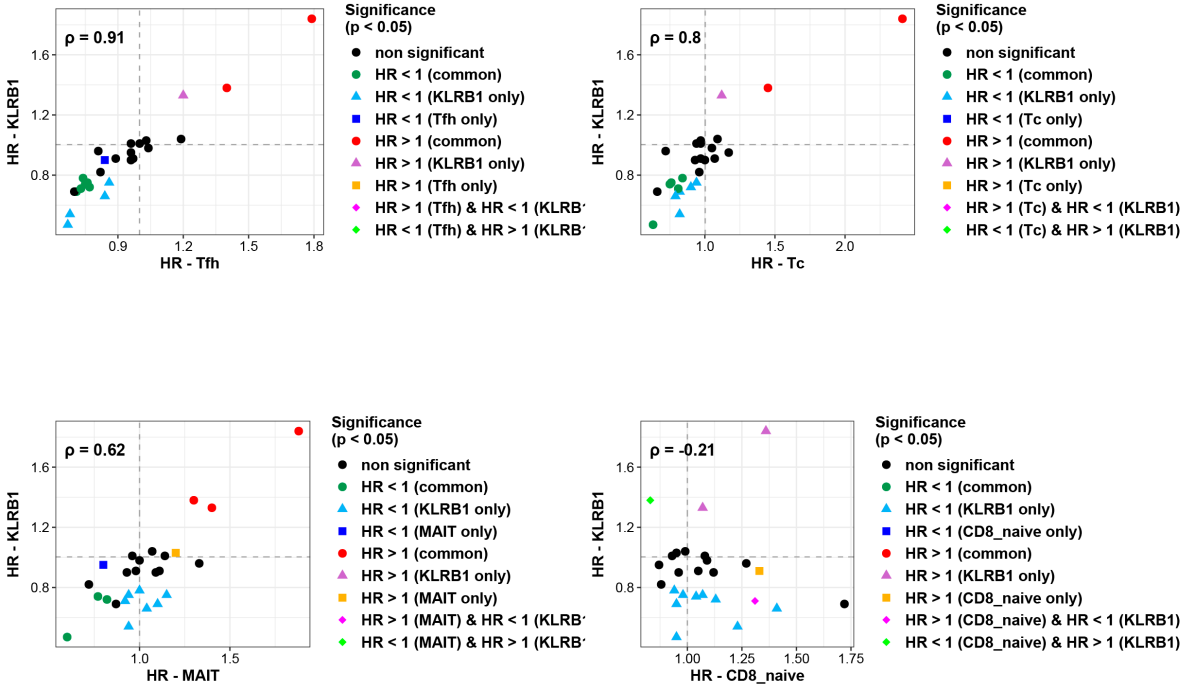
Appendix Table IV-3. List of *IL32* signature genes, including 1E-10, 1E-11, 1E-12, 1E-13, 1E-14, 1E-15, 1E-16, 1E-17, 1E-18, 1E-19 and 1E-20 *IL32* signatures.

1.E-10	1.E-11	1.E-12	1.E-13	1.E-14	1.E-15	1.E-16	1.E-17	1.E-18	1.E-19	1.E-20
IL32	IL32	IL32	IL32	IL32	IL32	IL32	IL32	IL32	IL32	IL32
MMP25	MMP25	MMP25	MMP25	MMP25	MMP25	MMP25	MMP25	UBD	UBD	UBD
UBD	UBD	UBD	UBD	UBD	UBD	UBD	UBD	IRF1	IRF1	IRF1
IRF1	IRF1	IRF1	IRF1	IRF1	IRF1	IRF1	IRF1	IL2RG	IL2RG	IL2RG
IL2RG	IL2RG	IL2RG	IL2RG	IL2RG	IL2RG	IL2RG	IL2RG	ICAM1	ICAM1	ICAM1
ICAM1	ICAM1	ICAM1	ICAM1	ICAM1	ICAM1	ICAM1	ICAM1	CCL5	CCL5	CCL5
CCL5	CCL5	CCL5	CCL5	CCL5	CCL5	CCL5	CCL5	PSMB9	PSMB9	PSMB9
PSMB9	PSMB9	PSMB9	PSMB9	PSMB9	PSMB9	PSMB9	PSMB9	LTB	LTB	LTB
RRAS	RRAS	RRAS	RRAS	RRAS	LTB	LTB	LTB	IL4I1	IL4I1	IL4I1
LTB	LTB	LTB	LTB	LTB	IL4I1	IL4I1	IL4I1	HLA-A	HLA-A	HLA-A
IL4I1	IL4I1	IL4I1	IL4I1	IL4I1	HLA-A	HLA-A	HLA-A	IL15RA	IL15RA	IL15RA
HLA-A	HLA-A	HLA-A	HLA-A	HLA-A	IL15RA	IL15RA	IL15RA	PSMB10	PSMB10	PSMB10
IL15RA	IL15RA	IL15RA	IL15RA	IL15RA	PSMB10	PSMB10	PSMB10	CD74	CD74	CD74
PSMB10	PSMB10	PSMB10	PSMB10	PSMB10	TAP1	TAP1	TAP1	HLA-F	HLA-F	HLA-F
TAP1	TAP1	TAP1	TAP1	TAP1	CD74	CD74	CD74	SH2D2A	SH2D2A	HLA-B
SOD2	SOD2	CD74	CD74	CD74	HLA-F	HLA-F	HLA-F	HLA-B	HLA-B	
CD74	CD74	GBP2	GBP2	HLA-F	TNFRSF4	TNFRSF4	APOL3	TYMP	TYMP	
GBP2	GBP2	HLA-F	HLA-F	TNFRSF4	APOL3	APOL3	SH2D2A	GZMH	GZMH	
HLA-F	HLA-F	TNFRSF4	TNFRSF4	APOL3	SH2D2A	SH2D2A	HLA-B	CD3E		
TNFRSF4	TNFRSF4	APOL3	APOL3	SH2D2A	HLA-H	HLA-B	TYMP	HAPLN3		
APOL3	APOL3	SH2D2A	SH2D2A	HLA-H	HLA-B	TYMP	GZMH			
SH2D2A	SH2D2A	HLA-H	HLA-H	HLA-B	TYMP	GZMH	CD3E			
BIRC3	BIRC3	HLA-B	HLA-B	TYMP	TMSB10	CD3E	ETV7			
HLA-H	HLA-H	TYMP	TYMP	GBP1	GZMH	ETV7	HAPLN3			
HLA-B	HLA-B	GBP1	GBP1	TMSB10	CD3E	HAPLN3	CD7			
TYMP	TYMP	TMSB10	TMSB10	GZMH	ETV7	CD7	GZMA			
GBP1	GBP1	GZMH	GZMH	CD3E	HAPLN3	GZMA	CD247			
TMSB10	TMSB10	CD3E	CD3E	ETV7	JAK3	CD247	NKG7			
GZMH	GZMH	ETV7	ETV7	HAPLN3	CD7	NKG7	CD2			
CD3E	CD3E	HAPLN3	HAPLN3	JAK3	GZMA	CD2	CD6			
ETV7	ETV7	JAK3	JAK3	CD7	CD247	CD6				
HAPLN3	HAPLN3	CD7	CD7	GZMA	NKG7	CD3D				
JAK3	JAK3	GZMA	GZMA	CD247	CXCL10	PSMB8				
CD7	CD7	CD247	CD247	NKG7	CD2	CD52				
GZMA	GZMA	NKG7	NKG7	CXCL10	CD6					
ICAM2	CD247	IL15	CXCL10	CD2	CD3D					
CD247	NKG7	CXCL10	CD2	CD6	PSMB8					
NKG7	IL15	CD2	CD6	CD3D	CD52					

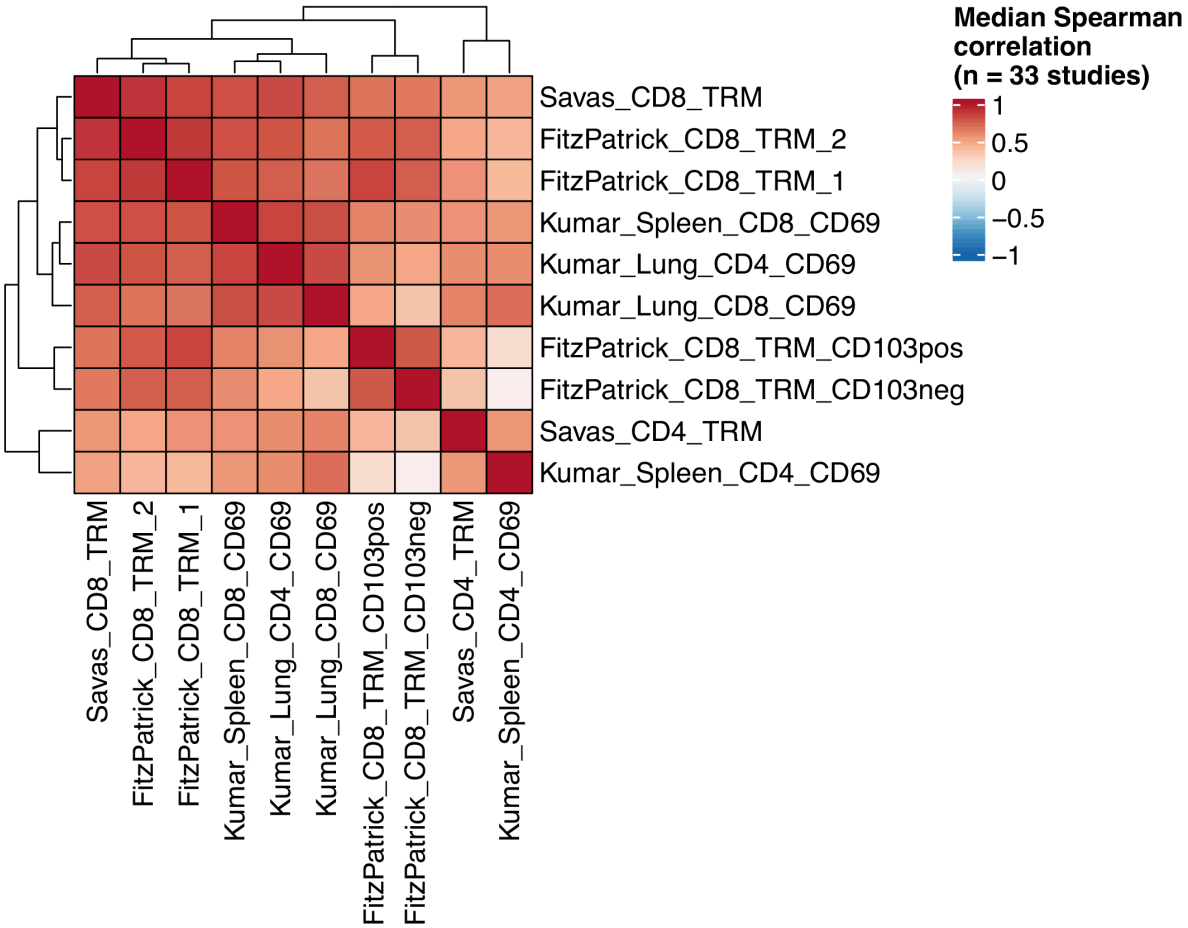
IL15	CXCL10	CD6	CD3D	PSMB8	LST1					
CXCL10	CD2	CD3D	PSMB8	CD52	RARRES3					
CD2	CD6	APOL1	CD52	IL2RB	CST7					
CD6	CD3D	PSMB8	IL2RB	LST1	VAMP5					
CD3D	APOL1	CD52	LST1	RARRES3	CXCR3					
APOL1	PSMB8	IL2RB	RARRES3	CST7	PRF1					
PSMB8	CD52	LST1	CST7	ZNF683	RASAL3					
CD52	IL2RB	RARRES3	ZNF683	VAMP5	HLA-DMA					
IL2RB	LST1	CST7	VAMP5	CXCR3						
LST1	RARRES3	ZNF683	CXCR3	BATF2						
RARRES3	CST7	VAMP5	BATF2	PRF1						
CST7	ZNF683	MVP	PRF1	RASAL3						
ZNF683	VAMP5	CXCR3	RASAL3	HLA-DMA						
VAMP5	MVP	BATF2	HLA-DMA	CARD16						
MVP	CXCR3	PRF1	CARD16	HLA-C						
CXCR3	BATF2	RASAL3	EBI3	CCL4						
BATF2	PRF1	HLA-DMA	HLA-C	CTSW						
PRF1	RASAL3	CXCL9	CCL4	GzmB						
RASAL3	HLA-DMA	CARD16	CTSW							
HLA-DMA	CXCL9	EBI3	GzmB							
CXCL9	CARD16	HLA-C	CXCL11							
CARD16	EBI3	CCL4	PTPN7							
EBI3	HLA-C	CTSW	BATF							
HLA-C	CCL4	HSD3B7	ODF3B							
CCL4	CTSW	GzmB	HLA-DPA1							
CTSW	HSD3B7	CXCL11	SIRPG							
HSD3B7	GzmB	PTPN7								
GzmB	CXCL11	BATF								
CXCL11	PTPN7	ODF3B								
PTPN7	BATF	HLA-DPA1								
BATF	ODF3B	SIRPG								
ODF3B	HLA-DPA1	CD5								
HLA-DPA1	SIRPG	IFITM3								
SIRPG	CD5	HCST								
CD5	IFITM3	SLAMF8								
IFITM3	HCST	HLA-DRA								
HCST	SLAMF8	IFI30								
SLAMF8	HLA-DRA	DOK2								
HLA-DRA	IFI30	HLA-DPB1								
IFI30	DOK2	AMICA1								
DOK2	HLA-DPB1									

STAT4	AMICA1									
HLA-DPB1	ACAP1									
AMICA1	LCP2									
NCR00152	ZAP70									
ACAP1	CD48									
LCP2	IL21R									
ZAP70	PSTPIP1									
CD48	FLT3LG									
CTSS	HMHA1									
IL21R	HLA-DRB1									
TMEM176A	FCER1G									
PSTPIP1										
FLT3LG										
HMHA1										
HLA-DRB1										
FCER1G										
CCRL2										
PLEKHO1										
GMFG										
RAC2										
LSP1										
TMEM176B										
PLAUR										
CCR5										
PTPRCAP										
LOC606724										
GSDMD										
TRPV2										
SLA2										
CD8A										
CXCR6										
SERPING1										
MYO1F										
SIT1										

V. Appendices V



Appendix Figure V-1. Correlation of the prognostic value of *KLRB1* and the prognostic value of selected immune subsets in cancer. Spearman's correlation between the HR of *KLRB1* and HR of indicated cell types, including Tfh (T follicular helper cells), Tc (cytotoxic T cells), MAIT and naive CD8 T cells (CD8_naive) was analysed across 26 cancer types from TCGA. Each dot represents a different cancer type.



Appendix Figure V-2. Intercorrelation between enrichment of different TRM signatures within TCGA data. Heatmap shows median Spearman's correlation across 33 analysed TCGA cancer types between ssGSEA enrichment scores of different TRM signatures.

REFERENCES

1. Chaplin, D. D. (2010). Overview of the immune response. *J. Allergy Clin. Immunol. 125*(2), S3–S23.

2. Corthay, A. (2014). Does the immune system naturally protect against cancer? *Front. Immunol. 5*, 197.

3. Julier, Z., A. J. Park, P. S. Briquez, and M. M. Martino. (2017). Promoting tissue regeneration by modulating the immune system. *Acta Biomater. 53*, 13–28.

4. Carrillo, J. L. M., F. P. C. García, O. G. Coronado, M. A. M. García, and J. F. C. Cordero. (2017). Physiology and Pathology of Innate Immune Response Against Pathogens. In *Physiology and Pathology of Immunology*, (N. Rezaei, ed). IntechOpen. 99–134.

5. Akira, S., S. Uematsu, and O. Takeuchi. (2006). Pathogen Recognition and Innate Immunity. *Cell 124*(4), 783–801.

6. Mogensen, T. H. (2009). Pathogen Recognition and Inflammatory Signaling in Innate Immune Defenses. *Clin. Microbiol. Rev. 22*(2), 240–273.

7. Long, E. O., and S. Rajagopalan. (2002). Stress Signals Activate Natural Killer Cells. *J. Exp. Med. 196*(11), 1399–1402.

8. Shimasaki, N., A. Jain, and D. Campana. (2020). NK cells for cancer immunotherapy. *Nat. Rev. Drug Discov. 19*(3), 200–218.

9. Kambayashi, T., and T. M. Laufer. (2014). Atypical MHC class II-expressing antigen-presenting cells: can anything replace a dendritic cell? *Nat. Rev. Immunol. 14*(11), 719–730.

10. Burnet, F. M. (1957). A Modification of Jerne's Theory of Antibody Production using the Concept of Clonal Selection. *Aust. J. Sci. 20*(3), 67–69.

11. Silverstein, A. M. (2002). The Clonal Selection Theory: what it really is and why modern challenges are misplaced. *Nat. Immunol. 3*(9), 793–796.

12. Schatz, D. G., and Y. Ji. (2011). Recombination centres and the orchestration of V(D)J recombination. *Nat. Rev. Immunol. 11*(4), 251–263.

13. Hodgkin, P. D., W. R. Heath, and A. G. Baxter. (2007). The clonal selection theory: 50 years since the revolution. *Nat. Immunol. 8*(10), 1019–1026.

14. Borghesi, L., and C. Milcarek. (2007). Innate versus Adaptive Immunity: A Paradigm Past Its Prime? *Cancer Res. 67*(9), 3989–3993.

15. Kirman, J. R., K. M. Quinn, and R. A. Seder. (2019). Immunological memory. *Immunol. Cell Biol. 97*(7), 615–616.

16. Romagnani, S. (2006). Immunological tolerance and autoimmunity. *Intern. Emerg. Med. 1*(3), 187–196.

17. Wencker, M., G. Turchinovich, R. Di Marco Barros, L. Deban, A. Jandke, A. Cope, and A. C. Hayday. (2014). Innate-like T cells straddle innate and adaptive immunity by altering antigen-receptor responsiveness. *Nat. Immunol. 15*(1), 80–87.

18. Godfrey, D. I., A. P. Uldrich, J. McCluskey, J. Rossjohn, and D. B. Moody. (2015). The burgeoning family of unconventional T cells. *Nat. Immunol. 16*(11), 1114–1123.

19. Germain, R. N. (2002). T-cell development and the CD4–CD8 lineage decision. *Nat. Rev. Immunol. 2*(5), 309–322.

20. Shah, D. K., and J. C. Zúñiga-Pflücker. (2014). An Overview of the Intrathymic Intricacies of T Cell Development. *J. Immunol. 192*(9), 4017–4023.

21. Qi, C., Y. Wang, P. Li, and J. Zhao. (2021). Gamma Delta T Cells and Their Pathogenic Role in Psoriasis. *Front. Immunol. 12*, 186.

22. Pellicci, D. G., H.-F. Koay, and S. P. Berzins. (2020). Thymic development of unconventional T cells: how NKT cells, MAIT cells and γδ T cells emerge. *Nat. Rev. Immunol. 20*(12), 756–770.

23. Chen, L., and D. B. Flies. (2013). Molecular mechanisms of T cell co-stimulation and co-inhibition. *Nat. Rev. Immunol. 13*(4), 227–242.

24. Jain, A., and C. Pasare. (2017). Innate Control of Adaptive Immunity: Beyond the Three-

Signal Paradigm. *J. Immunol. 198*(10), 3791–3800.
25. Zhu, J., H. Yamane, and W. E. Paul. (2010). Differentiation of Effector CD4 T Cell Populations. *Annu. Rev. Immunol. 28*(1), 445–489.
26. Kaech, S. M., E. J. Wherry, and R. Ahmed. (2002). Effector and memory T-cell differentiation: implications for vaccine development. *Nat. Rev. Immunol. 2*(4), 251–262.
27. Kaech, S. M., and W. Cui. (2012). Transcriptional control of effector and memory CD8+ T cell differentiation. *Nat. Rev. Immunol. 12*(11), 749–761.
28. Mahnke, Y. D., T. M. Brodie, F. Sallusto, M. Roederer, and E. Lugli. (2013). The who's who of T-cell differentiation: Human memory T-cell subsets. *Eur. J. Immunol. 43*(11), 2797–2809.
29. Vantourout, P., and A. Hayday. (2013). Six-of-the-best: unique contributions of γδ T cells to immunology. *Nat. Rev. Immunol. 13*(2), 88–100.
30. Papotto, P. H., B. Yilmaz, and B. Silva-Santos. (2021). Crosstalk between γδ T cells and the microbiota. *Nat. Microbiol. 6*(9), 1110–1117.
31. Ravens, S., A. S. Fichtner, M. Willers, D. Torkornoo, S. Pirr, J. Schöning, M. Deseke, I. Sandrock, A. Bubke, A. Wilharm, D. Dodoo, B. Egyir, K. L. Flanagan, L. Steinbrück, P. Dickinson, P. Ghazal, B. Adu, D. Viemann, and I. Prinz. (2020). Microbial exposure drives polyclonal expansion of innate γδ T cells immediately after birth. *Proc. Natl. Acad. Sci. U. S. A. 117*(31), 18649–18660.
32. Singer, A., S. Adoro, and J.-H. Park. (2008). Lineage fate and intense debate: myths, models and mechanisms of CD4- versus CD8-lineage choice. *Nat. Rev. Immunol. 8*(10), 788–801.
33. Overgaard, N. H., J.-W. Jung, R. J. Steptoe, and J. W. Wells. (2015). CD4+/CD8+ double-positive T cells: more than just a developmental stage? *J. Leukoc. Biol. 97*(1), 31–38.
34. D'Acquisto, F., and T. Crompton. (2011). CD3+CD4−CD8− (double negative) T cells: Saviours or villains of the immune response? *Biochem. Pharmacol. 82*(4), 333–340.
35. Brandt, D., and C. M. Hedrich. (2018). TCRαβ+CD3+CD4−CD8− (double negative) T cells in autoimmunity. *Autoimmun. Rev. 17*(4), 422–430.
36. Swain, S. L., K. K. McKinstry, and T. M. Strutt. (2012). Expanding roles for CD4+ T cells in immunity to viruses. *Nat. Rev. Immunol. 12*(2), 136–148.
37. Chatzileontiadou, D. S. M., H. Sloane, A. T. Nguyen, S. Gras, and E. J. Grant. (2021). The Many Faces of CD4+ T Cells: Immunological and Structural Characteristics. *Int. J. Mol. Sci. 22*(1), 73.
38. Appay, V., R. A. W. van Lier, F. Sallusto, and M. Roederer. (2008). Phenotype and function of human T lymphocyte subsets: Consensus and issues. *Cytom. Part A 73A*(11), 975–983.
39. Chen, X., and J. J. Oppenheim. (2011). Resolving the identity myth: Key markers of functional CD4+FoxP3+ regulatory T cells. *Int. Immunopharmacol. 11*(10), 1489–1496.
40. Schmitt, N., S.-E. Bentebibel, and H. Ueno. (2014). Phenotype and functions of memory Tfh cells in human blood. *Trends Immunol. 35*(9), 436–442.
41. Trapani, J. A., and M. J. Smyth. (2002). Functional significance of the perforin/granzyme cell death pathway. *Nat. Rev. Immunol. 2*(10), 735–747.
42. Martínez-Lostao, L., A. Anel, and J. Pardo. (2015). How Do Cytotoxic Lymphocytes Kill Cancer Cells? *Clin. Cancer Res. 21*(22), 5047–5056.
43. Paul, M. St., and P. S. Ohashi. (2020). The Roles of CD8+ T Cell Subsets in Antitumor Immunity. *Trends Cell Biol. 30*(9), 695–704.
44. Vivier, E., E. Tomasello, M. Baratin, T. Walzer, and S. Ugolini. (2008). Functions of natural killer cells. *Nat. Immunol. 9*(5), 503–510.
45. Kurioka, A., P. Klenerman, and C. B. Willberg. (2018). Innate-like CD8+ T-cells and NK cells: converging functions and phenotypes. *Immunology 154*(4), 547–556.
46. Kurioka, A., C. Cosgrove, Y. Simoni, B. van Wilgenburg, A. Geremia, S. Björkander, E. Sverremark-Ekström, C. Thurnheer, H. F. Günthard, N. Khanna, The Swiss HIV Cohort Study, Oxford IBD Cohort Investigators, L. J. Walker, C. V. Arancibia-Cárcamo, E. W. Newell, C. B. Willberg, and P. Klenerman. (2018). CD161 Defines a Functionally Distinct Subset of Pro-Inflammatory Natural Killer Cells. *Front. Immunol. 9*, 486.

47. Cooper, M. A., T. A. Fehniger, S. C. Turner, K. S. Chen, B. A. Ghaheri, T. Ghayur, W. E. Carson, and M. A. Caligiuri. (2001). Human natural killer cells: a unique innate immunoregulatory role for the CD56bright subset. *Blood 97*(10), 3146–3151.
48. Cooper, M. A., T. A. Fehniger, and M. A. Caligiuri. (2001). The biology of human natural killer-cell subsets. *Trends Immunol. 22*(11), 633–640.
49. Ivashkiv, L. B. (2018). IFNγ: signalling, epigenetics and roles in immunity, metabolism, disease and cancer immunotherapy. *Nat. Rev. Immunol. 18*(9), 545–558.
50. Chan, A., D.-L. Hong, A. Atzberger, S. Kollnberger, A. D. Filer, C. D. Buckley, A. McMichael, T. Enver, and P. Bowness. (2007). CD56bright Human NK Cells Differentiate into CD56dim Cells: Role of Contact with Peripheral Fibroblasts. *J. Immunol. 179*(1), 89–94.
51. Silva, A., D. M. Andrews, A. G. Brooks, M. J. Smyth, and Y. Hayakawa. (2008). Application of CD27 as a marker for distinguishing human NK cell subsets. *Int. Immunol. 20*(4), 625–630.
52. Lopez-Vergès, S., J. M. Milush, S. Pandey, V. A. York, J. Arakawa-Hoyt, H. Pircher, P. J. Norris, D. F. Nixon, and L. L. Lanier. (2010). CD57 defines a functionally distinct population of mature NK cells in the human CD56dimCD16+ NK-cell subset. *Blood 116*(19), 3865–3874.
53. Aldemir, H., V. Prod'homme, M.-J. Dumaurier, C. Retiere, G. Poupon, J. Cazareth, F. Bihl, and V. M. Braud. (2005). Cutting Edge: Lectin-Like Transcript 1 Is a Ligand for the CD161 Receptor. *J. Immunol. 175*(12), 7791–7795.
54. Rosen, D. B., J. Bettadapura, M. Alsharifi, P. A. Mathew, H. S. Warren, and L. L. Lanier. (2005). Cutting Edge: Lectin-Like Transcript-1 Is a Ligand for the Inhibitory Human NKR-P1A Receptor. *J. Immunol. 175*(12), 7796–7799.
55. Kleiveland, C. R. (2015). Peripheral Blood Mononuclear Cells. In *The Impact of Food Bioactives on Health: In Vitro and Ex Vivo Models*, (K. Verhoeckx, P. Cotter, I. López-Expósito, C. Kleiveland, T. Lea, A. Mackie, T. Requena, D. Swiatecka, and H. Wichers, eds). Springer, Cham. 161–167.
56. Spits, H., D. Artis, M. Colonna, A. Diefenbach, J. P. Di Santo, G. Eberl, S. Koyasu, R. M. Locksley, A. N. J. McKenzie, R. E. Mebius, F. Powrie, and E. Vivier. (2013). Innate lymphoid cells — a proposal for uniform nomenclature. *Nat. Rev. Immunol. 13*(2), 145–149.
57. Vivier, E., D. Artis, M. Colonna, A. Diefenbach, J. P. Di Santo, G. Eberl, S. Koyasu, R. M. Locksley, A. N. J. McKenzie, R. E. Mebius, F. Powrie, and H. Spits. (2018). Innate Lymphoid Cells: 10 Years On. *Cell 174*(5), 1054–1066.
58. Hazenberg, M. D., and H. Spits. (2014). Human innate lymphoid cells. *Blood 124*(5), 700–709.
59. Valdez, Y., S. K. Kyei, G. F. T. Poon, A. Kokaji, S. M. Woodside, A. C. Eaves, and T. E. Thomas. (2018). Efficient Enrichment of Functional ILC Subsets from Human PBMC by Immunomagnetic Selection. *J. Immunol. 200*(1 Supplement), 51.13.
60. Leite-de-Moraes, M. C., A. Hameg, A. Arnould, F. Machavoine, Y. Koezuka, E. Schneider, A. Herbelin, and M. Dy. (1999). A Distinct IL-18-Induced Pathway to Fully Activate NK T Lymphocytes Independently from TCR Engagement. *J. Immunol. 163*(11), 5871–5876.
61. Rossjohn, J., D. G. Pellicci, O. Patel, L. Gapin, and D. I. Godfrey. (2012). Recognition of CD1d-restricted antigens by natural killer T cells. *Nat. Rev. Immunol. 12*(12), 845–857.
62. Fan, X., and A. Y. Rudensky. (2016). Hallmarks of Tissue-Resident Lymphocytes. *Cell 164*(6), 1198–1211.
63. Wang, X., K. A. Bishop, S. Hegde, L. A. Rodenkirch, J. W. Pike, and J. E. Gumperz. (2012). Human invariant natural killer T cells acquire transient innate responsiveness via histone H4 acetylation induced by weak TCR stimulation. *J. Exp. Med. 209*(5), 987–1000.
64. Jo, J., A. T. Tan, J. E. Ussher, E. Sandalova, X.-Z. Tang, A. Tan-Garcia, N. To, M. Hong, A. Chia, U. S. Gill, P. T. Kennedy, K. C. Tan, K. H. Lee, G. De Libero, A. J. Gehring, C. B. Willberg, P. Klenerman, and A. Bertoletti. (2014). Toll-Like Receptor 8 Agonist and Bacteria Trigger Potent Activation of Innate Immune Cells in Human Liver. *PLoS Pathog.*

10(6), e1004210.

65. Ussher, J. E., M. Bilton, E. Attwod, J. Shadwell, R. Richardson, C. de Lara, E. Mettke, A. Kurioka, T. H. Hansen, P. Klenerman, and C. B. Willberg. (2014). CD161++CD8+ T cells, including the MAIT cell subset, are specifically activated by IL-12+IL-18 in a TCR-independent manner. *Eur. J. Immunol. 44*(1), 195–203.

66. Provine, N. M., B. Binder, M. E. B. FitzPatrick, A. Schuch, L. C. Garner, K. D. Williamson, B. van Wilgenburg, R. Thimme, P. Klenerman, and M. Hofmann. (2018). Unique and Common Features of Innate-Like Human Vδ2+ γδT Cells and Mucosal-Associated Invariant T Cells. *Front. Immunol. 9*, 756.

67. Gao, Y., and A. P. Williams. (2015). Role of Innate T Cells in Anti-Bacterial Immunity. *Front. Immunol. 6*, 302.

68. Fergusson, J. R., K. E. Smith, V. M. Fleming, N. Rajoriya, E. W. Newell, R. Simmons, E. Marchi, S. Björkander, Y.-H. Kang, L. Swadling, A. Kurioka, N. Sahgal, H. Lockstone, D. Baban, G. J. Freeman, E. Sverremark-Ekström, M. M. Davis, M. P. Davenport, V. Venturi, J. E. Ussher, C. B. Willberg, and P. Klenerman. (2014). CD161 defines a transcriptional and functional phenotype across distinct human T cell lineages. *Cell Rep. 9*(3), 1075–1088.

69. Montoya, C. J., D. Pollard, J. Martinson, K. Kumari, C. Wasserfall, C. B. Mulder, M. T. Rugeles, M. A. Atkinson, A. L. Landay, and S. B. Wilson. (2007). Characterization of human invariant natural killer T subsets in health and disease using a novel invariant natural killer T cell-clonotypic monoclonal antibody, 6B11. *Immunology 122*(1), 1–14.

70. Kleinschek, M. A., K. Boniface, S. Sadekova, J. Grein, E. E. Murphy, S. P. Turner, L. Raskin, B. Desai, W. A. Faubion, R. de Waal Malefyt, R. H. Pierce, T. McClanahan, and R. A. Kastelein. (2009). Circulating and gut-resident human Th17 cells express CD161 and promote intestinal inflammation. *J. Exp. Med. 206*(3), 525–534.

71. Cosmi, L., R. De Palma, V. Santarlasci, L. Maggi, M. Capone, F. Frosali, G. Rodolico, V. Querci, G. Abbate, R. Angeli, L. Berrino, M. Fambrini, M. Caproni, F. Tonelli, E. Lazzeri, P. Parronchi, F. Liotta, E. Maggi, S. Romagnani, and F. Annunziato. (2008). Human interleukin 17–producing cells originate from a CD161+CD4+ T cell precursor. *J. Exp. Med. 205*(8), 1903–1916.

72. Maggi, L., V. Santarlasci, M. Capone, A. Peired, F. Frosali, S. Q. Crome, V. Querci, M. Fambrini, F. Liotta, M. K. Levings, E. Maggi, L. Cosmi, S. Romagnani, and F. Annunziato. (2010). CD161 is a marker of all human IL-17-producing T-cell subsets and is induced by RORC. *Eur. J. Immunol. 40*(8), 2174–2181.

73. Fergusson, J. R., M. H. Hühn, L. Swadling, L. J. Walker, A. Kurioka, A. Llibre, A. Bertoletti, G. Holländer, E. W. Newell, M. M. Davis, E. Sverremark-Ekström, F. Powrie, S. Capone, A. Folgori, E. Barnes, C. B. Willberg, J. E. Ussher, and P. Klenerman. (2016). CD161intCD8+ T cells: a novel population of highly functional, memory CD8+ T cells enriched within the gut. *Mucosal Immunol. 9*(2), 401–413.

74. Nicol, B., M. Salou, I. Vogel, A. Garcia, E. Dugast, J. Morille, S. Kilens, E. Charpentier, A. Donnart, S. Nedellec, M. Jacq-Foucher, F. Le Frère, S. Wiertlewski, A. Bourreille, S. Brouard, L. Michel, L. David, P.-A. Gourraud, N. Degauque, A. B. Nicot, L. Berthelot, and D.-A. Laplaud. (2018). An intermediate level of CD161 expression defines a novel activated, inflammatory, and pathogenic subset of CD8+ T cells involved in multiple sclerosis. *J. Autoimmun. 88*, 61–74.

75. Fergusson, J. R., V. M. Fleming, and P. Klenerman. (2011). CD161-Expressing Human T Cells. *Front. Immunol. 2*, 36.

76. Rosen, D. B., W. Cao, D. T. Avery, S. G. Tangye, Y.-J. Liu, J. P. Houchins, and L. L. Lanier. (2008). Functional Consequences of Interactions between Human NKR-P1A and Its Ligand LLT1 Expressed on Activated Dendritic Cells and B Cells. *J. Immunol. 180*(10), 6508–6517.

77. Mathewson, N. D., O. Ashenberg, I. Tirosh, S. Gritsch, E. M. Perez, S. Marx, L. Jerby-Arnon, R. Chanoch-Myers, T. Hara, A. R. Richman, Y. Ito, J. Pyrdol, M. Friedrich, K. Schumann, M. J. Poitras, P. C. Gokhale, L. N. Gonzalez Castro, M. E. Shore, C. M. Hebert, B. Shaw, H. L. Cahill, M. Drummond, W. Zhang, O. Olawoyin, H. Wakimoto, O.

Rozenblatt-Rosen, P. K. Brastianos, X. S. Liu, P. S. Jones, D. P. Cahill, M. P. Frosch, D. N. Louis, G. J. Freeman, K. L. Ligon, A. Marson, E. A. Chiocca, D. A. Reardon, A. Regev, M. L. Suvà, and K. W. Wucherpfennig. (2021). Inhibitory CD161 receptor identified in glioma-infiltrating T cells by single-cell analysis. *Cell 184*(5), 1281-1298.e26.

78. Gherardin, N. A., A. N. Keller, R. E. Woolley, J. Le Nours, D. S. Ritchie, P. J. Neeson, R. W. Birkinshaw, S. B. G. Eckle, J. N. Waddington, L. Liu, D. P. Fairlie, A. P. Uldrich, D. G. Pellicci, J. McCluskey, D. I. Godfrey, and J. Rossjohn. (2016). Diversity of T Cells Restricted by the MHC Class I-Related Molecule MR1 Facilitates Differential Antigen Recognition. *Immunity 44*(1), 32–45.

79. Tilloy, F., E. Treiner, S.-H. Park, C. Garcia, F. Lemonnier, H. de la Salle, A. Bendelac, M. Bonneville, and O. Lantz. (1999). An Invariant T Cell Receptor α Chain Defines a Novel TAP-independent Major Histocompatibility Complex Class Ib–restricted α/β T Cell Subpopulation in Mammals. *J. Exp. Med. 189*(12), 1907–1921.

80. Kjer-Nielsen, L., O. Patel, A. J. Corbett, J. Le Nours, B. Meehan, L. Liu, M. Bhati, Z. Chen, L. Kostenko, R. Reantragoon, N. A. Williamson, A. W. Purcell, N. L. Dudek, M. J. McConville, R. A. J. O'Hair, G. N. Khairallah, D. I. Godfrey, D. P. Fairlie, J. Rossjohn, and J. McCluskey. (2012). MR1 presents microbial vitamin B metabolites to MAIT cells. *Nature 491*(7426), 717–723.

81. van Wilgenburg, B., I. Scherwitzl, E. C. Hutchinson, T. Leng, A. Kurioka, C. Kulicke, C. de Lara, S. Cole, S. Vasanawathana, W. Limpitikul, P. Malasit, D. Young, L. Denney, E. Barnes, J. Ball, G. Burgess, G. Cooke, J. Dillon, C. Gore, G. Foster, N. Guha, R. Halford, C. Herath, C. Holmes, A. Howe, E. Hudson, W. Irving, S. Khakoo, D. Koletzki, N. Martin, T. Mbisa, J. McKeating, J. McLauchlan, A. Miners, A. Murray, P. Shaw, P. Simmonds, C. Spencer, P. Targett-Adams, E. Thomson, P. Vickerman, N. Zitzmann, M. D. Moore, P. Fabris, M. T. Giordani, Y. H. Oo, S. M. Laidlaw, L. B. Dustin, L.-P. Ho, F. M. Thompson, N. Ramamurthy, J. Mongkolsapaya, C. B. Willberg, G. R. Screaton, and P. Klenerman. (2016). MAIT cells are activated during human viral infections. *Nat. Commun. 7*(1), 11653.

82. Leng, T., H. D. Akther, C.-P. Hackstein, K. Powell, T. King, M. Friedrich, Z. Christoforidou, S. McCuaig, M. Neyazi, C. V. Arancibia-Cárcamo, J. Hagel, F. Powrie, Oxford IBD Investigators, R. S. Peres, V. Millar, D. Ebner, R. Lamichhane, J. Ussher, T. S. C. Hinks, E. Marchi, C. Willberg, and P. Klenerman. (2019). TCR and Inflammatory Signals Tune Human MAIT Cells to Exert Specific Tissue Repair and Effector Functions. *Cell Rep. 28*(12), 3077-3091.e5.

83. Sattler, A., C. Dang-Heine, P. Reinke, and N. Babel. (2015). IL-15 dependent induction of IL-18 secretion as a feedback mechanism controlling human MAIT-cell effector functions. *Eur. J. Immunol. 45*(8), 2286–2298.

84. Dusseaux, M., E. Martin, N. Serriari, I. Péguillet, V. Premel, D. Louis, M. Milder, L. Le Bourhis, C. Soudais, E. Treiner, and O. Lantz. (2011). Human MAIT cells are xenobiotic-resistant, tissue-targeted, CD161hi IL-17–secreting T cells. *Blood 117*(4), 1250–1259.

85. Le Bourhis, L., M. Dusseaux, A. Bohineust, S. Bessoles, E. Martin, V. Premel, M. Coré, D. Sleurs, N.-E. Serriari, E. Treiner, C. Hivroz, P. Sansonetti, M.-L. Gougeon, C. Soudais, and O. Lantz. (2013). MAIT Cells Detect and Efficiently Lyse Bacterially-Infected Epithelial Cells. *PLoS Pathog. 9*(10), e1003681.

86. Kurioka, A., J. E. Ussher, C. Cosgrove, C. Clough, J. R. Fergusson, K. Smith, Y.-H. Kang, L. J. Walker, T. H. Hansen, C. B. Willberg, and P. Klenerman. (2015). MAIT cells are licensed through granzyme exchange to kill bacterially sensitized targets. *Mucosal Immunol. 8*(2), 429–440.

87. Billerbeck, E., Y.-H. Kang, L. Walker, H. Lockstone, S. Grafmueller, V. Fleming, J. Flint, C. B. Willberg, B. Bengsch, B. Seigel, N. Ramamurthy, N. Zitzmann, E. J. Barnes, J. Thevanayagam, A. Bhagwanani, A. Leslie, Y. H. Oo, S. Kollnberger, P. Bowness, O. Drognitz, D. H. Adams, H. E. Blum, R. Thimme, and P. Klenerman. (2010). Analysis of CD161 expression on human CD8+ T cells defines a distinct functional subset with tissue-homing properties. *Proc. Natl. Acad. Sci. U. S. A. 107*(7), 3006–3011.

88. Gherardin, N. A., M. N. T. Souter, H.-F. Koay, K. M. Mangas, T. Seemann, T. P. Stinear,

S. B. G. Eckle, S. P. Berzins, Y. D'Udekem, I. E. Konstantinov, D. P. Fairlie, D. S. Ritchie, P. J. Neeson, D. G. Pellicci, A. P. Uldrich, J. McCluskey, and D. I. Godfrey. (2018). Human blood MAIT cell subsets defined using MR1 tetramers. *Immunol. Cell Biol. 96*(5), 507–525.

89. Lamichhane, R., M. Schneider, S. M. de la Harpe, T. W. R. Harrop, R. F. Hannaway, P. K. Dearden, J. R. Kirman, J. D. A. Tyndall, A. J. Vernall, and J. E. Ussher. (2019). TCR- or Cytokine-Activated CD8+ Mucosal-Associated Invariant T Cells Are Rapid Polyfunctional Effectors That Can Coordinate Immune Responses. *Cell Rep. 28*(12), 3061-3076.e5.

90. Kurioka, A., L. J. Walker, P. Klenerman, and C. B. Willberg. (2016). MAIT cells: new guardians of the liver. *Clin. Transl. Immunol. 5*(8), e98.

91. Kurioka, A., A. S. Jahun, R. F. Hannaway, L. J. Walker, J. R. Fergusson, E. Sverremark-Ekström, A. J. Corbett, J. E. Ussher, C. B. Willberg, and P. Klenerman. (2017). Shared and Distinct Phenotypes and Functions of Human CD161++ Vα7.2+ T Cell Subsets. *Front. Immunol. 8*, 1031.

92. Reantragoon, R., A. J. Corbett, I. G. Sakala, N. A. Gherardin, J. B. Furness, Z. Chen, S. B. G. Eckle, A. P. Uldrich, R. W. Birkinshaw, O. Patel, L. Kostenko, B. Meehan, K. Kedzierska, L. Liu, D. P. Fairlie, T. H. Hansen, D. I. Godfrey, J. Rossjohn, J. McCluskey, and L. Kjer-Nielsen. (2013). Antigen-loaded MR1 tetramers define T cell receptor heterogeneity in mucosal-associated invariant T cells. *J. Exp. Med. 210*(11), 2305–2320.

93. Kalyan, S., and D. Kabelitz. (2013). Defining the nature of human γδ T cells: a biographical sketch of the highly empathetic. *Cell. Mol. Immunol. 10*(1), 21–29.

94. Rajoriya, N., J. R. Fergusson, J. A. Leithead, and P. Klenerman. (2014). Gamma delta T-lymphocytes in hepatitis C and chronic liver disease. *Front. Immunol. 5*, 400.

95. Kabelitz, D. (2012). CD277 takes the lead in human γδ T-cell activation. *Blood 120*(11), 2159–2161.

96. Kabelitz, D., and W. He. (2012). The Multifunctionality of Human Vγ9Vδ2 γδ T Cells: Clonal Plasticity or Distinct Subsets? *Scand. J. Immunol. 76*(3), 213–222.

97. Karunakaran, M. M., C. R. Willcox, M. Salim, D. Paletta, A. S. Fichtner, A. Noll, L. Starick, A. Nöhren, C. R. Begley, K. A. Berwick, R. A. G. Chaleil, V. Pitard, J. Déchanet-Merville, P. A. Bates, B. Kimmel, T. J. Knowles, V. Kunzmann, L. Walter, M. Jeeves, F. Mohammed, B. E. Willcox, and T. Herrmann. (2020). Butyrophilin-2A1 Directly Binds Germline-Encoded Regions of the Vγ9Vδ2 TCR and Is Essential for Phosphoantigen Sensing. *Immunity 52*(3), 487-498.e6.

98. Davey, M. S., C. R. Willcox, S. P. Joyce, K. Ladell, S. A. Kasatskaya, J. E. McLaren, S. Hunter, M. Salim, F. Mohammed, D. A. Price, D. M. Chudakov, and B. E. Willcox. (2017). Clonal selection in the human Vδ1 T cell repertoire indicates γδ TCR-dependent adaptive immune surveillance. *Nat. Commun. 8*(1), 14760.

99. Porcelli, S., M. B. Brenner, J. L. Greenstein, C. Terhorst, S. P. Balk, and P. A. Bleicher. (1989). Recognition of cluster of differentiation 1 antigens by human CD4−CD8− cytolytic T lymphocyte. *Nature 341*(6241), 447–450.

100. Reijneveld, J. F., T. A. Ocampo, A. Shahine, B. S. Gully, P. Vantourout, A. C. Hayday, J. Rossjohn, D. B. Moody, and I. Van Rhijn. (2020). Human γδ T cells recognize CD1b by two distinct mechanisms. *Proc. Natl. Acad. Sci. U. S. A. 117*(37), 22944–22952.

101. Bai, L., D. Picard, B. Anderson, V. Chaudhary, A. Luoma, B. Jabri, E. Adams, P. Savage, and A. Bendelac. (2012). The majority of CD1d-sulfatide-specific T cells in human blood use a semiinvariant Vδ1 TCR. *Eur. J. Immunol. 42*(9), 2505–2510.

102. Gapin, L. (2016). Development of invariant natural killer T cells. *Curr. Opin. Immunol. 39*, 68–74.

103. Krijgsman, D., M. Hokland, and P. J. K. Kuppen. (2018). The Role of Natural Killer T Cells in Cancer—A Phenotypical and Functional Approach. *Front. Immunol. 9*, 367.

104. Exley, M., S. Porcelli, M. Furman, J. Garcia, and S. Balk. (1998). CD161 (NKR-P1A) Costimulation of CD1d-dependent Activation of Human T Cells Expressing Invariant Vα24JαQ T Cell Receptor α Chains. *J. Exp. Med. 188*(5), 867–876.

105. Heidemann, S. C., V. Chavez, C. J. Landers, T. Kucharzik, J. L. Prehn, and S. R. Targan.

(2010). TL1A Selectively Enhances IL-12/IL-18-Induced NK Cell Cytotoxicity against NK-Resistant Tumor Targets. *J. Clin. Immunol. 30*(4), 531–538.
106. Lee, A. J., F. Mian, S. M. Poznanski, M. Stackaruk, T. Chan, M. V. Chew, and A. A. Ashkar. (2019). Type I Interferon Receptor on NK Cells Negatively Regulates Interferon-γ Production. *Front. Immunol. 10*, 1261.
107. Papadakis, K. A., J. L. Prehn, C. Landers, Q. Han, X. Luo, S. C. Cha, P. Wei, and S. R. Targan. (2004). TL1A Synergizes with IL-12 and IL-18 to Enhance IFN-γ Production in Human T Cells and NK Cells. *J. Immunol. 172*(11), 7002–7007.
108. Gorvel, L., D. Korenfeld, T. Tung, and E. Klechevsky. (2017). Dendritic Cell-Derived IL-32α: A Novel Inhibitory Cytokine of NK Cell Function. *J. Immunol. 199*(4), 1290–1300.
109. Kim, S. H., S. Y. Han, T. Azam, D. Y. Yoon, and C. A. Dinarello. (2005). Interleukin-32: A cytokine and inducer of TNFα. *Immunity 22*(1), 131–142.
110. Shoda, H., K. Fujio, Y. Yamaguchi, A. Okamoto, T. Sawada, Y. Kochi, and K. Yamamoto. (2006). Interactions between IL-32 and tumor necrosis factor alpha contribute to the exacerbation of immune-inflammatory diseases. *Arthritis Res. Ther. 8*(6), R166.
111. Burnet, M. (1957). Cancer: a biological approach. III. Viruses associated with neoplastic conditions. IV. Practical applications. *Br. Med. J. 1*(5023), 841–847.
112. Burnet, M. (1964). IMMUNOLOGICAL FACTORS IN THE PROCESS OF CARCINOGENESIS. *Br. Med. Bull. 20*(2), 154–158.
113. Burnet, F. M. (1970). The Concept of Immunological Surveillance. In *Progress in Experimental Tumor Research: Immunological Aspects of Neoplasia*, vol. 13. (R. S. Schwartz, and F. Homburger, eds). S. Karger, Basel. 1–27.
114. Thomas, L. (1959). Discussion. In *Cellular and Humoral Aspects of the Hypersensitive States*, (H. S. Lawrence, ed). Hoeber-Harper, New York. 529–532.
115. Thomas, L. (1982). On immunosurveillance in human cancer. *Yale J. Biol. Med. 55*(3–4), 329–333.
116. Dunn, G. P., L. J. Old, and R. D. Schreiber. (2004). The Immunobiology of Cancer Immunosurveillance and Immunoediting. *Immunity 21*(2), 137–148.
117. Swann, J. B., and M. J. Smyth. (2007). Immune surveillance of tumors. *J. Clin. Invest. 117*(5), 1137–1146.
118. Birkeland, S. A., H. H. Storm, L. U. Lamm, L. Barlow, I. Blohmé, B. Forsberg, B. Eklund, O. Fjeldborg, M. Friedberg, L. Frödin, E. Glattre, S. Halvorsen, N. V. Holm, A. Jakobsen, H. E. Jorgensen, J. Ladefoged, T. Lindholm, G. Lundgren, and E. Pukkala. (1995). Cancer risk after renal transplantation in the nordic countries, 1964-1986. *Int. J. Cancer 60*(2), 183–189.
119. Hollenbeak, C. S., M. M. Todd, E. M. Billingsley, G. Harper, A.-M. Dyer, and E. J. Lengerich. (2005). Increased incidence of melanoma in renal transplantation recipients. *Cancer 104*(9), 1962–1967.
120. Opelz, G., and B. Döhler. (2004). Lymphomas After Solid Organ Transplantation: A Collaborative Transplant Study Report. *Am. J. Transplant. 4*(2), 222–230.
121. Naito, Y., K. Saito, K. Shiiba, A. Ohuchi, K. Saigenji, H. Nagura, and H. Ohtani. (1998). CD8+ T Cells Infiltrated within Cancer Cell Nests as a Prognostic Factor in Human Colorectal Cancer. *Cancer Res. 58*(16), 3491–3494.
122. Schumacher, K., W. Haensch, C. Röefzaad, and P. M. Schlag. (2001). Prognostic Significance of Activated CD8+ T Cell Infiltrations within Esophageal Carcinomas. *Cancer Res. 61*(10), 3932–3936.
123. Oshi, M., M. Asaoka, Y. Tokumaru, L. Yan, R. Matsuyama, T. Ishikawa, I. Endo, and K. Takabe. (2020). CD8 T Cell Score as a Prognostic Biomarker for Triple Negative Breast Cancer. *Int. J. Mol. Sci. 21*(18), 6968.
124. Yarchoan, M., B. A. Johnson, E. R. Lutz, D. A. Laheru, and E. M. Jaffee. (2017). Targeting neoantigens to augment antitumour immunity. *Nat. Rev. Cancer 17*(4), 209–222.
125. Paul, S., and G. Lal. (2017). The Molecular Mechanism of Natural Killer Cells Function and Its Importance in Cancer Immunotherapy. *Front. Immunol. 8*, 1124.
126. Dunn, G. P., L. J. Old, and R. D. Schreiber. (2004). The Three Es of Cancer

Immunoediting. *Annu. Rev. Immunol. 22*(1), 329–360.
127. Dunn, G. P., C. M. Koebel, and R. D. Schreiber. (2006). Interferons, immunity and cancer immunoediting. *Nat. Rev. Immunol. 6*(11), 836–848.
128. Pardoll, D. M. (2012). The blockade of immune checkpoints in cancer immunotherapy. *Nat. Rev. Cancer 12*(4), 252–264.
129. Hanahan, D., and R. A. Weinberg. (2011). Hallmarks of Cancer: The Next Generation. *Cell 144*(5), 646–674.
130. Gentles, A. J., A. M. Newman, C. L. Liu, S. V Bratman, W. Feng, D. Kim, V. S. Nair, Y. Xu, A. Khuong, C. D. Hoang, M. Diehn, R. B. West, S. K. Plevritis, and A. A. Alizadeh. (2015). The prognostic landscape of genes and infiltrating immune cells across human cancers. *Nat. Med. 21*(8), 938–945.
131. Fulwyler, M. J. (1965). Electronic Separation of Biological Cells by Volume. *Science 150*(3698), 910–911.
132. Robinson, J. P., and M. Roederer. (2015). Flow cytometry strikes gold. *Science 350*(6262), 739–740.
133. Adan, A., G. Alizada, Y. Kiraz, Y. Baran, and A. Nalbant. (2017). Flow cytometry: basic principles and applications. *Crit. Rev. Biotechnol. 37*(2), 163–176.
134. Nolan, J. P., D. Condello, E. Duggan, M. Naivar, and D. Novo. (2013). Visible and near infrared fluorescence spectral flow cytometry. *Cytom. Part A 83A*(3), 253–264.
135. Ferrer-Font, L., C. Pellefigues, J. U. Mayer, S. J. Small, M. C. Jaimes, and K. M. Price. (2020). Panel Design and Optimization for High-Dimensional Immunophenotyping Assays Using Spectral Flow Cytometry. *Curr. Protoc. Cytom. 92*(1), e70.
136. Bandura, D. R., V. I. Baranov, O. I. Ornatsky, A. Antonov, R. Kinach, X. Lou, S. Pavlov, S. Vorobiev, J. E. Dick, and S. D. Tanner. (2009). Mass cytometry: Technique for real time single cell multitarget immunoassay based on inductively coupled plasma time-of-flight mass spectrometry. *Anal. Chem. 81*(16), 6813–6822.
137. Hennig, C., N. Adams, and G. Hansen. (2009). A versatile platform for comprehensive chip-based explorative cytometry. *Cytom. Part A 75A*(4), 362–370.
138. Hümmert, M. W., S. Alvermann, S. Gingele, C. C. Gross, H. Wiendl, A. Mirenska, C. Hennig, and M. Stangel. (2018). Immunophenotyping of cerebrospinal fluid cells by Chipcytometry. *J. Neuroinflammation 15*(1), 160.
139. Neves-Petersen, M. T., G. P. Gajula, and S. B. Petersen. (2012). UV Light Effects on Proteins: From Photochemistry to Nanomedicine. In *Molecular Photochemistry - Various Aspects*, (S. Saha, ed). IntechOpen. 125–158.
140. Abaskharon, R. M., and F. Gai. (2016). Direct measurement of the tryptophan-mediated photocleavage kinetics of a protein disulfide bond. *Phys. Chem. Chem. Phys. 18*(14), 9602–9607.
141. Bendall, S. C., G. P. Nolan, M. Roederer, and P. K. Chattopadhyay. (2012). A deep profiler's guide to cytometry. *Trends Immunol. 33*(7), 323–332.
142. Brummelman, J., C. Haftmann, N. G. Núñez, G. Alvisi, E. M. C. Mazza, B. Becher, and E. Lugli. (2019). Development, application and computational analysis of high-dimensional fluorescent antibody panels for single-cell flow cytometry. *Nat. Protoc. 14*(7), 1946–1969.
143. Sahir, F., J. M. Mateo, M. Steinhoff, and K. S. Siveen. (2020). Development of a 43 color panel for the characterization of conventional and unconventional T-cell subsets, B cells, NK cells, monocytes, dendritic cells, and innate lymphoid cells using spectral flow cytometry. *Cytom. Part A* , 1–7.
144. Rodriguez, L., P. T. Pekkarinen, T. Lakshmikanth, Z. Tan, C. R. Consiglio, C. Pou, Y. Chen, C. H. Mugabo, N. A. Nguyen, K. Nowlan, T. Strandin, L. Levanov, J. Mikes, J. Wang, A. Kantele, J. Hepojoki, O. Vapalahti, S. Heinonen, E. Kekäläinen, and P. Brodin. (2020). Systems-Level Immunomonitoring from Acute to Recovery Phase of Severe COVID-19. *Cell Reports Med. 1*(5), 100078.
145. Parra, E. R. (2018). Novel Platforms of Multiplexed Immunofluorescence for Study of Paraffin Tumor Tissues. *J. Cancer Treat. Diagnosis 2*(1), 43–53.
146. Parra, E. R., A. Francisco-Cruz, and I. I. Wistuba. (2019). State-of-the-Art of Profiling

Immune Contexture in the Era of Multiplexed Staining and Digital Analysis to Study Paraffin Tumor Tissues. *Cancers 11*(2), 247.

147. Francisco-Cruz, A., E. R. Parra, M. T. Tetzlaff, and I. I. Wistuba. (2020). Multiplex Immunofluorescence Assays. In *Biomarkers for Immunotherapy of Cancer: Methods in Molecular Biology*, vol. 2055. (M. Thurin, A. Cesano, and F. M. Marincola, eds). Humana, New York. 467–495.

148. Yaghoobi, V., S. Martinez-Morilla, Y. Liu, L. Charette, D. L. Rimm, and M. Harigopal. (2020). Advances in quantitative immunohistochemistry and their contribution to breast cancer. *Expert Rev. Mol. Diagn. 20*(5), 509–522.

149. Tan, W. C. C., S. N. Nerurkar, H. Y. Cai, H. H. M. Ng, D. Wu, Y. T. F. Wee, J. C. T. Lim, J. Yeong, and T. K. H. Lim. (2020). Overview of multiplex immunohistochemistry/immunofluorescence techniques in the era of cancer immunotherapy. *Cancer Commun. 40*(4), 135–153.

150. Von Waldeyer-Hartz, W. (1884). Ueber den lymphatischen Apparat des Pharynx. In *Deutsche Medizinische Wochenschrift*, (P. Boerner, ed). Georg Reimer Verlag, Berlin. 313.

151. Perry, M., and A. Whyte. (1998). Immunology of the tonsils. *Immunol. Today 19*(9), 414–421.

152. Nave, H., A. Gebert, and R. Pabst. (2001). Morphology and immunology of the human palatine tonsil. *Anat. Embryol. 204*(5), 367–373.

153. Scadding, G. K. (1990). Immunology of the tonsil: A review. *J. R. Soc. Med. 83*(2), 104–107.

154. Gebert, A., and R. Pabst. (1999). M cells at locations outside the gut. *Semin. Immunol. 11*(3), 165–170.

155. Brandtzaeg, P. (2015). Immunobiology of the Tonsils and Adenoids. In *Mucosal Immunology*, 4th ed. vol. 2. (J. Mestecky, W. Strober, M. W. Russell, B. L. Kelsall, H. Cheroutre, and B. N. Lambrecht, eds). Elsevier, Amsterdam. 1985–2016.

156. Kwak, K., H. Sohn, J. Brzostowski, J. Manzella-Lapeira, and S. K. Pierce. (2016). Human tonsil naive B cells and germinal center B cells show distinct behaviors upon contact of antigen in lipid bilayers. *J. Immunol. 196*(1 Supplement), 195.8.

157. Liu, Y. J., O. De Bouteiller, C. Arpin, F. Brière, L. Galibert, S. Ho, H. Martinez-Valdez, J. Banchereau, and S. Lebecque. (1996). Normal human IgD+IgM- germinal center B cells can express up to 80 mutations in the variable region of their IgD transcripts. *Immunity 4*(6), 603–613.

158. Kranich, J., and N. J. Krautler. (2016). How follicular dendritic cells shape the B-cell antigenome. *Front. Immunol. 7*, 225.

159. Crotty, S. (2011). Follicular helper CD4 T cells (TFH). *Annu. Rev. Immunol. 29*(1), 621–663.

160. Thornhill, J. P., S. Fidler, P. Klenerman, J. Frater, and C. Phetsouphanh. (2017). The role of CD4+ T follicular helper cells in HIV infection: From the germinal center to the periphery. *Front. Immunol. 8*, 46.

161. Breitfeld, D., L. Ohl, E. Kremmer, J. Ellwart, F. Sallusto, M. Lipp, and R. Förster. (2000). Follicular B helper T cells express CXC chemokine receptor 5, localize to B cell follicles, and support immunoglobulin production. *J. Exp. Med. 192*(11), 1545–1552.

162. Liu, X., X. Chen, B. Zhong, A. Wang, X. Wang, F. Chu, R. I. Nurieva, X. Yan, P. Chen, L. G. Van Der Flier, H. Nakatsukasa, S. S. Neelapu, W. Chen, H. Clevers, Q. Tian, H. Qi, L. Wei, and C. Dong. (2014). Transcription factor achaete-scute homologue 2 initiates follicular T-helper-cell development. *Nature 507*(7493), 513–518.

163. Radcliff, F. J., S. Waldvogel-Thurlow, F. Clow, M. Mahadevan, J. Johnston, G. Li, T. Proft, R. G. Douglas, and J. D. Fraser. (2019). Impact of superantigen-producing bacteria on T cells from tonsillar hyperplasia. *Pathogens 8*(3), 90.

164. Lepore, M., A. Kalinicenko, A. Colone, B. Paleja, A. Singhal, A. Tschumi, B. Lee, M. Poidinger, F. Zolezzi, L. Quagliata, P. Sander, E. Newell, A. Bertoletti, L. Terracciano, G. De Libero, and L. Mori. (2014). Parallel T-cell cloning and deep sequencing of human MAIT cells reveal stable oligoclonal TCRβ repertoire. *Nat. Commun. 5*(1), 3866.

165. Kawaguchi, T. (1993). [Gamma delta T cells in the palatine tonsil--immunohistological and functional study]. *Nippon Jibiinkoka Gakkai Kaiho 96*(5), 810-817_2,875.
166. Koay, H.-F., D. I. Godfrey, and D. G. Pellicci. (2018). Development of mucosal-associated invariant T cells. *Immunol. Cell Biol. 96*(6), 598–606.
167. Ussher, J. E., P. Klenerman, and C. B. Willberg. (2014). Mucosal-associated invariant T-cells: new players in anti-bacterial immunity. *Front. Immunol. 5*, 450.
168. Lukasik, Z., D. Elewaut, and K. Venken. (2020). MAIT Cells Come to the Rescue in Cancer Immunotherapy. *Cancers 12*(2), 413.
169. Van Gassen, S., B. Callebaut, M. J. Van Helden, B. N. Lambrecht, P. Demeester, T. Dhaene, and Y. Saeys. (2015). FlowSOM: Using self-organizing maps for visualization and interpretation of cytometry data. *Cytom. Part A 87*(7), 636–645.
170. Nowicka, M., C. Krieg, H. L. Crowell, L. M. Weber, F. J. Hartmann, S. Guglietta, B. Becher, M. P. Levesque, and M. D. Robinson. (2017). CyTOF workflow: differential discovery in high-throughput high-dimensional cytometry datasets [version 2; peer review: 2 approved]. *F1000Res. 6*, 748.
171. Beucke, N., D. Wesch, H. Oberg, C. Peters, J. Bochem, B. Weide, C. Garbe, G. Pawelec, S. Sebens, C. Röcken, H. Hashimoto, M. W. Löffler, P. Nocerino, S. Kordasti, D. Kabelitz, K. Schilbach, and K. Wistuba-Hamprecht. (2020). Pitfalls in the characterization of circulating and tissue-resident human γδ T cells. *J. Leukoc. Biol. 107*(6), 1097–1105.
172. Goltsev, Y., N. Samusik, J. Kennedy-Darling, S. Bhate, M. Hale, G. Vazquez, S. Black, and G. P. Nolan. (2018). Deep Profiling of Mouse Splenic Architecture with CODEX Multiplexed Imaging. *Cell 174*(4), 968-981.e15.
173. Stoeckius, M., C. Hafemeister, W. Stephenson, B. Houck-Loomis, P. K. Chattopadhyay, H. Swerdlow, R. Satija, and P. Smibert. (2017). Simultaneous epitope and transcriptome measurement in single cells. *Nat. Methods 14*(9), 865–868.
174. Peterson, V. M., K. X. Zhang, N. Kumar, J. Wong, L. Li, D. C. Wilson, R. Moore, T. K. McClanahan, S. Sadekova, and J. A. Klappenbach. (2017). Multiplexed quantification of proteins and transcripts in single cells. *Nat. Biotechnol. 35*(10), 936–939.
175. Hagel, J. P., K. Bennett, F. Buffa, P. Klenerman, C. B. Willberg, and K. Powell. (2021). Defining T Cell Subsets in Human Tonsils Using ChipCytometry. *J. Immunol. 206*(12), 3073–3082.
176. Lun, A. T. L., A. C. Richard, and J. C. Marioni. (2017). Testing for differential abundance in mass cytometry data. *Nat. Methods 14*(7), 707–709.
177. Van Gassen, S., B. Gaudilliere, M. S. Angst, Y. Saeys, and N. Aghaeepour. (2020). CytoNorm: A Normalization Algorithm for Cytometry Data. *Cytom. Part A 97*(3), 268–278.
178. Wilkerson, M. D., and D. N. Hayes. (2010). ConsensusClusterPlus: a class discovery tool with confidence assessments and item tracking. *Bioinformatics 26*(12), 1572–1573.
179. Ritchie, M. E., B. Phipson, D. Wu, Y. Hu, C. W. Law, W. Shi, and G. K. Smyth. (2015). limma powers differential expression analyses for RNA-sequencing and microarray studies. *Nucleic Acids Res. 43*(7), e47.
180. Weber, L. M., M. Nowicka, C. Soneson, and M. D. Robinson. (2019). diffcyt: Differential discovery in high-dimensional cytometry via high-resolution clustering. *Commun. Biol. 2*(1), 183.
181. Parks, D. R., M. Roederer, and W. A. Moore. (2006). A new “Logicle” display method avoids deceptive effects of logarithmic scaling for low signals and compensated data. *Cytom. Part A 69A*(6), 541–551.
182. Herzenberg, L. A., J. Tung, W. A. Moore, L. A. Herzenberg, and D. R. Parks. (2006). Interpreting flow cytometry data: A guide for the perplexed. *Nat. Immunol. 7*(7), 681–685.
183. Moore, W. A., and D. R. Parks. (2012). Update for the logicle data scale including operational code implementations. *Cytom. Part A 81A*(4), 273–277.
184. Fletez-Brant, K., J. Špidlen, R. R. Brinkman, M. Roederer, and P. K. Chattopadhyay. (2016). flowClean: Automated identification and removal of fluorescence anomalies in

flow cytometry data. *Cytom. Part A 89*(5), 461–471.
185. Kohonen, T. (1990). The Self-Organizing Map. *Proc. IEEE 78*(9), 1464–1480.
186. Wehrens, R., and L. M. C. Buydens. (2007). Self- and Super-organizing Maps in R: The kohonen Package. *J. Stat. Softw. 21*(5), 1–19.
187. Diggins, K. E., A. R. Greenplate, N. Leelatian, C. E. Wogsland, and J. M. Irish. (2017). Characterizing cell subsets using marker enrichment modeling. *Nat. Methods 14*(3), 275–278.
188. Diggins, K. E., J. S. Gandelman, C. E. Roe, and J. M. Irish. (2018). Generating Quantitative Cell Identity Labels with Marker Enrichment Modeling (MEM). *Curr. Protoc. Cytom. 83*(1), 10.21.1-10.21.28.
189. Bagwell, C. B. (2005). Hyperlog—A flexible log-like transform for negative, zero, and positive valued data. *Cytom. Part A 64A*(1), 34–42.
190. Monaco, G., H. Chen, M. Poidinger, J. Chen, J. P. de Magalhães, and A. Larbi. (2016). flowAI: automatic and interactive anomaly discerning tools for flow cytometry data. *Bioinformatics 32*(16), 2473–2480.
191. Meskas, J., S. Wang, and R. Brinkman. (2020). flowCut — An R package for precise and accurate automated removal of outlier events and flagging of files based on time versus fluorescence analysis. *bioRxiv* , 2020.04.23.058545.
192. normalizeBatch: Normalize intensities across batches in MarioniLab/cydar: Using Mass Cytometry for Differential Abundance Analyses. [Website, accessed on June 13, 2021]. Available from: https://rdrr.io/github/MarioniLab/cydar/man/normalizeBatch.html
193. Wogsland, C. E., H. E. Lien, L. Pedersen, P. Hanjra, S. M. Grondal, R. A. Brekken, J. B. Lorens, and N. Halberg. (2021). High-dimensional immunotyping of tumors grown in obese and non-obese mice. *Dis. Model. Mech. 14*(4), dmm048977.
194. Weber, L. M., and M. D. Robinson. (2016). Comparison of clustering methods for high-dimensional single-cell flow and mass cytometry data. *Cytom. Part A 89*(12), 1084–1096.
195. Liu, X., W. Song, B. Y. Wong, T. Zhang, S. Yu, G. N. Lin, and X. Ding. (2019). A comparison framework and guideline of clustering methods for mass cytometry data. *Genome Biol. 20*(1), 297.
196. Levine, J. H., E. F. Simonds, S. C. Bendall, K. L. Davis, E. D. Amir, M. D. Tadmor, O. Litvin, H. G. Fienberg, A. Jager, E. R. Zunder, R. Finck, A. L. Gedman, I. Radtke, J. R. Downing, D. Pe'er, and G. P. Nolan. (2015). Data-Driven Phenotypic Dissection of AML Reveals Progenitor-like Cells that Correlate with Prognosis. *Cell 162*(1), 184–197.
197. Stassen, S. V., D. M. D. Siu, K. C. M. Lee, J. W. K. Ho, H. K. H. So, and K. K. Tsia. (2020). PARC: Ultrafast and accurate clustering of phenotypic data of millions of single cells. *Bioinformatics 36*(9), 2778–2786.
198. Bodenheimer, T., M. Halappanavar, S. Jefferys, R. Gibson, S. Liu, P. J. Mucha, N. Stanley, J. S. Parker, and S. R. Selitsky. (2020). FastPG: Fast clustering of millions of single cells. *bioRxiv* , 2020.06.19.159749.
199. Gao, X., D. Hu, M. Gogol, and H. Li. (2019). ClusterMap: Compare multiple single cell RNA-Seq datasets across different experimental conditions. *Bioinformatics 35*(17), 3038–3045.
200. Bruggner, R. V., B. Bodenmiller, D. L. Dill, R. J. Tibshirani, and G. P. Nolan. (2014). Automated identification of stratifying signatures in cellular subpopulations. *Proc. Natl. Acad. Sci. U. S. A. 111*(26), E2770–E2777.
201. Arvaniti, E., and M. Claassen. (2017). Sensitive detection of rare disease-associated cell subsets via representation learning. *Nat. Commun. 8*(1), 14825.
202. Seiler, C., A. M. Ferreira, L. M. Kronstad, L. J. Simpson, M. Le Gars, E. Vendrame, C. A. Blish, and S. Holmes. (2021). CytoGLMM: conditional differential analysis for flow and mass cytometry experiments. *BMC Bioinformatics 22*(1), 137.
203. Xu, W., and A. Larbi. (2017). Markers of T cell senescence in humans. *Int. J. Mol. Sci. 18*(8), 1742.
204. Xu, W., G. Monaco, E. H. Wong, W. L. W. Tan, H. Kared, Y. Simoni, S. W. Tan, W. Z. Y. How, C. T. Y. Tan, B. T. K. Lee, D. Carbajo, K. G. Srinivasan, I. C. H. Low, E. W. H.

Mok, S. Foo, J. Lum, H. L. Tey, W. P. Tan, M. Poidinger, E. Newell, T. P. Ng, R. Foo, A. N. Akbar, T. Fülöp, and A. Larbi. (2019). Mapping of γ/δ T cells reveals Vδ2+ T cells resistance to senescence. *EBioMedicine 39*, 44–58.

205. Ibegbu, C. C., Y.-X. Xu, W. Harris, D. Maggio, J. D. Miller, and A. P. Kourtis. (2005). Expression of Killer Cell Lectin-Like Receptor G1 on Antigen-Specific Human CD8+ T Lymphocytes during Active, Latent, and Resolved Infection and its Relation with CD57. *J. Immunol. 174*(10), 6088–6094.

206. Knox, J. J., G. L. Cosma, M. R. Betts, and L. M. McLane. (2014). Characterization of T-bet and Eomes in peripheral human immune cells. *Front. Immunol. 5*, 217.

207. Bade, B., H. E. Boettcher, J. Lohrmann, C. Hink-Schauer, K. Bratke, D. E. Jenne, J. C. Virchow Jr, and W. Luttmann. (2005). Differential expression of the granzymes A, K and M and perforin in human peripheral blood lymphocytes. *Int. Immunol. 17*(11), 1419–1428.

208. Valiante, N. M., and G. Trinchieri. (1993). Identification of a novel signal transduction surface molecule on human cytotoxic lymphocytes. *J. Exp. Med. 178*(4), 1397–1406.

209. Jiang, W., N. R. Chai, D. Maric, and B. Bielekova. (2011). Unexpected Role for Granzyme K in CD56bright NK Cell-Mediated Immunoregulation of Multiple Sclerosis. *J. Immunol. 187*(2), 781–790.

210. Leong, J. W., and T. A. Fehniger. (2011). Human NK cells: SET to kill. *Blood 117*(8), 2297–2298.

211. Romee, R., B. Foley, T. Lenvik, Y. Wang, B. Zhang, D. Ankarlo, X. Luo, S. Cooley, M. Verneris, B. Walcheck, and J. Miller. (2013). NK cell CD16 surface expression and function is regulated by a disintegrin and metalloprotease-17 (ADAM17). *Blood 121*(18), 3599–3608.

212. Simoni, Y., and E. W. Newell. (2018). Dissecting human ILC heterogeneity: more than just three subsets. *Immunology 153*(3), 297–303.

213. Tominaga, K., T. Yoshimoto, K. Torigoe, M. Kurimoto, K. Matsui, T. Hada, H. Okamura, and K. Nakanishi. (2000). IL-12 synergizes with IL-18 or IL-1β for IFN-γ production from human T cells. *Int. Immunol. 12*(2), 151–160.

214. Munk, R. B., K. Sugiyama, P. Ghosh, C. Y. Sasaki, L. Rezanka, K. Banerjee, H. Takahashi, R. Sen, and D. L. Longo. (2011). Antigen-independent IFN-γ production by human naïve CD4+ T cells activated by IL-12 plus IL-18. *PLoS One 6*(5), e18553.

215. Strauss, L., C. Bergmann, and T. L. Whiteside. (2009). Human Circulating CD4+CD25highFoxp3+ Regulatory T Cells Kill Autologous CD8+ but Not CD4+ Responder Cells by Fas-Mediated Apoptosis. *J. Immunol. 182*(3), 1469–1480.

216. Bin Dhuban, K., E. D'Hennezel, E. Nashi, A. Bar-Or, S. Rieder, E. M. Shevach, S. Nagata, and C. A. Piccirillo. (2015). Coexpression of TIGIT and FCRL3 Identifies Helios+ Human Memory Regulatory T Cells. *J. Immunol. 194*(8), 3687–3696.

217. Feng, X., L. Zhang, C. Acharya, G. An, K. Wen, L. Qiu, N. C. Munshi, Y. T. Tai, and K. C. Anderson. (2017). Targeting CD38 suppresses induction and function of T regulatory cells to mitigate immunosuppression in multiple myeloma. *Clin. Cancer Res. 23*(15), 4290–4300.

218. Gu, J., X. Ni, X. Pan, H. Lu, Y. Lu, J. Zhao, S. G. Zheng, K. L. Hippen, X. Wang, and L. Lu. (2017). Human CD39hi regulatory T cells present stronger stability and function under inflammatory conditions. *Cell. Mol. Immunol. 14*(6), 521–528.

219. Yang, B. H., S. Hagemann, P. Mamareli, U. Lauer, U. Hoffmann, M. Beckstette, L. Föhse, I. Prinz, J. Pezoldt, S. Suerbaum, T. Sparwasser, A. Hamann, S. Floess, J. Huehn, and M. Lochner. (2016). Foxp3+ T cells expressing RORγt represent a stable regulatory T-cell effector lineage with enhanced suppressive capacity during intestinal inflammation. *Mucosal Immunol. 9*(2), 444–457.

220. Ziegler, S. F. (2006). FOXP3: Of Mice and Men. *Annu. Rev. Immunol. 24*(1), 209–226.

221. Ribeiro-Dias, F., R. Saar Gomes, L. L. de Lima Silva, J. C. dos Santos, and L. A. B. Joosten. (2017). Interleukin 32: a novel player in the control of infectious diseases. *J. Leukoc. Biol. 101*(1), 39–52.

222. Cole, S., J. Murray, C. Simpson, R. Okoye, K. Tyson, M. Griffiths, D. Baeten, S. Shaw,

and A. Maroof. (2020). Interleukin (IL)-12 and IL-18 Synergize to Promote MAIT Cell IL-17A and IL-17F Production Independently of IL-23 Signaling. *Front. Immunol. 11*, 2992.

223. Hinks, T. S. C., E. Marchi, M. Jabeen, M. Olshansky, A. Kurioka, T. J. Pediongco, B. S. Meehan, L. Kostenko, S. J. Turner, A. J. Corbett, Z. Chen, P. Klenerman, and J. McCluskey. (2019). Activation and In Vivo Evolution of the MAIT Cell Transcriptome in Mice and Humans Reveals Tissue Repair Functionality. *Cell Rep. 28*(12), 3249-3262.e5.

224. Pont, F., J. Familiades, S. Déjean, S. Fruchon, D. Cendron, M. Poupot, R. Poupot, F. L'Faqihi-Olive, N. Prade, B. Ycart, and J.-J. Fournié. (2012). The gene expression profile of phosphoantigen-specific human γδ T lymphocytes is a blend of αβ T-cell and NK-cell signatures. *Eur. J. Immunol. 42*(1), 228–240.

225. Dahl, C. A., R. P. Schall, H. L. He, and J. S. Cairns. (1992). Identification of a novel gene expressed in activated natural killer cells and T cells. *J. Immunol. 148*(2), 597–603.

226. Kang, J.-W., Y. S. Park, D. H. Lee, M. S. Kim, Y. Bak, S. Y. Ham, S. H. Park, H. Kim, J. H. Ahn, J. T. Hong, and D.-Y. Yoon. (2014). Interaction network mapping among IL-32 isoforms. *Biochimie 101*(1), 248–251.

227. Choi, J.-D., S.-Y. Bae, J.-W. Hong, T. Azam, C. A. Dinarello, E. Her, W.-S. Choi, B.-K. Kim, C.-K. Lee, D.-Y. Yoon, S.-J. Kim, and S.-H. Kim. (2009). Identification of the most active interleukin-32 isoform. *Immunology 126*(4), 535–542.

228. Kang, J.-W., Y. S. Park, D. H. Lee, M. S. Kim, Y. Bak, S. H. Park, S. Y. Ham, Y. Yang, J. T. Hong, and D.-Y. Yoon. (2013). Interleukin-32δ interacts with IL-32β and inhibits IL-32β-mediated IL-10 production. *FEBS Lett. 587*(23), 3776–3781.

229. Joosten, L. A. B., M. G. Netea, S.-H. Kim, D.-Y. Yoon, B. Oppers-Walgreen, T. R. D. Radstake, P. Barrera, F. A. J. van de Loo, C. A. Dinarello, and W. B. van den Berg. (2006). IL-32, a proinflammatory cytokine in rheumatoid arthritis. *Proc. Natl. Acad. Sci. U. S. A. 103*(9), 3298–3303.

230. Hasegawa, H., H. J. Thomas, K. Schooley, and T. L. Born. (2011). Native IL-32 is released from intestinal epithelial cells via a non-classical secretory pathway as a membrane-associated protein. *Cytokine 53*(1), 74–83.

231. dos Santos, J. C., B. Heinhuis, R. S. Gomes, M. S. M. A. Damen, F. Real, R. A. Mortara, S. T. Keating, C. A. Dinarello, L. A. B. Joosten, and F. Ribeiro-Dias. (2017). Cytokines and microbicidal molecules regulated by IL-32 in THP-1-derived human macrophages infected with New World Leishmania species. *PLoS Negl. Trop. Dis. 11*(2), e0005413.

232. Goda, C., T. Kanaji, S. Kanaji, G. Tanaka, K. Arima, S. Ohno, and K. Izuhara. (2006). Involvement of IL-32 in activation-induced cell death in T cells. *Int. Immunol. 18*(2), 233–240.

233. Meyer, N., M. Zimmermann, S. Bürgler, C. Bassin, S. Woehrl, K. Moritz, C. Rhyner, P. Indermitte, P. Schmid-Grendelmeier, M. Akdis, G. Menz, and C. A. Akdis. (2010). IL-32 is expressed by human primary keratinocytes and modulates keratinocyte apoptosis in atopic dermatitis. *J. Allergy Clin. Immunol. 125*(4), 858-865.e10.

234. Ota, K., M. Kawaguchi, J. Fujita, F. Kokubu, S.-K. Huang, Y. Morishima, S. Matsukura, M. Kurokawa, Y. Ishii, H. Satoh, T. Sakamoto, and N. Hizawa. (2015). Synthetic double-stranded RNA induces interleukin-32 in bronchial epithelial cells. *Exp. Lung Res. 41*(6), 335–343.

235. Li, W., Y. Liu, M. M. Mukhtar, R. Gong, Y. Pan, S. T. Rasool, Y. Gao, L. Kang, Q. Hao, G. Peng, Y. Chen, X. Chen, J. Wu, and Y. Zhu. (2008). Activation of Interleukin-32 Pro-Inflammatory Pathway in Response to Influenza A Virus Infection. *PLoS One 3*(4), e1985.

236. Li, W., F. Yang, Y. Liu, R. Gong, L. Liu, Y. Feng, P. Hu, W. Sun, Q. Hao, L. Kang, J. Wu, and Y. Zhu. (2009). Negative feedback regulation of IL-32 production by iNOS activation in response to dsRNA or influenza virus infection. *Eur. J. Immunol. 39*(4), 1019–1024.

237. Nold-Petry, C. A., M. F. Nold, J. A. Zepp, S.-H. Kim, N. F. Voelkel, and C. A. Dinarello. (2009). IL-32–dependent effects of IL-1β on endothelial cell functions. *Proc. Natl. Acad. Sci. U. S. A. 106*(10), 3883–3888.

238. Heinhuis, B., M. I. Koenders, F. A. van de Loo, M. G. Netea, W. B. van den Berg, and L. A. B. Joosten. (2011). Inflammation-dependent secretion and splicing of IL-32γ in

rheumatoid arthritis. *Proc. Natl. Acad. Sci. U. S. A. 108*(12), 4962–4967.
239. Nishida, A., A. Andoh, M. Shioya, S. Kim-Mitsuyama, A. Takayanagi, and Y. Fujiyama. (2008). Phosphatidylinositol 3-kinase/Akt signaling mediates interleukin-32α induction in human pancreatic periacinar myofibroblasts. *Am. J. Physiol. Liver Physiol. 294*(3), G831–G838.
240. Jeong, H.-J., S.-Y. Shin, H.-A. Oh, M.-H. Kim, J.-S. Cho, and H.-M. Kim. (2011). IL-32 up-regulation is associated with inflammatory cytokine production in allergic rhinitis. *J. Pathol. 224*(4), 553–563.
241. Nam, S.-Y., H.-A. Oh, Y. Choi, K.-Y. Park, H.-M. Kim, and H.-J. Jeong. (2014). Inhibition of IL-32 Signaling by Bamboo Salt Decreases Pro-Inflammatory Responses in Cellular Models of Allergic Rhinitis. *J. Med. Food 17*(9), 939–948.
242. Moschen, A. R., T. Fritz, A. D. Clouston, I. Rebhan, O. Bauhofer, H. D. Barrie, E. E. Powell, S.-H. Kim, C. A. Dinarello, R. Bartenschlager, J. R. Jonsson, and H. Tilg. (2011). Interleukin-32: A new proinflammatory cytokine involved in hepatitis C virus-related liver inflammation and fibrosis. *Hepatology 53*(6), 1819–1829.
243. Schenk, M., S. R. Krutzik, P. A. Sieling, D. J. Lee, R. M. B. Teles, M. T. Ochoa, E. Komisopoulou, E. N. Sarno, T. H. Rea, T. G. Graeber, S. Kim, G. Cheng, and R. L. Modlin. (2012). NOD2 triggers an interleukin-32–dependent human dendritic cell program in leprosy. *Nat. Med. 18*(4), 555–563.
244. Kang, J.-W., S.-C. Choi, M.-C. Cho, H.-J. Kim, J.-H. Kim, J.-S. Lim, S.-H. Kim, J.-Y. Han, and D.-Y. Yoon. (2009). A proinflammatory cytokine interleukin-32β promotes the production of an anti-inflammatory cytokine interleukin-10. *Immunology 128*(1pt2), e532–e540.
245. Nakayama, M., Y. Niki, T. Kawasaki, Y. Takeda, H. Ikegami, Y. Toyama, and T. Miyamoto. (2013). IL-32-PAR2 axis is an innate immunity sensor providing alternative signaling for LPS-TRIF axis. *Sci. Rep. 3*(1), 2960.
246. Netea, M. G., T. Azam, E. C. Lewis, L. A. B. Joosten, M. Wang, D. Langenberg, X. Meng, E. D. Chan, D.-Y. Yoon, T. Ottenhoff, S.-H. Kim, and C. A. Dinarello. (2006). Mycobacterium tuberculosis Induces Interleukin-32 Production through a Caspase- 1/IL-18/Interferon-γ-Dependent Mechanism. *PLoS Med. 3*(8), e277.
247. Novick, D., M. Rubinstein, T. Azam, A. Rabinkov, C. A. Dinarello, and S.-H. Kim. (2006). Proteinase 3 is an IL-32 binding protein. *Proc. Natl. Acad. Sci. U. S. A. 103*(9), 3316–3321.
248. Kim, S.-J., S.-Y. Lee, E. Her, S.-Y. Bae, J.-D. Choi, J.-W. Hong, J. JaeKal, D.-Y. Yoon, T. Azam, C. A. Dinarello, and S.-H. Kim. (2008). Proteinase 3-processed form of the recombinant IL-32 separate domain. *BMB Rep. 41*(11), 814–819.
249. Heinhuis, B., M. I. Koenders, W. B. van den Berg, M. G. Netea, C. A. Dinarello, and L. A. B. Joosten. (2012). Interleukin 32 (IL-32) Contains a Typical α-Helix Bundle Structure That Resembles Focal Adhesion Targeting Region of Focal Adhesion Kinase-1. *J. Biol. Chem. 287*(8), 5733–5743.
250. Turner-Brannen, E., K.-Y. G. Choi, R. Arsenault, H. El-Gabalawy, S. Napper, and N. Mookherjee. (2011). Inflammatory Cytokines IL-32 and IL-17 Have Common Signaling Intermediates despite Differential Dependence on TNF-Receptor 1. *J. Immunol. 186*(12), 7127–7135.
251. Mabilleau, G., and A. Sabokbar. (2009). Interleukin-32 Promotes Osteoclast Differentiation but Not Osteoclast Activation. *PLoS One 4*(1), e4173.
252. Kang, J.-W., Y. S. Park, M. S. Kim, D. H. Lee, Y. Bak, S. Y. Ham, Y.-S. Song, J. T. Hong, and D.-Y. Yoon. (2014). IL-32α down-regulates β2 integrin (CD18) expression by suppressing PU.1 expression in myeloid cells. *Cell. Signal. 26*(7), 1514–1522.
253. Kang, J.-W., Y. S. Park, M. S. Kim, D. H. Lee, Y. Bak, S. Y. Ham, S. H. Park, J. T. Hong, and D.-Y. Yoon. (2013). Interleukin (IL)-32β-mediated CCAAT/Enhancer-binding Protein α (C/EBPα) Phosphorylation by Protein Kinase Cδ (PKCδ) Abrogates the Inhibitory Effect of C/EBPα on IL-10 Production. *J. Biol. Chem. 288*(33), 23650–23658.
254. Jung, M. Y., M. H. Son, S. H. Kim, D. Cho, and T. S. Kim. (2011). IL-32γ Induces the Maturation of Dendritic Cells with Th1- and Th17-Polarizing Ability through Enhanced IL-

12 and IL-6 Production. *J. Immunol. 186*(12), 6848–6859.
255. Netea, M. G., T. Azam, G. Ferwerda, S. E. Girardin, M. Walsh, J.-S. Park, E. Abraham, J.-M. Kim, D.-Y. Yoon, C. A. Dinarello, and S.-H. Kim. (2005). IL-32 synergizes with nucleotide oligomerization domain (NOD) 1 and NOD2 ligands for IL-1β and IL-6 production through a caspase 1-dependent mechanism. *Proc. Natl. Acad. Sci. U. S. A. 102*(45), 16309–16314.
256. Wong, C.-K., J. Dong, and C. W.-K. Lam. (2014). Molecular mechanisms regulating the synergism between IL-32γ and NOD for the activation of eosinophils. *J. Leukoc. Biol. 95*(4), 631–642.
257. Sloot, Y. J. E., J. W. Smit, L. A. B. Joosten, and R. T. Netea-Maier. (2018). Insights into the role of IL-32 in cancer. *Semin. Immunol. 38*, 24–32.
258. Hong, J. T., D. J. Son, C. K. Lee, D.-Y. Yoon, D. H. Lee, and M. H. Park. (2017). Interleukin 32, inflammation and cancer. *Pharmacol. Ther. 174*, 127–137.
259. Netea, M. G., E. C. Lewis, T. Azam, L. A. B. Joosten, J. Jaekal, S.-Y. Bae, C. A. Dinarello, and S.-H. Kim. (2008). Interleukin-32 induces the differentiation of monocytes into macrophage-like cells. *Proc. Natl. Acad. Sci. U. S. A. 105*(9), 3515–3520.
260. Kim, M. S., J.-W. Kang, Y. S. Park, D. H. Lee, Y. Bak, T. Kwon, and D.-Y. Yoon. (2015). IL-32θ inhibits monocytic differentiation of leukemia cells by attenuating expression of transcription factor PU.1. *Oncotarget 6*(6), 4394–4405.
261. Nold, M. F., C. A. Nold-Petry, G. B. Pott, J. A. Zepp, M. T. Saavedra, S.-H. Kim, and C. A. Dinarello. (2008). Endogenous IL-32 controls cytokine and HIV-1 production. *J. Immunol. 181*(1), 557–565.
262. Osman, A., F. Bhuyan, M. Hashimoto, H. Nasser, T. Maekawa, and S. Suzu. (2014). M-CSF Inhibits Anti–HIV-1 Activity of IL-32, but They Enhance M2-like Phenotypes of Macrophages. *J. Immunol. 192*(11), 5083–5089.
263. Montoya, D., M. S. Inkeles, P. T. Liu, S. Realegeno, R. M. B. Teles, P. Vaidya, M. A. Munoz, M. Schenk, W. R. Swindell, R. Chun, K. Zavala, M. Hewison, J. S. Adams, S. Horvath, M. Pellegrini, B. R. Bloom, and R. L. Modlin. (2014). IL-32 is a molecular marker of a host defense network in human tuberculosis. *Sci. Transl. Med. 6*(250), 250ra114.
264. Bai, X., W. H. Kinney, W.-L. Su, A. Bai, A. R. Ovrutsky, J. R. Honda, M. G. Netea, M. Henao-Tamayo, D. J. Ordway, C. A. Dinarello, and E. D. Chan. (2015). Caspase-3-independent apoptotic pathways contribute to interleukin-32γ-mediated control of Mycobacterium tuberculosis infection in THP-1 cells. *BMC Microbiol. 15*(1), 39.
265. Cheon, S., J. H. Lee, S. Park, S. I. Bang, W. J. Lee, D.-Y. Yoon, S.-S. Yoon, T. Kim, H. Min, B. J. Cho, H. J. Lee, K. W. Lee, S. H. Jeong, H. Park, and D. Cho. (2011). Overexpression of IL-32α Increases Natural Killer Cell-mediated Killing through Up-regulation of Fas and UL16-binding protein 2 (ULBP2) Expression in Human Chronic Myeloid Leukemia Cells. *J. Biol. Chem. 286*(14), 12049–12055.
266. Park, M. H., M. J. Song, M.-C. Cho, D. C. Moon, D. Y. Yoon, S. B. Han, and J. T. Hong. (2012). Interleukin-32 enhances cytotoxic effect of natural killer cells to cancer cells via activation of death receptor 3. *Immunology 135*(1), 63–72.
267. Smith, A. J., C. M. Toledo, S. W. Wietgrefe, L. Duan, T. W. Schacker, C. S. Reilly, and A. T. Haase. (2011). The immunosuppressive role of IL-32 in lymphatic tissue during HIV-1 infection. *J. Immunol. 186*(11), 6576–6584.
268. Heinhuis, B., T. S. Plantinga, G. Semango, B. Küsters, M. G. Netea, C. A. Dinarello, J. W. A. Smit, R. T. Netea-Maier, and L. A. B. Joosten. (2016). Alternatively spliced isoforms of IL-32 differentially influence cell death pathways in cancer cell lines. *Carcinogenesis 37*(2), 197–205.
269. Marcondes, A. M., A. J. Mhyre, D. L. Stirewalt, S.-H. Kim, C. A. Dinarello, and H. J. Deeg. (2008). Dysregulation of IL-32 in myelodysplastic syndrome and chronic myelomonocytic leukemia modulates apoptosis and impairs NK function. *Proc. Natl. Acad. Sci. U. S. A. 105*(8), 2865–2870.
270. Wang, S., F. Chen, and L. Tang. (2015). IL-32 promotes breast cancer cell growth and invasiveness. *Oncol. Lett. 9*(1), 305–307.
271. Plantinga, T. S., I. Costantini, B. Heinhuis, A. Huijbers, G. Semango, B. Kusters, M. G.

Netea, A. R. M. M. Hermus, J. W. A. Smit, C. A. Dinarello, L. A. B. Joosten, and R. T. Netea-Maier. (2013). A promoter polymorphism in human interleukin-32 modulates its expression and influences the risk and the outcome of epithelial cell–derived thyroid carcinoma. *Carcinogenesis 34*(7), 1529–1535.

272. Zhai, J., Y. An, W. Wang, Y. Fan, and G. Yao. (2019). IL-32 expression indicates unfavorable prognosis in patients with colon cancer. *Oncol. Lett. 17*(5), 4655–4660.

273. Suga, H., M. Sugaya, T. Miyagaki, M. Kawaguchi, H. Fujita, Y. Asano, Y. Tada, T. Kadono, and S. Sato. (2014). The Role of IL-32 in Cutaneous T-Cell Lymphoma. *J. Invest. Dermatol. 134*(5), 1428–1435.

274. Yousif, N. G., F. G. Al-amran, N. Hadi, J. Lee, and J. Adrienne. (2013). Expression of IL-32 modulates NF-κB and p38 MAP kinase pathways in human esophageal cancer. *Cytokine 61*(1), 223–227.

275. Cui, Y., Z. Sun, X. Li, C. Leng, L. Zhang, X. Fu, L. Li, X. Zhang, Y. Chang, F. Nan, Z. Li, J. Yan, M. Zhang, W. Li, G. Wang, D. Zhang, and Y. Ma. (2016). Expression and clinical significance of cyclooxygenase-2 and interleukin-32 in primary gastric B-cell lymphoma. *Oncol. Lett. 11*(1), 693–698.

276. Kang, Y. H., M.-Y. Park, D.-Y. Yoon, S. R. Han, C. Il Lee, N. Y. Ji, P.-K. Myung, H. G. Lee, J. W. Kim, Y. Il Yeom, Y. J. Jang, D. K. Ahn, J. W. Kim, and E. Y. Song. (2012). Dysregulation of overexpressed IL-32α in hepatocellular carcinoma suppresses cell growth and induces apoptosis through inactivation of NF-κB and Bcl-2. *Cancer Lett. 318*(2), 226–233.

277. Nishida, A., A. Andoh, O. Inatomi, and Y. Fujiyama. (2009). Interleukin-32 Expression in the Pancreas. *J. Biol. Chem. 284*(26), 17868–17876.

278. Lee, S., J.-H. Kim, H. Kim, J. W. Kang, S.-H. Kim, Y. Yang, J. Kim, J. Park, S. Park, J. Hong, and D.-Y. Yoon. (2011). Activation of the interleukin-32 pro-inflammatory pathway in response to human papillomavirus infection and over-expressionof interleukin-32 controls the expression of the humanpapillomavirus oncogene. *Immunology 132*(3), 410–420.

279. Ishigami, S., T. Arigami, Y. Uchikado, T. Setoyama, Y. Kita, K. Sasaki, H. Okumura, H. Kurahara, Y. Kijima, A. Harada, S. Ueno, and S. Natsugoe. (2013). IL-32 expression is an independent prognostic marker for gastric cancer. *Med. Oncol. 30*(2), 472.

280. Sorrentino, C., and E. Di Carlo. (2009). Expression of IL-32 in Human Lung Cancer Is Related to the Histotype and Metastatic Phenotype. *Am. J. Respir. Crit. Care Med. 180*(8), 769–779.

281. Park, J. S., S. Y. Choi, J.-H. Lee, M. Lee, E. S. Nam, A. L. Jeong, S. Lee, S. Han, M.-S. Lee, J.-S. Lim, D. Y. Yoon, Y. Kwon, and Y. Yang. (2013). Interleukin-32β stimulates migration of MDA-MB-231 and MCF-7cells via the VEGF-STAT3 signaling pathway. *Cell. Oncol. 36*(6), 493–503.

282. Yang, Y., Z. Wang, Y. Zhou, X. Wang, J. Xiang, and Z. Chen. (2015). Dysregulation of over-expressed IL-32 in colorectal cancer induces metastasis. *World J. Surg. Oncol. 13*(1), 146.

283. Guenin, S., M. Mouallif, P. Hubert, N. Jacobs, N. Krusy, A. Duray, M. M. Ennaji, S. Saussez, and P. Delvenne. (2014). Interleukin-32 expression is associated with a poorer prognosis in head and neck squamous cell carcinoma. *Mol. Carcinog. 53*(8), 667–673.

284. Zeng, Q., S. Li, Y. Zhou, W. Ou, X. Cai, L. Zhang, W. Huang, L. Huang, and Q. Wang. (2014). Interleukin-32 contributes to invasion and metastasis of primary lung adenocarcinoma via NF-kappaB induced matrix metalloproteinases 2 and 9 expression. *Cytokine 65*(1), 24–32.

285. Lee, H.-J., Z. L. Liang, S. M. Huang, J.-S. Lim, D.-Y. Yoon, H.-J. Lee, and J. M. Kim. (2012). Overexpression of IL-32 is a novel prognostic factor in patients with localized clear cell renal cell carcinoma. *Oncol. Lett. 3*(2), 490–496.

286. Gruber, T., M. Kremenovic, H. Sadozai, N. Rombini, L. Baeriswyl, F. Maibach, R. L. Modlin, M. Gilliet, D. von Werdt, R. E. Hunger, S. M. Seyed Jafari, G. Parisi, G. Abril-Rodriguez, A. Ribas, and M. Schenk. (2020). IL-32γ potentiates tumor immunity in melanoma. *JCI Insight 5*(18), e138772.

287. Yu, X., B. Zhou, Z. Zhang, Q. Gao, Y. Wang, Y. Song, Y. Pu, Y. Chen, R. Duan, L. Zhang, and M. Xi. (2015). Significant association between IL-32 gene polymorphisms and susceptibility to endometrial cancer in Chinese Han women. *Tumor Biol. 36*(7), 5265–5272.
288. Jafrin, S., M. A. Aziz, and M. S. Islam. (2021). Impact of interleukin-32 germ-line rs28372698 and intronic rs12934561 polymorphisms on cancer development: A systematic review and meta-analysis. *Int. Immunopharmacol. 99*, 107964.
289. Luo, X., P. Bai, Q. Li, Y. Zhang, Y. Song, M. Su, X. Huang, B. Zhou, L. Zhang, and Y. Gong. (2020). Association between interleukin-32 polymorphisms and ovarian cancer in the Chinese Han population. *Int. J. Clin. Exp. Pathol. 13*(7), 1733.
290. Yong, H. J., J. S. Park, A. L. Jeong, S. Han, S. Lee, H. I. Ka, B. Sumiyasuren, H. J. Joo, S. J. So, J. Y. Park, D.-Y. Yoon, J.-S. Lim, M.-S. Lee, H. G. Lee, and Y. Yang. (2017). Von Hippel-Lindau regulates interleukin-32β stability in ovarian cancer cells. *Oncotarget 8*(41), 69833–69846.
291. Tsai, C.-Y., C.-S. Wang, M.-M. Tsai, H.-C. Chi, W.-L. Cheng, Y.-H. Tseng, C.-Y. Chen, C. D. Lin, J.-I. Wu, L.-H. Wang, and K.-H. Lin. (2014). Interleukin-32 Increases Human Gastric Cancer Cell Invasion Associated with Tumor Progression and Metastasis. *Clin. Cancer Res. 20*(9), 2276–2288.
292. Zhao, W.-B., Q.-L. Wang, Y.-T. Xu, S.-F. Xu, Y. Qiu, and F. Zhu. (2018). Overexpression of interleukin-32α promotes invasion by modulating VEGF in hepatocellular carcinoma. *Oncol. Rep. 39*(3), 1155–1162.
293. Bhat, S., N. Gardi, S. Hake, N. Kotian, S. Sawant, S. Kannan, V. Parmar, S. Desai, A. Dutt, and N. N. Joshi. (2017). Impact of intra-tumoral IL17A and IL32 gene expression on T-cell responses and lymph node status in breast cancer patients. *J. Cancer Res. Clin. Oncol. 143*(9), 1745–1756.
294. Ohmatsu, H., D. Humme, J. Gonzalez, N. Gulati, M. Möbs, W. Sterry, and J. G. Krueger. (2017). IL-32 induces indoleamine 2,3-dioxygenase+CD1c+ dendritic cells and indoleamine 2,3-dioxygenase+CD163+ macrophages: Relevance to mycosis fungoides progression. *Oncoimmunology 6*(2), e1181237.
295. Nabeki, B., S. Ishigami, Y. Uchikado, K. Sasaki, Y. Kita, H. Okumura, T. Arigami, Y. Kijima, H. Kurahara, K. Maemura, and S. Natsugoe. (2015). Interleukin-32 expression and Treg infiltration in esophageal squamous cell carcinoma. *Anticancer Res. 35*(5), 2941–2947.
296. Han, L., S. Chen, Z. Chen, B. Zhou, Y. Zheng, and L. Shen. (2021). Interleukin 32 Promotes Foxp3+ Treg Cell Development and CD8+ T Cell Function in Human Esophageal Squamous Cell Carcinoma Microenvironment. *Front. Cell Dev. Biol. 9*, 1962.
297. Raskov, H., A. Orhan, J. P. Christensen, and I. Gögenur. (2021). Cytotoxic CD8+ T cells in cancer and cancer immunotherapy. *Br. J. Cancer 124*(2), 359–367.
298. Tay, R. E., E. K. Richardson, and H. C. Toh. (2021). Revisiting the role of CD4+ T cells in cancer immunotherapy—new insights into old paradigms. *Cancer Gene Ther. 28*(1), 5–17.
299. Colaprico, A., T. C. Silva, C. Olsen, L. Garofano, C. Cava, D. Garolini, T. S. Sabedot, T. M. Malta, S. M. Pagnotta, I. Castiglioni, M. Ceccarelli, G. Bontempi, and H. Noushmehr. (2016). TCGAbiolinks: an R/Bioconductor package for integrative analysis of TCGA data. *Nucleic Acids Res. 44*(8), e71.
300. Silva, T. C., A. Colaprico, C. Olsen, F. D'Angelo, G. Bontempi, M. Ceccarelli, and H. Noushmehr. (2016). TCGA Workflow: Analyze cancer genomics and epigenomics data using Bioconductor packages [version 2; peer review: 1 approved, 2 approved with reservations]. *F1000Res. 5*, 1542.
301. Mounir, M., M. Lucchetta, T. C. Silva, C. Olsen, G. Bontempi, X. Chen, H. Noushmehr, A. Colaprico, and E. Papaleo. (2019). New functionalities in the TCGAbiolinks package for the study and integration of cancer data from GDC and GTEx. *PLoS Comput. Biol. 15*(3), e1006701.
302. Collado-Torres, L., A. Nellore, K. Kammers, S. E. Ellis, M. A. Taub, K. D. Hansen, A. E.

Jaffe, B. Langmead, and J. T. Leek. (2017). Reproducible RNA-seq analysis using recount2. *Nat. Biotechnol. 35*(4), 319–321.

303. Hoadley, K. A., C. Yau, T. Hinoue, D. M. Wolf, A. J. Lazar, E. Drill, R. Shen, A. M. Taylor, A. D. Cherniack, V. Thorsson, R. Akbani, R. Bowlby, C. K. Wong, M. Wiznerowicz, F. Sanchez-Vega, A. G. Robertson, B. G. Schneider, M. S. Lawrence, H. Noushmehr, T. M. Malta, The Cancer Genome Atlas Network, J. M. Stuart, C. C. Benz, and P. W. Laird. (2018). Cell-of-Origin Patterns Dominate the Molecular Classification of 10,000 Tumors from 33 Types of Cancer. *Cell 173*(2), 291-304.e6.

304. Liu, J., T. Lichtenberg, K. A. Hoadley, L. M. Poisson, A. J. Lazar, A. D. Cherniack, A. J. Kovatich, C. C. Benz, D. A. Levine, A. V. Lee, L. Omberg, D. M. Wolf, C. D. Shriver, V. Thorsson, and The Cancer Genome Atlas Network. (2018). An Integrated TCGA Pan-Cancer Clinical Data Resource to Drive High-Quality Survival Outcome Analytics. *Cell 173*(2), 400-416.e11.

305. Hao, Y., S. Hao, E. Andersen-Nissen, W. M. Mauck III, S. Zheng, A. Butler, M. J. Lee, A. J. Wilk, C. Darby, M. Zager, P. Hoffman, M. Stoeckius, E. Papalexi, E. P. Mimitou, J. Jain, A. Srivastava, T. Stuart, L. M. Fleming, B. Yeung, A. J. Rogers, J. M. McElrath, C. A. Blish, R. Gottardo, P. Smibert, and R. Satija. (2021). Integrated analysis of multimodal single-cell data. *Cell 184*(13), 3573-3587.e29.

306. Elizaga, M. L., S. S. Li, N. K. Kochar, G. J. Wilson, M. A. Allen, H. V. N. Tieu, I. Frank, M. E. Sobieszczyk, K. W. Cohen, B. Sanchez, T. E. Latham, D. K. Clarke, M. A. Egan, J. H. Eldridge, D. Hannaman, R. Xu, A. Ota-Setlik, M. J. McElrath, C. M. Hay, and NIAID HIV Vaccine Trials Network (HVTN) 087 Study Team. (2018). Safety and tolerability of HIV-1 multiantigen pDNA vaccine given with IL-12 plasmid DNA via electroporation, boosted with a recombinant vesicular stomatitis virus HIV Gag vaccine in healthy volunteers in a randomized, controlled clinical trial. *PLoS One 13*(9), e0202753.

307. Li, S. S., N. K. Kochar, M. Elizaga, C. M. Hay, G. J. Wilson, K. W. Cohen, S. C. De Rosa, R. Xu, A. Ota-Setlik, D. Morris, G. Finak, M. Allen, H.-V. Tieu, I. Frank, M. E. Sobieszczyk, D. Hannaman, R. Gottardo, P. B. Gilbert, G. D. Tomaras, L. Corey, D. K. Clarke, M. A. Egan, J. H. Eldridge, M. J. McElrath, N. Frahm, and NIAID HIV Vaccine Trials Network. (2017). DNA Priming Increases Frequency of T-Cell Responses to a Vesicular Stomatitis Virus HIV Vaccine with Specific Enhancement of CD8+ T-Cell Responses by Interleukin-12 Plasmid DNA. *Clin. Vaccine Immunol. 24*(11), e00263-17.

308. Azizi, E., A. Carr, G. Plitas, A. Cornish, C. Konopacki, S. Prabhakaran, J. Nainys, K. Wu, V. Kiseliovas, M. Setty, K. Choi, R. Fromme, P. Dao, P. McKenney, R. Wasti, K. Kadaveru, L. Mazutis, A. Rudensky, and D. Pe'er. (2018). Single-Cell Map of Diverse Immune Phenotypes in the Breast Tumor Microenvironment. *Cell 174*(5), 1293-1308.e36.

309. Hagel, J. P., L. C. Garner, M. Bilton, H. Mehta, T. Leng, C.-P. Hackstein, P. Phalora, A. Amini, H. D. Akther, N. M. Provine, M. Edmans, C. B. Willberg, and P. Klenerman. (2020). Human MAIT Cell Activation In Vitro. In *MAIT Cells. Methods in Molecular Biology*, vol. 2098. (H. Kaipe, I. Magalhaes, and J. M. Walker, eds). Humana, New York. 97–124.

310. Yan, H., D. He, X. Huang, E. Zhang, Q. Chen, R. Xu, X. Liu, F. Zi, and Z. Cai. (2018). Role of interleukin-32 in cancer biology. *Oncol. Lett. 16*(1), 41–47.

311. Kraha, A., H. Turner, K. Nimon, L. Zientek, and R. Henson. (2012). Tools to support interpreting multiple regression in the face of multicollinearity. *Front. Psychol. 3*, 44.

312. Hafemeister, C., and R. Satija. (2019). Normalization and variance stabilization of single-cell RNA-seq data using regularized negative binomial regression. *Genome Biol. 20*(1), 296.

313. Korsunsky, I., A. Nathan, N. Millard, and S. Raychaudhuri. (2019). Presto scales Wilcoxon and auROC analyses to millions of observations. *bioRxiv* , 653253.

314. Sareneva, T., I. Julkunen, and S. Matikainen. (2000). IFN-α and IL-12 Induce IL-18 Receptor Gene Expression in Human NK and T Cells. *J. Immunol. 165*(4), 1933–1938.

315. Liu, K., M. Catalfamo, Y. Li, P. A. Henkart, and N. Weng. (2002). IL-15 mimics T cell receptor crosslinking in the induction of cellular proliferation, gene expression, and

cytotoxicity in CD8+ memory T cells. *Proc. Natl. Acad. Sci. U. S. A. 99*(9), 6192–6197.
316. Tomkowicz, B., E. Walsh, A. Cotty, R. Verona, N. Sabins, F. Kaplan, S. Santulli-Marotto, C.-N. Chin, J. Mooney, R. B. Lingham, M. Naso, and T. McCabe. (2015). TIM-3 Suppresses Anti-CD3/CD28-Induced TCR Activation and IL-2 Expression through the NFAT Signaling Pathway. *PLoS One 10*(10), e0140694.
317. Lichtenegger, F. S., M. Rothe, F. M. Schnorfeil, K. Deiser, C. Krupka, C. Augsberger, M. Schlüter, J. Neitz, and M. Subklewe. (2018). Targeting LAG-3 and PD-1 to Enhance T Cell Activation by Antigen-Presenting Cells. *Front. Immunol. 9*, 385.
318. Ghandi, M., F. W. Huang, J. Jané-Valbuena, G. V. Kryukov, C. C. Lo, E. R. McDonald III, J. Barretina, E. T. Gelfand, C. M. Bielski, H. Li, K. Hu, A. Y. Andreev-Drakhlin, J. Kim, J. M. Hess, B. J. Haas, F. Aguet, B. A. Weir, M. V. Rothberg, B. R. Paolella, M. S. Lawrence, R. Akbani, Y. Lu, H. L. Tiv, P. C. Gokhale, A. de Weck, A. A. Mansour, C. Oh, J. Shih, K. Hadi, Y. Rosen, J. Bistline, K. Venkatesan, A. Reddy, D. Sonkin, M. Liu, J. Lehar, J. M. Korn, D. A. Porter, M. D. Jones, J. Golji, G. Caponigro, J. E. Taylor, C. M. Dunning, A. L. Creech, A. C. Warren, J. M. McFarland, M. Zamanighomi, A. Kauffmann, N. Stransky, M. Imielinski, Y. E. Maruvka, A. D. Cherniack, A. Tsherniak, F. Vazquez, J. D. Jaffe, A. A. Lane, D. M. Weinstock, C. M. Johannessen, M. P. Morrissey, F. Stegmeier, R. Schlegel, W. C. Hahn, G. Getz, G. B. Mills, J. S. Boehm, T. R. Golub, L. A. Garraway, and W. R. Sellers. (2019). Next-generation characterization of the Cancer Cell Line Encyclopedia. *Nature 569*(7757), 503–508.
319. Li, Y., J. Xie, X. Xu, L. Liu, Y. Wan, Y. Liu, C. Zhu, and Y. Zhu. (2013). Inducible Interleukin 32 (IL-32) Exerts Extensive Antiviral Function via Selective Stimulation of Interferon λ1 (IFN-λ1). *J. Biol. Chem. 288*(29), 20927–20941.
320. Kim, S. (2014). Interleukin-32 in Inflammatory Autoimmune Diseases. *Immune Netw. 14*(3), 123–127.
321. Shioya, M., A. Nishida, Y. Yagi, A. Ogawa, T. Tsujikawa, S. Kim-Mitsuyama, A. Takayanagi, N. Shimizu, Y. Fujiyama, and A. Andoh. (2007). Epithelial overexpression of interleukin-32α in inflammatory bowel disease. *Clin. Exp. Immunol. 149*(3), 480–486.
322. Nicholl, M. B., X. Chen, C. Qin, Q. Bai, Z. Zhu, M. R. Davis, and Y. Fang. (2016). IL-32α has differential effects on proliferation and apoptosis of human melanoma cell lines. *J. Surg. Oncol. 113*(4), 364–369.
323. Park, E.-S., J.-M. Yoo, H.-S. Yoo, D.-Y. Yoon, Y.-P. Yun, and J. Hong. (2014). IL-32γ enhances TNF-α-induced cell death in colon cancer. *Mol. Carcinog. 53*(S1), E23–E35.
324. Oh, J. H., M.-C. Cho, J.-H. Kim, S. Y. Lee, H. J. Kim, E. S. Park, J. O. Ban, J.-W. Kang, D.-H. Lee, J.-H. Shim, S. B. Han, D. C. Moon, Y. H. Park, D.-Y. Yu, J.-M. Kim, S. H. Kim, D.-Y. Yoon, and J. T. Hong. (2011). IL-32γ inhibits cancer cell growth through inactivation of NF-κB and STAT3 signals. *Oncogene 30*(30), 3345–3359.
325. Braud, V. M., J. Biton, E. Becht, S. Knockaert, A. Mansuet-Lupo, E. Cosson, D. Damotte, M. Alifano, P. Validire, F. Anjuère, I. Cremer, N. Girard, D. Gossot, A. Seguin-Givelet, M.-C. Dieu-Nosjean, and C. Germain. (2018). Expression of LLT1 and its receptor CD161 in lung cancer is associated with better clinical outcome. *Oncoimmunology 7*(5), e1423184.
326. Corbett, A. J., W. Awad, H. Wang, and Z. Chen. (2020). Antigen Recognition by MR1-Reactive T Cells; MAIT Cells, Metabolites, and Remaining Mysteries. *Front. Immunol. 11*, 1961.
327. Helmink, B. A., M. A. W. Khan, A. Hermann, V. Gopalakrishnan, and J. A. Wargo. (2019). The microbiome, cancer, and cancer therapy. *Nat. Med. 25*(3), 377–388.
328. Li, S., Y. Simoni, E. Becht, C. Y. Loh, N. Li, D. Lachance, S.-L. Koo, T. P. Lim, E. K. W. Tan, R. Mathew, A. Nguyen, J. Golovato, J. D. Berkson, M. Prlic, B. Lee, S. S. Minot, N. Nagarajan, N. Dey, D. S. W. Tan, I. B. Tan, and E. W. Newell. (2020). Human Tumor-Infiltrating MAIT Cells Display Hallmarks of Bacterial Antigen Recognition in Colorectal Cancer. *Cell Reports Med. 1*(3), 100039.
329. Haeryfar, S. M. M., C. R. Shaler, and P. T. Rudak. (2018). Mucosa-associated invariant T cells in malignancies: a faithful friend or formidable foe? *Cancer Immunol. Immunother. 67*(12), 1885–1896.

330. Zhao, J., X. Chen, T. Herjan, and X. Li. (2020). The role of interleukin-17 in tumor development and progression. *J. Exp. Med. 217*(1), e20190297.
331. Kuen, D.-S., B.-S. Kim, and Y. Chung. (2020). IL-17-Producing Cells in Tumor Immunity: Friends or Foes? *Immune Netw. 20*(1), e6.
332. Ling, L., Y. Lin, W. Zheng, S. Hong, X. Tang, P. Zhao, M. Li, J. Ni, C. Li, L. Wang, and Y. Jiang. (2016). Circulating and tumor-infiltrating mucosal associated invariant T (MAIT) cells in colorectal cancer patients. *Sci. Rep. 6*(1), 20358.
333. Won, E. J., J. K. Ju, Y.-N. Cho, H.-M. Jin, K.-J. Park, T.-J. Kim, Y.-S. Kwon, H. J. Kee, J.-C. Kim, S.-J. Kee, and Y.-W. Park. (2016). Clinical relevance of circulating mucosal-associated invariant T cell levels and their anti-cancer activity in patients with mucosal-associated cancer. *Oncotarget 7*(46), 76274–76290.
334. Peterfalvi, A., E. Gomori, T. Magyarlaki, J. Pal, M. Banati, A. Javorhazy, J. Szekeres-Bartho, L. Szereday, and Z. Illes. (2008). Invariant Vα7.2-Jα33 TCR is expressed in human kidney and brain tumors indicating infiltration by mucosal-associated invariant T (MAIT) cells. *Int. Immunol. 20*(12), 1517–1525.
335. Sundström, P., F. Ahlmanner, P. Akéus, M. Sundquist, S. Alsén, U. Yrlid, L. Börjesson, Å. Sjöling, B. Gustavsson, S. B. J. Wong, and M. Quiding-Järbrink. (2015). Human Mucosa-Associated Invariant T Cells Accumulate in Colon Adenocarcinomas but Produce Reduced Amounts of IFN-γ. *J. Immunol. 195*(7), 3472–3481.
336. Zabijak, L., C. Attencourt, C. Guignant, D. Chatelain, P. Marcelo, J. P. Marolleau, and E. Treiner. (2015). Increased tumor infiltration by mucosal-associated invariant T cells correlates with poor survival in colorectal cancer patients. *Cancer Immunol. Immunother. 64*(12), 1601–1608.
337. Shaler, C. R., M. E. Tun-Abraham, A. I. Skaro, K. Khazaie, A. J. Corbett, T. Mele, R. Hernandez-Alejandro, and S. M. M. Haeryfar. (2017). Mucosa-associated invariant T cells infiltrate hepatic metastases in patients with colorectal carcinoma but are rendered dysfunctional within and adjacent to tumor microenvironment. *Cancer Immunol. Immunother. 66*(12), 1563–1575.
338. Mitchell, J., E. Kvedaraite, T. von Bahr Greenwood, J.-I. Henter, D. G. Pellicci, S. P. Berzins, and G. Kannourakis. (2018). Altered Populations of Unconventional T Cell Lineages in Patients with Langerhans Cell Histiocytosis. *Sci. Rep. 8*(1), 16506.
339. Zheng, C., L. Zheng, J.-K. Yoo, H. Guo, Y. Zhang, X. Guo, B. Kang, R. Hu, J. Y. Huang, Q. Zhang, Z. Liu, M. Dong, X. Hu, W. Ouyang, J. Peng, and Z. Zhang. (2017). Landscape of Infiltrating T Cells in Liver Cancer Revealed by Single-Cell Sequencing. *Cell 169*(7), 1342-1356.e16.
340. Huang, W. C., Y. C. Hsiao, C. C. Wu, Y. T. Hsu, and C. L. Chang. (2019). Less circulating mucosal-associated invariant T cells in patients with cervical cancer. *Taiwan. J. Obstet. Gynecol. 58*(1), 117–121.
341. Favreau, M., K. Venken, S. Faict, K. Maes, K. De Veirman, E. De Bruyne, X. Leleu, L. Boon, D. Elewaut, K. Vanderkerken, and E. Menu. (2017). Both mucosal-associated invariant and natural killer T-cell deficiency in multiple myeloma can be countered by PD-1 inhibition. *Haematologica 102*(7), e266–e270.
342. Kabelitz, D., R. Serrano, L. Kouakanou, C. Peters, and S. Kalyan. (2020). Cancer immunotherapy with γδ T cells: many paths ahead of us. *Cell. Mol. Immunol. 17*(9), 925–939.
343. Park, J. H., and H. K. Lee. (2021). Function of γδ T cells in tumor immunology and their application to cancer therapy. *Exp. Mol. Med. 53*(3), 318–327.
344. Silva-Santos, B., S. Mensurado, and S. B. Coffelt. (2019). γδ T cells: pleiotropic immune effectors with therapeutic potential in cancer. *Nat. Rev. Cancer 19*(7), 392–404.
345. Godfrey, D. I., J. Le Nours, D. M. Andrews, A. P. Uldrich, and J. Rossjohn. (2018). Unconventional T Cell Targets for Cancer Immunotherapy. *Immunity 48*(3), 453–473.
346. Godder, K. T., P. J. Henslee-Downey, J. Mehta, B. S. Park, K.-Y. Chiang, S. Abhyankar, and L. S. Lamb. (2007). Long term disease-free survival in acute leukemia patients recovering with increased γδ T cells after partially mismatched related donor bone marrow transplantation. *Bone Marrow Transplant. 39*(12), 751–757.

347. Lamb Jr, L. S., P. J. Henslee-Downey, R. S. Parrish, K. Godder, J. Thompson, C. Lee, and A. P. Gee. (1996). Rapid Communication: Increased Frequency of TCRγδ+ T Cells in Disease-Free Survivors Following T Cell-Depleted, Partially Mismatched, Related Donor Bone Marrow Transplantation for Leukemia. *J. Hematother. 5*(5), 503–509.
348. Bialasiewicz, A. A., J.-X. Ma, and G. Richard. (1999). α/β− and γ/δ TCR+ lymphocyte infiltration in necrotising choroidal melanomas. *Br. J. Ophthalmol. 83*(9), 1069–1073.
349. Wu, Y., F. Kyle-Cezar, R. T. Woolf, C. Naceur-Lombardelli, J. Owen, D. Biswas, A. Lorenc, P. Vantourout, P. Gazinska, A. Grigoriadis, A. Tutt, and A. Hayday. (2019). An innate-like Vδ1+ γδ T cell compartment in the human breast is associated with remission in triple-negative breast cancer. *Sci. Transl. Med. 11*(513), eaax9364.
350. Ma, C., Q. Zhang, J. Ye, F. Wang, Y. Zhang, E. Wevers, T. Schwartz, P. Hunborg, M. A. Varvares, D. F. Hoft, E. C. Hsueh, and G. Peng. (2012). Tumor-Infiltrating γδ T Lymphocytes Predict Clinical Outcome in Human Breast Cancer. *J. Immunol. 189*(10), 5029–5036.
351. Chabab, G., C. Barjon, N. Abdellaoui, L. Salvador-Prince, C. Dejou, H.-A. Michaud, F. Boissière-Michot, E. Lopez-Crapez, W. Jacot, D. Pourquier, N. Bonnefoy, and V. Lafont. (2020). Identification of a regulatory Vδ1 gamma delta T cell subpopulation expressing CD73 in human breast cancer. *J. Leukoc. Biol. 107*(6), 1057–1067.
352. Peng, G., H. Y. Wang, W. Peng, Y. Kiniwa, K. H. Seo, and R.-F. Wang. (2007). Tumor-Infiltrating γδ T Cells Suppress T and Dendritic Cell Function via Mechanisms Controlled by a Unique Toll-like Receptor Signaling Pathway. *Immunity 27*(2), 334–348.
353. Rong, L., K. Li, R. Li, H.-M. Liu, R. Sun, and X.-Y. Liu. (2016). Analysis of tumor-infiltrating gamma delta T cells in rectal cancer. *World J. Gastroenterol. 22*(13), 3573–3580.
354. Chen, X., W. Shang, R. Xu, M. Wu, X. Zhang, P. Huang, F. Wang, and S. Pan. (2019). Distribution and functions of γδ T cells infiltrated in the ovarian cancer microenvironment. *J. Transl. Med. 17*(1), 144.
355. Wu, P., D. Wu, C. Ni, J. Ye, W. Chen, G. Hu, Z. Wang, C. Wang, Z. Zhang, W. Xia, Z. Chen, K. Wang, T. Zhang, J. Xu, Y. Han, T. Zhang, X. Wu, J. Wang, W. Gong, S. Zheng, F. Qiu, J. Yan, and J. Huang. (2014). γδT17 Cells Promote the Accumulation and Expansion of Myeloid-Derived Suppressor Cells in Human Colorectal Cancer. *Immunity 40*(5), 785–800.
356. Hu, G., P. Wu, P. Cheng, Z. Zhang, Z. Wang, X. Yu, X. Shao, D. Wu, J. Ye, T. Zhang, X. Wang, F. Qiu, J. Yan, and J. Huang. (2017). Tumor-infiltrating CD39+ γδTregs are novel immunosuppressive T cells in human colorectal cancer. *Oncoimmunology 6*(2), e1277305.
357. Patil, R. S., S. U. Shah, S. V. Shrikhande, M. Goel, R. P. Dikshit, and S. V. Chiplunkar. (2016). IL17 producing γδT cells induce angiogenesis and are associated with poor survival in gallbladder cancer patients. *Int. J. Cancer 139*(4), 869–881.
358. Nair, S., and M. V. Dhodapkar. (2017). Natural Killer T Cells in Cancer Immunotherapy. *Front. Immunol. 8*, 1178.
359. Pilones, K. A., J. Aryankalayil, and S. Demaria. (2012). Invariant NKT cells as novel targets for immunotherapy in solid tumors. *Clin. Dev. Immunol. 2012*, 720803.
360. Stolk, D., H. J. van der Vliet, T. D. de Gruijl, Y. van Kooyk, and M. A. Exley. (2018). Positive & Negative Roles of Innate Effector Cells in Controlling Cancer Progression. *Front. Immunol. 9*, 1990.
361. Yanagisawa, K., K. Seino, Y. Ishikawa, M. Nozue, T. Todoroki, and K. Fukao. (2002). Impaired Proliferative Response of Vα24 NKT Cells from Cancer Patients Against α-Galactosylceramide. *J. Immunol. 168*(12), 6494–6499.
362. Metelitsa, L. S., O. V. Naidenko, A. Kant, H.-W. Wu, M. J. Loza, B. Perussia, M. Kronenberg, and R. C. Seeger. (2001). Human NKT Cells Mediate Antitumor Cytotoxicity Directly by Recognizing Target Cell CD1d with Bound Ligand or Indirectly by Producing IL-2 to Activate NK Cells. *J. Immunol. 167*(6), 3114–3122.
363. Nicol, A., M. Nieda, Y. Koezuka, S. Porcelli, K. Suzuki, K. Tadokoro, S. Durrant, and T. Juji. (2000). Human invariant Vα24+ natural killer T cells activated by α-

galactosylceramide (KRN7000) have cytotoxic anti-tumour activity through mechanisms distinct from T cells and natural killer cells. *Immunology 99*(2), 229–234.

364. Tachibana, T., H. Onodera, T. Tsuruyama, A. Mori, S. Nagayama, H. Hiai, and M. Imamura. (2005). Increased Intratumor Vα24-Positive Natural Killer T Cells: A Prognostic Factor for Primary Colorectal Carcinomas. *Clin. Cancer Res. 11*(20), 7322–7327.

365. Hishiki, T., N. Mise, K. Harada, F. Ihara, M. Takami, T. Saito, K. Terui, M. Nakata, S. Komatsu, H. Yoshida, and S. Motohashi. (2018). Invariant natural killer T infiltration in neuroblastoma with favorable outcome. *Pediatr. Surg. Int. 34*(2), 195–201.

366. Hu, T., P. Yang, H. Zhu, X. Chen, X. Xie, M. Yang, S. Liu, and H. Wang. (2015). Accumulation of invariant NKT cells with increased IFN-γ production in persistent high-risk HPV-infected high-grade cervical intraepithelial neoplasia. *Diagn. Pathol. 10*(1), 20.

367. Tahir, S. M. A., O. Cheng, A. Shaulov, Y. Koezuka, G. J. Bubley, S. B. Wilson, S. P. Balk, and M. A. Exley. (2001). Loss of IFN-γ Production by Invariant NK T Cells in Advanced Cancer. *J. Immunol. 167*(7), 4046–4050.

368. Molling, J. W., W. Kölgen, H. J. J. van der Vliet, M. F. Boomsma, H. Kruizenga, C. H. Smorenburg, B. G. Molenkamp, J. A. Langendijk, C. R. Leemans, B. M. E. von Blomberg, R. J. Scheper, and A. J. M. van den Eertwegh. (2005). Peripheral blood IFN-γ-secreting Vα24+Vβ11+ NKT cell numbers are decreased in cancer patients independent of tumor type or tumor load. *Int. J. Cancer 116*(1), 87–93.

369. Yoneda, K., T. Morii, M. Nieda, N. Tsukaguchi, I. Amano, H. Tanaka, H. Yagi, N. Narita, and H. Kimura. (2005). The peripheral blood Vα24+ NKT cell numbers decrease in patients with haematopoietic malignancy. *Leuk. Res. 29*(2), 147–152.

370. Fujii, S., K. Shimizu, V. Klimek, M. D. Geller, S. D. Nimer, and M. V. Dhodapkar. (2003). Severe and selective deficiency of interferon-γ-producing invariant natural killer T cells in patients with myelodysplastic syndromes. *Br. J. Haematol. 122*(4), 617–622.

371. Chuc, A. E. N., L. A. M. Cervantes, F. P. Retiguin, J. V. Ojeda, and E. R. Maldonado. (2012). Low number of invariant NKT cells is associated with poor survival in acute myeloid leukemia. *J. Cancer Res. Clin. Oncol. 138*(8), 1427–1432.

372. Gorini, F., L. Azzimonti, G. Delfanti, L. Scarfò, C. Scielzo, M. T. Bertilaccio, P. Ranghetti, A. Gulino, C. Doglioni, A. Di Napoli, M. Capri, C. Franceschi, F. Caligaris-Cappio, P. Ghia, M. Bellone, P. Dellabona, G. Casorati, and C. de Lalla. (2017). Invariant NKT cells contribute to chronic lymphocytic leukemia surveillance and prognosis. *Blood 129*(26), 3440–3451.

373. Molling, J. W., J. A. E. Langius, J. A. Langendijk, C. R. Leemans, H. J. Bontkes, H. J. J. van der Vliet, B. M. E. von Blomberg, R. J. Scheper, and A. J. M. van den Eertwegh. (2007). Low Levels of Circulating Invariant Natural Killer T Cells Predict Poor Clinical Outcome in Patients With Head and Neck Squamous Cell Carcinoma. *J. Clin. Oncol. 25*(7), 862–868.

374. Schneiders, F. L., R. C. G. de Bruin, A. J. M. van den Eertwegh, R. J. Scheper, C. R. Leemans, R. H. Brakenhoff, J. A. Langendijk, H. M. W. Verheul, T. D. de Gruijl, J. W. Molling, and H. J. van der Vliet. (2012). Circulating Invariant Natural Killer T-Cell Numbers Predict Outcome in Head and Neck Squamous Cell Carcinoma: Updated Analysis With 10-Year Follow-Up. *J. Clin. Oncol. 30*(5), 567–570.

375. Metelitsa, L. S., H.-W. Wu, H. Wang, Y. Yang, Z. Warsi, S. Asgharzadeh, S. Groshen, S. B. Wilson, and R. C. Seeger. (2004). Natural Killer T Cells Infiltrate Neuroblastomas Expressing the Chemokine CCL2. *J. Exp. Med. 199*(9), 1213–1221.

376. Asadzadeh, Z., H. Mohammadi, E. Safarzadeh, M. Hemmatzadeh, A. Mahdian-Shakib, F. Jadidi-Niaragh, G. Azizi, and B. Baradaran. (2017). The paradox of Th17 cell functions in tumor immunity. *Cell. Immunol. 322*, 15–25.

377. Guéry, L., and S. Hugues. (2015). Th17 Cell Plasticity and Functions in Cancer Immunity. *Biomed Res. Int. 2015*, 314620.

378. Tosolini, M., A. Kirilovsky, B. Mlecnik, T. Fredriksen, S. Mauger, G. Bindea, A. Berger, P. Bruneval, W.-H. Fridman, F. Pagès, and J. Galon. (2011). Clinical Impact of Different Classes of Infiltrating T Cytotoxic and Helper Cells (Th1, Th2, Treg, Th17) in Patients

with Colorectal Cancer. *Cancer Res. 71*(4), 1263–1271.
379. Zhang, J.-P., J. Yan, J. Xu, X.-H. Pang, M.-S. Chen, L. Li, C. Wu, S.-P. Li, and L. Zheng. (2009). Increased intratumoral IL-17-producing cells correlate with poor survival in hepatocellular carcinoma patients. *J. Hepatol. 50*(5), 980–989.
380. Yamada, Y., H. Saito, and M. Ikeguchi. (2012). Prevalence and clinical relevance of Th17 cells in patients with gastric cancer. *J. Surg. Res. 178*(2), 685–691.
381. Chen, X., J. Wan, J. Liu, W. Xie, X. Diao, J. Xu, B. Zhu, and Z. Chen. (2010). Increased IL-17-producing cells correlate with poor survival and lymphangiogenesis in NSCLC patients. *Lung Cancer 69*(3), 348–354.
382. Galand, C., S. Donnou, L. Crozet, S. Brunet, V. Touitou, H. Ouakrim, W. H. Fridman, C. Sautès-Fridman, and S. Fisson. (2011). Th17 Cells Are Involved in the Local Control of Tumor Progression in Primary Intraocular Lymphoma. *PLoS One 6*(9), e24622.
383. Su, X., J. Ye, E. C. Hsueh, Y. Zhang, D. F. Hoft, and G. Peng. (2010). Tumor Microenvironments Direct the Recruitment and Expansion of Human Th17 Cells. *J. Immunol. 184*(3), 1630–1641.
384. Maruyama, T., K. Kono, Y. Mizukami, Y. Kawaguchi, K. Mimura, M. Watanabe, S. Izawa, and H. Fujii. (2010). Distribution of Th17 cells and FoxP3(+) regulatory T cells in tumor-infiltrating lymphocytes, tumor-draining lymph nodes and peripheral blood lymphocytes in patients with gastric cancer. *Cancer Sci. 101*(9), 1947–1954.
385. Sfanos, K. S., T. C. Bruno, C. H. Maris, L. Xu, C. J. Thoburn, A. M. DeMarzo, A. K. Meeker, W. B. Isaacs, and C. G. Drake. (2008). Phenotypic Analysis of Prostate-Infiltrating Lymphocytes Reveals TH17 and Treg Skewing. *Clin. Cancer Res. 14*(11), 3254–3261.
386. Hus, I., A. Bojarska-Junak, S. Chocholska, W. Tomczak, J. Woś, A. Dmoszyńska, and J. Roliński. (2013). Th17/IL-17A Might Play a Protective Role in Chronic Lymphocytic Leukemia Immunity. *PLoS One 8*(11), e78091.
387. Kryczek, I., M. Banerjee, P. Cheng, L. Vatan, W. Szeliga, S. Wei, E. Huang, E. Finlayson, D. Simeone, T. H. Welling, A. Chang, G. Coukos, R. Liu, and W. Zou. (2009). Phenotype, distribution, generation, and functional and clinical relevance of Th17 cells in the human tumor environments. *Blood 114*(6), 1141–1149.
388. Punt, S., J. M. Langenhoff, H. Putter, G. J. Fleuren, A. Gorter, and E. S. Jordanova. (2015). The correlations between IL-17 vs. Th17 cells and cancer patient survival: a systematic review. *Oncoimmunology 4*(2), e984547.
389. Takahashi, T., S. Dejbakhsh-Jones, and S. Strober. (2006). Expression of CD161 (NKR-P1A) Defines Subsets of Human CD4 and CD8 T Cells with Different Functional Activities. *J. Immunol. 176*(1), 211–216.
390. Trabanelli, S., A. Gomez-Cadena, B. Salomé, K. Michaud, D. Mavilio, B. N. Landis, P. Jandus, and C. Jandus. (2018). Human innate lymphoid cells (ILCs): Toward a uniform immune-phenotyping. *Cytom. Part B Clin. Cytom. 94*(3), 392–399.
391. Myers, J. A., and J. S. Miller. (2021). Exploring the NK cell platform for cancer immunotherapy. *Nat. Rev. Clin. Oncol. 18*(2), 85–100.
392. Addou-Klouche, L. (2017). NK Cells in Cancer Immunotherapy. In *Natural Killer Cells*, (M. Aribi, ed). IntechOpen.
393. Lo Nigro, C., M. Macagno, D. Sangiolo, L. Bertolaccini, M. Aglietta, and M. C. Merlano. (2019). NK-mediated antibody-dependent cell-mediated cytotoxicity in solid tumors: biological evidence and clinical perspectives. *Ann. Transl. Med. 7*(5), 105.
394. Mirjačić Martinović, K., N. Babović, R. Džodić, V. Jurišić, S. Matković, and G. Konjević. (2015). Favorable in vitro effects of combined IL-12 and IL-18 treatment on NK cell cytotoxicity and CD25 receptor expression in metastatic melanoma patients. *J. Transl. Med. 13*(1), 120.
395. Zhuang, L., R. J. Fulton, P. Rettman, A. E. Sayan, J. Coad, A. Al-Shamkhani, and S. I. Khakoo. (2019). Activity of IL-12/15/18 primed natural killer cells against hepatocellular carcinoma. *Hepatol. Int. 13*(1), 75–83.
396. Terrén, I., A. Orrantia, A. Mosteiro, J. Vitallé, O. Zenarruzabeitia, and F. Borrego. (2021). Metabolic changes of Interleukin-12/15/18-stimulated human NK cells. *Sci. Rep. 11*(1),

6472.
397. Prager, I., C. Liesche, H. van Ooijen, D. Urlaub, Q. Verron, N. Sandström, F. Fasbender, M. Claus, R. Eils, J. Beaudouin, B. Önfelt, and C. Watzl. (2019). NK cells switch from granzyme B to death receptor–mediated cytotoxicity during serial killing. *J. Exp. Med. 216*(9), 2113–2127.
398. Zamai, L., A. R. Mariani, G. Zauli, L. Rodella, R. Rezzani, F. A. Manzoli, and M. Vitale. (1998). Kinetics of In Vitro Natural Killer Activity Against K562 Cells as Detected by Flow Cytometry. *Cytometry 32*(4), 280–285.
399. Spinner, M. A., L. A. Sanchez, A. P. Hsu, P. A. Shaw, C. S. Zerbe, K. R. Calvo, D. C. Arthur, W. Gu, C. M. Gould, C. C. Brewer, E. W. Cowen, A. F. Freeman, K. N. Olivier, G. Uzel, A. M. Zelazny, J. R. Daub, C. D. Spalding, R. J. Claypool, N. K. Giri, B. P. Alter, E. M. Mace, J. S. Orange, J. Cuellar-Rodriguez, D. D. Hickstein, and S. M. Holland. (2014). GATA2 deficiency: a protean disorder of hematopoiesis, lymphatics, and immunity. *Blood 123*(6), 809–821.
400. Lorenzi, L., G. Tabellini, W. Vermi, D. Moratto, F. Porta, L. D. Notarangelo, O. Patrizi, S. Sozzani, G. de Saint Basile, S. Latour, D. Pace, S. Lonardi, F. Facchetti, R. Badolato, and S. Parolini. (2013). Occurrence of Nodular Lymphocyte-Predominant Hodgkin Lymphoma in Hermansky-Pudlak Type 2 Syndrome Is Associated to Natural Killer and Natural Killer T Cell Defects. *PLoS One 8*(11), e80131.
401. Moon, W. Y., and S. J. Powis. (2019). Does Natural Killer Cell Deficiency (NKD) Increase the Risk of Cancer? NKD May Increase the Risk of Some Virus Induced Cancer. *Front. Immunol. 10*, 1703.
402. Zhang, S., W. Liu, B. Hu, P. Wang, X. Lv, S. Chen, and Z. Shao. (2020). Prognostic Significance of Tumor-Infiltrating Natural Killer Cells in Solid Tumors: A Systematic Review and Meta-Analysis. *Front. Immunol. 11*, 1242.
403. Nersesian, S., S. L. Schwartz, S. R. Grantham, L. K. MacLean, S. N. Lee, M. Pugh-Toole, and J. E. Boudreau. (2021). NK cell infiltration is associated with improved overall survival in solid cancers: A systematic review and meta-analysis. *Transl. Oncol. 14*(1), 100930.
404. Lowdell, M. W., R. Craston, D. Samuel, M. E. Wood, E. O'Neill, V. Saha, and H. G. Prentice. (2002). Evidence that continued remission in patients treated for acute leukaemia is dependent upon autologous natural killer cells. *Br. J. Haematol. 117*(4), 821–827.
405. Carlsten, M., and M. Järås. (2019). Natural Killer Cells in Myeloid Malignancies: Immune Surveillance, NK Cell Dysfunction, and Pharmacological Opportunities to Bolster the Endogenous NK Cells. *Front. Immunol. 10*, 2357.
406. Guillerey, C. (2018). Roles of cytotoxic and helper innate lymphoid cells in cancer. *Mamm. Genome 29*(11), 777–789.
407. Crinier, A., E. Vivier, and M. Bléry. (2019). Helper-like innate lymphoid cells and cancer immunotherapy. *Semin. Immunol. 41*, 101274.
408. Salomé, B., A. Gomez-Cadena, R. Loyon, M. Suffiotti, V. Salvestrini, T. Wyss, G. Vanoni, D. F. Ruan, M. Rossi, A. Tozzo, P. Tentorio, E. Bruni, C. Riether, E.-M. Jacobsen, P. Jandus, C. Conrad, M. Hoenig, A. Schulz, K. Michaud, M. G. Della Porta, S. Salvatore, P.-C. Ho, D. Gfeller, A. Ochsenbein, D. Mavilio, A. Curti, E. Marcenaro, A. Steinle, A. Horowitz, P. Romero, S. Trabanelli, and C. Jandus. (2019). CD56 as a marker of an ILC1-like population with NK cell properties that is functionally impaired in AML. *Blood Adv. 3*(22), 3674–3687.
409. de Weerdt, I., V. van Hoeven, J. M. Munneke, S. Endstra, T. Hofland, M. D. Hazenberg, and A. P. Kater. (2016). Innate lymphoid cells are expanded and functionally altered in chronic lymphocytic leukemia. *Haematologica 101*(11), e461–e464.
410. Trabanelli, S., A. Curti, M. Lecciso, B. Salomé, C. Riether, A. Ochsenbein, P. Romero, and C. Jandus. (2015). CD127+ innate lymphoid cells are dysregulated in treatment naïve acute myeloid leukemia patients at diagnosis. *Haematologica 100*(7), e257–e260.
411. Trabanelli, S., M. F. Chevalier, A. Martinez-Usatorre, A. Gomez-Cadena, B. Salomé, M. Lecciso, V. Salvestrini, G. Verdeil, J. Racle, C. Papayannidis, H. Morita, I. Pizzitola, C.

Grandclément, P. Bohner, E. Bruni, M. Girotra, R. Pallavi, P. Falvo, E. O. Leibundgut, G. M. Baerlocher, C. Carlo-Stella, D. Taurino, A. Santoro, O. Spinelli, A. Rambaldi, E. Giarin, G. Basso, C. Tresoldi, F. Ciceri, D. Gfeller, C. A. Akdis, L. Mazzarella, S. Minucci, P. G. Pelicci, E. Marcenaro, A. N. J. McKenzie, D. Vanhecke, G. Coukos, D. Mavilio, A. Curti, L. Derré, and C. Jandus. (2017). Tumour-derived PGD2 and NKp30-B7H6 engagement drives an immunosuppressive ILC2-MDSC axis. *Nat. Commun. 8*(1), 593.

412. Xuan, X., J. Zhou, Z. Tian, Y. Lin, J. Song, Z. Ruan, B. Ni, H. Zhao, and W. Yang. (2020). ILC3 cells promote the proliferation and invasion of pancreatic cancer cells through IL-22/AKT signaling. *Clin. Transl. Oncol. 22*(4), 563–575.

413. Salimi, M., R. Wang, X. Yao, X. Li, X. Wang, Y. Hu, X. Chang, P. Fan, T. Dong, and G. Ogg. (2018). Activated innate lymphoid cell populations accumulate in human tumour tissues. *BMC Cancer 18*(1), 341.

414. Chevalier, M. F., S. Trabanelli, J. Racle, B. Salomé, V. Cesson, D. Gharbi, P. Bohner, S. Domingos-Pereira, F. Dartiguenave, A.-S. Fritschi, D. E. Speiser, C. A. Rentsch, D. Gfeller, P. Jichlinski, D. Nardelli-Haefliger, C. Jandus, and L. Derré. (2017). ILC2-modulated T cell–to-MDSC balance is associated with bladder cancer recurrence. *J. Clin. Invest. 127*(8), 2916–2929.

415. Moral, J. A., J. Leung, L. A. Rojas, J. Ruan, J. Zhao, Z. Sethna, A. Ramnarain, B. Gasmi, M. Gururajan, D. Redmond, G. Askan, U. Bhanot, E. Elyada, Y. Park, D. A. Tuveson, M. Gönen, S. D. Leach, J. D. Wolchok, R. P. DeMatteo, T. Merghoub, and V. P. Balachandran. (2020). ILC2s amplify PD-1 blockade by activating tissue-specific cancer immunity. *Nature 579*(7797), 130–135.

416. Carrega, P., F. Loiacono, E. Di Carlo, A. Scaramuccia, M. Mora, R. Conte, R. Benelli, G. M. Spaggiari, C. Cantoni, S. Campana, I. Bonaccorsi, B. Morandi, M. Truini, M. C. Mingari, L. Moretta, and G. Ferlazzo. (2015). NCR+ILC3 concentrate in human lung cancer and associate with intratumoral lymphoid structures. *Nat. Commun. 6*(1), 8280.

417. Irshad, S., F. Flores-Borja, K. Lawler, J. Monypenny, R. Evans, V. Male, P. Gordon, A. Cheung, P. Gazinska, F. Noor, F. Wong, A. Grigoriadis, G. O. Fruhwirth, P. R. Barber, N. Woodman, D. Patel, M. Rodriguez-Justo, J. Owen, S. G. Martin, S. E. Pinder, C. E. Gillett, S. P. Poland, S. Ameer-Beg, F. McCaughan, L. M. Carlin, U. Hasan, D. R. Withers, P. Lane, B. Vojnovic, S. A. Quezada, P. Ellis, A. N. J. Tutt, and T. Ng. (2017). RORγt+ Innate Lymphoid Cells Promote Lymph Node Metastasis of Breast Cancers. *Cancer Res. 77*(5), 1083–1096.

418. Koh, J., H. Y. Kim, Y. Lee, I. K. Park, C. H. Kang, Y. T. Kim, J.-E. Kim, M. Choi, W.-W. Lee, Y. K. Jeon, and D. H. Chung. (2019). IL23-Producing Human Lung Cancer Cells Promote Tumor Growth via Conversion of Innate Lymphoid Cell 1 (ILC1) into ILC3. *Clin. Cancer Res. 25*(13), 4026–4037.

419. Huang, Q., N. Jacquelot, A. Preaudet, S. Hediyeh-zadeh, F. Souza-Fonseca-Guimaraes, A. N. J. McKenzie, P. M. Hansbro, M. J. Davis, L. A. Mielke, T. L. Putoczki, and G. T. Belz. (2021). Type 2 Innate Lymphoid Cells Protect against Colorectal Cancer Progression and Predict Improved Patient Survival. *Cancers 13*(3), 559.

420. Monaco, G., B. Lee, W. Xu, S. Mustafah, Y. Y. Hwang, C. Carré, N. Burdin, L. Visan, M. Ceccarelli, M. Poidinger, A. Zippelius, J. P. de Magalhães, and A. Larbi. (2019). RNA-Seq Signatures Normalized by mRNA Abundance Allow Absolute Deconvolution of Human Immune Cell Types. *Cell Rep. 26*(6), 1627-1640.e7.

421. Miao, Y.-R., Q. Zhang, Q. Lei, M. Luo, G.-Y. Xie, H. Wang, and A.-Y. Guo. (2020). ImmuCellAI: A Unique Method for Comprehensive T-Cell Subsets Abundance Prediction and its Application in Cancer Immunotherapy. *Adv. Sci. 7*(7), 1902880.

422. FitzPatrick, M. E. B., N. M. Provine, L. C. Garner, K. Powell, A. Amini, S. L. Irwin, H. Ferry, T. Ambrose, P. Friend, G. Vrakas, S. Reddy, E. Soilleux, P. Klenerman, and P. J. Allan. (2021). Human intestinal tissue-resident memory T cells comprise transcriptionally and functionally distinct subsets. *Cell Rep. 34*(3), 108661.

423. Savas, P., B. Virassamy, C. Ye, A. Salim, C. P. Mintoff, F. Caramia, R. Salgado, D. J. Byrne, Z. L. Teo, S. Dushyanthen, A. Byrne, L. Wein, S. J. Luen, C. Poliness, S. S. Nightingale, A. S. Skandarajah, D. E. Gyorki, C. M. Thornton, P. A. Beavis, S. B. Fox,

Kathleen Cuningham Foundation Consortium for Research into Familial Breast Cancer (kConFab), P. K. Darcy, T. P. Speed, L. K. Mackay, P. J. Neeson, and S. Loi. (2018). Single-cell profiling of breast cancer T cells reveals a tissue-resident memory subset associated with improved prognosis. *Nat. Med. 24*(7), 986–993.

424. Kumar, B. V., W. Ma, M. Miron, T. Granot, R. S. Guyer, D. J. Carpenter, T. Senda, X. Sun, S.-H. Ho, H. Lerner, A. L. Friedman, Y. Shen, and D. L. Farber. (2017). Human Tissue-Resident Memory T Cells Are Defined by Core Transcriptional and Functional Signatures in Lymphoid and Mucosal Sites. *Cell Rep. 20*(12), 2921–2934.

425. Llibre, A., P. Klenerman, and C. B. Willberg. (2016). Multi-functional lectin-like transcript-1: A new player in human immune regulation. *Immunol. Lett. 177*, 62–69.

426. Germain, C., T. Guillaudeux, E. D. Galsgaard, C. Hervouet, N. Tekaya, A.-S. Gallouet, J. Fassy, F. Bihl, G. Poupon, A. Lazzari, P. Spee, F. Anjuère, C. Pangault, K. Tarte, P. Tas, L. Xerri, and V. M. Braud. (2015). Lectin-like transcript 1 is a marker of germinal center-derived B-cell non-Hodgkin's lymphomas dampening natural killer cell functions. *Oncoimmunology 4*(8), e1026503.

427. Li, N., V. van Unen, T. Höllt, A. Thompson, J. van Bergen, N. Pezzotti, E. Eisemann, A. Vilanova, S. M. Chuva de Sousa Lopes, B. P. F. Lelieveldt, and F. Koning. (2018). Mass cytometry reveals innate lymphoid cell differentiation pathways in the human fetal intestine. *J. Exp. Med. 215*(5), 1383–1396.

428. Poggi, A., P. Costa, M. R. Zocchi, and L. Moretta. (1997). NKRP1A molecule is involved in transendothelial migration of CD4+ human T lymphocytes. *Immunol. Lett. 57*(1–3), 121–123.

429. Llibre, A., C. López-Macías, T. Marafioti, H. Mehta, A. Partridge, C. Kanzig, F. Rivellese, J. D. Galson, L. J. Walker, P. Milne, R. E. Phillips, D. F. Kelly, G. J. Freeman, M. E. El Shikh, P. Klenerman, and C. B. Willberg. (2016). LLT1 and CD161 Expression in Human Germinal Centers Promotes B Cell Activation and CXCR4 Downregulation. *J. Immunol. 196*(5), 2085–2094.

430. Chan, J.-A., F. de Labastida Rivera, J. Loughland, J. A. Engel, H. J. Lee, A. SheelaNair, B. D. Wines, F. H. Amante, L. Webb, P. Mukhopadhyay, A.-M. Patch, P. M. Hogarth, J. G. Beeson, J. S. McCarthy, A. Haque, C. R. Engwerda, and M. J. Boyle. (2020). Th2-like T-follicular helper cells promote functional antibody production during Plasmodium falciparum infection. *bioRxiv* , 2020.05.18.101048.

431. Newman, A. M., C. L. Liu, M. R. Green, A. J. Gentles, W. Feng, Y. Xu, C. D. Hoang, M. Diehn, and A. A. Alizadeh. (2015). Robust enumeration of cell subsets from tissue expression profiles. *Nat. Methods 12*(5), 453–457.

432. Bindea, G., B. Mlecnik, M. Tosolini, A. Kirilovsky, M. Waldner, A. C. Obenauf, H. Angell, T. Fredriksen, L. Lafontaine, A. Berger, P. Bruneval, W. H. Fridman, C. Becker, F. Pagès, M. R. Speicher, Z. Trajanoski, and J. Galon. (2013). Spatiotemporal Dynamics of Intratumoral Immune Cells Reveal the Immune Landscape in Human Cancer. *Immunity 39*(4), 782–795.

433. Gu-Trantien, C., S. Loi, S. Garaud, C. Equeter, M. Libin, A. de Wind, M. Ravoet, H. Le Buanec, C. Sibille, G. Manfouo-Foutsop, I. Veys, B. Haibe-Kains, S. K. Singhal, S. Michiels, F. Rothé, R. Salgado, H. Duvillier, M. Ignatiadis, C. Desmedt, D. Bron, D. Larsimont, M. Piccart, C. Sotiriou, and K. Willard-Gallo. (2013). CD4+ follicular helper T cell infiltration predicts breast cancer survival. *J. Clin. Invest. 123*(7), 2873–2892.

434. Singh, D., A. Ganesan, B. Panwar, S. Eschweiler, C. Hanley, A. Madrigal, C. Ramírez-Suástegui, A. Wang, J. Clarke, O. Wood, E. Garrido-Martin, S. Chee, G. Seumois, S. Belanger, A. Alzetani, E. Woo, P. Friedmann, S. Crotty, G. Thomas, T. Sanchez-Elsner, F. Ay, C. Ottensmeier, and P. Vijayanand. (2020). CD4+ follicular helper-like T cells are key players in anti-tumor immunity. *bioRxiv* , 2020.01.08.898346.

435. Phillips, D., C. M. Schürch, M. S. Khodadoust, Y. H. Kim, G. P. Nolan, and S. Jiang. (2021). Highly Multiplexed Phenotyping of Immunoregulatory Proteins in the Tumor Microenvironment by CODEX Tissue Imaging. *Front. Immunol. 12*, 687673.

436. Hartmann, F. J., E. F. Simonds, N. Vivanco, T. Bruce, L. Borges, G. P. Nolan, M. H. Spitzer, and S. C. Bendall. (2019). Scalable Conjugation and Characterization of

Immunoglobulins with Stable Mass Isotope Reporters for Single-Cell Mass Cytometry Analysis. In *Methods in Molecular Biology*, vol. 1989. Humana Press Inc. 55–81.

437. Kashima, Y., Y. Sakamoto, K. Kaneko, M. Seki, Y. Suzuki, and A. Suzuki. (2020). Single-cell sequencing techniques from individual to multiomics analyses. *Exp. Mol. Med. 52*(9), 1419–1427.

438. Baron, M., and I. Yanai. (2017). New skin for the old RNA-Seq ceremony: The age of single-cell multi-omics. *Genome Biol. 18*(1), 159.

439. Wang, Y. J., D. Traum, J. Schug, L. Gao, C. Liu, HPAP Consortium, M. A. Atkinson, A. C. Powers, M. D. Feldman, A. Naji, K.-M. Chang, and K. H. Kaestner. (2019). Multiplexed In Situ Imaging Mass Cytometry Analysis of the Human Endocrine Pancreas and Immune System in Type 1 Diabetes. *Cell Metab. 29*(3), 769-783.e4.

440. Akoya Biosciences. CODEX® Grant Support Document - Perform Deep Spatial Phenotyping to Reveal the Diverse Cellular Landscape Across Whole Tissue Sections. [Website, accessed on June 14, 2021]. Available from: https://www.akoyabio.com/wp-content/uploads/2021/05/CODEX-Grant-Support-Document.pdf

441. Heinhuis, B., C. D. Popa, B. L. J. H. van Tits, S. H. Kim, P. L. Zeeuwen, W. B. van den Berg, J. W. M. van der Meer, J. A. van der Vliet, A. F. H. Stalenhoef, C. A. Dinarello, M. G. Netea, and L. A. B. Joosten. (2013). Towards a role of interleukin-32 in atherosclerosis. *Cytokine 64*(1), 433–440.

442. Xu, Q., X. Pan, X. Shu, H. Cao, X. Li, K. Zhang, J. Lu, Y. Zou, X. Li, H. Liu, Y. Zhang, D. Yang, Q. Ning, G. Shen, and G. Li. (2012). Increased interleukin-32 expression in chronic hepatitis B virus-infected liver. *J. Infect. 65*(4), 336–342.

443. Zou, Y., J. Bao, X. Pan, Y. Lu, S. Liao, X. Wang, G. Wang, and D. Lin. (2015). NKP30-B7-H6 Interaction Aggravates Hepatocyte Damage through Up-Regulation of Interleukin-32 Expression in Hepatitis B Virus-Related Acute-On-Chronic Liver Failure. *PLoS One 10*(8), e0134568.

444. El-Far, M., M. Durand, I. Turcotte, E. Larouche-Anctil, M. Sylla, S. Zaidan, C. Chartrand-Lefebvre, R. Bunet, H. Ramani, M. Sadouni, I. Boldeanu, A. Chamberland, S. Lesage, J.-G. Baril, B. Trottier, R. Thomas, E. Gonzalez, A. Filali-Mouhim, J.-P. Goulet, J. A. Martinson, S. Kassaye, R. Karim, J. R. Kizer, A. L. French, S. J. Gange, P. Ancuta, J.-P. Routy, D. B. Hanna, R. C. Kaplan, N. Chomont, A. L. Landay, and C. L. Tremblay. (2021). Upregulated IL-32 Expression And Reduced Gut Short Chain Fatty Acid Caproic Acid in People Living With HIV With Subclinical Atherosclerosis. *Front. Immunol. 12*, 1235.

445. Bai, X., S.-H. Kim, T. Azam, M. T. McGibney, H. Huang, C. A. Dinarello, and E. D. Chan. (2010). IL-32 Is a Host Protective Cytokine against Mycobacterium tuberculosis in Differentiated THP-1 Human Macrophages. *J. Immunol. 184*(7), 3830–3840.

446. Bai, X., S. Shang, M. Henao-Tamayo, R. J. Basaraba, A. R. Ovrutsky, J. L. Matsuda, K. Takeda, M. M. Chan, A. Dakhama, W. H. Kinney, J. Trostel, A. Bai, J. R. Honda, R. Achcar, J. Hartney, L. A. B. Joosten, S.-H. Kim, I. Orme, C. A. Dinarello, D. J. Ordway, and E. D. Chan. (2015). Human IL-32 expression protects mice against a hypervirulent strain of Mycobacterium tuberculosis. *Proc. Natl. Acad. Sci. U. S. A. 112*(16), 5111–5116.

447. Zepp, J. A., C. A. Nold-Petry, C. A. Dinarello, and M. F. Nold. (2011). Protection from RNA and DNA Viruses by IL-32. *J. Immunol. 186*(7), 4110–4118.

448. Rasool, S. T., H. Tang, J. Wu, W. Li, M. M. Mukhtar, J. Zhang, Y. Mu, H. X. Xing, J. Wu, and Y. Zhu. (2008). Increased level of IL-32 during human immunodeficiency virus infection suppresses HIV replication. *Immunol. Lett. 117*(2), 161–167.

449. Bang, B.-R., H.-S. Kwon, S.-H. Kim, S.-Y. Yoon, J.-D. Choi, G. H. Hong, S. Park, T.-B. Kim, H.-B. Moon, and Y. S. Cho. (2014). Interleukin-32γ Suppresses Allergic Airway Inflammation in Mouse Models of Asthma. *Am. J. Respir. Cell Mol. Biol. 50*(6), 1021–1030.

450. McCarthy, N. E., Z. Bashir, A. Vossenkämper, C. R. Hedin, E. M. Giles, S. Bhattacharjee, S. G. Brown, T. J. Sanders, K. Whelan, T. T. MacDonald, J. O. Lindsay, and A. J. Stagg. (2013). Proinflammatory Vδ2+ T Cells Populate the Human Intestinal Mucosa and

Enhance IFN-γ Production by Colonic αβ T Cells. *J. Immunol. 191*(5), 2752–2763.
451. McCarthy, N. E., C. R. Hedin, T. J. Sanders, P. Amon, I. Hoti, I. Ayada, V. Baji, E. M. Giles, M. Wildemann, Z. Bashir, K. Whelan, I. Sanderson, J. O. Lindsay, and A. J. Stagg. (2015). Azathioprine therapy selectively ablates human Vδ2+ T cells in Crohn's disease. *J. Clin. Invest. 125*(8), 3215–3225.
452. Amini, A., D. Pang, C.-P. Hackstein, and P. Klenerman. (2020). MAIT Cells in Barrier Tissues: Lessons from Immediate Neighbors. *Front. Immunol. 11*, 3040.
453. Toia, F., S. Buccheri, A. Anfosso, F. Moschella, F. Dieli, S. Meraviglia, and A. Cordova. (2016). Skewed Differentiation of Circulating Vγ9Vδ2 T Lymphocytes in Melanoma and Impact on Clinical Outcome. *PLoS One 11*(2), e0149570.
454. Eberl, M. (2020). Antigen recognition by human γδ T cells: one step closer to knowing. *Immunol. Cell Biol. 98*(5), 351–354.
455. Rigau, M., S. Ostrouska, T. S. Fulford, D. N. Johnson, K. Woods, Z. Ruan, H. E. G. McWilliam, C. Hudson, C. Tutuka, A. K. Wheatley, S. J. Kent, J. A. Villadangos, B. Pal, C. Kurts, J. Simmonds, M. Pelzing, A. D. Nash, A. Hammet, A. M. Verhagen, G. Vairo, E. Maraskovsky, C. Panousis, N. A. Gherardin, J. Cebon, D. I. Godfrey, A. Behren, and A. P. Uldrich. (2020). Butyrophilin 2A1 is essential for phosphoantigen reactivity by gd T cells. *Science 367*(6478), eaay5516.
456. Fergusson, J. R., J. E. Ussher, A. Kurioka, P. Klenerman, and L. J. Walker. (2018). High MDR-1 expression by MAIT cells confers resistance to cytotoxic but not immunosuppressive MDR-1 substrates. *Clin. Exp. Immunol. 194*(2), 180–191.
457. Turtle, C. J., H. M. Swanson, N. Fujii, E. H. Estey, and S. R. Riddell. (2009). A Distinct Subset of Self-Renewing Human Memory CD8+ T Cells Survives Cytotoxic Chemotherapy. *Immunity 31*(5), 834–844.
458. Deroost, K., and J. Langhorne. (2018). Gamma/Delta T Cells and Their Role in Protection Against Malaria. *Front. Immunol. 9*, 2973.
459. Wang, H., Z. Chen, J. McCluskey, and A. J. Corbett. (2021). Mouse models illuminate MAIT cell biology. *Mol. Immunol. 130*, 55–63.
460. Yu, K. K. Q., D. B. Wilburn, J. A. Hackney, P. A. Darrah, K. E. Foulds, C. A. James, M. T. Smith, L. Jing, R. A. Seder, M. Roederer, D. M. Koelle, W. J. Swanson, and C. Seshadri. (2019). Conservation of molecular and cellular phenotypes of invariant NKT cells between humans and non-human primates. *Immunogenetics 71*(7), 465–478.
461. Ren, Y., E. Sekine-Kondo, M. Tateyama, T. Kasetthat, S. Wongratanacheewin, and H. Watarai. (2018). New Genetically Manipulated Mice Provide Insights Into the Development and Physiological Functions of Invariant Natural Killer T Cells. *Front. Immunol. 9*, 1294.
462. Wen, X., P. Rao, L. J. Carreño, S. Kim, A. Lawrenczyk, S. A. Porcelli, P. Cresswell, and W. Yuan. (2013). Human CD1d knock-in mouse model demonstrates potent antitumor potential of human CD1d-restricted invariant natural killer T cells. *Proc. Natl. Acad. Sci. U. S. A. 110*(8), 2963–2968.
463. Nowak, M., and I. G. H. Schmidt-Wolf. (2011). Natural Killer T Cells Subsets in Cancer, Functional Defects in Prostate Cancer and Implications for Immunotherapy. *Cancers 3*(3), 3661–3675.
464. Masopust, D., C. P. Sivula, and S. C. Jameson. (2017). Of Mice, Dirty Mice, and Men: Using Mice To Understand Human Immunology. *J. Immunol. 199*(2), 383–388.

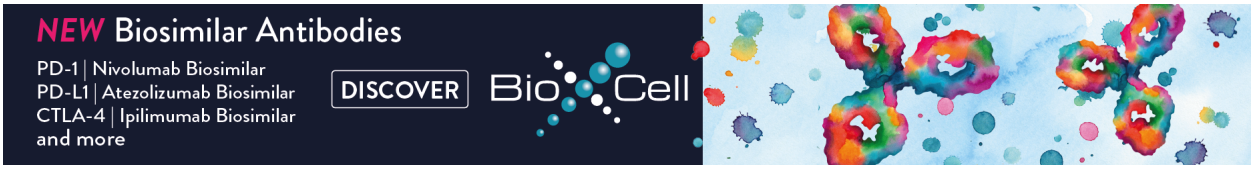
LIST OF PUBLICATIONS

- **Hagel JP,** Bennett K, Buffa F, Klenerman P, Willberg CB, Powell K (2021). Defining T Cell Subsets in Human Tonsils Using ChipCytometry. *J Immunol*. 206(12), 3073–3082.

- **Hagel JP**, Garner LC, Bilton M, Mehta H, Leng T, Hackstein CP, Phalora P, Amini A, Akther HD, Provine NM, Edmans M, Willberg CB, Klenerman P (2020). Human MAIT Cell Activation In Vitro. In *MAIT Cells. Methods in Molecular Biology*, vol. 2098. (H. Kaipe, I. Magalhaes, and J. M. Walker, eds). Humana, New York. 97–124

- Leng T, Akther HD, Hackstein CP, Powell K, King T, Friedrich M, Christoforidou Z, McCuaig S, Neyazi M, Arancibia-Cárcamo CV, **Hagel J**, Powrie F; Oxford IBD Investigators, Peres RS, Millar V, Ebner D, Lamichhane R, Ussher J, Hinks TSC, Marchi E, Willberg C, Klenerman P (2019). TCR and Inflammatory Signals Tune Human MAIT Cells to Exert Specific Tissue Repair and Effector Functions. *Cell Rep*. 28(12), 3077–3091.e5.

- Zinser ME, Highton AJ, Kurioka A, Kronsteiner B, **Hagel J**, Leng T, Marchi E, Phetsouphanh C, Willberg CB, Dunachie SJ, Klenerman P (2018). Human MAIT cells show metabolic quiescence with rapid glucose-dependent upregulation of granzyme B upon stimulation. *Immunol Cell Biol*. 96(6), 666–674.



The Journal of Immunology

Defining T Cell Subsets in Human Tonsils Using ChipCytometry

Joachim P. Hagel, Kyle Bennett, Francesca Buffa, Paul Klenerman, Christian B. Willberg and Kate Powell

This information is current as of January 8, 2022.

J Immunol 2021; 206:3073-3082; Prepublished online 7 June 2021;
doi: 10.4049/jimmunol.2100063
http://www.jimmunol.org/content/206/12/3073

Supplementary Material **http://www.jimmunol.org/content/suppl/2021/06/07/jimmunol.2100063.DCSupplemental**

References This article **cites 44 articles**, 5 of which you can access for free at:
http://www.jimmunol.org/content/206/12/3073.full#ref-list-1

Why *The JI*? Submit online.

- **Rapid Reviews! 30 days*** from submission to initial decision
- **No Triage!** Every submission reviewed by practicing scientists
- **Fast Publication!** 4 weeks from acceptance to publication

**average*

Subscription Information about subscribing to *The Journal of Immunology* is online at:
http://jimmunol.org/subscription

Permissions Submit copyright permission requests at:
http://www.aai.org/About/Publications/JI/copyright.html

Author Choice Freely available online through *The Journal of Immunology* Author Choice option

Email Alerts Receive free email-alerts when new articles cite this article. Sign up at:
http://jimmunol.org/alerts

The Journal of Immunology is published twice each month by
The American Association of Immunologists, Inc.,
1451 Rockville Pike, Suite 650, Rockville, MD 20852
Copyright © 2021 The Authors All rights reserved.
Print ISSN: 0022-1767 Online ISSN: 1550-6606.

Downloaded from http://www.jimmunol.org/ by guest on January 8, 2022

Defining T Cell Subsets in Human Tonsils Using ChipCytometry

Joachim P. Hagel,* Kyle Bennett,* Francesca Buffa,[†,1] Paul Klenerman,[*,‡,§,1] Christian B. Willberg,[*,‡,1] and Kate Powell,[*,1]

ChipCytometry is a multiplex imaging method that can be used to analyze either cell suspensions or tissue sections. Images are acquired by iterative cycles of immunostaining with fluorescently labeled Abs, followed by photobleaching, which allows the accumulation of multiple markers on a single sample. In this study, we explored the feasibility of using ChipCytometry to identify and phenotype cell subsets, including rare cell types, using a combination of tissue sections and single-cell suspensions. Using ChipCytometry of tissue sections, we successfully demonstrated the architecture of human palatine tonsils, including the B and T cell zones, and characterized subcompartments such as the B cell mantle and germinal center zone, as well as intrafollicular PD1-expressing $CD4^+$ T cells. Additionally, we were able to identify the rare tonsillar T cell subsets, mucosal-associated invariant T (MAIT) and γδ-T cells, within tonsil tissue. Using single-cell suspension ChipCytometry, we further dissected human tonsillar T cell subsets via unsupervised clustering analysis as well as supervised traditional manual gating. We were able to show that $PD1^+CD4^+$ T cells are comprised of $CXCR5^+BCL6^{high}$ follicular Th cells and $CXCR5^-BCL6^{mid}$ pre–follicular Th cells. Both supervised and unsupervised analysis approaches identified MAIT cells in single-cell suspensions, confirming a phenotype similar to that of blood-derived MAIT cells. In this study, we demonstrate that ChipCytometry is a viable method for single-cell suspension cytometry and analysis, with the additional benefit of allowing phenotyping in a spatial context using tissue sections. ***The Journal of Immunology*****, 2021, 206: 3073–3082.**

Many novel technologies have recently emerged for multiparameter cytometry analysis of cells and tissues, offering the exciting prospect of visualizing cellular phenotyping within a spatial context. These methods use a variety of immunostaining methodologies applied to fluorescence microscopy or mass spectrometry imaging techniques to acquire information on the expression of multiple markers. Each method has its own advantages and disadvantages. For example, the number of markers that can be assessed on a single sample, the sample processing time and throughput, the commercial availability of reagents, operating costs, and system purchasing costs are system specific (1–5).

ChipCytometry is an imaging-based multiplex-immunophenotyping method in which samples, either cell suspensions or tissue sections, are immobilized on slides inside a microfluidic chip (6). Through consecutive and iterative cycles of staining with fluorophore-labeled Abs, imaging and subsequent photobleaching, a theoretically unlimited number of markers can be measured on a single sample. Advantages of ChipCytometry over other methods include that samples are preserved after analysis and can be stored for at least 20 mo without significant degradation (7). This allows reanalysis with additional markers or sample collection and storage at different sites with subsequent centralized analysis. In addition, the development of a panel of markers is relatively straightforward using standard flow cytometry Abs. Combinations of up to five fluorophores can be used for each cycle.

To explore the feasibility of using ChipCytometry for immunephenotyping, we employed lymphoid palatine tonsil tissue, as it is very rich in immune cells and has a well-established and distinct architecture. Palatine tonsils are secondary lymphoid tissues that belong to the Waldeyer's ring, which further includes the adenoids and tubal and lingual tonsils (8, 9). They are located at the transition between the mouth and oropharynx and are a part of the mucosal-associated lymphoid tissues (10, 11). The tonsils are covered by an epithelium that increases the tonsil surface by forming crypts in which specialized cells can take up Ag and transport it to subepithelial areas where it can get in contact with immune cells (10, 12). The immune cells are organized in two major zones within the tonsils: B cell follicles and the extrafollicular region in which T cells and B cells become activated. Lymphoid follicles contain B cells and are therefore characterized by CD19 expression. Primary lymphoid follicles do not have a germinal center (13). Secondary lymphoid follicles consist of a mantle zone including naive (IgD^+CD10^-) B cells; they also contain a germinal center including germinal center (IgD^-CD10^+) B cells (14, 15). Germinal centers are places of B cell proliferation, differentiation, and maturation (13). Besides B cells, lymphoid follicles also contain a network of stromal-derived follicular dendritic cells, which are important for Ag presentation to B cells (16). Additionally, B cell follicles contain T cells that are critical for the humoral immune response (17). The extrafollicular region (also called the T cell zone) contains T cells that are primarily $CD4^+$ T cells with fewer $CD8^+$ T cells. Besides T cells, the extrafollicular region includes interdigitating dendritic cells, macrophages, and high-endothelial venules. The latter are

*Peter Medawar Building for Pathogen Research, Nuffield Department of Medicine, University of Oxford, Oxford, United Kingdom; [†]Computational Biology and Integrative Genomics, Department of Oncology, University of Oxford, Oxford, United Kingdom; [‡]NIHR Biomedical Research Centre, John Radcliffe Hospital, Oxford University Hospitals NHS Foundation Trust, Oxford, United Kingdom; and [§]Translational Gastroenterology Unit, Nuffield Department of Medicine, University of Oxford, Oxford, United Kingdom

[1]F.B., P.K., C.B.W., and K.P. are joint last authors.

ORCIDs: 0000-0002-9952-1812 (J.P.H.); 0000-0003-0220-9097 (K.B.); 0000-0003-0409-406X (F.B.); 0000-0003-4307-9161 (P.K.); 0000-0001-5299-9344 (C.B.W.); 0000-0002-1826-953X (K.P.).

Received for publication January 22, 2021. Accepted for publication April 15, 2021.

This work was supported in whole or in part by the Wellcome Trust (WT109965MA). This work was also supported by the NIHR Senior Fellowship (to P.K.), the John Fell Fund, the Laidlaw Foundation, and the Human Immune Discovery Initiative Oxford.

Address correspondence and reprint requests to Prof. Paul Klenerman and Joachim P. Hagel, Peter Medawar Building for Pathogen Research, University of Oxford, South Parks Road, Oxford OX1 3SY, U.K. E-mail addresses: paul.klenerman@medawar.ox.ac.uk (P.K.) and joachim.hagel@ndm.ox.ac.uk (J.P.H.)

The online version of this article contains supplemental material.

Abbreviations used in this article: DN, double negative; GZMB, Granzyme B; MAIT, mucosal-associated invariant T; SOM, self-organizing map; TFH, follicular Th; TIFF, tagged image file format; *t*-SNE, *t*-distributed stochastic neighbor embedding.

This article is distributed under the terms of the CC BY 4.0 Unported license.

Copyright © 2021 The Authors

Downloaded from http://www.jimmunol.org/ by guest on January 8, 2022

specialized venules that allow circulating lymphocytes to enter the lymphoid tissue (13).

Tonsillar $CD4^+$ T cell subsets can be divided into three major groups (18). Most intrafollicular T cells belong to the follicular B helper T cell group (follicular Th [TFH], $CD4^+PD1^+CXCR5^+BCL6^{high}$) (17, 18). B cell and TFH interactions are crucial for the formation of the humoral immune response and support B cell somatic hypermutation and Ab class switching (17, 19). Other tonsillar $CD4^+$ T cell subsets include non-TFH ($CD4^+PD1^-CXCR5^-BCL6^{low}$) and pre-TFH ($CD4^+PD1^+CXCR5^-BCL6^{mid}$). Pre-TFH cells develop from activated Ag-specific $CD4^+$ T cells. The transcriptional program that is initiated in pre-TFH cells can induce CXCR5 expression, enabling the cells to migrate toward the B cell follicle (18, 20).

Most $CD4^+$ and $CD8^+$ T cells that enter palatine tonsils are naive cells competing for Ag to reach maturity (10, 13), but there are also unconventional T cell subsets found within the tonsil, for example, innate-like T cells including mucosal-associated invariant T (MAIT) cells and γδ-T cells (21–23). MAIT cells are memory-type and Ag-experienced cells with peripheral tissue homing properties (24, 25). They are characterized by their semi-invariant TCR that recognizes microbial-derived riboflavin metabolites presented by a conserved MHC class I–like molecule called MR1 (26, 27). MAIT cells can, however, also be activated in a TCR-independent manner by cytokines such as IL-12, IL-18, and IL-15 (28, 29). Most MAIT cells are $CD8^+$ or double negative (DN) in blood. They can be identified by tetramer staining or using a combination of markers including Vα7.2 and CD161 (30, 31). MAIT cells also express the innate-like marker CD218a (IL-18Rα) and the transcription factor PLZF (31). MAIT cell selection and development begin in the thymus, and MAIT cells are thought to acquire their memory Ag-experienced phenotype via contact with microbes in the periphery (32). MAIT cell frequencies in tonsil are ∼10 times lower than in blood (21). MAIT cell responses play multiple roles in infection, inflammation, and cancer (29, 33, 34).

To establish the utility of the ChipCytometry technique, using both cell suspensions and tissue sections, we aimed to depict the general tonsil architecture, showing different tonsillar regions and subcompartments. We localized and phenotyped immune subsets including follicular $CD4^+$ T cell subsets and rarer immune cells such as MAIT cells and finally analyzed data obtained from ChipCytometry of cell suspensions for more stringent phenotyping of immune subsets.

Materials and Methods

Tissues and cells

Human tonsillar tissue was obtained from routine tonsillectomies collected by the Translational Gastroenterology Unit Biobank, John Radcliffe Hospital (Oxford, U.K.) following informed consent under approved study protocol 16/YH/O247. Tissue sections were prepared by snap-freezing samples in OCT cutting medium (OCT embedding matrix; CellPath) and cryosectioning onto glass coverslips. Single-cell suspensions were prepared by mechanical disruption of tonsil samples. Human blood samples were obtained from the National Health Service Blood and Transplant, John Radcliffe Hospital. PBMCs were isolated from on a Lymphoprep gradient (STEMCELL Technologies) according to the manufacturer's instructions.

ChipCytometry of cell suspensions

Tonsil-derived $CD3^+$ T cells were isolated by positive selection from single-cell suspensions using magnetic CD3 Microbeads (Miltenyi Biotec) and treated with Human TruStain FcX (BioLegend) to block unwanted Fc receptor–mediated staining. Cells from different donors were barcoded with anti-CD45 Abs (pan–leukocyte marker) coupled to FITC, PE, or PerCP-Cy5.5 to allow analysis of multiple donors on a single chip. Barcodes consisted of different single anti-CD45 stains or combinations of differently labeled anti-CD45 Abs. The CXCR5 Ab does not recognize fixed epitope, and therefore, staining was performed simultaneously with CD45 barcode staining for 5 min at 4°C. Donor-derived cells were mixed and loaded into cell suspension chips (ZellSafe Cells – Chips; Zellkraftwerk, Leipzig, Germany), allowed to adhere to the chip surface for 10 min at room temperature, then nonadhered cells were washed off with PBS. The initial acquisition, performed with the ChipCytometer (Zellscanner ONE; Zellkraftwerk), included barcodes and CXCR5 stain. Samples were fixed (fixation buffer; Zellkraftwerk) for 5 min at room temperature, and subsequent markers were acquired in iterative rounds of photobleaching, staining, and imaging. FITC-, PE-, or PerCP/PerCP-Cy5.5–coupled Abs were applied in mixes (up to three per round). Surface Abs were incubated for 10 min at room temperature. For intracellular markers, True-Nuclear Transcription Factor Buffer Set (BioLegend) was used as follows: chips were rinsed and incubated with permeabilization buffer for 1 h, followed by rinsing and incubation with fixation buffer for 1 further h before finally washing with permeabilization buffer. Ab mixes for intracellular staining were prepared in permeabilization buffer and incubated for 30 min (all permeabilization and staining steps performed at room temperature). The following 19 markers were applied to the samples: BCL6, CD3, CD4, CD8, CD19, CD44, CD45, CD45RA, CD56, CD69, CD161, CXCR5, FASL, FOXP3, Granzyme B (GZMB), ICOS, IL-18Rα (CD218a), PD1, and Vα7.2. For Ab details, please see Tables I and II.

ChipCytometry of tissue sections

Cryosections were cut directly onto poly-L-lysine– or APES-coated coverslips (Sigma-Aldrich) and fixed immediately using freshly prepared 0.1 M phosphate-buffered 4% paraformaldehyde (Sigma-Aldrich) or Zellkraftwerk

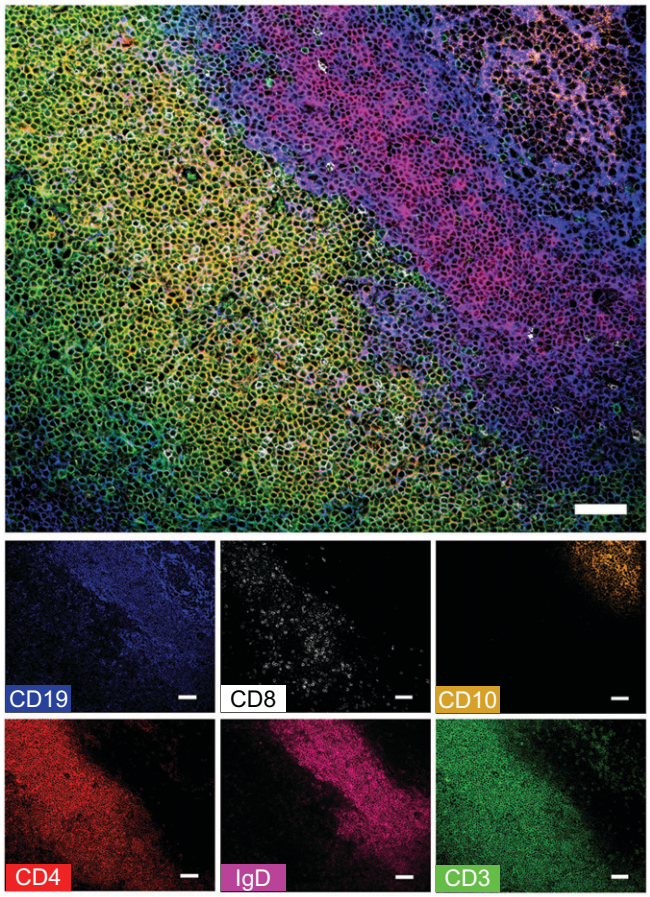


FIGURE 1. Human tonsil architecture resolved using ChipCytometry. Sections of paraformaldehyde-fixed human tonsil tissue mounted in microfluidic chips were immunostained in consecutive runs using a panel of 12 fluorochrome-labeled Abs. The top image was compiled by selecting six markers: CD19 (blue), CD8 (white), CD10 (orange), CD4 (red), IgD (magenta), and CD3 (green), assigning colors arbitrarily from the lookup table and merging to form a composite image. Expression of individual markers is shown in the small panels. The B cell zone (B cell follicle) is characterized by CD19 expression, in which IgD outlines the mantle zone containing IgD-expressing naive B cells, and CD10 outlines the germinal center containing $CD10^+$ germinal center B cells. Adjacent to the B cell zone, CD3 expression outlines the T cell zone (extrafollicular zone), including $CD4^+$ and $CD8^+$ T cells. Scale bars, 50 μm.

Downloaded from http://www.jimmunol.org/ by guest on January 8, 2022

fixation buffer (Zellkraftwerk) for 10 min at room temperature. After washing in PBS, sections on coverslips were assembled into tissue chips (ZellSafe Tissue – Chips; Zellkraftwerk), which were immediately filled with PBS or storage buffer (Zellkraftwerk). Before use, the storage buffer was washed out of the chip with ∼5 ml of PBS. Tonsil sections were initially blocked by incubating in 3% normal goat serum with 2% BSA (Thermo Fisher Scientific) in PBS for at least 1 h at room temperature. Immunostaining was performed at room temperature for 30 min using 0.5 ml of diluted Ab solution per chip. Ab mixtures were diluted in PBS alone or PBS containing 2% BSA or 2% normal goat serum. A total of 12 markers were acquired in iterative rounds of photobleaching, staining, and imaging: CD3, CD4, CD8, CD10, CD19, CD161, γδTCR, IgD, PD1, PLZF, Vα7.2, and histone H3 (not shown). For Ab details please see Table III.

Flow cytometry

Cells were stained with a viability dye (LIVE/DEAD Fixable Near-IR Dead Cell Stain Kit; Invitrogen) and fluorochrome-labeled Abs for 30 min at 4°C. The following Abs were used: CD3–eFluor 450 (OKT3; eBioscience), CD8-VioGreen (BW135/80; Miltenyi Biotec), γδTCR-FITC (5A6.E9; Invitrogen), CD161-PE and CD161-APC (191B8; Miltenyi Biotec), Vδ2-PerCP-Cy5.5 (B6; BioLegend), CD56–PE-Cy7 (HCD56; BioLegend), Vα7.2-APC and Vα7.2-PerCP-Cy5.5 (3C10; BioLegend), CCR7-FITC (G043H7), and CD62L-PE (DREG-56; BioLegend). Data were acquired by a MACSQuant Analyzer 10 (Miltenyi Biotec).

Data processing and statistical methods

Flow cytometry and ChipCytometry data were analyzed using FlowJo (versions 10.6.2 and 10.7.1; Beckton Dickinson), and bar charts were generated using GraphPad Prism software (version 8.4.3). For supervised manual gating analysis of flow cytometry and ChipCytometry data, biexponential transformation was applied in FlowJo. For unsupervised clustering analysis, ChipCytometry cell suspension data were first transformed and preprocessed in FlowJo and then exported to R (RStudio version 1.2.5042 and R version 3.6.2). The data were transformed using HyperLog transformation. The parameters of this transformation were adjusted, and rescaling was performed so that for each marker, the distribution spanned the whole dynamic range. The transformed data were binned into integer histogram channels ranging from 0 to 1023. Outliers and fluorescence anomalies outside the axis limits after transformation were assigned to either the minimum or maximum value. All datapoints with an assigned value of 0 or 1023 after the transformation were removed from further analysis. An exception was made for CXCR5, which was transformed using logarithmic transformation, because suitable rescaling could not be achieved with HyperLog in FlowJo. Data were preprocessed by excluding $CD19^+$ cells and gating on $CD3^+$ cells in FlowJo. FlowSOM R package (version 1.18.0) (35) was used to identify cell clusters within the dataset using all markers except for CD45, which was used for barcoding, and CD3 and CD19, as these were used for gating during preprocessing. Parameters chosen were self-organizing map (SOM) grid = 10 × 10 and seed = 1234. The resulting SOM nodes were used in the R package ConsensusClusterPlus (1.50.0) to obtain the final optimal clusters (36). A delta area plot was created with a maximum of $k = 20$ metaclusters, which indicated cluster stability at a metacluster number of $k = 12$. Cluster information for 12 metaclusters was exported, and data were further analyzed in FlowJo for visualization, including *t*-distributed stochastic neighbor embedding (*t*-SNE) analysis (fast Fourier transform–accelerated interpolation-based *t*-SNE, iteration: 3000, perplexity: 50, *k*-nearest neighbors algorithm: exact, and learning rate: auto [optimized *t*-SNE]). For cluster characterization, the distribution of the intensity of each marker was considered in each cluster and the median value taken (median marker expression). This was displayed as heatmap using pheatmap package (version 1.0.12). In addition to comparing median marker expression directly, Marker Enrichment Modeling was performed for cluster characterization using the R package Marker Enrichment Modeling (version 2.0.0) (37, 38).

Image processing

Images for publication were downloaded from the ChipCytometer as 16-bit uncompressed tagged image file format (TIFF) files and converted to 8-bit per channel RGB TIFF files in ImageJ/Fiji (version 1.5). Scale bars were added in Adobe Photoshop CS4 according to the metadata stored with the image. Images were cropped, annotations (arrows, text, etc.) were added, and brightness and contrast adjusted as necessary in Photoshop. Files were exported as flattened 300 dpi TIFF files with Lempel–Ziv–Welch compression. Files of each image processing stage were saved.

Results

Defining tonsillar architecture in humans using tissue ChipCytometry

A panel of 12 Abs was employed to establish the anatomy of the palatine tonsil by ChipCytometry. A combination of T cell markers (CD3, CD4, and CD8) and B cell markers (CD19, CD10, and IgD) were chosen to depict general palatine tonsil architecture (Fig. 1, Supplemental Figs. 1A, 2A). Specifically, the lymphoid follicle zone (B cell zone) was defined by CD19 expression and could be further characterized by the differential expression of IgD and CD10. Naive B cells (IgD^+CD10^-) are mainly located in the B cell mantle zone, and germinal center B cells (IgD^-CD10^+) are located in the B cell germinal center zone (14, 15). The extrafollicular zone (T cell zone) adjacent to the B cell zone was defined by CD3 expression. $CD3^+$ T cells included CD4-expressing and CD8-expressing cells. A few $CD3^+$ T cells could also be found within the B cell zone.

Identification of CD4 T cell subsets in human tonsils

From the full panel of 12 markers, a combination of CD3, CD4, PD1, and CD19 staining was chosen to identify palatine tonsillar T cell subsets expressing PD1 (Fig. 2, Supplemental Figs. 1B, 2B). CD3 expression was concentrated within the extrafollicular T cell zone; however, we were also able to identify some intrafollicular $CD3^+$ T cells. Many of those T cells were $CD4^+$ and $PD1^+$. A few rare $CD4^+PD1^+$ T cells could also be found within the extrafollicular region (T cell zone). Tonsillar $CD3^+CD4^+PD1^+$ T cells most likely include pre-TFH and TFH subsets (18) as opposed to $CD3^+CD4^+PD1^-$ cells that most likely include non-TFH cells. Examples of some of the many $CD3^+CD4^+PD1^+$ T cells are indicated in Fig. 2 and Supplemental Fig. 1B by white arrowheads.

Identification and phenotyping of tonsillar CD3 T cell subsets by cell suspension ChipCytometry

To identify and phenotype tonsillar CD3 T cell subsets, cell suspensions produced by dissociation of human palatine tonsil tissue were enriched for $CD3^+$ T cells ($n = 4$). Cells from each donor were barcoded with CD45 Abs coupled to different fluorochromes, allowing individual donors to be distinguished in the pooled samples. A staining

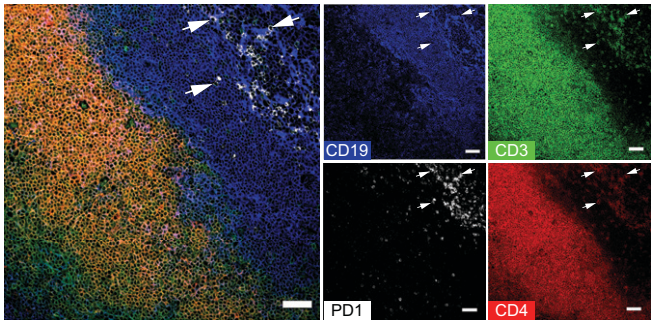


FIGURE 2. Identification of $CD4^+$ T cell subsets in human tonsils. A combination of CD4, CD19, CD3, and PD1 were chosen from the full marker panel to identify $CD4^+$ T cells in the tonsil. The large multicolor composite image shows a merged image of CD19 (blue), CD3 (green), PD1 (white), and CD4 (red), whereas the smaller images demonstrate the expression of each marker individually. The T cell zone is characterized by CD3 expression and includes $CD4^+$ T cells; $CD3^+CD4^+$ cells appear yellow/orange in combination. PD1-expressing $CD3^+CD4^+$ are predominantly located in the B cell zone, but a few are also located in the T cell zone. This subset most likely includes prefollicular (pre-TFH) and TFH cells. $CD3^+CD4^+PD1^-$ cells are predominantly located in the extrafollicular region and include non-TFH cells. Arrowheads indicate examples of $CD3^+CD4^+PD1^+$ cells. Scale bars, 50 μm.

Downloaded from http://www.jimmunol.org/ by guest on January 8, 2022

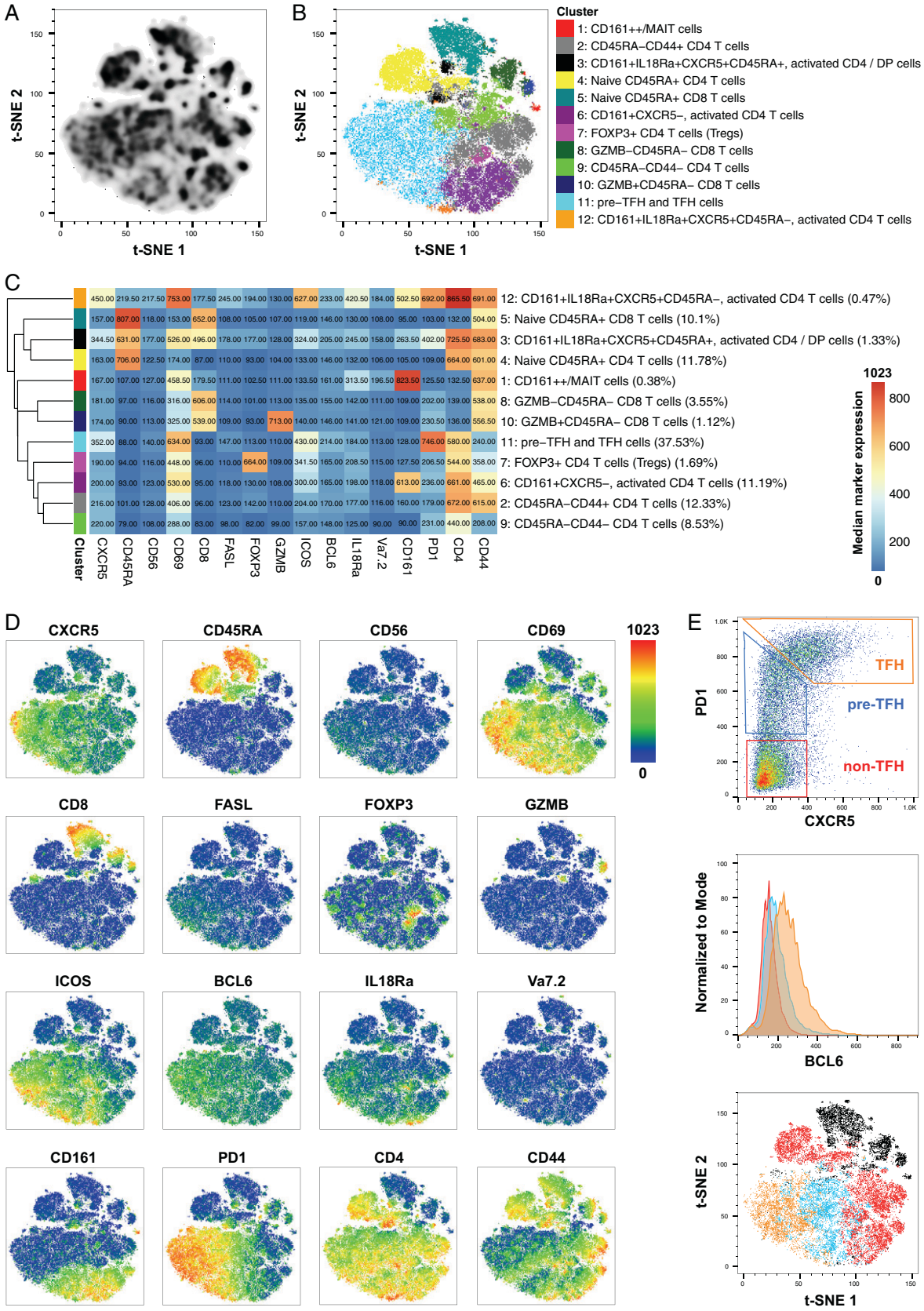


FIGURE 3. Phenotyping of tonsil-derived, CD3-enriched cells by cell suspension ChipCytometry. Four human tonsils were processed to single-cell suspensions, positively enriched for $CD3^+$ T cells, barcoded, loaded onto a microfluidic chip, fixed, and subsequently analyzed by ChipCytometry with a panel of 19 fluorochrome-labeled Abs. (**A**) Density plot shows *t*-SNE analysis of concatenated samples, including all $CD3^+CD19^-$ cells. (**B**) Clusters that were identified via FlowSOM were projected onto the *t*-SNE coordinates and color coded as indicated. (**C**) A heatmap showing median marker intensities within each cell cluster was generated to characterize cell clusters and derive cell labels. The heatmap color represents median marker expression across all four aggregated samples. (**D**) T-SNE plots show the expression of 16 markers within the aggregated samples. (**E**) Top panel, *(Figure legend continues)*

Downloaded from http://www.jimmunol.org/ by guest on January 8, 2022

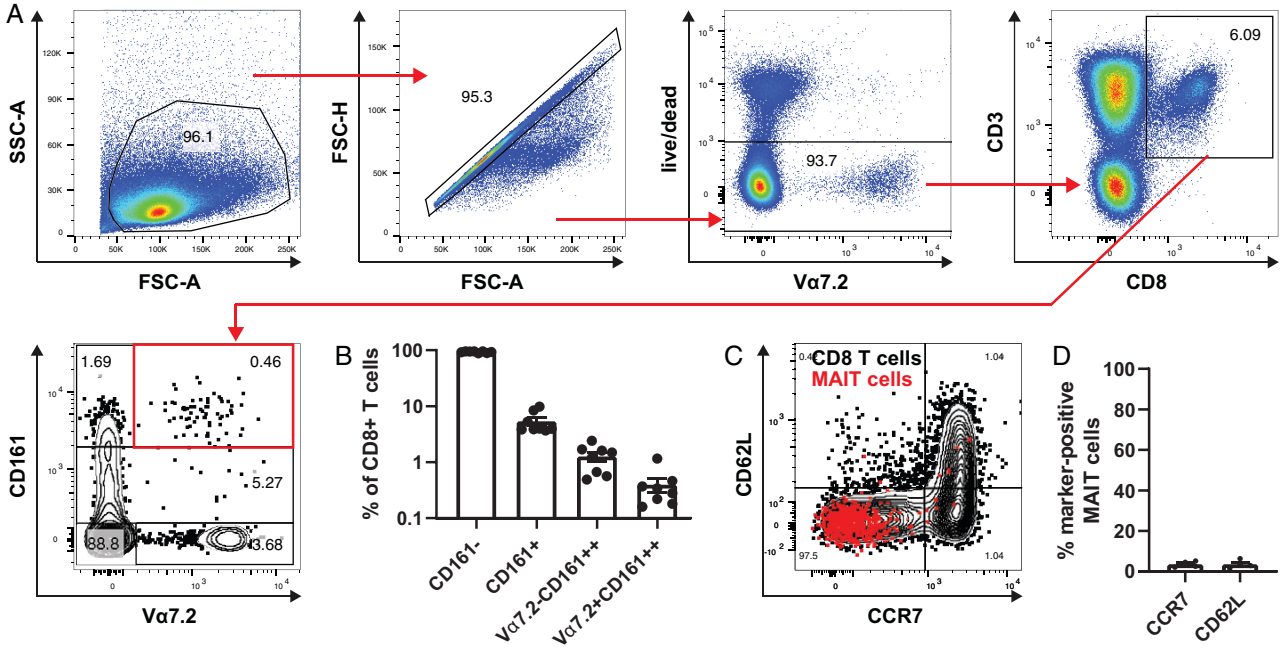


FIGURE 4. Flow cytometry identifies $CD8^+$ MAIT cells as a rare subset within human tonsils. Human tonsils were processed to single-cell suspensions and analyzed by flow cytometry. Stains included LIVE/DEAD Fixable dye, CD3, CD8, Vα7.2, CD161, CCR7, and CD62L. (**A**) Gating strategy is shown to identify $CD8^+$ MAIT cells ($Vα7.2^+CD161^{++}$) within tonsils. (**B**) Enumeration of CD8 T cell subsets (eight tonsils from six donors). (**C**) CCR7 and CD62 expression of total CD8 T cells (black) and MAIT cells (red). The flow cytometry plot is representative of four biological replicates. (**D**) Enumeration of CCR7 and CD62L expressing MAIT cells ($n = 4$).

panel consisting of the following 19 markers was used: BCL6, CD3, CD4, CD8, CD19, CD44, CD45, CD45RA, CD56, CD69, CD161, CXCR5, FASL, FOXP3, GZMB, ICOS, IL-18Rα (CD218a), PD1, and Vα7.2. T cell subsets were identified via unsupervised clustering using FlowSOM, a method based on SOM clustering (35, 39), and visualized using *t*-SNE (Fig. 3A). ConsensusClusterPlus was used to estimate the optimal number of clusters within the dataset, and FlowSOM clustering was performed into 12 groups (Fig. 3B). As the process for labeling cell clusters is not established, we applied a layered approach for cluster labeling using median marker expression together with Marker Enrichment Modeling in a semisupervised manner in addition to gating in FlowJo (Fig. 3C, Supplemental Fig. 3A, 3B). The identified $CD3^+$ T cell subsets included various $CD4^+$ T cell subsets, $CD8^+$ T cell subsets, and unconventional, innate-like T cell subsets such as MAIT cells. We found one naive $CD4^+CD45RA^+$ T cell subset (cluster 4) and two $CD4^+CD45RA^-$ subsets that differed in regard to CD44 expression (cluster 2 = $CD44^+$ and cluster 9 = $CD44^-$). Each of these subsets comprised ∼10% of total T cells. Additionally, we found three subsets that contained $CD4^+$ T cells expressing CD161, which is a marker generally associated with innate-like and memory cell types (40). Those were $CD161^+CXCR5^-CD69^+ICOS^+CD45RA^-$ (cluster 6, ∼10% of total T cells), $CD161^+CXCR5^+IL\text{-}18Rα^+CD69^+PD1^+ICOS^+CD45RA^-$ (cluster 12, 0.47% of total T cells), and $CD161^+CXCR5^+IL\text{-}18Rα^+CD69^+PD1^+ICOS^+CD45RA^+$ (cluster 3, 1.33% of total T cells). The latter included, besides $CD4^+$ T cells, a substantial fraction of double-positive T cells and showed lower levels of CD161, CXCR5, IL-18Rα, CD69, PD1, and ICOS expression compared with cluster 12. Other $CD4^+$ T cell subsets included $FOXP3^+$ cells, which represent the T regulatory cell population (cluster 7, 1.69% of total T cells) and prefollicular/follicular CD4 Th cells (cluster 11, $CD4^+CXCR5^{+/-}PD1^+ICOS^+CD69^+$), which comprised 37.53% of total T cells. In addition to CD4 T cell subsets, we found a naive $CD8^+CD45RA^+$ subset (cluster 5, ∼10% of total T cells) and two $CD8^+CD45RA^-$ subsets, of which one was $GZMB^+$ (cluster 10, 1.12% of total T cells), and the other was $GZMB^-$ (cluster 8, 3.55% of total T cells), respectively. We also found a cluster that contained $CD161^{++}$ T cells, including MAIT cells ($CD161^{++}Vα7.2^{+/-}IL\text{-}18Rα^+CD69^+$, cluster 1, 0.38% of total T cells), which were either $CD8^+$ or DN. The expression of the 16 phenotyping markers that were used for clustering are displayed on *t*-SNE plots in Fig. 3D.

We further analyzed the dataset via manual gating to elaborate on the characterization of PD1-expressing and follicular CD4 T cell subsets. We stratified $CD4^+$ T cells according to PD1 and CXCR5 expression (Fig. 3E), as previously shown by Thornhill et al. (18). The subsets included $CXCR5^+PD1^+$ TFH, $CXCR5^-PD1^+$ pre-TFH, and $CXCR5^-PD1^-$ non-TFH cells. These cell types differed in BCL6 expression; TFH cells had the highest levels of BCL6 expression, pre-TFH intermediate levels of BCL6 expression, and non-TFH the lowest levels of BCL6 expression. These three CD4 subsets also segregated on the *t*-SNE plot. With our characterization of tonsil-derived CD4 T cell subsets, we were able to replicate results previously described in the literature by Thornhill et al. (18).

Identifying rarer T cell subsets in tonsils by tissue ChipCytometry including MAIT cells and γδ-T cells

Next, we aimed to identify and phenotype rare cell subsets within palatine tonsillar tissue. MAIT cells have been described as a rare

Within $CD4^+$ T cells, the subsets TFH, pre-TFH, and non-TFH cells were identified according to expression of CXCR5 and PD1. Center panel, BCL6 expression is shown within non-TFH (red), pre-TFH (blue), and TFH (orange) cell subsets in human tonsils. Bottom panel, T-SNE plot shows non-TFH (red), pre-TFH (blue), TFH (orange), and non-CD4 T cells (black). Plots in (E) are derived from one donor and are representative of four donors.

Downloaded from http://www.jimmunol.org/ by guest on January 8, 2022

cell subset within human palatine tonsil tissue (21, 22). We could confirm this by the analysis of eight palatine tonsils of six different donors using flow cytometry (Fig. 4A, 4B). MAIT cells were defined as $CD3^+CD8^+V\alpha7.2^+CD161^{++}$. The frequency of MAIT cells ranged from ~0.1 to 1% of total CD8 T cells. This is 10-fold lower compared with blood (41). Interestingly, palatine tonsillar MAIT cells did not show typical lymphoid tissue homing marker expression CCR7 and CD62L (Fig. 4C, 4D).

We were able to identify $CD8^+$ MAIT cells in palatine tonsil tissue sections by ChipCytometry using a combination of CD3, CD8, Vα7.2, CD161, PLZF, and CD19 markers (Fig. 5, Supplemental Fig. 4). MAIT cells were identified as $CD3^+V\alpha7.2^+CD161^+PLZF^+$ cells. In Fig. 5, all MAIT cells were $CD8^+$ and were located within the T cell zone and adjacent to the B cell zone (indicated by white arrows). In Supplemental Fig. 4, we found $CD8^+$ as well as $CD8^-$ MAIT cells (a few examples are indicated by white arrows) side by side with another relatively rare tonsillar innate-like T cell subset, the γδ-T cells (white arrows with asterisk). Interestingly, MAIT as well as γδ-T cells were not only found within the T cell zone in the second example, but a few also adjacent and within the $CD19^+$ area.

Identification and phenotyping of human tonsillar MAIT cells by cell suspension ChipCytometry

Besides the identification of $CD161^{++}$/MAIT cells within CD3-enriched tonsil-derived single-cell suspensions via unsupervised clustering (Fig. 3B, 3C, Supplemental Fig. 3), we also identified and phenotyped MAIT cells by a traditional manual gating approach using the same dataset (Fig. 6A–F). After de-barcoding of the different donors (Fig. 6A), MAIT cells were identified using the following gating strategy (Fig. 6B, 6C): first, we gated on $CD19^-CD3^+$ T cells, and within this gate $CD4^+$, $CD8^+$, and DN T cell subsets were identified. Within each of those subsets, MAIT cells were defined as $V\alpha7.2^+CD161^{++}$, and their frequencies were determined. The MAIT cell frequencies within the $CD8^+$ T cells were similar to the frequencies observed in the flow cytometry experiment (Fig. 4A, 4B). Using ChipCytometry, we identified ~6-fold higher frequency of tonsillar DN MAIT cells than tonsillar $CD8^+$ MAIT cells (Fig. 6D); however, we did not observe any considerable frequencies of $CD4^+$ MAIT cells. By determining the frequencies of MAIT cells expressing different phenotyping markers, we found that $CD8^+$ and DN MAIT cells shared a similar phenotype (Fig. 6E, 6F). Most MAIT cells were $CD69^+$, indicating an activated phenotype. In addition, most MAIT cells were $CD45RA^-CD44^+$, indicating a memory and Ag-experienced phenotype. MAIT cells also expressed high levels of IL-18Rα, and ~30% of MAIT cells expressed the costimulatory receptor ICOS. There was a very small fraction of $FASL^+$ and $GZMB^+$ MAIT cells, however. MAIT cells were considered negative for BCL6, CXCR5, PD1, and FOXP3. In summary, we found that tonsillar MAIT cells have an activated memory phenotype ($CD44^+CD45RA^-CD69^+ICOS^+$) and express typical innate-associated markers such as IL-18Rα. This correlates well with the generally accepted phenotype of MAIT cells described in the literature (40–42).

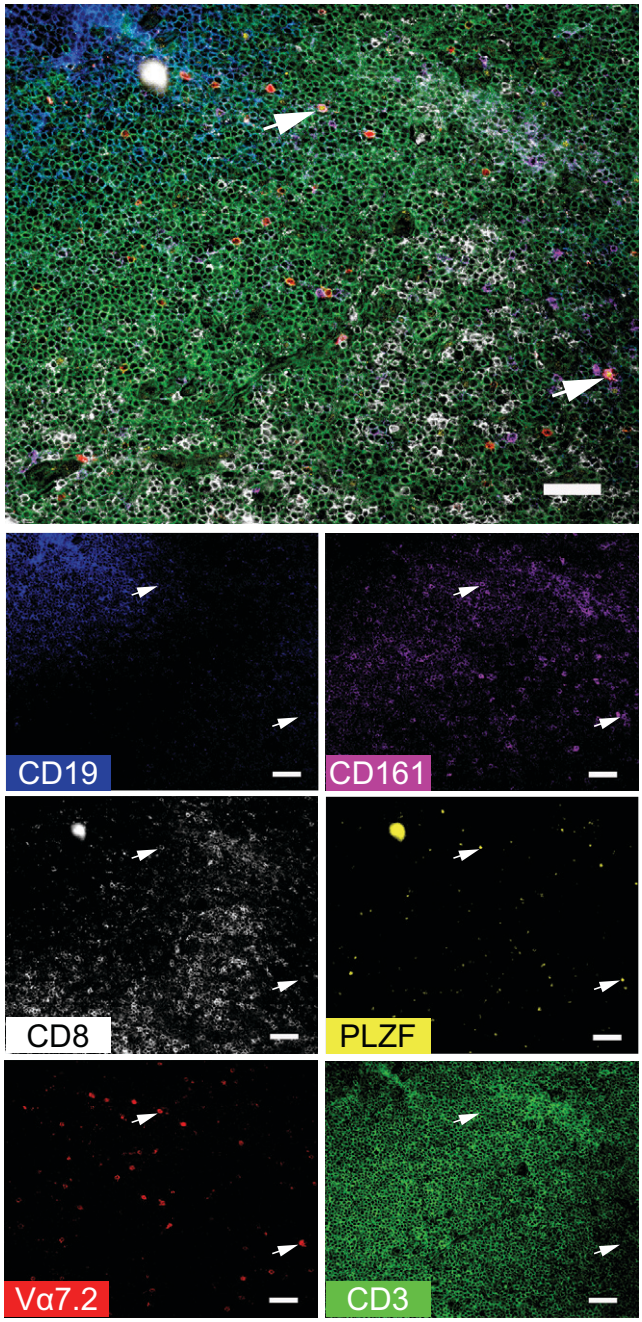


FIGURE 5. Identification of rare immune subsets in human tonsils. A combination of Vα7.2 (shown in red), CD8 (white), CD161 (magenta), PLZF (yellow), CD3 (green), and CD19 (blue) markers were selected from the available panel to illustrate the presence of MAIT cells within the tonsil. Single-color images demonstrate the expression of each marker individually, whereas the larger image shows a merged composite of all six markers. Arrowheads indicate examples of cells that coexpress CD3, CD8, Vα7.2, CD161, and PLZF, which represent $CD8^+$ MAIT cells. During the iterative staining process, dust particles can be introduced into the microfluidic chip, generating autofluorescent artifacts such as those seen in this study at the top left of the CD8, PLZF, and merged images. Scale bars, 50 μm.

Discussion

We have demonstrated, using the palatine tonsil as a test case, that ChipCytometry is a viable method that combines the power of traditional cytometry with the spatial information available from tissue sections. Using this method, we were able to demonstrate the immune cell compartments of the palatine tonsil, including the B cell zone with its subcompartments of naive (IgD^+CD10^-) and germinal center (IgD^-CD10^+) B cells and the T cell zone (Fig. 1, Supplemental Figs. 1A, 2A). Within the $CD3^+$ T cell compartment, we could identify multiple T cell subsets, for example $CD4^+PD1^+$ T cells, most of which were located within the $CD19^+$ B cell zone, with a few cells present within the T cell zone (Fig. 2, Supplemental Figs. 1B, 2B). We performed more stringent phenotyping of tonsillar T cells using cell suspension ChipCytometry and identified two subtypes of $CD4^+PD1^+$ cells including pre-TFH ($CD4^+PD1^+$

Downloaded from http://www.jimmunol.org/ by guest on January 8, 2022

$CXCR5^{-}BCL6^{mid}$) and TFH ($CD4^{+}PD1^{+}CXCR5^{+}BCL6^{high}$) cells, which were distinct from non-TFH ($CD4^{+}PD1^{-}CXCR5^{-}BCL6^{low}$) cells (Fig. 3E). TFH cells are a specialized immune subset that is crucial for forming protective immunity by providing T cell help to B cells (17, 19). We were able to demonstrate that ChipCytometry is sufficiently sensitive to identify very rare palatine tonsillar immune subsets such as the innate-like T cell subset MAIT cells. We identified and located MAIT cells in tissue sections (Fig. 5, Supplemental Fig. 4) and could further phenotype them using single-cell suspension ChipCytometry (Fig. 6). We confirmed that tonsillar MAIT cells have an activated, memory-like, and innate-like phenotype similar to that seen in blood-derived MAIT cells. Additionally, we identified a second innate-like T cell subset, the γδ-T cells, distributed alongside MAIT cells and located predominately in the T cell zone but with a few cells scattered within the $CD19^{+}$ B cell zone (Fig. 5, Supplemental Fig. 4). Besides manual and supervised identification of compartments and cell types (Figs. 3E, 6), we successfully performed unsupervised clustering using FlowSOM to identify different cell types that are included in the cell suspension ChipCytometry dataset (Fig. 3A–D), which is an analysis strategy similar to what has been used for similar data obtained from other methods such as mass cytometry (35, 39). We identified 12 cell groups within the $CD3^{+}$

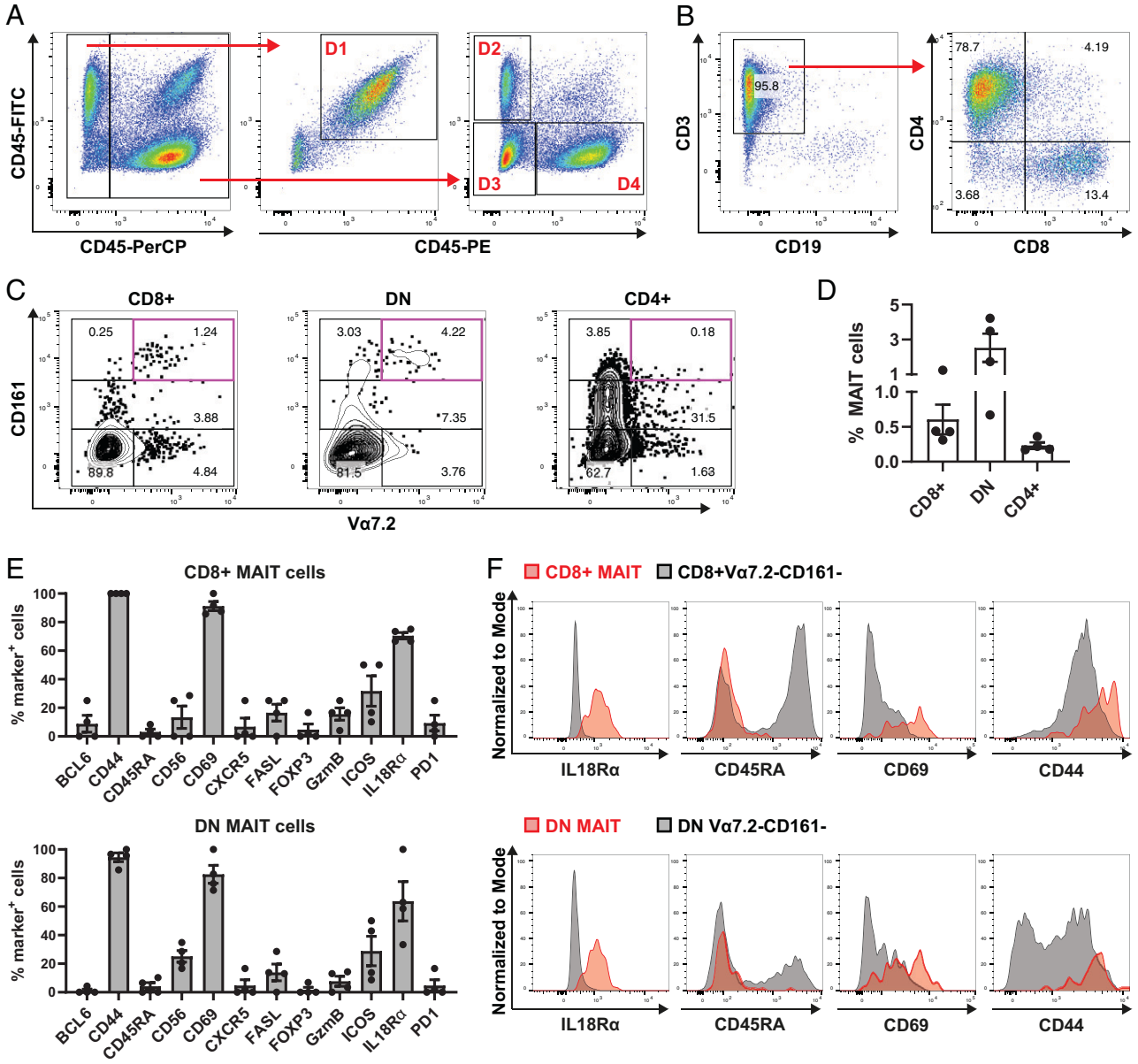


FIGURE 6. Identification and phenotyping of tonsillar MAIT cells using cell suspension ChipCytometry. Cell suspensions of four human tonsils were enriched for $CD3^{+}$ cells and analyzed by ChipCytometry with a panel of 19 fluorochrome-labeled Abs. (**A**) Pooled samples were de-barcoded to identify different donors. Barcodes consisted of combinations of CD45 Abs that were labeled with different fluorochromes. Donor 1 (D1) = $PerCP^{-}FITC^{+}PE^{+}$; donor 2 (D2) = $PerCP^{+}FITC^{+}PE^{-}$, donor 3 (D3) = $PerCP^{+}FITC^{-}PE^{-}$, and donor 4 (D4) = $PerCP^{+}FITC^{-}PE^{+}$. (**B**) The following gating strategy was applied to identify MAIT cells: first, we gated on $CD3^{+}CD19^{-}$ cells. Within this gate, subpopulations according to CD4 and CD8 expression were defined, including $CD4^{+}$, $CD8^{+}$, and DN T cells. (**C**) Within each T cell subset, MAIT cells were identified by Vα7.2 and $CD161^{++}$ expression. (**D**) Enumeration of MAIT cells within T cell subsets. (**E**) Phenotype of $CD8^{+}$ and DN MAIT cells. (**F**) Representative plots of IL-18Rα, CD45RA, CD69, and CD44 expression by $CD8^{+}$ and DN MAIT cells (red) compared with $Vα7.2^{-}CD161^{-}$ conventional T cells within $CD8^{+}$ and DN T cells, respectively.

Downloaded from http://www.jimmunol.org/ by guest on January 8, 2022

Table I. Extracellular markers for ChipCytometry cell suspension staining

	Marker	Clone	Label	Manufacturer
1	CD3	UCHT 1	PerCP-Cy5.5	BioLegend
2	CD4	RPA-T4	FITC	BioLegend
3	CD8α	SK1	PerCP-Cy5.5	BioLegend
4	CD19	LT19	PE	Miltenyi Biotec
5	CD44	DB105	PE	Miltenyi Biotec
6	CD45	HI30	FITC, PE, PerCP	BioLegend
7	CD45RA	HI100	PerCP-Cy5.5	BioLegend
8	CD56*	AF12-7H3	PE	Miltenyi Biotec
9	CD69	FN50	PE	BioLegend
10	CD161	191B8	PE	Miltenyi Biotec
11	CD178 (FASL)*	NOK-1	PE	BioLegend
12	CD185 (CXCR5)	J252D4	BV421	BioLegend
13	CD218a (IL-18Ra)*	H44	PE	BioLegend, eBioscience
14	CD278 (ICOS)	C398.4A	PerCP-Cy5.5	BioLegend
15	CD279 (PD-1)	eBioJ105	PE	eBioscience
16	TCR Vα7.2	3C10	PE	BioLegend

Markers that are sensitive toward repeated cycles of photobleaching are indicated with an asterisk and should be stained early in the process.

tonsillar T cells, including expected cell types such as pre-TFH/TFH cells and $CD161^{++}$/MAIT cells. The grouping of $V\alpha7.2^{-}CD161^{++}$ cells with MAIT cells in one cluster confirms that they share a similar phenotype (40). The FlowSOM algorithm partitioned some cell types based on the heterogenous expression of a single marker (e.g., CD44 within $CD4^{+}CD45RA^{-}$ cells or GZMB within $CD8^{+}CD45RA^{-}$ cells). Clustering into fewer, but potentially biologically more meaningful cell groups can be achieved by performing manual merging of similar clusters, as suggested by Nowicka et al. (39). Direct FlowSOM clustering into a smaller number of clusters can be problematic. First, cluster stability could suffer, and second, there is the danger that not all expected and rare cell types would be detected (39).

The examples above outline the advantages of ChipCytometry in which multiplex tissue cytometry data, including phenotyping and spatial information from intact tissue, can be combined with cell suspension data that include phenotyping information on a single-cell level. Multiple adjacent positions of a tissue section can be scanned and stitched together to obtain a relatively large image for analysis (theoretically up to a limit of 1×2 cm^2) (Supplemental Fig. 2). In addition, the method allows users to acquire a theoretically unlimited number of markers on a single sample (6).

The ChipCytometry technique uses directly labeled primary Abs that are commercially widely available for flow cytometry. Panel design is straightforward, as no or little compensation is required. Imaging for each fluorochrome in an Ab mixture is performed sequentially for each fluorochrome at each position. Samples are preserved after analysis and can be stored up to 20 mo without significant biomarker degradation (7). This allows reanalysis of samples even after project completion or sample collection and processing and storage on different sites with subsequent centralized analysis.

As ChipCytometry includes two imaging steps, pre- and poststaining, some correction can be made for autofluorescence by the subtraction of the background from the poststaining image. Further advantages of ChipCytometry in comparison with alternative methods include a greater resolution limit of 500 nm as opposed to 1000 nm for imaging mass cytometry, and wider dynamic range (eight decades versus two to three decades in conventional fluorescence microscopy). ChipCytometry also has a higher scannable area than imaging mass cytometry (1×2 cm^2 versus 1 mm^2) (5, 6).

There are, however, some limitations to the ChipCytometry technique. This method is a serial and iterative process in which Abs from each subsequent round of staining are left in place and the signal is removed by photobleaching. In theory, issues due to steric hindrance could, therefore, be anticipated. Despite the highly multiplexed nature of ChipCytometry, we have not yet encountered any issues due to steric hindrance beyond any well-known Ab pairs from other applications such as flow cytometry or mass cytometry. An example is steric hindrance between the Ab pair Vδ2 clone B6 and γδTCR clone 11F2 (43).

Another factor is the negative impact of repeated photobleaching cycles on Ag integrity, most likely caused by photodamage of proteins that can absorb high-energy light in the UV region (44). A device upgrade from the manufacturer consisting of a longpass filter that blocks damaging UV in the white light filter module during the photobleaching process was provided to mitigate the destructive effect of repeated photobleaching cycles. Further mitigation can be accomplished by limiting the use of dyes to fluorochromes with a higher excitation wavelength (FITC, PE, and PerCP) and photobleaching only through their respective filters instead of using the universal white light filter module for photobleaching. Although these precautions generally minimize the destructive effect of repeated photobleaching, particular sensitive epitopes need to be stained early in the process. This requires, however, that each new epitope is tested to determine its relative sensitivity before its consideration in panel design. Sensitive markers applied in the panels of this study are indicated with an asterisk in Tables I–III.

Because of the optimization required, we find that ChipCytometry has a relatively slow sample throughput. In addition, each position on a sample chip is scanned one after another, and staining is performed in a serial iterative process. Sample throughput of cell suspensions can be increased using barcodes, which allows simultaneous analysis of multiple pooled samples as shown in Fig. 6A. This approach limits, however, the maximum cell number per sample. Alternatively, sample throughput can no doubt be increased substantially through the use of automated ChipCytometry systems.

In summary, ChipCytometry is a viable and versatile method for immunophenotyping for both tissue sections as well as cell suspensions. We were able to show the general palatine tonsil architecture including immune compartments and localize and phenotype immune subsets, including very rare immune cell types. ChipCytometry overcomes some technical and practical

Table II. Intracellular markers for ChipCytometry cell suspension staining

	Marker	Clone	Label	Manufacturer
1	BCL6	REA373	PE	Miltenyi Biotec
2	GZMB	GB11	PE	eBioscience
3	FOXP3	259D/C7	PE	BD Biosciences

Downloaded from http://www.jimmunol.org/ by guest on January 8, 2022

Table III. Markers for ChipCytometry tissue section staining

	Marker	Clone	Label	Manufacturer
1	CD3	UCHT1	PerCP	BioLegend
2	CD4	RPA-T4	PerCP	BioLegend
3	CD8	SK1	FITC	BioLegend
4	CD10	HI10a	PE	BioLegend
5	CD19	LT19	PerCP	ExBio
6	CD161	HP-3G10	PE	eBioscience
7	CD279 (PD-1)	eBioJ105	PE	eBioscience
8	IgD	IA6-2	PerCP	BioLegend
9	Histone H3	17H2L9	AF488	Invitrogen
10	PLZF	R17-809	PE	BD Pharmingen
11	TCR-γ/δ (γδTCR)	5A6.E9	FITC, PE	Life Technologies
12	TCR Vα7.2	3C10	PE	BioLegend

AF488, Alexa Fluor 488.

method–specific limitations of other similar methods, although it has a relatively low throughput and requires substantial stain-specific optimization. This approach does lend itself to specific applications in immunology research through multistain imaging of specific immune subsets, which require multiple markers for definition, especially when applied in parallel with current high-content analysis of cell suspensions and single-cell RNA sequencing approaches.

Acknowledgments

We acknowledge the Translational Gastroenterology Unit Biobank (John Radcliffe Hospital) and National Health Service Blood and Transplant (John Radcliffe Hospital) for collecting and making available the samples used in the generation of this article.

Disclosures

The authors have no financial conflicts of interest.

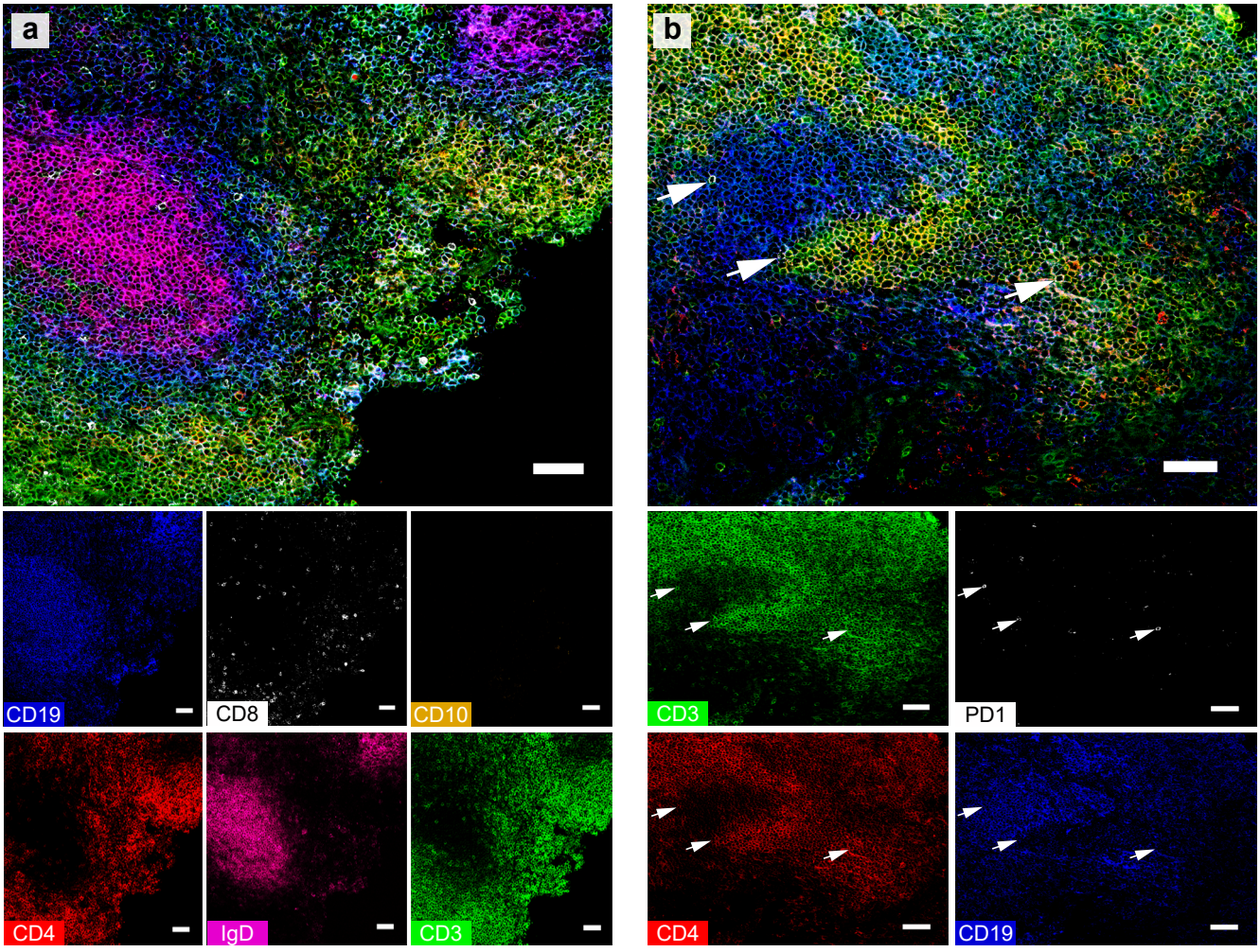
References

1. Parra, E. R. 2018. Novel platforms of multiplexed immunofluorescence for study of paraffin tumor tissues. *J. Cancer Treatment Diagn.* 2: 43–53.
2. Parra, E. R., A. Francisco-Cruz, and I. I. Wistuba. 2019. State-of-the-art of profiling immune contexture in the era of multiplexed staining and digital analysis to study paraffin tumor tissues. *Cancers (Basel)* 11: 247.
3. Francisco-Cruz, A., E. R. Parra, M. T. Tetzlaff, and I. I. Wistuba. 2020. Multiplex immunofluorescence assays. In *Biomarkers for Immunotherapy of Cancer: Methods and Protocols, Methods in Molecular Biology*. M. Thurin, A. Cesano, and F. M. Marincola, eds. Vol. 2055. Humana Press Inc., Totowa, NJ, p. 467–495.
4. Yaghoobi, V., S. Martinez-Morilla, Y. Liu, L. Charette, D. L. Rimm, and M. Harigopal. 2020. Advances in quantitative immunohistochemistry and their contribution to breast cancer. *Expert Rev. Mol. Diagn.* 20: 509–522.
5. Tan, W. C. C., S. N. Nerurkar, H. Y. Cai, H. H. M. Ng, D. Wu, Y. T. F. Wee, J. C. T. Lim, J. Yeong, and T. K. H. Lim. 2020. Overview of multiplex immunohistochemistry/immunofluorescence techniques in the era of cancer immunotherapy. *Cancer Commun. (Lond.)* 40: 135–153.
6. Hennig, C., N. Adams, and G. Hansen. 2009. A versatile platform for comprehensive chip-based explorative cytometry. *Cytometry A* 75: 362–370.
7. Hümmert, M. W., S. Alvermann, S. Gingele, C. C. Gross, H. Wiendl, A. Mirenska, C. Hennig, and M. Stangel. 2018. Immunophenotyping of cerebrospinal fluid cells by Chipcytometry. *J. Neuroinflammation* 15: 160.
8. Von Waldeyer-Hartz, W. 1884. Ueber den lymphatischen apparat des pharynx. In *Deutsche Medizinische Wochenschrift*, Vol. 10. P. Boerner, ed. Georg Reimer Verlag, Berlin, p. 313.
9. Perry, M., and A. Whyte. 1998. Immunology of the tonsils. *Immunol. Today* 19: 414–421.
10. Nave, H., A. Gebert, and R. Pabst. 2001. Morphology and immunology of the human palatine tonsil. *Anat. Embryol. (Berl.)* 204: 367–373.
11. Scadding, G. K. 1990. Immunology of the tonsil: a review. *J. R. Soc. Med.* 83: 104–107.
12. Gebert, A., and R. Pabst. 1999. M cells at locations outside the gut. *Semin. Immunol.* 11: 165–170.
13. Brandtzaeg, P. 2015. Immunobiology of the tonsils and adenoids. In *Mucosal Immunology*, 4th Ed. Vol. 2. J. Mestecky, W. Strober, M. W. Russell, B. L. Kelsall, H. Cheroutre, and B. N. Lambrecht, eds. Elsevier, Amsterdam, p. 1985–2016.
14. Kwak, K., H. Sohn, J. Brzostowski, J. Manzella-Lapeira, and S. K. Pierce. 2016. Human tonsil naive B cells and germinal center B cells show distinct behaviors upon contact of antigen in lipid bilayers. *J. Immunol.* 196 (Suppl. 1): 195.8.
15. Liu, Y. J., O. de Bouteiller, C. Arpin, F. Brière, L. Galibert, S. Ho, H. Martinez-Valdez, J. Banchereau, and S. Lebecque. 1996. Normal human IgD+IgM- germinal center B cells can express up to 80 mutations in the variable region of their IgD transcripts. *Immunity* 4: 603–613.
16. Kranich, J., and N. J. Krautler. 2016. How follicular dendritic cells shape the B-cell antigenome. *Front. Immunol.* 7: 225.
17. Crotty, S. 2011. Follicular helper CD4 T cells (TFH). *Annu. Rev. Immunol.* 29: 621–663.
18. Thornhill, J. P., S. Fidler, P. Klenerman, J. Frater, and C. Phetsouphanh. 2017. The role of CD4+ T follicular helper cells in HIV infection: from the germinal center to the periphery. *Front. Immunol.* 8: 46.
19. Breitfeld, D., L. Ohl, E. Kremmer, J. Ellwart, F. Sallusto, M. Lipp, and R. Förster. 2000. Follicular B helper T cells express CXC chemokine receptor 5, localize to B cell follicles, and support immunoglobulin production. *J. Exp. Med.* 192: 1545–1552.
20. Liu, X., X. Chen, B. Zhong, A. Wang, X. Wang, F. Chu, R. I. Nurieva, X. Yan, P. Chen, L. G. van der Flier, et al. 2014. Transcription factor achaete-scute homologue 2 initiates follicular T-helper-cell development. *Nature* 507: 513–518.
21. Radcliff, F. J., S. Waldvogel-Thurlow, F. Clow, M. Mahadevan, J. Johnston, G. Li, T. Proft, R. G. Douglas, and J. D. Fraser. 2019. Impact of superantigen-producing bacteria on T cells from tonsillar hyperplasia. *Pathogens* 8: 90.
22. Lepore, M., A. Kalinichenko, A. Colone, B. Paleja, A. Singhal, A. Tschumi, B. Lee, M. Poidinger, F. Zolezzi, L. Quagliata, et al. 2014. Parallel T-cell cloning and deep sequencing of human MAIT cells reveal stable oligoclonal TCRβ repertoire. [Published erratum appears in 2014 *Nat. Commun.* 5: 4493.] *Nat. Commun.* 5: 3866.
23. Kawaguchi, T. 1993. [Gamma delta T cells in the palatine tonsil–immunohistological and functional study]. *Nippon Jibiinkoka Gakkai Kaiho* 96: 810–817.
24. Billerbeck, E., Y.-H. Kang, L. Walker, H. Lockstone, S. Grafmueller, V. Fleming, J. Flint, C. B. Willberg, B. Bengsch, B. Seigel, et al. 2010. Analysis of CD161 expression on human CD8+ T cells defines a distinct functional subset with tissue-homing properties. *Proc. Natl. Acad. Sci. USA* 107: 3006–3011.
25. Dusseaux, M., E. Martin, N. Serriari, I. Péguillet, V. Premel, D. Louis, M. Milder, L. Le Bourhis, C. Soudais, E. Treiner, and O. Lantz. 2011. Human MAIT cells are xenobiotic-resistant, tissue-targeted, CD161hi IL-17-secreting T cells. *Blood* 117: 1250–1259.
26. Tilloy, F., E. Treiner, S. H. Park, C. Garcia, F. Lemonnier, H. de la Salle, A. Bendelac, M. Bonneville, and O. Lantz. 1999. An invariant T cell receptor alpha chain defines a novel TAP-independent major histocompatibility complex class Ib-restricted alpha/beta T cell subpopulation in mammals. *J. Exp. Med.* 189: 1907–1921.
27. Kjer-Nielsen, L., O. Patel, A. J. Corbett, J. Le Nours, B. Meehan, L. Liu, M. Bhati, Z. Chen, L. Kostenko, R. Reantragoon, et al. 2012. MR1 presents microbial vitamin B metabolites to MAIT cells. *Nature* 491: 717–723.
28. Ussher, J. E., M. Bilton, E. Attwod, J. Shadwell, R. Richardson, C. de Lara, E. Mettke, A. Kurioka, T. H. Hansen, P. Klenerman, and C. B. Willberg. 2014. CD161++ CD8+ T cells, including the MAIT cell subset, are specifically activated by IL-12+IL-18 in a TCR-independent manner. *Eur. J. Immunol.* 44: 195–203.
29. van Wilgenburg, B., I. Scherwitzl, E. C. Hutchinson, T. Leng, A. Kurioka, C. Kulicke, C. de Lara, S. Cole, S. Vasanawathana, W. Limpitikul, et al; STOP-HCV consortium. 2016. MAIT cells are activated during human viral infections. *Nat. Commun.* 7: 11653.
30. Reantragoon, R., A. J. Corbett, I. G. Sakala, N. A. Gherardin, J. B. Furness, Z. Chen, S. B. G. Eckle, A. P. Uldrich, R. W. Birkinshaw, O. Patel, et al. 2013. Antigen-loaded MR1 tetramers define T cell receptor heterogeneity in mucosal-associated invariant T cells. *J. Exp. Med.* 210: 2305–2320.
31. Gherardin, N. A., M. N. Souter, H.-F. Koay, K. M. Mangas, T. Seemann, T. P. Stinear, S. B. Eckle, S. P. Berzins, Y. d'Udekem, I. E. Konstantinov, et al. 2018. Human blood MAIT cell subsets defined using MR1 tetramers. *Immunol. Cell Biol.* 96: 507–525.
32. Koay, H.-F., D. I. Godfrey, and D. G. Pellicci. 2018. Development of mucosal-associated invariant T cells. *Immunol. Cell Biol.* 96: 598–606.
33. Ussher, J. E., P. Klenerman, and C. B. Willberg. 2014. Mucosal-associated invariant T-cells: new players in anti-bacterial immunity. *Front. Immunol.* 5: 450.
34. Lukasik, Z., D. Elewaut, and K. Venken. 2020. Mait cells come to the rescue in cancer immunotherapy? *Cancers (Basel)* 12: 413.
35. Van Gassen, S., B. Callebaut, M. J. Van Helden, B. N. Lambrecht, P. Demeester, T. Dhaene, and Y. Saeys. 2015. FlowSOM: Using self-organizing maps for visualization and interpretation of cytometry data. *Cytometry A* 87: 636–645.
36. Wilkerson, M. D., and D. N. Hayes. 2010. ConsensusClusterPlus: a class discovery tool with confidence assessments and item tracking. *Bioinformatics* 26: 1572–1573.
37. Diggins, K. E., A. R. Greenplate, N. Leelatian, C. E. Wogsland, and J. M. Irish. 2017. Characterizing cell subsets using marker enrichment modeling. *Nat. Methods* 14: 275–278.
38. Diggins, K. E., J. S. Gandelman, C. E. Roe, and J. M. Irish. 2018. Generating quantitative cell identity labels with Marker Enrichment Modeling (MEM). *Curr. Protoc. Cytom.* 83: 10.21.1–10.21.28.
39. Nowicka, M., C. Krieg, H. L. Crowell, L. M. Weber, F. J. Hartmann, S. Guglietta, B. Becher, M. P. Levesque, and M. D. Robinson. 2017. CyTOF workflow: differential discovery in high-throughput high-dimensional cytometry datasets. *F1000 Res.* 6: 748.

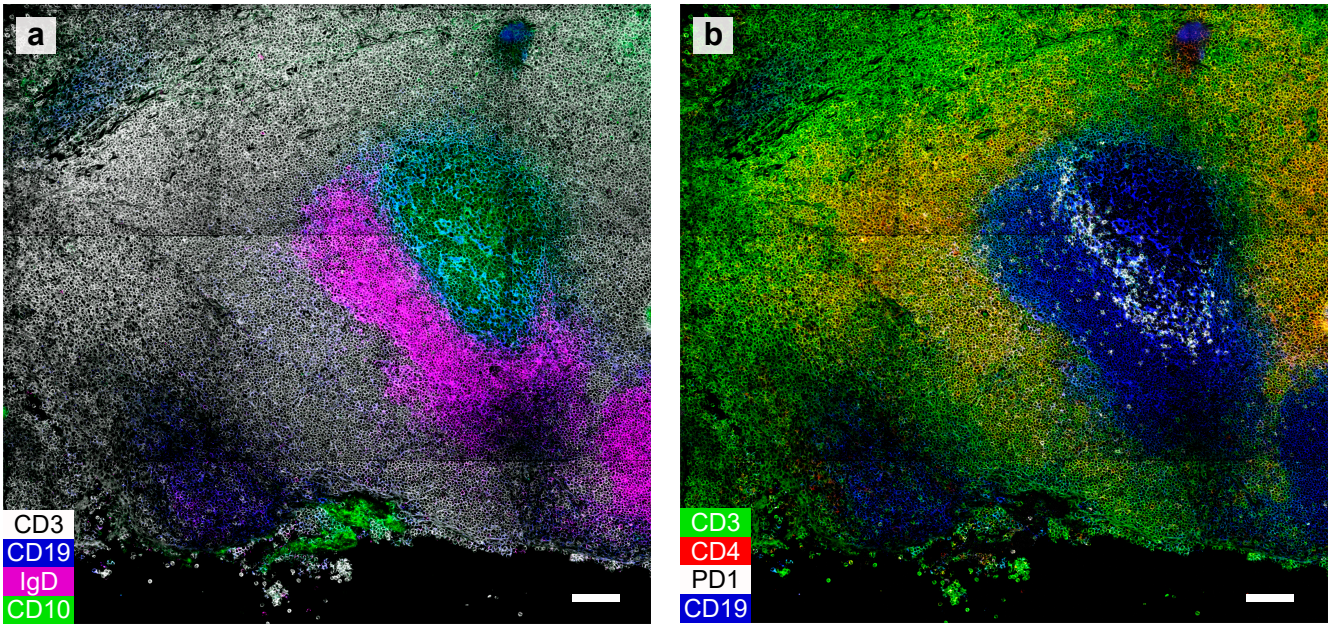
Downloaded from http://www.jimmunol.org/ by guest on January 8, 2022

40. Fergusson, J. R., K. E. Smith, V. M. Fleming, N. Rajoriya, E. W. Newell, R. Simmons, E. Marchi, S. Björkander, Y.-H. Kang, L. Swadling, et al. 2014. CD161 defines a transcriptional and functional phenotype across distinct human T cell lineages. *Cell Rep.* 9: 1075–1088.
41. Kurioka, A., L. J. Walker, P. Klenerman, and C. B. Willberg. 2016. MAIT cells: new guardians of the liver. *Clin. Transl. Immunology* 5: e98.
42. Fergusson, J. R., V. M. Fleming, and P. Klenerman. 2011. CD161-expressing human T cells. *Front. Immunol.* 2: 36.
43. Beucke, N., D. Wesch, H. H. Oberg, C. Peters, J. Bochem, B. Weide, C. Garbe, G. Pawelec, S. Sebens, C. Röcken, et al. 2020. Pitfalls in the characterization of circulating and tissue-resident human γδ T cells. *J. Leukoc. Biol.* 107: 1097–1105.
44. Abaskharon, R. M., and F. Gai. 2016. Direct measurement of the tryptophan-mediated photocleavage kinetics of a protein disulfide bond. *Phys. Chem. Chem. Phys.* 18: 9602–9607.

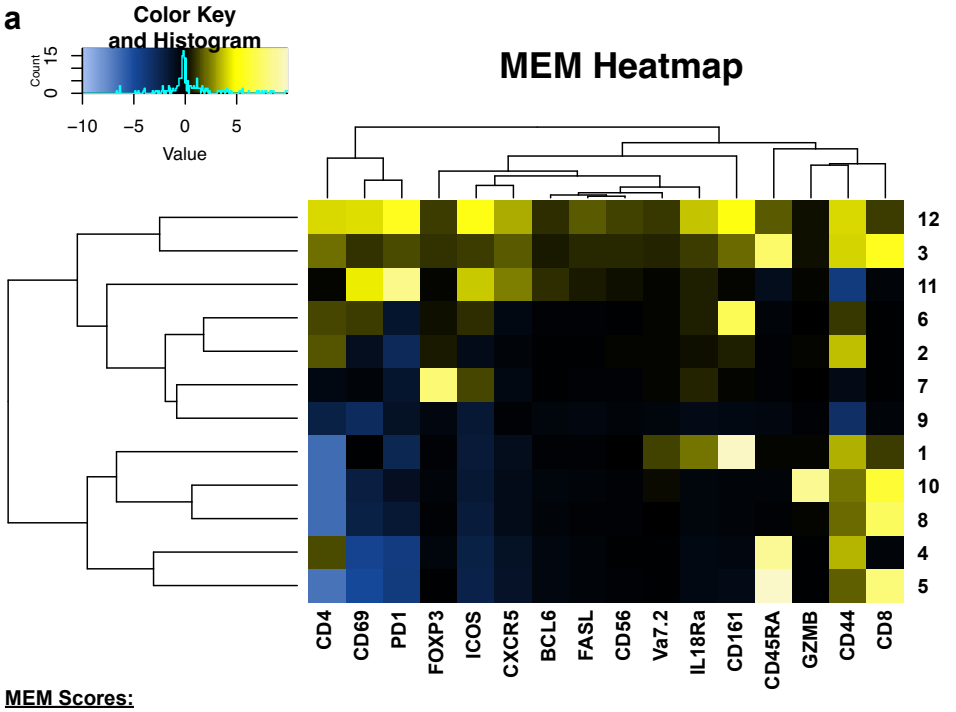
Downloaded from http://www.jimmunol.org/ by guest on January 8, 2022

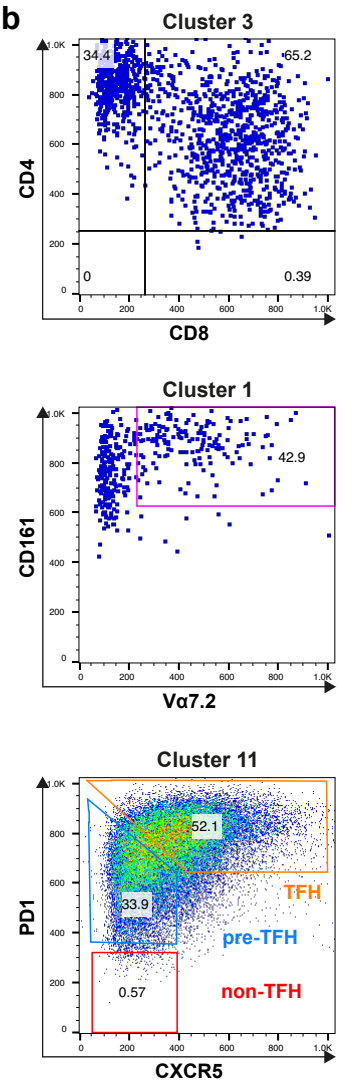


Suppl. Figure 1: Identification of the general human tonsil architecture and tonsillar CD4+ T-cell subsets using Chipcytometry (second example). Sections of paraformaldehyde-fixed human tonsil tissue mounted in microfluidic chips were immunostained in consecutive runs using a panel of 12 fluorochrome-labelled antibodies. (**a**) Six markers were selected to depict the general human tonsil architecture: CD19 (blue), CD8 (white), CD10 (orange), CD4 (red), IgD (magenta) and CD3 (green). The large multicolour image shows a composite image of all the 6 markers, whereas the expression of individual markers is shown in the small panels. The B-cell zone (B-cell follicle) is characterised by CD19 expression, in which IgD outlines the mantle zone containing IgD-expressing naive B cells, and CD10 outlines the germinal centre containing CD10+ germinal centre B cells. Adjacent to the B-cell zone, CD3 expression outlines the T-cell zone (extrafollicular zone), including CD4+ and CD8+ T cells. Scale bars represent 50 µm. (**b**) A combination of CD4, CD19, CD3 and PD1 was chosen from the full marker panel to identify tonsillar CD4+ T cells and their subsets according to PD1-expression. The large multicolour composite image shows a merged image of CD19 (blue), CD3 (green), PD1 (white) and CD4 (red), while the smaller images demonstrate the expression of each marker individually. The T-cell zone is characterised by CD3 expression and includes CD4+ T cells; CD3+CD4+ cells appear yellow / orange in combination. PD1-expressing CD3+CD4+ are predominantly located in the B-cell zone, but a few are also located in the T-cell zone. This subset most likely includes pre-follicular (pre-TFH) and follicular T-helper cells (TFH). CD3+CD4+PD1- cells are predominantly located in the extrafollicular region and include non-follicular T helper cells (non-TFH). White arrowheads indicate examples of CD3+CD4+PD1+ cells. Scale bars represent 50 µm.



Suppl. Figure 2: Chipcytometry allows the acquisition of multiple adjacent positions of a tissue section that can be tiled to obtain a larger field of view. Human tonsil tissue was fixed, mounted on microfluidic chips and analysed by chip cytometry with panel of 12 fluorochrome-labelled antibodies. Multiple adjacent positions were recorded and stitched together to obtain an overview over a larger tissue area. Different combinations of markers were chosen to illustrate different immune compartments in the tissue. (**a**) CD19 (blue), CD10 (green), IgD (purple) and CD3 (white) were chosen to illustrate different tonsil regions including extrafollicular T-cell zone (CD3+), B cell follicle (CD19+) and B cell sub-compartments including mantle zone (IgD+CD10-) and germinal centre zone (IgD-CD10+). For further information please refer to **Figure 1** and **Suppl. Figure 1a**. (**b**) CD3 (green), CD4 (red), CD19 (blue) and PD1 (white) was chosen to depict PD1 expressing CD4 T cells and their location relative to B cell and T-cell zones. For further information refer to **Figure 2** and **Suppl. Figure 1b**. Scale bars represent 100 µm.





MEM Scores:

Cluster 1: ▲ CD161+10 CD44+3 IL18Ra+2 CD8+1 Va7.2+1 ▼ CD4-6 PD1-3 ICOS-2 CXCR5-1

Cluster 2: ▲ CD44+4 CD4+2 CD161+1 ▼ PD1-3 CD69-1 ICOS-1

Cluster 3: ▲ CD45RA+7 CD8+6 CD44+4 CXCR5+2 CD161+2 CD4+2 CD56+1 CD69+1 FASL+1 FOXP3+1 ICOS+1 IL18Ra+1 Va7.2+1 PD1+1 ▼ None

Cluster 4: ▲ CD45RA+9 CD44+3 CD4+1 ▼ CD69-5 PD1-4 ICOS-2 CXCR5-1 IL18Ra-1

Cluster 5: ▲ CD45RA+10 CD8+8 CD44+2 ▼ CD4-7 CD69-5 PD1-4 ICOS-2 CXCR5-1 IL18Ra-1 CD161-1

Cluster 6: ▲ CD161+7 CD69+1 ICOS+1 IL18Ra+1 CD4+1 CD44+1 ▼ PD1-2 CXCR5-1

Cluster 7: ▲ FOXP3+8 ICOS+1 IL18Ra+1 ▼ CXCR5-1 PD1-1 CD4-1 CD44-1

Cluster 8: ▲ CD8+7 CD44+2 ▼ CD4-6 CD69-2 ICOS-2 PD1-2 CXCR5-1

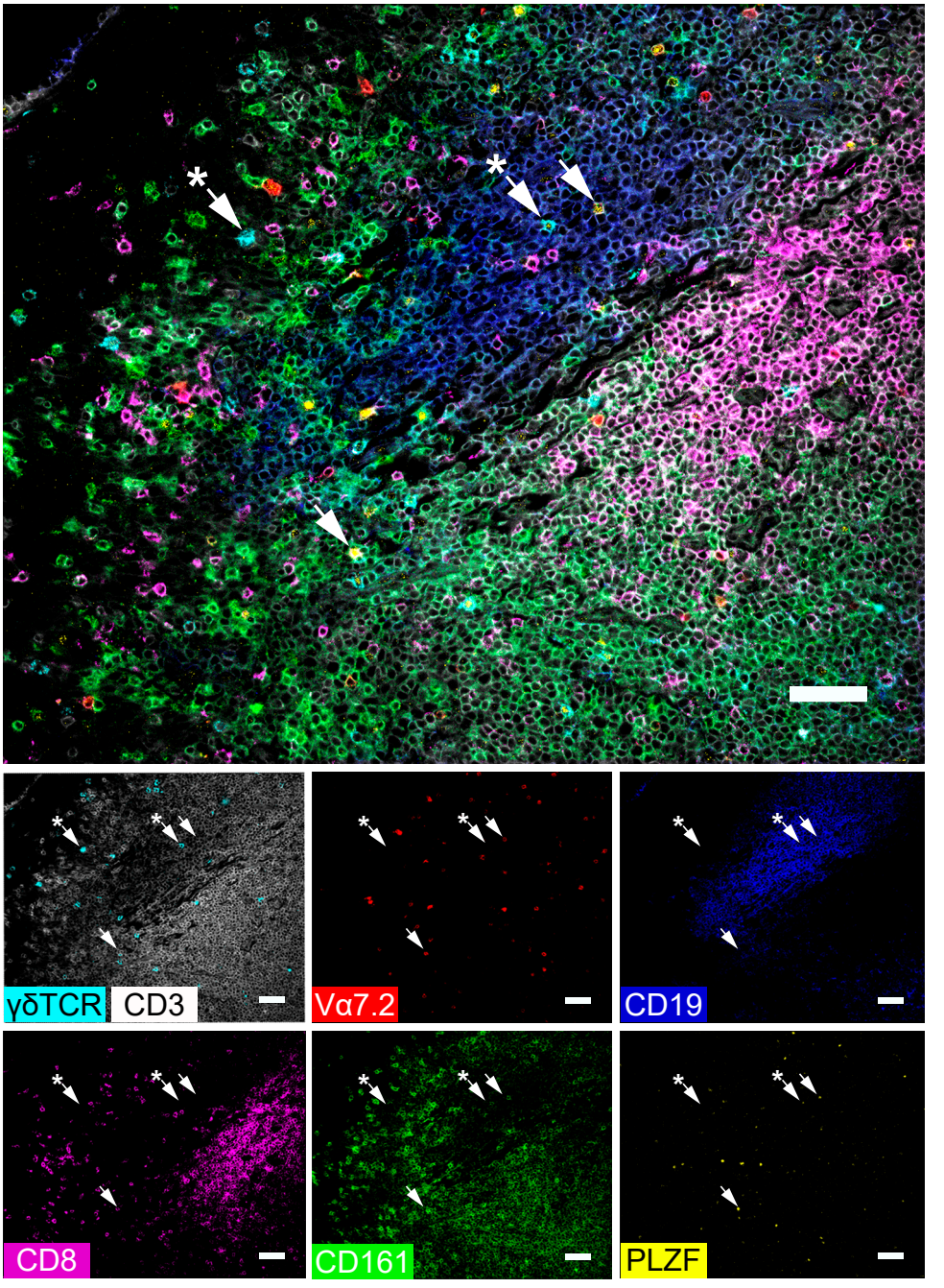
Cluster 9: ▲ None ▼ CD69-3 CD44-3 ICOS-2 CD4-2 IL18Ra-1 CD161-1 PD1-1

Cluster 10: ▲ GZMB+9 CD8+6 CD44+2 ▼ CD4-6 CD69-2 ICOS-2 CXCR5-1 PD1-1

Cluster 11: ▲ PD1+8 CD69+4 ICOS+4 CXCR5+2 BCL6+1 IL18Ra+1 ▼ CD44-4 CD45RA-1

Cluster 12: ▲ PD1+6 ICOS+5 CD161+5 CD69+4 IL18Ra+4 CD4+4 CD44+4 CXCR5+3 CD45RA+2 FASL+2 CD56+1 CD8+1 FOXP3+1 BCL6+1 Va7.2+1 ▼ None

Suppl. Figure 3: Cluster characterisation using Marker Enrichment Modeling (MEM) and FlowJo gating. (**a**) Cell clusters that were identified using FlowSOM as shown in **Figure 3b** were characterised with the help of Marker Enrichment Modeling in R as described by Diggins et al. (37, 38). MEM scores ranging from -10 to +10 indicate positive or negative enrichment of each marker within a population compared to the average of all other populations. (**b**) Examples of using FlowJo gating for cluster characterisation. Median marker expression (**Figure 3c**) and MEM scores (**Suppl. Figure 3a**) provided in certain cases ambiguous information for cell cluster labelling. An example is cluster 3, which showed increased median marker expression values and positive MEM scores for both CD8 and CD4 compared to the other clusters. To determine whether the cluster contained single positive CD4 and CD8 T cells or DP (double-positive) T cells, we inspected CD4 and CD8 expression in FlowJo within cluster 3 as shown in the top panel. This revealed that cluster 3 contained both single positive CD4 T cells and DP T cells, but no single positive CD8 T cells. Another example is cluster 1, for which FlowJo inspection (middle panel) revealed that it contained CD161++ T cells including both Vα7.2+ MAIT cells (pink gate) and V α7.2- non-MAIT cells. The dichotomy of Vα7.2 expression in this cluster was not obvious from evaluating Vα7.2 median marker expression or MEM score. The last example of FlowJo cluster inspection (bottom panel) showed that cluster 11 contained both pre-TFH (CXCR5-PD1+) as well as TFH (CXCR5+PD1+) cells. Final labels for all cell clusters were determined in a multi-pronged approach considering median marker expression of each marker, MEM Scores and manual inspection of clusters in FlowJo.



Suppl. Figure 4: Identification of rare immune subsets in human tonsils including MAIT and γδ-T cells. A combination of the markers γδ-TCR (cyan), CD3 (white), Vα7.2 (red), CD19 (blue), CD8 (magenta), CD161 (green) and PLZF (yellow) were selected from the available panel to illustrate the presence of MAIT cells and γδ-T cells within the tonsil. The large panel shows a merged multicolour composite image with all seven markers and the smaller panels show single- and dual-colour images as indicated. A few examples of MAIT cells (CD3+Vα7.2+CD161+PLZF+) are indicated by white arrowheads without an asterisk. CD8 was co-expressed in some of the MAIT cells, but there were also CD8- MAIT cells. γδ-T cells can be recognised side by side with MAIT cells in the T-cell zone (CD3+, white) but also adjacent and within the B cell zone (CD19+, blue). A few examples of many γδ-T cells are indicated by white arrows with an asterisk. Scale bars represent 50 µm.